DEVELOPMENTS OF ADVANCED SOLUTIONS FOR SEISMIC RESISTING PRECAST CONCRETE FRAMES

Alejandro Dario Amaris Mesa

A thesis presented for the degree of

Doctor of Philosophy

in

Civil Engineering

at the University of Canterbury

Christchurch, New Zealand

March, 2010

ABSTRACT

Major advances have been observed during the last two decades in the field of seismic engineering with further refinements of performance-based seismic design philosophies and the subsequent definition of corresponding compliance criteria. Following the globally recognized expectation and ideal aim to provide a modern society with high (seismic) performance structures able to sustain a design level earthquake with limited or negligible damage, alternative solutions have been developed for high-performance, seismic resisting systems.

In the last two decades, an alternative approach in seismic design has been introduced for precast concrete buildings in seismic regions with the introduction of “dry” jointed ductile systems also called “hybrid” systems based on unbonded post-tensioned rocking connections. As a result structural systems with high seismic performance capabilities can be implemented, with the unique capability to undergo inelastic displacement similar to their traditional monolithic counterparts, while limiting the damage to the structural system and assuring full re-centring capabilities (negligible residual or permanent deformations).

The continuous and rapid development of jointed ductile connections for seismic resisting systems has resulted in the validation of a wide range of alternative arrangements, encompassed under the general umbrella of “hybrid” systems.

This research provides a comprehensive experimental and analytical investigations of 2- and 3-Dimensional, 2/3 scaled, exterior beam-column joints subjected both uni and bi-directional (four clove) quasic-static loading protocols into the behaviour, modelling, design and feasibility of new arrangements for “dry” jointed ductile systems for use in regions of high seismicity. In order to further emphasize the enhanced performance of these systems, a comparison with the experimental response and observed damage of 2-D and 3-D monolithic beam-column benchmark specimens is presented.

However, after a lot of attention given to the behaviour of the skeleton structure, more recently the focus of research in Earthquake Engineering has concentrated on the behaviour of the floor system within the overall 3D behaviour of the building and the effects of beam elongation. The effects of beam elongation in precast frame systems have been demonstrated to be a potential source of un-expected damage, unless adequate detailing is provided in order to account for displacement incompatibilities between the lateral resisting systems and the floor. Two contributions to beam elongation are typically recognized: a) the material contribution due to

the cumulative residual strain within the steel, and b) the geometrical contribution due to the presence of a neutral axis and actual depth of the beam.

Regarding jointed ductile connections with re-centering characteristics, the extent of beam elongation is significantly reduced, being limited to solely the geometrical contribution. Furthermore, such effects could be minimized when a reduced depth of the beam is adopted due to the use of internal prestressing or external post-tensioning. However, damage to precast floor systems, resulting from a geometric elongation of the beam, has yet to be addressed in detail.

In order to emphasize the enhanced performance in controlling and minimizing the damage of the structural elements via the use of the proposed advanced hybrid solutions, this research presents via experimental and analytical validation of two alternative and innovative solutions to reduce the damage to the floor using 2 and 3-Dimensional, 2/3 scaled, exterior beam-column joints.

The first approach consists of using standard precast rocking/dissipative frame connections (herein referred to as “gapping”) in combination with an articulated or “jointed” floor. This system uses mechanical devices to connect the floor and the lateral beams which can accommodate the displacement incompatibilities in the connection. The second approach to reduce the floor damage investigates the implementation of a “non-gapping” connection, also called non-tearing-floor connection, using a top hinge at the beam-column interface, while still relying on more traditional floor-to-frame connections (i.e. topping and continuous starter bars). Additionally, further refinements and constructability issues for the non gapping connection are investigated under the experimental and analytical validation of a major 2-Dimensional, 2/3 scaled, two-story one-bay frame using non-tearing floor connections.

Based on the non-tearing floor connections, a series of parametric analysis for beam-column joints and frames are carried out. Furthermore, the analysis and design of two prototype frames using different solutions is presented. The frames are subjected to cyclic adaptive pushover and inelastic time history analysis in order to investigate analytically the response characteristics of hybrid frames using non-tearing connections, as well as how the beam growth affects the frame response under earthquake loading. Computational models for hybrid PRESSS frames and a conventional reinforced concrete frames are developed and compared with the ones using non-tearing connections.

ACKNOWLEDGEMENTS

This research investigation presented in this thesis was carried out at the Department of Civil Engineering, University of Canterbury, New Zealand, made possible by the financial support provided by the New Zealand Foundation of Research, Science and Technology under Grant P2075 as part of the "Future Building System" research project. I highly appreciate the research scholarship provided to me during my candidature in this PhD programme.

My most sincere gratitude must go to Associate Professor Stefano Pampanin, Prof. Des Bull and Prof. Athol Carr for their guidance, invaluable advice, patience and continuous encouragement, without which the research would not have been successful. Special thanks to Senior Lecturer Alessandro Palermo for his contribution on the experimental response on the advanced solutions for Hybrid beam-column joints.

I want to extend my gratitude to the technical staff of the Department of Civil Engineering for their assistance in the construction and testing of the different test specimens, in particular to Mr. Gary Harvey for the construction of the beam-column joints specimens, Mr. Gavin Keats, Mr. Russell McConchie and Mr. Nigel Dixon for the construction for the two stories frame subassembly.

This acknowledgment would not suffice without mentioning the contributions and special gratitude to my fellow postgraduate students, Dion Marriott, Umut Akguzel, Kam Weng, Masoud Moghaddasi, Michael Newcombe, Tobias Smith and many others for their enthusiasm and friendship.

Special thanks to my wife Luisa and little son Samuel and my parents Roberto and Ines for their encouragement love and support.

TABLE OF CONTENT

LIST OF FIGURES

LIST OF TABLES

CHAPTER 1
INTRODUCTION

1.1 DAMAGE IN THE BEAM SIDES-SWAY SEISMIC DESIGN APPROACH

Most of the standards and codes around the world allow the use of design forces that are generally smaller than those required for elastic response, providing that the critical regions of the structure have adequate ductility and energy dissipation capacity. Such approaches are fundamentally based on a casualty-prevention principle, where structural damage is accepted providing that collapse is avoided.

Designers must select a proper mechanism of plastic deformation and using capacity design principles they have to ensure that the chosen mechanism can be developed. Normally, the use of beam sidesway mechanism of plastic deformation is a common design practice for multi-storey buildings. This mechanism distributes the plasticity throughout the height of the building by ensuring the formation of plastic hinges in most beams.

When the plastic hinge forms in the beam elements of a reinforced concrete frame, the distance between the beam ends increases (beam growth) because the neutral axis at the beam ends is on compression and on the tensile strain at mid-depth of the member [1.1, 1.2, 1.3].

This beam growth has an enormous impact on frames behaviour because frames elongate horizontally at the floor where beam yields significantly which normally occurs at the lower stories because columns are fixed against translation at their bases and frames will primarily deform in a shear mode when subjected to lateral forces. This beam growth then causes curvature in the columns that is not considered in conventional analysis of sway mechanism behaviour.

When the frames are subjected to lateral forces, column moments tend to increase at one end of the building and diminish at the other end. The differences between the individual column shears cause axial forces in the beams, which reduce the magnitude of the beam growth. However, these additional axial forces may change the hierarchy of strength capacity of the structural elements making the beams stronger and also increasing the joint shear demands above the values computed by conventional analysis. The forces also cause larger moments in the columns, and increase the possibility of hinges forming in the column.

Beam elongation effects not only change the strength of the structural elements but also affect the floor system, which in most cases will be forced to elongate, and therefore to crack, with the beams but in some cases result in the loss of support for precast floor systems and possible collapse [1.4].

1.2 EMERGING TECHNOLOGIES IN PERFORMACE-BASED SEISMIC DESIGN

Recent advances in Performance-Based Seismic Design have focused on controlling the damage after an earthquake within repairable limits, in order to reduce post event costs as well as business interruption. However, due to this traditionally accepted seismic design approach, based on the development of a desired inelastic mechanism through the formation of plastic hinge regions in the discrete and controlled locations within the structure (i.e. weak beam, strong column mechanism), different levels of structural damage and, consequently, repair cost, will be expected and, depending on the seismic intensity, typically accepted as unavoidable results of the inelastic behaviour itself.

The construction of seismic moment resisting frames with precast concrete elements generally fall into two broad categories based on the design of the connection between the precast concrete elements: the first type are called wet connections relying on cast-in-place techniques to provide equivalent “monolithic” connections (i.e. equivalent strength and toughness to their cast-in-place counterparts).

The second alternative to the traditional emulation of cast-in-place solutions had been developed in the last two decades as a revolutionary alternative approach to seismic design, under the U.S. PRESSS program coordinated by the University of California, San Diego [1.5, 1.6, 1.7] for precast concrete buildings in seismic regions with the introduction of “dry” jointed ductile systems also called “hybrid systems” and based on the use of unbonded post-tensioning techniques. As a result, high seismic performance structural systems can be obtained, with the unique potentiality to undergo inelastic displacement similar to their traditional monolithic counterparts, while limiting the damage to the structural system and assuring full re-centring (negligible residual or permanent deformations).

After a lot of attention given to the behaviour of the skeleton structure, more recently the focus of research in Earthquake Engineering has concentrated on the behaviour of the floor system within the overall 3D behaviour of the building and the effects of beam elongation. These effects could be relevant in the response of the first-story columns since the building foundation

at this level may try to restrain elongation of the beams of the first story at the formation of their plastic hinges. This restriction may cause shear force in the columns not considered in conventional analysis, with the possibility of also creating additional plastic hinges in the columns (weak-column, strong-beam mechanism) and possible collapse of the structure or in loss of support for precast floor systems due to an elongation of the beam elements.

It is worth emphasising that beam elongation effects are typical of both cast-in-situ concrete and precast concrete frames. Two contributions to beam elongation are typically recognized: a) the material contribution due to the cumulative residual strain within the steel, and b) the geometrical contribution due to the presence of a neutral axis and actual depth of the beam.

In the wet connections or "equivalent monolithic", the beam growth is the sum of the widths of the beam-column interface cracks at the beam centreline and is often neglected in design practice; meanwhile for the dry connections or "jointed" systems the rotations are deliberately concentrated at the connections with a single joint opening and the center-to-center distance between two adjacent columns increases as the gap opens at the beam-column interface.

With regards to jointed ductile connections with re-centering characteristics, the extent of beam elongation is significantly reduced, being limited to the geometrical contribution alone. Furthermore, such effects could be minimized when a reduced depth of the beam is adopted due to the use of internal prestressing or external post-tensioning. However, damage to precast floor systems, resulting from a geometric elongation of the beam, has yet to be addressed in detail.

1.3 OBJECTIVES AND SCOPE OF RESEARCH

One of the major problems in the use of hybrid systems had been the limitations placed by code provisions for practical implementation based on experimental-analytical case-by-case application [1.8, 1.9]. This research investigates alternative and innovative connections that have resulted through the validation of a wide range of alternative arrangements, under the general umbrella of "hybrid" systems, currently available to designers and contractors. Additionally, analytical-experimental validation is implemented using simple analytical models already presented in the literature, providing a reliable control over the expected hysteresis and dynamic behaviour.

It is clear from the introduction that effects of beam elongation in precast frame systems have been demonstrated to be a potential source of un-expected damage to precast floor systems, unless adequate detailing is provided to account for displacement incompatibilities between the

lateral resisting systems and the floor. Therefore, the research presented herein seeks also to explore innovative developments on new seismic resistant structural connection and devices in precast systems based on jointed ductile connections to reduce the damage in the floor systems in order to maintain the interaction between diaphragm and lateral load resisting systems at their connections functionally after a major earthquake event.

This study focuses on the investigation into the practical feasibility and efficiency of simple technical solutions to connect precast floor systems and lateral resisting frame systems using these alternative "hybrid" connections, without incurring damage due to displacement incompatibilities. Additionally, the evolutions on hybrid connections, lead to an innovative floor-to-lateral-load-resisting, "non-tearing floor" connection, designed to minimize the problems associated with beam elongation effects. The main key features investigated are:

- the shear transfer mechanism: friction due to the post-tensioned tendons contribution, single or double shear keys or metallic slotted or cables stayed corbel;
- the sources and location of energy dissipation: internal or external supplemental damping devices; and
- the longitudinal profile of post-tensioned tendons: straight, draped tendons/cable solutions or combination of profiles depending on the ratio between gravity and lateral loads effects, as a consequence of different level of seismicity (target design earthquake) as well as of the assigned role of the system during the seismic response (i.e. pure gravity-load carrying system, pure seismic resisting system or intermediate solutions).

This research also investigates the efficiency of analytical methods to properly represent the behaviour of the proposed connections through analytical-experimental validation of the experimental results.

Finally, this research will investigate the numerical studies on multi-storey frames using the innovative "non-tearing floor" connections under cyclic adaptive push over analysis and a series of time history analyses changing the earthquake intensities as well as the energy content characteristics for far and near field earthquake records.

Special attention will be given to compare the multi-storey frames which will be designed considering three different systems: traditional hybrid PRESSS, Hybrid using non-tearing connection and a monolithic (cast-in-situ or emulation of cast-in-situ concrete) solution.

1.4 ORGANIZATION OF THIS THESIS

In order to achieve the above mentioned objectives, the thesis consists of eight chapters as outlined in this section. Chapter 1 describes the problems associated with the traditional capacity design approach where structural damage is accepted providing that collapse is avoided by assuming the formation of plastic deformation in most of the beams and the effects of beam elongation which has an impact on the frame behaviour. However, new technologies in emulation of cast-in-place and the introduction of "dry" jointed ductile "hybrid systems" are available to undergo inelastic displacement similar to their traditional monolithic counterparts, while limiting the damage to the structural system and assuring full re-centring capabilities (negligible residual or permanent deformations). However the effects of geometric beam elongation have not yet been addressed in detail.

Chapter 2 provides a comprehensive review survey of relevant research of various connection details in precast concrete moment-resisting frames for high seismic zones initiated at the National Institute of Standards and Technology (NIST) in 1987 and followed by the Precast Seismic Structural Systems (PRESSS) research program in 1990 which also investigated the behaviour of the precast floor systems within the overall 3D behaviour of the building through the implementation of a floor-frame connections available to accommodate the effects of beam elongation by the testing of a 60% scale five-storey two-bay by two bay frame. The Chapter ends with recent developments on new alternative on dry "jointed" ductile connections around the world specially in New Zealand, Italy, Turkey and Japan.

Chapter 3 investigates alternative and innovative connections that have resulted from the validation of a wide range of alternative arrangements, under the general umbrella of dry jointed ductile "hybrid" systems. Three main parameters are experimentally investigated: shear transfer mechanism, the sources and location of energy dissipation and the longitudinal profile of post-tensioned tendons.

Several hybrid beam-column connections with different configurations and arrangements are shown. Evaluation and comparisons with the experimental response and observed damage of 2-D and 3-D monolithic and traditional Hybrid PRESSS beam-column specimens designed according to the NZ3101:2006 code provision are presented. Additionally, analytical-experimental validation is being implemented using simple analytical models already presented in the literature, providing a reliable control over the expected hysteresis and dynamic behaviour.

As described in the introduction and literature survey (Chapter 2), it is clear that effects of beam elongation in precast frame systems have been demonstrated to be a potential source of un-expected damage to precast floor systems, unless adequate detailing is provided to account for displacement incompatibilities between the lateral resisting systems and the floor. Chapter 4 introduces two types of floor-frame connections available to accommodate or reduce the effects of beam elongation and reduce the floor damage via experimental results on 2-D and 3-D beam column joint subassemblies.

The first approach consists of using standard precast rocking/dissipative frame connections (herein referred to as "gapping") in combination with an articulated or "jointed" floor by using mechanical devices (presented and implemented in Chapter 3) connecting the floor and the lateral beams accommodating the displacement incompatibilities in the connection. The second approach would rely upon a top hinge "non-gapping" system also called "non-tearing floor" connection designed to minimize the problems associated with beam elongation effects that could be use in combination with a standard floor solution (i.e. topping and continuous starter bars).

Additionally, analytical-experimental validation is being implemented using simple analytical models already presented in the literature, providing a reliable control over the expected hysteresis and dynamic behaviour.

Chapter 5 further investigates the concept evolution of the "non-gapping" systems by the construction details and experimental results of a major 2-D, 2/3 scaled, two stories, single bay, hybrid precast concrete frame system with the innovative "non-tearing floor" connection which consist of a single top-hinge connection in combination with anti-symmetric profile of unbonded post-tensioned tendons and external and replaceable mild-steel dissipater devices which provide additional supplemental damping and connection strength while the re-centering is provided mainly by the column base moments.

The results of the quasi-static cyclic tests of the 2-D precast concrete frame system able to obtain an efficient floor to lateral load resisting system connection are presented. Additionally, analytical-experimental validation is implemented using simple analytical models already presented in the literature, providing a reliable control over the expected hysteresis and dynamic behaviour.

Chapter 6 is a parametric analysis for a series of beam-column joints using non-tearing connection to determine the local characteristics of the connections. Additionally, the structural

behaviour of hybrid H-frames with multiple spans using non-tearing connections is presented and parametric analysis is carried out to evaluate the overall response of the H-frames in terms of stiffness and strength. The analysis consists of three beam sections with different bay lengths, changing the location of the tendons along the beam section, the unbonded length and initial post-tensioned force and the steel area content to determine the characteristics of the top hinge connections.

Chapter 7 presents the design, modeling and push over analysis of 5 and 10 multi-storey building prototypes with different solutions. The buildings were designed using direct displacement based design principles for a traditional hybrid PRESSS type and base shear was calculated and distributed throughout the structures.

The design of the beam members and their connections were considered for three different systems for comparison purposes: traditional hybrid PRESSS, Hybrid using non-tearing connection and a monolithic (cast-in-situ or emulation of cast-in-situ concrete) solution. Additionally, the effects of beam elongation were modelled. Therefore, for comparison purposes five different models have been implemented to compare the behaviour of the systems: Hybrid PRESSS without beam elongation (Hy), Hybrid PRESSS including beam elongation (Hy_beam-elong), Hybrid non tearing connection (Hy_non-tear), monolithic without beam elongation (Mon) and monolithic including beam elongation (Mon_beam-elong).

Chapter 8 presents the engineering design parameters based on a series of time history analysis carried out on the models designed in Chapter 7 and special attention is given to the Hybrid frames using non-tearing floor connections to investigate and evaluate the performance of this type of system to earthquake loading.

An initial set of five earthquake motions were selected and scaled to represent the likely ground motion for the 500-year return period. This chapter also assesses each 5 and 10-storey frame model by a sensitivity analysis by changing intensities from 0.5x to 2.0x the earthquake intensity. Therefore, a design earthquake (DEQ) and maximum credible earthquake (MCE) proposed by the NZ 1170:5 with a probability of exceedence of 10% and 2% in 50 years corresponding to an average return period of 500 years and 2500 years respectively is evaluated.

A second set of 30 earthquake motions were selected and scaled to represent the likely ground motion for the 500-year return period. 20 records were considered for far field and 10 for near field faults events. The records are included in order to investigate the behaviour of the hybrid systems with non-tearing connections in these types of events.

1.5 REFERENCES

1.1 Fenwick, R.C. and Fong, A., "The Behaviour of Reinforced Concrete beams Under Cyclic Loading," Research Report, Department of Civil Engineering, University of Auckland. 1979

1.2 Douglas, K.T., "Elongation in Reinforced Concrete Frames," PhD Thesis, Department of Civil Engineering, University of Auckland. 1992.

1.3 Fenwick, R. C. and Megget, L. M., "Elongation and Load Deflection Characteristics of Reinforced Concrete Members containing Plastic Hinges," Bulletin of the New Zealand National Society for Earthquake Engineering, 26, 1, pp. 28-41, 1993

1.4 Matthews, J., D. Bull, Mander J., "Hollowcore floor slab performance following a severe earthquake. Concrete Structures in Seismic Regions," Proceeding of the First fib Symposium. Athens, Greece. 2003.

1.5 Priestley, M. J. N., "Overview of PRESSS Research Program," PCI Journal, V. 36, No. 4, Jul.-Aug. 1991, pp. 50-57.

1.6 Priestley, M. J. N., "The PRESSS program – Current Status and Proposed Plans for Phase III," PCI Journal, V. 41, No. 2, Mar.-Apr. 1996, pp. 22-40.

1.7 Priestley, M. J. N., Sritharan, S., Conley, J., and Pampanin, S., "Preliminary Results and Conclusion from the PRESSS Five-Story Precast Concrete Test Building," PCI Journal, V.44, No. 6, Nov.-Dec. 1999, pp. 44-67.

1.8 ACI Committee 374.1-05 "Acceptance Criteria for Moment Frames Based on Structural Testing and Commentary", American Concrete Institute, Farmington Hill, Michigan. 2005

1.9 New Zealand Standards (NZS). "Appendix B: Special Provisions for the Seismic Design of Ductile Jointed Precast Concrete Structural Systems," NZS3101:2006, Concrete Standard, Wellington, New Zealand.

CHAPTER 2
LITERATURE REVIEW

2.1 INTRODUCTION

In 1986 a series of workshops took place in Los Angeles (U.S) to examine the problems and needs of the Precast Concrete Industry. Results from this workshop noticed the higher cost of precast concrete construction in comparison with more traditional systems followed by a lack of prescriptive design provisions of precast elements in seismic regions.

In response to these needs, a study of the behavior of precast beam-column connections subjected to cyclic inelastic loading with emphasis being placed on an economical and constructible connection was initiated at the National Institute of Standards and Technology (NIST) in 1987 and then followed by the Precast Seismic Structural Systems (PRESSS) research program in 1990. The goal of these test programs was to develop recommended guidelines for the design of beam-column connections in high seismic regions.

Emerging solutions developed from the PRESSS research program with the concept of a "dry-jointed" ductile hybrid connection achieving a high seismic performance, able to sustain a design level earthquake with limited or negligible damage based on a combination of traditional materials and available, cost-effective, technology.

After the NIST and the PRESSS research programs developed in the United States, extended research with additional implementation of alternative arrangements of hybrid dry–jointed ductile connections have been carried out through out the world especially in Italy, Turkey and Japan. Although a lot of attention was given to the behaviour of the skeleton structure, significant focus in Earthquake Engineering has been placed on the behaviour of the floor system, with the study of the overall 3D behaviour of the building and the effects of beam elongation. In addition to this, the damage to precast floor systems due to a geometric elongation of the beam has yet to be addressed in detail.

The following sections describe the NIST study as well as the PRESSS research program followed by extended research carried out around the world on innovative developments for high-performance seismic resisting precast systems based on jointed ductile connections and the interaction between diaphragm and lateral load resisting systems at their connections.

2.2 EXPERIMENTAL PROGRAM AT THE NATIONAL INSTITUTE OF STANDARDS AND TECHNOLOGY (NIST)

In 1986 a series of workshops under the control of the Precast/Prestressed Concrete Institute (PCI) with cooperation of the Precast Concrete Manufactures Association of California (PCMAC) took place in Los Angeles (U.S) to examine the problems and needs of the Precast Concrete Industry. Six main areas were examined: 1) Construction; 2) Systems Engineering; 3) Codification needs; 4) Research; 5) Overview/Rebuttal; and 6) Tackling seismic resistance by design innovations. Results from this workshop noticed the higher cost of precast concrete construction in comparison with more traditional systems followed by a lack of prescriptive design provision of precast elements in seismic regions [2.1].

In response to these needs, a study of the behaviour of precast beam-column connections subjected to cyclic inelastic loading was initiated at the National Institute of Standards and Technology (NIST) in 1987. The NIST research program was divided in four phases. The main objective of phase I was to determine the viability of post-tensioning for precast concrete elements as a connecting methodology. Experimental data showed a very satisfactory result for the bonded post-tensioned beam-column joints in terms of ductility, strength and initial stiffness. However, at a high level of drift significant stiffness degradation in the unloading phase was observed as well as limited energy dissipation capacity when compared to the monolithic solutions [2.2].

Phase II had the objective to improve the cyclic energy dissipation characteristics of the bonded post-tensioned precast elements. A possible method of improving the energy absorption characteristics of the precast concrete connection was to move the location of the post-tensioning steel closer to the centre of the beam in order to reduce the strain and retain their post-tensioning force for a longer period. Also, prestressing strands are used more commonly than post-tensioned bars in practice mainly due to the lengths required when post-tensioning several bays at a time. Results showed that locating the post tensioned steel from top or bottom to the centroid of the cross section can change the strain level in the post tensioned steel, maintaining the clamping force at higher drift levels. Failure of all precast concrete specimens in Phase II was similar and was a result of the inability of the connection to sustain additional load. Also, some pinching in the force-displacement hysteretic loops was observed, with an unloading branch with zero-slope stiffness at loads near zero due to debonding of the prestressing strands. Finally the use of prestressing strands as opposed to the use of post-

tensioning bars seemed to improve the energy absorption characteristics of the precast concrete connections [2.3].

Of particular importance was Phase III of the NIST program [2.4] where the concept of "partially bonded" or "fully unbonded" post-tensioned tendons in beam-column connections took place. This phase proposed to keep the presstressing strands in the elastic domain as suggested by the Precast Seismic Structural Systems (PRESSS) Research Program which was initiated as part of the United States-Japan protocol on large scale testing for seismic response of precast concrete buildings [2.5, 2.6].

It was believed that the observed zero-slope stiffness in the earlier precast specimens during the latter stages of the tests was caused by the inelastic response of the post-tensioned steel; it was proposed to keep the post-tensioned steel elastic with the use of partially bonded tendons. This was done by leaving the prestressing strands unbonded in the column region and for a short length in the beams at each side, with the remaining length of the post-tensioned steel was bonded with the surrounding ducts.

Results showed very similar performance in comparison with the tests reported for Phase II with near zero-slope stiffness observed for only the final hysteresis loops. Additionally, the hysteresis loops were slightly narrower than those obtained for the precast concrete connections in Phases I and II. Considering that failure for Phase II was characterized by yielding of the post-tensioning steel, beam crushing and opening at the junction between the beam and the column, specimens in Phase III were not tested to failure. At the final of this phase comparisons between the precast concrete connections and their monolithic counterparts indicated that the latter failed in shear in the joint region. The post-tensioned precast connections tested were able to resist the shear at the beam-column interface without corbels. Shear resistance was provided by the friction between the beam and the column as a result of the force in the Post-tensioned steel. However, it was noted that gravity forces were not included in the tests performed so far.

Phase IV examined the use of non-prestressed low strength (mild) steel used in conjunction with post-tensioned steel with the objective of improving the energy dissipation characteristics of the precast specimens. The specimens were termed "hybrid connections" because they combined the use of mild steel or low strength steel used as an energy dissipater while the friction forces developed between the beam and column by post-tensioning force will be used to provide the necessary shear resistance. Additional concern was established where the shear resistant connection would not be sufficient to resist the applied seismic shear loads in addition to gravity

loads, therefore the use of simulated gravity loads were applied to the beams for the Phase IV tests.

Phase IV was divided into two phases. Phase IV A involved four specimens of three different configurations with the objective of testing the concept of hybrid connections and to determine the optimum combination of mild and post-tensioned steel. The beams specimens had "dogbones"- over and under the expanded flange. Two specimens had fully bonded post-tensioned tendons in the middle of the beam while fully bonded mild steel was located at the top and bottom of the beam (Figure 2.1).

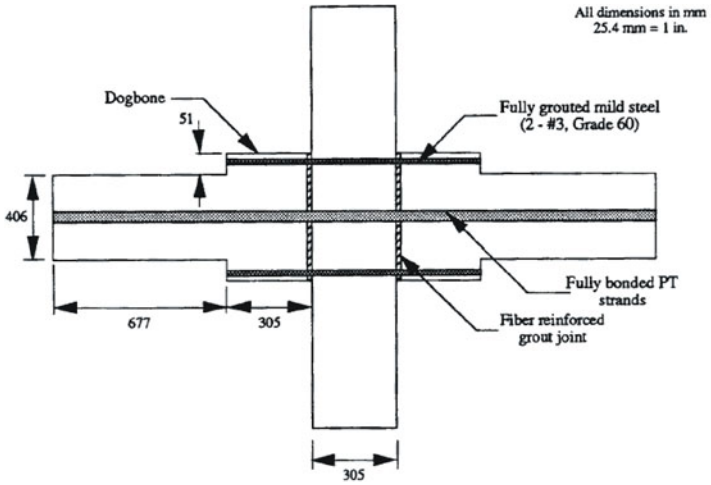

Figure 2.1.Basic detail for specimens I-P-Z4 and K-P-Z4 [2.7]

The second specimen (Figure 2.2) used fully bonded mild steel and unbonded post-tensioned bars all located at the top and bottom of the beam where highest flexural strain are reached but the delay in yielding of the post-tensioned steel was accomplished through the use of unbonded post-tensioned bars.

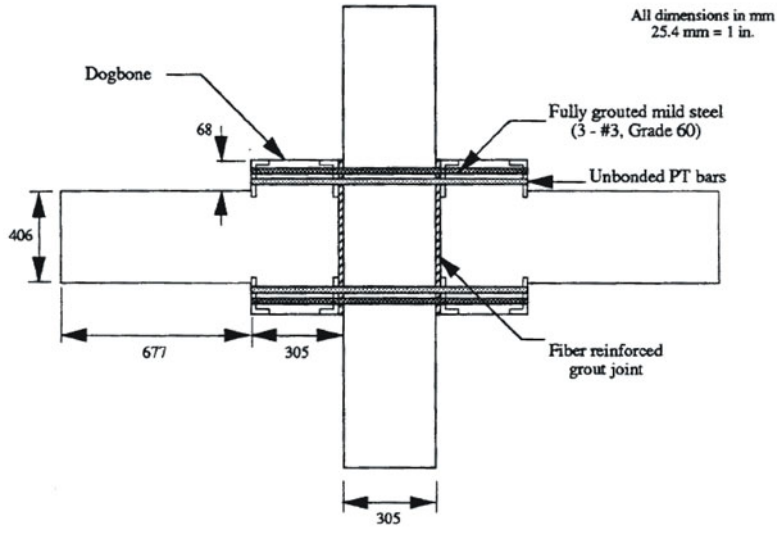

Figure 2.2.Basic detail for specimen J-P-Z4 [2.7]

The third specimen (Figure 2.3) in Phase IV A incorporated replaceable unbonded mild steel (also called the "replaceable system") and the use of unbonded post-tensioning bars [2.7]. The results of these tests were fracture of the mild steel causing failure of the specimens with the first two configurations and very good agreements in terms of strength and ductility in comparison with the monolithic benchmark. Finally the replaceable system failed prematurely at a story drift of 2.0% and it was concluded that the cost of such replaceable connection may prohibit its use in practice.

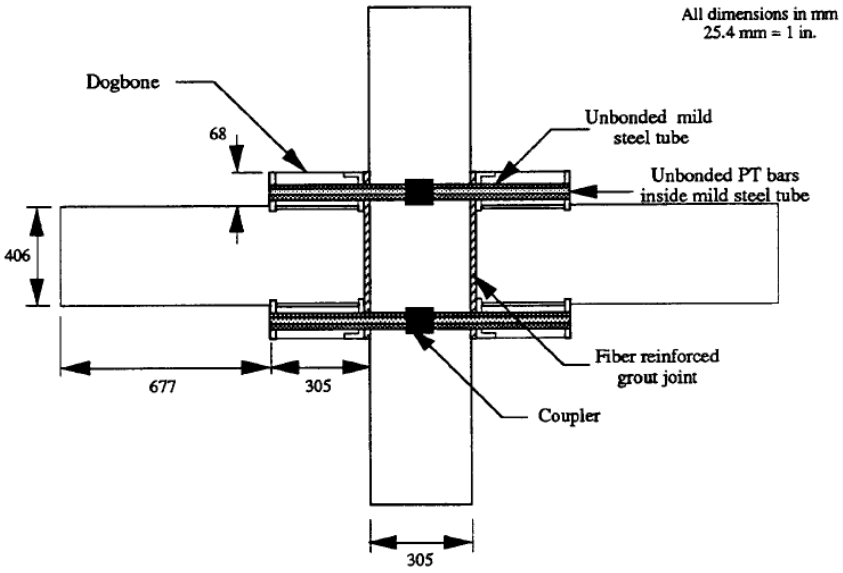

Figure 2.3.Basic detail for specimen L-P-Z4 [2.7]

Results obtained from Phase IV A were then used to determine the specimen details for Phase IV B which consisted of four specimens. The primary variables in this phase were the amount and the type of mild steel (unbonded over a certain length to delay fracture of the bars) and the use of partially bonded post-tensioned steel as a compromise between fully bonded and unbonded post-tensioned steel where in the first case the bonded portion provides corrosion protection and anchorage redundancy, while the unbonded portion delays inelastic strain in the post-tensioned steel. For the sake of brevity only one specimen is illustrated in Figure 2.4 while the others had the same design details but varied only the amount and type of mild steel. Details can be found in [2.8].

The post-tensioned steel was located at the centroid of the beam since this location produced the largest drift capacity prior to yield of the post-tensioned steel in the previous phase. Additionally, the presence of the "dog-bones" was eliminated due to mainly cost and excessive fabrication. Results showed that a hybrid connection can be designed to perform in a similar

manner as a monolithic connection in terms of connection strength, drift capacity, energy dissipation, residual drift, and damage to the concrete [2.8].

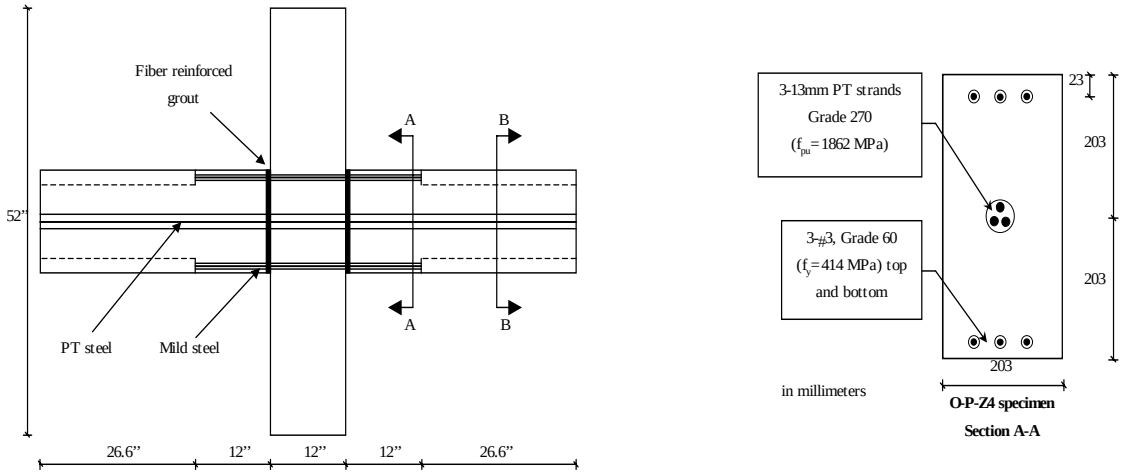

Figure 2.4.Specimen O-P-Z4 and beam section reinforcement details [2.8]

2.3 THE PRECAST SEISMIC STRUCTURAL SYSTEM (PRESSS) RESEARCH PROGRAM

The PREcast Seismic Structural System (PRESSS) Research Program was initiated as part of the United States-Japan protocol on large scale testing for seismic response of precast concrete buildings and it was conceived in three phases [2.5]. Phase I was focused on identifying and evaluating the most promising structural concepts for precast concrete building systems in seismically active regions while phases II and III were improvement of the concepts, definitions and a major test on a five-story precast building was implemented.

Phase I of the PRESSS program in collaboration with Phase III of the NIST research program, identified that the use of unbonded tendons partially debonded through the joint and for some distance on either side was a viable solution for precast concrete ductile connections [2.5].

An extensive dynamic inelastic analysis of single degree of freedom oscillators was carried out to investigate the theoretical seismic response of precast-prestressed concrete frames with partially unbonded tendons and the results were compared with fully bonded or monolithic solutions, with different initial periods and ideal hysteretic rules: Linear elastic, bilinear elastic (unbonded tendons), bilinear elastoplastic (monolithic), bilinear degrading (fully bonded). Analytical results indicated that force displacement response using bilinear elastic model would be less than 35% larger than elasto-plastic systems for displacement for medium to long period structures. Also, it was found that the stiffness degradation phenomenon, previously described,

is caused by a reduction of the effective prestressed clamping force through the column, resulting from the inelastic strain of the prestressing steel at the critical section.

Phase II provided rational design recommendations for seismic design of precast frame systems using ductile connections. Experimental studies were conducted at the University of California in San Diego on full scale exterior and interior unbonded post-tensioned precast beam-column subassemblies to investigate the seismic performance of these types of connection [2.9]. The results from this research proposed a more refined strut and tie mechanism for the shear joint transfer in an interior connection.

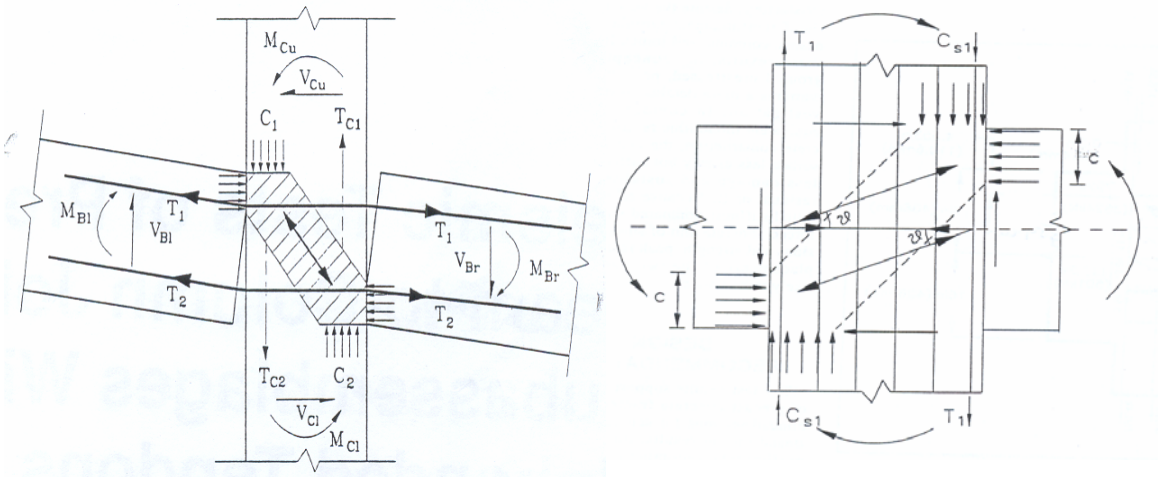

Figure 2.5. Forces contributing to joint shears (left) and Joint strut-and-tie model for the design of transverse reinforcing steel (right). [2.9].

Also, as part of the Phase II, innovative connections were developed at the University of Minnesota and University of Texas in Austin [2.10] based on a experimental campaign representing four types of categories of connections: 1) Non-linear Elastic (NLE) Connection 2) Tension-compression Yield (TCY) Connection Systems, 3) Energy Dissipating/coulomb Friction (CF) connection and 4) Shear Yield (SY) Connection system.

2.3.1 Non-linear Elastic connection

The first category consisted of precast elements jointed using some form of unbonded post-tensioning steel to form the connection. Three connections were investigated: two of the connections UMn-PTS (Figure 2.6-left) and UMn-PTB (Figure 2.6-right) used the concept of horizontal “dogbones” located at the beam ends to anchor the post-tensioning steel. The difference between the two specimens consisted in member sizes and post-tensioning type: one used prestressing strands (UMn-PTS) while the second connection (UMn-PTB) used high strength threaded bars.

Results obtained showed very stable hysteresis behaviour. The self-centring nature of the systems resulted in negligible residual deformations upon unloading with very little damage observed outside the connection region.

The third connection UT-PTS was designed with pre-tensioning instead of post-tensioning. It was reported that the prestressed concrete specimens exhibited the desired nonlinear elastic behaviour through the 3% drift level.

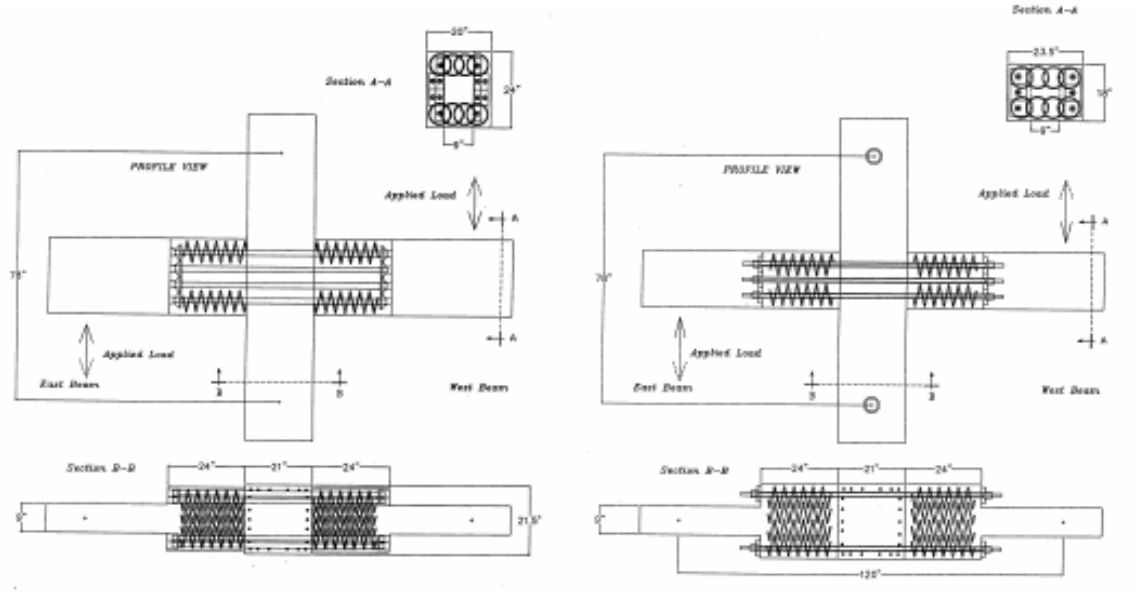

Figure 2.6.Specimen UMn-PTS (left) and UMn-PTB (right) [2.10]

2.3.2 Tension Compression Yield connection

The second category of connection is relying on axial tension and compression yield of the connection elements where mild strength steel, are designed to yield in tension and compression under opposing directions of seismic response. Behaviour is thus similar to monolithic reinforced concrete response and is characterized by reasonably high energy dissipation. Disadvantages of the tension-compression yield systems include high residual displacement and low residual stiffness after inelastic seismic response.

Four connections were tested using the TCY concept: UT specimens GAP and DB; and UMn specimens GAP and TCY. The GAP connections were intended to be restrained from translation at the bottom of the beam-column interface using the concept of “gap-joint system” where the lateral movement was accommodated by rotation about that point through opening and closing of a gap at the top of the interface.

The specimen UT-GAP incorporated tapered threaded couplers in the columns to mate with mild reinforcement in the cast-in place toping of the beam (Figure 2.7-left). The bottom horizontal connection and resistance to beam-end uplift was provided by four high-strength vertical rods anchored in the corbel while oversized holes in the beam provided sufficient construction tolerances to slip the beam ends over the rods. After the placement of the beams, nuts were fastened to the ends of the rods, then the voids around the rods were grouted. Each beam was seated on a neoprene pad to accommodate the rotation of the beam without causing damage to the corbel. Finally, fiber-reinforced grout was placed in the bottom of the gap between beams and columns to facilitate direct transfer of compression forces from the bottom of each beam to the column. The tops of the beams were cast after the beam top bars were screwed into the threaded couplers embedded in the columns.

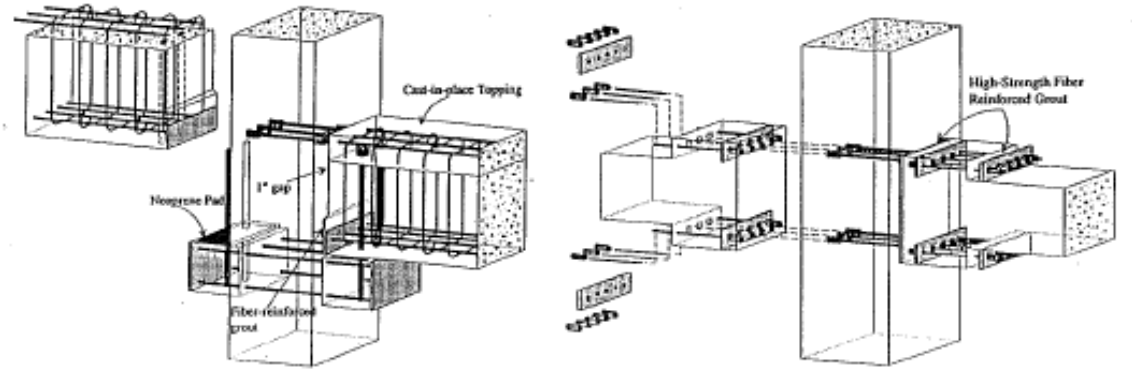

Figure 2.7. Specimen UT-GAP (left) and UT-DB (right) [2.10].

The specimen UT-DB (Figure 2.7-right) used vertical “dogbones” and high-strength threaded bars to connect precast beams and columns. High-strength fiber reinforced grout was placed between the beam ends and the column before the beams were connected to the column. Ducts that contained the threaded bars were grouted after the threaded bars were snug tightened.

The experimental results of the UT-GAP and UT-DB connections showed less energy dissipation as well as pinching behaviour due to shear and flexural deformations that occurred in the interface of the components connecting the elements. As a result of these tests and previous tests carried out in the NIST program Phase IV B [2.7], it was conclude that connections that provided an indirect path for force transfer between precast elements precipitated the premature failure of the specimens.

In order to eliminate this indirect path of force transfer, two connections were developed the UMn-TCY and UMn-GAP. The first type (UMn-TCY) used a simple “block-outs” system through the beam and embedded corrugated pipes in the column to accommodate placement of continuous reinforcement in the beam block-out that could be slid and tied in place through the

column during construction and subsequently grouted instead of using couplers that caused discontinuities in the load path (Figure 2.8-left). Experimental results showed very good performance for the design at high drift levels. Significant pinching behaviour was observed at high drift levels and was attributed to several factors: a) slip between the corrugated pipes (where the longitudinal beam bars are located) and the surrounding column concrete b) buckling of the longitudinal bars in the connection region close to the beam column interfaces, and c) relative vertical movement (slip) between column and beams as a result of the elongation, due to yielding a kinking of the beam longitudinal reinforcement.

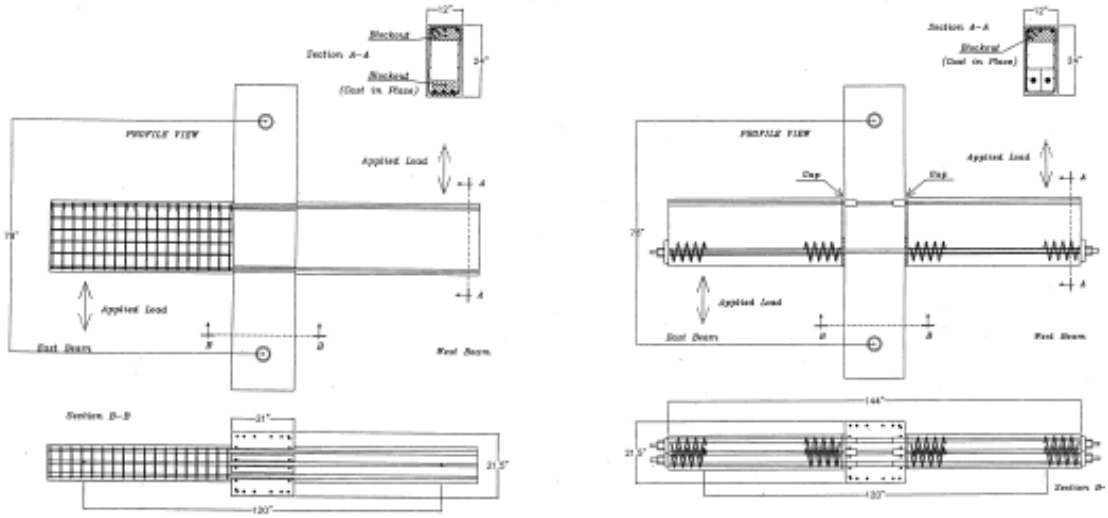

Figure 2.8. Specimen UMn-TCY (left) and UMn-GAP (right) [2.10].

The final TCY connection called UMn-GAP (Figure 2.8-right) used a grout pad at the bottom third of the beam-column interface while two post-tensioned bars passing through grout and column prevented relative opening of the bottom face of the connection and provided a pivot point for the beam rotation. The post-tensioning was used to provide sufficient clamping force to sustain gravity and lateral shear loads without experiencing inelastic deformations during cyclic behaviour. At the top of the connection reinforcing bars were connected through couplers at the beam column interface. Additional transverse reinforcement was placed in the beam to prevent bucking experienced in the previous connection UMn-TCY.

Experimental results of the connection performed satisfactorily up to 2% drift. Good energy dissipation characteristics were observed until premature fracture of the top bars occurred at the face of the couplers due to the high inelastic demands imposed. However, this connection was not attractive due to the difficulties and time effort required in the assembled of the connection. Initially, the grout was applied and cured within approximately the bottom third of the beam-column interface while the post-tensioning rods were lightly post-tensioned. The beam top reinforcement was threaded into the couplers cast through the column and the beam block-outs

were grouted. Finally the couplers were threaded after post-tensioning to ensure no significant initial stresses were induced in the beam top reinforcement.

2.3.3 Energy Dissipating/coulomb Friction (CF) connection

The four connection types consisted of special damping devices, typically involving some form of friction sliding, which could be placed in the connections between precast frame or panel elements. The specimen UT-FR was tested incorporating this concept (Figure 2.9). The top of each beam was connected to the column by a steel plate assembly that was embedded in the beam and bolted onto the side of the column. The plate assemblies contained slotted holes that permitted sliding along vertical plate surfaces on the sides of the beams. Depending on the level of moment capacity in the connection, the friction force could be obtained using thick brass plates between all sliding surfaces using conical washers beneath the high-strength bolts that clamped the plates together.

The bottom connection between the beams and column was developed to replace the corbel which performed poorly on the UT-GAP connection (Figure 2.7-left) and establish a continuous force path mechanism so that all inelastic action occurred in the top connection.

Experimental results showed very stable hysteresis behaviour and high energy dissipation similar to elasto-plastic behaviour until failure occurred in a weld in between steel plates due to a larger force than anticipated being developed in the top connection. It was also observed that the assemblage of plates used in the top connections and the high strength bolts used at the bottom of the connection introduced flexibility at low drift levels.

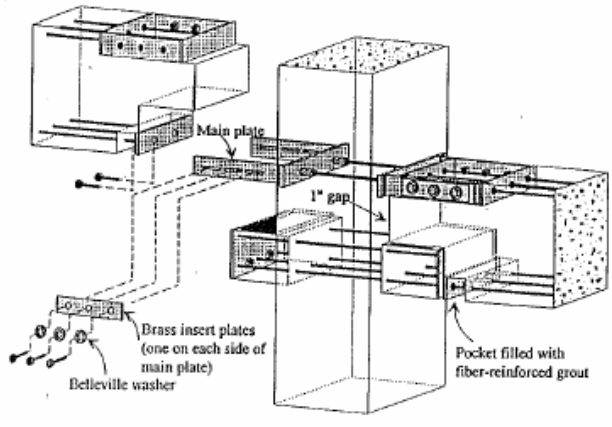

Figure 2.9. Specimen UT-FR [2.10].

However, as it was pointed out [2.10] in the UMn-GAP (Figure 2.8-right) and UT-GAP (Figure 2.9) connections, the concept of the restrained from translation at the bottom of the beam-

column interface using the concept of "gap-joint system" could be inverted so that the hinge connection was located at the top with the friction sliding at the bottom. Therefore, this would have the advantage of avoiding large inelastic displacements thus reducing damage in the floor [2.11].

An experimental program of five precast beam-column sub assemblages had been tested in Japan [2.12] and a flexural hysteresis model for prestressed concrete members considering bond-slip between prestressing steel and concrete was also developed [2.13]. The beams did not contain mild steel continuity bars. The parameters investigated were the eccentricity and size of PT steel and the amount of longitudinal mild steel bars on the columns. All specimens showed stable hysteretic curves with narrow hysteresis loops, and almost no residual displacements. At 0.05 radians of beam rotation angle, the contribution of shear deformation at the beam-column joint core was less than 5% of the overall drift and most of the deformation was attributed to the rotation at the beam-column interface.

The Building Research Institute (BRI) in Japan tested a three-story precast prestressed concrete frame, as shown in Figure. 2.10 [2.14]. The 36% scale specimen represented the lower stories of an eleven-story prototype building. The frame had two bays in one direction and one bay in the other. The beams consisted of prestressing bars and strands but no mild steel bars, and thus were expected to dissipate little energy. The frame was subjected to both static and pseudo-dynamic loadings. Under static loading, the frame performed well and reached 4% drift with no deterioration of its load carrying capacity. The maximum residual displacement was 14% of the maximum displacement. Under pseudo dynamic testing, the frame showed higher mode effects and the maximum story drift was observed at the second story.

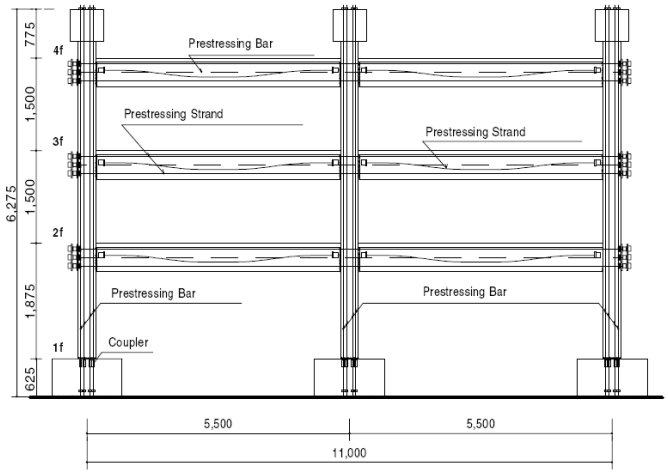

Figure 2.10. BRI three storey frame tested at the BRI [2.14]

2.4 DEVELOPMENT OF THE BEAM-COLUMN HYBRID JOINT AND FLOOR-FRAME MECHANICAL CONNECTORS

After a lot of attention given to the behaviour of the skeleton structure and under the previous premise, the focus of research in Earthquake Engineering has focused on the behaviour of the floor system, within the overall 3D behaviour of the building and the effects of beam elongation [2.15, 2.16, 2.17, 2.18, 2.19, 2.20]. These effects could be relevant in the response of the first-story columns since the building foundation at this level may try to restrain elongation of the beams of the first story at the formation of their plastic hinges. This restriction may cause shear force in the columns not considered in conventional analysis, with the possibility of also creating additional plastic hinges in the columns (weak-column, strong-beam mechanism) and possible collapse of the structure; or in loss of support for precast floor systems due to an elongation of the beam elements.

It is worth emphasising that beam elongation effects are typical of both cast-in-situ and precast concrete frames. With regards to jointed ductile connections with re-centering characteristics, the extent of beam elongation is significantly reduced, being limited to the geometrical contribution alone due to the presence of a neutral axis and actual depth of the beam. Furthermore, such effects could be minimized when a reduced depth of the beam is adopted due to the use of internal prestressing or external post-tensioning. However, damage to precast floor systems, resulting from a geometric elongation of the beam, has yet to be addressed in detail.

In order to investigate the response of all the structural components The PRESSS Phase III [2.21, 2.22] was conceived to integrate the components of experimental and analytical research developed in Phase I and II and consist of a 60% scale five-story two-bay by two bay frame. In addition to providing experimental verification of the design and analysis procedures, particular interest in the testing was focused on the performance of the precast floor system and the gravity support system and to investigate the floor connection.

In one direction of the PRESSS building, seismic resistance is provided by two precast frame systems with and without prestressing connections, with a precast wall system and gravity frames in the orthogonal direction. Four different beam-column connection details, based on the past NIST and PRESSS research program were modelled at different levels in the two parallel seismic frames (Figure 2.11).

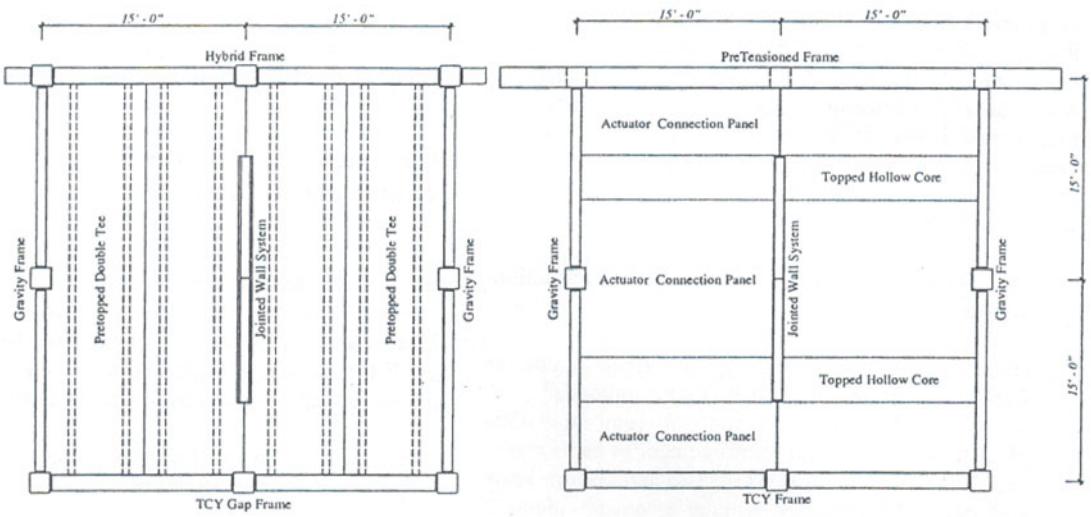

Figure 2.11. Floor plan view of the test building at Levels 1 to 3 (left) and levels 4 and 5 (right) [2.21]

In the prestressed frame an improved hybrid connection [2.23] (floors 1 to 3) and Pretensioned connection (floors 4 and 5) were used. Figure 2.12-left shows the Hybrid Frame connection where the beams were connected to multi-storey columns by unbonded post-tensioned strands that run through a duct in the centre of the beam and through the columns. Mild steel passes from the beams through the columns and dissipates energy in large earthquakes.

The Pre-Tensioned connection (Figure 2.12-right) consisted of multi-span beams which were cast with partially debonded pretensioning strand set on one-story columns. As the frame displaces laterally, the debonded strand remains elastic and re-centres the structure after a major seismic event. The hybrid frame also has this characteristic.

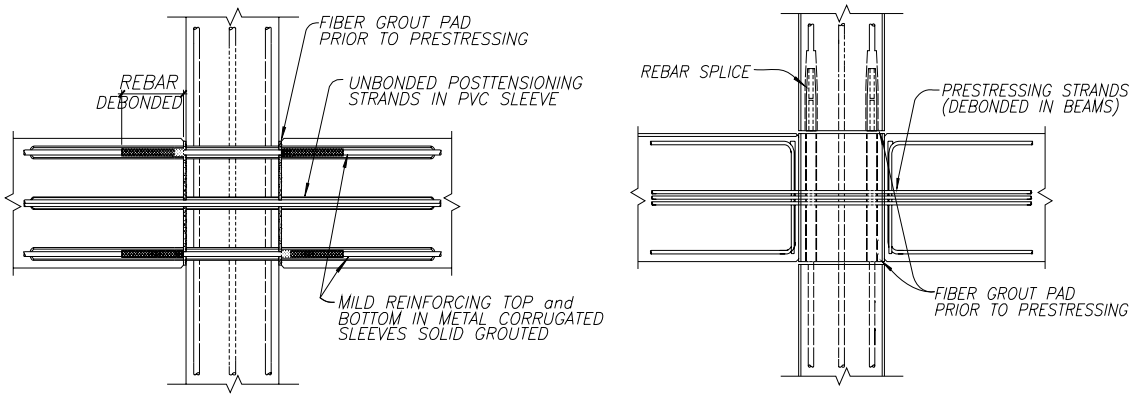

Figure 2.12. Hybrid connection (left) and Pretensioned connection (right) [2.21].
Note: for clarity beam reinforcement is not shown

For the second frame with the no use of prestressing the Tension-compression Yield (TCY) GAP connection (floors 1 to 3) and TCY connection (floors 4 and 5) were implemented. Figure

2.13-left shows the Tension-Compression Yielding (TCY) Gap connection where beams were erected between columns, leaving a small gap between the end of the beam and the face of the column. Only the bottom portion of this gap is grouted to provide contact between the beam and column. The reinforcing steel is debonded for a specified length at the gap so it can yield alternately in tension and compression without fracture. This solution was developed to avoid the primary elongation effects associated with both geometric and material beam elongation and thus the centre-to-centre distance between columns did not grow with lateral drift. However, such a solution would not account for the tearing floor actions occurring due to the gap-opening at the top of the beam.

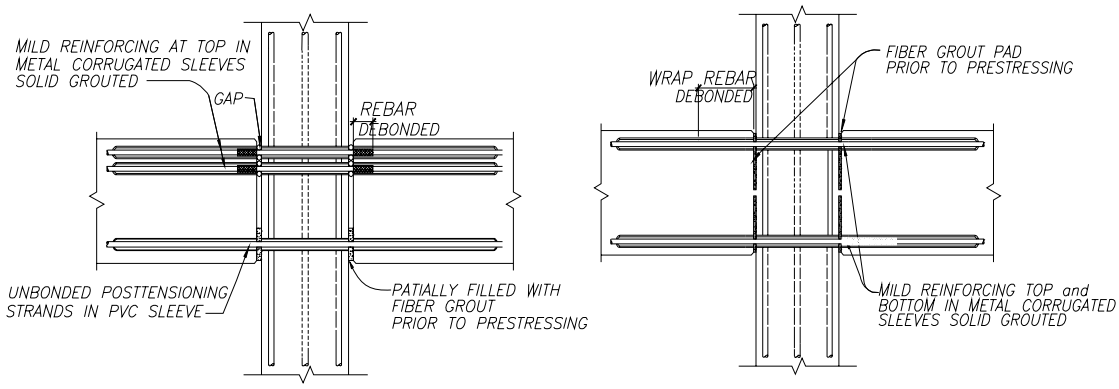

Figure 2.13. TCY-GAP connection (left) and TCY connection (right) [2.21].
Note: for clarity beam reinforcement is not shown.

The TCY connection (Figure 2.13-right) consisted of a traditional tension/compression-yielding connection similar to that used in cast-in-place concrete construction. The yielding is concentrated in the connection, rather than creating distributed yielding over the finite length of a plastic hinge.

In addition, two precast flooring systems were included in the building. The first three floors were constructed using pretopped double tees attached to the frame with an X-plate connector (Figure 2.14) such that vertical and horizontal displacement would be taken by the connector. Hollow-core panels were used in the upper floors. The connection of the hollow-core with the frame was using drag bars from the topping connecting into pockets in the top of the frame beams.

The structure was subjected to four successive levels of seismic excitation, using multi-degree of freedom pseudo-dynamic test techniques. The building was independently tested in the two orthogonal directions. In each direction three different schemes of test were used. Stiffness measurement test, pseudo dynamic test and triangular load test.

Figure 2.14. PRESSS test building (left) and X-plate mechanical connector type (right) [2.22]

The Structural response of the structure was extremely satisfactory as reported [2.22] with minimal damage to the beam column connections while the response of the two precast flooring systems with the frame was very satisfactory. Minor cracking in the topping of the hollow-core was reported despite of the high level of floor forces during the test. The X-plate connector used to connect the double-tees with the seismic resisting frame performed well, although significant inelastic deformations and permanent distortion was reported at the end of the test.

During the design phase of the PRESSS prototype building, dynamic analysis was performed using two earthquake records [2.24]. Analysis of the hybrid frames confirmed that the beam growth forces the columns further apart, thus inducing additional shear and moment in the columns. The beam growth causes column shears that are opposite in sign at each end of the building. At one end they add to the seismic shear, while they counteract it at the other end.

Similarly, analytical models were developed to investigate the response of the hybrid frames with different configurations, as well as how the beam growth affects the frame response under seismic loading [2.25]. It was found that ignoring the effects of beam growth could underestimate the structural demands on some of the framing members. In particular, the demands on the outer columns were much greater than those on the columns in the middle, especially at the lower floors. The response of the frames, including inter-story column drifts and demands on individual framing members, was closely related to the geometry of the frame, such as the clear span-to-beam depth ratio, and the number of bays. A simplified analytical model for predicting the effects of beam growth, based largely on geometry, was developed.

Experimental research on the three-dimensional behaviour of precast super-assemblages consisting of precast moment-resisting frames and precast hollow-core floor units [2.26] had reported total collapse of the floor units due to lost of seating (Figure 2.15). Similarly, another recent research on a two-story precast concrete dual system, using double tees floor units [2.27] reported excessive cracks on the topping in the slab-wall joint.

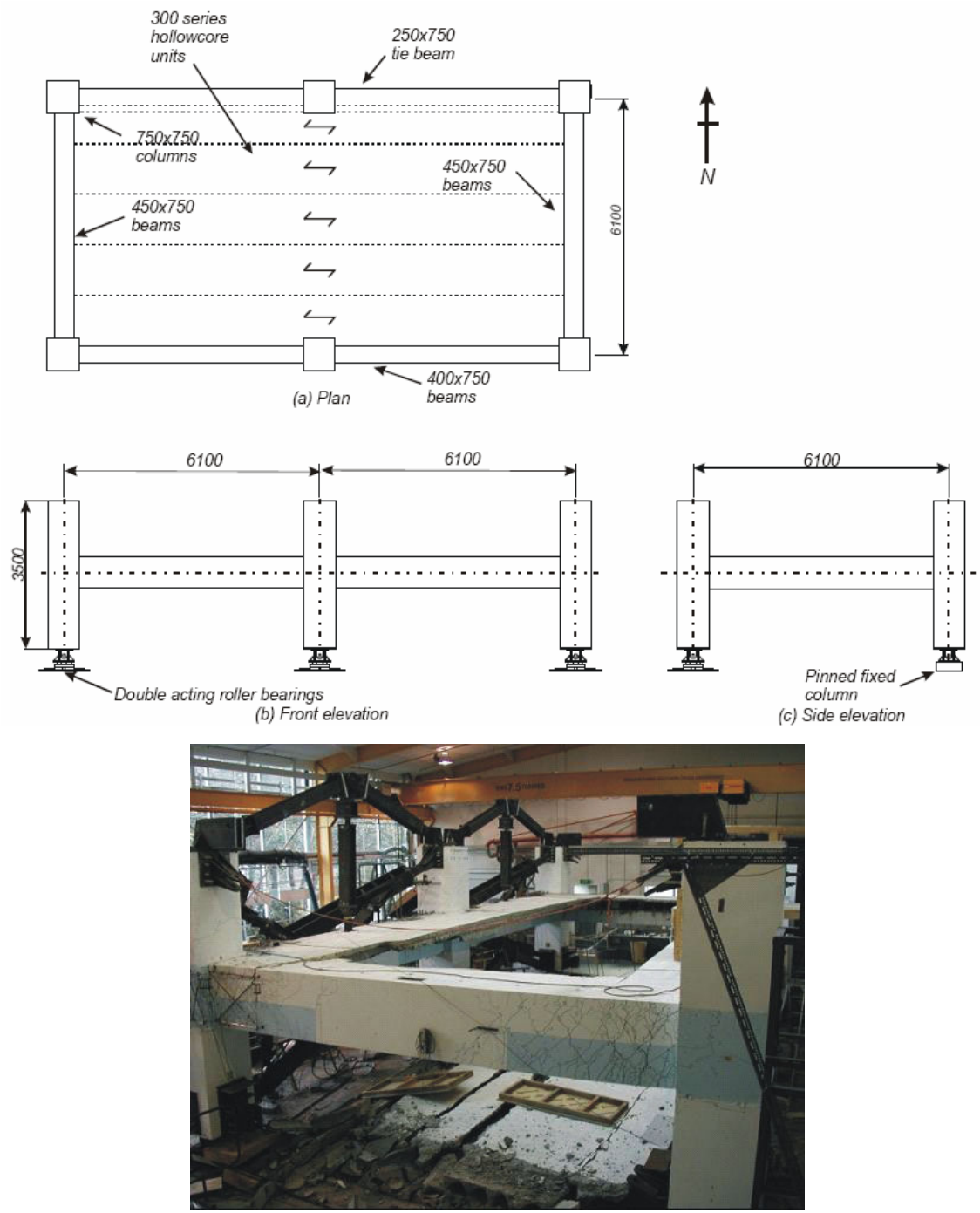

Figure 2.15. Geometry and test set-up (top); lost of support in the floor unit (bottom). [2.26]

Recent experimental research at the University of Canterbury on the effect of beam elongation on the response of a three-dimensional sub-assemblage consisting of a two-bay moment resisting frame with deep precast prestressed rib floor units have shown that the presence of the slab can significantly increase the strength of the beam plastic hinges, by acting as deep beams to restrain their elongation. This effect is shown in Figure 2.16 where the diagonal cracks inclined towards the central column restrain the elongation and the longitudinal cracks parallel to frame, near the end slab, show the deep beam actions of the floor [2.28].

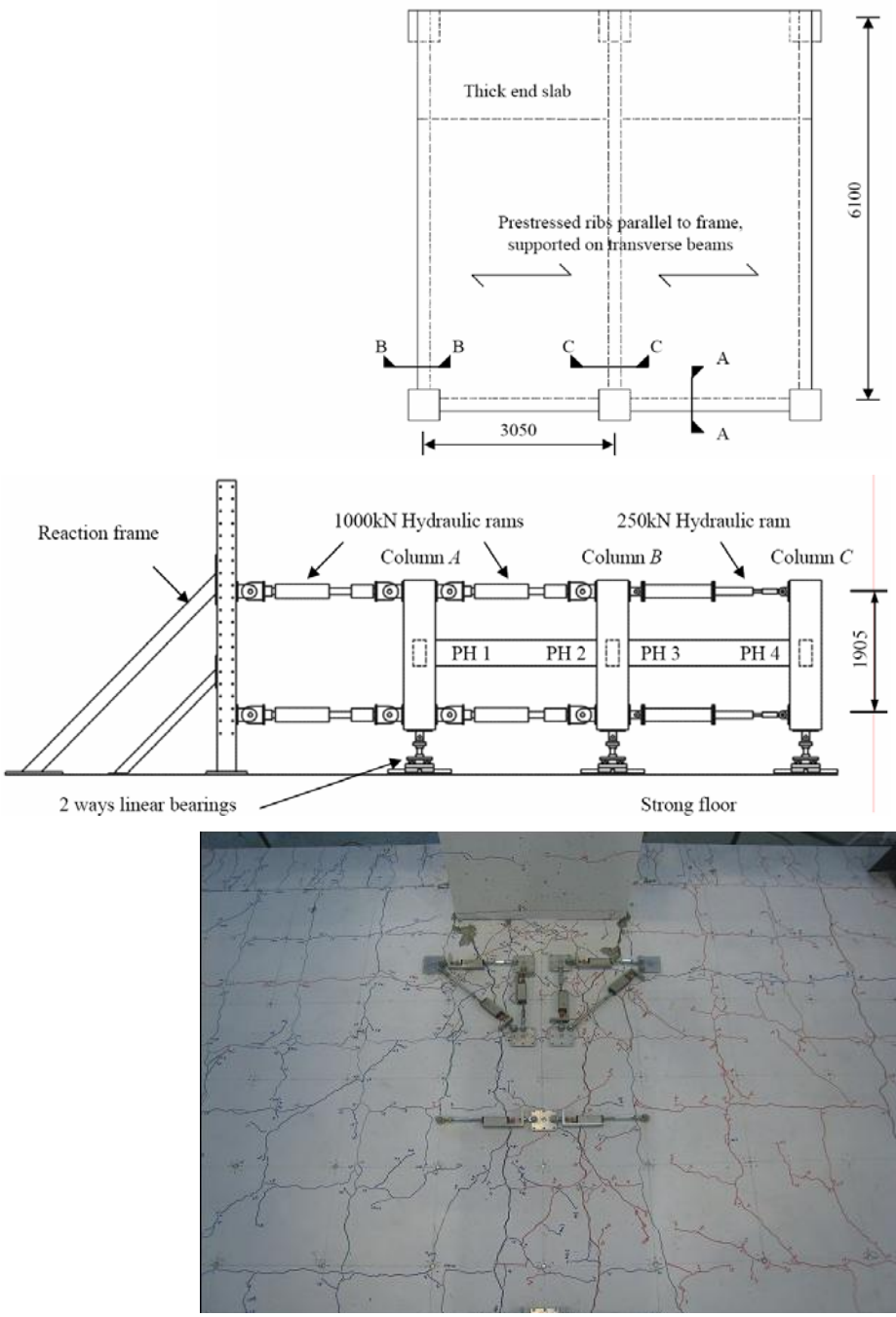

Figure 2.16. Geometry and test set-up (top); Floor slab crack patterns (bottom). (Courtesy: Brian Peng [2.28]).

All the above mentioned researchers further underlined issues related to the displacement incompatibility between precast floors and the lateral resisting system, including the effects of beam-elongation. Appropriate design criteria and detailed technical solutions are thus required to overcome such issues.

2.5 NEW ARRANGEMENTS OF THE HYBRID CONNECTIONS

Recent research at Italy, Turkey and New Zealand had lead after the culmination of the PRESSS program with the continuous and rapid development of jointed ductile connections for seismic resisting systems in the validation of a wide range of alternative arrangements, under the general umbrella of "hybrid" systems, currently available to designers and contractors for practical applications based on a case-by-case (cost-benefit) evaluation.

Based on similar concepts developed in the PRESSS program, a natural evolution connection solution and construction system able to accommodate higher seismic demand, named "Brooklyn" system, has been studied and developed for gravity-load-dominated frame buildings with the intent of combining the structural concept and efficiency of cable-stayed (Figure 2.17-left) or suspended bridges (Figure 2.17-right) within a typical multi-storey building system [2.29, 2.30]. The key peculiarities of the system were the use of alternative solutions for steel shear bracket/corbel and the use of a draped tendon profile in order to supply an adequate moment resistance at the critical sections under combined gravity and low-to-moderate lateral loads.

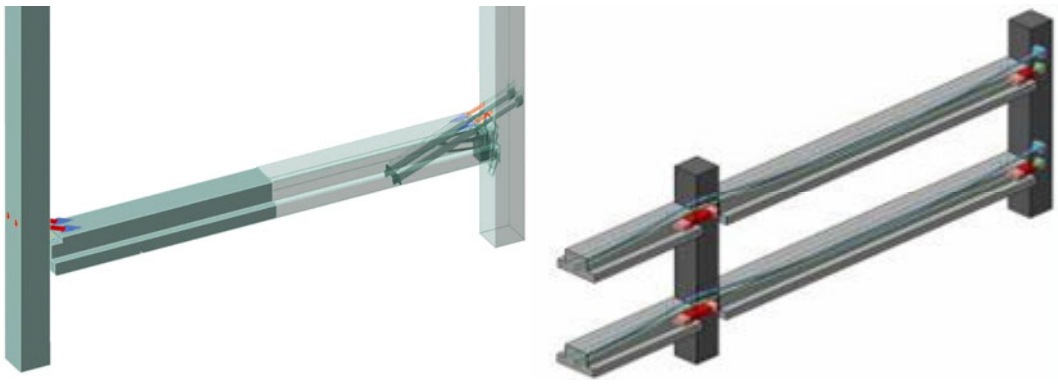

Figure 2.17. Alternative solutions for the Brooklyn system: cable stayed (left) and suspended solution (right) [2.29, 2.30]

The experimental results showed a very satisfactory performance of both the proposed solutions for the Brooklyn system (cable-stayed and suspended). Significant reduction of vertical

deformation/deflection under service load with also some significant displacement ductility capacity up to the ultimate limit state was found. Furthermore, the design of the tendons can provide self-centring properties to the overall system, when unloading from the service (dead + live) load level to the condition of permanent load (i.e. slab-load) were obtained.

More recently, further experimental investigations under lateral loading on beam column joints for lateral load only [2.31] or lateral and gravity load systems [2.32] (Figure 2.18-right) had been carried out. Post-tensioned precast concrete beam and column elements were permitted to rock at the connection interface. Steel plate armouring was used to protect the rocking surfaces and prevent spalling or crushing of concrete. Straight prestressing bars for the lateral load only or draped prestressing bars anchored in the column at floor level act to provide the connections with moment resistance and to balance an applied gravity load.

Supplemental energy dissipaters were use at the rocking connection in the form of (a) a 'dog-bone' plate tension-compression yielding dissipator; (b) a threaded rod tension-compression yielding dissipator; and (c) 'boomerang' mild steel flexural yielding dissipater (Figure 2.19). For all of these cases, the dissipater forces were transferred from the dissipater to the connection armourment and then into the beam mild steel reinforcement.

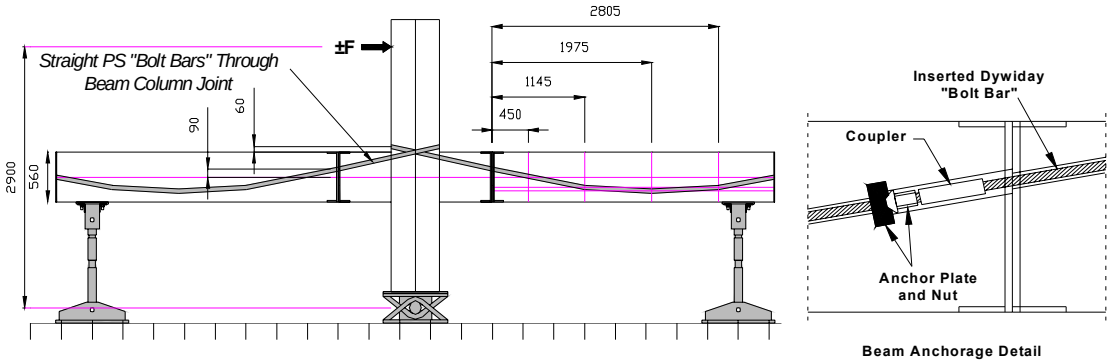

Figure 2.18. Beam-Column joint test set up (left) and anchorage details (right) [2.32]

The experimental testing showed that the connection system and adopted design procedures satisfactorily prevent damage to the structure even at drift levels of 4%. The systems were shown to be capable of achieving equivalent strengths to conventionally designed connections but with minimal residual drifts resulting from the recentring effect of the elastic prestressing. It was also demonstrated that this class of frame can be primarily designed on the basis of balancing structural dead load with the seismic capacity of the frame checked as an after consideration. However, it was found that although the specimen's performance was

satisfactory, several design improvements relating to the coupler system and the armoured ends were required [2.33].

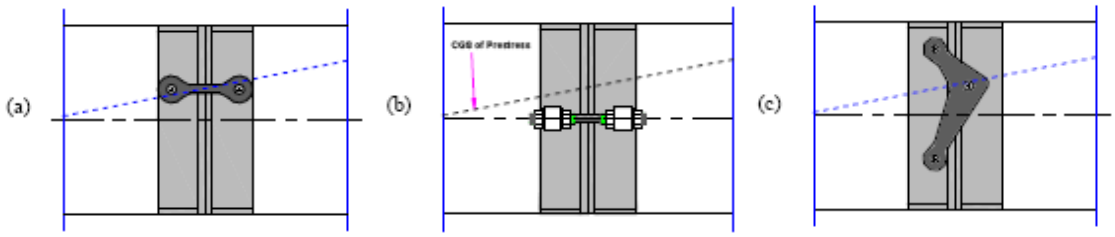

Figure 2.19. Mechanical Energy Dissipators: (a) Tension-Compression 'Dog-bone'; (b) Threaded Rod Fuse; (c) Flexural 'Boomerang'.

An experimental campaign with the aim to reduce the damage in reinforced concrete structures was conceived after the 1995 Hyogo-ken Nanbu earthquake in Japan. It was found that the costs associated with repairing the structures were about 70% of the costs of building a new structure and in some cases it was difficult or impossible to repair the structures. Experimental research on "emulative" cast-in-situ concrete beam column joints has shown that the damage to the floor using a "slotted beam" (Figure 2.20), constructed with a narrow vertical slot at the beam ends running from the bottom of the beam up to the bottom of the floor [2.34] reduces the floor damage.

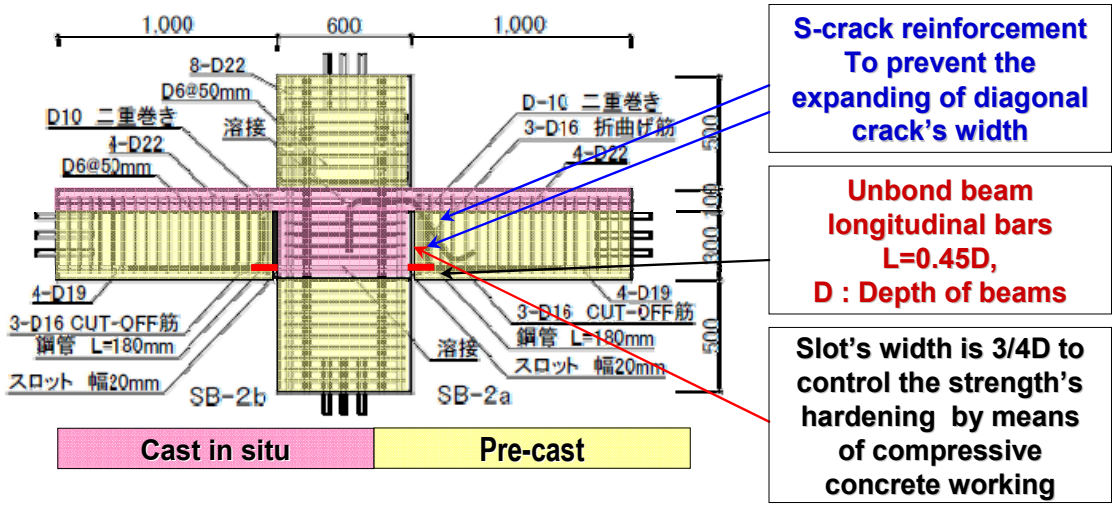

Figure 2.20 Slotted Articulated floor connection proposed in Japan. [2.34]

Experimental results indicated that the flexural strength of the system is governed by the bottom beam reinforcement which is continuous through the slot; meanwhile yielding of the top reinforcement is avoided. The depth of the compressive concrete was proposed as ¼ of beam depth to control the increasing strength. Special shear reinforcement is required in the connection for a phenomenon called S-crack generated due to the tensile stresses created in the concrete in the beam-bottom, even when the bottom reinforcement is in compression, that is

required to equilibrate the compressive strut forces in the concrete carrying the shear to the end of the region of the beam where the longitudinal reinforcement is unbonded.

Finally, the bottom reinforcement was inserted through a close fitting steel tube to break the bond over the reinforcement bars and to spread the plastic elongation over a longer length. They also prevent or delay buckling with the bottom reinforcement is in compression.

Experimental results showed that beam elongation effects were minimized and minor floor cracks were observed when compared with conventional solutions. However, the special detailing required to guarantee an efficient and reliable mechanism and structural performance are yet to be properly developed and translated in simple design recommendations, particularly when using precast concrete solutions.

Similarly, recent research [2.35] based on experimental tests on 2/3 scale in plane beam-column joints were carried out using the slotted reinforced concrete beam similar as proposed [2.34] as an alternative non-tearing floor solution which minimises beam elongation, and the damage to the yielding connection and adjacent floor diaphragms. The objective of this research was to implement of this technology in New Zealand construction practice.

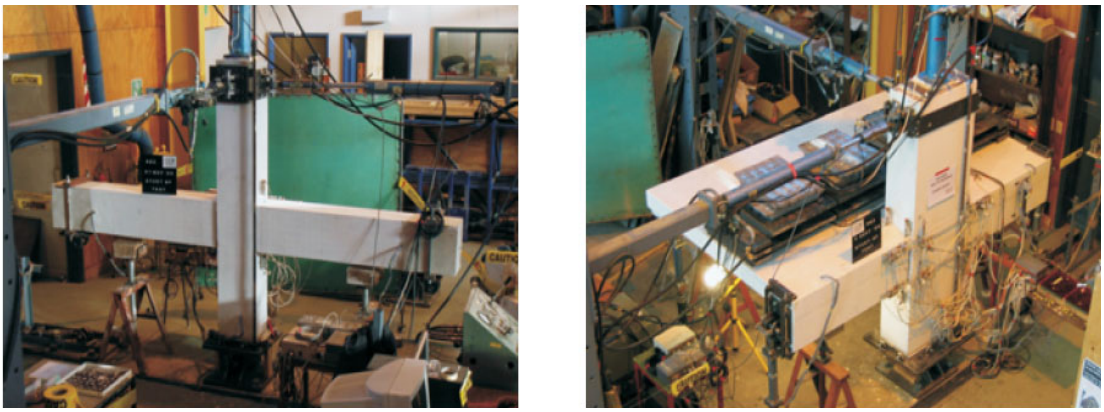

Figure 2.21 Experimental tests on beam-column connections using slotted articulated floor proposed in New Zealand. [2.35]

Experimental tests revealed some design issues associated with slotted-beams as buckling and low cycle fatigue failure of bottom longitudinal reinforcement, insufficient anchorage to bottom reinforcement passing through interior joints, increased joint shear demands on lower horizontal joint stirrups and beam torsion resulting from eccentric floor gravity loads. However, it was shown that all these issues could be resolved with modified detailing or additional reinforcement.

Simultaneously, an experimental and analytical research [2.36] at 2 dimensional frame incorporating different beam-to-column connection details has shifted from detailing for significant localised damage to beams and adjacent floors to that of minimising damage to the structural system of beam and floor by creating a "Non-Tearing (of the floor)" beam-to-column connection.

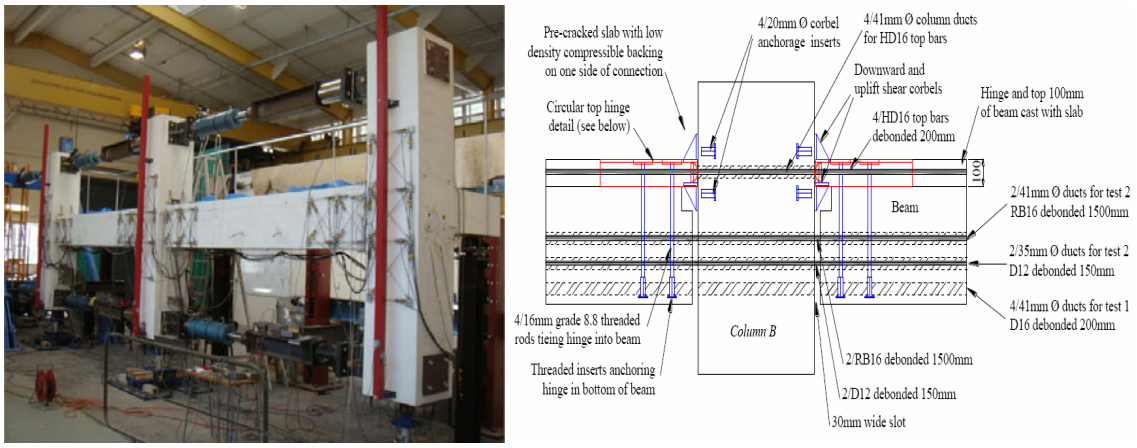

Figure 2.22 Experimental tests on 2-dimensional frame using slotted articulated floor (left) and interior beam-column connection details (right) proposed in New Zealand. [2.36]

Results had underline that non-tearing connection technology significantly reduces damage and collapse potential in precast concrete seismic moment frames. With the further research, development and refinement of connection details, non-tearing connection technology shows impressive potential for enhancing the seismic safety, efficiency and performance of precast concrete frame buildings.

Recent experimental research on post-tensioned precast concrete moment-resisting, beam-column connections containing different mild steel reinforcement contents had been carried out [2.37] to determine the effect of mild steel reinforcement content on the behaviour and performance of post-tensioned precast concrete hybrid connections. Five hybrid connections were tested. The main variable was the mild steel's percentage of contribution to the flexural capacity of the connection, ranging from 0% to 65% of the connection's moment capacity.

Results of this experimental campaign showed that the response of the hybrid connections approached that of the monolithic subassembly as the mild steel reinforcement content increased. Connection capacities were well predicted by the joint gap opening approach. The design assumptions of hybrid connections are best satisfied with a 30% mild steel reinforcement contribution to the connection's flexural capacity.

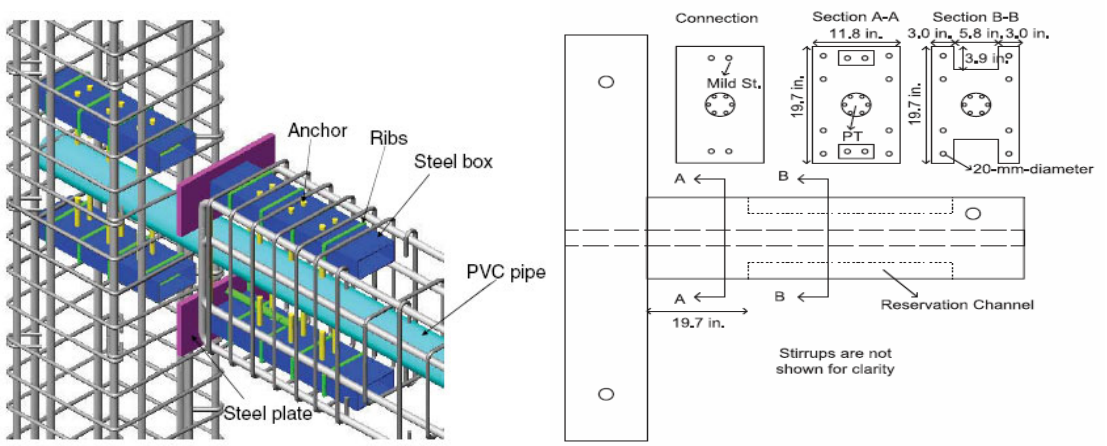

Figure 2.23 Details of the connection details (left) and post-tensioned specimens (right) proposed in Turkey. [2.37]

2.6 CHAPTER SUMMARY

In 1986 a workshop took place in Los Angeles (U.S) to examine the problems and needs of the Precast Concrete Industry. Results from this workshop noticed the higher cost of precast concrete construction in comparison with more traditional systems followed by a lack of prescriptive design provision for the designers in the design of precast elements in seismic regions [2.1].

In response to these needs, a long term program was initiated at the National Institute of Standards and Technology (NIST) in 1987 to study of the behavior of precast beam-column connections subjected to cyclic inelastic loading [2.2]. As part of the experimental program, the concept known as the "hybrid connection" was developed [2.7] and in conjunction "replaceable systems" which involve replaceable dissipaters was also developed [2.8]. In this connection, the use of non-prestressed low strength (mild) steel is used with post-tensioned steel with the objective of improving the energy dissipation characteristics of the precast specimens while the post-tensioned steel provides the clamping force necessary for shear resistance.

Simultaneously, The Precast Seismic Structural Systems (PRESSS) Research Program [2.5] was initiated as part of the United States-Japan protocol on large scale testing for seismic response of precast concrete buildings. As part of the PRESSS program, different ductile connections were developed [2.10, 2.23] and incorporated on the testing of a large scale, five-storey building using both frame and wall systems [2.21]. The Structural response of the structure was extremely satisfactory as reported [2.22] with minimal damage to the beam column connections.

After a lot of attention given to the behaviour of the skeleton structure, the research interest in earthquake engineering has focused on the behaviour of the floor system, within the overall 3D behaviour of the building and the effects of beam elongation [2.15, 2.16, 2.17, 2.18, 2.19, 2.20].

Experimental and numerical studies [2.25, 2.26, 2.27, 2.28] have shown that plastic beam hinges cause growth in the beam length depending on the beam depth, expected position of the neutral axis and rotation (drift) demand. As the structure moves laterally, the gap at the beam column joint interface opens and increases the distance between the columns. This beam growth pushes the columns apart and induces additional shear and moment demands on the columns. Furthermore, as the gap opens, the floor next to the beam must be allowed to crack open, since preventing a crack from opening would affect the behaviour of the beam. Therefore the detailing should accommodate deliberate crack opening at the floor diaphragm.

Based on similar concepts developed in the PRESSS program, alternative and innovative connections to accommodate higher seismic demands have resulted through the validation of a wide range of alternative arrangements under the general umbrella of "hybrid" systems are currently available to designers and contractors around the world [2.29, 2.30, 2.31, 2.32, 2.33, 2.37]. The key peculiarities of the system were the use of alternative solutions for steel shear bracket/corbel, the use of straight or draped tendon profile in order to supply an adequate moment resistance at the critical sections under combined gravity and low-to-moderate lateral loads.

Recently focus of research has shifted from detailing for significant localised damage to beams and adjacent floors to that of minimising damage to the structural system of beam and floor by creating a "Non-Tearing (of the floor)" beam-to-column connection [2.34, 2.35, 2.36]. This is where the relative rotation of the beam to the column, under lateral displacement of the building, does not result in large plasticity of the beam and avoids the detrimental damage (tearing) of the floor-to-column junction.

2.7 REFERENCES

2.1 Englekirk, R. E., "Overview of PCI Workshop on Effective Use of Precast Concrete for Seismic Resistance," PCI Journal, V. 31, No. 6, Nov.-Dec. 1986, pp. 48-58.

2.2 Cheok, G. S., and Lew, H. S., "Performance of 1/3-Scale Model Precast Concrete Beam-Column Connections Subjected to Cyclic Inelastic Loads – Report No. 1,"

NISTR 4433, National Institute of Standard and Technology, Gaithersburg, MD, October 1990.

2.3 Cheok, G. S., and Lew, H. S., "Performance of 1/3-Scale Model Precast Concrete Beam-Column Connections Subjected to Cyclic Inelastic Loads – Report No. 2," NISTR 4589, National Institute of Standard and Technology, Gaithersburg, MD, June 1991.

2.4 Cheok, G. S., and Lew, H. S., "Model Precast Concrete Beam-to-Column Connections Subjected to Cyclic Loading," PCI Journal, V. 38, No. 4, Jul.-Aug. 1993, pp. 80-92.

2.5 Priestley, M. J. N., "Overview of PRESSS Research Program," PCI Journal, V. 36, No. 4, Jul.-Aug. 1991, pp. 50-57.

2.6 Priestley, M. J. N., and Tao, J. R., "Seismic Response of Precast Prestressed Concrete Frames with Partially Debonded Tendons," PCI Journal, V. 38, No. 1, Jan.-Feb. 1993, pp. 58-69.

2.7 Cheok, G. S., Stone, W. C., and Lew, H. S., "Performance of 1/3-Scale Model Precast Concrete Beam-Column Connections Subjected to Cyclic Inelastic Loads – Report No. 3," NISTR 5246, National Institute of Standard and Technology, Gaithersburg, MD, August 1993.

2.8 Cheok, G. S., and Stone, W. C., "Performance of 1/3-Scale Model Precast Concrete Beam-Column Connections Subjected to Cyclic Inelastic Loads – Report No. 4," NISTR 5436, National Institute of Standard and Technology, Gaithersburg, MD, June 1994.

2.9 MacRae, G. and Priestley, M.J.N., "Precast Post-Tensioned Ungrouted Concrete Beam-Column Sub assemblage Tests," Report No. SSRP 94/10, Department of Applied Mechanics and Engineering Sciences, University of California, San Diego, CA, March 1994, 124 pp.

2.10 Palmieri, L., Saqan, E., French, C., and Kreger, M., "Ductile Connections for Precast Concrete Frame Systems," Proceedings of the Mete Sozen Symposium, SP-162-13, American Concrete Institute, Farmington Hills, MI., Oct. 1996, pp. 313-355.

2.11 Priestley, M. J. N., "The PRESSS program – Current Status and Proposed Plans for Phase III," PCI Journal, V. 41, No. 2, Mar.-Apr. 1996, pp. 22-40.

2.12 Adachi, M. and Nishiyama, M., "Hysteretic behaviour of precast post-tensioned beam-column joint assemblage," Transactions of the Japan Concrete Institute, Vol. 19 pp. 211-218, 1997.

2.13 Adachi, M. and Nishiyama, M. "Idealization of hysteretic behavior of prestessed concrete members and assemblages considering bond-slip between prestressing steel and concrete," 12th World Conference on Earthquake Engineering, Paper No. 2259, Upper Hutt, New Zealand. New Zealand Society for Earthquake Engineering. 2000.

2.14 Kato, H., Ichisawa, Y., Takamatsu, K., and Okamoto, N., "Earthquake response of an eleven-story precast prestressed concrete building by substructure pseudo dynamic test," 12th World Conference on Earthquake Engineering, Paper No. 2223, Upper Hutt, New Zealand. New Zealand Society for Earthquake Engineering. 2000.

2.15 Fenwick, R. and Fong, A. "The behaviour of reinforced concrete beams under cyclic loading," Technical Report 176, Dept. of Civil Engineering, Univ. of Auckland, New Zealand. 1979

2.16 Douglas, K.T., "Elongation in Reinforced Concrete Frames, PhD Thesis, Department of Civil Engineering, University of Auckland. 1992.

2.17 Restrepo-Posada, J., Park, R., and Buchanan, A. H., "Seismic behaviour of connections between precast concrete elements," Technical Report Research Report 93-03, Dept. of Civil Eng., Univ. of Canterbury, New Zealand.

2.18 Fenwick, R. C. and Megget, L. M., "Elongation and Load Deflection Characteristics of Reinforced Concrete Members containing Plastic Hinges," Bulletin of the New Zealand National Society for Earthquake Engineering, V.26, Jan.-Mar. 1993, pp. 28-41.

2.19 Fenwick, R. and Davidson, B., "Elongation in ductile seismic-resistant reinforced concrete frame," Priestley, N., Collins, M., and Seible, F., editors, Recent Development in Lateral Force Transfer in Buildings, Proceedings of the Tom Paulay Symposium, pp. 143-170, Farmington Hills, MI. American Concrete Institute. 1995.

2.20 Fenwick, R., Ingham, J., andWuu, P., "The performance of ductile R/C frames under seismic loading," NZSEE Conference, pp. 20-26, New Plymouth, New Zealand. 1996

2.21 Nakaki, S., Stanton, J. F., Sritharan, S., "An Overview of the PRESSS Five-Story Precast Test Building," PCI Journal, V.44, No.2, Mar-Apr 1999, pp. 26-39.

2.22 Priestley, M. J. N., Sritharan, S., Conley, J., and Pampanin, S., "Preliminary Results and Conclusion from the PRESSS Five-Story Precast Concrete Test Building," PCI Journal, V.44, No. 6, Nov.-Dec. 1999, pp. 44-67.

2.23 Stanton, J. F., Stone, W. C., Cheok, G. S., "A Hybrid Reinforced Precast Frame for Seismic Regions", PCI Journal, Vol. 42, No. 2. Mar-Apr. 1997, pp. 20-32.

2.24 Collins, R. H., "Design of a precast concrete building for seismic loading," Master's thesis, Dept. of Civil & Environmental Engineering., Univ. of Washington. 1999.

2.25 Kim, J., "Behaviour of Hybrid Frames Under Seismic Loading", PhD Thesis, Department of Civil and Environmental Engineering, University of Washington, U.S.A, 2002.

2.26 Matthews, J., "Hollow-core floor slab performance following a severe earthquake," PhD Thesis, Department of Civil and Environmental Engineering, University of Canterbury, New Zealand, 2004.

2.27 Rodriguez, M.E., Blandon J.J. "Tests on a Half-Scale Two-Story Seismic-Resisting Precast Concrete Building," PCI Journal, V. 50, No. 1, Jan-Feb 2005, pp.94-114.

2.28 B.H.H. Peng, R.C. Fenwick, R.P. Dhakal and D.K. Bull. "Experimental study on the seismic performance of RC moment resisting frames with precast-prestressed floor units," Proceedings of The New Zealand Society of Earthquake Engineering Annual Conference. Taupo, New Zealand, 2008.

2.29 Pagani, C., "Four is Better than Two – The Principle of Cable-Stayed Bridges Applied to Building Beams," Elite Journal, V. 4, No. 5, Nov.-Dec. 2001, pp. 42-57.

2.30 Pampanin, S., Pagani, C., and Zambelli, S., "Cable-Stayed and Suspended Post-tensioned Solutions for Precast Concrete Frames," Proceedings of New Zealand Concrete Industry Conference, Queenstown, New Zealand, 2004.

2.31 Davies, M. N., "Seismic Damage Avoidance Design of Beam-Column Joints using Unbonded Post-Tensioning: Theory, Experiments and Design Example," ME thesis, Department of Civil Engineering, University of Canterbury, Christchurch, New Zealand, 2004, 155 pp.

2.32 Arnold, D. M., "Development and Experimental Testing of a Seismic Damage Avoidance Designed Beam to Column Connection Utilizing Draped Unbonded Post-Tensioning," ME thesis, Department of Civil Engineering, University of Canterbury, Christchurch, New Zealand, 2004, 108 pp.

2.33 Li, L., "Further Experiments on Damage Avoidance design of Beam to-Column Joints," ME thesis, Department of Civil Engineering, University of Canterbury, Christchurch New Zealand, 2006, 147 pp.

2.34 Ohkubo, M., Hamamoto, T. "Developing Reinforced Concrete Slotted Beam Structures to Reduce Earthquake Damage and to Enhance Seismic Structural Performance," Proceedings of the 13th World conference on Earthquake Engineering. 2004, Vancouver, Canada.

2.35 Au, E. V., "the Mechanics and Design of a Non-tearing Floor Connection Using Slotted Reinforced Concrete Beams," ME thesis, Department of Civil Engineering, University of Canterbury, Christchurch New Zealand, 2010, 335pp.

2.36 Leslie, B.J. "The Development and Validation of a Non-tearing floor Precast concrete Structural System for Seismic Regios," ME thesis, Department of Civil Engineering, University of Canterbury, Christchurch New Zealand, 2010, 481pp.

2.37 Ozden, S. and Ertas, O., "Behaviour of Unbonded, Post-tensioned, Precast Concrete Connections with Different Percentages of Mild Steel Reinforcement," PCI Journal, V. 52, No. 2, Mar.-Apr. 2007, pp. 32-44.

CHAPTER 3
ADVANCED SEISMIC PERFORMANCE OF JOINTED DUCTILE PRECAST CONCRETE FRAME SYSTEMS

3.1 INTRODUCTION

The use of hybrid systems had been limited by code provisions for practical implementation based on experimental-analytical case-by-case applications. This research investigates alternative and innovative connections that have resulted from the validation of a wide range of alternative arrangements, under the general umbrella of "hybrid" systems, currently available to designers and contractors.

In order to emphasize the enhanced performance of the proposed advanced hybrid solutions, comparisons with the experimental response and observed damage of 2-D and 3-D monolithic beam-column specimens designed according to the NZ3101:1995 code provisions were carried out.

Additionally, analytical-experimental validation is being implemented using simple analytical models already presented in the literature, providing a reliable control over the expected hysteresis and dynamic behaviour.

3.2 THE JOINTED HYBRID CONNECTION

3.2.1 Behavioural Concept

The precast elements are jointed together by post-tensioning the precast beams to the columns using strands that are not bonded to the concrete as shown in Figure 3.1. The inelastic demand is accommodated within the connection itself, through the opening and closing of an existing gap at the critical beam-column interface. The clamping force between beam and column provides vertical shear force transfer at the interface between the beam and column while ensuring that the limit of proportionality is not reached as a result of the elongation caused by the opening of the gap during the largest expected lateral displacement demand.

Energy dissipation capacity can be introduced into the beam-column connection by different means. Normally the use of mild steel bars inserted into a corrugated steel tube and then

grouted. Energy dissipation occurs from the yielding in tension and compression when the gap occurs.

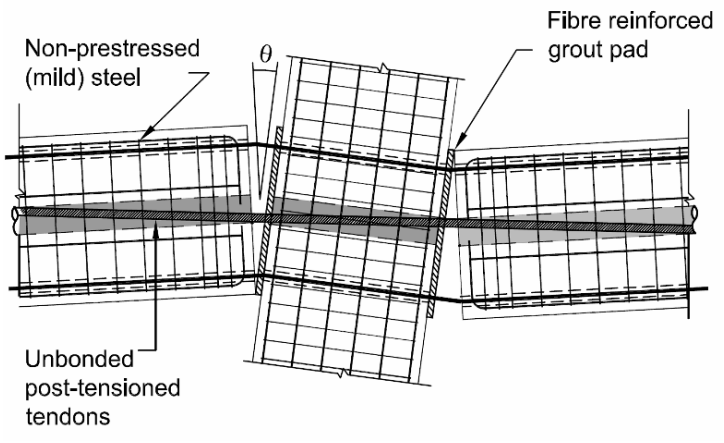

Figure 3.1. Hybrid beam-column connection. Modify after [3.6]

The rocking mechanism at the connection can be control by the relative ratio of moment contribution between post-tensioning and mild steel which governs the so-called "flag-shaped" hysteresis behaviour (Figure 3.2). Depending on this moment ratio also typically referred to as λ a wide range of hybrid solutions can be obtained [3.1].

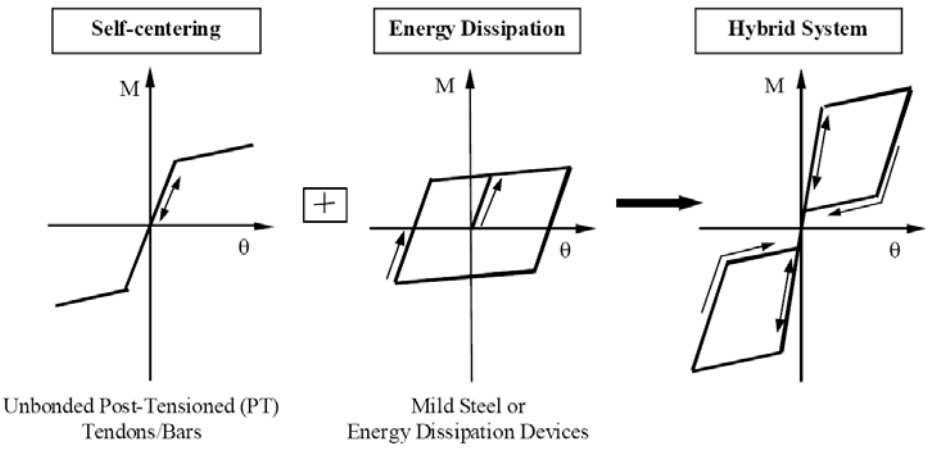

Figure 3.2. Idealized flag-shape hysteretic rule. From fib Bulleting 27 [3.2]

3.2.2 Generic Procedure for Analytical Modelling

As the gap at the beam-column interface opens and closes it forms an infinite curvature at the critical section of the beam column joint. This violates strain compatibility and Bernoulli's "plane sections remain plane" theory. Therefore, the use of a moment-rotation relationship is more appropriate when compared to traditional moment-curvature relationship.

Several different approaches are described in literature to model the connection of the precast concrete system with differing levels of complexity: section analysis [3.3], fibre element analysis [3.4], multi-spring macro-models [3.5] and lumped plasticity model using moment-curvature/rotation [3.6, 3.7] implemented via rotational springs.

3.2.3 Moment-Rotation Analysis of Ductile Connection

The lumped plasticity modelling approach adopts non-linear inelastic rotational springs located in parallel at the rocking interface. The spring properties can be evaluated via a monotonic moment-rotation analysis which is evaluated based on a global member compatibility condition using the monolithic beam analogy principles [3.6] and implemented in the New Zealand code provisions [3.1]. The analysis allows each moment contribution (mild steel, post-tensioned tendons and axial load) to be isolated, defining their individual contributions and allowing individual spring properties to be defined.

This analysis requires a trial and error calculation of the neutral axis position c, where for a given column rotation θ, the effective beam rotation developed at the beam-column joint zone θ_b can be evaluated using rigid body geometrical considerations shown in Figure 3.3 without taken into account the elastic deformation of the of the elements. The amount of elastic deformation can be a percentage of the lateral drift of the frame. Therefore, the column rotation θ can be express as the design drift θ_d minus the yield rotation θ_y and therefore the effective beam rotation can be evaluated as

$$\theta_b = \frac{\theta}{\left(1 - \frac{h_c}{l_b}\right)} \tag{3.1}$$

Where l_b is the ideal beam length from centre to centre of the joints and h_c is the column depth.

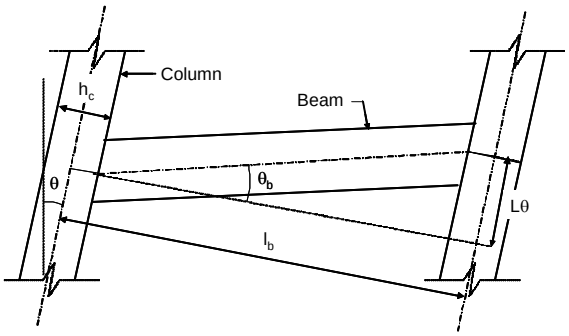

Figure 3.3. Effective beam rotation and inter-storey drift rotation using rigid body of the elements Modify after [3.6]

The next step is to evaluate the strain and the elongation in the unbonded post-tensioned tendons and energy dissipation due to the gap opening. Assuming that the tendon location is at mid-height of the section (Figure 3.4), the elongation (elastic + plastic) at the level of the tendon can be calculated as:

$$\Delta_{pt} = \theta_b \left(\frac{h}{2} - c \right) \tag{3.2}$$

The unbonded post-tensioned tendon strain is calculated as

$$\varepsilon_{pt} = \frac{n\Delta_{pt}}{l_{unb}} \tag{3.3}$$

where h is the beam section height, c the neutral axis position, n the number of total openings along the beam and l_{unb} is the unbonded length of the tendons.

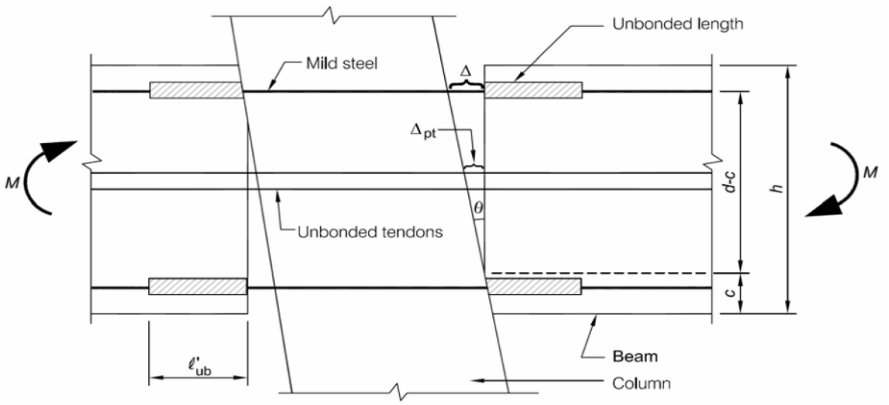

Figure 3.4. Rocking mechanism of the hybrid beam-column connection. Modify after [3.6]

Similarly, the elongation at the level of the mild steel, due to the gap opening Δ can be evaluated according with (3.4) where d is the beam section depth

$$\Delta = \theta_b (d - c) \tag{3.4}$$

And the strain in the mild steel ε_s can be evaluated as

$$\varepsilon_s = \frac{(\Delta - 2\Delta_{sp})}{l'_{unb}} \tag{3.5}$$

Where l'_{unb} is the unbonded length of the mild steel and Δ_{sp} is the elongation due to strain penetration, assumed to occur at both ends of the unbonded region, which can be evaluated as a portion of the elastic strain and plastic strain steel contributions [3.8].

$$\Delta_{sp} = \frac{2}{3} l_{sp} \varepsilon_e + l_{sp} \varepsilon_p \tag{3.6}$$

Where ε_e and ε_p are the elastic and plastic strains in the beam reinforcement, and l_{sp} is the length of the strain penetration equal to $l_{sp} = 0.022 d_b f_y$ evaluated as a product of the bar diameter d_b and the yield stress of the bar f_y

Doing some simplifications, the strain in the mild steel can be calculated as:

$$\varepsilon_s = \frac{(\Delta - \frac{2}{3} l_{sp} \alpha \varepsilon_y)}{\left(l'_{unb} + 2 l_{sp}\right)} \tag{3.7}$$

Where α is the ratio of the elastic and yield strain in the steel $\alpha = \varepsilon_e / \varepsilon_y$

The next step in the calculation is the estimation of the strain in the concrete ε_c which can be derived from any stress-strain concrete models available in literature. Two equations are required to solve the two unknown values. Section analysis and member compatibility conditions (the monolithic beam analogy) are used. However, a simplified procedure can be used assuming a triangular or rectangular concrete stress-block where there is no need to calculate the strain in the concrete.

If a refined stress-strain concrete relationship is adopted, two more equations are required to solve the system. The basis of the monolithic beam analogy is the assumption that a pre-cast ductile connection and a monolithic connection are compatible. Therefore, a pre-cast ductile connection and a monolithic connection will give the same beam deflection at the point of contra-flexure. This is illustrated in Figure 3.5.

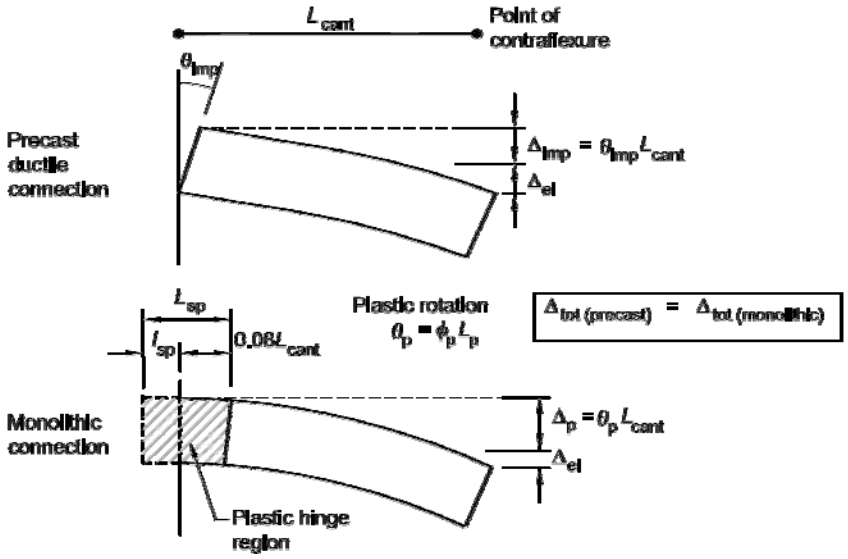

Figure 3.5 Monolithic beam analogies. Modify after [3.6]

Based on previously proposed yield curvature concepts [3.9], the plastic deformations from the precast and monolithic joints can be equated. Therefore, the strain in the concrete ε_c can be found by the tri-angular relationship between the ultimate curvature ϕ_u and the neutral axis position c.

$$\phi_u = \frac{\varepsilon_c}{c} = \left[\frac{\theta_{imp} L_{cant}}{\left(L_{cant} - \frac{L_p}{2} \right) L_p} + \phi_y \right] \tag{3.8}$$

Where L_{cant} is the distance from the interface and the point of contra flexure, θ_{imp} the imposed rigid rotation at the beam column joint interface, ϕ_y the yield curvature, L_p the plastic hinge length proposed [3.9] as $L_p = 0.08l + 0.022 d_b f_y$ and c neutral axis position.

The next step in the process is the section equilibrium by evaluating the compression concrete stress block, the forces in the energy dissipation and the force in the tendon. Once sectional equilibrium is obtained, the moment capacity is evaluated by taking moments about the compression concrete centroid. This process is iterative and so the calculations were performed using an excel spread sheet.

3.3 ALTERNATIVE SOLUTIONS FOR HYBRID SYSTEMS

Innovative alternative arrangements on improved and advanced solutions of post-tensioned jointed ductile “hybrid” connections for precast concrete buildings have been presented in the literature [3.10]. The proposed solutions accommodate different structural or architectural needs while respecting considerations on cost-effectiveness by varying the following key parameters:

3.3.1 Shear Transfer Mechanism

Shear transfer mechanism was investigated by relying either on friction due to the post-tensioned tendon contributions, and/or the dowel action in the mild steel. Additionally, other sources of shear transfer were investigated by using metallic slotted connections using single or double mechanical hinges acting as shear keys.

3.3.2 Sources and Location of Energy Dissipation

Internal or external supplemental damping devices relying on mild steel and implemented following a passive control approach were investigated. Internal mild steel dissipaters were inserted in embedded metallic corrugated ducts and grouted.

External replaceable mild steel dissipaters were proposed due to the peculiar "undamageable" properties of an hybrid systems, where only the energy dissipaters act as sacrificial fuses and might be required to be substituted after a test (or after an earthquake event). Location can be either protruding from the beam face or hidden inside of a cage for architectural purposes.

3.3.3 Post-tensioned Tendon Profile

Different arrangements for the longitudinal post-tensioned tendons profile were studied: straight, draped tendons/cable profile solutions or combination of profiles depending on the contribution of the gravity and lateral loads effects, considering different levels of seismicity (target design earthquake) as well as of the assigned role of the system during the seismic response (i.e. gravity-load only system, seismic resisting system or intermediate solutions).

3.4 EXPERIMENTAL INVESTIGATION ON ALTERNATIVE SOLUTIONS FOR HYBRID CONNECTIONS

The experimental program shows the results obtained in the Structural Laboratory at the University of Canterbury on the refinement and development of alternative arrangements for hybrid precast building systems.

Particular attention will be given to the quasi-static cyclic tests, under uni- and/or bi-directional testing regimes, on a series of exterior 2-D or 3-D, 2/3 scaled, beam-column joint subassemblies with the intent of evaluating the performance of recently implemented concepts and details as well as to validate the efficiency of the numerical/analytical models used for design and analysis purposes.

According to the previously defined key features of alternative hybrid systems, the configurations herein presented comprise of solutions with either straight or parabolic tendons, relying on either unbonded post-tensioned tendons only or on the addition of internal or external energy dissipaters. Implementation and testing of simple and effective shear keys at the critical

section interface, as an alternative to the friction mechanism due to the unbonded post-tensioned tendons as accepted in literature [3.2] will also be presented.

3.4.1 Specimen Description

A five-storey monolithic reinforced concrete frame prototype building (3.0m inter-storey height) consisting of three bays of 4.5m long was designed following a direct displacement based design (DDBD) procedure [3.11] for which the calculations can be found in Appendix A. After distributing the base shear, the internal actions were scaled to respect similitude requirements for the test specimen given a beam moment capacity of $M_b^* = 30\ kNm$. Therefore, as part of the experimental research investigation herein reported, MJ1 and MJ2 are two monolithic beam column joints designed according to the NZ3101:1995 code provisions subjected to uni-directional and bi-directional "four clove" protocol respectively.

HJ1 represents a Hybrid PRESSS beam column joint solution described in literature [3.11]. HJ2 is a 2-D hybrid PRESSS – Brooklyn type beam column joint which consists of a PRESSS-Brooklyn hybrid system with parabolic tendon profile and the use of corbel for shear transfer mechanism at initial stage and double hinge at the second stage of testing.

HJ3 was prepared with a modular configuration such that 2-D or 3-D exterior (corner) beam-column joint subassemblies with several alternative arrangements of post-tensioning profiles could be tested after replacing the dissipating devices. Shear transfer mechanism was obtained using metallic spherical balls acting as double hinges. Table 3.1 summarizes the specimen ID and the material properties for each specimen.

Table 3.1 Sub assemblage ID and material properties of the specimens.

Specimen ID	Connection Type	Test Type	f'c (MPa)	fy (MPa)				
				Bar Diameter (mm)				
				6	7	8	10	12
MJ1	Monolithic	2-D	32.9	390	-	-	-	320
MJ2	Monolithic	3-D	29.2	390	-	-	-	320
HJ1	Hybrid PRESSS	2-D	21.8	-	-	-	336	-
HJ2	Hybrid PRESSS-Brooklyn corbel / double hinge	2-D	38.7	-	350	-	-	-
HJ3	Advanced Hybrid double Hinge	2-D and 3-D	55.2	-	330	330	-	-

3.4.1.1 2-D (MJ1) and 3-D (MJ2) Monolithic Beam-Column Subassemblies

The 2-D and 3-D monolithic exterior beam-column joint reinforced concrete specimens MJ1 and MJ2 (Table 3.2) were designed according to NZS3101: 1995 as it is representative of a large number of existing buildings. The amount of longitudinal steel reinforcement for the column and beam was fixed to equal approximately 2% and 0.55% of their concrete gross cross-sectional areas (NZS3101:1995 allows a minimum of 0.8% and 0.42% for columns and beams respectively). The beam was reinforced using 4-D12 deformed longitudinal bars top and bottom and D6 plain transverse steel spaced 70mm in plastic hinge zones. The column was reinforced with 12-D12 longitudinal bars and D6 ties spaced 60 mm in potential plastic hinge zones.

For MJ1, the specimen was cast flat rather in contrast to MJ2 which was cast vertically as in actual construction. After the reinforcing cage was assembled and placed inside the formwork, the concrete was placed and internally vibrated. The specimen was moist cured for a period of seven days inside the formwork. Forms were removed after seven days and the specimen was stored in the laboratory until it was tested. A concrete mix using Type I Portland cement and coarse aggregate with maximum dimension of 13 mm was used. The slump was kept at about 130 mm for ease of placement. The test day compressive strength for the concrete cylinders and the average yield stress for the reinforcing steel are presented in Table 3.1.

3.4.1.2 Hybrid PRESSS Beam-Column Subassembly (HJ1)

Table 3.2 shows HJ1, a Hybrid PRESSS type connection. The specimen comprised a) straight profile longitudinal tendons; b) internal mild steel bars as dissipation devices and c) friction at the critical beam-column section as the shear transfer mechanism. To ensure a certain hierarchy of strength in the joint and for comparison purpose, the specimen was designed to have approximately the same flexural capacity of the Monolithic solution specimen (MJ1). Two tests were carried out using this specimen:

First test HJ1-60PT corresponds to the unbonded post-tensioned only solution using a seven wire strand with an area of A_{pt} = 99mm^2 and an initial post-tensioning force at 60% of the ultimate stress $\sigma_{pt\ ult}$ = 1860MPa, thus equal to an initial post-tensioning force of $F_{pt\ ini}$=110 kN.

The second test HJ1-60PT-10D was implemented adding energy dissipation to the unbonded post-tensioned solution in the form of four deformed longitudinal mild steel reinforcing bars (two top and bottom 10 mm diameter), inserted in embedded metallic corrugated ducts and grouted. In order to prevent premature fracturing of the steel, an unbonded length of 50 mm

was adopted by wrapping plastic tape around the bars in the vicinity of the critical section (Figure 3.6).

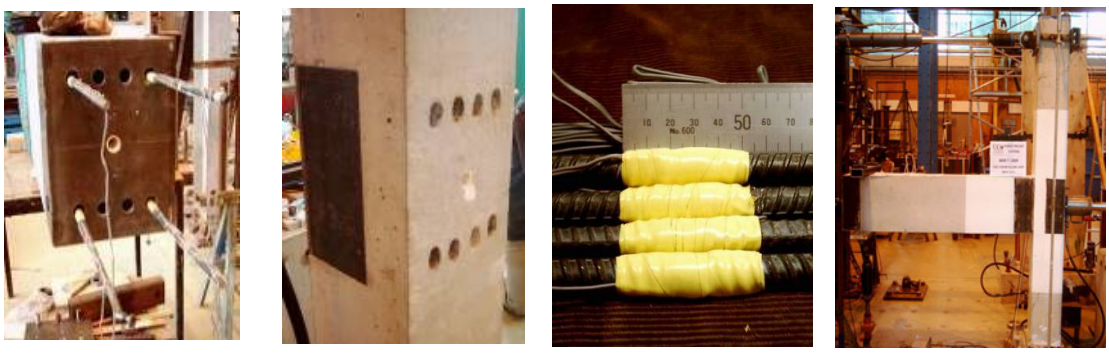

Figure 3.6. Construction details of HJ1 Specimen

Table 3.2–Geometry of Sub assemblages

Specimen ID	Geometry	Section A-A	Section B-B
MJ1 and MJ2	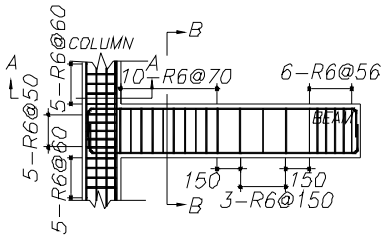	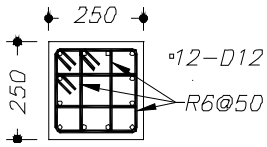	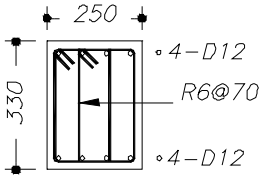
HJ1	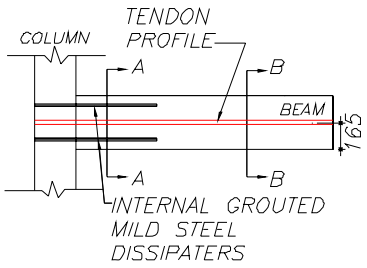	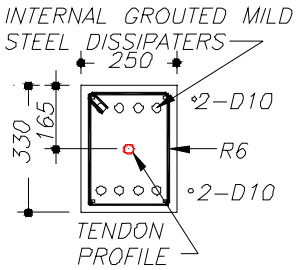	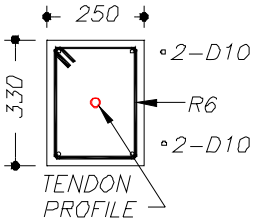
HJ2	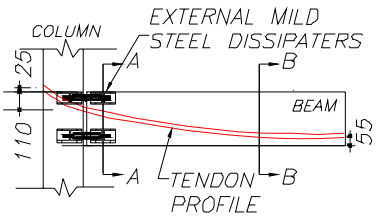	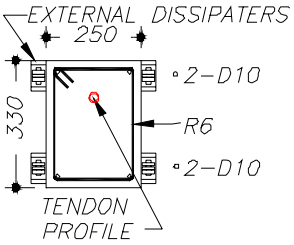	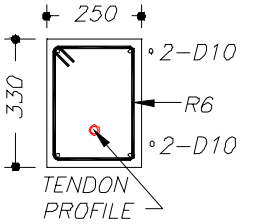
HJ3	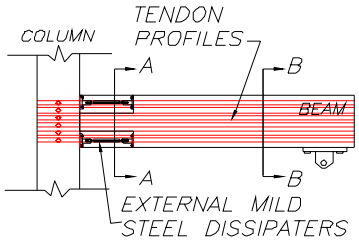	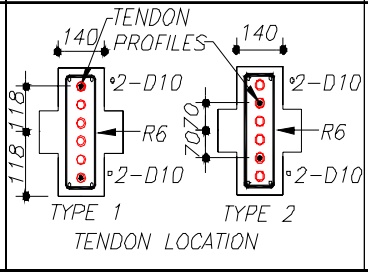	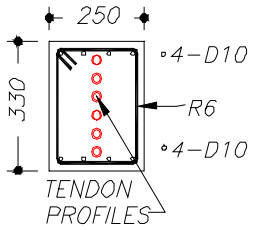

3.4.1.3 Hybrid PRESSS-Brooklyn Beam-Column Subassembly (HJ2)

Based on similar concepts to the hybrid systems, Table 3.2 shows HJ2 which was constructed using similar principles as the "Brooklyn" system [3.12]. The key peculiarities of the connection are:

a) External energy dissipaters: the design criterion for external energy dissipaters was to allow replacement after a seismic event. Permanent 10 mm steel plates acting as a footings were cast flush with the surface of the concrete and support was provided by welding 12 mm dowels between the plates. The plates and dowels were then welded to the reinforcing cage and placed in the formwork prior to casting of the concrete. Eight energy dissipater footings were made from 75 x 40 mm PFC cut down to 150 mm lengths with an 18 mm steel bar welded centrally between the flanges as shown in Figure 3.7-left.

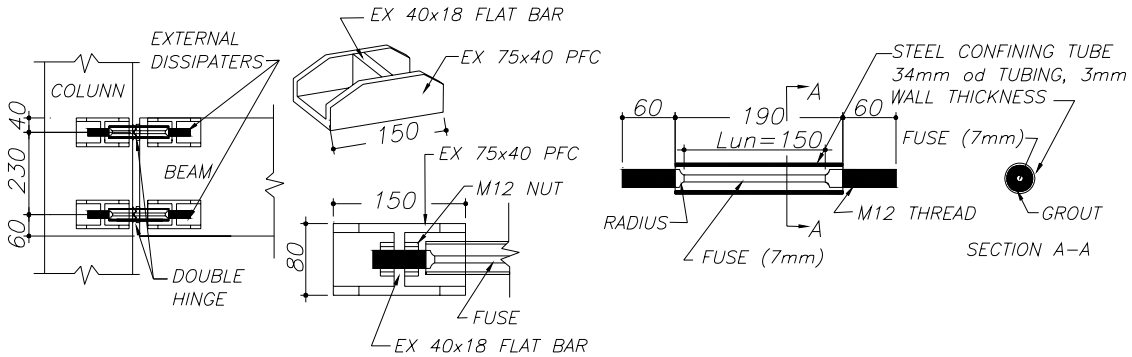

Fig. 3.7 Energy dissipater footing (left) and rods (right) used in HJ2 Specimen.

The flat bar has a 12.5 mm hole drilled in it for the threaded dissipater rods to fit through. These rods were then fastened to a 12 mm bar with a nut on either side to prevent movement during both compression and tension of the energy dissipater. The dissipater rods were fastened to the footings so that they are able to be replaced easily and consisted of a 12 mm round bar threaded at the bar ends and machined down at 7 mm with a 150 mm unbonded length (Figure 3.7-right) and inserted into grouted metallic cylinders (anti-buckling restrainers). The rods ends were designed such that no yield stress would occur at the ends while all the plastic deformation occurred in the critical section.

b) Corbel: The use of alternative solutions for steel shear bracket/corbel (Figure 3.8-left), able to fully counteract the shear force transmitted at the beam-column interface. In this way the prestressing tendons have only to balance flexural stresses and a large floor slab span can be achieved. Undesirable consequences related to the yielding or failure of the tendons, or in

general, due to the loss of the shear friction transfer mechanism, are thus overcome, in line with recent requirements in code provisions [3.1]. Also, by "hiding" the corbel in the depth of the beam, architectural and aesthetic requirements (in addition to fire resistance) can be met.

The corbel was designed to support the beam in shear before the post tensioning of the tendon was applied and during cyclic seismic loading. The corbel comprised of a 50 mm length of 100x50 RHS, welded to a 10 mm plate that is bolted to pre-cast mounts in the column. The RHS had a semi-circular slot taken out of the two sides and the upper face folded down. This was to provide a bearing surface that would maintain bearing contact with the beam above without inducing any uplift. A thin cover of foam was glued to the bearing surface to minimize damage the corbel would cause to the concrete bearing surface in the beam.

It is worth mentioning that in the first phase, experimental tests were carried out adopting a typical friction-type shear transfer mechanism at the beam-column interface, with the corbel acting only as a support for the gravity loads. However, the excessive slipping observed at the rocking interface, due to the combination of upward seismic shear force and the vertical component of the tendon force, suggested the adoption of a bilateral restraining corbel solution.

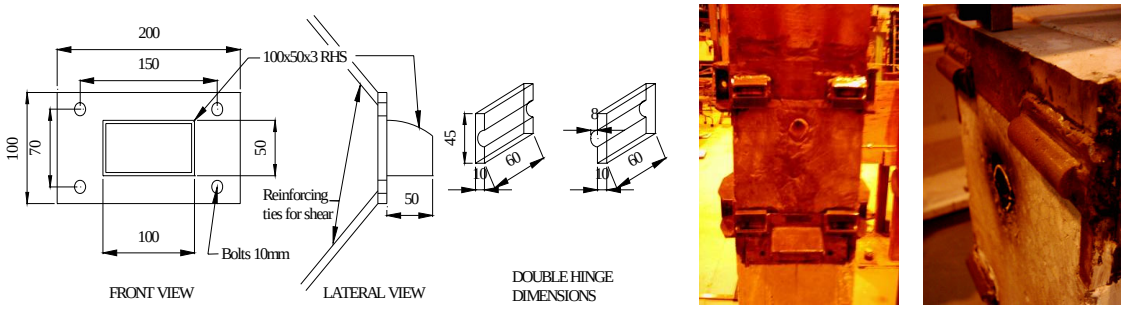

Figure 3.8–Corbel details (left) and double hinge solution (right) used in HJ2 Specimen.

c) Given the previous considerations the concept of a "double hinge" shear key was developed and successfully implemented with the intent to provide adequate bilateral (i.e. either upwards or downwards direction) shear transfer mechanism at the critical section.

As shown in Figure 3.8-right, two shear key "hinges" consisting of two half cylinders with convex and concave edge were respectively welded to a steel plate at the end of the beam and column faces at the level of the external dissipation devices. As a result, the controlled rocking motion occurs about two pivot points and is thus significantly simplified. For this test the locations of the hinges were at 40 mm and 60 mm from the top and bottom of the beam section respectively.

d) Draped tendon profile: the use of a draped tendon profile anchored at the exterior columns of the frame in order to supply an adequate moment resistance at the critical sections under combined gravity and low-to-moderate lateral loads was considered. Three tests were carried out considering different levels of initial post-tensioning using a seven wire strand A_{pt} = 99mm^2 to obtain the unbonded post-tensioned only solution.

The tests HJ2-35PT, HJ2-55PT and HJ2-70PT correspond to the unbonded post-tensioned only solution varying the initial post-tensioning force at 35%, 55% and 70% of the ultimate stress $\sigma_{pt\,ult}$ = 1860MPa, thus equal to an initial post-tensioning forces of $F_{pt\,ini}$ = 65kN, 100kN and 125kN respectively. A fourth test HJ2-70PT-7D was performed adding external energy dissipation to the unbonded post-tensioned force of 70% in the form of 7 mm fuse bars with 150 mm of unbonded length for comparison results.

3.4.1.4 Advanced Hybrid beam-column Subassembly (HJ3)

Using similar principles as explained for specimen HJ2, specimen HJ3 (Table 3.2) was designed using a modular configuration, such that several alternative arrangements of hybrid systems could be tested. The specimen comprised of:

a) Double Hinges: a flexible face plate, acting as a sort of “mask”, was located at both the beam and column faces with different possible locations of the mechanical hinges acting as shear key solutions. These hinges were metallic spherical balls of 15 mm diameter inserted into the steel plates which were previously milled and allowed for a gap between the column and beam at the critical section of 4 mm. The selection of aspheric balls over the previous cylinder solution was due to the implementation of 3-D testing in the beam-column joint subassembly. Figure 3.9-left shows the location and implementation in the beam-column joint subassembly. For this set of tests the hinge location was at 47 mm from the top and bottom of the beam section.

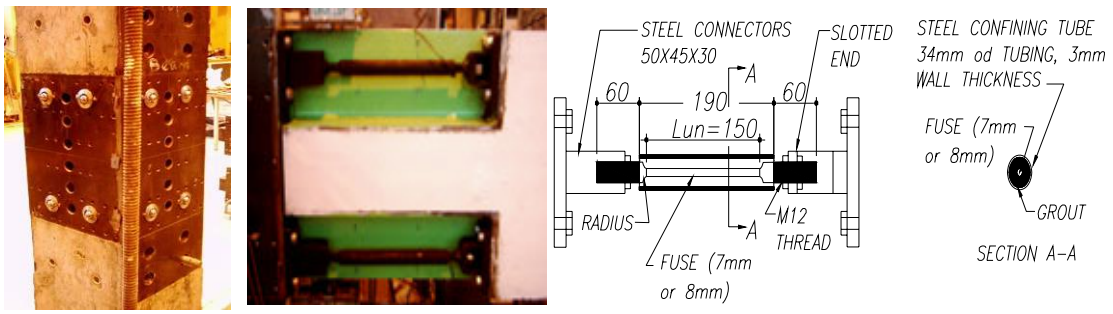

Figure 3.9. Double hinge shear key (left) and external dissipater (centre) and dissipators rods detail (right) used in HJ3

b) Replaceable external energy dissipaters: These dissipaters were located 47mm from the top and bottom at the beam end inside of a pocket "hidden" for architectural use. Steel connectors of 50 x 45 x 30 mm were used to attach the dissipaters to the column and beam elements. At one end these connectors consisted of a block having a single threaded hole while at the opposite end a slotted connection was used. This meant that the dissipater could be bolted in, thus solving the tolerances issues usually associated with precast construction (Figure 3.9-centre).

The mild steel dissipater (Figure 3.9-right) is fabricated from a round mild steel bar, threaded at each end and machined down to a specific bar diameter over a pre-determined length; defined as the unbonded length. The unbonded length prevents premature fracture of the bar by limiting the strains to allowable values. A steel tube is placed over the machined area of the steel bar, temporarily fixed in place and filled with epoxy or grout meaning the steel confinement tube acts as an anti-buckling restraint.

c) Straight tendon profile: six different configurations for straight longitudinal tendon profiles could be implemented. This report for analysis and comparison refers to two tendon profiles. Tendon location type 1 corresponds to two tendons (one each) located at 118 mm from the beam centerline (Table 3.2). Two unbonded post-tensioned only solutions were adopted. HJ3-15PT1 and HJ3-25PT1 correspond to initial post-tensioning forces of 15% and 25% of the ultimate stress $\sigma_{pt\ ult}$ = 1860MPa, thus equal to an initial post-tensioning force of $F_{pt\ ini}$ = 27.5kN and 46.0kN respectively.

In order to compare the behavior of the mechanical hinges and the effects in the beam-column joint moment contribution, a third test HJ3-27PT2 was carried out using location type 2 where the two tendons were located at 70 mm from the beam centerline (Table 3.2). Two more tests HJ3-25PT1-7D and HJ3-27PT2-8D were performed adding external energy dissipation to the unbonded post-tensioned solution in the form of 7 and 8 mm fuse bars with 150 mm of unbonded length for result comparisons.

In order to explore the response of the advanced hybrid subassembly under a combined bidirectional "four clove" loading protocol, two tests were carried out: HJ3-X25PT1-Y27PT2 and HJ3-X25PT1-Y27PT2-X7D-Y8D where the prefix X and Y means the two orthogonal directions (Figure 3.11). A summary of these tests is presented in table 3.3

3.5 TEST SET UP AND LOADING PROTOCOL

Figure 3.10-left shows an elevation view of the typical set-up of the beam-column joint subassemblies. In the setup, beam and column elements are extended between points of contra flexure, assumed to be at mid-span of the beams and at mid-height of the columns, where pins are introduced. The column was displaced horizontally by a servo-controlled hydraulic actuator located at the point of inflexion. Simple supports at the beam ends were provided by connecting pin-end steel members to the floor. Axial load was applied on the top of the column using a jack pushing against a top steel plate and clamping down with the bottom column pin.

Table 3.3–Test summary

Specimen ID	Test Type	Test ID	$T_{pt\,ini}$ (kN)	$(N/No)_{min,ini,max}$ (%)	Description
MJ1	2-D	MJ1	N/A	0.6, 1.0, 1.4	Monolithic beam column subassembly
MJ2	3-D	MJ2	N/A	0.5, 1.0, 1.6	Monolithic beam column subassembly
HJ1	2-D	HJ1-60PT	110.0	1.0	Hybrid PRESSS only PT solution (60%PTult)
		HJ1-60PT-10D	110.0	1.0	Hybrid PRESSS 10mm fuse and 60%PT_{ult}
HJ2	2-D	HJ2-35PT	64.5	1.0	Hybrid PRESSS-Brooklyn only PT solution (35%PT_{ult})
		HJ2-55PT	101.2	1.0	Hybrid PRESSS-Brooklyn only PT solution (55%PT_{ult})
		HJ2-70PT	128.9	1.0	Hybrid PRESSS-Brooklyn only PT solution (70%PT_{ult})
		HJ2-70PT-7D	128.9	1.0	Hybrid PRESSS-Brooklyn 7mm fuse and 70%PT_{ult}
HJ3	2-D	HJ3-15PT1	27.6	1.0	Advanced Hybrid double hinge only PT solution (15%PT_{ult}) tendon location type 1
		HJ3-25PT1	46.0	1.0	Advanced Hybrid double hinge only PT solution (27%PT_{ult}) tendon location type 1
		HJ3-27PT2	49.7	1.0	Advanced Hybrid double hinge only PT solution (27%PT_{ult}) tendon location type 2
		HJ3-25PT1-7D	46.0	1.0	Advanced Hybrid double hinge 7mm fuse and 25%PT_{ult} tendon location type 1
		HJ3-27PT2-8D	49.7	1.0	Advanced Hybrid double hinge 8mm fuse and 27%PT_{ult} tendon location type 2
	3-D	HJ3-X25PT1-Y27PT2	46.0 in X and 49.7 in Y	1.0	Advanced Hybrid double hinge only PT solution (25%PT_{ult} tendon location type 1 in X and 27PT_{ult} tendon location type 2 in Y)
		HJ3-X25PT1-Y27PT2-X7D-Y8D	46.0 in X and 49.7 in Y	1.0	Advanced Hybrid double hinge 7mm fuse and 25%PT_{ult} tendon location type 1 in X; 8mm fuse and 27PT_{ult} tendon location type 2 in Y

Variation in column axial load was considered only for the monolithic beam-column joints MJ1 and MJ2 with an initial load of $N_o = 65\text{kN}$ which represents the load of the prototype structure. Variation of the load was changed through the protocol software as the specimen was displaced; meanwhile a constant axial load of $N_o = 100\text{kN}$ was applied to the rest of the subassemblies since axial load has no effect on the joint shear strength for these particular systems. Table 3.3 shows the initial, minimum and maximum axial load values with respect to the initial axial load.

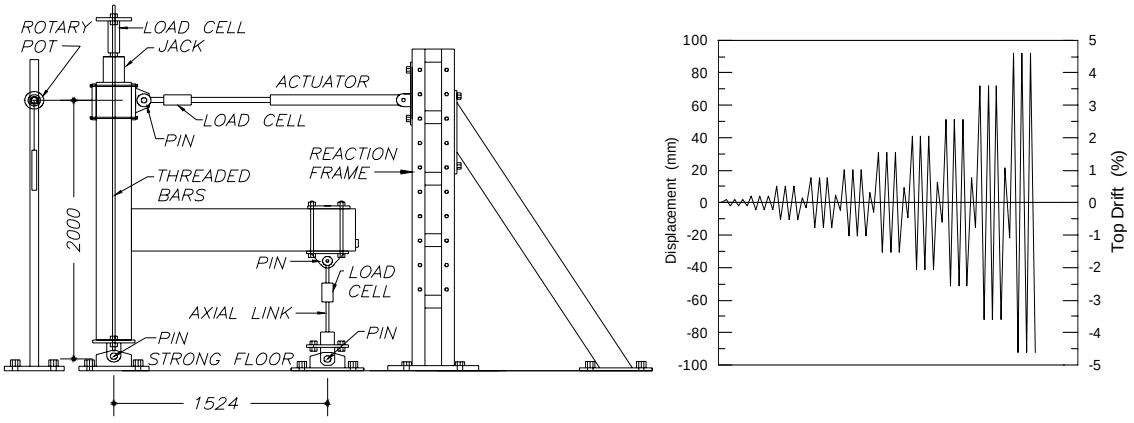

Figure 3.10. General uni-directional test set-up (left) and uni directional loading protocol (right).

The specimens were extensively instrumented. Internal strain gauges were used on the longitudinal bars and ties in both beam and column for the monolithic beam column joint subassembly. Strain gauges were used in the hybrid beam column joint subassemblies especially for the internal or external mild steel bars used as energy dissipation devices. Potentiometers and LVDTs were located selectively at the critical sections such that measurements of curvature, rotations, deformations and displacements could be obtained from the experiments. Load cells were installed on top of the column, at the level of the hydraulic actuator, at the end of the beam element and at the post-tensioning anchorages for the hybrid beam column joint subassemblies.

The 2-Dimensional loading regime consisted of quasi-static cycles of applied displacements at the top of the column using a rotary pot transducer independently installed from the specimen (Figure 3.10-right). The testing protocol complied with the recently proposed “acceptance criteria” [3.13] and consisted of a series of three identical cycles at same drift level with the amplitude increasing of each set not less than one and one-quarter times, and no more than one and one-half times, the previous drift ratio, followed by a smaller single cycle of one third of the last cycle.

As mentioned previously, MJ2 and HJ3 specimen were subjected to a combined bidirectional "four clove" loading protocol shown in Figure 3.11. Three cycles per combined drift level, plus one smaller amplitude cycle, were carried out in each quadrant, with similar conceptual protocol adopted for the uni-directional testing [3.13]. As a result, it is worth noting that the specimen is actually subjected to a more demanding protocol, with a cumulative number of six cycles in each direction per drift level, instead of the three cycles in the uni-directional testing protocol.

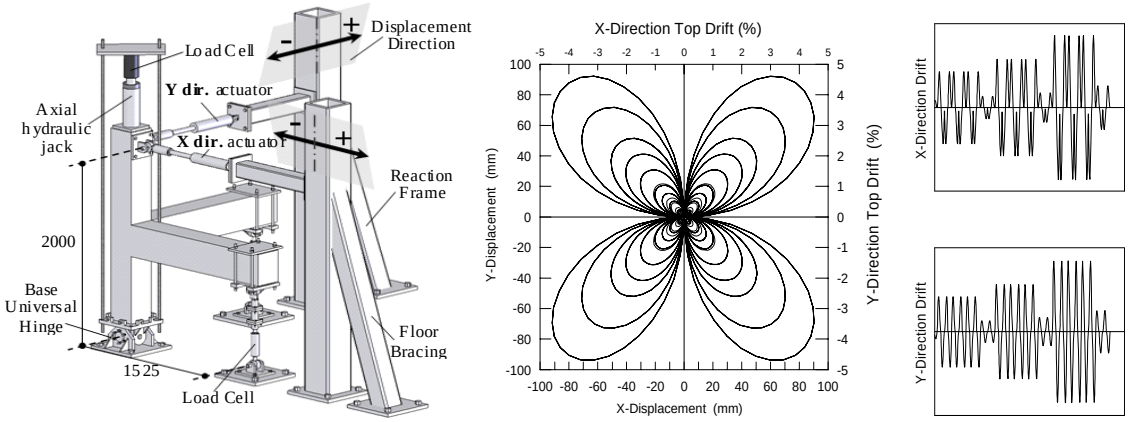

Figure 3.11. Test set-up and four cove bi-directional displacement regime for MJ2 and HJ3. (Courtesy: Umut Akgüzel [3.14]).

3.6 EXPERIMENTAL RESPONSE

3.6.1 Response of the Monolithic specimen MJ1

The total lateral force versus drift and the observed damage at 4.5% of drift level are presented in Figure 3.12. As expected by the adoption of capacity design considerations targeting the development of a weak beam strong column mechanism, the damage is concentrated in the plastic hinge region leading to progressing flexural cracking and spalling of the concrete. In general, a very stable fat hysteresis loop typical of ductile cast-in-place reinforced concrete connection with high energy dissipation capacity was observed.

The response of the specimen was elastic at 0.1% drift; the first flexural cracks appeared at 0.2% drift as hair line cracks at the beam-column interface. At 0.5% of drift, new flexural cracks from top and bottom beam plastic hinge location were formed. Additionally, the cracks that formed in the beam-column interface at 0.2% drift, encircled the whole perimeter of the joint with 0.1mm crack widths. At 0.75% drift, first hairline diagonal crack was observed from top end beam crossing down the beam-column joint core and flexural cracks were observed around the outer column face which continued propagating until 1.0% of drift.

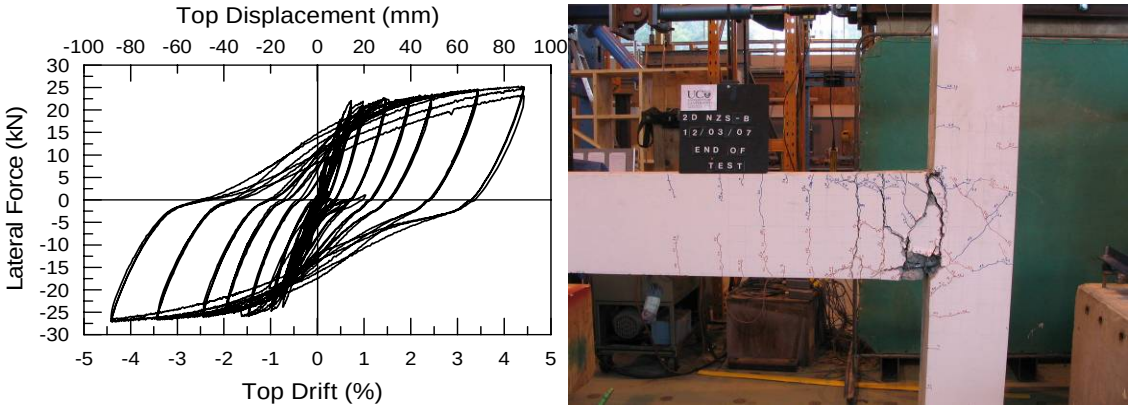

Figure 3.12. Hysteresis response of MJ1 (left) and Observed damage at 4.5% drift (right).

Initial cracks developed at the beam column interface continued to propagate creating a hinge mechanism (1.8mm crack widths) and additional hair line diagonal crack was formed from bottom beam end up the beam-column joint core at 1.5% of drift. From 2.0% to 4.5% of drifts, the development of flexural cracking along the plastic hinge beam region was observed. Small cracks from beam top and bottom at the outer column face were developed as well as increments of diagonal cracking at the beam column joint core.

3.6.2 Response of the Monolithic specimen MJ2

The general behaviour and failure mechanisms are described as follows:

The response of the specimen was elastic during the first cycle (0.1% drift). The first flexural cracks appeared as hair line cracks concurrently at both beam-column interfaces at 2nd cycle (0.2% drift). In addition, minor flexural cracks occurred in both directions at a distance of 100 mm and 240 mm from the faces of the column respectively. Apart from the new flexural cracks formed in the X and Y directions at a distance of 300 mm and 500 mm, during the 3rd cycle (0.5% drift) previously formed flexural cracks on the beams extended so that the bottom and top flexural cracks joined together. Cracks that formed in the beam-column interfaces encircled the whole perimeter of the joint.

During the 4th cycle (0.75% drift), the first hairline diagonal cracks were observed in the beam-column joint core in both directions. In the following cycle (1.0% drift), flexural cracks were observed around the column tension sides approximately 200mm and 150mm below and above the beam level respectively. At the 6th and 7th cycles (1.5% and 2.0% drift), uniformly distributed cracks materialized in the joint region and propagated into the adjacent beams and horizontally into the column. Planar cracks developed in the joint cover concrete but did not

detach and fall. Spalling initiated in the upper and bottom interfaces of the joint. At the end of the 7th cycle, residual crack widths on beams and columns were around 0.1-0.4mm and on joint were 0.2-1.4mm. Residual crack width of the interface crack in the middle was 3.5mm.

At the 8th and 9th cycle (2.5% and 3.5% drift), with the extension of cracks formed at the joint 175mm under the beam, concrete crushing and spalling at the corner occurred. At first sight it can be seen that since the specimen was designed according to current NZS3101:1995 code, plastic deformation or hinging of the beam was expected which is the current design target.

Figure 3.13 and Figure 3.14 shows the hysteresis response and the observed level of damage at 2.5% drift for X and Y direction respectively. It is interesting to note that, in spite of the adoption of code-design provisions based on capacity design considerations, the bi-directional loading regime proved to be very demanding for the joint region. Extensive cracking of the joint panel zone developed at 2.5% drift level, progressively leading to crushing and spalling of the whole cover concrete in the joint panel zone region at 4.5% drift (Figure 3.15).

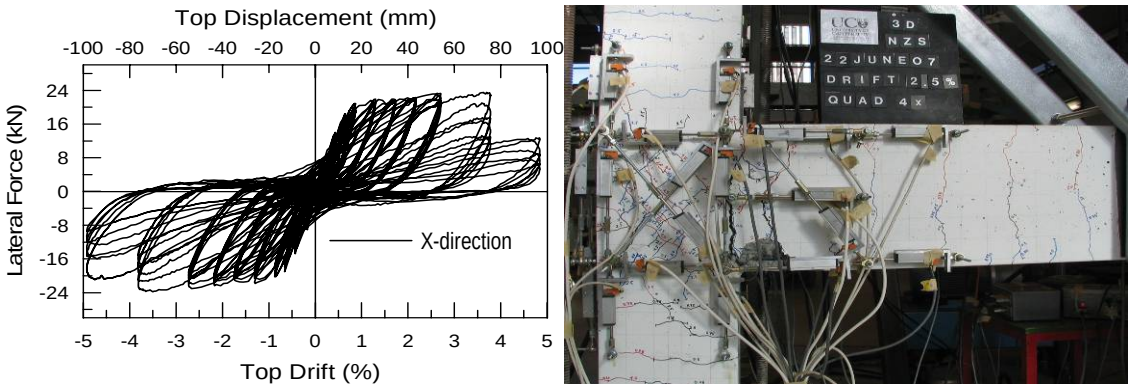

Figure 3.13. Hysteresis response of MJ2 in X-direction (left) and Observed damage at 2.5% drift (right)

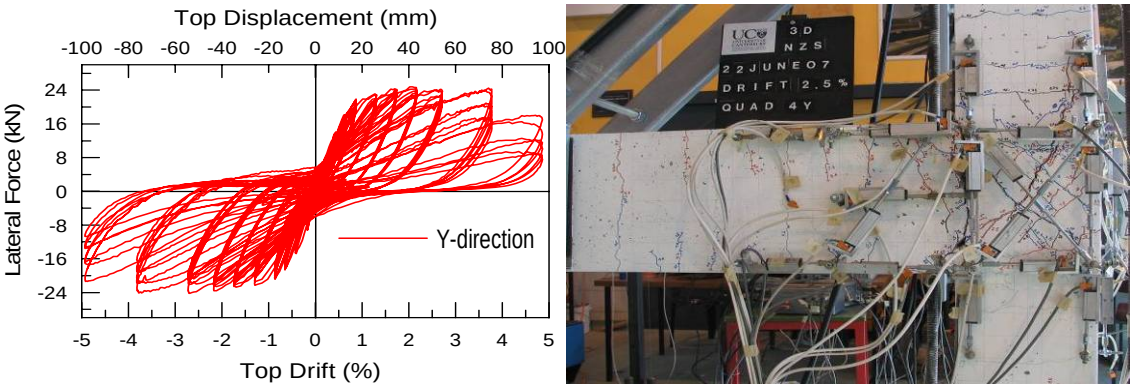

Figure 3.14. Hysteresis response of MJ2 in Y-direction (left) and Observed damage at 2.5% drift (right)

Due to the bond deterioration under the combined bi-directional loading, flexural cracking in the beam concentrated at the interface with the column through opening of a single crack, instead of developing within a traditional plastic hinge region. As a result, a marked pinching behaviour was observed in the hysteresis response at earlier level of drift, in addition to increasing level of stiffness and strength degradation.

Figure 3.15. Observed damage of MJ2 in X (left) and Y (centre) directions and joint damage (right) at end of test.

On the other hand, by visual inspection, it was observed during the experiment that, the transverse shear reinforcement that was provided within the joint region serves to add efficient confinement to the concrete, thereby increasing its compressive resistance and preserving integrity of the connection. Moreover, the cracks were well distributed over the beam region, no buckling of the longitudinal steel reinforcement or bond slip failure of the beam which is found to be a more brittle type of failure when compared with shear failure associated with a higher rate of strength deterioration reinforcement occurred.

3.6.3 Response of the Hybrid PRESSS specimen HJ1

Figure 3.16-left show the responses of HJ1-60PT and HJ1-60PT-10D. Typical of a jointed ductile hybrid solution, no damage was reported in the structural members. It can be seen a stable non linear elastic hysteresis behaviour for HJ1-60PT without remarkable losses of stiffness at any reloading stage while a very stable hysteresis loop with higher energy dissipation capacity was developed when adding energy dissipation devices. The onset of stiffness degradation between mild steel longitudinal bars and the grout due to the bond deterioration became more evident at the first cycle of 4.5% of drift.

Crushing of the concrete at the top and bottom of the column face in the critical section due to the protection of the beam by a steel plate started to occur at 2.5% drift (Figure 3.13-right) and additional torsion rotation about the longitudinal axis was observed at levels of 3.5% drift. This

torsion effect was primary due to the different strain demand that occurs in the mild steel bars. However, previous research [3.15] stated that torsional rotation effects occurred in hybrid connections due to the heavy floor hung eccentrically from the side of the beam. Therefore, a possible corbel detailing that takes into account this effect needs to be addressed.

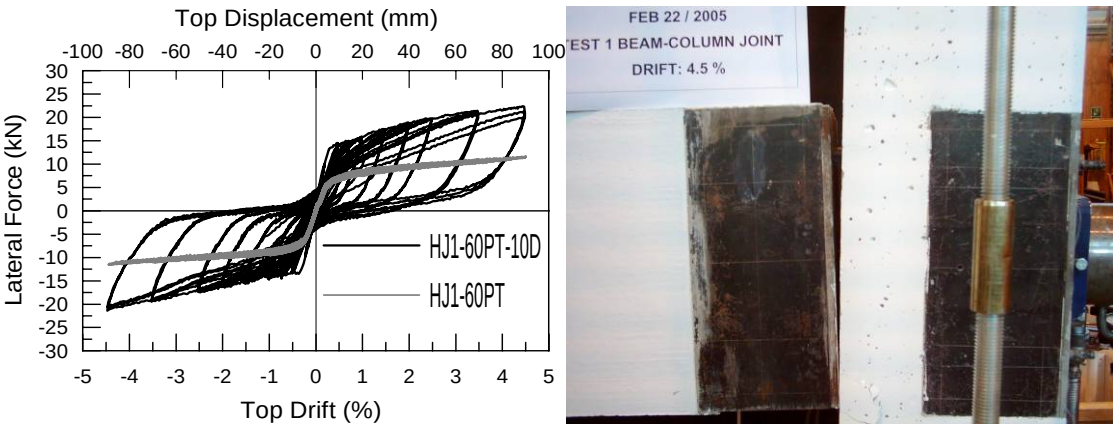

Figure 3.16. Hysteresis response of HJ1 with and without internal dissipaters (left) and gap opening at 4.5% of drift (right).

Figure 3.17 reports the variation of the tendon force versus the drift level as well as location of the neutral axis position along the beam height for test HJ1-60PT-10D. Due to this local column face damage a relocation of the neutral axis position is observed for the higher displacement demand.

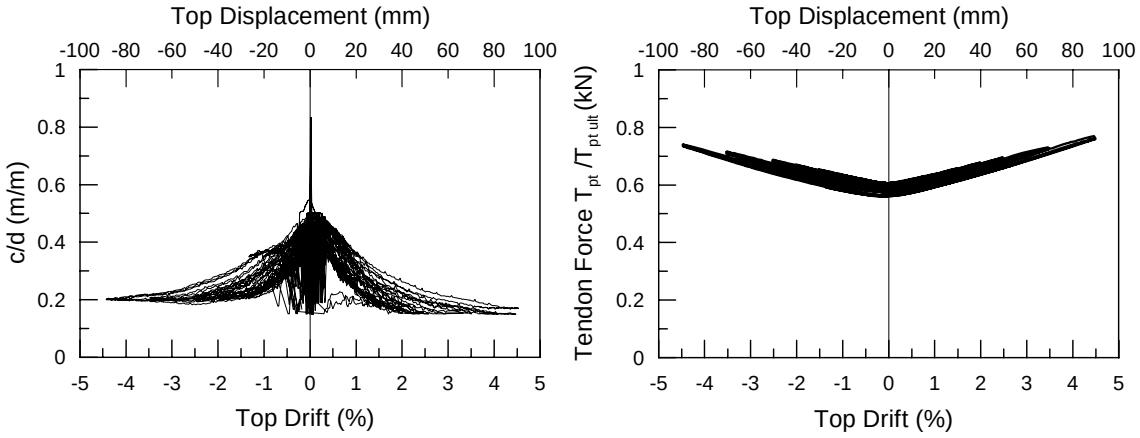

Figure 3.17. Location of the neutral axis position (left) and variation of tendon post-tensioning force (right).

3.6.4 Response of the Hybrid PRESSS-Brooklyn Beam-Column Subassembly HJ2

As it was described before, three tests were carried out considering different levels of initial prestressing to obtain the unbonded post-tensioned only solution and one hybrid test using

external energy dissipaters. It is shown in Figure 3.18-left the force displacement responses of HJ2-35PT, HJ2-55PT and HJ2-70PT with very stable non-linear elastic hysteresis behaviours. Some friction between the tendons and the duct is observed due to the draped profile.

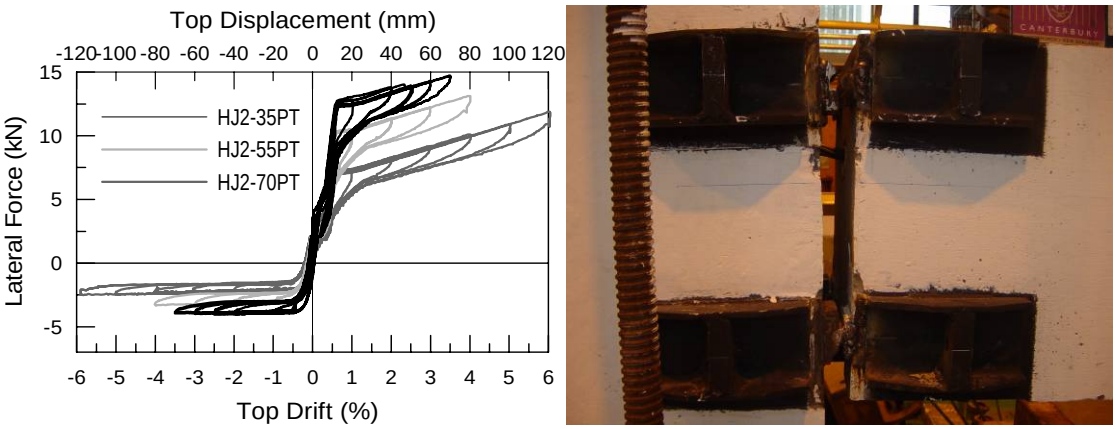

Figure 3.18. Hysteresis response of HJ2 for unbonded post-tensioned only solutions (left) and gap opening at 4.5% of drift (right)

As the system rocks around the two hinges located at the beam column joint interface (Figure 3.18-right), the neutral axis position is easily determined by simple triangular relationships and showed in Figure 3.19-left for HJ2-70PT. Very similar results are obtained for the other two tests. Due to the asymmetry of the hinges location along the beam section, it is observed that the gap opening of the top hinge is less than the bottom hinge as a result of the asymmetry of the hinge locations within the beam section (40 mm and 60 mm from the top and bottom of the beam section respectively).

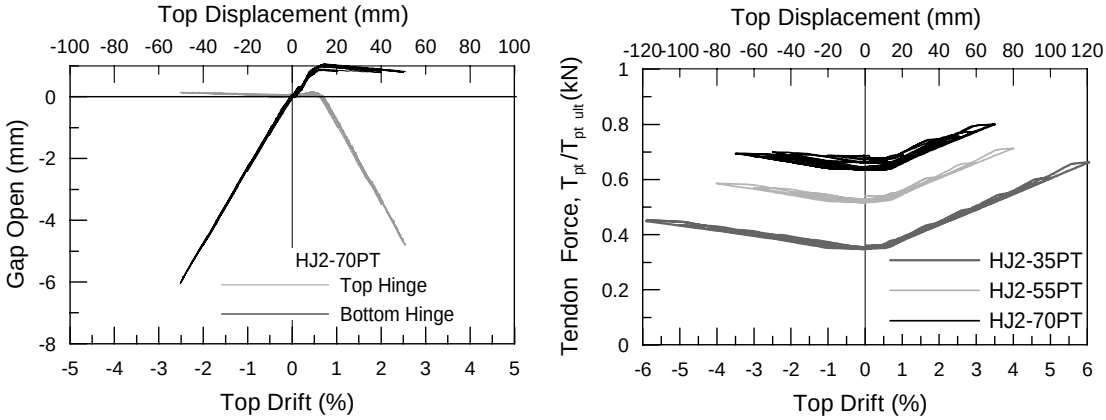

Figure 3.19. Gap opening variation at rocking (left) and variation of tendon post-tensioning forces for HJ2 (right).

The tendon force behaviour is shown in Fig. 3.19-right. As the top and bottom hinges are not located symmetrically at the critical section, an asymmetric behaviour is also shown for the

post-tensioned forces. It can be seen that as the gap opens at the bottom, higher tendon forces were obtained when compare to the gap opening at the top (negative drift) due to the higher distance between the location of tendon and the bottom hinge.

Figure 3.20-left shows the total force displacement response of HJ2-70PT and HJ2-70PT-7D. The later with a well defined flag-shape behaviour with full re-centering capability due to the external dissipater adopted (7mm with an unbonded length of 150mm, grouted into a steel cylinder acting as an anti-buckling restrainer) in addition to some friction between the tendons and the duct due to the draped profile already reported in the unbonded post-tensioned solution. In all cases, the observed asymmetric behaviour in terms of strength was due, as expected, to the non-central position of the cable within the section. Furthermore, no damage occurred up to design drift in the beam or column structural elements, a typical characteristic of a well-designed ductile jointed connection.

Similar to what is displayed in Figure 3.19-right, the variation of the gap open at the rocking interface is shown in Figure 3.21-left for test HJ2-70PT-7D. Some energy release is observed when compared to the post-tensioned only solution due to the energy dissipaters. As the gap opens, the dissipater elongates and yields in tension, as soon as the maximum displacement is reached and the reverse loading occurs, and the dissipater start compressing leaving some residual displacements after yield.

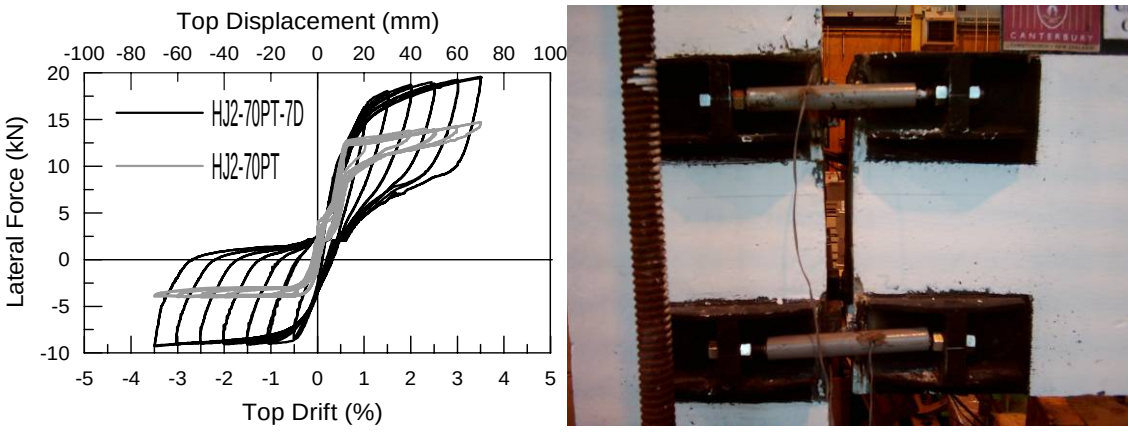

Figure 3.20. Hysteresis response of HJ2 with and without external dissipaters (left) and gap opening at 3.5% drift (right).

Figure 3.21-right shows the cyclic stress-strain / force-displacement for the 7 mm fuse adopted with an unbonded length of 150 mm. Very stable cyclic hysteresis behaviour is observed with failure of the dissipater at 8mm elongation which corresponds to 6% of axial strain.

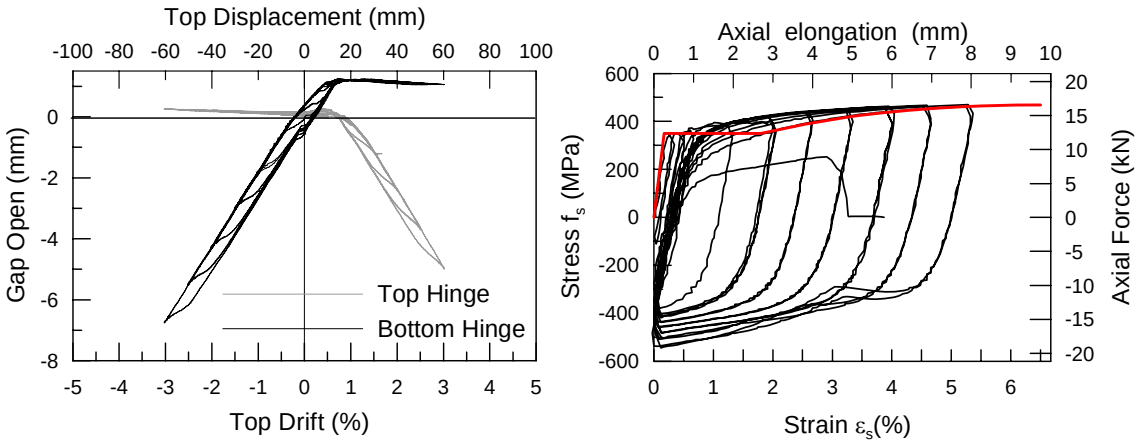

Figure 3.21. Gap opening variation at rocking (left) and Stress-strain / force-displacement of the external dissipaters used for HJ2 (right).

3.6.5 Response of the Advanced Hybrid Beam-Column Subassembly HJ3

Figure 3.22-left shows the responses of HJ3-15PT1 and HJ3-25PT1 with extremely satisfactory results. As expected, the bigger the initial post-tension force, the higher the lateral force and moment at the beam-column connection. It is important to mention that the geometric non linearity is due to the sudden relocation of the neutral axis along the section depth.

In order to compare the behavior of the different location of the tendon profiles, an additional test HJ3-27PT2 was carried and is shown with HJ3-25PT1 in Figure 3.22-left. The force displacement response shows a very stable non-linear elastic hysteresis loop. However, due to the fact that the location of the metallic hinges and location of the tendons in HJ3-25PT1 are in a very similar location from the beam centerline, when the gap closes, there is no moment contribution from the tendon which is at the same level of the hinge in compression and the tendon force remains constant and only elongates or shortens according with its elastic properties keeping the hinge in compression (Figure 3.23-right). Meanwhile for test HJ3-27PT2 (where the tendon profile is closer to the beam centerline), when the gap closes there are two lever arms from the compression hinge to the tendon forces.

Similar to the results obtained with the Hybrid PRESSS-Brooklyn subassembly (HJ2 specimen) when the system rocks with the use of two hinges at the critical section, Figure 3.23-left show the gap opening and closing of the top and bottom hinges as the neutral axis position is fixed for the HJ3-27PT2. Identical results were obtained for the other tests. A Symmetric behaviour is obtained which is compared with the previous specimen HJ2 as the hinges were symmetrically located in the beam section.

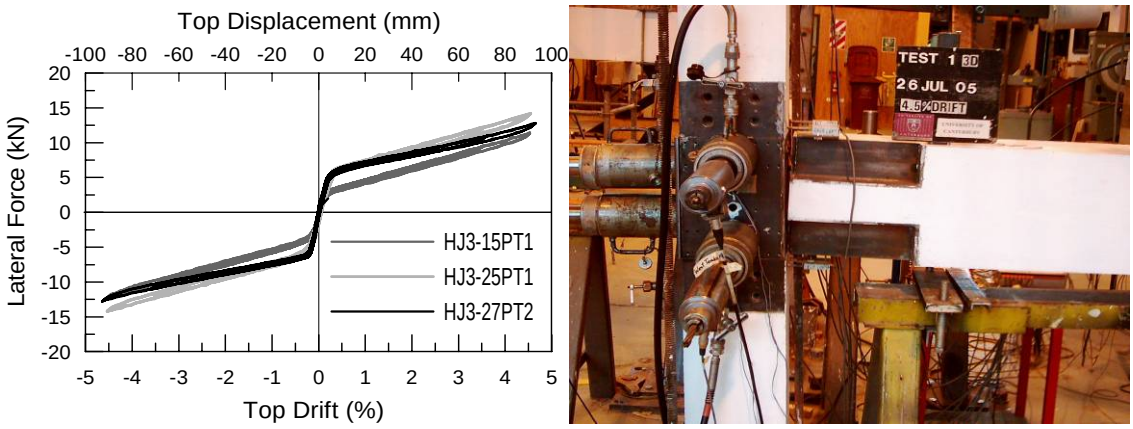

Figure 3.22. Hysteresis response of HJ3: unbonded post-tensioned only solution (left) and gap opening at 4.5% drift (right).

Figure 3.23-right shows the tendon force behaviors for HJ3-15PT1 and HJ3-25PT1 which have similar behavior. Due to the difference in the initial post-tensioned force all the forces during the cyclic behavior are shift up by the same amount.

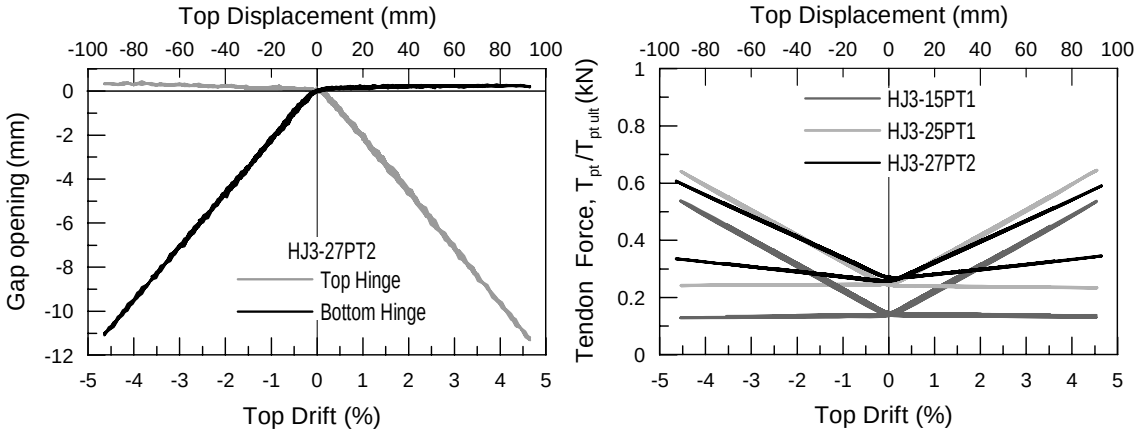

Figure 3.23. Gap opening variation at rocking (left) and variation of tendon forces for HJ3 (right).

Additional external energy dissipation was added to the previous configuration. Test results for HJ3-27PT1-7D and HJ3-27PT2-8D are shown in Figure 3.24. An extremely efficient and stable hysteresis behavior can be seen. Less energy dissipation is observed for HJ3-25PT1-7D in comparison with HJ3-27PT2-8D due to the smaller dissipater used. Valuable confirmations of the reliability of a flexible design approach were obtained, where dissipaters, post-tensioning location and levels can be varied while maintaining the desired level of moment capacity and overall dissipation/recentring properties. The presence of the double-hinge shear key solutions (small metallic balls, Figure 3.22-right) guaranteed two fixed pivot points, with no stiffness or strength losses up to a high level of drift (4.5%) because of only minor damage at the contact level.

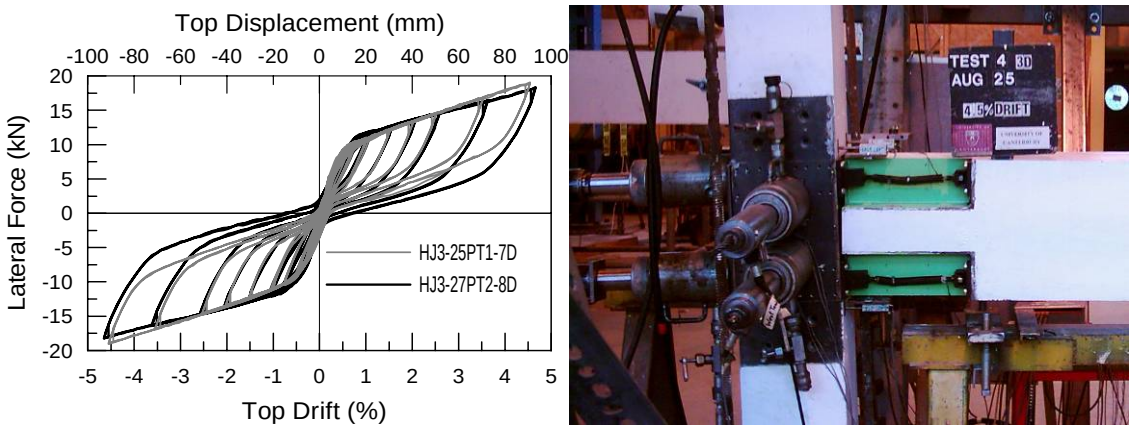

Figure 3.24. Hysteresis response of HJ3 with two different energy dissipaters (left) and gap opening at 4.5% (right).

Gap opening is showed in Figure 3.25-left and is similar to that recorded for the same test without energy dissipation. However, it can be seen that there is small increase in the residual displacement of the dissipaters as the gap opens and closes due to the dissipaters yielding in tension. This is represented as a widening of the hysteretic loop in the plot of gap opening vs displacement. The symmetric behaviour of the gap opening is obtained due to the symmetry of the hinges located in the beam section.

Tendons forces for the two tests are showing in Figure 3.25-right and are very similar to those obtain in the unbonded post-tensioned solution (Figure 3.23-right). Minor tendon losses are observed for test HJ3-27PT2-8D as a result of slip on the head of the anchorage during the test.

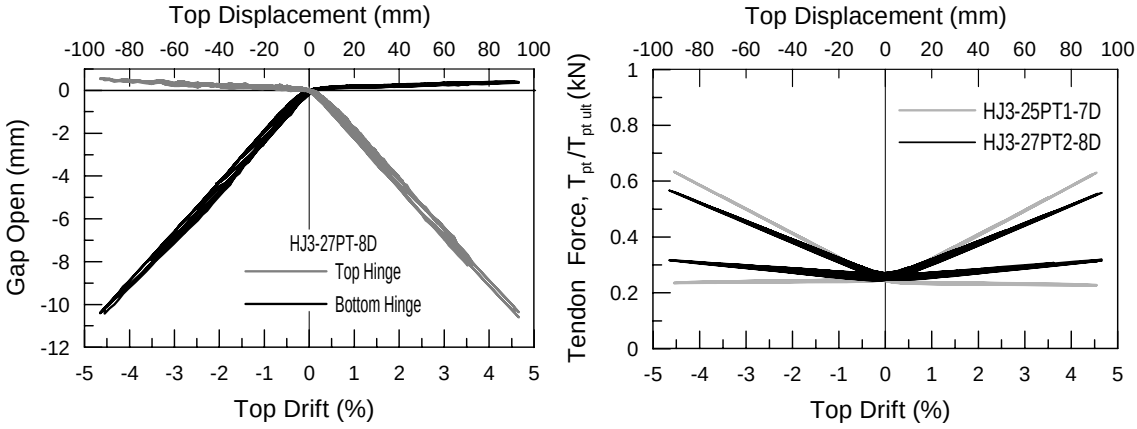

Figure 3.25. Gap opening variation at rocking (left) and variation of tendon forces for HJ3 (right).

Two sizes of external dissipater were implemented for specimen HJ3. Figure 3.26 shows the monotonic uni-axial and cyclic stress-strain / force-displacement for the 7 mm and 8 mm fuses adopted with an unbonded length of 150 mm.

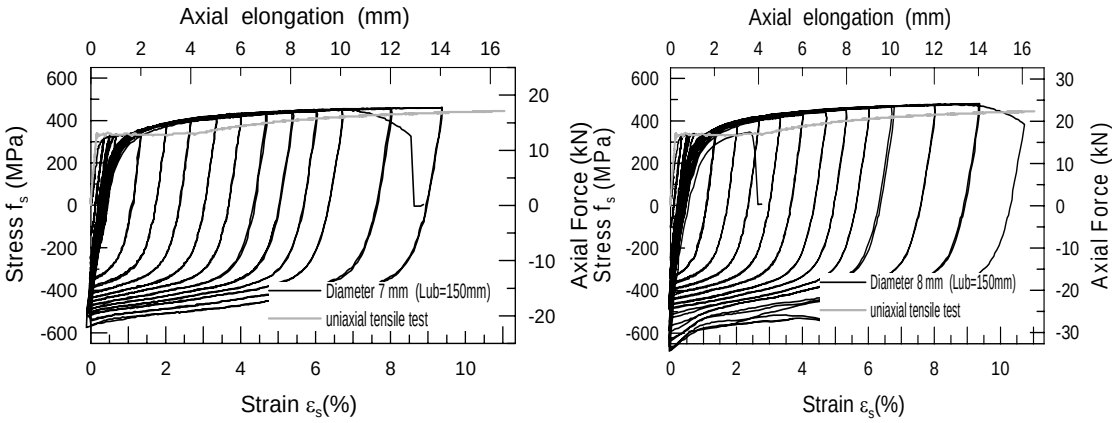

Figure 3.26. Stress-strain and force displacement curve of the external dissipaters used in HJ3.

The dissipater failed at a level of elongation of 14 mm and 16mm corresponding to a 9% and 11% of the axial strain for 7mm and 8mm fuse respectively. Comparison between monotonic and cyclic behaviour of the dissipaters shows a reduction of the yield plateau under cyclic loading and increase of the yield strength due to strain rate effects. This phenomenon is commonly known as the Bauschinger effects. As expected, the two dissipaters failed at similar level of elongation which is controlled by the unbonded length assumed.

HJ3 was also subjected to combined bi-directional "four clove" loading protocol as shown in Figure 3.27. The response of test HJ3-X25PT1-Y27PT2 was extremely satisfactory in both directions as shown in Figure 3.28-left. An increasing level of damage or reduction of strength/stiffness was not observed as shown in Figure 3.24-Right at maximum response, as would be expected in a monolithic configuration (Figure 3.13 to Figure 3.15).

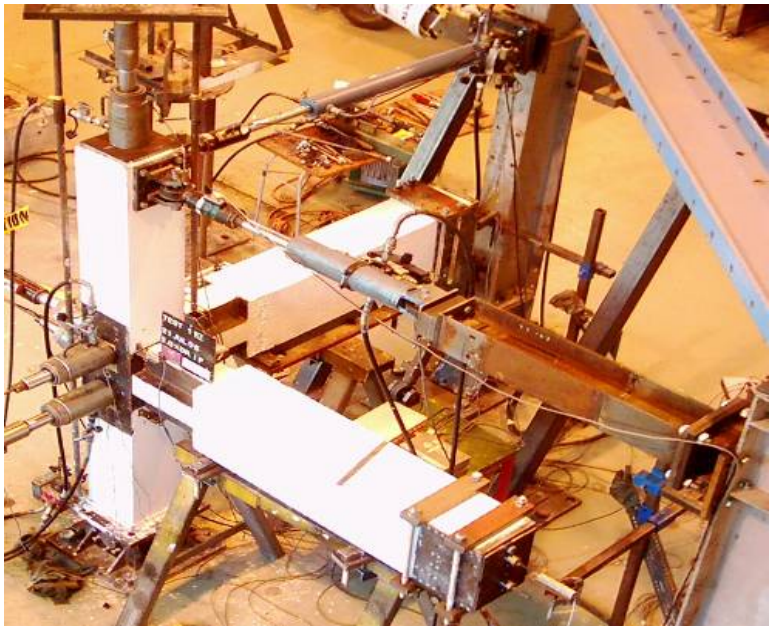

Figure 3.27. Test set up for HJ3 under bi-directional loading.

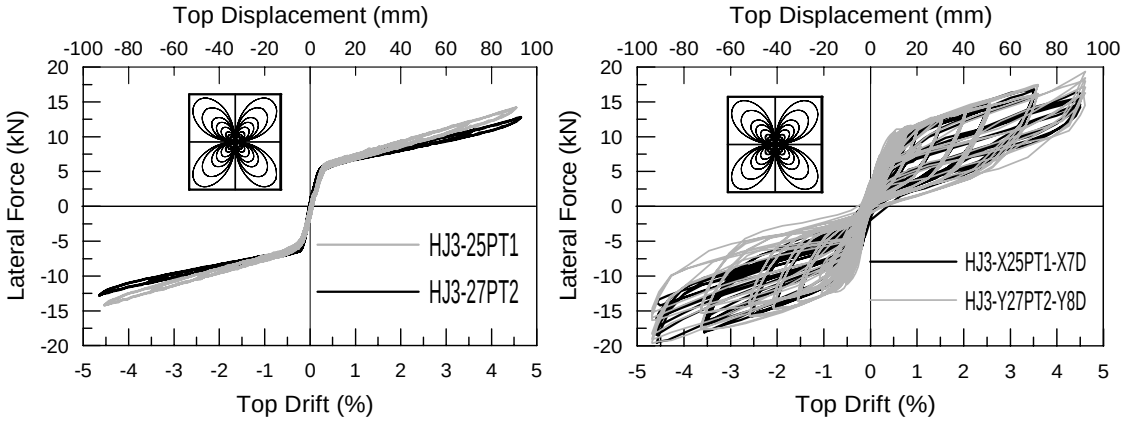

Figure 3.28. Hysteresis response of HJ3 under bi-directional loading: unbonded post-tensioned only solution (left) and Hybrid solution (right).

The effects of bi-axial cyclic loading were almost negligible when comparing the response to that of the same specimen under independent uni-directional loading (Figure 3.29). Nevertheless, comparisons indicate that the increase on the lateral forces is due to partial constraints in the test set-up (movement of the beam pinned arm in the out-of plane direction). No losses of pre-stress in the tendons were recorded during all tests as is shown in Figure 3.30.

Test HJ3-X25PT1-Y27PT2-X7D-Y8D represents the hybrid solution under bi-directional loading with the addition of external dissipaters, with the clear aim of demonstrating the flexibility of the design and the possibility of having a reliable control of the flag-shape behaviour. The same moment capacity at target drift (4.5%) and similar energy dissipation were thus aimed for as the uni-directional loading.

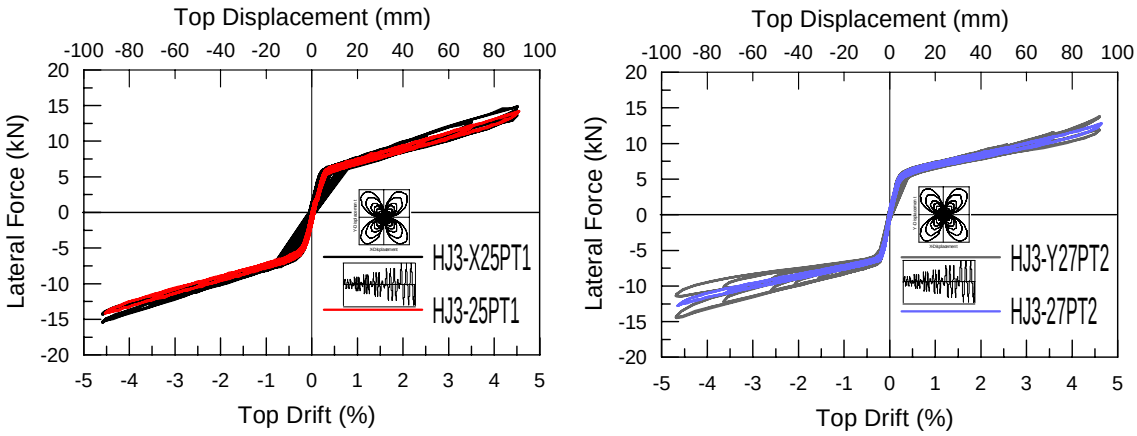

Figure 3.29. Comparisons between bi-directional and uni-directional loading for unbonded post-tensioned only solution specimen HJ3: Lateral force vs. displacement in X-direction (left) and Y-direction (right).

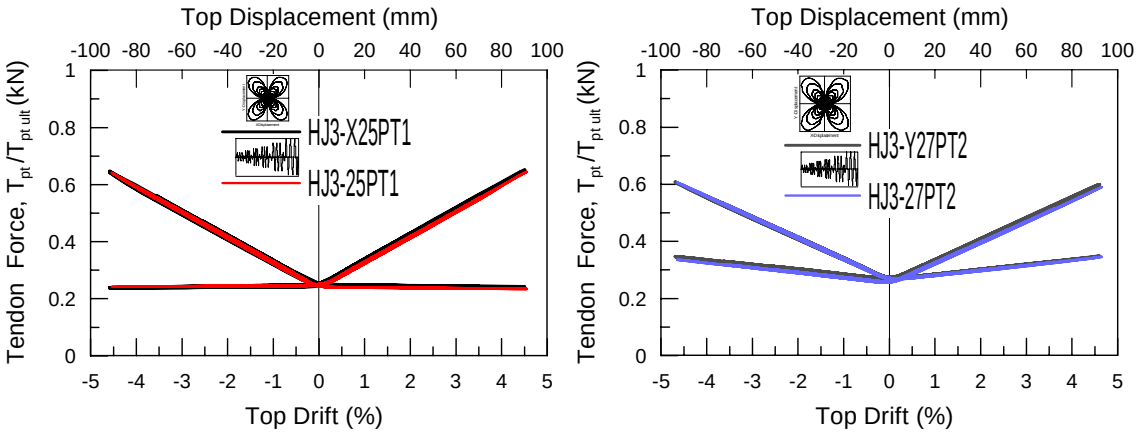

Figure 3.30. Comparison between bi-directional and uni-directional loading for unbonded post-tensioned only solution specimen HJ3: variation of tendon forces in X-direction (left) and Y-direction (right).

The response of the hybrid system under the bi-directional (four clove) testing regime was very satisfactory up to 3.5% of drift (Figure 3.28-right). Up to this stage, the effects of bi-axial loading seemed to be negligible, when compared with the uni-directional response (Figure 3.31).

At higher level of drifts, however, the torsion effects on the beam, observed during the tests on the post-tensioned solution and mainly due to the test set-up constraints, led to losses of prestress in the tendon in the X direction (Figure 3.32) as well as to general stiffness degradation. The subsequent increased level of strain demand in the dissipaters, combined with the aforementioned highly demanding testing protocol, led to the premature fracture of dissipaters when moving to 4.5% drift in the X-direction.

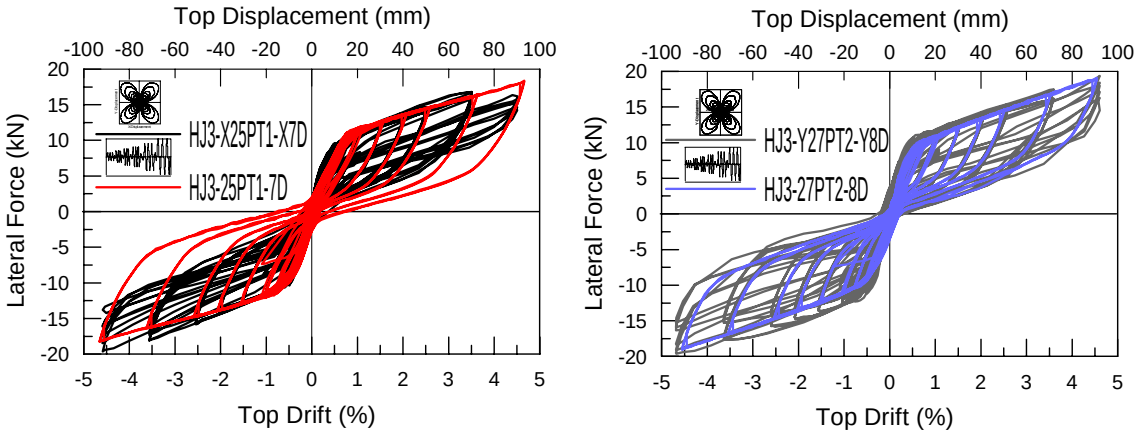

Figure 3.31. Comparisons between bi-directional and uni-directional loading for hybrid solution specimen HJ3: Lateral force vs. displacement in X-direction (left) and Y-direction (right).

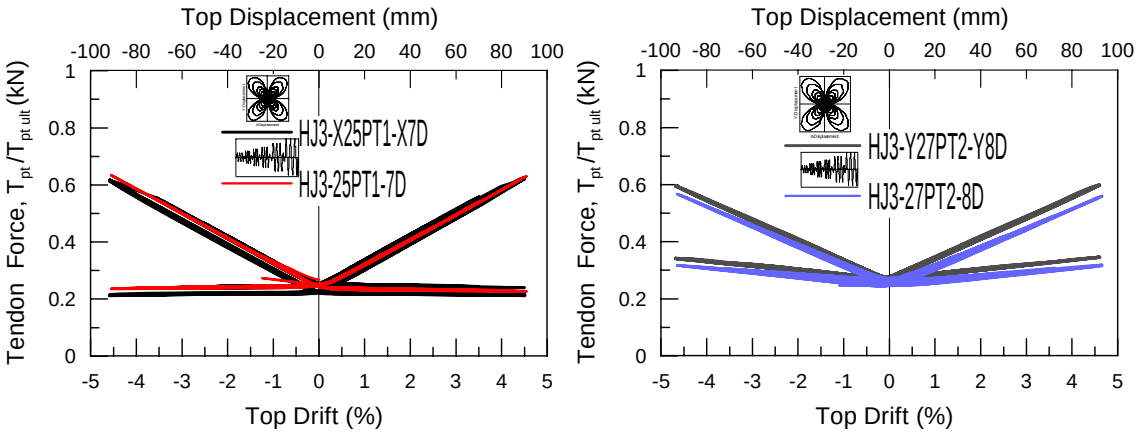

Figure 3.32. Comparison between bi-directional and uni-directional loading for hybrid solution specimen HJ3: variation of tendon forces in X-direction (left) and Y-direction (right).

3.7 EVALUATION OF THE TEST RESULTS

All connections had an adequate performance in terms of strength, stiffness and ductility. Comparison between different subassemblies responses are presented in the following sections.

3.7.1 Stiffness Degradation

Secant stiffness is defined as the slope taken at the maximum load obtained from the last cycle of each imposed drift. Each value of secant stiffness was normalized with respect to the value obtained at 0.1% inter-story drift level for comparison purposes. Figure 3.33 shows the normalized stiffness degradation for some of the tests performed.

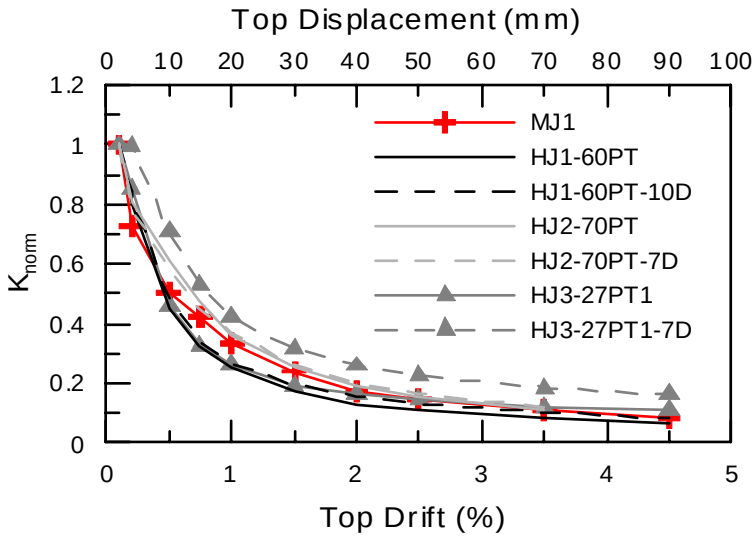

Figure 3.33. Stiffness degradation: MJ1, HJ1, HJ2and HJ3.

The tests HJ1-60PT and HJ1-60PT-10D presented a faster decrease in the stiffness at early drift levels but almost the same at 4.5% drift when compared to MJ1. Other research [3.16] had underline that the use of gross section properties to calculate the total base shear for hybrid systems determined by force based design methods is non conservative, and therefore, the Displacement Based Design method is a more rational design approach. However, stiffness degradation for tests HJ2-70PT and HJ2-70PT-7D are very similar to those obtained for MJ1.

Comparison between the hybrid test using unbonded post-tensioned only solutions (without energy dissipaters) and including energy dissipaters for the specimens HJ1 and HJ2 indicate that there is no difference in the residual stiffness. However, results obtained for specimen HJ3 with and without energy dissipation show that residual stiffness is different using the unbonded post-tensioned solution and energy dissipaters.

Furthermore, tests HJ3-25PT1 decrease about 70% in comparison with HJ3-25PT1-7D at 4.5% of drift, however the latter show an decrease of approximately 50% of stiffness degradation in comparison with MJ1. Similarly, tests HJ3-27PT2 decrease 60% in comparison with test HJ3-27PT2-8D at maximum drift but an increase of 60% when compared with the monolithic solution MJ1.

Most importantly, comparative results among HJ2, HJ3 and the monolithic solution MJ1, show that the use of external dissipaters decreases the secant stiffness degradation. An explanation is that the external dissipater does not suffer stiffness degradation effects due to bond deterioration.

3.7.2 Energy Dissipation

The equivalent viscous damping ratio (ξ_{eq}) is defined as the ratio between the energy absorbed through the inelastic response of the actual structure and an equivalent viscous system. Figure 3.34 shows the equivalent viscous damping (ξ_{eq})-ductility relationship for the monolithic specimen MJ1 and three different tests performed in HJ1 and HJ3 specimens calculated as the ratio between the area under the force-displacement curve in the third cycle of each imposed drift level and the area defined at maximum displacements and pick force assuming linear elastic behaviour.

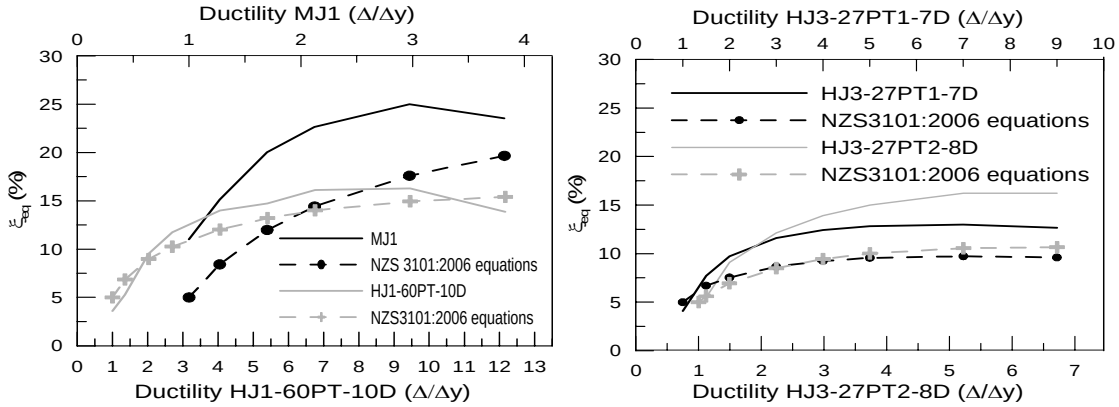

Figure 3.34. Equivalent viscous damping ratio for MJ, HJ1 and HJ3 tests.

Figure 3.34-left shows a maximum of 25% and 15% of ξ_{eq} for tests MJ1 and HJ1-60PT-10D respectively at 3.5% of drift. Figure 3.34-right shows a maximum of 13% and 16% of ξ_{eq} for tests HJ3-27PT1-7D and HJ3-27PT2-8D respectively at 4.5% drift. As expected, the second tests had more ξ_{eq} due to the increase in the dissipaters fuse.

Comparison between the tests performed using HJ3 subassembly with HJ1 display a similar equivalent viscous damping (ξ_{eq}=15%) however it is less than the monolithic specimens. However, displacement ductility was higher for HJ1-60PT-10D with a ductility of 12 while MJ1 was had a ductility value of 4 and smaller ductility levels were observed for those obtained for the HJ3 subassembly with ductilities of 9 and 6.5 respectively at 4.5% of drift.

3.7.3 Residual Displacements

Figure 3.35 shows the residual displacement obtained from different tests using the differing subassemblies as an indicator each systems performance. MJ1 had a 68 mm residual displacement at 4.5% drift, almost half of the residual displacement (38 mm) was obtained for the traditional hybrid HJ1 subassembly at the same drift level with 15 mm being recorded for the HJ3 subassembly.

As expected, minimum residual displacements were obtained for HJ1, HJ2 and HJ3, the post-tensioned only solutions. However, adding energy dissipation in the form of external dissipaters HJ2 experienced a residual displacement comparable to the monolithic solution MJ1 as a result of the asymmetry of the behaviour and the inclusion of friction between the tendon and the plastic duct due to the draped profile. Specimen HJ3 with external energy dissipation experience very low values of residual displacements for both types of dissipater.

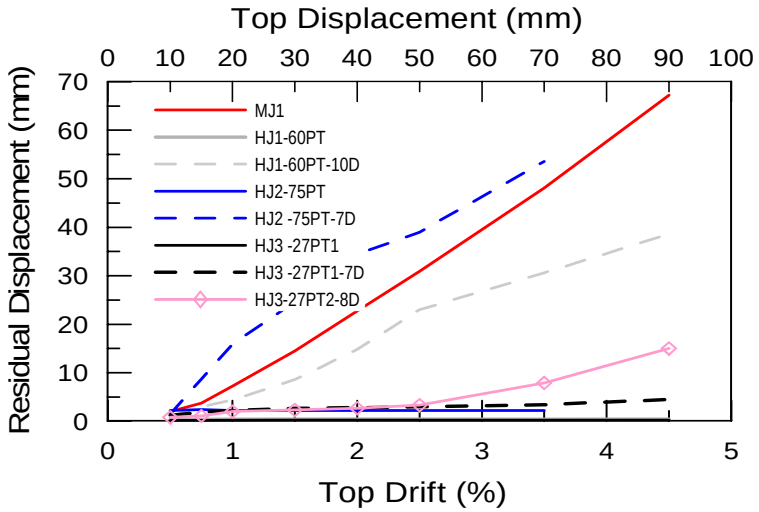

Figure 3.35. Residual displacements for test MJ1, HJ2, HJ2 and HJ3

3.7.4 Comparative Behaviour of MJ1 and HJ1

A further confirmation of the higher performance of the jointed ductile connection when compared to an equivalent monolithic solution is provided by the combination of the total force - displacement hysteresis response and the observed damage of the experimental tests of the hybrid and the monolithic solution for approximately the same flexural capacity.

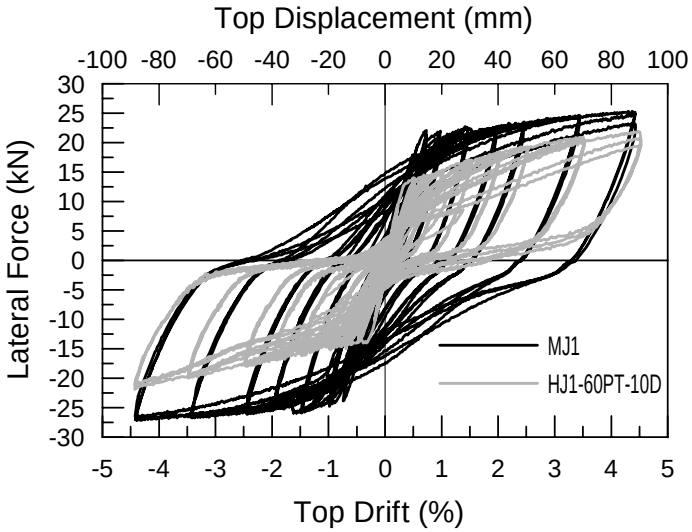

Figure 3.36. Comparison of Hysteresis responses between MJ1 and HJ1-60PT-10D.

As expected due to the adoption of capacity design considerations targeting the development of a weak beam strong column mechanism, the damage of MJ1 was concentrated in the beam plastic hinge region leading to progressing flexural cracking and spalling of the concrete, while hairline cracks were observed in HJ1-60PT-10D at full load and these cracks closed completely

when the load was removed. MJ1 present a higher energy dissipation capacity, when compared HJ1-60PT- 10D. In spite of this very satisfactory behavior when referring to traditional systems, the differences in terms of level of damage and residual deformations between the monolithic and jointed ductile system are evident.

3.8 EXPERIMENTAL ANALYTICAL COMPARISON

As explained in Section 3.2 the lumped plasticity modeling approach was implemented in this research. This model adopts non-linear inelastic springs in parallel located at the rocking interface. The analysis allows each contribution of the mild steel, post-tensioned tendons and axial load to be isolated, defining their individual contributions and allowing individual spring properties to be defined. The non-linear finite element program Ruaumoko2D [3.17] was used to model the series of experimental tests imposing the same time history displacements applied to the tests.

3.8.1 2-D Monolithic Beam-Column Subassembly MJ1

Before the model could be inputted into Ruaumoko, moment-curvature relations were required for the column and beam members. In Ruaumoko, the beam was considered one component (Gibelson) type member while the column was modelled using the beam-column type member as the column axial load changed during the test. However, the design of the monolithic connection was following the capacity design principles and no plastic hinge was expected in the columns.

The program XTRACT was used for the beam and column section analysis. A bilinear approximation to the actual curve was derived for the beam, using the yield, nominal and ultimate conditions as proposed by other researchers [3.9] and values for initial stiffness k_0=5.32 kN/m^{2}and the ratio of post-yield stiffness (bilinear factor) r = 0.0002, were obtained. The plastic hinge length was assumed as proposed [3.9] $L_p = 0.08l + 0.022d_b f_y$ = 0.165m.

A modified Takeda hysteresis model was assumed for the plastic hinge region. The three extra parameters, namely unloading proportional to inverse square root of ductility reached (α), reloading points towards maximum moment-curvature point reached (β), and the unloading and reloading behaviour parameter (*NF*). Also, a fourth parameter (*KKK*) is required to specify which of the two types of unloading behaviour are used. In these analyses, the following values for the parameters were calibrated to match the experimental results: α = 0.18, β = 3, *NF* = 10

(recommended values for reloading stiffness power factor) and *KKK* = 1 (Unloading as in Drain 2-D).

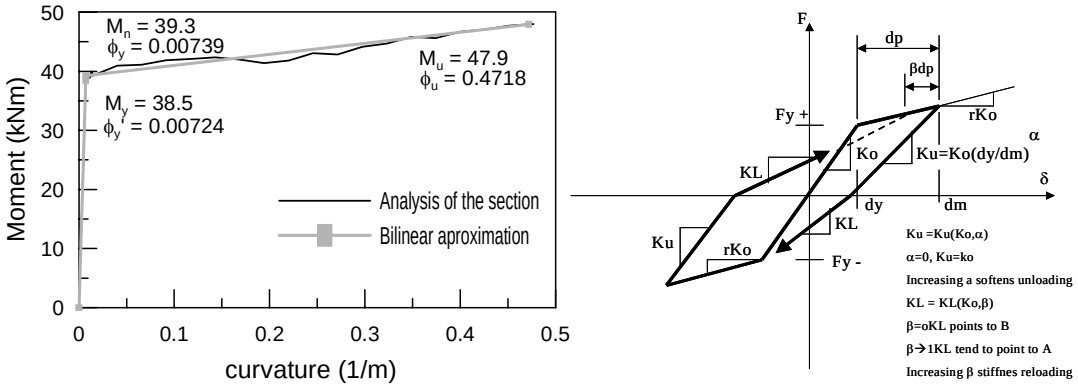

Figure 3.37. Beam moment curvature for MJ1 (left) and Modified Takeda hysteretic rule (right)

Figure 3.38 shows the analytical experimental comparison using the Takeda hysteretic model. It can be seen a good approximation to the experimental results in terms of strength and stiffness but the model presents some inconsistencies in the small cycles and higher residual deformations were observed.

Modelling the 3 dimensional monolithic beam-column joint MJ2 failure occurred through shear of the beam column joint region and not by flexural behaviour as observed in Figure 3.15. Ongoing research at the University of Canterbury investigating joint shear failure in combination with providing analytical modes and retrofitting techniques for this type of failure is being performed; however it is not part of this research and therefore analysis of this type of behaviour will not be addressed in detail.

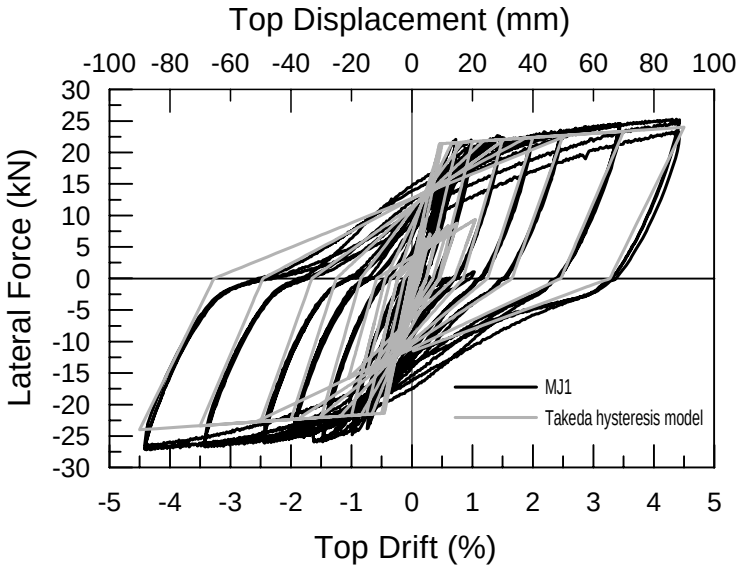

Figure 3.38. MJ1 Experimental analytical comparison using using Takeda hysteresis model

3.8.2 Hybrid PRESSS Beam-Column Subassembly HJ1

Using the lumped plasticity model based on the combination of two rotational springs in parallel as proposed [3.6, 3.7] is shown in Figure 3.39. The moment rotation contribution for the unbonded post tensioned tendon was modelled using a Non Linear Elastic hysteresis rule while two hysteresis models were considered to represent the energy dissipation contribution: Bi-linear inelastic and Bounded Ramberg-Osgood while elastic elements were used to represent the structural members.

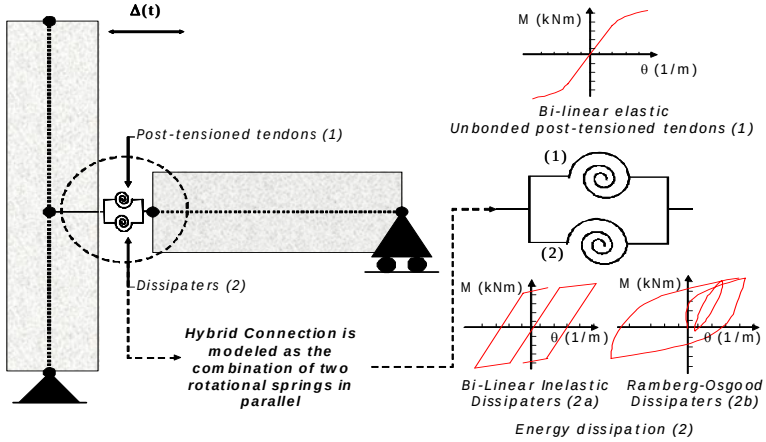

Figure 3.39 Rotational Spring model used for HJ1

Figure 3.40 shows the validation of the results for the hybrid solution test HJ1-60PT-10D. It can be noted that the model is, in general, able to satisfactorily reproduce the experimental results either in terms of monotonic and cyclic behaviour, while still not fully capturing the stiffness degradation effects due to bond deterioration.

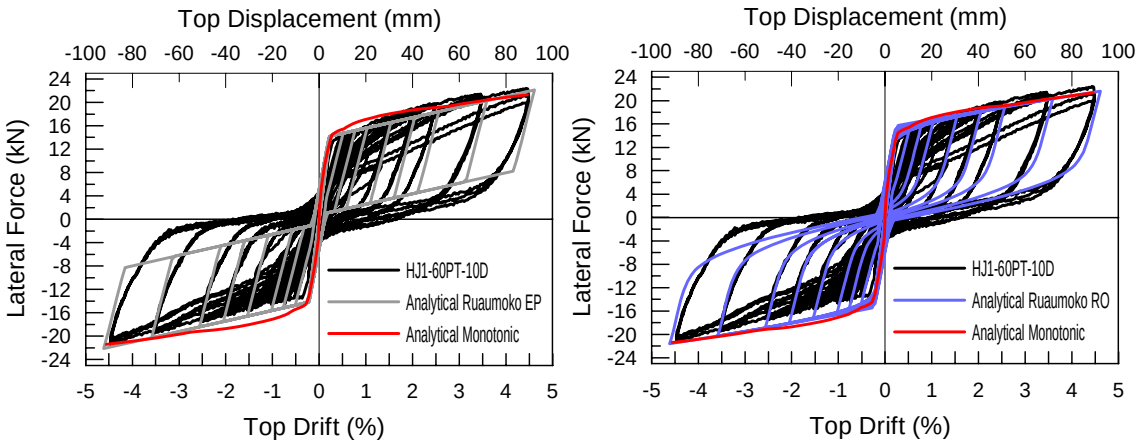

Figure 3.40 Experimental analytical comparison for HJ1-60PT-10D: force Displacement using Elasto-plastic (left) and using Ramberg-Osgood (right).

The elasto-plastic behaviour (EP), assumed to model the internal grouted bars acting as energy dissipation (Figure 3.40-left), under-estimates the energy dissipated due the reversal cyclic of loading while the Romberg-Osgood hysteresis behaviour (RO) present a more realistic approximation of the energy dissipater. However, the Ramberg-Osgood factor r used in the model was calibrated accordingly to match the experimental response.

In terms of local response, Figure 3.41, show the neutral axis position along the beam height and the post-tensioned tendon behaviour compared with the analytical monotonic model. Both behaviour shown a good agreement with the experimental results, however, as explained previously, due to a local damage on the column face, a relocation of the neutral axis position is observed and leading to Prestress losses in the post-tensioned tendon which can not be accounted in the analytical model.

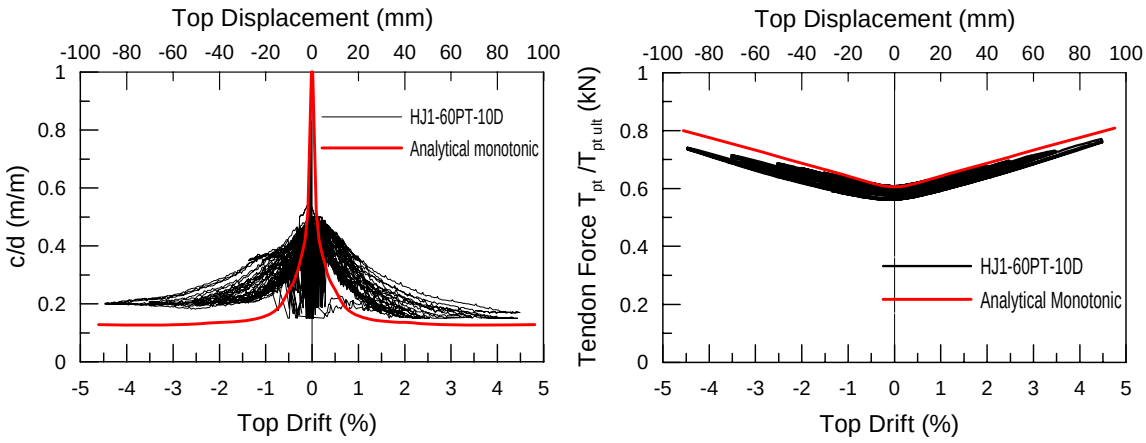

Figure 3.41 Experimental analytical comparison for HJ1-60PT-10D: Neutral axis postion (left) and Post-tensioned tendon force (right).

3.8.3 Hybrid PRESSS-Brooklyn Beam-Column Subassembly HJ2

Using the moment-rotation model, three springs were assigned at the beam column connection interface as shown in Figure 3.42. Due to the asymmetric behaviour caused by the non-central position of the tendon within the section two rotational springs with bi-linear slackness in tension or compression were assigned to the unbonded post-tensioned tendon. Two different types of hysteresis behaviour were analyzed to represents the steel dissipation contribution: Bi-linear inelastic and bounded Ramberg-Osgood.

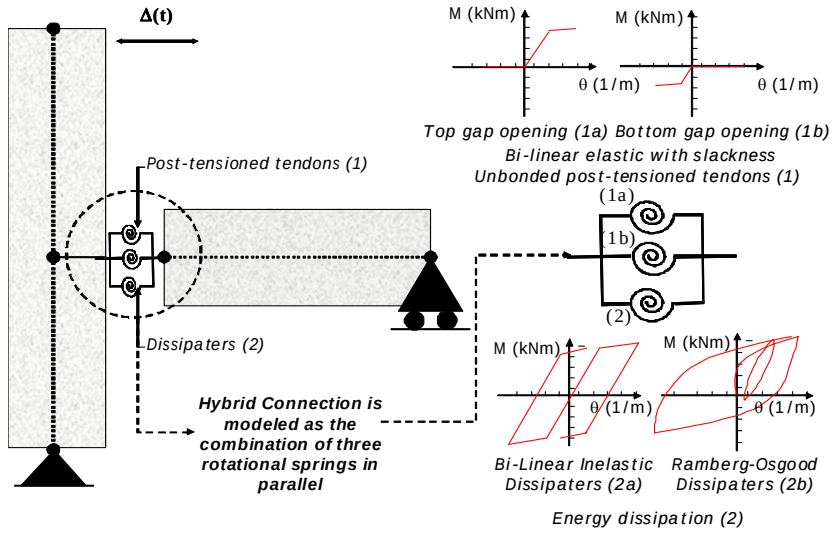

Figure 3.42 Rotational Spring model used for HJ2

Figure 3.43 shows the force-displacement experimental validation of test HJ2-70PT-7D using bi-linear (EP) or considering a Romberg-Osgood (RO) hysteresis rules (RO) (Figure 3.43-left and Figure 3.34-right respectively).

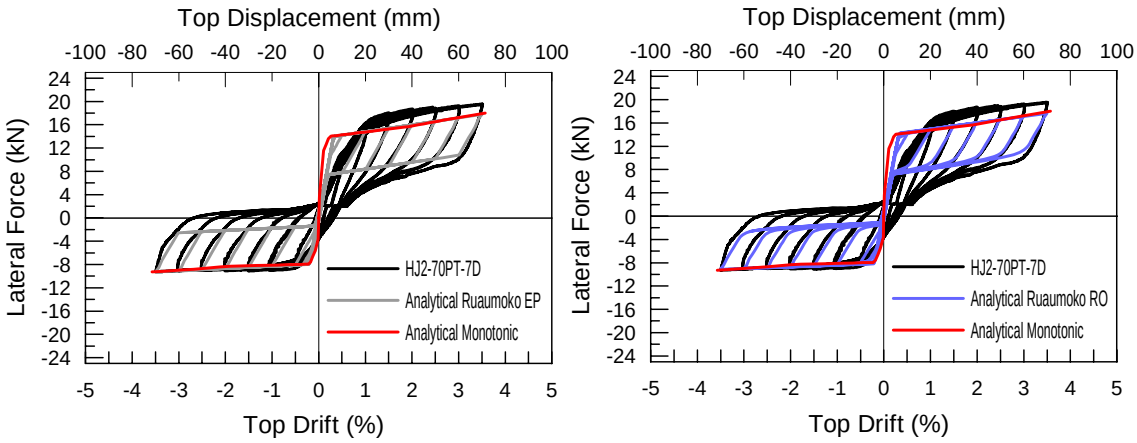

Figure 3.43 Experimental analytical comparison using monotonic steel behaviour for HJ2-70PT-7D: Force Displacement using Elasto-plastic (left) and Ramberg-Osgood (right).

In general the lumped plasticity model using the monolithic beam analogy can validate the results in terms of monotonic behaviour. Initial stiffness was over estimated in the models while not fully capturing the strength at higher drift levels due to the Bauschinger effects arising from the cyclic behaviour of the dissipaters. Additional energy dissipation is observed in the test due to friction of the parabolic tendon within the plastic duct and is not accounted for in the models.

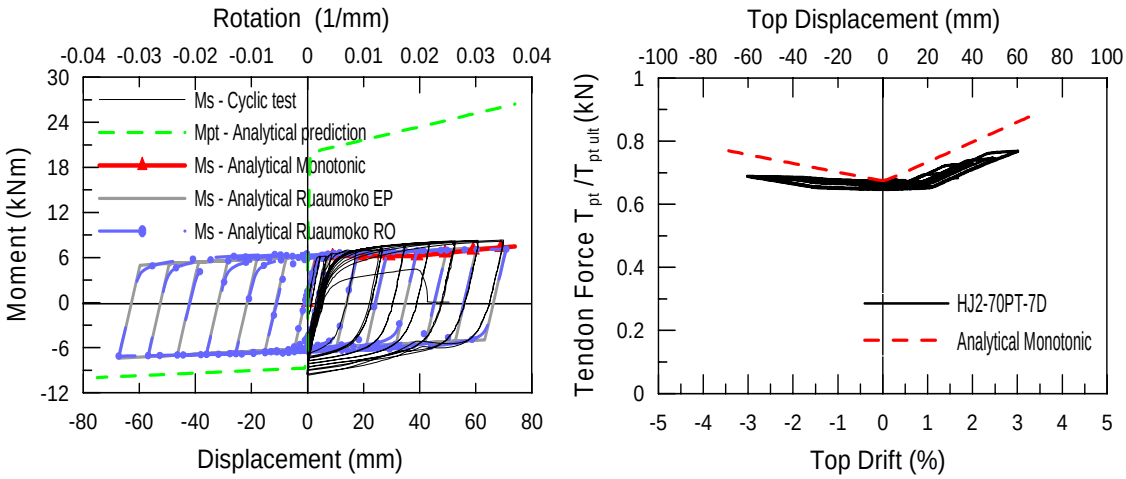

Figure 3.44 Experimental analytical comparison for HJ2-70PT-7D: Steel and post-tensioned moment contribution (Left) and Post-tensioned tendon force (right).

Figure 3.44-left shows the analytical comparison among the cyclic experimental dissipater test and the analytical hysteresis used for the Ruaumoko model. As it can be seen, the cyclic test of the dissipaters (calculated as the distance between the hinge and location of the dissipater) showed additional residual moments in the unloading behaviour which are not accounted for in the analytical models. Figure 3.44-right shows the experimental validation of the post-tensioned tendon force. In the analytical model friction forces generated by the parabolic profile and pre-stress losses between the tendon and the plastic duct during the test were not considered in the models.

3.8.4 Advanced Hybrid Beam-Column Subassembly HJ3

Using the lumped plasticity model based on the combination of two rotational springs in parallel as proposed in Figure 3.39 is used for the validation of the different tests carried out on the HJ3 specimen. The moment rotation contribution for the unbonded post tensioned tendon was modelled using a Non Linear Elastic hysteresis rule while two hysteresis models were considered to represent the energy dissipation contribution: Bi-linear inelastic and Bounded Ramberg-Osgood while elastic elements were used to represent the structural members.

Figure 3.45 shows the force-displacement experimental validation of test HJ3-25PT1-7D using bi-linear (EP) and Romberg-Osgood (RO) hysteresis rules (Figure 3.45-left and Figure 3.45-right respectively). In general the lumped plasticity model using the monolithic beam analogy can validate the results in terms of monotonic steel behaviour. However, it does not fully capture the strength at higher drift levels due to the Bauschinger effects in the dissipaters as explained in section 3.6.5.

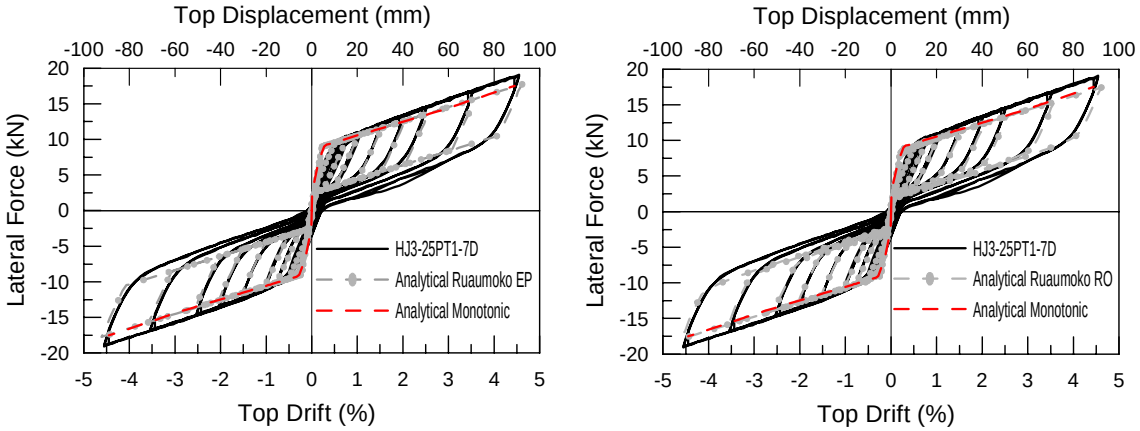

Figure 3.45 Experimental analytical comparison for HJ3-25PT1-7D: Force Displacement using monotonic steel characteristics: Elasto-plastic (left) and Ramberg-Osgood (right).

Figure 3.46-left shows the uni-axial and cyclic tensile tests of the dissipaters in combination with the analytical approximation used for the monotonic moment-rotation analysis. Notice that the plateau zone under cyclic behaviour is reduced and additional strength at early loading cycles is observed. Figure 3.46-right shows the extremely good agreement between the analytical behaviour of the post-tensioned force compared with the experimental results.

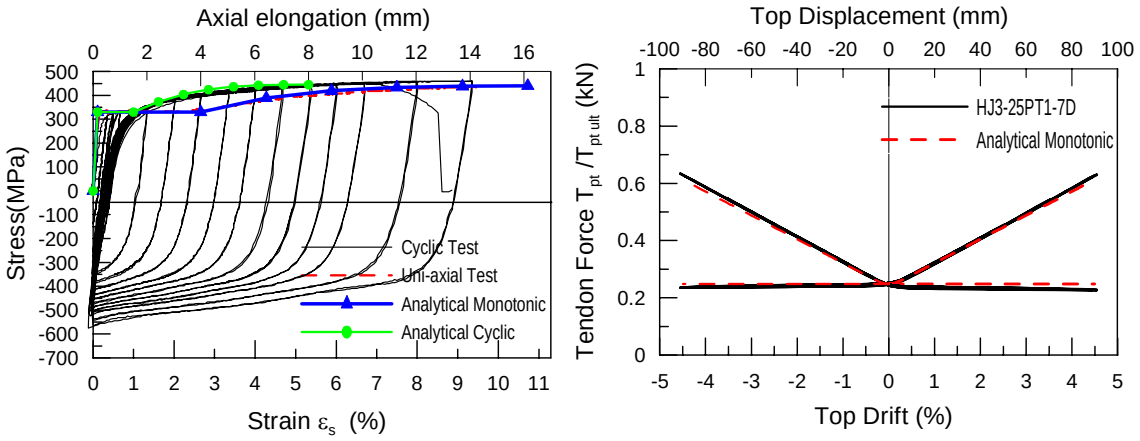

Figure 3.46 Experimental analytical comparison for HJ2-25PT1-7D: Cyclic and monotonic steel behaviour (left) and Post-tensioned tendon force (right).

From the experimental testing of the dissipater (Figure 3.21) and knowing that the neutral axis position is fixed, it is easy to calculate the moment contribution of the dissipater and compare it with the analytical results (Figure 3.47-left). In addition, post-tensioned and mild steel moment rotation contributions using the uni-axial tensile test are also shown in Figure 3.47-left.

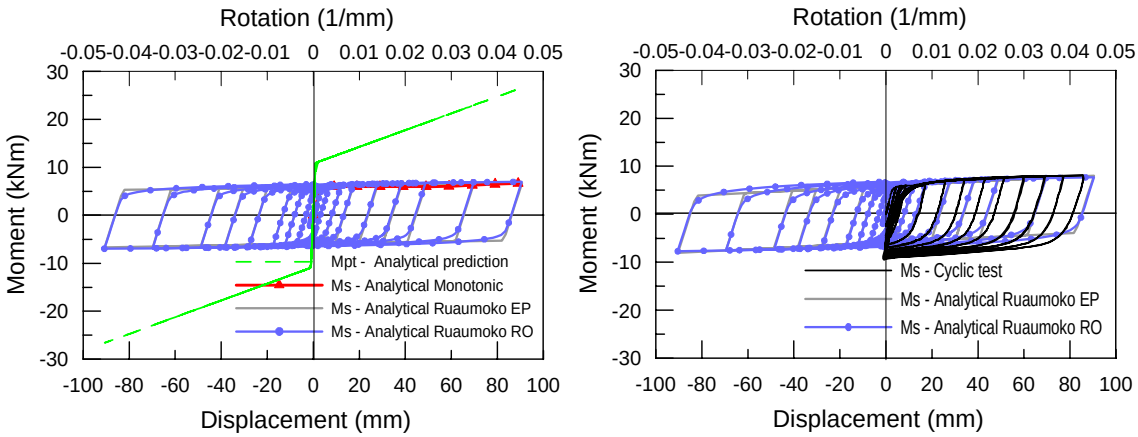

Figure 3.47 Experimental analytical comparison for HJ2-25PT1-7D: Monotonic steel and post-tensioned moment contribution (left) and Cyclic steel moment contribution (right).

It can be seen that the cyclic test of the dissipaters showed an increase in the strength at earlier cyclics of loading and additional residual moments in the unloading behaviour. Therefore additional modelling was carried out using the results from the cyclic test of the dissipaters for both the Elasto plastic (EP) and Romberg-Osgood (RO) hysteresis behaviour.

Using the cyclic test behaviour of the dissipaters and using both the Elasto-Plastic and Ramberg-Osgood hysteresis rule can successfully represent the experimental response in terms of strength at higher drift levels (Figure 3.48-left and Figure 3.48-right respectively). However, it does not fully capture the full amount of energy dissipated due in the un-loading path with the buckling of the dissipaters under the cyclic condition.

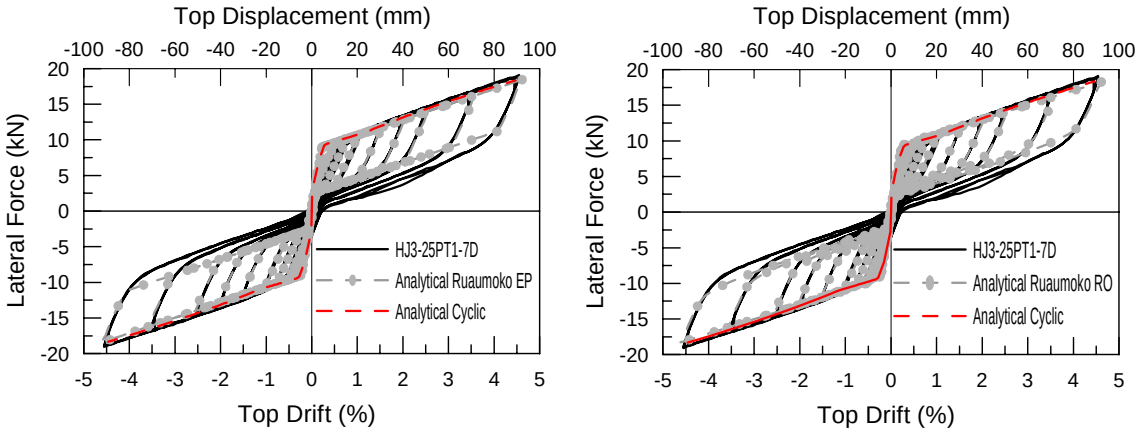

Figure 3.48 Experimental analytical comparison for HJ3-25PT1-7D: Force Displacement using cyclic steel characteristics: Elasto-plastic (left) and Ramberg-Osgood (right).

Finally, similar results were obtained for the test HJ3-X25PT1-Y27PT2-X7D-Y-8D using the same moment-rotational model presented previously for the test HJ3-27PT1-7D. Figure 3.49

shows the analytical validation in terms of total lateral response for the two orthogonal directions using Elasto-Plastic and Ramberg-Osgood hysteresis behaviour with very good agreements. However, as explained before at a maximum drift of 4.5% the fracture of one dissipater led to the premature fracture of all of the dissipaters in the X-direction.

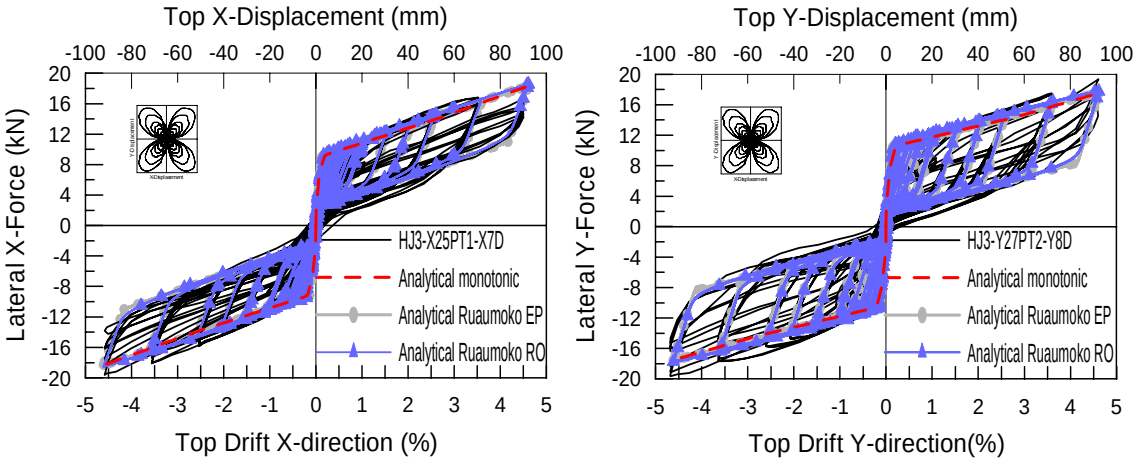

Figure 3.49 Experimental analytical comparison for HJ3-X25PT1-Y27PT2-X7D-Y8D: Force Displacement using monotonic steel characteristics: Elasto-plastic (left) and Ramberg-Osgood (right).

3.9 CHAPTER SUMMARY

Alternative arrangements for jointed ductile connections to accommodate different structural or architectural needs have been implemented and validated through quasi-static cyclic tests on a series of exterior beam-column subassemblies under uni- or bi-directional loading regimes. The results confirmed the unique flexibility and efficiency of these systems for the development of the next generation of seismic resisting structures, able to undergo high inelastic displacement with limited levels of damage and negligible residual displacement when compared to traditional monolithic (cast-in-situ) ductile solutions.

In order to further emphasize the enhanced performance of these systems, a comparison with the experimental response and observed damage of 2-D and 3-D monolithic beam-column benchmark specimens designed according to the NZ3101:1995 seismic code provisions has been presented. The reliability and simplicity of recently implemented special code provisions for the design and analysis of jointed ductile systems is also confirmed by satisfactory results of analytical-experimental comparison. Based on the results of this test program, the following conclusions can be made:

1. All the experimental results of quasi-static tests on new advanced dry ductile hybrid connection using different configurations of tendon profile, shear transfer mechanism and energy dissipation provided encouraging confirmation of the enhanced performance of these connections respecting considerations on cost-effectiveness when compared to the traditional hybrid solution.

2. The longitudinal profile of post-tensioned tendons herein presented (straight, draped tendons/cable) had shown very satisfactory results. The choice will depend on the contribution of the gravity and lateral loads effects, considering different level of seismicity (target design earthquake) as well as of the assigned role of the system during the seismic response (i.e. gravity-load only carrying system, seismic resisting system or intermediate solutions). However, the parabolic profile can provide an asymmetric behaviour in terms of strength as a result of the non-central position of the cable within the section.

3. The performance of the external mild steel dissipater rods as a supplemental damping device was extremely satisfactory. The external location of these dissipaters gives an important advantage over the traditional hybrid system such that after a major earthquake they can be replaceable. The location in the connection (laterally connected or inside of a pocket) will depend on the architectural needs.

4. The implementation to accommodate alternative shear transfer mechanisms at the rocking critical section can be obtained by relying either on friction due to the post-tensioned tendons contribution, and/or on the dowel actions in the mild steel, and/or using the single or double shear keys or metallic slotted or cables stayed corbel depending on different structural (both seismic or gravity loading) systems.

5. Comparison in terms of flexural strength with the monolithic subassembly underline the flexibility of the hybrid systems to be designed with the same flexural strength as its cast-in place counterparts.

6. Experimental results showed that traditional hybrid systems substantially reduced their secant stiffness with the gap opening specially the unbonded post-tensioned solution. However, the proposed advanced solution using external mild steel dissipater had shown a decreased in the secant stiffness degradation as the external dissipaters do not have bond deterioration.

7. The response of the hybrid system under bi-directional (four clove) testing regime was very satisfactory and the effects of bi-axial loading seemed to be negligible, when compared

with the uni-directional response. At high drift levels, torsion effects on the beam were observed during the tests leading to losses of prestress in the tendon as well as to general stiffness degradation in addition to a highly demanding testing protocol, excessive strain demand in the dissipaters were observed leading to a premature fracture.

8. All the tests showed that the equivalent energy dissipation ratio increased with an increased of story drift. The monolithic specimen showed a higher equivalent viscous damping in comparison with the hybrid solutions. However, higher displacement ductility levels were obtained for the hybrid solutions. This result is important in the analysis of hybrid connections in determining the correct level of energy dissipation.

9. Hybrid connections and especially the unbonded post-tensioned only solution showed much less residual displacement than the monolithic solution due to the self-centering properties of the connection. The advanced hybrid solution showed minimum residual displacements than the others connections. However, solutions with parabolic profile (which provides asymmetric behaviour in terms of strength) in addition to the energy dissipation and friction can cause higher residual displacements than expected.

10. The analytical-experimental comparisons, mostly based on pure predictions (i.e. pre-testing numerical simulations) confirmed a very satisfactory accuracy of the simplified modelling proposed and adopted to describe the behaviour of the hybrid connections. Modelling the cyclic behaviour of the dissipaters gives a very close approximation to the experimental results. Furthermore, rotational spring model shows a good approximation in term of overall strength. However, the model is unable to properly capture the unloading stiffness due to the inaccuracy of the moment-rotation parameters adopted to model the hysteresis steel rules.

3.10 REFERENCES

3.1 New Zealand Standards (NZS). “Appendix B: Special Provisions for the Seismic Design of Ductile Jointed Precast Concrete Structural Systems,” NZS3101:2006, Concrete Standard, Wellington, New Zealand.

3.2 fib, International Federation for Structural Concrete. Seismic Design of Precast Concrete Building Structures, Bulletin 27, Lausanne, 254 pp, 2003.

3.3 Priestley, M. J. N., and Tao, J. R., “Seismic Response of Precast Prestressed Concrete Frames with Partially Debonded Tendons,” PCI Journal, V. 38, No. 1, Jan.-Feb. 1993, pp. 58-69.

3.4 El-Sheikh, M., Sause, R., Pessiki, S. and Lu, L.-W., "Seismic Behavior and Design of Unbonded Post-tensioned Precast Concrete Frames," PCI Journal. V. 44, No. 3, May.-Jun. 1999, pp. 54-71.

3.5 Kurama, Y., Sause, R., Pessiki, S., and Lu, L.-W., "Lateral Load Behaviour and Seismic Design of Unbonded Post-tensioned Precast Concrete Walls." ACI Journal. V.96, No. 4, Jul.-Aug. 1999, pp. 622-632

3.6 Pampanin S., Priestley N., and Sritharan S., "Analytical Modeling of the Seismic Behavior of Precast Concrete Frames Designed with Ductile Connections," Journal of Earthquake Engineering. Vol. 5, No. 3, May.-Jun, 2001, pp. 329-367.

3.7 Palermo, A., "The use of controlled rocking in the Seismic Design of Bridges," Ph.D. dissertation, Politecnico di Milano, Milano, Italy. 2004.

3.8 ACI Committee 374.1-05 "Acceptance Criteria for Moment Frames Based on Structural Testing and Commentary", American Concrete Institute, Farmington Hill, Michigan. 2005

3.9 Paulay, T. and Priestley, M. J. N. "Seismic Design of Reinforced Concrete and Mansory Buildings", John Wiley and Sons, Inc. New York. 1992

3.10 Pampanin S., Amaris A., Akguzel U., Palermo A.,. "Experimental Investigations on High-Performance Jointed Ductile Connections for Precast Frames." Proceedings of the First European Conference on Earthquake Engineering and Seismology. Geneva, Switzerland. 2006.

3.11 Priestley, M.J.N. Calvi, G.M. and Kowalsky M.J. "Displacement-Based Seismic Design of Structures". IUSS PRESS, Pavia, Italy. 2007, pp. 721

3.12 Pampanin, S., Pagani, C., and Zambelli, S., "Cable-Stayed and Suspended Post-tensioned Solutions for Precast Concrete Frames," Proceedings of New Zealand Concrete Industry Conference, Queenstown, New Zealand, 2004.

3.13 ACI Innovation Task Group 1 and Collaborators. "Special Hybrid Moment Frames Composed of Discretely Jointed Precast and Post-tensioned Concrete Members (T1.2-03) and Commentary (T1.2R-03)". American Concrete Institute, Farmington Hills, Michigan. 2003.

3.14 Akgüzel U., and Pampanin, S., "Effects of variation of axial load and bidirectional loading on seismic performance of GFRP retrofitted reinforced concrete exterior beam-column joints," Journal of Composites for Construction, Vol. 14, No 1, pp 94-104, 2010

3.15 Priestley, M. J. N., Sritharan, S., Conley, J., and Pampanin, S., "Preliminary Results and Conclusion from the PRESSS Five-Story Precast Concrete Test Building," PCI Journal, V. 44, No. 6, Nov.-Dec. 1999, pp. 44-67.

3.16 Ozden, S. and Ertas, O., "Behaviour of Unbonded, Post-tensioned, Precast Concrete Connections with Different Percentages of Mild Steel Reinforcement," PCI Journal, V. 52, No. 2, Mar.-Apr. 2007, pp. 32-44.

3.17 Carr, A. "RUAUMOKO program for Inelastic Dynamic Analysis – User Manual". Department of Civil Engineering, University of Canterbury, Christchurch, New Zealand. 2006.

CHAPTER 4
DEVELOPMENT OF NON-TEARING FLOOR SOLUTIONS FOR HYBRID CONNECTIONS

4.1 INTRODUCTION

As the structure moves laterally, the gap at the beam column joint interface opens increasing the distance between column centrelines. This beam growth pulls apart the columns and induces additional shear and moment demands in the columns. Furthermore, as the gap opens, the floor next to the beam must be allowed to crack, since preventing a crack from opening would affect the behaviour of the beam. Therefore detailing should accommodate deliberate crack opening at the floor diaphragm.

The effects of beam elongation in precast frame systems have been demonstrated to be a potential source of un-expected damage to precast floor systems, unless adequate detailing is provided to account for displacement incompatibilities between the lateral resisting systems and the floor.

In order to emphasize the enhanced performance in controlling and minimizing the damage of the structural elements via the use of the proposed advanced hybrid solutions, an alternative innovative solution has been implemented to reduce the damage to the floor as presented in Chapter 2.

In this research two types of connection have been implemented. The first approach consists of using standard precast rocking/dissipative frame connections (herein referred to as “gapping”) in combination with an articulated or “jointed” floor. This system uses mechanical devices to connect the floor and the lateral beams which can accommodate the displacement incompatibilities in the connection. The second approach would rely upon a top hinge “non-gapping” system that could be used in combination with a standard floor solution (i.e. topping and continuous starter bars).

Additionally, analytical-experimental validation is being implemented using simple analytical models already present in literature, providing a reliable control over the expected hysteresis and dynamic behaviour.

4.2 GAPPING FRAME SYSTEMS WITH AN ARTICULATED FLOOR CONNECTION

As described in Chapter 2, a welded X-plate mechanical connector between (double-tee) floor units and the lateral seismic resisting frame system to perform under in-plane seismic forces was developed during the PRESSS research program [4.1] showing very satisfactory results.

Similarly, during further developments of this work, an articulated "jointed" floor system to be combined with a traditional jointed ("gapping") hybrid connection or, in principle, with any other standard moment resisting connection has been developed and implemented.

In this solution, the floor is connected to the lateral beams on special sliding/shear mechanical connectors which act as shear keys when the floor moves (relatively) in the direction orthogonal to the beam and as sliders when the floor moves in the direction parallel to the beam (Figure 4.1). As a result, the system is able efficiently to transfer the inertial forces and to accommodate, with no damage to the floor, the displacement incompatibility between floor and frame by creating an articulated or jointed mechanism decoupled in the two directions

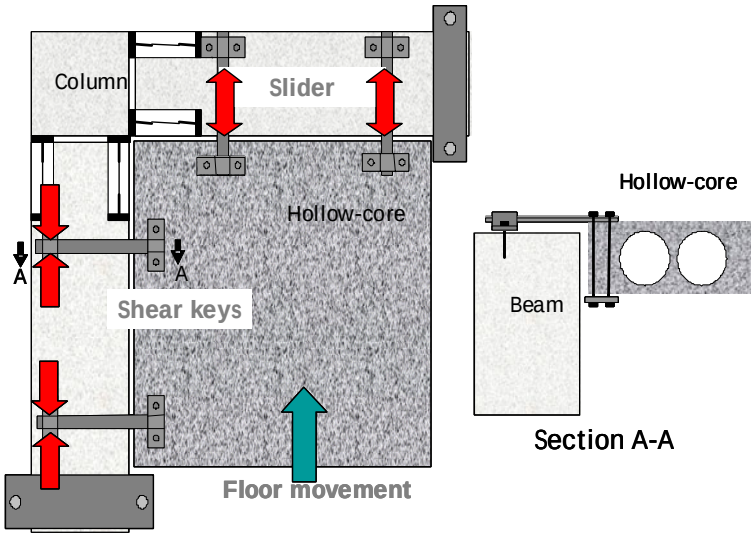

Figure 4.1. Articulated floor connection.

4.3 EXPERIMENTAL INVESTIGATIONS ON HYBRID FRAME CONNECTIONS WITH AN ARTICULATED JOINTED FLOOR

The experimental program shows the results obtained in the Structural Laboratory at the University of Canterbury based on the advanced hybrid beam column connection HJ3

subassembly, 2/3 scaled, with the intent of evaluating the performance of an articulated non tearing connection decouple in the two directions tested under both a uni-directional and bi-directional loading protocol.

4.3.1. Specimen Description

The specimen HJ3 was prepared with a modular configuration such that 2-D or 3-D exterior (corner) beam-column joint subassemblies with several alternative arrangements of post-tensioning profile could be tested after replacing the dissipating devices. Shear transfer mechanism was obtained using metallic spherical balls acting as double hinges as described in Chapter 3.

A piece of hollow-core unit series 200 was seated on a 75x50 piece of steel angle connected laterally to each precast beam by epoxy drilled fasteners; mechanical connectors were used on top of the floor, consisting of sliding/shear steel plates of 600x40x5mm which were attached to each end by steel plates and bolted to both the beams and the hollow-core by fasteners (Figure 4.2). A minimum tolerance of 1mm was left between the steel plates within the sliding/shear steel plates to reduce friction forces and allow the movement.

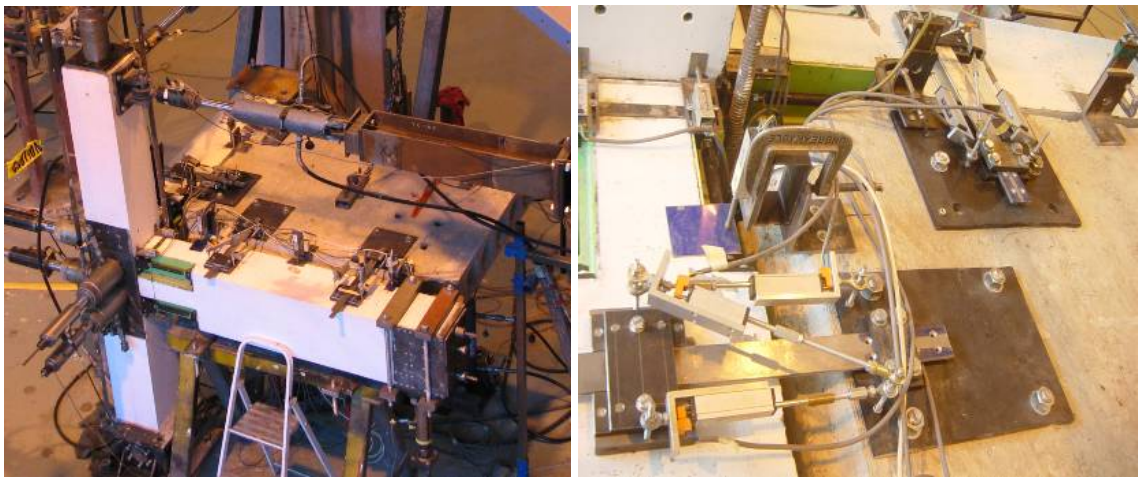

Figure 4.2. Beam-column joint with articulated floor unit: Top view (left) and connection details (right).

In order to explore the response of implementing an articulated "jointed" floor system to be combined with a traditional jointed hybrid connection tested in Chapter 3, or in principle, with any other standard moment resisting connection under a uni or combined bi-directional "four cloves" loading protocol, six tests were carried out using the beam column joint subassembly HJ3-HC where HC means hollow-core unit was used. The same initial post-tensioning and

energy dissipater content was used as those described in Chapter 3. A summary of the tests are presented in table 4.1

Table 4.1–Test summary

Specimen ID	Test Type	Test ID	Description
HJ3-HC	2-D	HJ3-HC-25PT1	Advanced Hybrid with hollow-core, only PT solution (27%PT_{ult}) profile 1
		HJ3-HC-27PT2	Advanced Hybrid with hollow-core, only PT solution (27%PT_{ult}) profile 2
		HJ3-HC-25PT1-7D	Advanced Hybrid with hollow-core, 7mm fuse and 25%PT_{ult} profile 1
		HJ3-HC-27PT2-8D	Advanced Hybrid with hollow-core, 8mm fuse and 27%PT_{ult} profile 2
	3-D	HJ3-HC-X25PT1-Y27PT2	Advanced Hybrid with hollow-core, only PT solution (25%PT_{ult} in X profile 1 and 27PT_{ult} in Y profile 2)
		HJ3-HC-X25PT1-Y27PT2-X7D-Y8D	Advanced Hybrid with hollow-core, 7mm fuse and 25%PT_{ult} profile 1 in X; 8mm fuse and 27PT_{ult} profile 2 in Y

4.3.2. Test set up and Loading Protocol.

A similar test set-up as those shown in Figure 3.10 and Figure 3.11 were used for the 2 Dimensional and 3 Dimensional tests (Figure 4.2-left). Beam and column elements are extended between points of contra flexure, assumed to be at the mid-span of the beams and at the mid-height of the column, where pins were introduced. The column was loaded vertically by a servo-controlled hydraulic actuator located at the point of inflexion. Simple supports at the beam ends were provided by connecting pin-end steel members to the floor.

An universal pinned connection able to move in both directions was located diagonally to the column and at the bottom corner of the hollow-core to provide support. A load cell attached to a hydraulic actuator controlled the hollow-core from the out plane movements (e.g. up down lifting) during the tests (Figure 4.3).

Since axial load has no effect in the joint shear strength for these particular systems, constant axial load was applied on the top of the column with 100kN.

The 2-Dimensional and 3-Dimensional loading regime was the same used previously for the beam column joints subassemblies presented in chapter 3 which complied with the “acceptance criteria” for jointed ductile connections proposed in the literature [4.2].

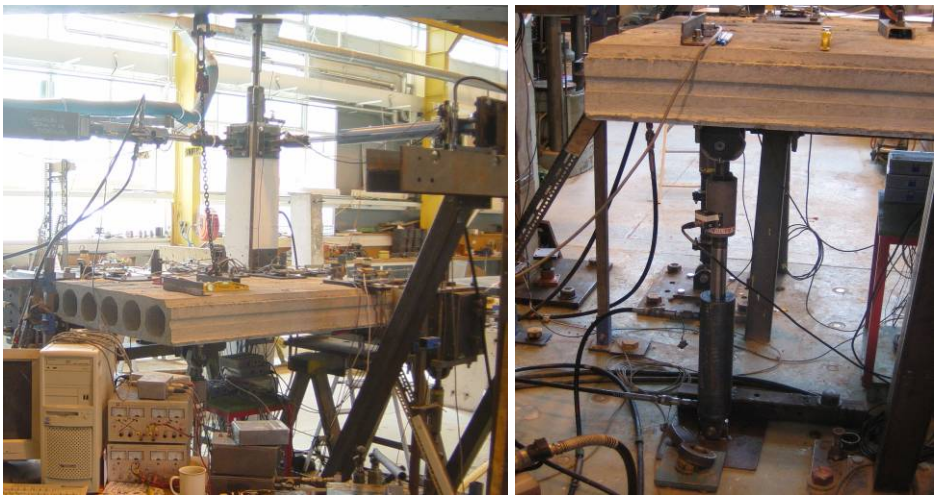

Figure 4.3. Beam-column joint with articulated floor unit: Back view (left), detail of strong floor-hollow-core connection (right).

4.4. EXPERIMENTAL RESPONSE OF THE SPECIMEN HJ3-HC

Figure 4.4 shows the lateral force vs. displacement responses of the unbonded post-tensioned only solution HJ3-HC-25PT1 and HJ3-HC-27PT2 in combination with the hybrid solution with external energy dissipaters HJ3-HC-25PT1-7D and HJ3-HC-27PT2-8D with extremely satisfactory results. The response without hollow-core is found in Figure 3.22 and Figure 3.24 for the post-tensioned only and adding energy dissipation solution respectively. Comparison shows no interaction between the hollow-core and the seismic resisting frame system.

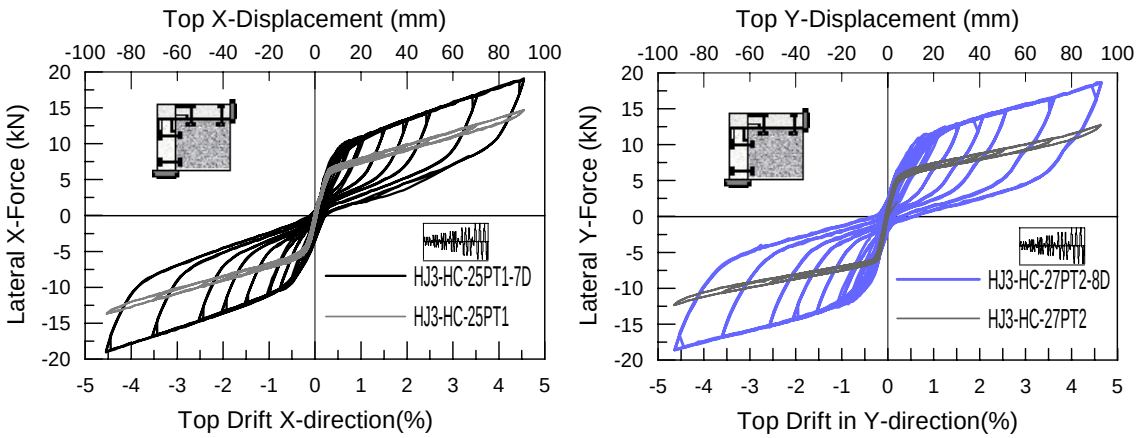

Figure 4.4. Hysteresis response of HJ3-HC under uni-directional loading with and without energy dissipaters.

Specimen HJ3-HC was also subjected to a combined bi-directional "four cloves" loading protocol. The response of tests HJ3-HC-X25PT1-Y27PT2 (unbonded post-tensioned only solution) and HJ3-HC-X25PT1-Y27PT2-X7D-Y8D (hybrid solution with external dissipaters),

was extremely satisfactory in both directions as shown in Figure 4.5. However, due to the aforementioned highly demanding nature of the testing protocol as explained in Chapter 3 (a total of 12 cycles in total for each drift) excessive steel strain in the dissipaters lead to a premature failure of one of the dissipaters in the last cycle of last quadrant towards 4.5% of drift.

In addition, in the Y direction some strength losses were observed due to torsion effects on the beam in the Y direction mainly due to the test set-up constraints (movement of the pinned beam arm in the out-of plane direction).

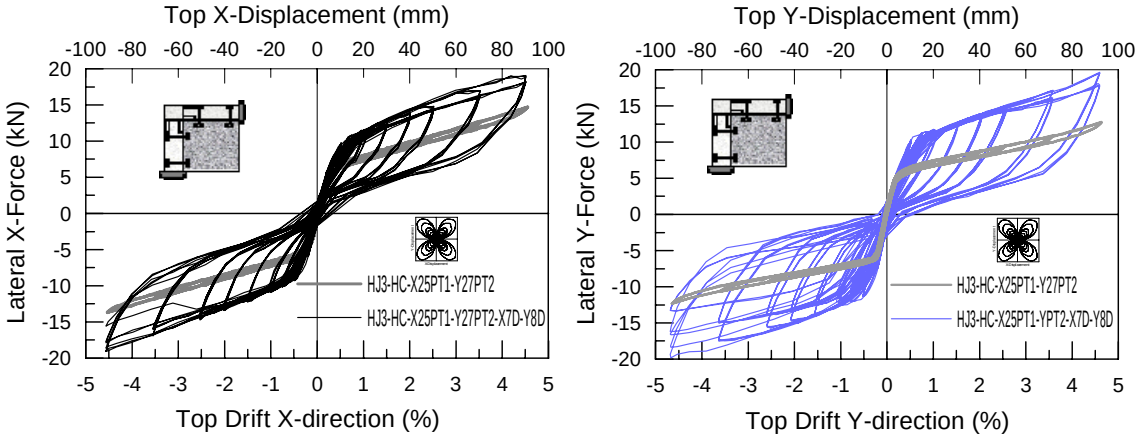

Figure 4.5. Hysteresis response of HJ3-HC under bi-directional loading: Hybrid solution (left) and overall response at 4.5% drift (right).

The effects of bi-axial cyclic loading were almost negligible when comparing the response to that of the same specimen under independent uni-directional loading (Figure 4.4) and no differences can be noted in the response of the 3-D beam-column joints subassemblies, due to over-strength or interaction, when compared to the response of the bare beam-column joint without floor (Figure 3.30 and Figure 3.31).

The gap opening of the top of the connection and movement the mechanical connector is shown in Figure 4.6 for test HJ3-HC-X25PT1-Y27PT2. As expected, similar displacements are observed between the beam-column connection and the movement at the hollow-core due to sliding of the mechanical connector. However, in the Y-direction there is some restrain when the gap closes at the top mainly due to the test set-up constraints in the beam pinned arm leading to torsion effects in the Y-direction.

Tendon force behaviour for all the tests were similar to the results obtained with the Hybrid subassembly without hollow-core slab and presented in Figure 3.23 and Figure 3.25 in Chapter 3.

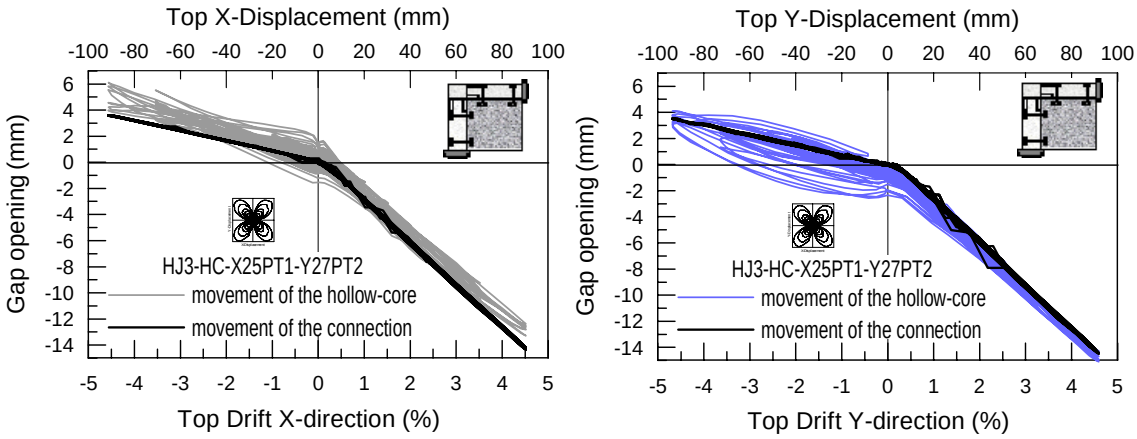

Figure 4.6. Gap opening of HJ3-HC at the beam column joint connection and movement of the floor in X-direction (left) and Y-direction (right).

4.5. NON-GAPPING FRAME SYSTEMS AND TOP HINGE CONNECTION

The previous concept of reducing the impact of displacement compatibilities using discrete shear connectors located at some points through the span of the seismic beam present some problems. As described previously, the floor will be free from having to follow the deformation pattern of the beam and needs to deflect together with the beam at the points of the shear key connectors only. However, this requirement could be easily obtained if the shear connectors are provided at the locations of zero vertical deflection of the beam.

From structural analysis it is known that there will be at least one point in the beam deflected in double curvature (i.e. where the vertical deflection is zero), this point varies from structure to structure and also within the same structure depending on the drift level. Hence, a general solution to completely avoid the compatibility requirement cannot be achieved through this approach.

A second approach is to have a frame system where displacement incompatibilities and the effects of beam elongation can be eliminated. The unique properties of a jointed ductile connection consisting of an articulated assembly of precast elements can be exploited and extended in order to avoid beam elongation effects.

As described in Chapter 2, as part of Phase II of the PREcast Seismic Structural System (PRESSS) Research Program, four beam-to-column connections and mechanical connectors limiting the issues of beam elongation between the precast floor units and the lateral resistant elements were developed [4.3, 4.4]. One of the connections - called the Hybrid frame connection (Figure 4.7-left) - combined unbonded post-tensioning through the centre of the joint which acts as a clamping force thus having self-centring properties and the use of mild-steel reinforcement inside ducts and grouted for bond conditions.

Another innovative beam-column connection called the Tension-Compression Yield–GAP solution (TCY GAP) (Figure 4.7-centre) was introduced using top mild-steel bars inserted into grouted sleeves and the use of unbonded post-tension tendons at the bottom of the beam. The peculiarity of this system was that beams and columns were separated by a small gap partially grouted to avoid the primary elongation effects, thus not affecting the centre-to-centre distance between columns. However, such a solution would not account for the tearing floor actions occurring due to the gap-opening at the top of the beam. Furthermore, no re-centering contribution was provided by the tendons located with a straight profile in the centre of the compression grout.

An inverted TCY-Gap solution (Figure. 4.7-right), based on a single top hinge (top pad or similar contact thick element) with a gap on the bottom part of the beam and grouted internal mild steel bars in the bottom part of the beam would naturally represent an evolution of the previous schemes. This modification prevents both elongation and tearing effects in the floor whilst no-recentring capacities can be provided due to the location and straight profile of the tendons.

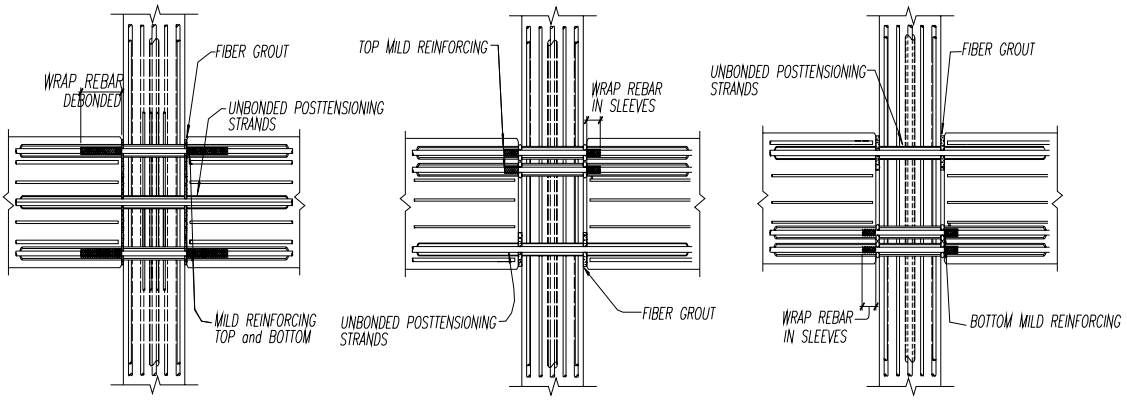

Figure 4.7. Evolution of the Hybrid systems: Hybrid PRESSS(left),TCY-GAP(centre), & Inverted TCY-GAP(right) Note. Beam reinforcement is not shown for clarity.

4.6 BEHAVIOURAL CONCEPT OF THE HYBRID TOP HINGE CONNECTION

The rocking of the top hinge or which from now shall be known as the non-tearing-floor-connection with a single top hinge, with different configuration of unbonded tendon profiles (straight or parabolic) and bottom energy dissipaters are shown in Figure 4.8.

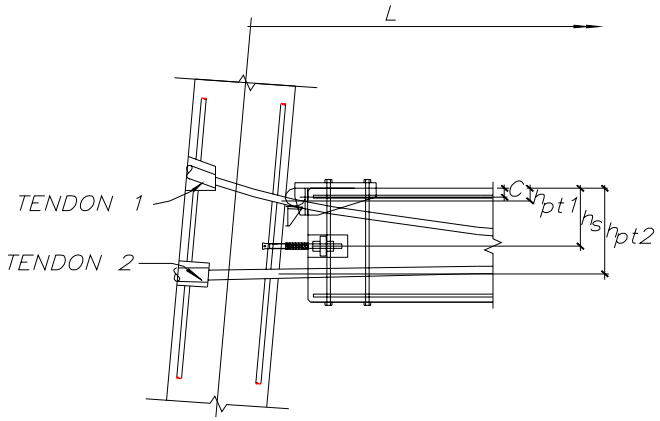

Figure 4.8. Rocking of the Hybrid B/C connection with top hinge and unbonded tendons.

Given that the single hinge acts as a pivot point, the neutral axis depth position c is given and fixed by the designer, the moment capacity of the beam column connection is simply achieved using equilibrium of the section and then taking moments from the neutral axis position.

4.6.1 Step 1: Evaluation of strain and stress in the post-tensioned tendons

To evaluate the strain and forces in the unbonded post-tensioned tendons, first it is required to find the elongation (elastic + plastic) at the level of the tendon which can be calculated as

$$\Delta_{pt1} = \theta_b \left(h_{pt1} - c \right) \tag{4.1a}$$

$$\Delta_{pt2} = \theta_b \left(h_{pt2} - c \right) \tag{4.1b}$$

where θ_b is the column rotation established as the design drift and h_{pt1} and h_{pt2} are the height of the tendon 1 and 2 respectively and c the neutral axis depth position.

The increase in the strain in the post-tensioned tendons due to the beam deformation is taken into account. The additional post-tension strain can be calculated as

$$\varepsilon_{pt1} = \Delta_{pt1} / l_{unb} \tag{4.2a}$$

$$\varepsilon_{pt2} = \Delta_{pt2} / l_{unb} \tag{4.2b}$$

where l_{unb} is the unbonded length of the post-tension tendons. The additional post-tension stress can be calculated as

$$\Delta\sigma_{pt1} = E_{pt} \Delta_{pt1} / l_{unb} \tag{4.3a}$$

$$\Delta\sigma_{pt2} = E_{pt}\Delta_{pt2} / l_{unb} \tag{4.3b}$$

where E_{pt} is the modulus of elasticity. Total post-tension tendon stress is easily calculated as $\sigma_{pt} = \sigma_{pt\,ini} + \Delta\sigma_{pt}$ where $\sigma_{pt\,ini}$ is the initial stress applied to the tendon expressed as a percentage of the ultimate stress.

4.6.2 Step 2: Evaluation of strain and stress in the mild steel dissipators

Estimating the strain and force in the mild steel can be achieved using a simple equation which by neglecting the strain penetration effects can be estimated as:

$$\varepsilon_s = \theta_b (h_s - c) / l'_{unb} \tag{4.4}$$

where h_s is the height of the dissipater, c the neutral axis position and l'_{unb} the unbonded length of the mild-steel.

In order to avoid fracturing of the bars at the design earthquake intensity level, the maximum permissible strain shall not exceed $0.9\varepsilon_{ult}$. Finally, the steel stress in dissipaters can be calculated through constitutive relationships. Recognising that it is possible for the tension strain to enter the strain hardening region of the stress-strain curve, an approximate multi-linear or parabolic stress curve proposed [4.5] can be adopted for design: Therefore, an evaluation of the strain obtained is required to obtain the mild steel stress:

$$f_s = E_s\varepsilon_s \text{ if } \varepsilon_s \le \varepsilon_y \tag{4.5a}$$

$$f_s = f_{su} + (f_y - f_u)\left(\frac{\varepsilon_{su} - \varepsilon_s}{\varepsilon_{su} - \varepsilon_{sh}}\right)^p \text{ where } p = \frac{\log\left(\frac{f_{su} - f_x}{f_{su} - f_y}\right)}{\log\left(\frac{\varepsilon_{su} - \varepsilon_x}{\varepsilon_{su} - \varepsilon_{sh}}\right)} \text{ if } \varepsilon_s \ge \varepsilon_{sh} \tag{4.5b}$$

Where ε_s and f_s are the generic stress-strain situation, ε_y and f_y corresponds to the yielding point, ε_{sh} defines the onset of the hardeing, ε_{su} and f_{su} are the ultimate strain and stress point and ε_x and f_x are the generic data point on the hardeing portion.

4.6.3 Step 3: Section equilibrium and moment capacity

The moment capacity of the beam column connection is simply achieved using equilibrium of the section and then taking moments from the neutral axis position. The total moment contribution M can be evaluated as:

$$M = \left(T_{pt1\,ini} + \Delta T_{pt1}\right)\left(h_{pt1} - c\right) + \left(T_{pt2\,ini} + \Delta T_{pt2}\right)\left(h_{pt2} - c\right) + T_s\left(h_s - c\right) \quad (4.6)$$

4.7 COMPARISON BETWEEN HYBRID PRESSS AND HYBRID NON-TEARING CONNECTION

In a traditional Hybrid PRESSS frame system a local connection or global force displacement re-centering can be achieved by combining the contribution of the post-tensioned tendons and the energy dissipation devices as presented in Chapter 3.

Figure 4.9, shows an idealized hysteresis loops a pure yielding system (Figure 4.9-left), a pure unbonded post-tensioned system (Figure 4.9-centre) and a hybrid PRESSS system and the Hybrid Non-tearing systems (Figure 4.9-right) using the equations (4.1) to (4.6). The pure yielding system dissipates energy, but will exhibit residual drift because the displacement is not zero when the force drops to zero.

In the pure unbonded post-tensioned Hybrid PRESSS, the relationship is elastic but nonlinear; that is, it loads and unloads along the same path so there is no hysteresis and no energy dissipated, but the path is non-linear because of the opening and closing of the cracks.

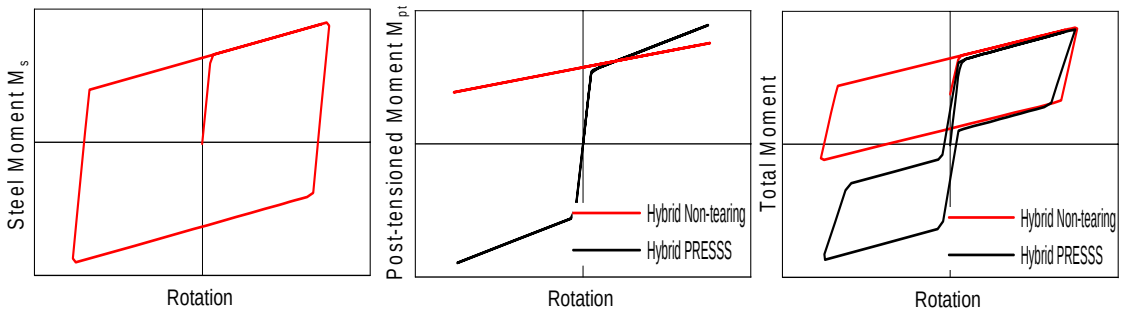

Figure 4.9. Idealized hysteresis loop for Hybrid and hybrid non-tearing rocking systems

For the Hybrid Non-tearing system, a linear elastic relationship is observed for the pure unbonded post-tensioned system (Figure 4.9-centre). The no zero offset of the initial post-tensioned moment is due to the initial post-tensioned force applied which induces an initial moment in the connection. The Hybrid non-tearing connection has small initial stiffness when it is compared with the high initial stiffness of the Hybrid PRESSS system.

The Hybrid PRESSS system presents a geometric non linearity of the stiffness onset when the gap at the critical section opens due to the sudden relocation of the neutral axis position over the beam depth, while for the Hybrid Non-tearing system this stiffness remains constant.

The total moment contribution for the Hybrid PRESSS and Hybrid Non-tearing systems are a combination of the two hysteresis curves. For the Hybrid PRESSS system (Figure 4.9-right), the prestressing force is designed to be large enough so that the elastic restoring force will overcome the yield strength of the mild reinforcing steel and return the system to zero or near zero displacement when external load is removed.

The curve in black from Figure 4.9-right, therefore, goes back through the origin. However, for the Hybrid Non-tearing system the total moment contribution is based on the same pure yielding system moment offset by the initial post-tensioned moment with an initial stiffness determined by the pure yield system and post-yield stiffness by the contribution of both systems (pure yield and linear elastic).

While the mild steel bar is yielding in the Hybrid PRESSS connection, energy is dissipated by hysteresis, as shown as the area under the curve. The area of the loop and the point at which the unloading curve rejoins the loading curve depends on the relative quantities of the two types of reinforcement.

Depending on the moment contribution ratio between the self-centering and dissipating contributions, a wide range of hybrid solutions such as those presented in Chapter 2 can be obtained varying from no energy dissipation and the use of an unbonded post-tensioned solution (also called Non linear elastic systems - NLE) [4.6] to systems with full capacity coming from the energy dissipation (Tension-Compression Yielding Systems - TCY) [4.6].

In the NLE systems, the unbonded post-tensioned tendons will provide all the moment capacities at the connection with the characteristic of having full re-centering capabilities which can be achieve with or without additional axial load. For the TCY systems the hysteresis behaviour is similar to an equivalent “emulative” monolithic connection.

Appendix B of New Zealand Standard 3101:2006 [4.7], determines the full self-centering of a general jointed connection shall be achieved by selecting in the design phase, an appropriate moment contribution ratio λ as the ratio between the restoring forces and the dissipation forces $\lambda = \left(M_{pt} + M_N / M_s\right) \geq \alpha_o$ where M_{pt}, M_N and M_s are the flexural strength contributions of the post-tensioned tendons, the axial load where present, and the non-prestressed steel reinforcement respectively. The Value α_0 is the overstrength factor for the non-prestressed steel reinforcement or the energy dissipating devices and is constrained by $\alpha_0 \geq 1.15$.

However, in the Hybrid Non-tearing connection, the energy dissipated under the curve and the point at which the unloading curve rejoins the loading curve does not go to zero due to the low stiffness of the post-tensioning behaviour and therefore no re-centering can be achieved at the connection. Also, a relatively low initial stiffness of the connections undergo the structure to higher displacement (more flexible) until the lateral resistance is achieved. Push over analysis and time history analysis will be carried out to examine the response of hybrid frame systems using non-tearing connections.

For the latter, a rubber pad working only in compression located at the gap of the connection would be sufficient to increase the stiffness when the gap closes. Therefore, it is require that the compression forces the rubber can sustain at the design drift will not surpass the forces in the monohinge. Chapter 5 shows the results obtained using the rubber pad concept.

4.8 EXPERIMENTAL INVESTIGATIONS ON A HYBRID BEAM COLUMN JOINT WITH TOP HINGE CONNECTIONS

The main objectives of the experimental campaign with the same specimen HJ3 described previously in Chapter 3 was to study a top hinge solution and the floor tearing effects due to the gap opening. It is important to mention that the full re-centering properties of the connection can not in this case be appreciated due to the use of a straight tendon configuration in addition to the use of a single beam-column connection solution.

4.8.1 Specimen Description

As part of the experimental research herein reported, the same 2-D exterior (corner) beam-column joint subassembly HJ3 was used and is described for this set of tests as HJ3-TH (where the TH means Top hinge). The modular face plate, acting as a “mask”, located at both the beam and column faces allowed for the location of mechanical top hinges acting as shear keys positioned at 47mm from top of the beam (Figure 4.10-left).

The location of the dissipaters was within the beam rectangular lateral profile (hidden) to represent a more aesthetically pleasing arrangement located at 47mm from the bottom beam end (Figure 4.10-centre). No energy dissipaters were located at the top of the beam due to the fact that there is no lever arm and therefore no additional force would be added into the system. The unbonded tendon locations were type 1 as shown in Table 3.2 in Chapter 3.

A compression-only block (buffer) at the bottom of the beam depth was implemented (Figure 4.10-right) in order to avoid instability of the beam-column subassembly that arises from the selected to the test set up. This compression block acts only in compression when the gap closes which added minor energy dissipation into the system from the compression stiffness of the block.

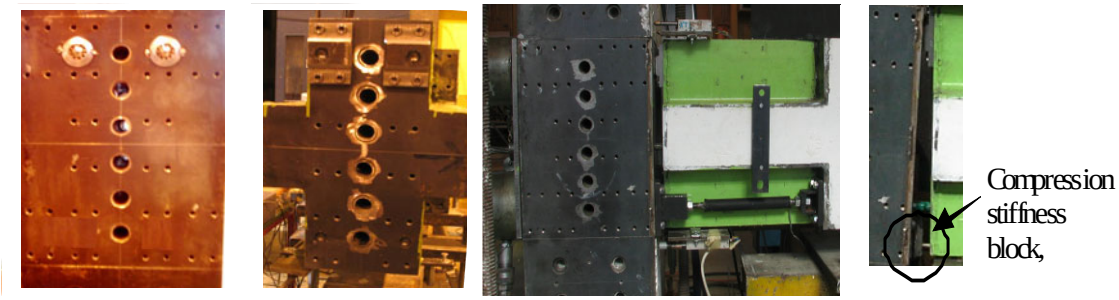

Figure 4.10. Modular configuration of the Hybrid beam-column joint HJ3-TH: location of hinges, dissipaters, and compression stiffness block.

An unbonded post-tensioned tendon-only solution (test HJ3-TH-20/38PT1) was performed varying the level of initial post-tensioning. Two seven wire strands (Apt = 99 mm2) located at top and bottom were used with initial post-tensioning level equal to 20% and 38% of the ultimate stress $\sigma_{pt\ ult}$ = 1860MPa, thus equal to an initial post-tensioning force of $F_{pt\ ini}$ = 37kN and 70kN respectively.

The hybrid non-tearing floor connection solution (test HJ3-TH-20/38PT1-7D) was obtained by adding external dissipaters, given the same tendon layout and prestressing force as in the post-tensioned only solution. Two external dissipators consisting of 7mm diameter fuses (with 150 mm unbonded length) were installed and inserted in existing slots on both sides of the beam (Figure 4.10-centre).

4.8.2 Test set up and Loading Protocol.

The set-up and imposed displacement regime of the exterior beam-column joint subassemblies are similar to those used for the subassemblies tested in Figure 3.10 presented in Chapter 3. Beam and column elements are extended between points of contra-flexure, assumed to be at mid-span of the beams and at mid-height of the column, where pins were introduced. Simple supports at the beam ends were provided by connecting pin-end steel members to the floor.

Quasi-static cyclic tests were carried out under increasing levels of lateral top displacement. The testing protocol complied with the “acceptance criteria” for jointed ductile connections

proposed in the literature [4.2] and consisted of a series of three cycles of drift, followed by a single smaller cycle.

Since axial load has no effect in the joint shear strength for these particular systems, constant axial load was applied on the top of the column with 100kN.

4.9 EXPERIMENTAL RESPONSE OF THE SPECIMEN HJ3-TH

Figure 4.11 shows the lateral force vs. displacement responses of the unbonded post-tensioned only solution test HJ3-TH-20/38PT1. In general the behaviour was satisfactory. As typical of a jointed ductile hybrid solution, no damage was reported in the structural members, while a very stable linear elastic hysteresis loop was developed. The initial force of the actuator of 8 kN is generated by the test set up, due to the fact that the bottom tendon is trying to close the gap and the actuator is acting as a reacting force.

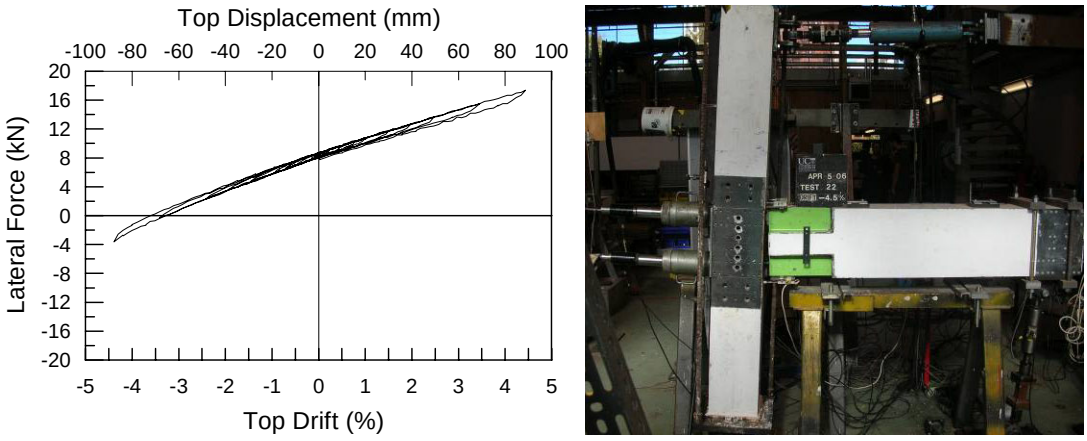

Figure 4.11. Hysteresis response of HJ3-TH-20/38PT1: Unbonded post-tensioned only solution (left) and overall response at 4.5 % drift (right)

The top hinge acting as a shear key, remained, as expected in compression during the test (due to the presence of the top tendon) while allowing the controlled rotation of the beam. Negligible elongation and shortening on the floor systems would thus be expected. Clearly, the closer the hinge is located to the top of the beam section, the less the damage from the floor will be. Figure 4.12 shows the top and bottom gap opening and tendon force behaviour for this specific test where the mechanical hinge was located at 47 mm from top of the beam section (Figure 4.10).

A maximum gap displacement of 2.5 mm at the top and 13 mm at the bottom were obtained at 4.5% drift. Considering that the neutral axis position remains constant at any drift level, a

simple calculation is required to maintain the required moment capacity in the joint. As was expected, the top tendon force remains constant and only elongates or shortens according with its elastic properties, keeping the beam column interface in compression, while the bottom tendon force needs to be designed to provide the required moment capacity.

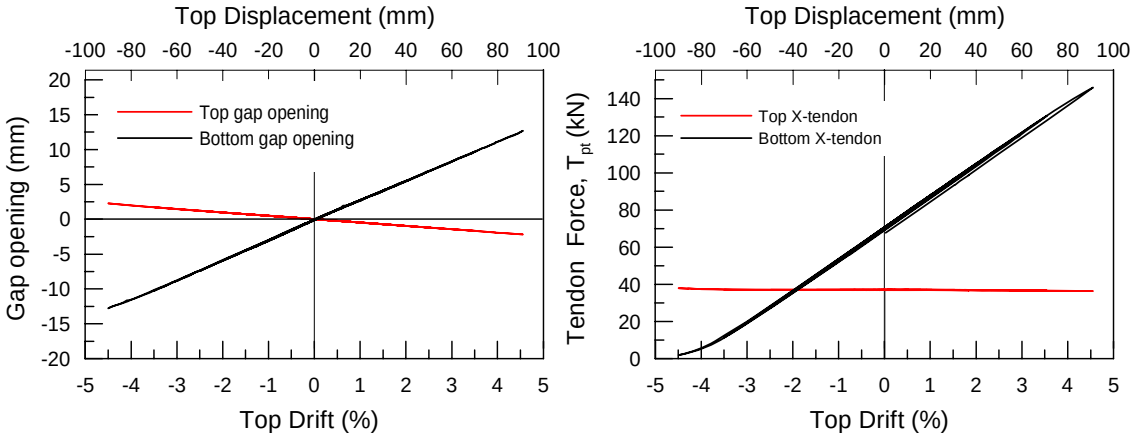

Figure 4.12. Gap opening variation at rocking (left) and variation of tendon forces for HJ3-TH-20/38PT1 (right)

The hybrid non-tearing-floor connection solution test HJ3-TH-20/38PT1-7D was obtained by adding external dissipaters, given the same tendon layout and prestressing force as in the post-tensioned only solution (Figure 4.11). Two external dissipaters consisting of 7mm diameter fuses (with 150 mm unbonded length) were installed and inserted in existing slots on both sides of the beam (Figure 4.10).

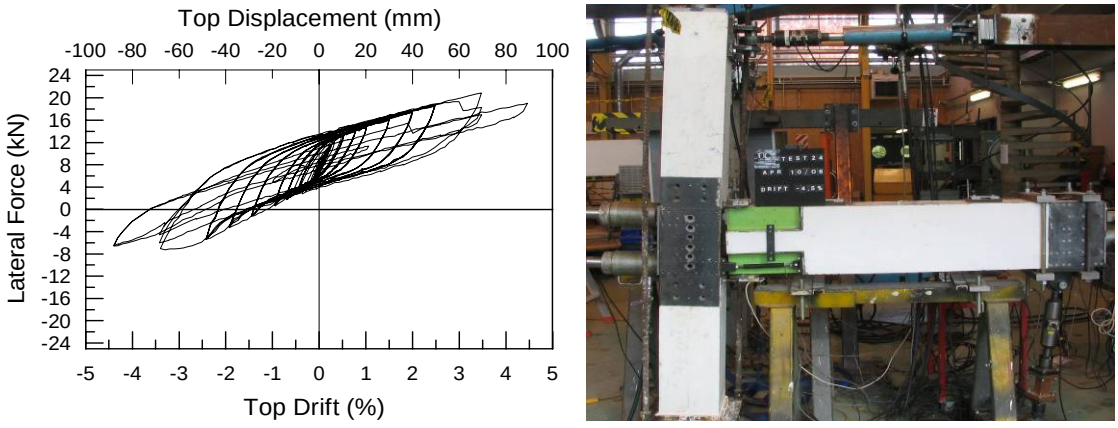

Figure 4.13. Hysteresis response of HJ3-TH-20/38PT1-7D: Hybrid solution with external dissipaters (Left) and overall response at 4.5 % drift (Right)

The experimental response under uni-directional testing showed (Figure 4.13) stable bi-linear hysteresis loop given by the combination of the non-linear elastic post-tensioned tendon and the bi-linear inelastic contribution of the mild steel bars. At higher drift levels (3.0%) however,

stiffness degradation is observed due to a fracture of one dissipater. As mentioned before, no re-centring is obtained in the connection due to the straight tendon profile.

As expected, same maximum gap displacements were obtained as those recorded in the unbonded post-tensioned solution (Figure 4.12). The presence of the single-hinge shear key solution which consists of small metallic balls, as shown in Figure 4.10 guaranteed one fixed pivot point, with no stiffness or strength losses up to a high level of drift (4.5%).

4.10 EXPERIMENTAL ANALYTICAL COMPARISON

Using a lumped plasticity model approach which adopts non-linear inelastic springs located in parallel at the rocking interface as described in Section 3.2 (Chapter 3), can successfully represent the response of the tests. The non-linear finite element program Ruaumoko2D [4.8] was used to model the series of experimental tests by imposing the same time history displacements applied during testing.

4.10.1 Hybrid PRESSS Beam-Column Subassembly HJ3-HC

Similarly as the validation of the results for the specimen HJ3 in Chapter 3, a lumped plasticity model based on the combination of two rotational springs in parallel was used for the validation of the different tests carried out on the HJ3-HC specimen (Figure 4.14).

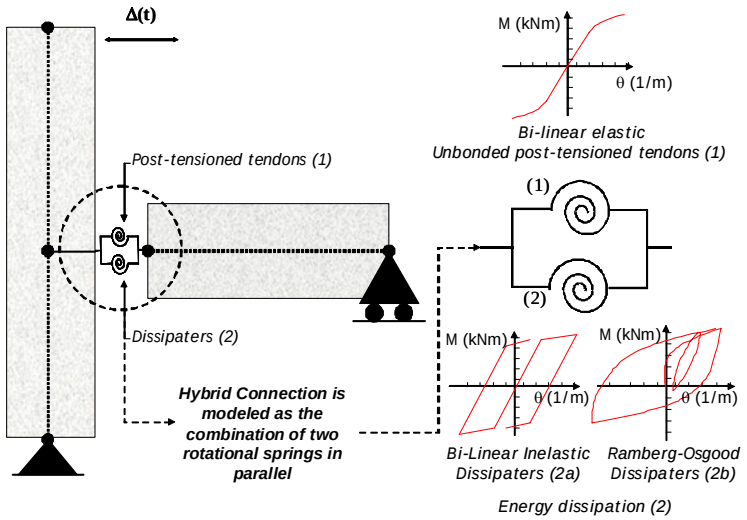

Figure 4.14 Rotational spring model used for HJ3-HC

The moment rotation contribution of the unbonded post tensioned tendon was modelled using a Non Linear Elastic hysteresis rule while two hysteresis models were considered to represent the

energy dissipation contribution: Bi-linear inelastic and Bounded Ramberg-Osgood. Elastic elements were used to represent the structural members.

Figure 4.15 shows the force-displacement experimental validation of test HJ3-HC-25PT1-7D using bi-linear (EP) and Romberg-Osgood (RO) hysteresis rules under monotonic steel behaviour. In general the lumped plasticity model can validate the results; however, the monotonic steel behaviour assumed does not fully capture the strength at higher drift levels due to the Bauschinger effects in the dissipaters as explained in Section 3.6.5.

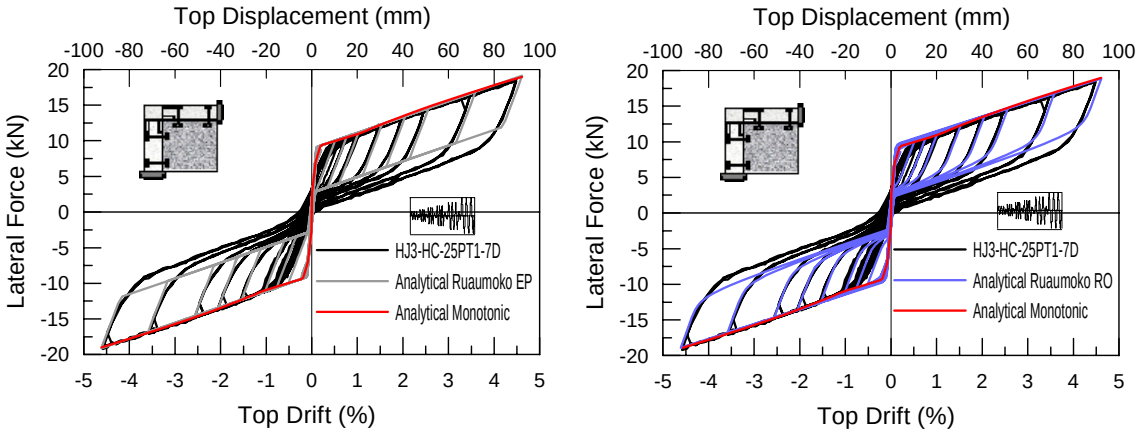

Figure 4.15 Experimental analytical comparison for HJ3-HC-25PT1-7D: Force displacement using monotonic steel characteristics: Elasto-plastic (left) and Ramberg-Osgood (right).

Figure 4.16-left shows the analytical comparison among experimental dissipater tests converted into moment rotation and the analytical hysteresis used for the Ruaumoko model. As it can be seen, the uni-axial tensile test of the dissipaters (calculated as the distance between the hinge and location of the dissipater) showed good agreement with the hysteresis behaviour used as input for the program. Figure 4.16-right shows the excellent agreements between the experimental results and the simple calculations using the monolithic beam analogy principles.

Finally, similar results were obtained for the test HJ3-HC-X25PT1-Y27PT2-X7D-Y-8D using the same moment-rotational model presented previously for the test HJ3-HC-27PT1-7D. Figure 4.17 shows the analytical validation in terms of total lateral response for the two orthogonal directions using Elasto-Plastic and Ramberg-Osgood hysteresis behaviour with very good agreements, however, it does not capture the failure of the dissipater at the maximum drift level of 4.5% and the subsequent strength losses in the Y direction.

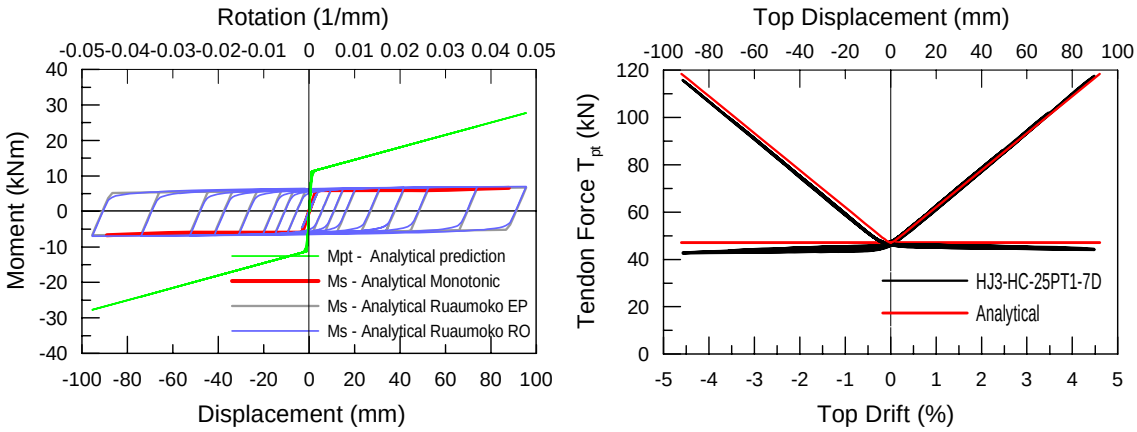

Figure 4.16 Experimental analytical comparison for HJ3-HC-25PT1-7D: Steel and post-tensioned moment contribution (left) and post-tensioned tendon force (right).

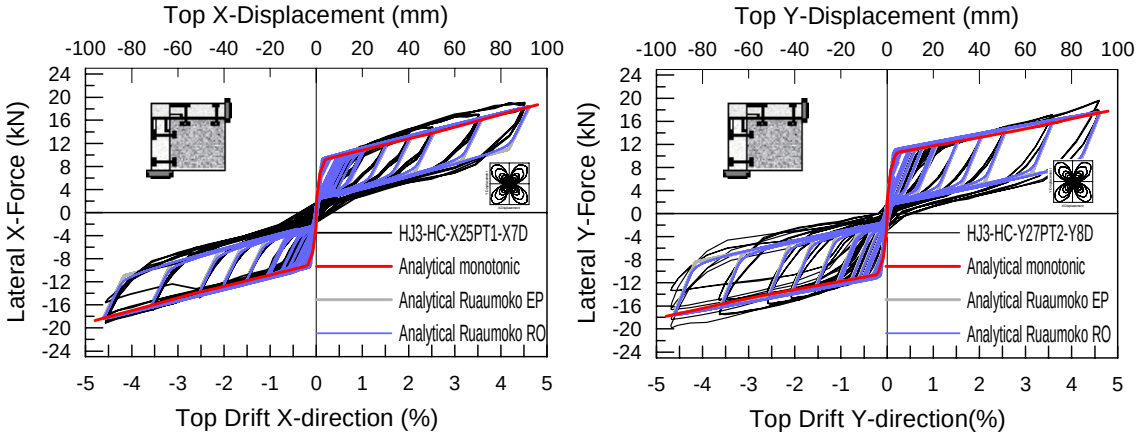

Figure 4.17 Experimental analytical comparison for HJ3-HC-X25PT1-Y27PT2-X7D-Y8D: Force displacement: Elasto-plastic (left) and Ramberg-Osgood (right).

4.10.2 Hybrid PRESSS Beam-Column Subassembly HJ3-TH

Two models were used to reproduce the experimental results, providing a reliable control over the expected hysteresis and dynamic behaviour. The first model is based on the moment rotation spring model acting in parallel (Figure 4.18-left). The second lumped plasticity model is based on the combination of three axial springs and shown in Figure 4.18-right.

In the moment rotation model, the unbonded post-tensioned tendon was using a rotational spring with the Linear Elastic rule behaviour, while for the second spring a Ramberg-Osgood hysteresis rule was considered. The top tendon was not modelled because there is not any contribution to the lateral response of the system.

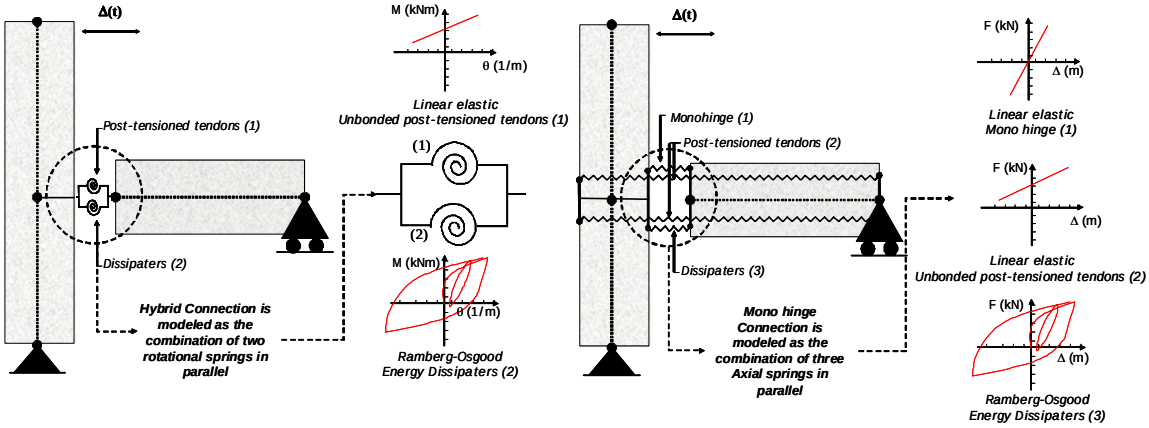

Figure 4.18. Models used for HJ3-TH: Moment rotational spring (left) and axial spring (right)

For the axial spring model, the mono-hinge axial stiffness is modelled with longitudinal and transverse linear elastic springs with significantly high stiffness (axial stiffness of metallic ball connection) to allow the analysis to include the resultant compressive force within the output. The unbonded post tensioned tendon is modelled using a Linear Elastic spring, while a spring having a Ramberg-Osgood hysteresis rule represents the steel dissipation contribution.

Figure 4.19-left and Figure 4.20-left show the experimental analytical comparison response of the model using moment rotational and axial spring models respectively. Given the simple hysteresis rules adopted, the model can reproduce the experimental results with reasonable accuracy. Both models can reproduce the behaviour of the post-tensioned force (Figure 4.19-right and Figure 4.20-right). However, due to the simple steel rule adopted, the models are unable to properly capture the behaviour when the dissipaters are loaded in compression (closing of the mono-hinge).

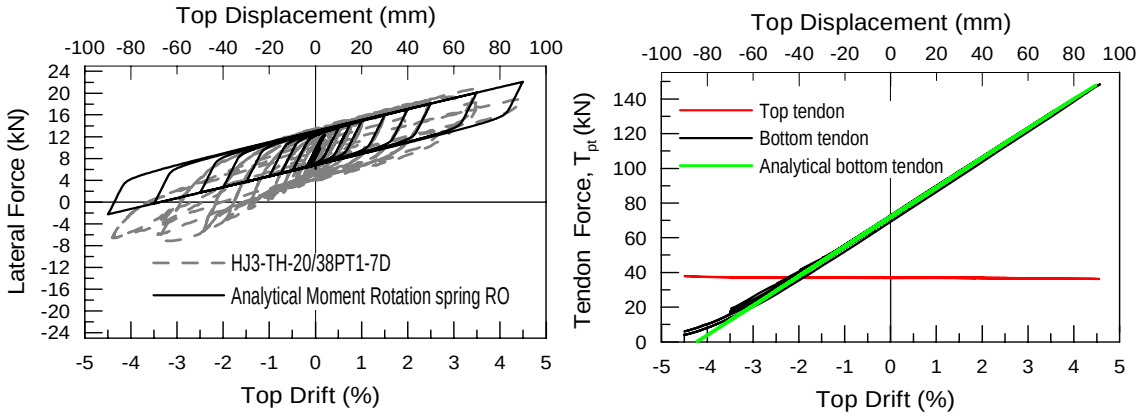

Figure 4.19. Experimental analytical comparison for HJ3-TH--20/38PT1 -7D using moment rotational springs: Force displacement response (left) and post-tensioned tendon force (right).

Comparison between the two models indicates that the axial spring model can better represent the overall response in terms of the force displacement as the additional stiffness of the mono hinge is taken into account while for the moment rotational model only the post-tensioned stiffness and dissipater contributions are considered.

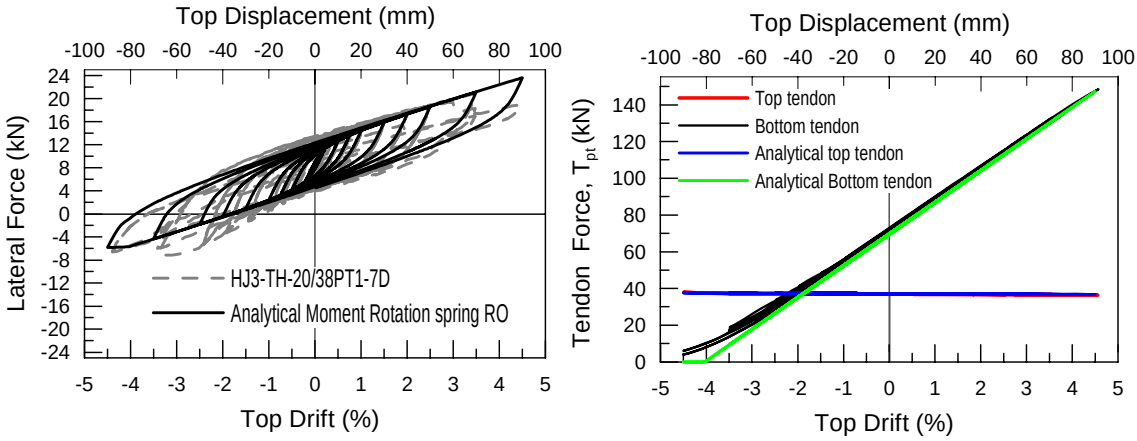

Figure 4.20. Experimental analytical comparison for HJ3-TH--20/38PT1 -7D using axial springs: Force displacement response (left) and Post-tensioned tendon force (right).

4.11 CHAPTER SUMMARY

In this Chapter an overview of issues related to displacement incompatibilities between floor and lateral load resisting systems including vertical displacement incompatibility, beam elongation and seating connections has been presented.

In order to emphasize the enhanced performance in controlling and minimizing the damage of the structural elements via the use of the proposed advanced hybrid solutions presented in Chapter 3, two types of connection able to reduce the damage in the floor by reducing the effects of beam elongation have been implemented through experimental and analytical comparison of the results.

The first approach consists of using standard precast rocking/dissipative frame connections referred to “gapping” connection in combination with an articulated or “jointed” floor which uses mechanical devices to connect the floor and the lateral beams which can accommodate the displacement incompatibilities in the connection.

The second approach would rely upon a top hinge “non-gapping” system that could be used in combination with a standard floor solution (i.e. topping and continuous starter bars). This connection is an innovative “non-tearing floor” solution for precast jointed frame systems able

to obtain an efficient floor to lateral load resisting system connection, while negating the problems associated to beam elongation effects.

Based on the results of quasi-static cyclic tests on 2/3 scaled beam-column joint subassemblies implementing the proposed non-tearing floor solutions, the following conclusions can be made:

1. The efficiency of a simple and practical floor-to-frame system connection, able to accommodate displacement incompatibility due to the effects of the beam elongation (gap opening), in this case limited to the geometrical contribution, can be avoided by using a traditional gapping solution and a "smarter" floor-frame connection. No damage in the floor system due to the gap opening mechanism is thus expected. Also, due to the low flexural stiffness of the shear key-connectors in the out of plane direction, torsion of the beam elements due to pull out of the floor or relative rotation of floor and edge support, can be limited.

2. Minimum or no bi-axial effects were observed due to cyclic loading when comparing the response under uni-directional loading. Additionally, no differences were observed in the response of the 3-D specimen due to over-strength or, in general, interaction, when compared to the response of the bare beam-column joint without floor analyzed in Chapter 3.

3. The second approach to reduce the floor damage has been investigated implementing a non-tearing-floor seismic resisting system using a top hinge connector at the beam-column interface, while still relying on more traditional floor-to-frame connections (i.e. topping and continuous starter bars). The main objectives of the experimental campaign under beam-column joint subassembly with the proposed specimen were to study the top hinge solution and the tearing floor effects due to the gap opening. Therefore, the full re-centering properties of the connection can not in this case be appreciated due to the use of a straight tendon configuration as well as the impact of the test set-up by using the beam-column connection.

4. A comparison between the hybrid non-tearing beam-column joint behaviour with that of the traditional Hybrid PRESSS or the advanced hybrid connection proposed in Chapter 3 has indicated that the hybrid non-tearing connection exhibits a no zero offset of initial post-tension moment with a small initial stiffness when compared to the traditional hybrid connection.

5. The total moment contribution for the Hybrid PRESSS system is designed such that the prestressing force is designed to be large enough so that the elastic restoring force will overcome the yield strength of the mild reinforcing steel and return the system to zero or near zero displacement when the external load is removed. However, for the Hybrid Non-tearing

system the total moment contribution is based on the same pure yielding system moment offset by the initial post-tensioned moment with the initial stiffness determined by the pure yield system and post-yield stiffness by the contribution of both systems (pure yield and linear elastic).

6. A further conceptual evolution of this top hinge solution has led to the development of the non-tearing floor solution able to avoid the beam elongation and tearing effects in the floor with the use of anti symmetric profile of the unbonded post-tensioned tendons and external and replaceable energy dissipaters. By doing this the flexural capacity of the connection can be achieved by the combination of post-tensioning and energy dissipation, while the desired self-centering capacity can be obtained through the implementation of a rocking foundation in combination of the gravity loads and/or the use of post-tensioning leading to limited or no residual deformation and cost of repairing. The concept will be presented in Chapter 5 with the experimental results obtained from a 2-Dimensional, 2/3 scale, two storey, single bay, precast concrete frame system along with a simplified procedure for the design and modelling of the proposed connection.

4.12 REFERENCES

4.1. Priestley, M.J.N., Sritharan, S., Conley, J.R. and Pampanin, S. 1999. “Preliminary Results and Conclusions From the PRESSS Five-Storey Precast Concrete Test Building,” PCI Journal. 44 (6). 42-67.

4.2. Innovation Task Group 1 and Collaborators and ACI Committee 374. “Acceptance Criteria for Moment Frames Based on Structural Testing (T1.1-01) and Commentary (T1.1R-01),” American Concrete Institute, Farmington Hill, Michigan. 2001.

4.3. Priestley, M.J.N 1996. “The PRESSS Program-Current Status and Proposed Plans for Phase III,” PCI Journal, 41 (2), 22-40.

4.4. Nakaki, S.E., Stanton, J. F., Sritharan S., 1999. “An Overview of the Presss Five-Story Precast Test Building,” PCI Journal, 44 (2), 26-39

4.5. Restrepo, J. I., 1993 “Seismic behaviour of connections between precast concrete elements,” Ph.D. Dissertation, Department of Civil engineering, University of Canterbury, Christchurch, New Zealand

4.6. Palmieri, L., Saqan, E., French, C., and Kreger, M., “Ductile Connections for Precast Concrete Frame Systems,” Proceedings of the Mete Sozen Symposium, SP-162-13, American Concrete Institute, Farmington Hills, MI., Oct. 1996, pp. 313-355.

4.7. New Zealand Standards (NZS). “Appendix B: Special Provisions for the Seismic Design of Ductile Jointed Precast Concrete Structural Systems,” *NZS3101:2006, Concrete Standard*, Wellington, New Zealand.

4.8. Carr, A. "RUAUMOKO program for Inelastic Dynamic Analysis – User Manual". Department of Civil Engineering, University of Canterbury, Christchurch, New Zealand. 2006.

CHAPTER 5
REFINEMENTS OF A NON-TEARING FLOOR CONNECTION FOR HYBRID FRAME SYSTEMS

5.1 INTRODUCTION

As described in Chapter 2 and Chapter 4, it is clear that effects of beam elongation in precast frame systems have been demonstrated to be a potential source of un-expected damage to precast floor systems, unless adequate detailing is provided to account for displacement incompatibilities between the lateral resisting systems and the floor.

Two solutions to control and minimize the floor damage for hybrid connections have been presented in Chapter 4: the first solution consists of using standard precast rocking frame connections in combination with an articulated or "jointed" floor by using mechanical devices connecting the floor and the lateral beams and the second approach would rely upon a top hinge "non-gapping" system that could be use in combination with a standard floor solution (i.e. topping and continuous starter bars).

Very satisfactory results were obtained through experimental quasi-static cyclic testing on 2/3 scaled beam-column joint sub-assemblies, implementing the proposed non-tearing floor solution and presented in Chapter 4. However, as in the original TCY-gap solution, a full re-centering behaviour cannot be developed due to the use of a straight tendon configuration.

In this chapter, with the aim to obtain to minimized the residual displacements using re-centering frame capabilities, and investigate further connection refinements and constructability issues, a further conceptual evolution of the system is proposed on a 2-D, 2/3 scale, two storey, single bay, precast concrete frame system with the innovative "non-tearing floor" connection which consists of a single top-hinge connection while the re-centering is provided mainly by the column base moments, the anti-symmetric profile of the unbonded post-tensioned tendons provide additional re-centering capacity and the proposed external and replaceable mild-steel dissipaters devices can be used in addition to provide the required supplemental damping and connection strength.

The results of the quasi-static cyclic tests of the 2-D precast concrete frame system able to obtain an efficient floor to lateral load resisting system connection are presented. Additionally,

analytical-experimental validation is implemented using simple analytical models already presented in the literature, providing a reliable control over the expected hysteresis and dynamic behaviour.

5.2 CONCEPTUAL DEVELOPMENT

The evolution of the connection started from an inverted TCY-Gap solution as proposed [5.1] based on a single top hinge (top pad or similar contact thick element) with a gap and grouted internal mild steel bars in the bottom part of the beam. This modification prevents both elongation and tearing effects in the floor whilst no-recentring capacities can be provided due to the location and straight profile of the tendons.

In order to obtain a system with re-centering properties, while allowing for longer span construction (large open space) typical of prestressed or post-tensioned solutions, a further conceptual evolution of the top hinge connection has been proposed and presented in the literature under this research program [5.2, 5.3]. A single top-hinge connection guarantees no beam elongation in addition to the use of anti-symmetric profile of the unbonded post-tensioned tendons and external and replaceable energy dissipations to provide the require flexural capacity and damping capacity, while the re-centering properties will be provided by the column base moments (by providing a rocking foundation in combination of the gravity loads and/or the use of post-tensioning) and with the use of anti symmetric profile of the unbonded post-tensioned tendons and external and replaceable energy dissipaters. (Figure 5.1).

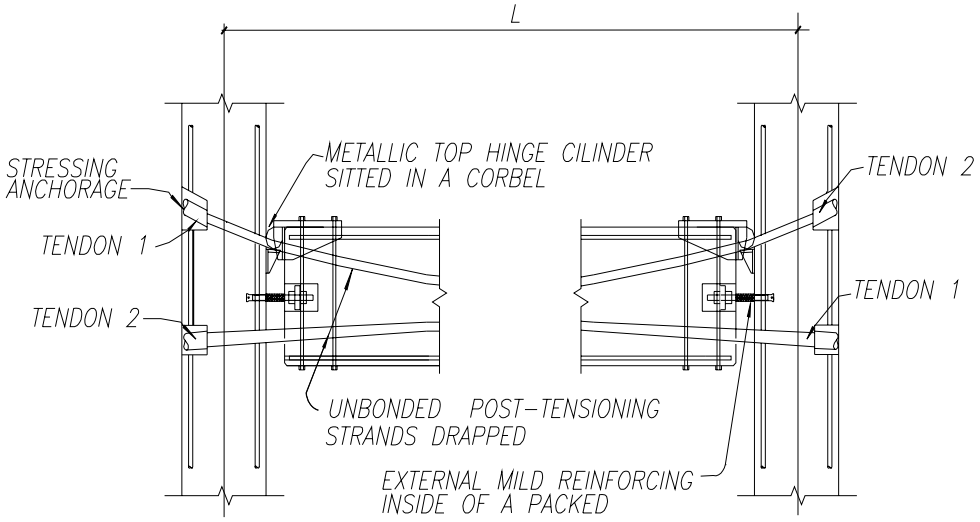

Figure 5.1. Hybrid Frame with draped unbonded tendons and metallic top hinge.

The connection inherently minimises the problems associated with beam elongation effects while also providing global system re-centring and minimising damage to the hybrid connection.

The connection detail (Figure 5.2) comprises of a top mono-hinge, steel armouring at the beam ends and a hidden corbel (acting as the beam-shear transfer mechanism). A T-shaped steel element is used as a shear key to prevent beam uplift and torsion while accommodating the tolerances in the beam length. An asymmetric unbonded post-tensioned tendon profile is adopted and combined with external energy dissipaters for supplementary damping.

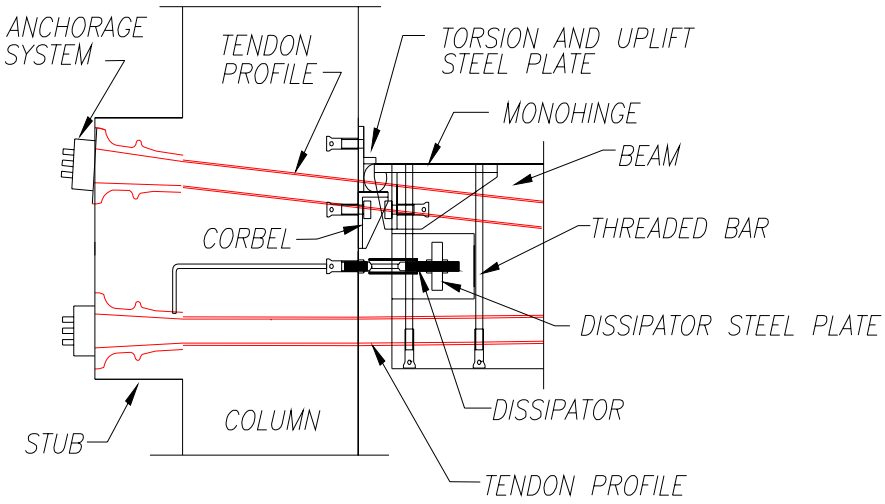

Figure 5.2. Connection detail.

5.2.1 Monohinge

Steel armouring was cast into the concrete during construction of the beams which consist of three steel plates (one top and two lateral) welded together. A steel cylinder (with one quarter removed) was connected to the top of the steel plate and welded to the steel armouring. The steel hinge element is attached to the beam using four high strength threaded bars bolted to the top steel plate and threaded into the underside of the beam.

5.2.2 Corbel

The corbel consisted of a steel angle, stiffened with four welded steel plates which added to the shear and bending capacity of the corbel. The steel corbel was attached to the column using high strength bolts, threaded into cast in-situ inserts.

5.2.3 Torsion, uplift steel plate and construction tolerances

The T-shape steel section (located directly above the steel cylinder) was located at both ends of the beam (Figure 5.2) to prevent torsion, beam uplift and tolerance issues. Uplifting occurs due to the vertical component of the post-tensioned forces (static case) and the laterally induced beam shear. Torsion could occur (as typical of any other system) when the precast floor units sit on the beam with an eccentricity.

Typical construction tolerances expected in real application were represented and addressed in the following manner:

- Product tolerances were considered for the precast beam by making them 20mm shorter than the required length. Steel shims were used to make up these tolerances and to transmit the axial compression forces from the beam to the column.

- Erection tolerances were expected to be, in general terms, not dissimilar from what would typically occur in normal construction process.

5.2.4 Mild steel dissipater fuse and steel plate

An important component for hybrid solutions are the external energy dissipaters used as supplemental damping devices. The objective of adding external energy dissipation is to dissipate the earthquake-induced energy via sacrificial elements that can be easily replaced after a strong earthquake. This minimises costs associated with repair and downtime when compared to conventional buildings.

The mild steel dissipater is fabricated from round mild steel bar, threaded at each end and machined down to a specific bar diameter over a pre-determined length; defined as the unbonded length.

The unbonded length prevents premature fracture of the bar by limiting the strains to allowable limits. An steel confining tube with bigger diameter than the energy dissipater bar is located over the machined area of the steel bar and filled with epoxy or grout into the steel confinement tube acting as anti-buckling restraint. Section 5.4.4 will explain the construction of the energy dissipaters

5.3 FLEXURAL CONNECTION DESIGN

Design of the connection can be done using a simplified procedure developed for jointed ductile connections [5.4] and implemented in the code provisions included in the Appendix B of the NZS3101:2006 [5.5]. When the structure is subjected to a high ground motion, the moment and shear envelopes (considering gravity and earthquake forces) occurs at the column face and is taken by the moment at the connection.

A non-tearing-floor-connection solution with a single top hinge, anti-symmetric tendon profile and bottom energy dissipaters are shown in Figure 5.3. Given that the single hinge acts as a pivot point, the neutral axis depth position c is given and fixed by the designer, so the next step is to evaluate the strain and forces in the unbonded post-tensioned tendons.

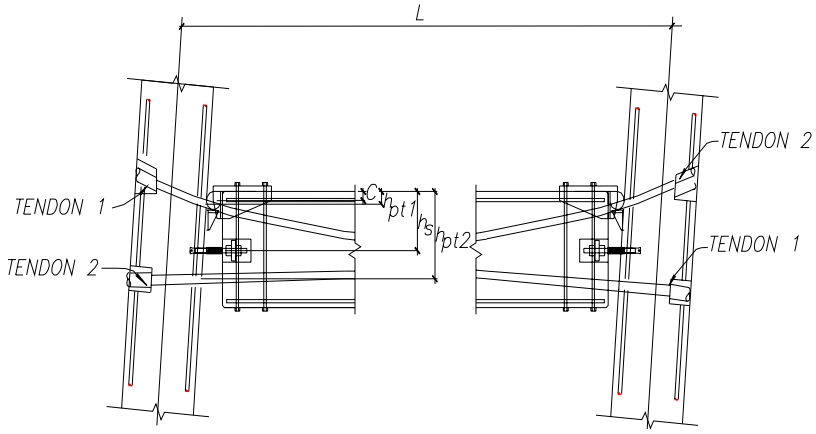

Figure 5.3. Rocking of the Hybrid Frame with draped unbonded tendons and metallic top hinge.

5.3.1 Step 1: Calculation of post-tensioned tendons elongation

Given that the single hinge acts as a pivot point, the neutral axis depth position c is given and fixed by the designer, so the next step is to evaluate the strain and forces in the unbonded post-tensioned tendons. The elongation (elastic + plastic) at the level of the tendon can be calculated as

$$\Delta_{pt1} = \theta_b \left(h_{pt1} - c \right) \tag{5.1a}$$

$$\Delta_{pt2} = \theta_b \left(h_{pt2} - c \right) \tag{5.1b}$$

where θ_b is the column rotation established as the design drift, h_{pt1} and h_{pt2} are the height of the tendon 1 and 2 respectively and c the neutral axis depth position.

Considering that the unbonded tendons are anti-symmetric and the open gap is at the bottom of the left connection (Figure 5.3), tendon 1 will shorten by an amount $\Delta_{pt1\,right}$ due to the closing

of the bottom of the right-side connection and elongate by the amount $\Delta_{pt1\,left}$ due to the open of the gap on the top of the left-side connection. Tendon 2 will be subjected to an anti-symmetric behaviour, implying elongation at the bottom of the left connection and shortening in the top of the right connection.

Assuming no friction between the post-tensioned tendon and the duct wall, the total contribution of the post-tensioned tendon deformations are based on the single contribution of each tendon at the left and right gap openings $\Delta_{pt1} = \Delta_{pt1\,left} + \Delta_{pt1\,right}$ and $\Delta_{pt2} = \Delta_{pt2\,left} + \Delta_{pt2\,right}$ respectively, where the two contributions are summed with their proper positive or negative signs.

To ensure that the correct force is applied to a set of tendons, calculations are made to account for losses (friction, wobble, wedge-set and anchor friction) along the length of a tendon profile and to estimate the elongation as a check against the gauge pressure on the jack.

Stressing the unbonded tendons may be performed from one or both ends. Stressing from both ends may be sequential, first from one end then the other, or simultaneous using two jacks. In some types of construction, it may only be necessary to stress from one end; for example, where tendons are relatively short, (about 50m) and have relatively small friction loss. However, for long tendon profiles, especially those within internal ducts set to a curved profile that passes continuously through three or four spans, friction loss may be so significant that it is essential to stress the tendon from both ends to ensure adequate force throughout.

Wedge-set should be taken into account for both the stressing end and dead end of a tendon. For long tendons, often the elongation may be greater than the travel on the jack. It is then necessary to take more than one pull of the jack. Each time the jack is released, the wedge-set occurs again at the jacking end. Since the load is picked up again upon re-gripping, the wedge set of individual pulls is not cumulative. Only the final wedge set affects the loss of tendon force. However, keeping account of cumulative elongations and wedge-sets during repeated pulls by a jack is always helpful for resolving unforeseen problems.

5.3.2 Step 2: Calculation of the strain in the unbonded post-tensioned tendon

The increase in the strain in the post-tensioned tendons due to the beam deformation is taken into account. The additional post-tension strain can be calculated as

$$\varepsilon_{pt1} = \Delta_{pt1} / l_{unb} \tag{5.2a}$$

$$\varepsilon_{pt2} = \Delta_{pt2} / l_{unb} \tag{5.2b}$$

where l_{unb} is the unbonded length of the post-tension tendon.

5.3.3 Step 3: Evaluation of stresses in the unbonded post-tensioned tendons

The additional post-tension stress can be calculated as

$$\Delta\sigma_{pt1} = E_{pt}\Delta_{pt1} / l_{unb} \tag{5.3a}$$

$$\Delta\sigma_{pt2} = E_{pt}\Delta_{pt2} / l_{unb} \tag{5.3b}$$

where E_{pt} is the modulus of elasticity and l_{unb} is the unbonded length of the post-tensioned tendon. Total post-tension tendon stress is easily calculated as $\sigma_{pt} = \sigma_{pt\,ini} + \Delta\sigma_{pt}$ where $\sigma_{pt\,ini}$ is the initial stress applied to the tendon expressed as a percentage of the ultimate stress. The condition for the upper bound limit for the initial prestress and the total stress should be checked and shall be expressed as $\sigma_{pt\,ini} \le 0.9\sigma_{pty} - \Delta\sigma_{pt}$.

5.3.4 Step 4: Evaluation of strain and stress in the mild steel dissipators

Estimating the strain and force in the mild steel can be achieved using a simple equation neglecting the strain penetration effects and can be estimated as:

$$\varepsilon_s = \theta_b (h_s - c) / l'_{unb} \tag{5.4}$$

where h_s is the height of the dissipater, c the neutral axis position and l'_{unb} the unbonded length of the mild-steel.

In order to avoid fracturing of the bars at the design earthquake intensity level, the maximum permissible strain shall not exceed $0.9\varepsilon_{ult}$. Finally, the steel stress in dissipaters can be calculated through constitutive relationships. Recognising that it is possible for the tension strain to enter the strain hardening region of the stress-strain curve, an approximate multi-linear or parabolic stress curve proposed [5.6] can be adopted for design: Therefore, an evaluation of the strain obtained is required to obtain the mild steel stress:

$$f_s = E_s\varepsilon_s \text{ if } \varepsilon_s \le \varepsilon_y \tag{5.5a}$$

$$f_s = f_{su} + (f_y - f_u)\left(\frac{\varepsilon_{su} - \varepsilon_s}{\varepsilon_{su} - \varepsilon_{sh}}\right)^p \text{ where } p = \frac{\log\left(\frac{f_{su} - f_x}{f_{su} - f_y}\right)}{\log\left(\frac{\varepsilon_{su} - \varepsilon_x}{\varepsilon_{su} - \varepsilon_{sh}}\right)} \text{ if } \varepsilon_s \ge \varepsilon_{sh} \tag{5.5b}$$

Where ε_s and f_s are the generic stress-strain situation, ε_y and f_y corresponds to the yielding point, ε_{sh} defines the onset of the hardeing, ε_{su} and f_{su} are the ultimate strain and stress point and ε_x and f_x are the generic data point on the hardeing portion.

5.3.5 Step 5: Section equilibrium and moment capacity

Moment capacity of the beam column connection is simply achieved using equilibrium of the section and then taking moments from the neutral axis position. Adopting a positive convention for moments (anti-clockwise direction) the moment at the left and right beam column connection are self-equilibrated in each floor at zero drift. For a positive joint rotation (gap opening), the left moment capacity increases while the right moment decreases in the same proportion due to the asymmetric tendon profiles. The moment contribution in the left connection M_{left} and right connection M_{right} can be evaluated as:

$$M_{left} = T_{pt1\,left}(h_{pt1} - c) + T_{pt2\,left}(h_{pt2} - c) + T_s(h_s - c) \quad (5.5a)$$

$$M_{right} = T_{pt1\,right}(h_{pt1} - c) + T_{pt2\,right}(h_{pt2} - c) + T_s(h_s - c) \quad (5.5b)$$

5.4 EXPERIMENTAL INVESTIGATIONS ON HYBRID FRAME CONNECTIONS WITH A NON-TEARING CONNECTION

A precast concrete prototype building consisting of a six storey, five bay by four bay floor plan was designed following the direct displacement based design (DDBD) procedure [5.7]. After distributing the base shear, the internal actions were scaled to respect similitude requirements for the test specimen. However, due to the space and capacity limitations within the structural laboratory, a two-storey frame, 2/3 scaled, was tested in the laboratory, taken as a super assemblage of the prototype for a proof of concept of the “non-tearing-floor” system.

5.4.1 Test set-up and specimen description

The test set-up is shown in Figure 5.4. The precast frame consists of two storeys of 2.06m and 2.10m inter-storey height respectively and one bay of 6.86m long.

The precast beams are composed of a rectangular section of 470x300mm. An I-shape section was designed at the beam ends to accommodate hidden energy dissipaters (limiting the architectural invasiveness). A 500mm square column cross section was adopted. External column end Stubs of 600x250mm at the beam column joint were used on both sides of the joint

to accommodate the post-tensioning anchorages with a more efficient distribution of compression stresses within the joint and to reduce reinforcement congestion in the joint region.

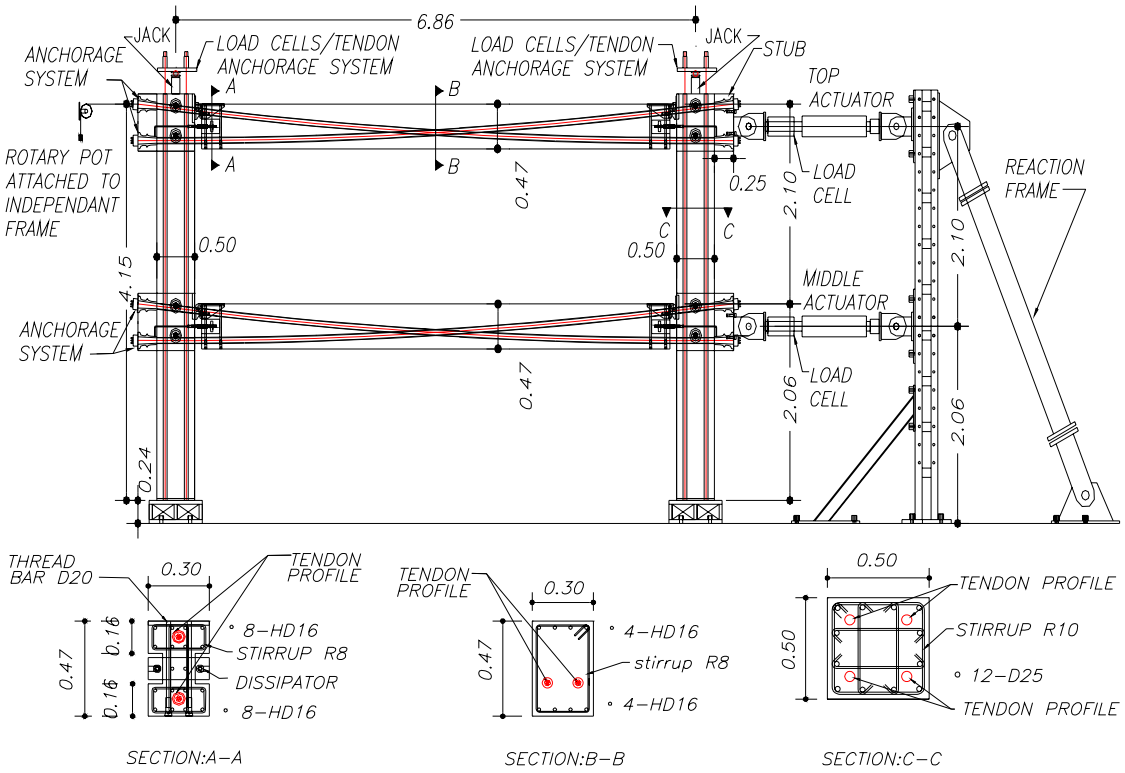

Figure 5.4. Test set up and specimen description.

The connection design and the precast beams and columns were designed according to the New Zealand Concrete Structures Standard NZ3101:2006 and Appendix B for jointed ductile connections [5.5].

Three types of tests were considered, 1) Only self weight of the elements and no additional column axial load, 2) maintaining a constant column axial load (PT), or 3) varying the column axial load (PT_{NC}). Section 5.4.5 defines the types of tests considered using the column post-tensioned tendons.

5.4.2 Construction process

Beams were caged and stirrups at each end were loose in order to accommodate steel armour (Figure 5.5-left). Special attention was required in this point to have the desire beam length. Therefore, the beam was up-side down and locked at each end in order to have the correct distance between the monohinges and minor tolerances will be taken into account with the T-shape steel plate. The steel monohinge element is attached to the beam using four high strength

threaded bars bolted to the top steel plate and threaded into the underside of the beam (Figure 5.5-right).

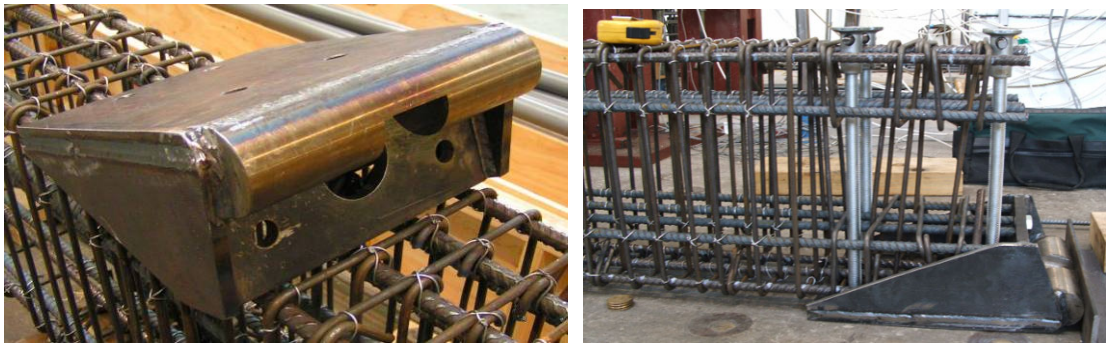

Figure 5.5. Construction process: Beam caging (left) and inserting of the hinge connection using threaded bars (right)

After this process, the plastic ducts were inserted into the beams (Figure 5.6-left) and tided with the reinforcement according to the designed profile. At the beam ends the energy dissipater steel plates were inserted and located (Figure 5.6-right).

Figure 5.6. Construction process: inserting tendon profile (left) and adding energy dissipator steel plate (right).

Finally, the detail of the beam is shown in Figure 5.7-left. The red circles correspond to the location of the threaded inserts for the floor starter bars for a future research. Beams were cast up-side down and located into the formwork to provide that the steel armour will be filled with concrete (Figure 5.7-right).

The columns on the other hand were caged separately (Figure 5.8-left). The stubs reinforcement was also attached to the columns. Note that two stubs were located in each floor and in the two orthogonal directions for further research. Spiral reinforcement was used in order to provide additional concrete confinement due to the high forces in the anchorage. Special attention was required in the location of the threaded inserts along the column height (Figure 5.8-right).

These inserts will support the steel corbel and the T-shape steel plate and were located on top a steel plate to provide a better distribution of shear, tension and compression forces into the core of concrete column concrete.

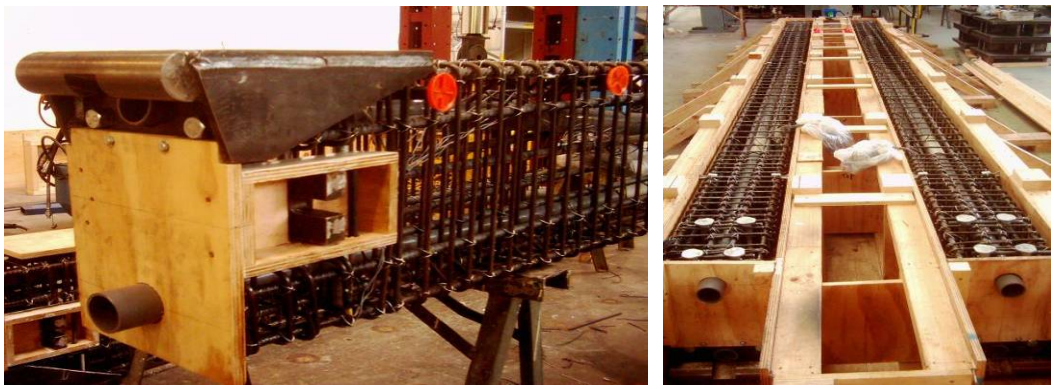

Figure 5.7. Construction process: final connection detail (left) and formwork ready to cast (right).

The final process is the insertion of the column steel cage into the formwork (Figure 5.9-left). Some minor clashes were found between the column stirrups and the threaded inserts. The stirrups at the joints were loose such that was easy to have them moved thus avoiding steel congestion.

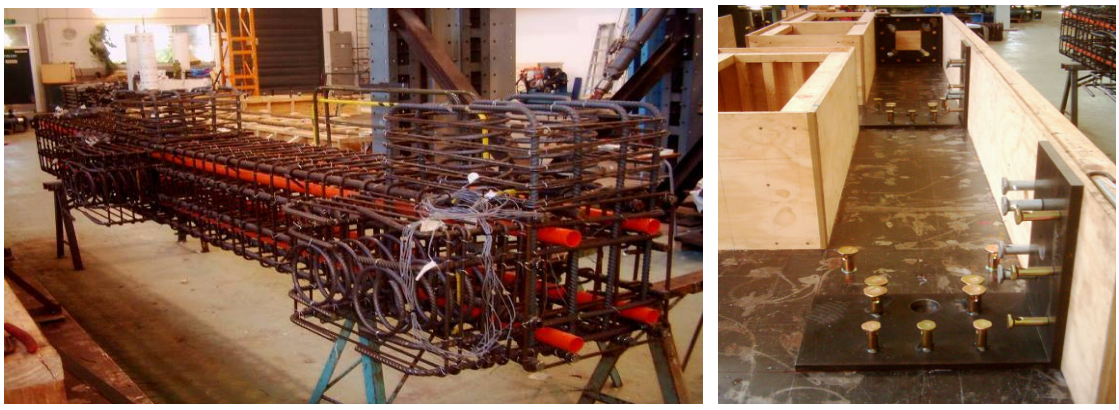

Figure 5.8. Construction process: column steel caging (left) and detailing of threaded insert locations (right).

Figure 5.9-right shows the columns inside the formwork. It can be seen that the stubs were cast together with the column, therefore special caging was provided for them. Columns were cast horizontally. A vibrator was used to flow the concrete into the beams and columns (Figure 5.10).

Figure 5.9. Construction process: inserting steel caging into the formwork (left) and column ready to cast (right).

The concrete mix design was provided by external contractors with a specified concrete capacity at 28 days of $f_c^{'}$=50 MPa. The concrete slump on the day of casting was 190mm and the required concrete capacity at 28 days was $f_c^{'}$=55 MPa.

Figure 5.10. Construction process: Casting Beams (left) and Columns (right)

5.4.3 Frame assembling

The columns were lifted and located into position on top of a steel base and braced to the floor for safety (Figure 5.11-left). Beams were lifted (Figure 5.11-right) and located on top of the steel corbel previously installed using mechanical bolts inserted into the threaded inserts (Figure 5.12-left).

After the beams had been installed, special attention in the column levels was required in order to guarantee a orthogonal relationship between the foundation and the beam-column joint interface. As mentioned before, in order to address tolerances issues it is common that the beams are shorter in length such that additional length can be given by grouting at the beam column joint.

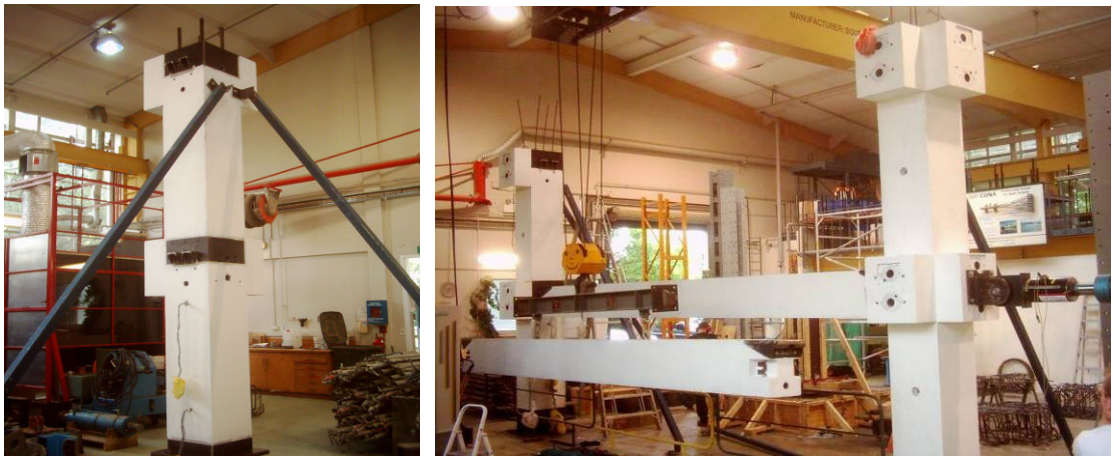

Figure 5.11. Assembling: Column standing into position (left) and lifting the beams (right).

For this particular frame, a 10mm gap was deliberately left at each beam column joint (Figure 5.12-left). The use of the T-shape steel section was located at both ends of the beam (Figure 5.12-right) to prevent torsion, beam uplift and tolerance issues.

Figure 5.12. Assembling: sitting beams on the corbels (left) and solving tolerances issues (right)

A total of eight 7-wire prestressing strands (0.5 in diameter, A_{pt} = 99mm^2) were used for each beam, with two ducts of four tendons each (Figure 5.13-left). Although the subassembly does not represent the prototype structure due to laboratory space limitations, from the structural analysis was obtained the required design beam moment of 180kNm at 2% lateral drift. An initial post-tensioning of 50% the ultimate stress $F_{pt\ ult}$ (1860MPa) was applied, resulting to a total initial post-tensioning force per beam-column connection of approximately 744kN.

The post-tensioning was applied on one side of the frame due to the space limitations and was carried out initially on the top anchor of the first floor with 25% of the ultimate stress $F_{pt\ ult}$. After the force had been achieved, the jack was release and located on the bottom anchor and a

full load (50% the ultimate stress $F_{pt\ ult}$) was applied. This process was according to the design considerations of the beam stress distribution profile during the post-tensioning. A set of four load cells (one on each anchorage) were locked and left for the testing.

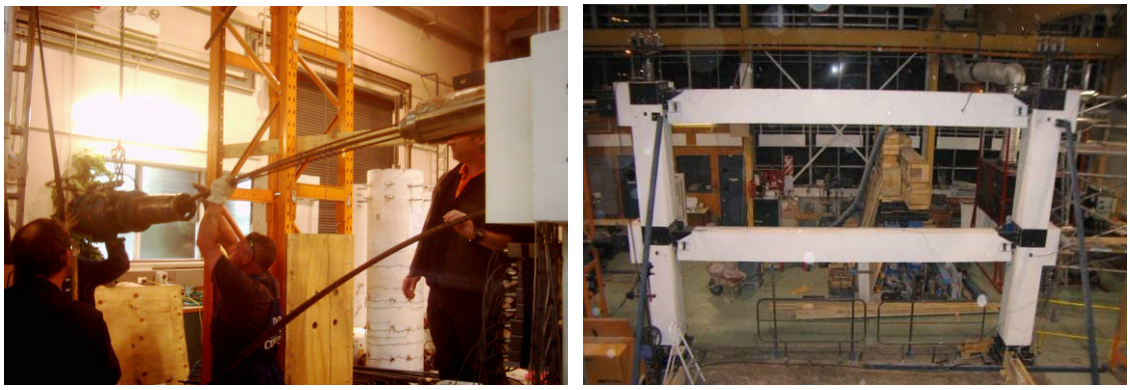

Figure 5.13. Assembling: post-tensioning (left) and test specimen (right).

Finally, a rocking mechanism was designed to develop at the column base using an axial load force of 162kN, representing 22% the ultimate stress $F_{pt\ ult}$ applied to each column via four unbonded post-tensioned tendons (Apt = 396mm^2) and illustrated in Figure 5.5.

5.4.4 Construction of Energy Dissipaters

The external energy dissipaters were designed to ensure that all the plastic deformation is confined to the fused region of the steel bar and is fabricated from round mild steel bars, threaded at each end and machined down to a specific bar diameter over a pre-determined length; defined as the unbonded length (Figure 5.14).

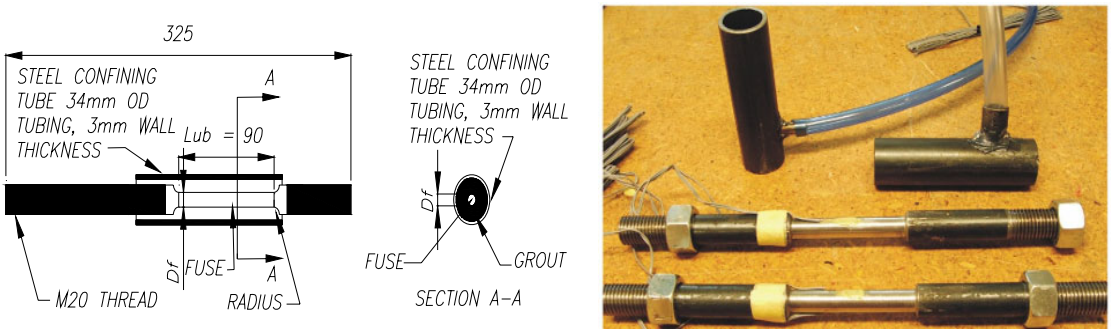

Figure 5.14. Dissipater rod details

Three different fuse diameters (Df) were considered: 7mm, 10mm and 13mm with an unbonded length of 90mm. A 34mm (outside diameter) steel tube with a wall thickness of 2mm (anti-buckling restraint), is located over the machined area of the steel bar and temporary fixed in

place. Epoxy was then injected into a hole (Figure 5.14) drilled into the bottom of the steel confinement tube to ensure that all the air was expelled out from the top.

The dissipaters are expected to be displaced in both tension and compression due to the specific nature of the mono-hinge connection. Uni-axial and cyclic tests were performed in the dissipaters. The energy dissipaters were tested to characterise their stability under cyclic loading and energy dissipation. The test set-up for is shown in Figure 5.15 where displacement is measured over a gauge length provided when installed within the beam-column connection. A 250 kN capacity, Instron test-rig was used to imposed a displacement time-history similar to that expected during testing when installed. Uni-axial tensile tests indicating a yield strength f_y =315 Mpa.

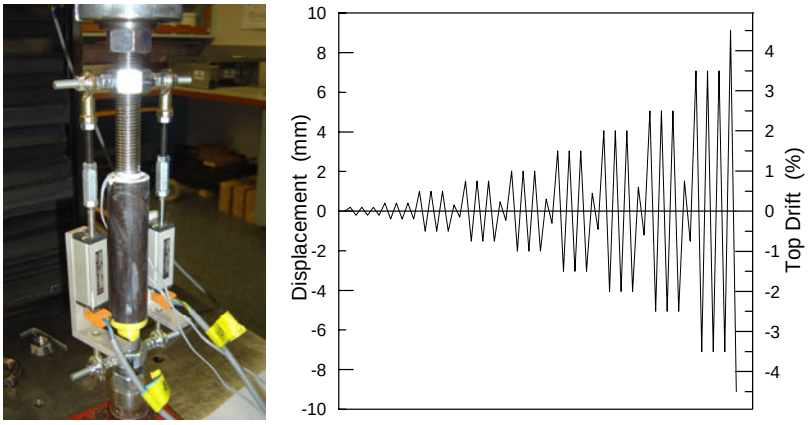

Figure 5.15. Dissipater test rig (left) and cyclic test protocol (right).

5.4.5 Loading history

A series of quasi-static cyclic displacement control tests were carried out under increasing levels of lateral top displacement, where the structure was displacement controlled for the top floor and force controlled for the first floor: this ensured the correct lateral load distribution between the two levels. The testing protocol complied with the "acceptance criteria" proposed by the ACI [5.8], [5.9] and consisted of a series of three cycles of drift, followed by a smaller single cycle.

5.4.6 Testing program

During the imposed displacement protocol, a rocking mechanism was developed at the column base. Three types of tests were considered, 1) Only the self weight of the columns and beams were acting at the column base (PT_{SW}); 2) maintaining a constant column axial load (PT), and 3)

varying the column axial load (PT_{NC}). In the first case no additional axial load was applied to the column bases. The second case, representing a solution without vertical post-tensioning in the column but simulating a higher constant load representing the gravity load of 162kN in each column applied and maintained constant during testing using a release valve within the hydraulic jack system (Figure 5.4).

In the third case, representing a solution with vertical tendons in the columns, the post-tensioned tendons were locked off resulting in an increase to the column axial load due to the elongation of the post-tensioned tendons as the columns rocked upon their foundation. In normal construction practice, when vertical tendons are adopted, they would likely be initially post-tensioned. However, in this experimental programme the initial post-tensioned forces were assumed to equal the gravity load of 162kN, which would represent the case of slack (no initial prestressing) vertical tendons. This test parameter was chosen to limit the demands imposed to the strong floor within the Civil Engineering Laboratory.

Table 5.1 summarizes the entire test program where the column axial load is represented by self weight (PT_{SW}), constant (PT) or variable (PT_{NC}), while 7, 10 and 13 denotes the diameter of the mild steel dissipater considered for each axial load regime above to demonstrate the re-centring capabilities of the frame.

Table 5.1. Test Summary.

Test	Column Axial Load Type	Dissipation Type
PT_{SW}	Self-weight	Post-tensioned only solution
PT_{NC}	Not Constant	Post-tensioned only solution
PT	Constant	Post-tensioned only solution
PT_{RP}	Constant	Post-tensioned only solution + rubber pad
$PT_{NC}7$	Not Constant	7mm fuse
PT7	Constant	7mm fuse
$PT_{NC}10$	Not Constant	10mm fuse
PT10	Constant	10mm fuse
$PT_{NC}13$	Not Constant	13mm fuse

As mention in Section 4.8 in Chapter 4, the need of additional lateral stiffness might be necessary for hybrid systems with Non-tearing connections. Therefore, Test PT_{RP} represents a test with applied constant column axial load and no energy dissipation was added into the system, but instead a Rubber pad was located at the location of the energy dissipation at the beam column joints. The intension with this test was to provide additional sources of increasing

lateral stiffness into the system. The rubber pads were designed such that acts in compression only when the gap in the connection closes.

5.5 TEST FRAME EXPERIMENTAL RESPONSE

5.5.1 Behaviour of Unbonded Post-Tensioned-only Solution

Three tests were first carried out on an unbonded post-tensioned only solution: a) only self-weight of the columns and beams were carried by the columns (Test PT_{SW}) b) varying the column axial load (Test PT_{NC}) and c) having a constant axial load (Test PT). Figure 5.16 shows the force displacement hysteretic behaviour up to 3.5% drift for the post-tensioned solution having no axial load (only self weight).

In general the behaviour was stable with some re-centring response coming from the weight of the elements acting at the columns base. Some dissipation can be observed which is coming from the friction occurring between the beam post-tensioned tendons within the ducts. No significant reduction in stiffness on loading was observed.

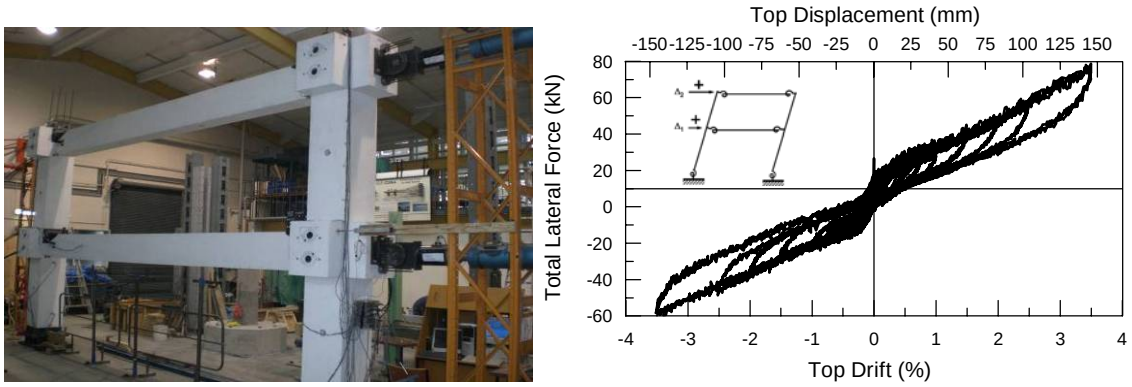

Figure 5.16. Unbonded post-tensioned only solution for test PT_{SW}: global hysteresis loop at 3.5 % drift.

Figure 5.17 shows the behaviour from the tests with non constant axial load (Test PT_{NC}) and constant axial load (Test PT). In general the behaviours were stable with better re-centring properties with a non linear elastic response with small dissipation coming from friction within the ducts. An increase in the energy dissipation is observed in Test PT when compared to Test PT_{NC} due to additional friction forces being introduced into the system as a result of the setup controlling the axial load during testing.

A larger bi-linear stiffness is observed for Test PT_{NC} when compared to Test PT due to that the increment in axial load increase the column moment and thus the lateral capacity.

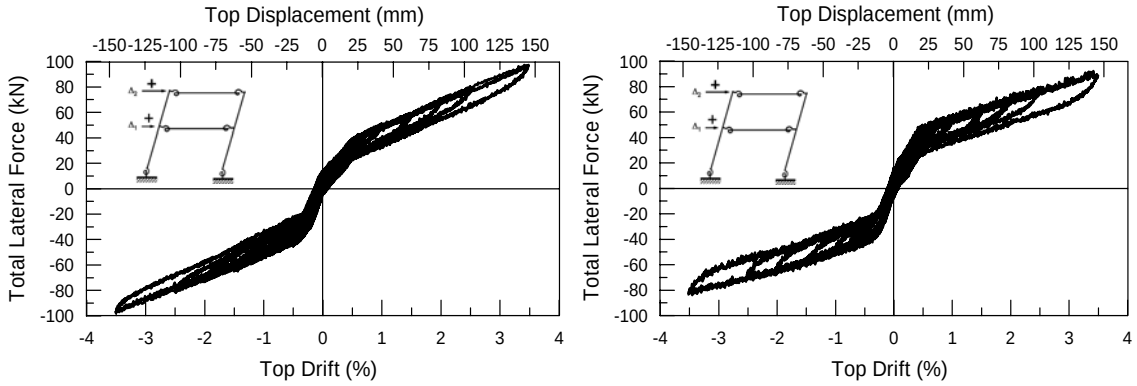

Figure 5.17. Global hysteresis loop at 3.5 % drift for Test PT_{NC} (left) and Test PT (right).

As mentioned before, the need of additional lateral stiffness might be necessary for hybrid systems with Non-tearing connections. Test PT_{RP} was performed with constant axial load and the use of a rubber pad which acts only in compression. The rubber pads were located at the same location as the dissipaters (mid-height of the beams) and designed such that no double hinging was created at the connection.

In order to ensure that no double hinging will occur, it is require that the compression forces that are sustained by the rubber at maximum drift will not surpass the forces in the monohinge. It is well known that the compressive modulus of elasticity depends on the shape factor S [5.10]. Therefore depending on the size of the rubber pad the effective compression modulus $E_c = E_o(1+2kS^2)$ can be determined in each rubber layer where E_o is the young's modulus for unconfined rubber, k is the numerical factor dependent on rubber hardness, S is the shape factor determined by the ratio of the loaded area to the force-free area for the layer.

For a rectangular rubber pad of bearing length L = 155mm and breadth B = 50mm and layer thickness t = 10mm with a hardness of IRHD of 55 [5.10], Table 5.2 presents the results obtained indicating that the force in the rubber is less than the forces acting on the monohinge (which is the total post-tension force) and the total moment due to the additional compression force is small. However, the use of the proposed rubber was tested as proof of concept.

Table 5.2. Rubber pad Material properties.

IRHD	B (mm)	L (mm)	t (mm)	h (mm)	S (-)	k (-)	Eo (MPa)	Ec (MPa)	θ imp (rad)	I (mm)	Δ (mm)	Axial Stiffness (MPa)	Axial Force (kN)	Moment (kNm)
55	50	155	10	90	1.89	0.64	3.25	18.11	0.035	203	7.09	1559.80	11.06	2.24

Figure 5.18 show the global hysteresis loop at 3.5% of drift. It can be seen similar results as per Tests PT_{NC} and PT. Comparison between Test PT and Test PT_{RP} indicate that the latter has a small amount of total base shear. This result is particularly of interest because effectively it is possible to induce additional lateral stiffness into the system without increase the amount of energy dissipation.

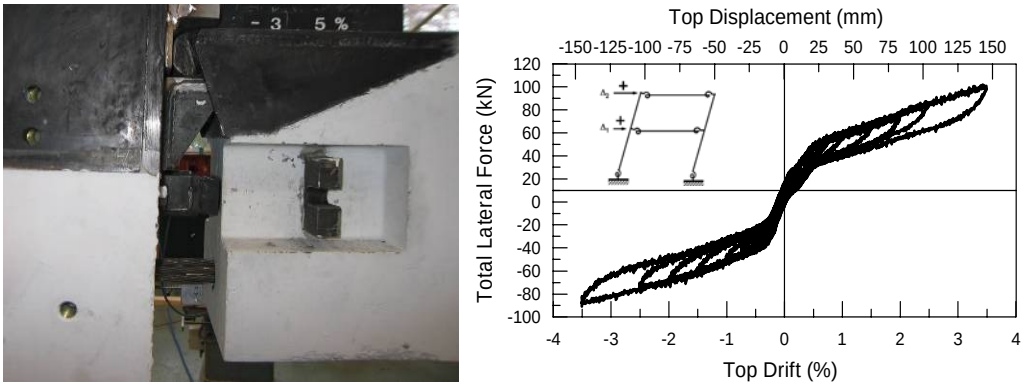

Figure 5.18. Unbonded post-tensioned only solution for test PT_{RP}: global hysteresis loop at 3.5 % drift.

The column axial load behaviour for Test PT_{NC} and Test PT is shown in Figure 5.19 left and right respectively. When the gap opens at the column base, the tendon elongation provides additional axial load for test PT_{NC} (Figure 5.19-left), while Figure 5.19-right shows axial load variations of $\pm$ 10kN for test PT due to the accuracy of the axial load control system. Similar results can be observed in Figure 5.20 where the column base moment rotation for the non constant (left) and constant (right) column axial load is shown.

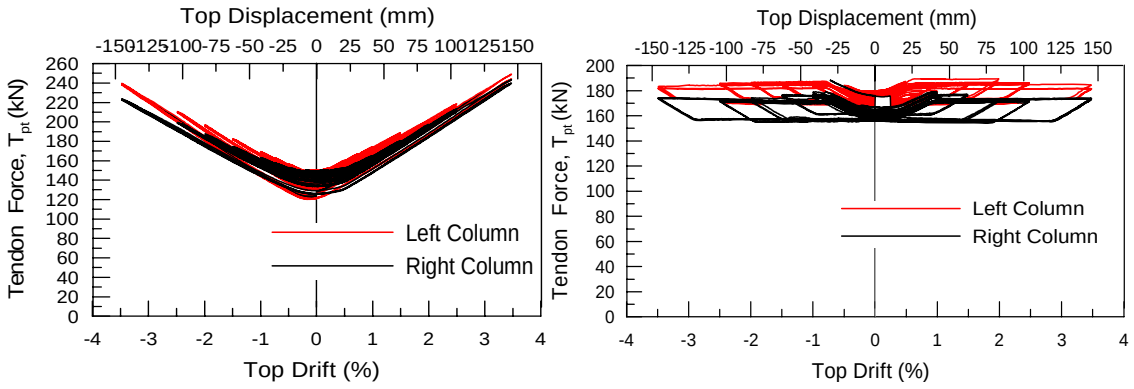

Figure 5.19. Behaviour of the post-tensioned tendons in the columns: test PT_{NC} (left) and test PT (right).

It is worth emphasising that while a majority of the re-centring is being provided by the columns, an allowance for column gravity loads and additional post-tensioned tendons within

the columns can be used to achieve a full static re-centring solution combined with the benefits of a non-tearing floor system. It should be noted that such a system does not necessarily require full static re-centring in order to have zero (or near zero) permanent deformations following an earthquake. In fact, the natural dynamic re-centring due to the small cycle hysteretic behaviour following the major excursions during the earthquake can be sufficient to restore the entire system to the original position after the free oscillations.

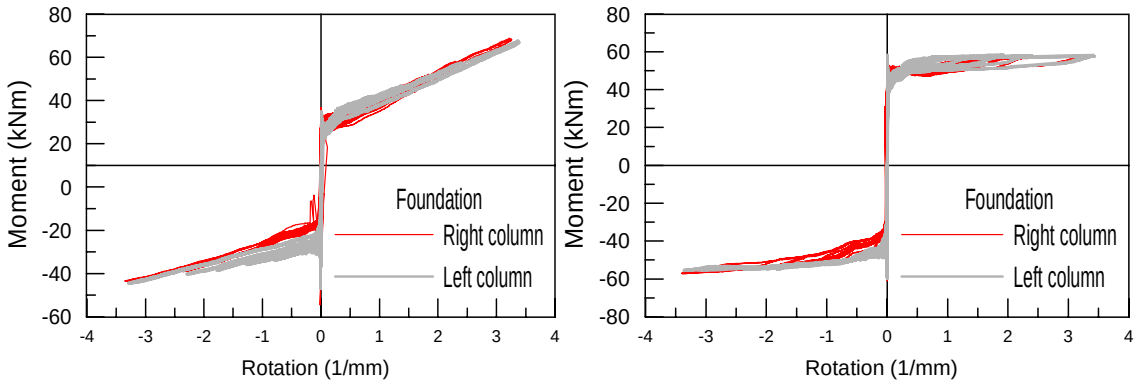

Figure 5.20. Moment-rotation behaviour in the foundation: test PT_{NC} (left) and test PT (right).

In terms of local responses, Figure 5.21 shows the gap opening response at the top and bottom of the beam depth. Maximum gap displacements of 1.3 mm (top) and 16 mm (bottom) were obtained at a lateral drift of 3.5%.

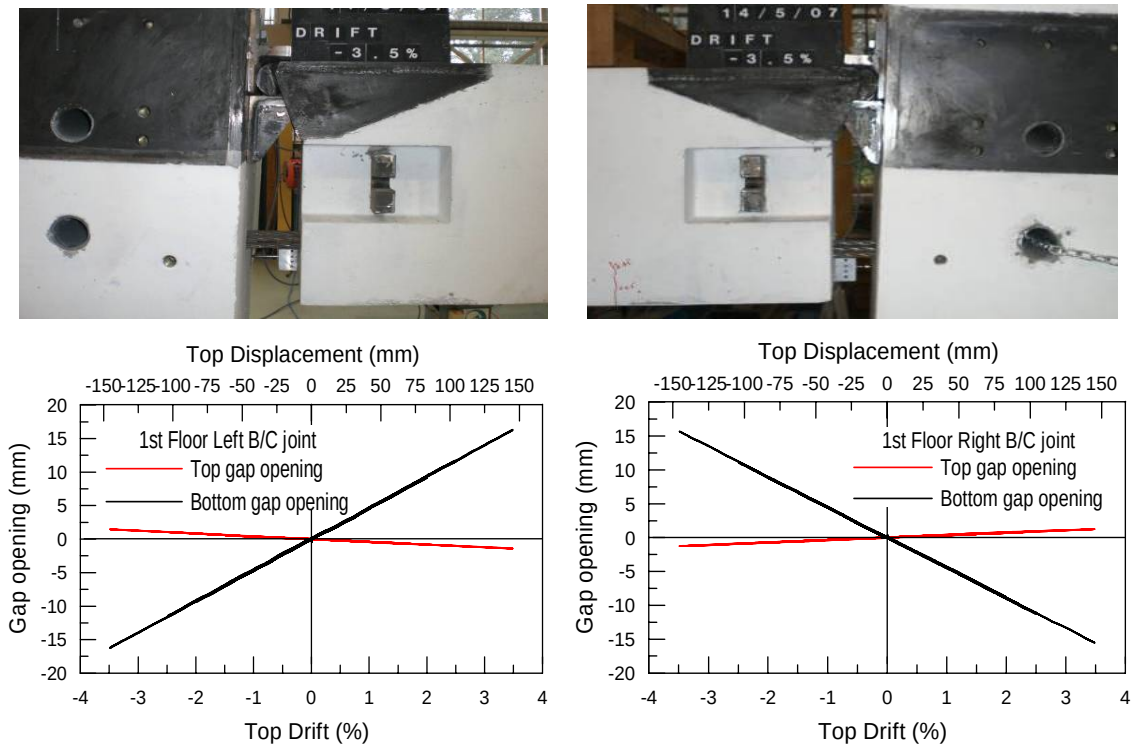

Figure 5.21. Gap opening of the B/C Joint at 3.5% of drift.

Post-tensioned forces in the tendons were obtained from the load cells attached to the left end of the subassembly (Figure 5.22-left). Considering that the neutral axis position remains constant at any drift level, a simple calculation can be used to determine the moment capacity in the joint, knowing the unbonded post-tensioned force and the distance from the monohinge to the tendons. Rotations were calculated using Potentiometers located at the beam-column interface.

Figure 5.22-right shows the moment versus rotation response of the beam-column connection. As expected, a linear elastic behaviour is observed with an initial moment of 150 kNm due to the initial post-tensioned force of the tendons. Adopting a positive convention for moments (anti-clockwise direction) the moment at the left and right beam column connection are self-equilibrated in each floor at zero drift. For a positive joint rotation (gap opening), the left moment capacity increases while the right moment decreases in the same proportion due to the asymmetric tendon profile.

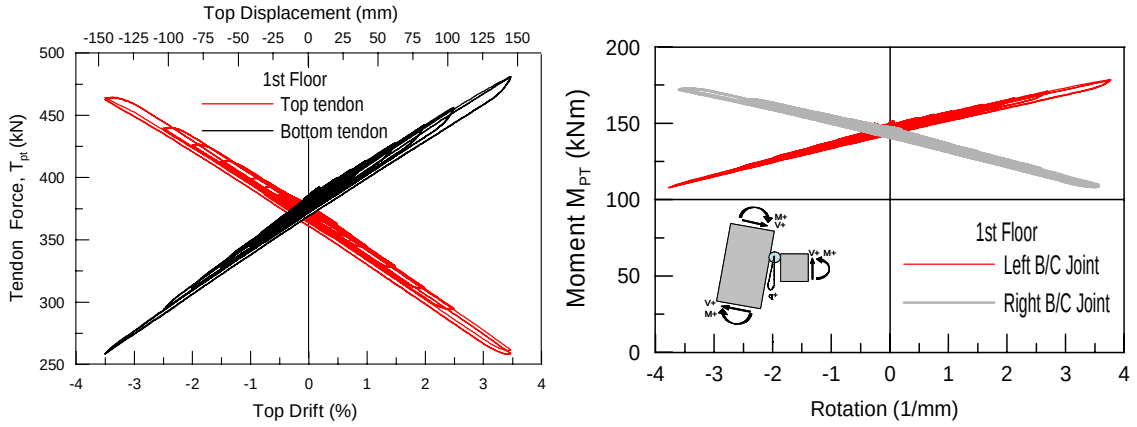

Figure 5.22. Beam post-tensioned forces (left) and B/C joint moment rotation behaviour (right).

5.5.2 Behaviour of the Hybrid Solution

Additional energy dissipation capability was added to the unbonded post-tensioned only solution in the form of mild steel external dissipater and test were carried out for the hybrid solution. The experimental results presented in Figure 5.23 correspond to the force displacement hysteresis behaviour of test $PT_{NC}7$ with variable axial load (Figure 5.23-left) and test PT7 with constant axial load (Figure 5.23-right).

A stable flag shape hysteresis is observed for both tests with higher dissipation when compared to the unbonded post-tensioned only solution. Furthermore, re-centring is achieved up to a lateral drift of 3.5%. The concave bilinear slope (pinching behaviour) indicates the onset of

stiffness degradation as a result of buckling of the external dissipaters in compression that occur during the second and third cycle of the tests.

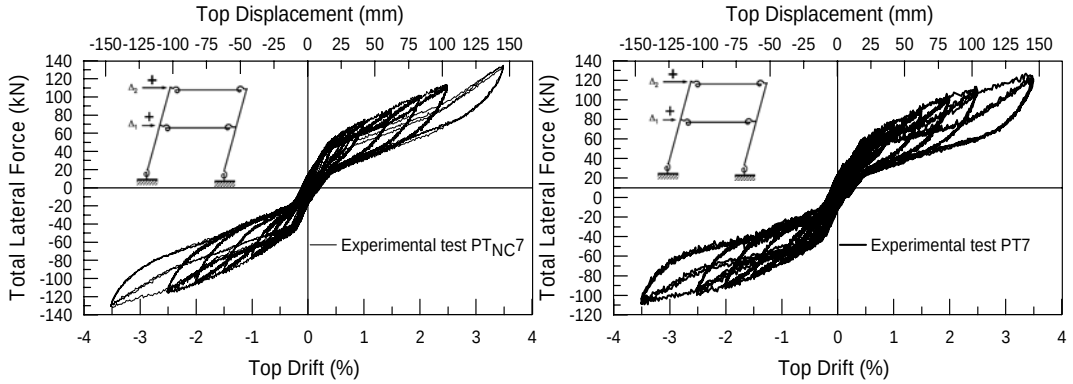

Figure 5.23. Hybrid system with external dissipaters: global hysteresis loop for TEST $PT_{NC}7$ (left) and TEST PT7 (right).

Comparisons drawn between test $PT_{NC}7$ and test PT7, show that PT7 has a reduction in total strength and lower bilinear stiffness due to the constant moment contribution at the column base with higher energy dissipation being provided by friction from the axial load control system.

As mentioned before, the dissipaters underwent net tension and compression displacements due to the specific nature of the mono-hinge connection. Figure 5.24-left show the test results of the uni axial-tensile test and the cyclic tests for dissipater with 7mm fuse. It can be seen that the dissipater has a reduced energy dissipation capacity when displaced into net negative displacements and then was reduced further by buckling at relatively low displacements. A reduction in length of the dissipater would reduce the premature buckling and hence improve the cyclic histeresis behaviour.

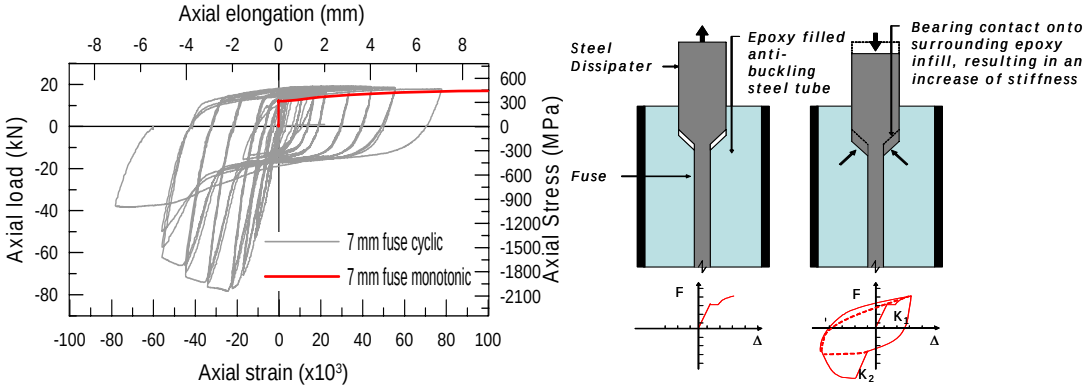

Figure 5.24. Cyclic and monotonic dissipater test (left) and behaviour in compression (right).

Figure 5.24-right illustrates the mechanics of the dissipater as it comes into contact with the surrounding epoxy when displaced in compression, increasing the stiffness and strength of the element. Depending on the relative capacity of the dissipater, failure can occur either by the dissipater yielding in compression or the epoxy crushing in compression.

Similar results are obtained in Figure 5.25 which shows the total force displacement for tests $PT_{NC}10$ and PT10. As previously illustrated with the tests of 7mm fuse, comparating tests $PT_{NC}10$ and test PT10 (10mm fuse) indicates that the latter shows a reduction in the total strength and lower bilinear stiffness doe to the constant moment contribution at the column base with higher energy dissipation being provided by friction from the axial load control system.

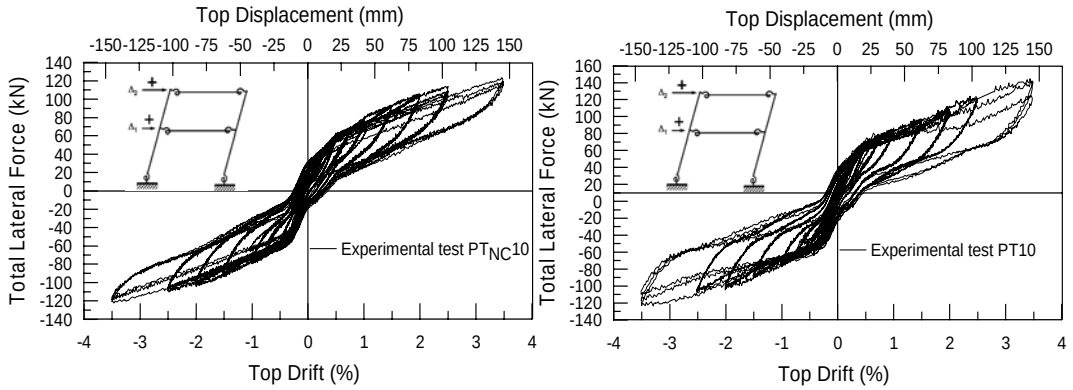

Figure 5.25. Hybrid system with external dissipaters: global hysteresis loop for TEST $PT_{NC}10$ (left) and TEST PT10 (right).

5.6 EVALUATION OF THE TEST RESULTS

All the tests had an adequate performance in terms of strength, stiffness and ductility. Comparison between the different tests responses are presented in the following sections.

5.6.1 Stiffness Degradation

Secant stiffness is defined as the slope defined at the maximum loads obtained on the last cycle of each imposed drift. Each value of secant stiffness was normalized with respect to the value obtained at 0.1% inter-story level for comparison purposes. Figure 5.26 shows the stiffness degradation normalized for all the tests performed.

Comparison among the only unbonded post-tensioned solutions and the hybrid solutions for the frame indicate that only the unbonded solution has reduced stiffness degradation at early drift levels. This is as expected because there were no energy dissipaters in the frame. There is no

difference between variable and constant axial load. However, results obtained for Tests $PT_{NC}10$ and PT10 show that residual stiffness are different because for Test $PT_{NC}10$, the use of a shorter steel confining tube reduced the capacity of the dissipater and induce premature buckling of the dissipater at early drift levels. This confining detail was improved for the other tests and as a result all the hybrid tests have similar stiffness degradation

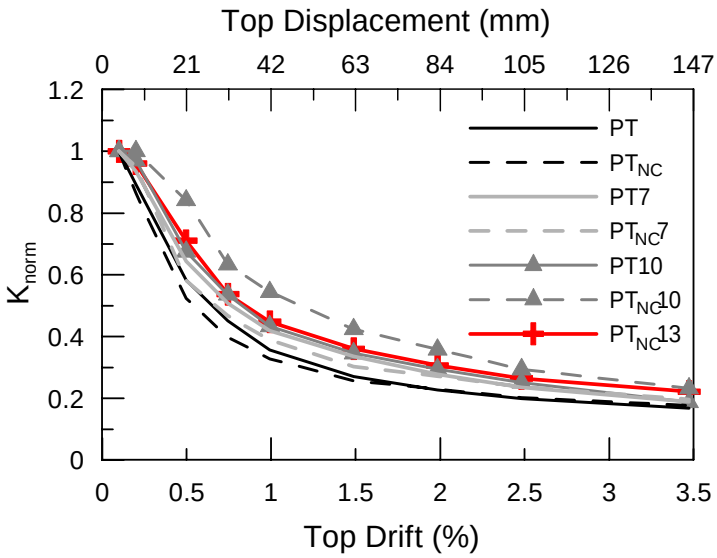

Figure 5.26. Stiffness degradation for test PT, PT_{NC}, PT7, $PT_{NC}7$, PT10, $PT_{NC}10$ and $PT_{NC}13$.

Furthermore, at a maximum drift level of 3.5% of drift, tests using the unbonded post-tensioned only solution (PT and PT_{NC}) decrease about 20% in comparison with the hybrid solution (PT7, $PT_{NC}7$, PT10, $PT_{NC}10$ and $PT_{NC}13$).

5.6.2 Energy Dissipation

The equivalent viscous damping ratio (ξ_{eq}) is defined as the energy absorbed by inelastic response of the actual structure to an equivalent viscous system. Figure 5.27 shows the equivalent viscous damping (ξ_{eq})-drift relationship for Tests $PT_{NC}7$, PT7, $PT_{NC}10$, PT10 and $PT_{NC}13$ calculated as the ratio between the area under the force-displacement curve in the third cycle of each imposed drift level and the area defined at maximum displacements and pick force assuming linear elastic behaviour.

As the dissipation content is increased the higher the equivalent viscous damping is observed. A maximum of 14% of equivalent viscous damping is observed for test $PT_{NC}13$.

Due to buckling of the dissipaters between a lateral drift of 2% and of 2.5%, a reduction in the ζ_{eq} is observed there after. The dissipaters within test $PT_{NC}13$ have greater anti-buckling resistance and thus no ζ_{eq} degradation is observed. A comparison between the constant and variable load tests shows no significant differences for the ζ_{eq} value.

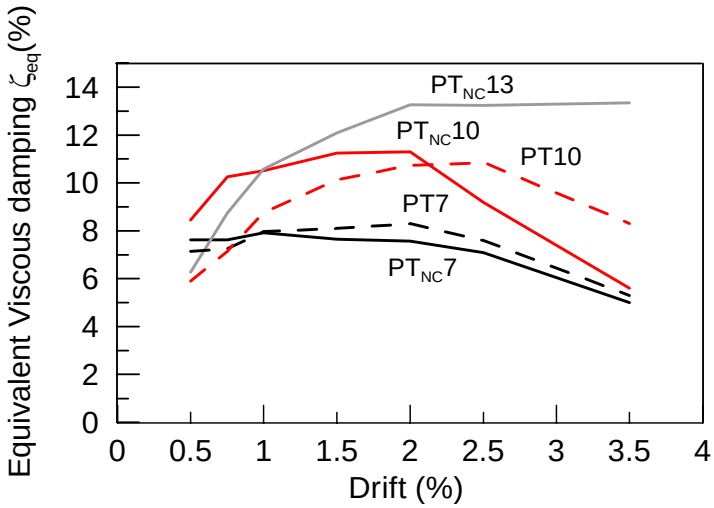

Figure 5.27. Equivalent viscous damping ratio for tests $PT_{NC}7$, PT7, $PT_{NC}10$, PT10 and $PT_{NC}13$

5.7 ANALYTICAL-EXPERIMENTAL COMPARISON

Two models were used to reproduce the experimental results, providing a reliable control over the expected hysteresis and dynamic behaviour. The first model is based on the moment rotation spring model acting in parallel while the second lumped plasticity model is based on the combination of axial springs. The non-linear finite element program Ruaumoko2D [5.12] was used to model the series of experimental tests. The use of the axial spring model has the advantage of properly capturing the beam axial forces induced by the post-tensioned tendons.

5.7.1 Moment Rotation spring Model

As explained in Chapter 3, a lumped plasticity modelling approach adopts non-linear inelastic rotational springs located in parallel at the rocking interface. The spring properties can be evaluated via a monotonic moment-rotation analysis which is evaluated based on a global member compatibility condition using monolithic beam analogy principles [5.4] and [5.11]. The analysis allows each moment contribution (mild steel, post-tensioned tendons and axial load) to be isolated, defining their individual contributions and allowing individual spring properties to be defined.

As an example, an analytical-experimental comparison using a lumped plasticity model based on the combination of different non-linear inelastic rotational springs located in parallel at the rocking interface is shown in Figure 5.28. Elastic elements are used to represent the precast structural members as proposed [5.4]. The recorded lateral force time history during testing was used as the input loading history for the model at each floor.

The unbonded post-tensioned tendon was modelled using a linear elastic rotational spring, while a second non-linear inelastic spring was used to represent the mild steel energy dissipation contribution using the Dodd-Restrepo hysteresis rule [5.13].

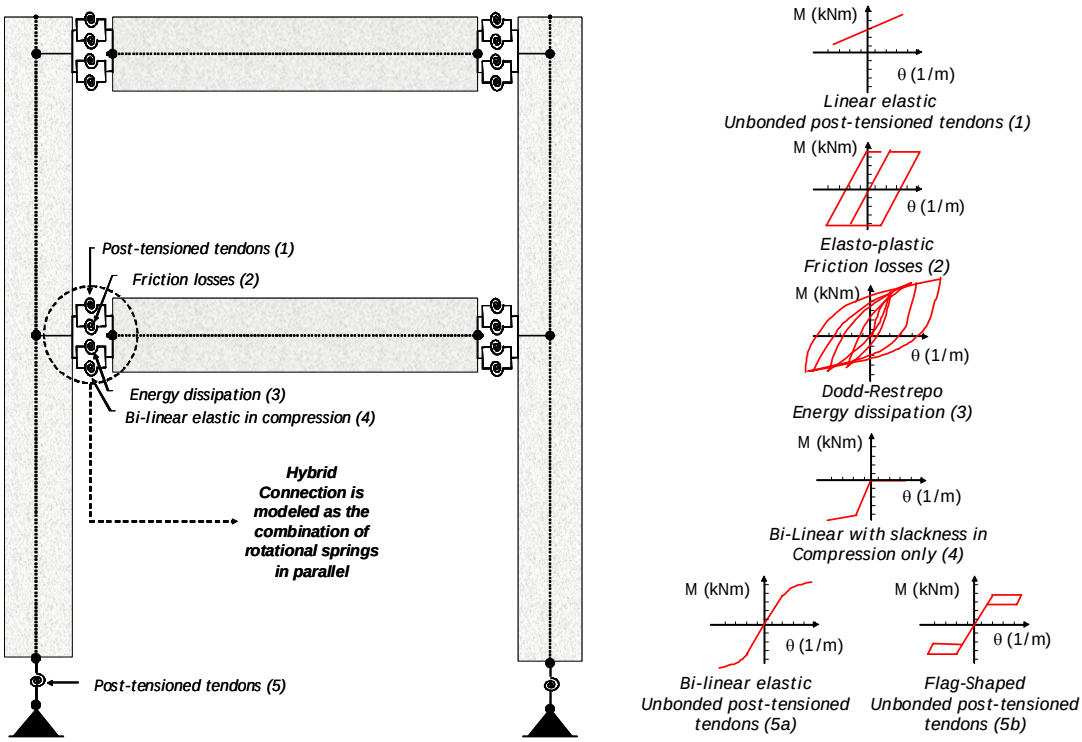

Figure 5.28. Moment Rotational spring model.

As the dissipaters are displaced into net negative displacements and buckling is initiated the dissipater does not contribute to the energy dissipated in the system. However, the bearing effect onto the epoxy filled material increases the compression stiffness and strength as was previously explained and illustrated in the experimental results presented earlier (Figure 5.24). An additional compression-only moment-rotational spring is added at the same location as the dissipaters such that the combined stiffness and strength between the two springs in parallel represents the observed behaviour during testing of the dissipater elements.

Friction forces occurring between the tendons and the plastic ducts were also considered. The friction force is determined using fundamental prestress theory where the vertical force components from the post-tensioned tendon are multiplied by the code recommendations for friction coefficients (between 0.05 and 0.15). A simple moment rotational spring was implemented with an elasto-plastic hysteresis rule considering a high initial stiffness where the yield moment corresponded to the friction force in each tendon multiplied by the individual internal lever arms.

Simple bi-linear elastic hysteresis rule was adopted at the column base to model the changed in the column axial force moment contribution due to the post-tensioned tendons. Additional friction forces were observed in the experimental results for the tests using constant column axial force (due to the test-set up). Therefore, the flag shape hysteresis model was implemented to account for the additional energy from the dissipated. The value Beta used for the energy dissipated was obtained by try an error from the experimental results.

Given the simple hysteresis rules adopted, Figure 5.29 illustrates how the global hysteresis response is accurately represented for Tests PT_{NC} and $PT_{NC}7$ (Figure 5.29 left and right respectively). It can be seen the excellent agreement between the model and the experimental results for Test PT_{NC} and a good approximation for Test $PT_{NC}7$ despite the complexity in the modelling the energy dissipation in compression.

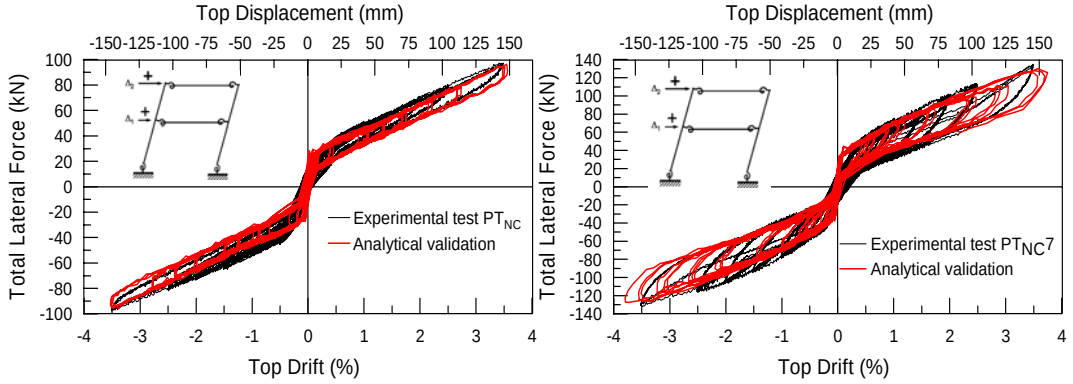

Figure 5.29. Analytical-experimental comparison using moment rotation model: Force displacement response of test PT_{NC} (left) and $PT_{NC}7$ (right).

Similar results are obtained for test PT and PT7 (Figure 5.30) where the model successfully reproduces the experimental results. The analytical validation of test PT was simpler than adding energy dissipation solution (test PT7) due to the complexity of the dissipation behaviour in compression.

Analytical experimental comparisons between the moment rotation of the unbonded post-tensioned tendons and the energy dissipation are shown in Figure 5.31-left and right respectively. The linear elastic behaviour of the post-tensioned tendons was combined with the bi-linear inelastic hysteresis representing the friction in the tendons (Figure 5.31-left). A small reduction in the tendon forces is required to discount the higher strength of forces in the model due to the friction force contribution.

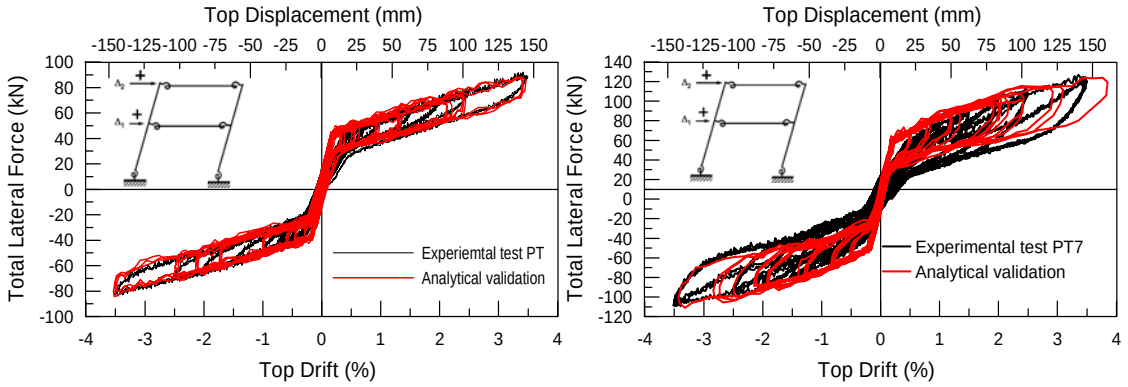

Figure 5.30. Analytical-experimental comparison using moment rotation model: Force displacement response of test PT (left) and PT7 (right).

Modelling the energy dissipater (Figure 5.31-right) required a proper understanding of the response. Different hysteresis rules were adopted in order to capture the real behaviour of the dissipater. Non-linear inelastic rules such as Ramberg-Osgood and Dodd-Restrepo were implemented. The bi-linear inelastic hysteresis rule was not appropriate for the model as Bauschinger effects could not be captured; meanwhile the Ramberg-Osgood hysteresis rule requires iteration on the power factor to obtain the desired monotonic moment-rotation response. The Dodd-Restrepo hysteresis rule is more appropriate in modelling the dissipaters as proper material non-linearity and Bauschinger effects are accounted for.

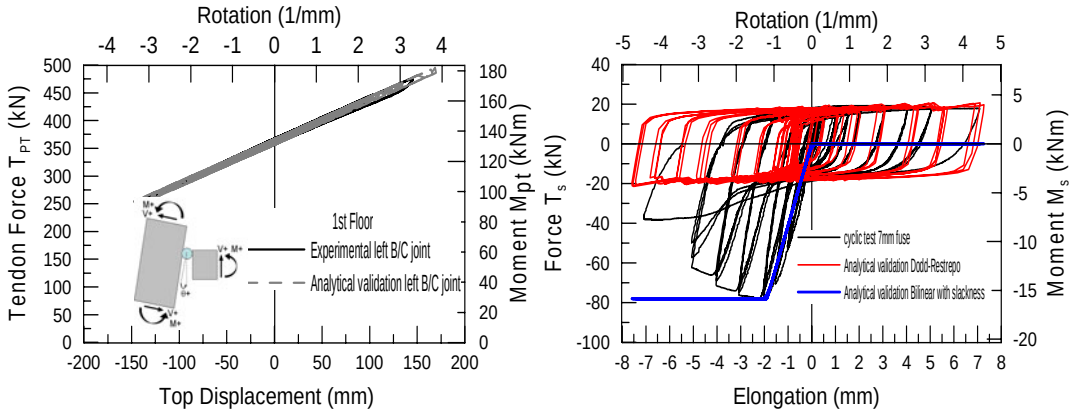

Figure 5.31. Analytical-experimental comparison for B/C connection using both models: unbonded post-tensioned tendon (left) and energy dissipater (right).

Figure 5.31-right shows the response using the Dodd-Restrepo hysteresis rule. An additional bilinear, compression-only spring is also presented to model the bearing contact in compression. The calculation of the stiffness and maximum yield moment is difficult to predict due to the unknown epoxy properties and the possible contribution of the outer steel tube. The stiffness and strength was simply calibrated from cyclic steel testing of the dissipaters.

The moment rotation response at the column foundation was modelled using a non-linear elastic hysteresis rule at the base of the frame. Figure 5.32 illustrates the analytical experimental-validation agreement considering variable or constant axial load. The experimental tests having variable axial load (PT_{NC}, $PT_{NC}7$ and $PT_{NC}10$) were modelled using a bi-linear elastic hysteresis (Figure 5.32-left). Meanwhile, the constant axial load tests (PT, PT7 and PT10) were modelled using flag-shaped hysteresis behaviour (Figure 5.32-right). Energy dissipation was considered in the hysteresis model to account for the additional energy loss due to the axial load setup and control.

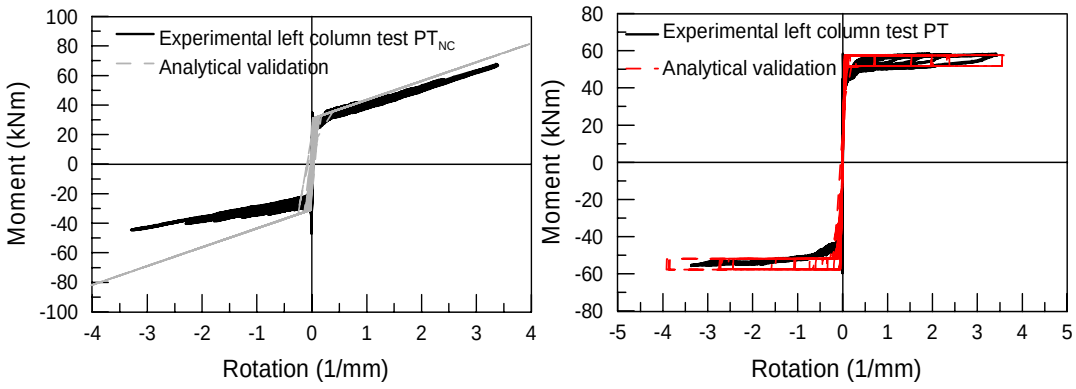

Figure 5.32. Analytical-experimental comparison moment rotational model: Column-foundation connection test PT_{NC} (left) and test PT (right) moment rotation behaviours.

5.7.2 Axial Spring Model

For the axial spring model (Figure 5.33), the mono-hinge axial stiffness was modelled with elasto-plastic springs to account for friction losses occurring between the tendons and the plastic ducts and with significantly high stiffness (axial stiffness of metallic ball connection) to allow the analysis to include the resultant compressive force of the tendons within the output of the beam elements and as a shear component in the column elements. The friction forces were determined using fundamental prestress theory where the vertical force components from the post-tensioned tendon are multiplied by the code recommendations for friction coefficients (between 0.05 and 0.15).

The unbonded post tensioned tendon is modelled using a Linear Elastic spring with an axial stiffness represented as the total area of the tendons, the steel modulus of elasticity steel and the unbonded length of the tendons. The spring elements were placed accordingly to the draped profile in different points and slaving the nodes profiles in the vertical direction with the beam nodes. The mild energy dissipaters were modelled using Dodd-Restrepo hysteresis rule [5.13].

Similar to what was presented in the moment rotational model, as the dissipaters are displaced into net negative displacements and buckling is initiated the dissipater does not contribute to the energy dissipated in the system. However, the bearing effect onto the epoxy filled material increases the compression stiffness and strength as was previously explained and illustrated in the experimental results presented earlier (Figure 5.24). An additional compression-only axial spring was added at the same location as the dissipaters such that the combined stiffness and strength between the two springs in parallel represents the observed behaviour during testing of the dissipater elements.

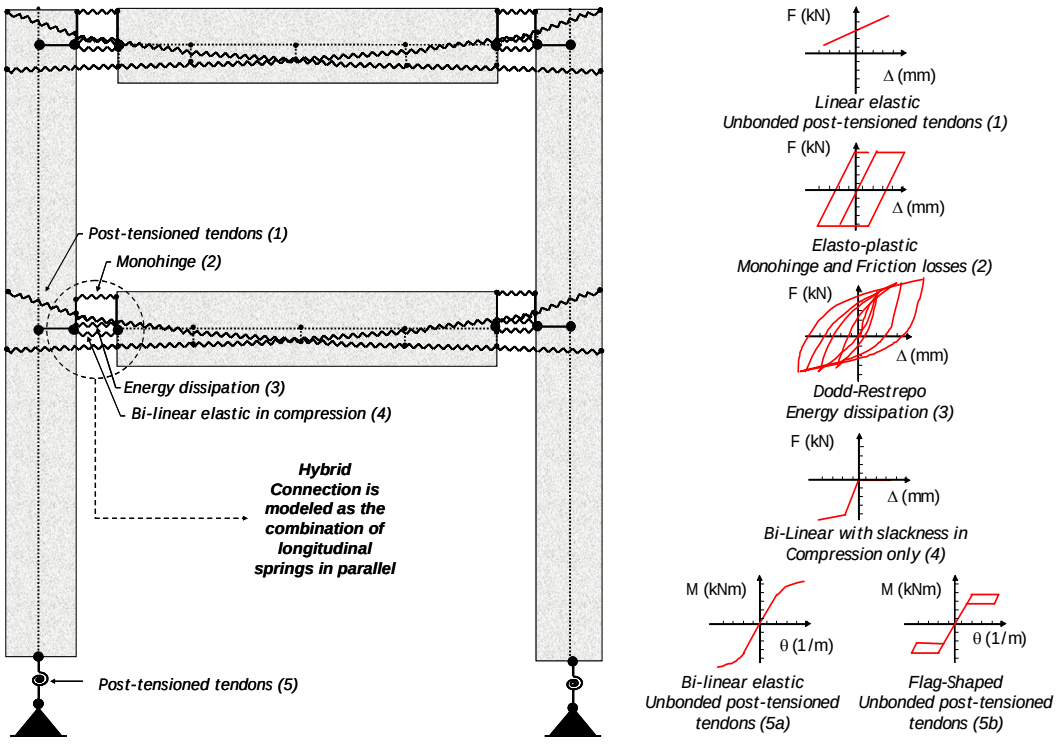

Figure 5.33. Axial spring model.

Similarly, as mentioned for the moment rotational spring model, a simple bi-linear elastic or flag shape hysteresis rule was adopted at the column base to model the axial force moment contribution due to the post-tensioned tendons.

Figure 5.34-left and right shows the global hysteresis response for tests PT_{NC} and $PT_{NC}7$ respectively. It can be seen the excellent agreement between the model and the experimental results for Test PT_{NC} and a good approximation for Test $PT_{NC}7$ despite the complexity in the modelling the energy dissipation in compression.

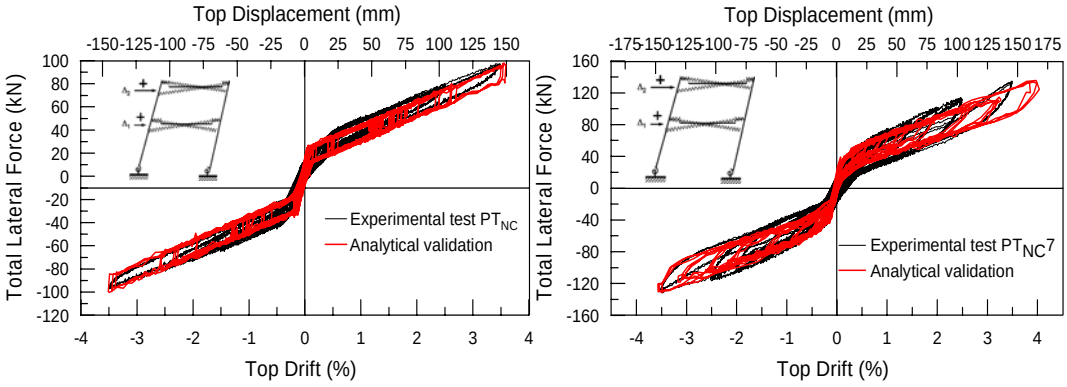

Figure 5.34. Analytical-experimental comparison using axial spring model: Force displacement response of test PT_{NC} (left) and $PT_{NC}7$ (right).

Similar experimental comparison of the results were obtained for Test PT and PT7 (Figure 5.35) where the model successfully reproduces the experimental results. The analytical validation of Test PT presents better agreement than the Test PT7 due to the simplicity hysteresis rule used to model the unbonded-post-tensioned tendons when compared to the additional Dodd-Restrepo and Bi-linear with slackness in compression hysteresis behaviours to capture energy dissipation used for the test.

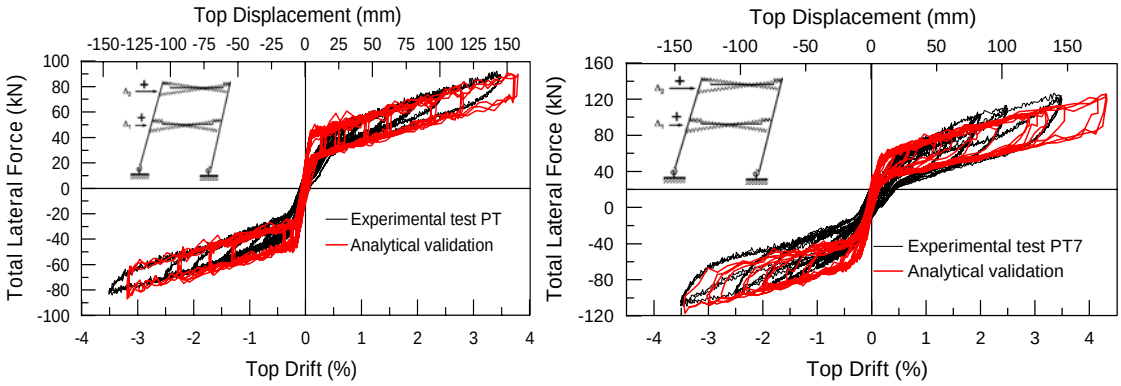

Figure 5.35. Analytical-experimental comparison using axial spring model: Force displacement response of test PT (left) and PT7 (right).

Similar results were obtained for the analytical experimental comparison using axial spring model between the unbonded post-tensioned tendons and the energy dissipation as those

obtained for the moment-rotation model shown in Figure 5.31 left and right respectively. As mentioned before, the linear elastic behaviour of the post-tensioned tendons was combined with the bi-linear inelastic hysteresis representing the friction in the tendons (Figure 5.31-left).

Different hysteresis rules were also adopted in order to capture the real behaviour of the dissipaters being the Dodd-Restrepo hysteresis rule the more appropriated in modelling the dissipaters. Additionally, the bilinear, compression-only spring hysteresis to account for the bearing contact in compression of the dissipater was also implemented. The calculation of the stiffness and maximum yield moment is difficult to predict due to the unknown epoxy properties and the possible contribution of the outer steel tube. The stiffness and strength was simply calibrated from cyclic steel testing of the dissipaters.

For this model, the column bases were modelled using the moment rotation response presented in the moment rotational model and results were identical as presented in the previous section of this chapter.

5.8 CHAPTER SUMMARY

In this Chapter a conceptual evolution of a non-tearing connection able to avoid the beam elongation and tearing effects in the floor with the use of anti symmetric profile of the unbonded post-tensioned tendons and external and replaceable energy dissipaters has been presented.

The flexural capacity of the connection can be achieved by the combination of post-tensioning and energy dissipation, while the desired self-centering capacity of the overal frame behaviour can be obtained through the implementation of a rocking foundation in combination of the gravity loads and/or the use of post-tensioning leading to limited or no residual deformation and cost of repairing.

The experimental results on cyclic testing of a two-story, one bay precast frame, implementing the proposed non-tearing floor, provide satisfactory confirmation that the effects associated with beam elongation can be eliminated, thus significantly reducing the expected damage in the floor.

Based on the results of quasi-static cyclic tests on 2/3 scaled, two-story, one bay precast frame implementing the proposed non-tearing floor solutions, the following conclusions can be made:

1. It was demonstrated that a global re-centring/dissipating response (typically referred to as a flag-shape behaviour) can be controlled either by only relying upon the contribution of the self weight of the structure and/or by adding unbonded post-tensioned tendons such that full re-centring can be achieved by the ratio between axial force and dissipation.

2. Although the innovative floor solution presented herein significantly reduces the effects of beam elongation, further refinements will include improvements in the energy dissipater devices as well as to guarantee the actual constructability (tolerances issues) targeting a wider adoption by the construction industry.

3. Experimental results showed that the systems using an unbonded post-tensioned solution substantially reduced their secant stiffness in comparison with the hybrid systems due to the external dissipaters' contribution to the secant stiffness of the frame.

4. As the dissipation content is increased the higher the equivalent viscous damping is perceived. Due to bucking of the dissipater between a lateral drift of 2% and 2.5%, a reduction in the equivalent viscous damping is observed. The equivalent viscous damping is highly dependent of the size of the fuse of the dissipater: the smaller the fuse is the lesser the equivalent viscous damping will be due to the poor bucking resistance and thus equivalent viscous damping degradation is observed. Dissipaters with bigger size in fuse diameter will have better performance in the cyclic behaviour and higher equivalent viscous damping under higher drift levels. A comparison between the constant and variable axial load shows no significant differences for the equivalent viscous damping.

5. The analytical-experimental comparisons for moment rotation or longitudinal spring models confirmed a very satisfactory accuracy in the overall strength response. Therefore, the proposed simplified models can be adopted to describe the behaviour of the hybrid non-tearing connection.

6. In terms of local response, the linear elastic hysteresis model use to represent the unbonded post-tensioned tendons showed very good agreement with the experimental response. Simple rules can be adopted to predict the behaviour of the energy dissipaters. However, due to the poor behaviour in compression and excessive buckling and bearing effects of the energy dissipaters exhibit in the tests new designs are highly recommended. One possible solution could be the reduction in length of the dissipater to increase the bucking capacity and a smoth transition zone slope about 3:1 between the fuse and the bar.

7. For the validation of the experimental results, modelling the energy dissipaters were using more refined hysteresis rules to capture the cyclic behaviour of the dissipaters and obtained a close approximation to the experimental results. However, the hysteresis rules were unable to properly capture the unloading stiffness and the buckling observed during the tests in the dissipaters due to the meaningless of the moment-rotation or axial force-elongation parameters adopted.

8. Comparison between the moment-rotation and longitudinal spring models indicates no significant difference in the global or local beam column joint validation. However, considering the number of nodes and the specific node coordinates to generate the geometry and create the proper action in the joint, in addition to the increase in number of elements that the longitudinal spring model requires, the moment rotational model seems to be more appropriate. Although, when it is require that a more refine internal forces distribution in the elements be determined (e.g. beam axial forces due to post-tensioned tendons) the longitudinal model is require.

5.9 REFERENCES

5.1 Palmieri, L., French, C., Sagan, E. I., and Kreger, M. E. 1997. "Ductile Connections for Precast Concrete Frames Systems." Mete A. Sozen Symposium, ACI SP 162, American Concrete Institute, Farmington Hill, MI, 1997, pp. 313-355.

5.2 Amaris, A. Pampanin, S., Bull, D., and Carr, A. "Development of a Non-tearing Floor Solution for Jointed Precast Frame Systems," Proceedings of the New Zealand Society of Earthquake Engineering Annual Conference, Parmerston North, New Zealand, 2007.

5.3 Amaris, A. Pampanin, S., Bull, D., and Carr, A. "Experimental Investigation on a Hybrid Jointed Precast Frame with Non-tearing Floor Connections," Proceedings of the New Zealand Society of Earthquake Engineering Annual Conference, Taupo, New Zealand, 2008.

5.4 Pampanin S., Priestley N., and Sritharan S., "Analytical Modeling of the Seismic Behavior of Precast Concrete Frames Designed with Ductile Connections." Journal of Earthquake Engineering. Vol. 5, No. 3, May.-Jun, 2001, pp. 329-367.

5.5 New Zealand Standards (NZS). "Appendix B: Special Provisions for the Seismic Design of Ductile Jointed Precast Concrete Structural Systems," NZS3101:2006, Concrete Standard, Wellington, New Zealand.

5.6 Restrepo, J. I., 1993 "Seismic behaviour of connections between precast concrete elements," Ph.D. Dissertation, Department of Civil engineering, University of Canterbury, Christchurch, New Zealand.

5.7 Priestley, M.J.N. “Direct Displacement-Based Design of Precast/Prestressed Concrete Buildings”. PCI Journal. Vol. 47 No. 6, Nov-Dec 2002, pp. 66-78

5.8 ACI Innovation Task Group 1 and Collaborators. “Special Hybrid Moment Frames Composed of Discretely Jointed Precast and Post-tensioned Concrete Members (T1.2-03) and Commentary (T1.2R-03)”. American Concrete Institute, Farmington Hills, Michigan. 2003.

5.9 Innovation Task Group 1 and Collaborators and ACI Committee 374. “Acceptance Criteria for Moment Frames Based on Structural Testing (T1.1-01) and Commentary (T1.1R-01),” American Concrete Institute, Farmington Hill, Michigan. 2001

5.10 Tyler, R. G. “Rubber Bearing in Base-Isolated Structures-A summary Paper” Bulletin of the NZ National Society for Earthquake Engineering, Vol 24, No. 3, Sep, 1991, pp. 251-274.

5.11 Palermo, A., “The use of controlled rocking in the Seismic Design of Bridges,” Ph.D. dissertation, Politecnico di Milano, Milano, Italy. 2004.

5.12 Carr, A. “RUAUMOKO program for Inelastic Dynamic Analysis – User Manual”. Department of Civil Engineering, University of Canterbury, Christchurch, New Zealand. 2006

5.13 Dodd, L., and Restrepo-Posado, J. “Model for Predicting Cyclic behaviour of Reinforcing Steel”. ASCE Journal of Structural Engineering, Vol. 121, No. 3, May–Jun, 1995, pp. 433-445.

CHAPTER 6
PARAMETRIC ANALYSIS FOR NON-TEARING FLOOR CONNECTIONS

6.1 INTRODUCTION

As described in Chapter 4 and Chapter 5, the concept of a non-tearing floor connection was presented along with the results of cyclic tests on a series of 2/3 scaled, precast beam-column joints and the 2-D, 2/3 scale, two story, single bay, precast concrete frame. Additionally, analytical-experimental validations were implemented using simple analytical models already presented in the literature, providing a reliable control over the expected hysteresis and dynamic behaviour.

In this chapter, a discussion of the structural behaviour of hybrid H-frames with multiple spans using non-tearing connections is presented. Parametric analysis is carried out for a series of beam-column joints and H-frames with multiple spans using non-tearing connection to determine the characteristics of the non-tearing connections in terms of local (moment capacity) and global (base shear) response. The variables considered consist of three beams sections with different bay lengths, changing the location of the tendons along the beam section, the unbonded length and initial post-tensioned force as well as the steel area content.

Finally, a design example of a non-tearing beam-column joint is presented under a given moment demand and evaluation of the storey shear is obtained through the equations formulated in the chapter.

6.2 STRUCTURAL BEHAVIOUR OF A HYBRID BEAM-COLUMN JOINT WITH TOP HINGE CONNECTION

As presented in the literature as part of this research program [6.1, 6.2], a further conceptual evolution of the rocking of the non-tearing floor beam-column connection with a single top hinge, anti-symmetric tendon profile and energy dissipaters had been shown in Chapter 5. Given that the single hinge acts as a pivot point, the neutral axis depth position c is given and fixed by the designer, the moment capacity of the beam column connection is simply achieved using equilibrium of the section and then taking moments from the neutral axis position. Under

an initial post-tensioned force $T_{pt1\,ini}$ and $T_{pt2\,ini}$ for tendons 1 and 2 respectively, the increase or decrease (when the gap closes) in force due to the rocking mechanism at the connection, can be evaluated as shown in Figure 6.1.

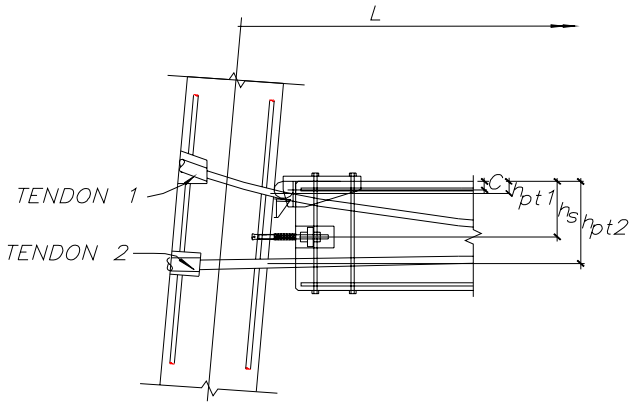

Figure 6.1. Rocking of the Hybrid non-tearing beam column connection.

$$\Delta T_{pt1} = \theta_b \left(h_{pt1} - c\right)\frac{EA_{pt}}{L_{unb}} \tag{6.1a}$$

$$\Delta T_{pt2} = \theta_b \left(h_{pt2} - c\right)\frac{EA_{pt}}{L_{unb}} \tag{6.1b}$$

where θ_b is the column rotation established as the design drift and h_{pt1} and h_{pt2} are the height of the tendon 1 and 2 respectively, c the neutral axis depth position, L_{unb} the length of the tendons without grout along the tendon profile, E and A_{pt} the modulus of elasticity and steel area of the tendons respectively.

Adopting a positive convention for moments (anti-clockwise direction) and a positive joint rotation (gap opening), the total moment contribution at the beam column connection can be calculated taking the forces from the centre of the top hinge as

$$M = M_{pt\,ini} + \Delta M_{pt} + M_s \tag{6.2}$$

Where $M_{pt\,ini}$ is the initial post-tension moment due to the initial post-tensioned forces and equal to $M_{pt\,ini} = T_{pt1\,ini}(h_{pt1} - c) + T_{pt2\,ini}(h_{pt2} - c)$, ΔM_{pt} is the change in the post-tensioned moment due to the elongation or shortening of the post-tensioned tendons and can be calculated as $\Delta M_{pt} = \Delta T_{pt1}(h_{pt1} - c) + \Delta T_{pt2}(h_{pt2} - c)$ where ΔT_{pt1} and ΔT_{pt2} can be calculated according to equation 6.1 and M_s is the moment contribution of the steel disipaters which is equal to $M_s = f_s A_s (h_s - c)$. The equation 6.2 can be rewritten as

$$M = \left(T_{pt1\,ini} + \Delta T_{pt1}\right)\left(h_{pt1} - c\right) + \left(T_{pt2\,ini} + \Delta T_{pt2}\right)\left(h_{pt2} - c\right) + T_s\left(h_s - c\right) \quad (6.3)$$

From equation 6.2, the total moment contribution of the connection depends on the material contribution of the energy dissipaters ($T_s = f_s A_s$) and post-tension tendons (EA_{pt}) and the geometrical contribution determined by the location of the tendons along the section (h_{pt1} and h_{pt2}), the unbonded post-tensioned length (L_{unb}) of the tendons and the initial post-tensioned forces ($T_{pt1\,ini}$ and $T_{pt2\,ini}$).

6.3 PARAMETRIC ANALYSIS IN A HYBRID B/C JOINT WITH NON TEARING CONNECTION

The natural characteristics of the connection determine an initial post-tensioned moment at zero drift which depends on the initial post-tensioned force. As the connection opens and closes, the post-tensioned moments will undergo to positive moment when the gap at the connection opens (positive rotation) and minimum of zero moment when the gap closes (negative rotation). The moments in the negative rotation can not have negative magnitudes as elongation of the tendon at the negative target rotation will be higher than the initial post-tensioned force meaning that the tendon will have a minimal compression force and buckling is occurring.

A parametric analysis is carried out for three beam section with different bay lengths, changing the location of the post-tensioned tendons along the beam section (h_{pt1}/h_b and h_{pt2}/h_b), the unbonded length of the post-tensioned tendons (L_{unb}/L_b), and the initial post-tensioned force as a percentage of the ultimate post-tensioned force ($T_{pt\,ini}/T_{ult}$) and changing the steel area content from A_{pt}/A_s to determine the characteristics of the connection. Table 6.1 shows a summary of the variables assumed.

6.3.1 Beam Section (h_b) and location of the post-tensioned tendons ratio (h_{pt2}/h_b).

Three beam sections (h_b) with different post-tensioned tendons location ratio (h_{pt2}/h_b) were evaluated for each bay length (L_b) with different unbonded length ratios (L_{unb}/L) and initial post-tensioned force ratios ($T_{pt\,ini}/T_{ult}$).

Figures 6.2 to 6.4 show $\Delta M_{pt} / M_{pt\,ini}$ vs. rotation for three beam sections with different initial post-tensioned forces and bay lengths changing the unbonded post-tensioned length. The variation between $h_{pt2} / h_b = 0.63\ and\ 0.85$ indicates as far h_{pt1} and h_{pt2} are from the top hinge (pivot point), higher the post-tensioned moments due to the increase in the lever arm.

Table 6.1. Parametric analysis of the B/C connection and frames with top hinge connection

h_b (mm)	L_b (mm)	L_{unb}/L_b	T_{ini}/T_{ult}	h_{pt1}/h_b	h_{pt2}/h_b	A_{pt}/A_s	No. Bays
500	6000	1.00	0.4, 0.5 and 0.6	0.17	0.63* and 0.85	0.0	1
		0.75				0.5	2
		0.50				1.0	3
		0.25				1.5	4
		0.00				2.0	5
	9000	1.00	0.4, 0.5 and 0.6	0.17	0.63* and 0.85	0.00	1
		0.75				0.25	2
		0.50				0.50	3
		0.25				1.00	4
		0.00				1.50	5
	12000	1.00	0.4, 0.5 and 0.6	0.17	0.63* and 0.85	0.00	1
		0.75				0.25	2
		0.50				0.50	3
		0.25				1.00	4
		0.00				1.50	5
700	6000	1.00	0.4, 0.5 and 0.6	0.17	0.63* and 0.85	0.00	1
		0.75				0.25	2
		0.50				0.50	3
		0.25				1.00	4
		0.00				1.50	5
	9000	0.67	0.4, 0.5 and 0.6	0.17	0.63* and 0.85	0.00	1
		0.50				0.25	2
		0.33				0.50	3
		0.17				1.00	4
		0.00				1.50	5
	12000	0.50	0.4, 0.5 and 0.6	0.17	0.63* and 0.85	0.00	1
		0.38				0.25	2
		0.25				0.50	3
		0.13				1.00	4
		0.00				1.50	5
900	6000	1.00	0.4, 0.5 and 0.6	0.17	0.63* and 0.85	0.00	1
		0.75				0.25	2
		0.50				0.50	3
		0.25				1.00	4
		0.00				1.50	5
	9000	0.67	0.4, 0.5 and 0.6	0.17	0.63* and 0.85	0.00	1
		0.50				0.25	2
		0.33				0.50	3
		0.17				1.00	4
		0.00				1.50	5
	12000	0.50	0.4, 0.5 and 0.6	0.17	0.63* and 0.85	0.00	1
		0.38				0.25	2
		0.25				0.50	3
		0.13				1.00	4
		0.00				1.50	5

* only for parametric analysis of B/C connection

Similarly, for a given L_b, L_{unb}/L_b and $T_{pt\,ini}/T_{ult}$, the change in the in the post-tensioned moments ΔM_{pt} increase due to the increase in the eccentricity of the post-tensioned lever arm with respect to the hinge located at the top of the connection.

6.3.2 Initial post-tensioned force ratio ($T_{pt\,ini}/T_{ult}$).

Figures 6.2 to 6.4 show that for a given bay length (L_b) and unbonded post-tensioned length (L_{unb}/L_b) an increase of the initial post-tensioned force from $T_{pt\,ini}/T_{ult} = 0.4$ to 0.6, the change in the post-tensioned moments over the initial post-tensioned force ($\Delta M_{pt}/M_{pt\,ini}$) decrease. Note that $M_{pt\,ini}$ increase as $T_{pt\,ini}$ increases, therefore in Figures 6.2 to 6.4 $\Delta M_{pt}/M_{pt\,ini}$ is reducing because of $M_{pt\,ini}$ increase. However, ΔM_{pt} is constant indicating that is independent of $T_{pt\,ini}$.

6.3.3 Bay length (L_b) and unbonded post-tensioned length ratio (L_{unb}/L_b).

Keeping in mind that ΔM_{pt} is reducing because of the increase in $M_{pt\,ini}$ due to the initial force $T_{pt\,ini}$, as the bay length (L_b) increases for a given unbonded post-tensioned length (L_{unb}/L_b), the post-tensioned moments (M_{pt}) and the change in the post-tensioned moments (ΔM_{pt}) increase.

Finally given a bay length (L_b), as the unbonded length ratio (L_{unb}/L) increased from partially bonded ($L_{unb}/L = 0.25$) to fully unbonded ($L_{unb}/L = 1.0$, the post-tensioned moments (M_{pt}) and the change in the post-tensioned moments (ΔM_{pt}) decreased.

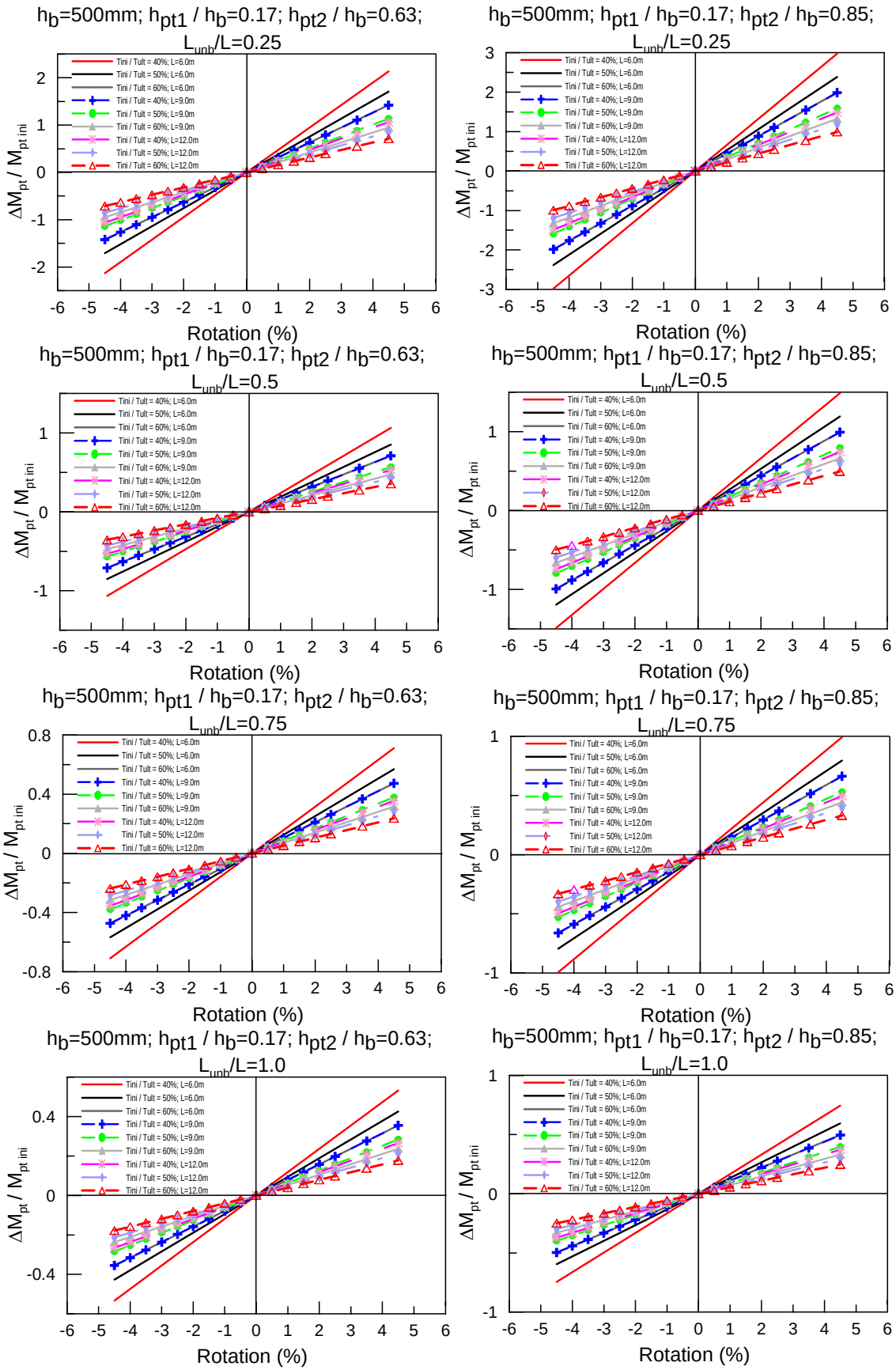

Figure 6.2. M_{pt} / $M_{pt\ ini}$ vs rotation for h_b=500 varying bay length, initial post-tensioning and unbonded length.

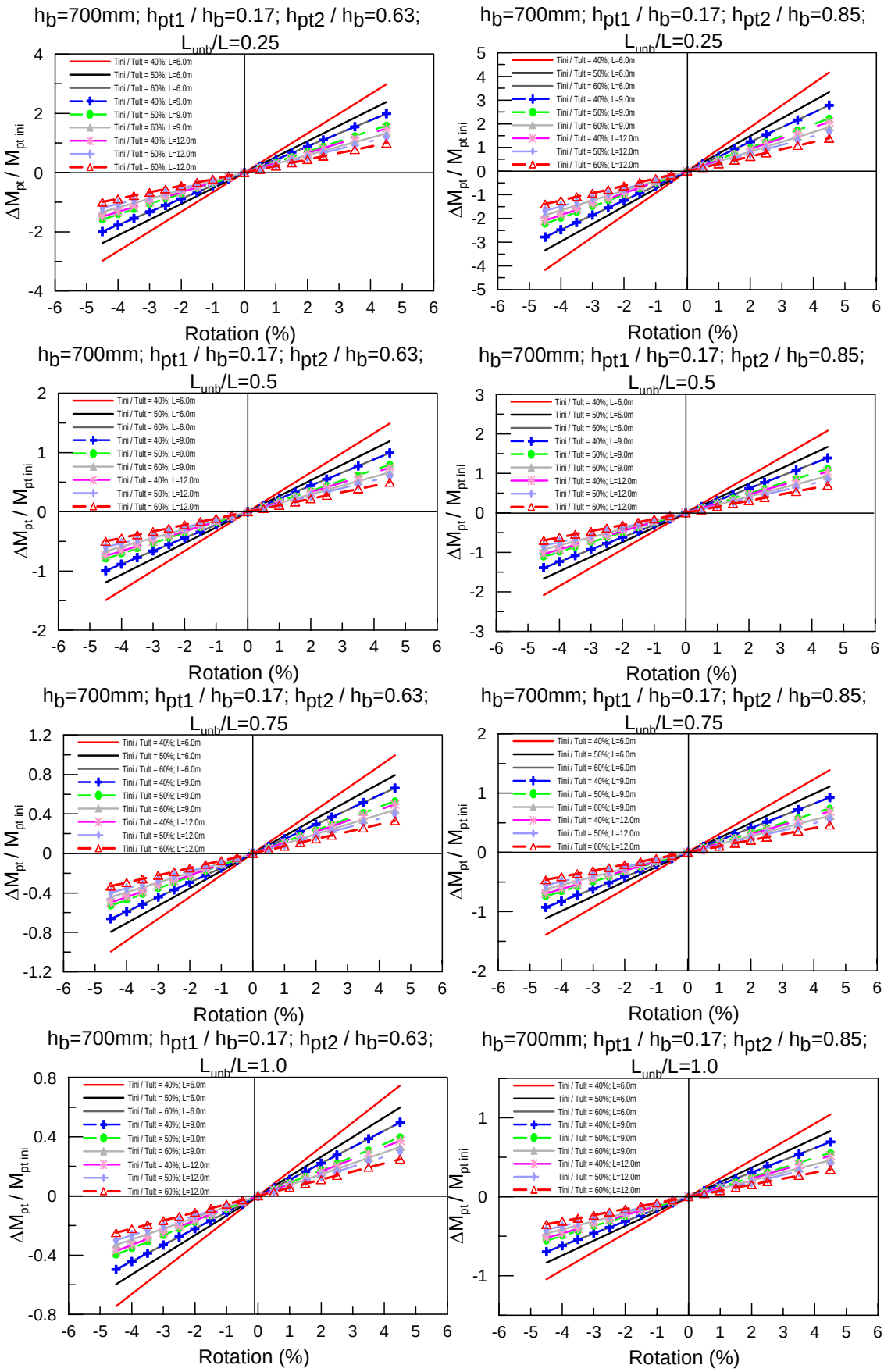

Figure 6.3. M_{pt} / $M_{pt\ ini}$ vs rotation for h_b=700 varying bay length, initial post-tensioning and unbonded length.

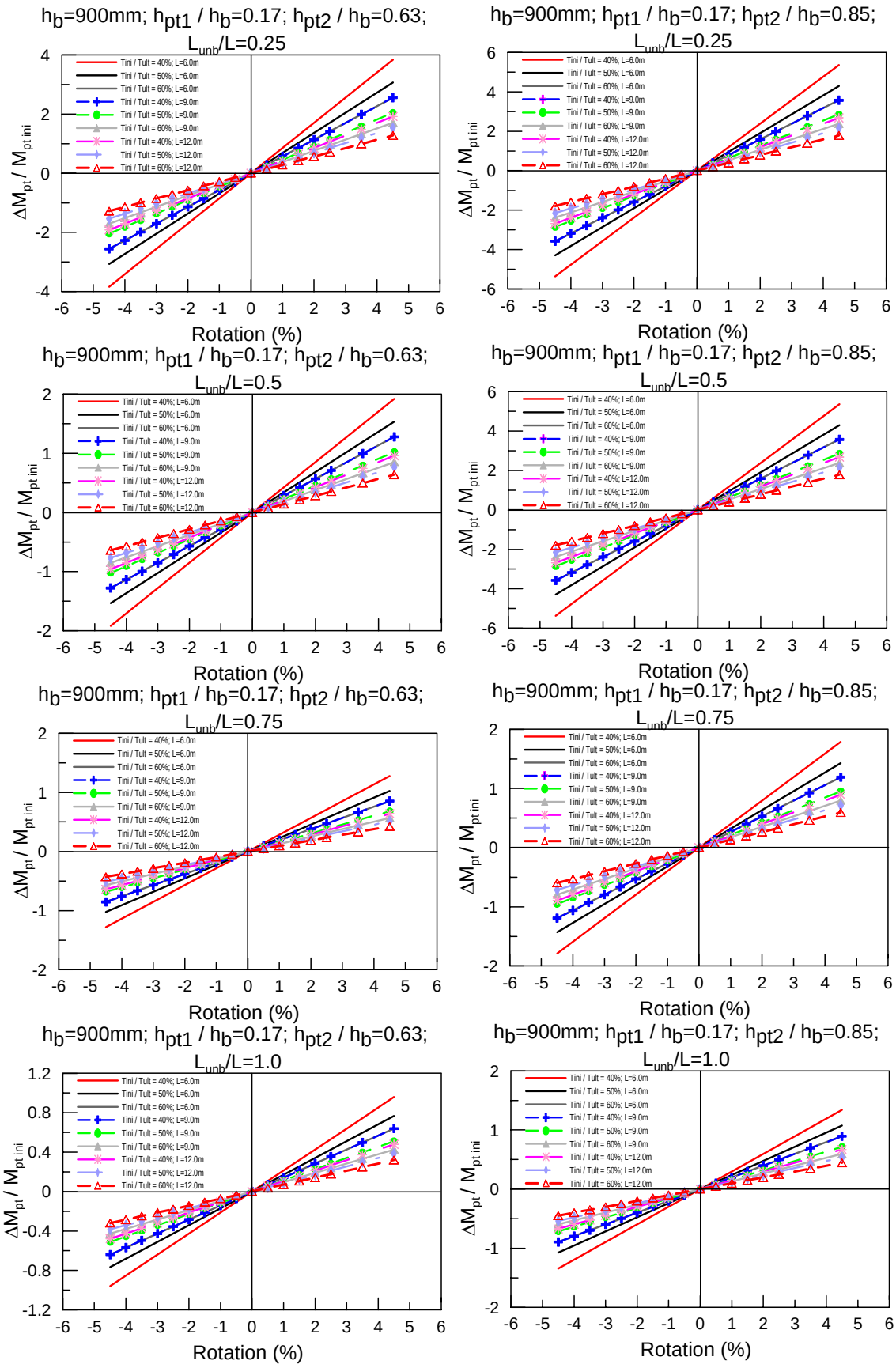

Figure 6.4. M_{pt} / $M_{pt\ ini}$ vs rotation for h_b=900 varying bay length, initial post-tensioning and unbonded length.

As the post-tensioned moments behave linearly, for design purposes Figure 6.5, shows the ratio of $\Delta M_{pt\ at\ 2.0\%} / M_{pt\ ini}$ vs. L_{unb} / L for three different initial post-tensioned forces ratio ($T_{pt\ ini} / T_{ult}$) and bay lengths (L_b). It can be seen that higher post-tensioned moments were obtained for $h_{pt2} / h_b = 0.85$ when compared with $h_{pt2} / h_b = 0.63$ especially for short bay lengths and small unbonded lengths up to half of the bay lengths this difference was significantly high.

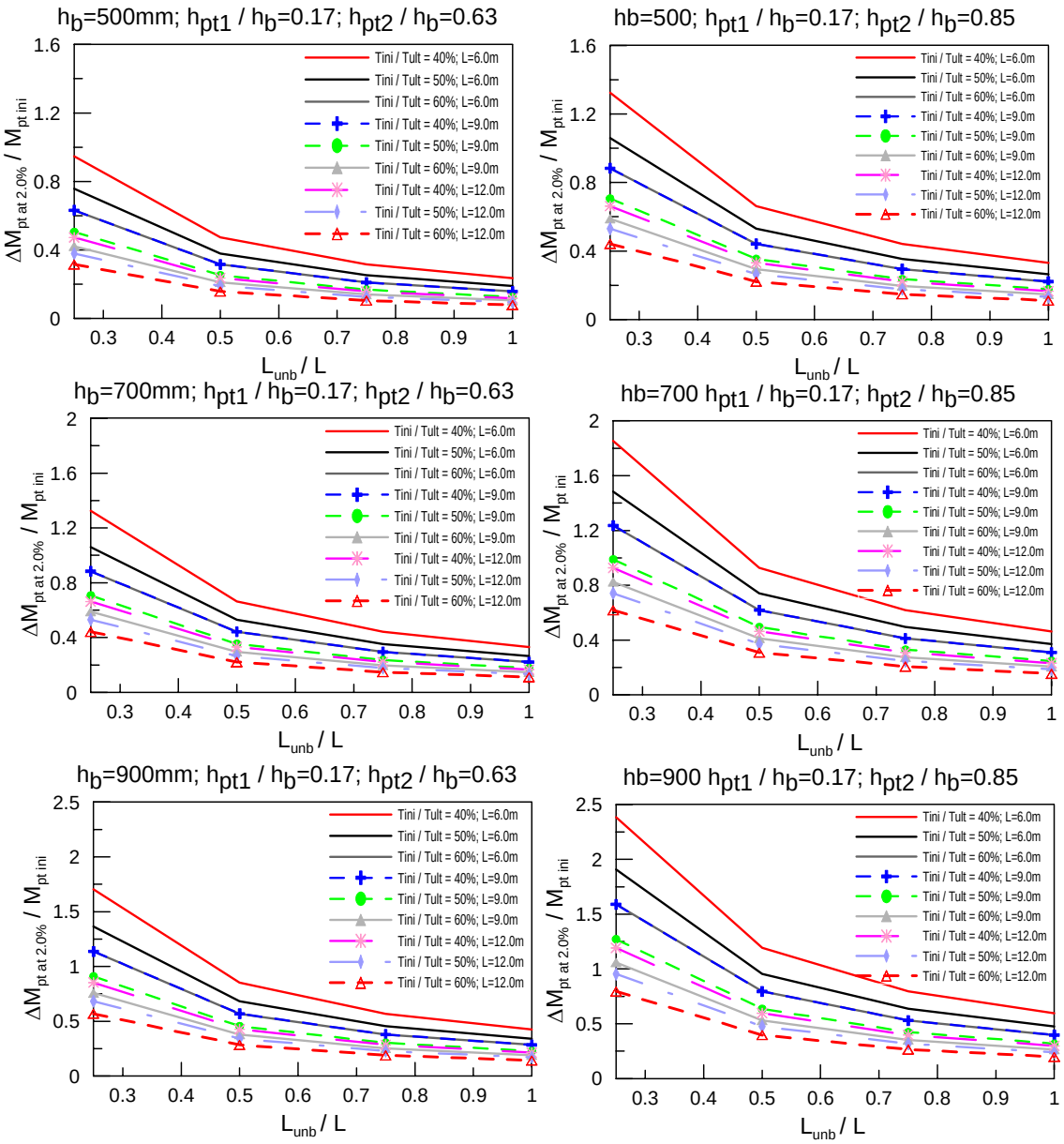

Figure 6.5. $M_{pt\ at\ 20\%} / M_{pt\ ini}$ vs L/L_{unb} for different bay lengths and initial post-tensioning.

The connection solution with partially bonded tendons ($L_{unb} / L = 0.25$) shows a higher post-tensioned moment contribution in the connection. As the unbonded length increases, there is a

decrease in the post-tensioned moment capacity of the connection until it becomes fully unbonded. These results indicate that higher beam shear can be obtained by reducing the unbonded length by one quarter of the total length and keeping an unbonded length low (e.g. quarter of the bay length).

Keeping in mind that ΔM_{pt} is reducing because of the increase in $M_{pt\ ini}$ due to $T_{pt\ ini}$, as the bay length (L_b) increases for a given unbonded post-tensioned length (L_{unb}/L), the post-tensioned moments (M_{pt}) and the change in the post-tensioned moments (ΔM_{pt}) increase.

6.3.4 Steel area content ratio.

A parametric analysis was carried out with the addition of external energy dissipation to the connection by changing the steel area content from A_{pt}/A_s for different types of beam sections, unbonded length ratios (L_{unb}/L), and bay lengths to determine the characteristics of the connection. Figures 6.6 to 6.14 show the $M_{total}/M_{pt\ ini}$ vs. rotation for three beam sections (h_b =500, 700 and 900mm) and different initial post-tensioned forces (T_{ini}/T_{ult} =40%, 50% and 60%).

Comparison between $M_{total}/M_{pt\ ini}$ changing the beam sections (h_b) indicate that as the beam depth increases, the total moments also increase due to the increase in the lever arm between the location of the tendons and the top hinge.

Given a bay length (L_b) and unbonded length ratio (L_{unb}/L), as the steel area content increases from $A_{pt}/A_s = 0$ to 2.0, for gap opening in the connection (positive rotation), the total moments increase as expected due to the higher contribution of the post-tensioned steel area. However as the initial post-tensioned moment increases, the total $M_{total}/M_{pt\ ini}$ ratio decreases. Note that as the gap closes (negative rotations), the total moment contribution will be significantly reduced due to the prestressing tendons having no force, therefore only the energy dissipation contribution is provided in the connection. This reduction in the total moments is more severe for small initial post-tensioned forces.

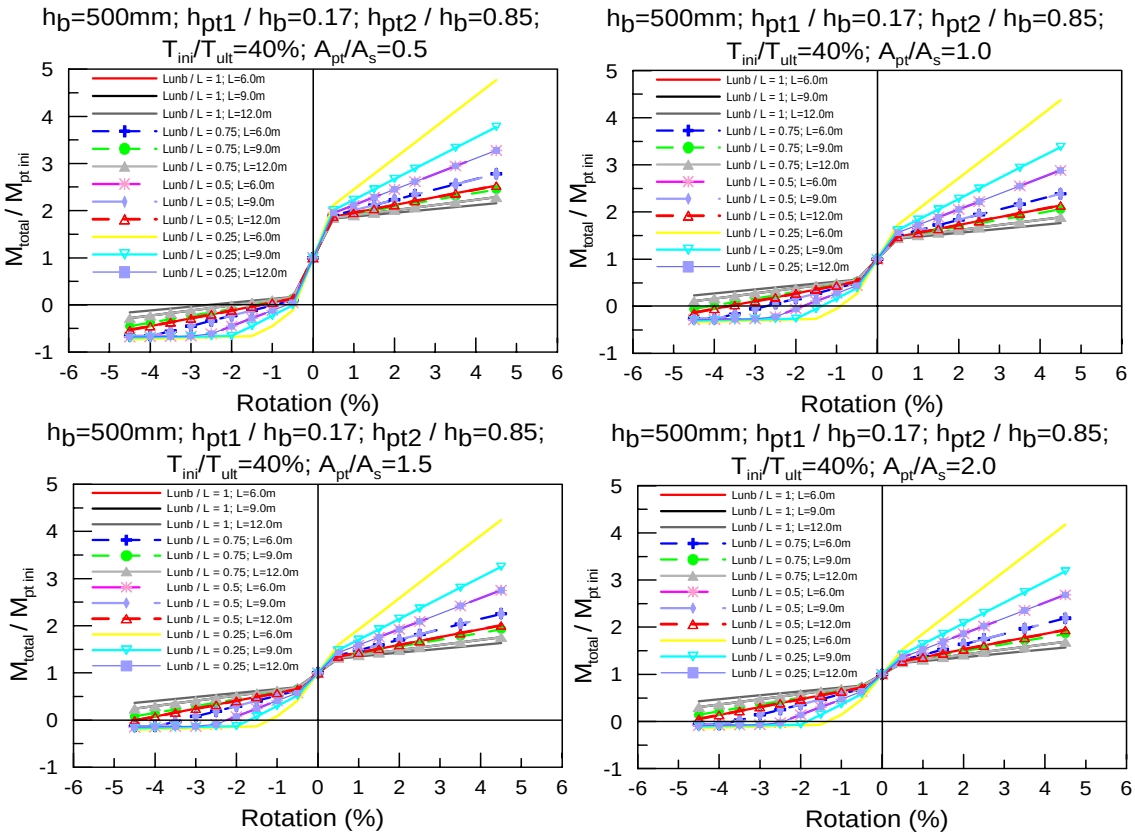

Figure 6.6. M_{total} / $M_{pt\ ini}$ vs rotation for h_b=500 and T_{ini}/ T_{ult}=40% varying bay length and unbonded length.

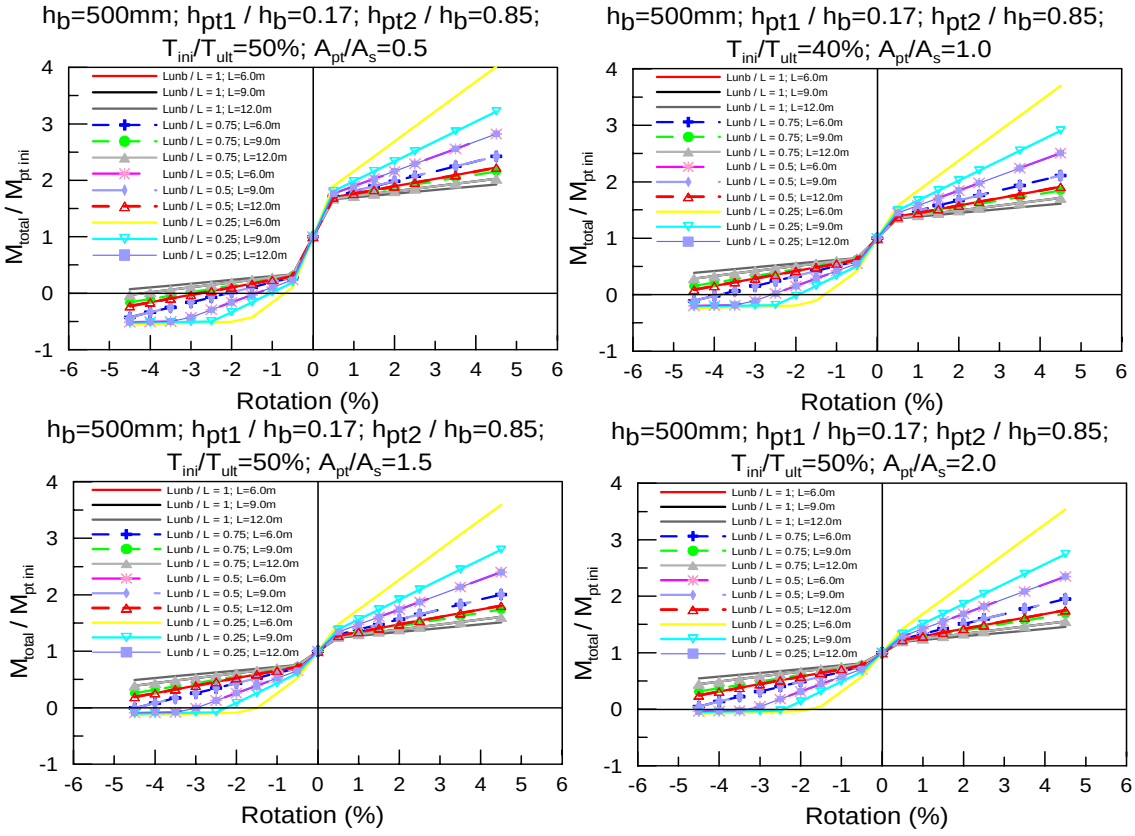

Figure 6.7. M_{total} / $M_{pt\ ini}$ vs rotation for h_b=500 and T_{ini}/ T_{ult}=50% varying bay length and unbonded length.

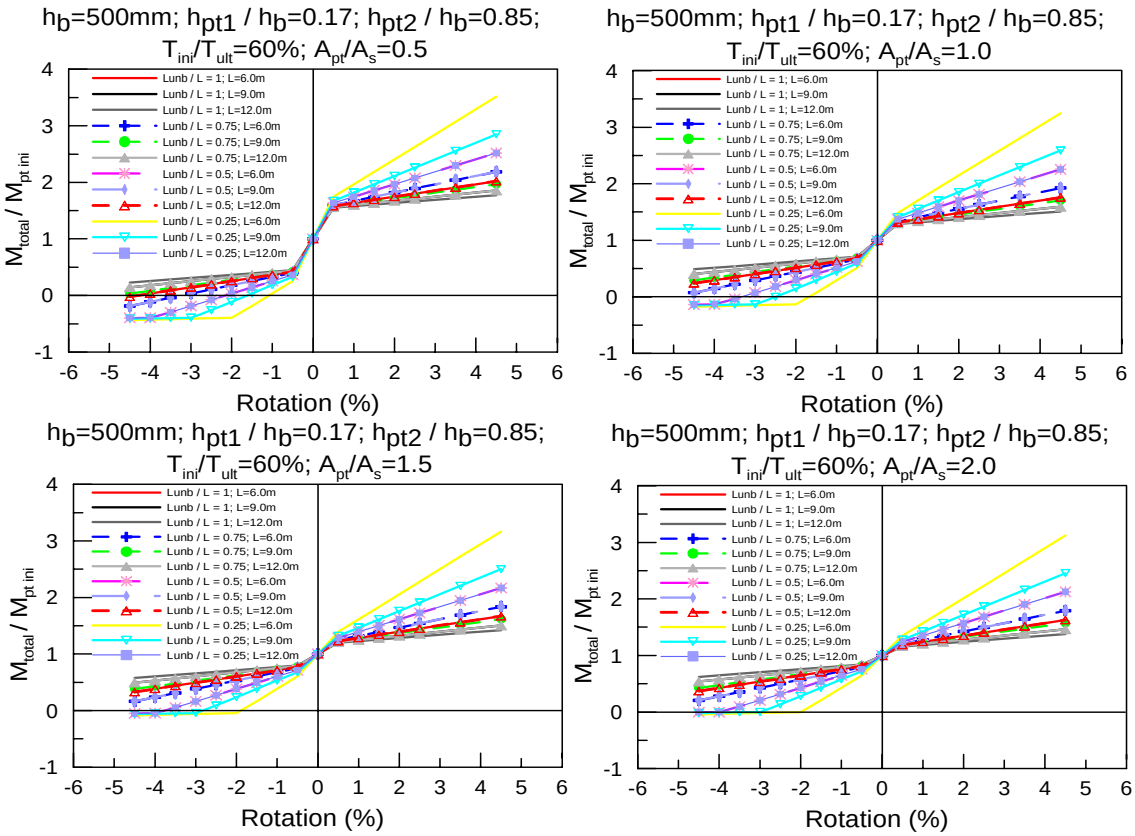

Figure 6.8. M_{total} / $M_{pt\ ini}$ vs rotation for h_b=500 and T_{ini}/ T_{ult}=60% varying bay length and unbonded length.

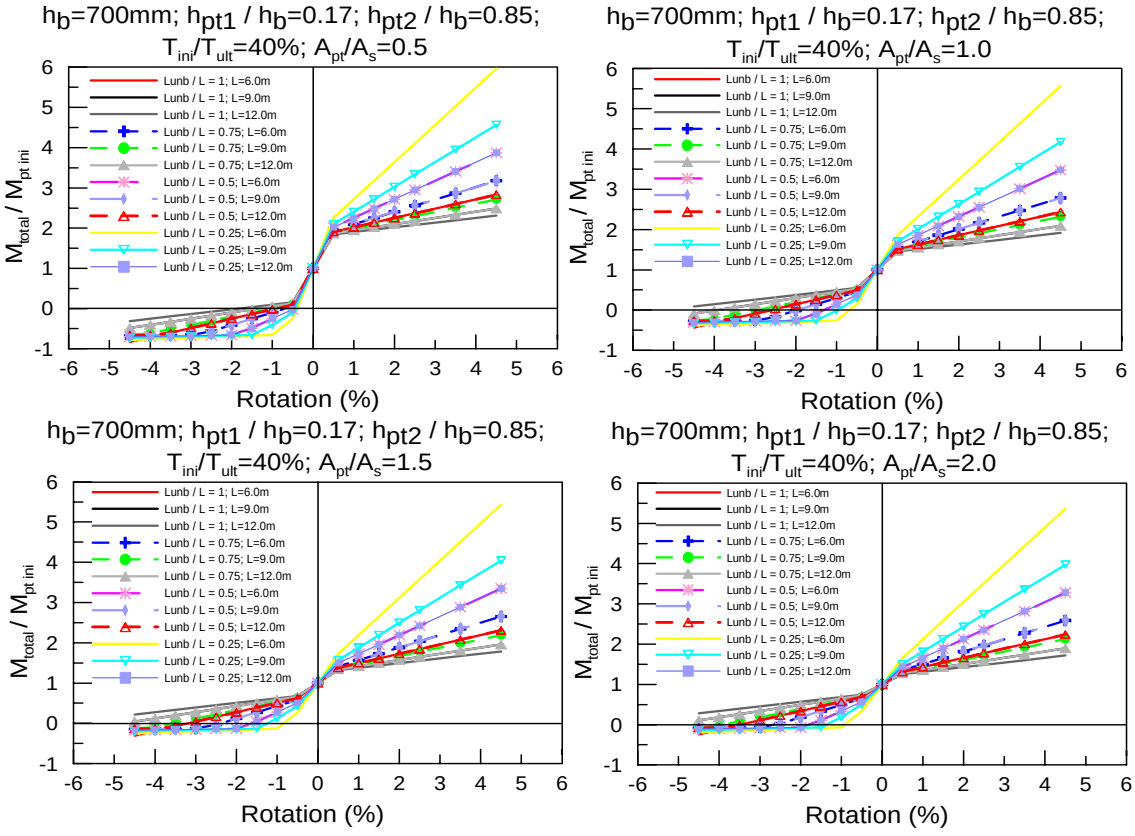

Figure 6.9. M_{total} / $M_{pt\ ini}$ vs rotation for h_b=700 and T_{ini}/ T_{ult}=40% varying bay length and unbonded length.

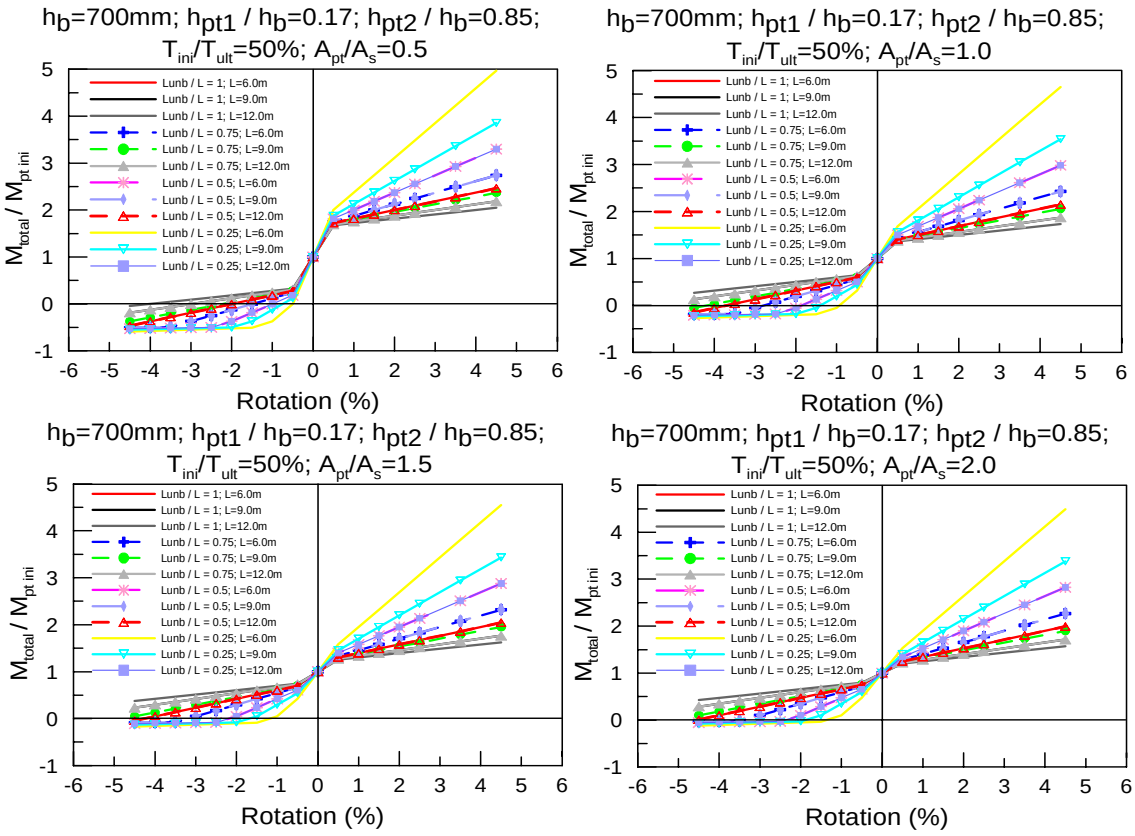

Figure 6.10. M_{total} / $M_{pt\ ini}$ vs rotation for h_b=700 and T_{ini}/ T_{ult}=50% varying bay length and unbonded length.

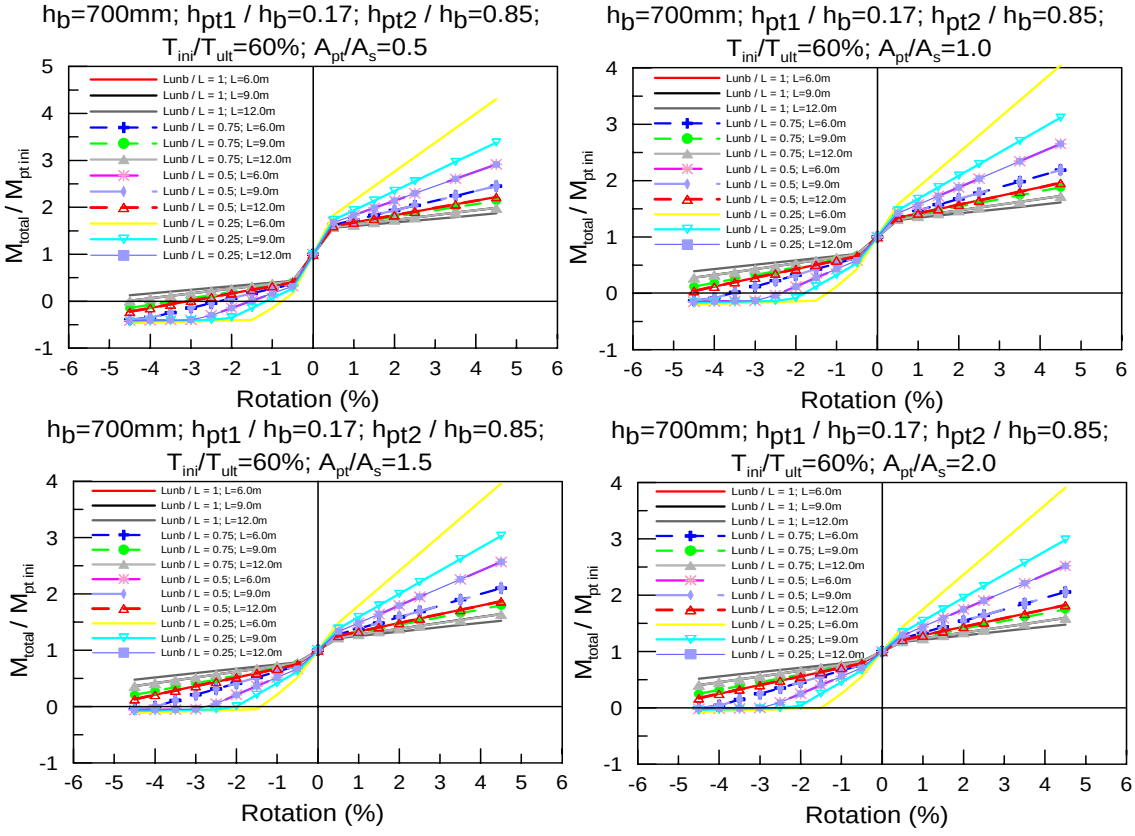

Figure 6.11. M_{total} / $M_{pt\ ini}$ vs rotation for h_b=700 and T_{ini}/ T_{ult}=60% varying bay length and unbonded length.

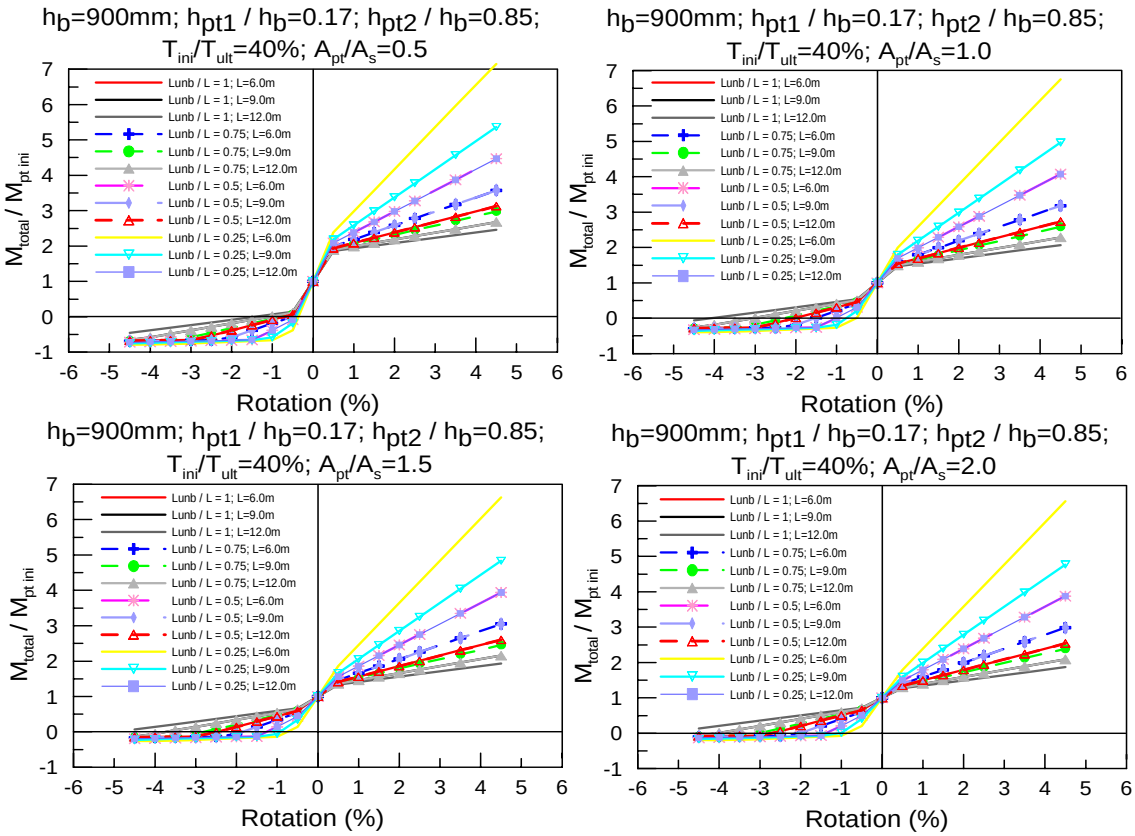

Figure 6.12. M_{total} / $M_{pt\ ini}$ vs rotation for h_b=900 and T_{ini}/ T_{ult}=40% varying bay length and unbonded length.

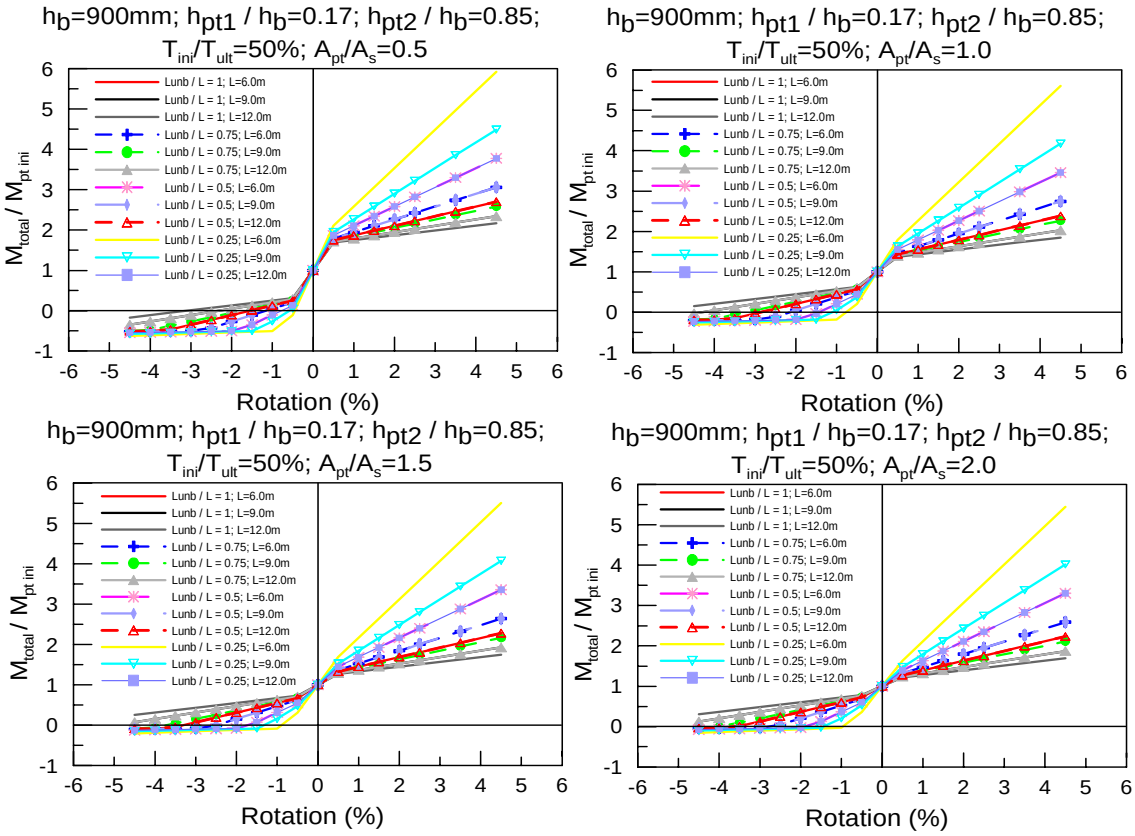

Figure 6.13. M_{total} / $M_{pt\ ini}$ vs rotation for h_b=900 and T_{ini}/ T_{ult}=50% varying bay length and unbonded length.

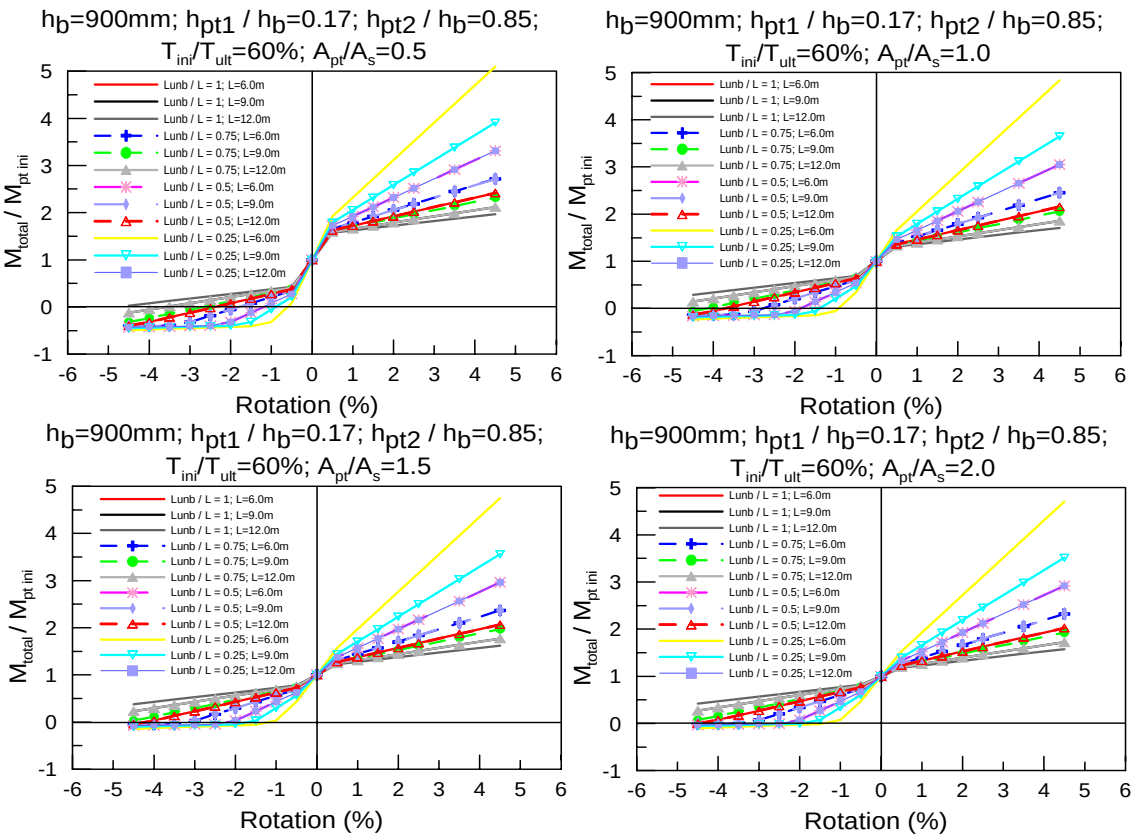

Figure 6.14. M_{total} / $M_{pt\ ini}$ vs rotation for h_b=900 and T_{ini}/ T_{ult}=60% varying bay length and unbonded length.

Similarly, given a bay length (L_b) and steel content ratio A_{pt}/A_s, as the L_{unb}/L decreases from fully unbonded $L_{unb}/L=1$ to fully bonded $L_{unb}/L=0$, the total moment at the connection when the gap closes (negative rotations) is severely decreased and increased when the gap opens (positive rotations). This is because as mentioned before, as the unbonded length decreases, the post-tensioned moment contribution increases. However, when the connection closes, the negative post-tensioned moments might be zero due to the small unbonded length.

Finally, by a given steel area content A_{pt}/A_s and unbonded length ratio L_{unb}/L, as the bay length increases from $L=6$ m to 12m the total moments decrease. Particularly this result indicates that for longer span construction (large open space) higher post-tensioned forces/increase dissipation or reduced unbonded length will be required to provide the required total moment capacity at the connection.

6.4 STRUCTURAL BEHAVIOUR OF HYBRID H-FRAMES WITH ONE SINGLE SPAN USING NON-TEARING CONNECTIONS

From the previous section the identification and parametric analysis of the beam column connection with non-tearing connection was carried out. In this section a structural analysis of an H-frame using non-tearing connection is presented along with the equilibrium equations to determine the shear forces and bending moments in the beam and columns.

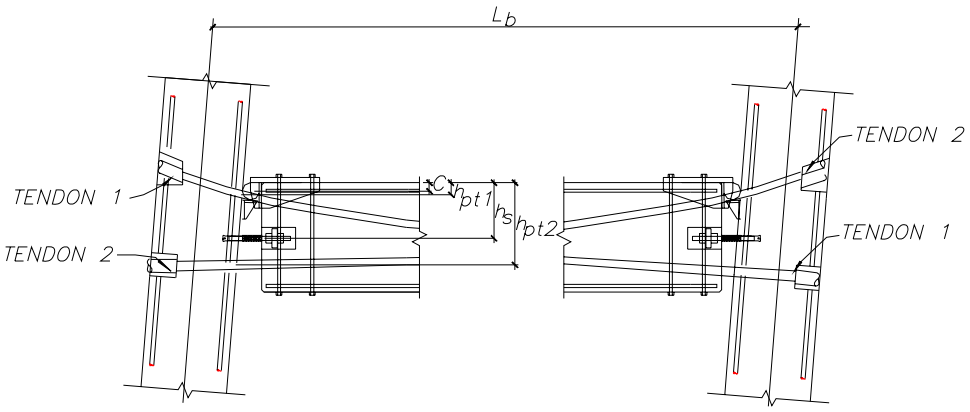

Figure 6.15. Rocking of the Hybrid frame with non-tearing connections.

Figure 6.15 shows an H frame with non-tearing connection under an initial post-tensioned force $T_{pt1\,ini}$ and $T_{pt2\,ini}$ for tendons 1 and 2 respectively, the increase or decrease (when the gap closes) in force due to the rocking mechanism of the connection, can be evaluated as:

$$\Delta T_{pt1} = \left[\theta_b\left(h_{pt1} - c\right) - \theta_b\left(h_{pt2} - c\right)\right]\frac{EA_{pt}}{L_{unb}} \tag{6.4a}$$

$$\Delta T_{pt2} = \left[\theta_b\left(h_{pt2} - c\right) - \theta_b\left(h_{pt1} - c\right)\right]\frac{EA_{pt}}{L_{unb}} \tag{6.4b}$$

where θ_b is the column rotation established as the design drift and h_{pt1} and h_{pt2} are the height of the tendon 1 and 2 respectively, c the neutral axis depth position, L_{unb} the length of the tendons without grout along the tendon profile, E and A_{pt} the modulus of elasticity and steel area of the tendons respectively.

Adopting a positive convention for moments (anti-clockwise direction), for a positive joint rotation (gap opening), The moment contribution in the left connection M_{left} and right connection M_{right} can be evaluated using equilibrium of the section and then taking moments from the neutral axis position:

$$M_{left} = \left(T_{pt1\,ini} + \Delta T_{pt1}\right)(h_{pt1} - c) + \left(T_{pt2\,ini} + \Delta T_{pt2}\right)(h_{pt2} - c) + T_s(h_s - c) \quad (6.5a)$$

$$M_{right} = \left(T_{pt1\,ini} + \Delta T_{pt1}\right)(h_{pt1} - c) + \left(T_{pt2\,ini} + \Delta T_{pt2}\right)(h_{pt2} - c) + T_s(h_s - c) \quad (6.5b)$$

From equation 6.5, the total moment contribution of the connection depend on the material contribution of the energy dissipaters ($T_s = f_s A_s$) and post-tension tendons (EA_{pt}) and the geometrical contribution determined by the location of the tendons in the section (h_{pt1} and h_{pt2}), the unbonded post-tensioned length (L_{unb}) and the initial post-tensioned forces ($T_{pt1\,ini}$ and $T_{pt2\,ini}$) which determine the initial moment contribution of the connection.

Figure 6.16 shows the moments and shears due to a right sway mechanism of a frame with non-tearing connections. As mention in the previous section, the post-tensioned moment contribution at the right connection ($M_{pt-right}$) will always be positive and greater or equal to zero.

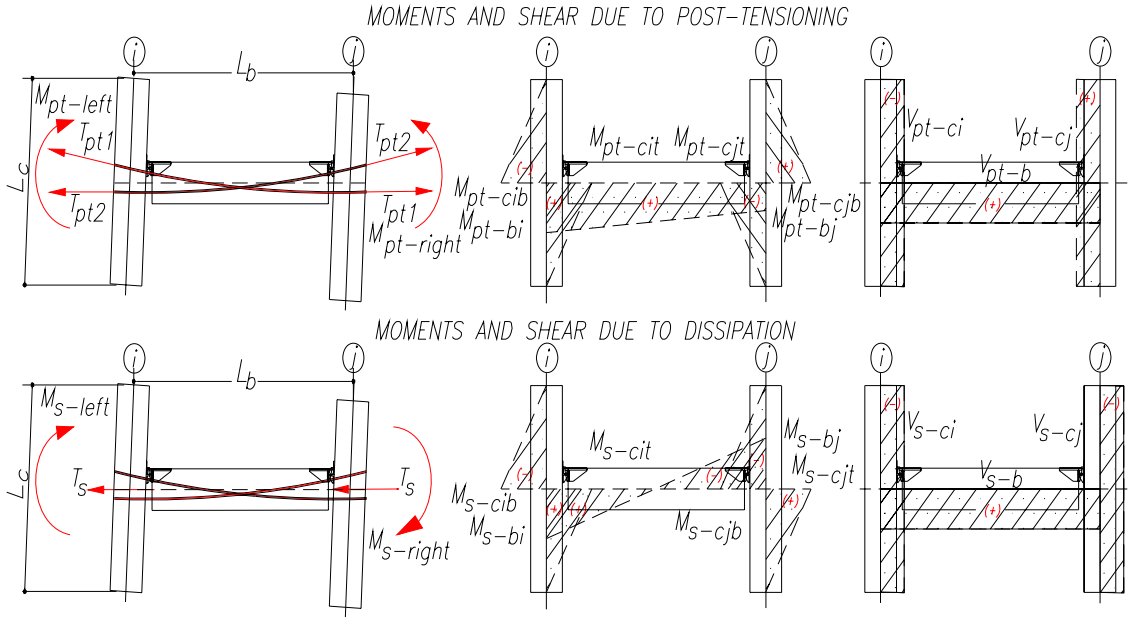

Figure 6.16. Moment and shear forces in a one bay H-Frame with non-tearing connection.

The total moment at the right connection M_{right} can be negative depending on the ratio $M_{pt-right}/M_s < 1$ which depends on the initial post-tensioned force, the location of the tendons along the beam depth, the unbonded length and the mild steel dissipation contribution. If this occurs, the column moments would have an inverse sign convention.

At rest (zero drift), the column moments are half of the beam moments which are the initial post-tensioned moments and the column shears (the gradient of the column moments) are self equilibrated

$$M_{cib} = M_{cit} = M_{pt\,ini} / 2 \tag{6.6a}$$

$$M_{cjb} = M_{cjt} = M_{pt\,ini} / 2 \tag{6.6b}$$

$$V_{ci} = V_{cj} = \frac{M_{pt\,ini}}{L_c / 2} \tag{6.6c}$$

$$V_b = \frac{(M_{pt\,ini} + M_{pt\,ini})}{L_b} \tag{6.6d}$$

Where M_{cib}, M_{cit}, M_{cjb}, M_{cjt}, V_{ci} and V_{cj} are the column moments and column shear at i and j axes respectively; V_b is the beam shear, $M_{pt\,ini}$ is the initial post-tensioned moment, L_c is the inter-storey height between point of contra flexure assumed to be at the mid-height of the columns and L_b the beam length.

As the gap opens at the i axis, the connection moment M_{left} increases while M_{right} decreases in the same proportion due to the asymmetry in the tendon profiles. The column moments changed according to the change in the post-tensioned moment ΔM_{pt} (due to the elongation or shortening of the post-tensioned tendon) and the moment contribution of the energy dissipation M_s can be calculated from Equations 6.4 and 6.5.

$$M_{cib} = -M_{left} / 2 = -(M_{pt\,ini} + \Delta M_{pt} + M_s) / 2 \tag{6.7a}$$

$$M_{cit} = M_{left} / 2 = (M_{pt\,ini} + \Delta M_{pt} + M_s) / 2 \tag{6.7b}$$

$$M_{cjb} = M_{right} / 2 = (M_{pt\,ini} - \Delta M_{pt} - M_s) / 2 \tag{6.7c}$$

$$M_{cjt} = -M_{right} / 2 = -(M_{pt\,ini} - \Delta M_{pt} - M_s) / 2 \tag{6.7d}$$

$$V_{ci} = \frac{M_{cib}}{L_c / 2} = \frac{-(M_{pt\,ini} + \Delta M_{pt} + M_s) / 2}{L_c / 2} \tag{6.7e}$$

$$V_{cj} = \frac{M_{cjb}}{L_c / 2} = \frac{(M_{pt\,ini} - \Delta M_{pt} - M_s) / 2}{L_c / 2} \tag{6.7f}$$

$$V_b = \frac{M_{left} - M_{right}}{L_b} = \frac{(M_{pt\,ini} + \Delta M_{pt} + M_s) - (M_{pt\,ini} - \Delta M_{pt} - M_s)}{L_b} \tag{6.7g}$$

Where M_{cib}, M_{cit}, M_{cjb}, M_{cjt}, V_{ci} and V_{cj} are the are the column moments and column shear at i and j axes respectively; V_b is the beam shear, $M_{pt\,ini}$ is the initial post-tensioned moment,

L_c is the inter-storey height between point of contra flexure assumed to be at mid-height of the columns, L_b is the beam length and ΔM_{pt} is the change in post-tensioned moment which can be calculated as $\Delta M_{pt} = \Delta T_{pt1}(h_{pt1} - c) + \Delta T_{pt2}(h_{pt2} - c)$ where ΔT_{pt1} and ΔT_{pt2} can be calculated from Equation 6.4.

Normally the column shear force V_{cj} at the j axis is positive because the initial moment ($M_{pt\,ini}$) which is based on the initial post-tensioned force is higher than the dissipation moment (M_s). This occurs when the ratio $(M_{pt\,ini} - \Delta M_{pt})/M_s > 1$. Conversely, the column shear V_{cj} at the j axis can become negative and more lateral shear contribution could be added to the frame. The total base shear can be calculated as the sum of the column shears as (6.7e) and (6.7f)

$$V_{base} = V_{ci} + V_{cj} = \frac{-2(\Delta M_{pt} + M_s)}{L_c} \tag{6.8}$$

The total base shear is directly proportional to the energy dissipation moment M_s and the change in moment due to the post-tensioned tendons ΔM_{pt}.

In addition to supplying adequate moment connection resistance, a beam with a top hinge connection is subjected to additional moments and shear forces in the beam member. Therefore, beam flexural detailing reinforcement must satisfy the code detailing requirements for an adequate ductility.

Secondary moments will occur as fixed end moments. Following the sign convention in which a moment is positive when it causes compression in the top beam fiber and negative when it causes compression in the bottom fiber. A flexural member is defined as a member in whom the axial load does not significantly contribute to the member's behaviour. Axial force is applied to the beams at the top hinge height. These forces induces a positive moment applied at the centreline of the beam element M_b^2 and shear force V_b^2 which all remain constant during sway of the frame. A criterion to neglect the compressive axial force is found to be less than one tenth of the gross section member and concrete strength $(A_g f_c^{'}/10)$.

$$M_b^2 = (T_{pt1} + T_{pt2})\, e \tag{6.9a}$$

$$V_b^2 = (2M_b^2 / L_b) \tag{6.9b}$$

Where e is the eccentricity between the geometric centre of the section (c.g.c) and the top hinge location.

6.5 STRUCTURAL BEHAVIOUR OF HYBRID H-FRAMES WITH MULTIPLE SPANS USING NON-TEARING CONNECTIONS

Four H-frames with multiple spans are shown in Figure 6.17. In the first case (Figure 6.17a) an anti-symmetric tendon profile is used and anchored inside the exterior columns. Assuming a frame with the same tendon profile, initial post-tensioning force (with no prestress losses) and bay length which was equal for all the spans, in an interior beam-column connection a elongation of the tendons is expected when the gap opens on the right side of the connection while in the left side of the connection, the gap closes and shorten of the tendons by the same amount; therefore, no change in the interior beam-column moment capacity will occur.

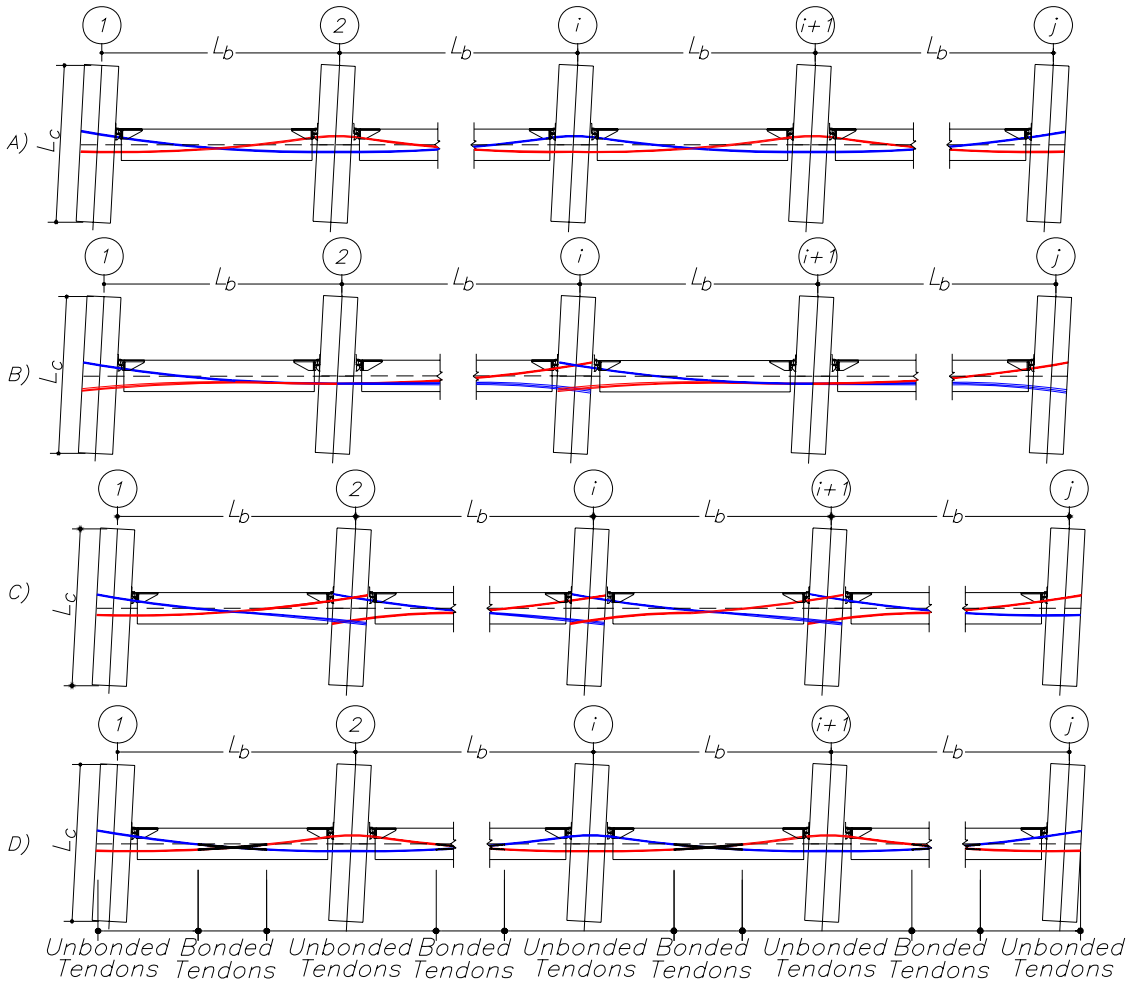

Figure 6.17. Different tendon profiles for an H-Frame with multiple bays using non-tearing connection.

The exterior beam-columns connections will increase and decrease their moment capacity when the gap opens and closes at the left and right column due to elongation and shorten in the tendon which produce increase and decrease in the tendon force respectively. These beam-column moment connections are small due to the high unbonded length of the tendons. The total base shear contribution will come from the moment contribution of the energy dissipaters in addition to the small contribution from the post-tensioned moments of the exterior columns.

A second case would consist of the unbonded tendons profiles being anti-symmetric and anchorage at the exterior columns and every two or three spans as shown in Figure 6.17b. Additional moment contribution in the interior columns where the tendons are anchored will occur due to the post-tensioning moments. These moments will be higher as the moments obtained from the previous solution (Figure 6.17a) due to a reduction in the unbonded length of the tendons. Therefore, in terms of the total response of the frame, an increase in the total base shear is evident when compared to the previous solution.

Figure 6.17c shows a third configuration where the tendons are anti-symmetric and anchored at every span. This solution seems to be uneconomical considering the cost associate with the construction and post-tensioning, however, in terms of the total response of the frame, an increase in the base shear would be observed due to the additional unbonded post-tensioned moment contribution coming from all interior columns as well for the to the exterior columns.

A fourth case consists on assume the same tendon profile (with no prestress losses and equal bay length for all the spans) as shown in Figure 6.17a where tendons are anchored at the exterior columns a more practical solution is to partially bond the post-tensioning tendons at mid-span of each bay (Figure 6.17d) instead of anchored at every single span as proposed in the third case (Figure 6.17c). The beam-column moment connections due to post-tensioning for interior columns at left and right side cancel out and no column shears for post-tensioning are obtained. Therefore, the total base shear contribution is coming from the change in the post-tensioned columns of the exterior columns and the moments coming from the energy dissipaters located at all the connections. The post-tensioned moment contribution over the total beam-column moment contribution depends on the unbonded length assumed for each span which is smaller than the bay length and therefore higher post-tensioned moments can be achieved in comparison with the first case Figure 6.17a

Multiple solutions can be obtained depending on a case by case application and Figure 6.17 presents only a few of them. The ideal solution would combine the use of post-tensioning and

energy dissipation to provide not only the require moment demand of the connection but also the global stiffness and strength.

Therefore, the solutions presented in Figure 6.17c and Figure 6.17d show a good local and global response; however, the latter solution would question the use of tendons in the interior spans if no extra benefit can be taken from them. Recent reseachers [6.3, 6.4] had been carried out using the benefits of the non-tearing connections without the use of un-bonded tendos with satisfactory results. However, the connection developed required cast-in-situ concrete to provide the moment resistant connection.

A parallel reseach [6.5] had developed a purely precast method of construction for non-tearing connection with the use of structural steel top hinge and column corbels to locate and support the beam during construction. Such solution is acceptable for short span where no post-tensioned is required to achive higher spans and where gravity loads are not dominant. However the use of drapped unbonded or partially bonded post-tensioned tendon solutions can be adopted for long spans and for both high gravity and seismic dominated frame systems.

An extension of the equations to calculate the column moments and shears for an H frame with multiple spans is presented as follows where an H-frame with unbonded post-tensioned tendons being anchored at each single span and partially bonded at the mid-span of each bay are shown in Figure 6.18 and Figure 6.19 respectively. Assuming no friction presstress losses in the tendon profiles, as the frame sways to the right, the gap opens at the right side of each axis and closes on the left side. The connection moment at the exterior column in axis 1 will increase due to an increment of the tendon elongation $M_{con-1l} = M_{pt-b1l} + M_{s-b1l}$, while for the axis j the left side of the connection will decrease in the same proportion $M_{con-jr} = M_{pt-bjr} - M_{s-bjr}$.

For the first solution (Figure 6.18), the interior column moments shows that the post-tensioned moments are opposite to each other but their magnitudes are different. Therefore a post-tensioned moment contribution is generated at the columns in addition to the energy dissipation contribution.

However, for the second solution (Figure 6.19), the interior column moments shows no change in the post-tensioning force, no additional moments are registered and no shears forces are generated. Therefore, the moments and shear forces in the interior columns are totally from the contribution of the energy dissipation.

For both solutions, the exterior columns moments are based on the equations (6.4) and (6.7) as follows

$$M_{c1b} = -M_{con-1l}/2 = -(M_{pt\,ini} + \Delta M_{pt} + M_s)/2 \quad (6.10a)$$

$$M_{c1t} = M_{con-1l}/2 = (M_{pt\,ini} + \Delta M_{pt} + M_s)/2 \quad (6.10b)$$

$$M_{cjb} = M_{con-jr}/2 = (M_{pt\,ini} - \Delta M_{pt} - M_s)/2 \quad (6.10c)$$

$$M_{cjt} = -M_{con-jr}/2 = -(M_{pt\,ini} - \Delta M_{pt} - M_s)/2 \quad (6.10d)$$

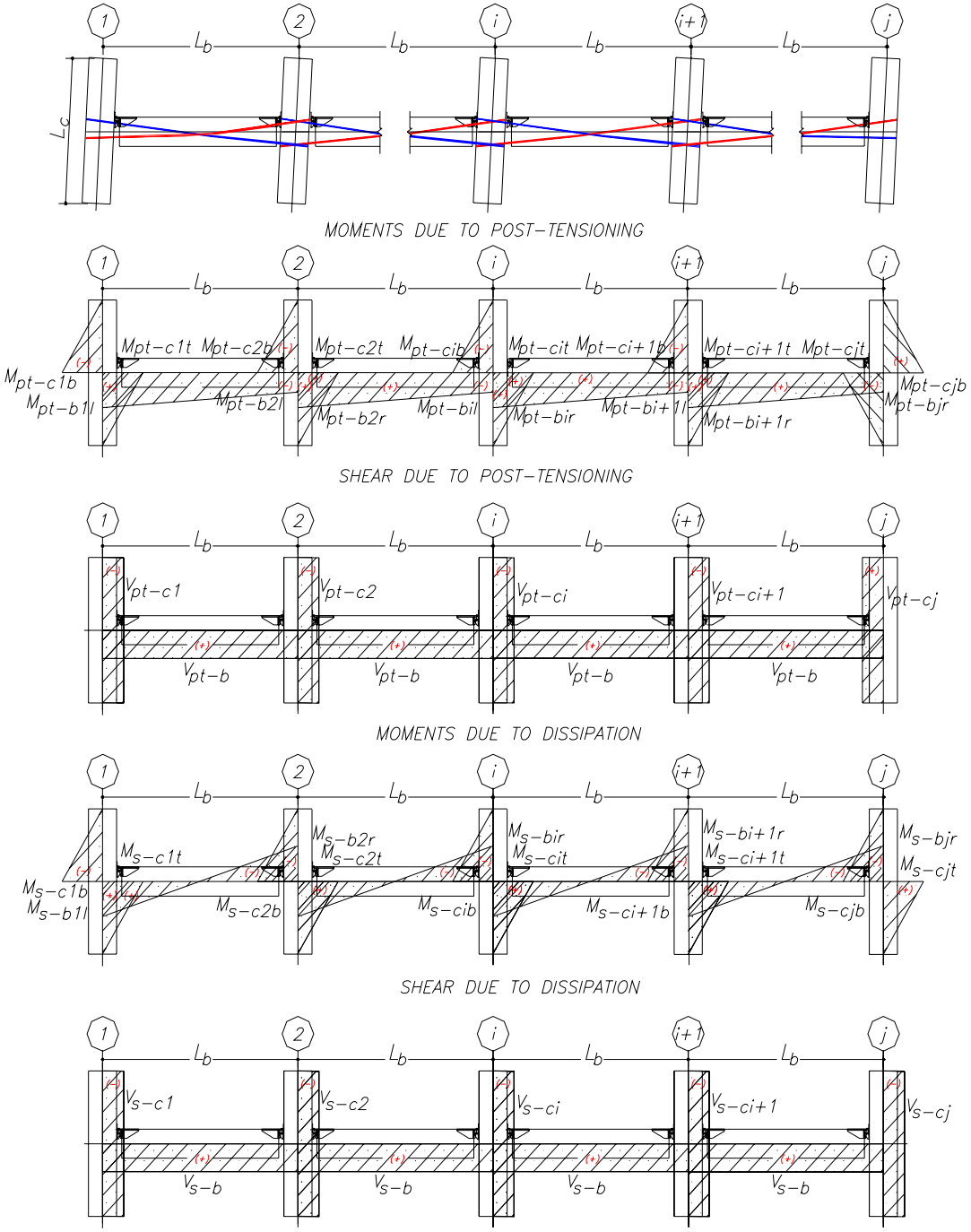

Figure 6.18. Moment and shear forces in a H-Frame with multiple bays using non-tearing connection with unbonded tendons anchored at each span.

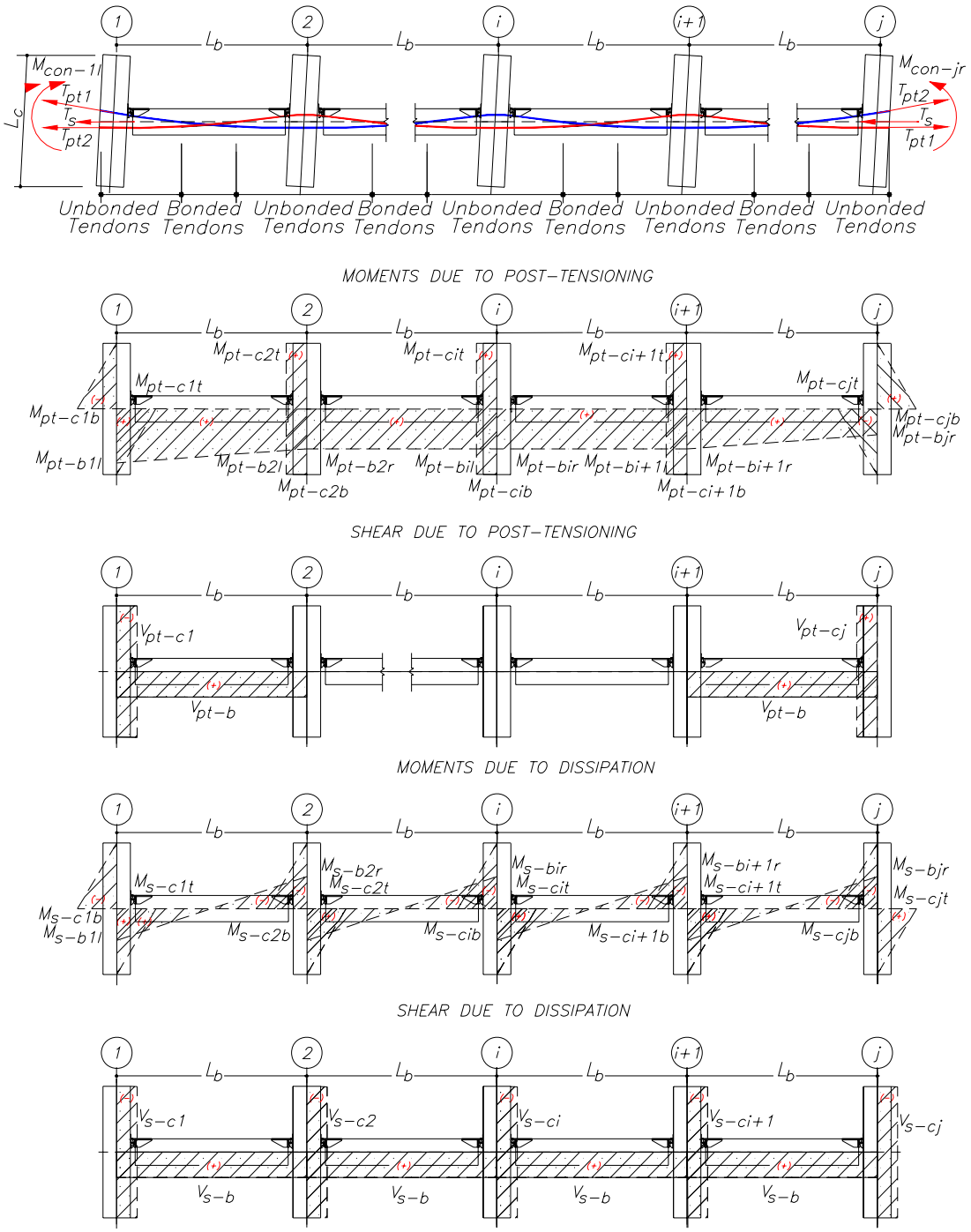

Figure 6.19. Moment and shear forces in a H-Frame with multiple bays using non-tearing connection with partially bonded tendons at mid- span.

The column shear therefore is the column moment divided by half the inter-storey height

$$V_{c1} = \frac{M_{c1b}}{L_c/2} = \frac{-(M_{pt\,ini} + \Delta M_{pt} + M_s)/2}{L_c/2} \qquad (6.10e)$$

$$V_{cj} = \frac{M_{cjb}}{L_c/2} = \frac{(M_{pt\,ini} - \Delta M_{pt} - M_s)/2}{L_c/2} \tag{6.10f}$$

$$V_{b1} = \frac{M_{con-1l} - M_{con-1r}}{L_b} = \frac{(M_{pt\,ini} + \Delta M_{pt} + M_s) - (M_{pt\,ini} - M_s)}{L_b} \tag{6.10g}$$

$$V_{bj} = \frac{M_{con-j-1r} - M_{con-jl}}{L_b} = \frac{(M_{pt\,ini} + M_s) - (M_{pt\,ini} - \Delta M_{pt} - M_s)}{L_b} \tag{6.10h}$$

Where M_{c1b}, M_{c1t}, M_{cjb}, M_{cjt}, V_{c1} and V_{cj} are the are the column moments and column shear at the 1 and j axes respectively; V_{b1} and V_{bj} are the beam shears for spans 1 and j, $M_{pt\,ini}$ is the initial post-tensioned moment, ΔM_{pt} is the change in post-tensioned moment, L_c is the inter-storey height between point of contra flexure assumed to be at mid-height of the columns and L_b is the beam length.

For interior columns, the column moments and shear forces can be obtained as an extension of equation (6.10). However, as mentioned before, different column moment distributions are obtained depending on the solution type. For the case where the tendons are anchored at each single span, the interior columns moments and shear forces depend on the change in the post-tensioned moment and the energy dissipation contribution as shown in equations (6.11)

$$M_{cib} = \left[(M_{pt\,ini} - \Delta M_{pt} - M_s) - (M_{pt\,ini} + \Delta M_{pt} + M_s)\right]/2 = -\Delta M_{pt} - M_s \tag{6.11a}$$

$$M_{cit} = \Delta M_{pt} + M_s \tag{6.11b}$$

$$V_{ci} = \frac{M_{cib}}{L_c/2} = \frac{-2(\Delta M_{pt} + M_s)}{L_c} \tag{6.11c}$$

$$V_{bi} = \frac{M_{b-i-1r} - M_{b-il}}{L_b} = \frac{2\Delta M_{pt} + 2M_s}{L_b} \tag{6.11d}$$

For the second solution where the tendons are partially bonded at mid-span, the interior columns moments depends only of the contribution of the energy dissipation contribution as shown in equation (6.12)

$$M_{cib} = \left[(M_{pt\,ini} - M_s) - (M_{pt\,ini} + M_s)\right]/2 = -M_s \tag{6.12a}$$

$$M_{cit} = M_s \tag{6.12b}$$

$$V_{ci} = \frac{M_{cib}}{L_c/2} = \frac{-2M_s}{L_c} \tag{6.12c}$$

$$V_{bi} = \frac{M_{b-i-1r} - M_{b-il}}{L_b} = \frac{(M_{pt\,ini} + M_s) - (M_{pt\,ini} - M_s)}{L_b} = \frac{2M_s}{L_b} \qquad (6.12d)$$

Similarly as explained before, the column shear force V_{cj} at the j axis is positive because the initial post-tensioned moment ($M_{pt\,ini}$) which is based on the initial post-tensioned force is higher than the dissipation moment (M_s). This occurred when the moment ratio $(M_{pt\,ini} - \Delta M_{pt})/M_s > 1$. Conversely, the column shear V_{cj} at the j axis can become negative and more lateral shear contribution could be added to the frame

The total base shear can be calculated as the sum of the column shears as (6.10e) (6.10f) and (6.11.c) or (6.12c). For the first solution where the tendons are anchored at each span the total base shear is shown in equation (6.13) where the total base shear is directly proportional to the sum of the energy dissipation moment M_s and the change in moments due to the post-tensioned tendons ΔM_{pt}.

$$V_{base} = V_{c1} + V_{cj} + \sum_{i=2}^{i=j-1} V_{ci} = \frac{-2}{L_c}\left[\sum_{i=1}^{i=j-1} \Delta M_{pt\,i} + M_{si}\right] \qquad (6.13)$$

While for the second solution, the total base shear shown in equation (6.14) is directly proportional to the contribution the change in moment due to post-tensioned tendons ΔM_{pt} generated in the exterior column and the sum of all energy dissipation moment M_s

$$V_{base} = V_{c1} + V_{cj} + \sum_{i=2}^{i=j-1} V_{ci} = \frac{-2}{L_c}\left[\Delta M_{pt} + \sum_{i=1}^{i=j-1} M_{si}\right] \qquad (6.14)$$

6.6 COMPARISON BETWEEN H-FRAMES USING HYBRID PRESSS AND NON-TEARING CONNECTIONS

As explained in Chapter 4 Section 4.7, in a traditional hybrid PRESSS frame connection, the initial stiffness depends on the contribution of the post-tensioning and the energy dissipation.

Depending on the moment contribution ratio between self-centering and dissipating contribution (typically referred to as λ) governs the so-called "flag-shaped" hysteresis behaviour, a wide range of hybrid solutions as presented in Chapter 2 and Chapter 3 can be obtained varying from Non linear elastic systems (NLE) to Tension-Compression Yielding Systems (TCY) [6.6].

In the NLE system, the unbonded post-tensioned tendons will provide all the moment capacity of the connection with the characteristic of being full re-centering capability which can be achieved with or without additional axial load. For the TCY systems the hysteresis behaviour is similar to an equivalent "emulative" monolithic connection.

The Appendix B of the New Zealand Standard 3101:2006 [6.7], states that the full self-centering of a general jointed connection shall be achieved by selecting in the design phase, an appropriate moment contribution ratio λ as the ratio between the restoring forces and the dissipation forces $\lambda = \left(M_{pt} + M_N / M_s\right) \geq \alpha_o$ where M_{pt}, M_N and M_s are the flexural strength contributions of the post-tensioned tendons, the axial load where present, and the non-prestressed steel reinforcement respectively. The Value α_0 is the overstrength factor for the non-prestressed steel reinforcement or the energy dissipating devices and is defined as $\alpha_0 \geq 1.15$.

In contrast a relatively low initial stiffness can be identified in the frame with non tearing connections when it is compared to more traditional systems such as hybrid PRESSS type connection or equivalent monolithic solutions. This low initial stiffness could assist the structure using non-tearing connections to undergo higher lateral displacements (more flexible) until the desired lateral resistance is achieved. Push over analysis and time history analysis will be carried out to examine the response of hybrid frame systems using non-tearing connections.

Improvements in the lateral stiffness can be obtained by using an equivalent amount of steel reinforcement from the monolithic connection in the energy dissipaters and/or locating the dissipaters at the bottom face and therefore higher mild steel moment contribution will be obtained. Additionally, Chapter 5 showed the results obtained using the use of a rubber pad working only in compression located at the gap of the connection which can be sufficient to increase the stiffness when the gap closes. It is require in the design that the rubber compression forces will not surpass the forces in the monohinge.

In the Hybrid Non-tearing connection, the energy dissipated under the curve, and the point at which the unloading curve rejoins the loading curve, does not go to zero due to the low stiffness of the post-tensioning compared with the high stiffness of the dissipaters and re-centering can not be achieved at the connection. In any case, if re-centering is requiring by design, column rocking base with self weight and/or additional post-tensioning at the column base can provide some or full re-centering of the structure.

6.7 PARAMETRIC ANALYSIS OF HYBRID H-FRAMES WITH NON-TEARING CONNECTIONS

A parametric analysis was carried out in Section 6.3 for a series of beam column joints with non-tearing connection. In this section, a parametric study to determine the characteristics of different H-frames using non tearing connection is presented. Two types of H-frames are considered from the previous section. The first case uses a draped tendon solution anchored at each span while second proposed the use of partially bonded tendons at mid-span.

These parameters consist of three beam sections (h_b), with different bay lengths (L_b) and number of bays (n_b), the initial post-tensioned force as a percentage of the ultimate post-tensioned force ($T_{pt\,ini}/T_{ult}$), the steel area content A_{pt}/A_s and for the second solution the changing the unbonded length of the post-tensioned tendons ratio (L_{unb}/L_b) was investigated. A summary of the parameters is presented in Table 6.1

6.7.1 Initial post-tensioned force ratio ($T_{pt\,ini}/T_{ult}$).

Changing the ratio of initial post-tensioned force as a percentage of the ultimate force indicated that there is no change in the total base shear of the frame system, however the internal shear forces and bending moments in the columns change.

The change in the post-tensioned moment (ΔM_{pt}) is the difference of the initial post-tensioned moment and the increase or decrease in moment due to elongation or shorten of the tendon due to the gap opening or closing. Therefore, as the initial post-tensioned moment increases, the additional moment due to the elongation of the tendon increases, but the change in the post-tensioned moment remains the same, meaning that the change of the initial post-tensioned force does not have any effect on the total lateral response of the frames.

6.7.2 Beam section (h_b) and bay length (L_b).

Three beam sections (h_b) with different location of post-tensioned tendons ratio (h_{pt2}/h_b) were evaluated for each bay length (L_b) with different unbonded length ratios (L_{unb}/L) and initial post-tensioned force ratios ($T_{pt\,ini}/T_{ult}$).

Figures 6.20 to 6.22 show the normalized base shear ($V_b / V_{b\ at\ Apt/As=0}$) vs displacement for one-bay H-frame with three beam sections using both solutions (i.e First solution is a frame which uses fully unbonded tendons anchored at each span and second solution is a frame with partially bonded tendons at mid-span and anchored at exterior columns). For the second solution will show different unbonded length ratios (L_{unb} / L_b). The normalized base shear ($V_b / V_{b\ at\ Apt/As=0}$) is the base shear with respect to the base shear obtained from a fully elasto-plastic system with no post-tensioning (i.e. A_{pt} / A_s =0).

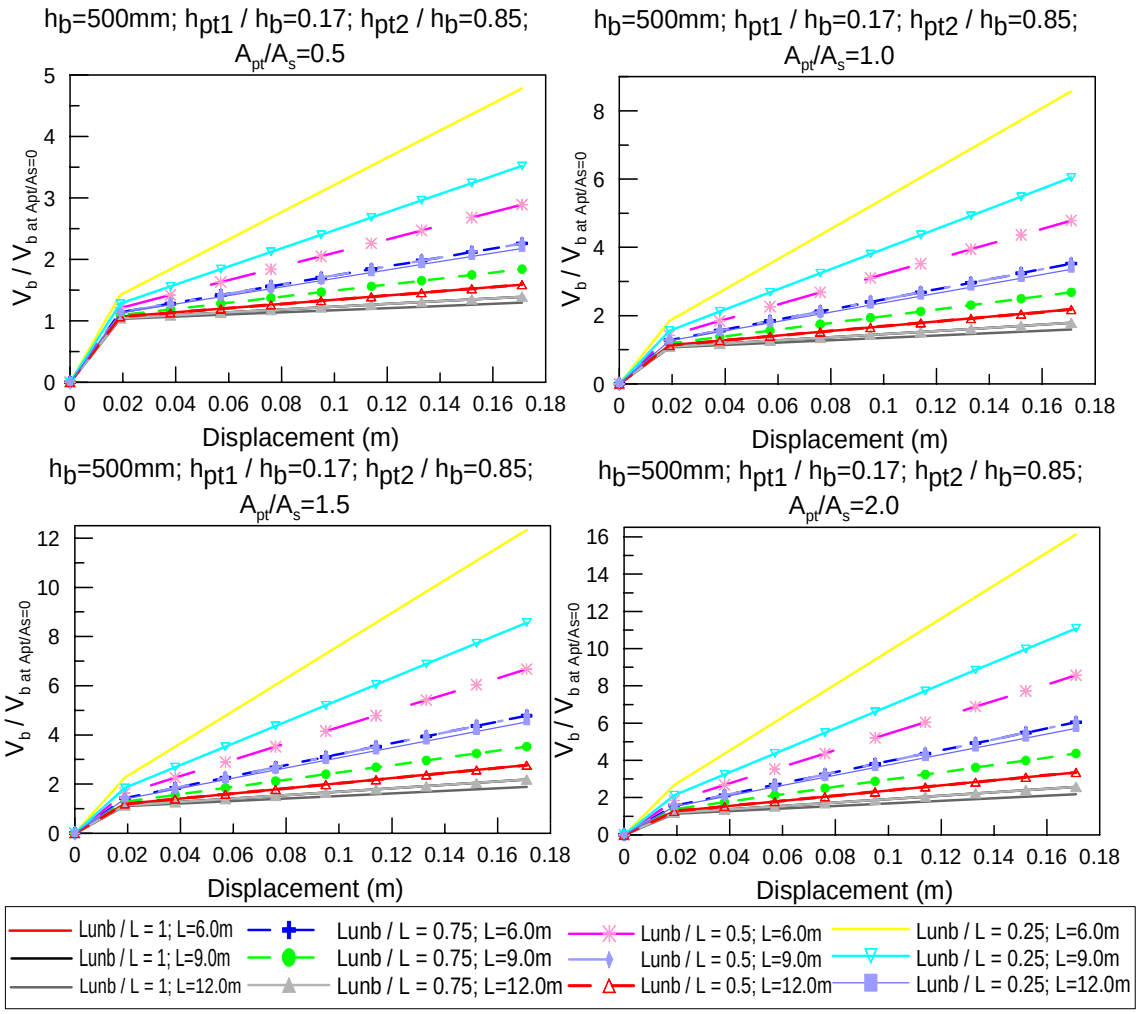

Figure 6.20. Normalized base shear (V_b / $V_{b\ atApt/As=0}$) vs displacement for h_b=500 varying bay length, the unbonded length and steel area content.

The variation between different beam sections (h_b) indicates that as the beam section increases, the base shear also increases due to the increase in the lever arm in the post-tensioned moments and mild steel dissipaters with respect to the top hinge.

However, increasing the bay length (L_b) from 6m to 12m, keeping constant the area content ratio (A_{pt} / A_s), the bay length (h_b) and the unbonded post-tensioned length ratio (L_{unb} / L_b) the normalized base shear decreases. This result indicates that frames with non-tearing connection present higher lateral response for short bay lengths.

6.7.3 Steel area content ratio (A_{pt} / A_s).

Three different bay lengths were investigated (L_b =6.0m, 9.0m and 12.0m) for three different beam sections (h_b =500mm, 700mm and 900mm). Figures 6.20 to 6.22 shows the normalized base shear with respect to the base shear obtained from a fully elasto-plastic system with no post-tensioning (i.e. A_{pt} / A_s =0).

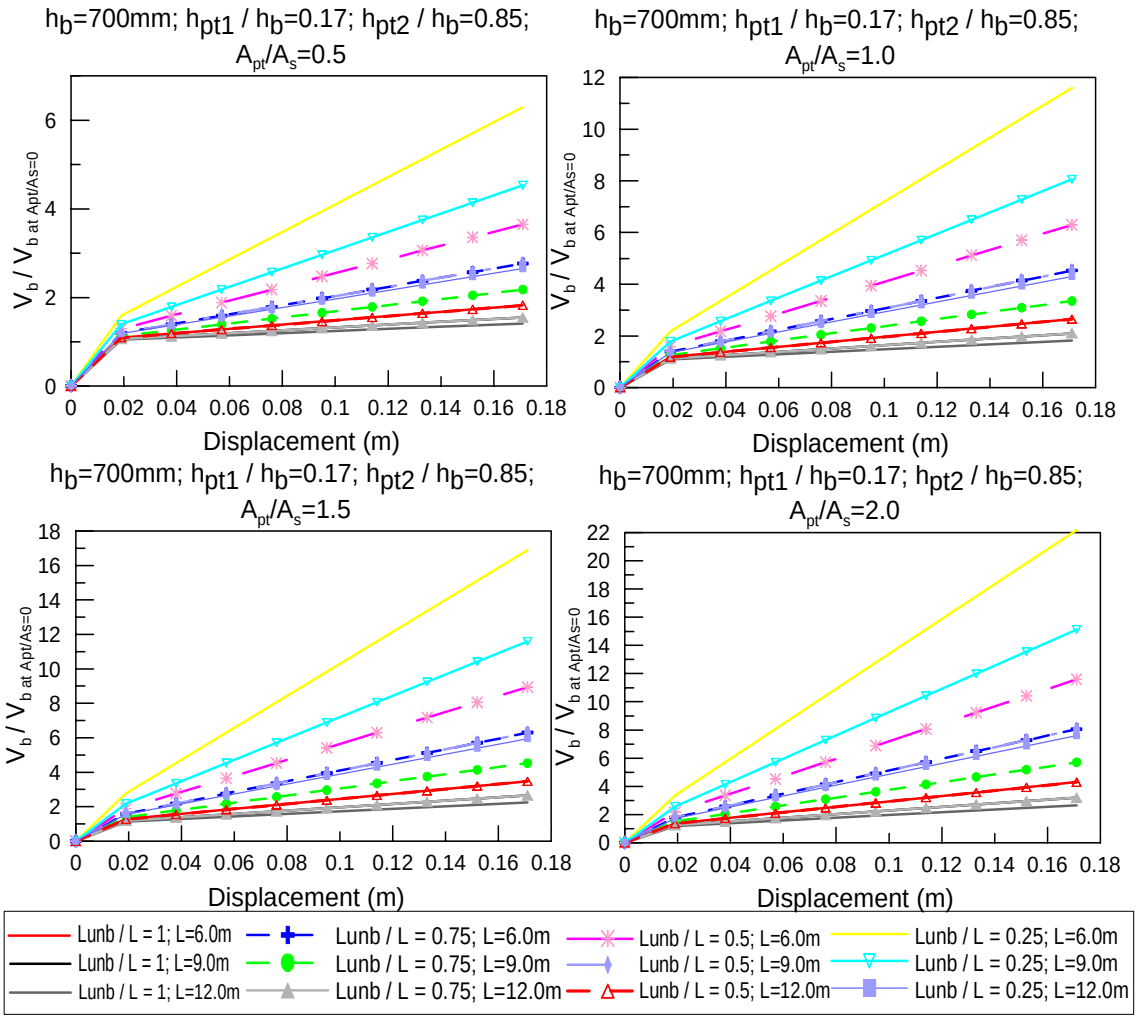

Figure 6.21. Normalized base shear (V_b / $V_{b\ atApt/As=0}$) vs displacement for h_b=700 varying bay length, the unbonded length and steel area content.

It can be seen that for an increase in the steel area content (A_{pt} / A_s =0.5 to 2.0) and keeping constant both the unbonded-post-tensioned length ratio (L_{unb} / L_b) and the beam section (h_b), the base shear increases due to higher moment capacity coming from the post-tensioned moments.

In terms of stiffness, as discuss previously, the initial stiffness depends basically on the mild steel dissipaters and a small contribution from the post-tensioning. As the steel area content increases A_{pt} / A_s and keeping constant the unbonded length ratio (L_{unb} / L_b), the bay length (L_b) and the beam section (h_b), a very small increase in the initial stiffness is observed up to yield of the dissipaters. As the unbonded length decrease from L_{unb} / L_b =1 (fully unbonded) to L_{unb} / L_b =0 (fully bonded), the initial stiffness increases due to the contribution of the post-tensioned tendons.

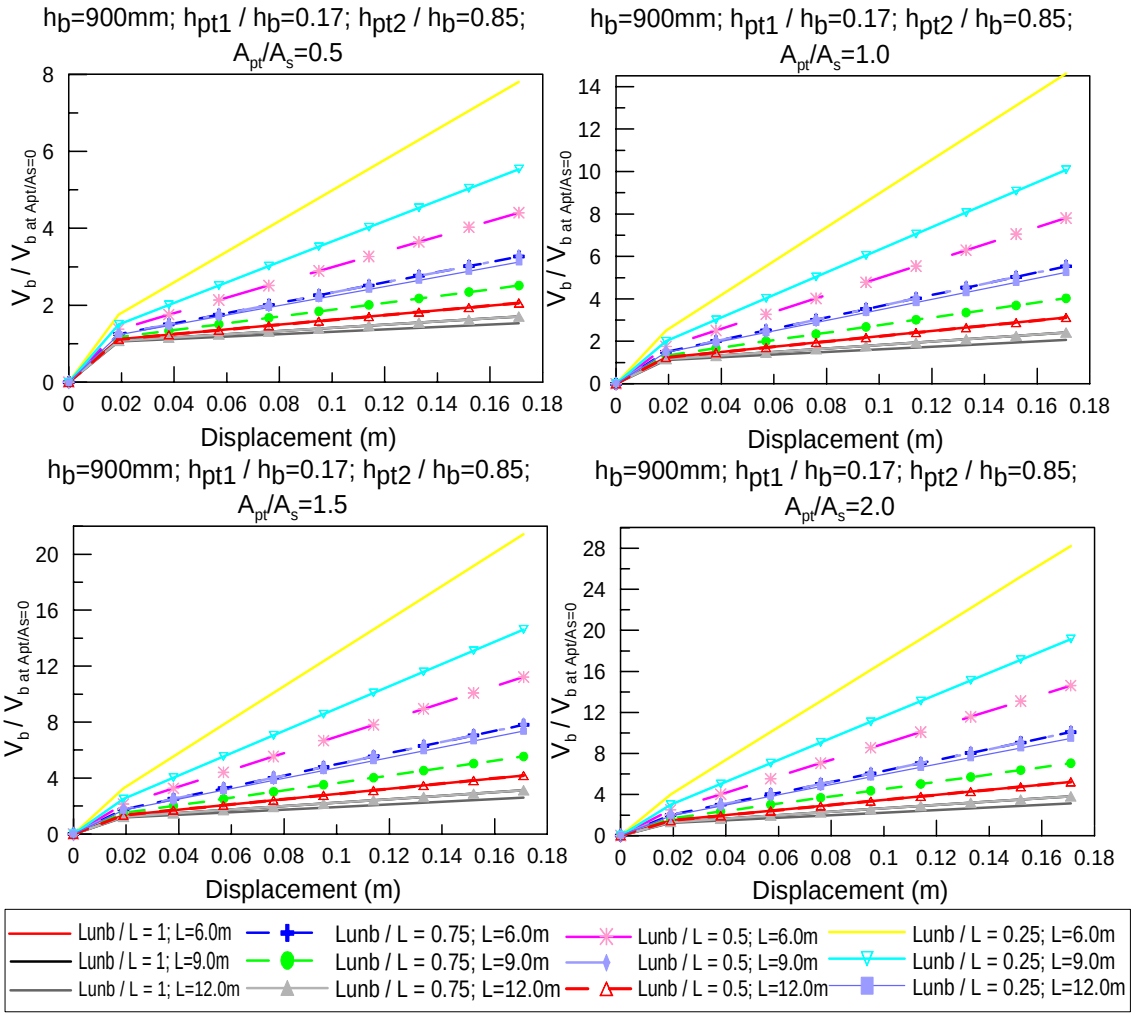

Figure 6.22. Normalized base shear (V_b / $V_{b\ atApt/As=0}$) vs displacement for h_b=900 varying bay length, the unbonded length and steel area content.

6.7.4 Unbonded post-tensioned length ratio (L_{unb} / L_b).

It was identified in Section 6.3 that as the unbonded length decreased from fully unbonded to fully bonded, that a larger contribution from the post-tensioning was present in the response of the connection in addition to a higher lateral response of the frames.

For a one-bay H-frame using the second solution (e.g. partially bonded tendons at mid-span) of a given bay length (L_b) and steel content ratio A_{pt} / A_s, as the L_{unb} / L_b decreases from fully unbonded $L_{unb} / L = 1$ to full bonded $L_{unb} / L = 0$, Figures 6.10 to 6.22 indicates that the total base shear increases. As mentioned in the previous section, these results indicate that higher beam shear can be obtained by reducing the unbonded length by one quarter of the total length.

6.7.5 Number of bays (n_b)

From Equation (6.13) the total base shear of the system where the tendons are anchored in each bay is directly proportional to the sum of all energy dissipation moment M_s and the change in moments due to the post-tensioned tendons ΔM_{pt} generated at the exterior and interior columns while for the second solution, the total base shear shown in equation (6.14) is directly proportional to the contribution of the change in moment due to post-tensioned tendons ΔM_{pt} generated in the exterior columns and the sum of all energy dissipation moment M_s.

Parametric analyses were carried out for three different beam sections (h_b), changing the bay lengths (L_b), the unbonded-post-tensioned length ratio (L_{unb} / L_b) for the second H-frame solution and the area content (A_{pt} / A_s) for different frames with a different number of bays ranging from n_b =1 to 5. Figures 6.23 to 6.34 show the normalized base shear ($V_b / V_{b\ at\ Apt/As=0}$) vs displacement for three beam sections with different unbonded length ratios (L_{unb} / L_b) and bay lengths (L_b). The normalized base shear ($V_b / V_{b\ at\ Apt/As=0}$) is the base shear with respect to the base shear obtained from a fully elasto-plastic system with no post-tensioning (i.e. A_{pt} / A_s =0).

Note that the shear of the frame considering fully elasto-plastic system $V_{b\ at\ Apt/As=0}$ increased as the number of bays increased. For the first H-frame solution where the post-tensioned tendons are anchored to each bay, it can be seen that $V_b / V_{b\ at\ Apt/As=0}$ remains constant as n_b increases. However, for the second H-frame solution, it can be seen that $V_b / V_{b\ at\ Apt/As=0}$ is reducing as n_b increases because of the increase in $V_{b\ at\ Apt/As=0}$. This result indicates that although the total base shear increases as the number of bays (n_b) increases, the shear contribution due to the change in the post-tensioned tendons in the exterior columns is becoming negligible and therefore, this solution is not particularly optimum in terms of lateral response.

Similarly as explained in the previous section for one-bay H-frames, it can be seen that for constant h_b, L_b and A_{pt} / A_s, changing L_{unb} / L_b from fully unbonded (L_{unb} / L_b =1) to fully bonded (L_{unb} / L_b =0) the base shear increases as the unbonded length reduces from fully unbonded to fully bonded. Similar results are observed keeping constant L_{unb} / L_b and changing A_{pt} / A_s.

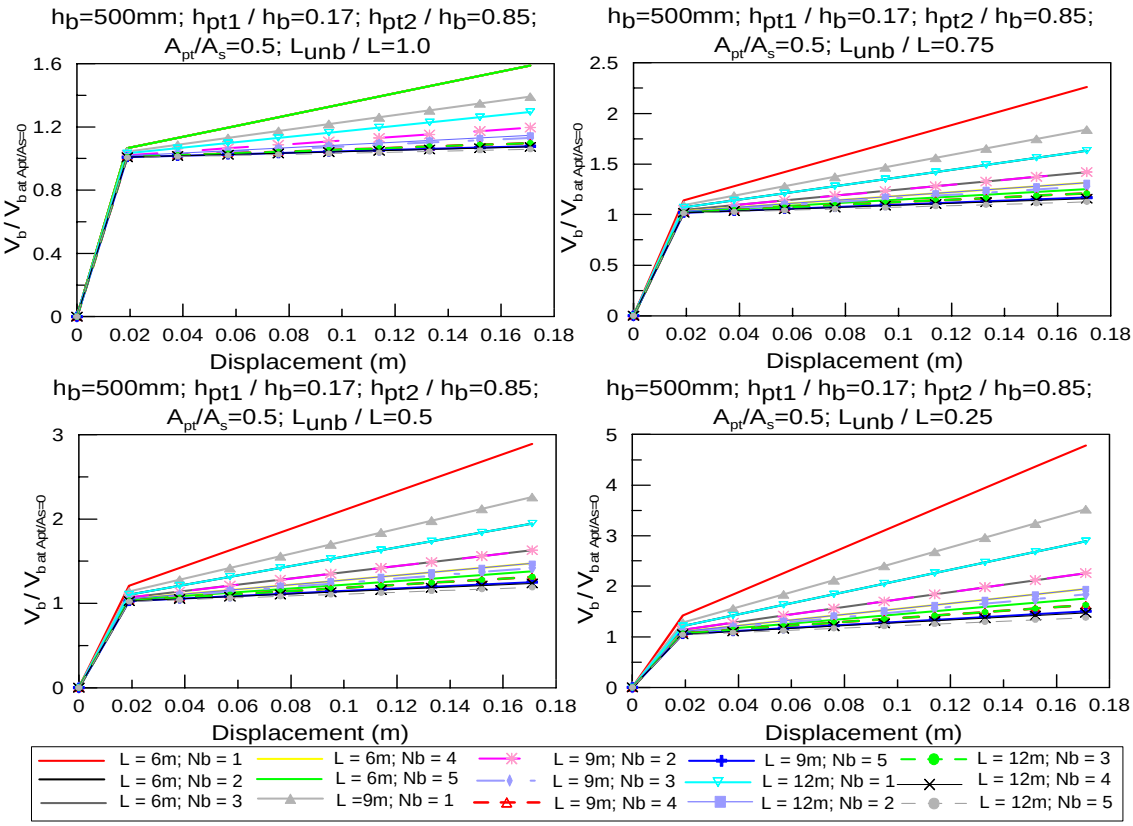

Figure 6.23. Normalized base shear (V_b / $V_{b\ atApt/As=0}$) vs displacement for h_b=500 and A_{pt}/A_s=0.5 varying the number of bays, the bay length and the unbonded length.

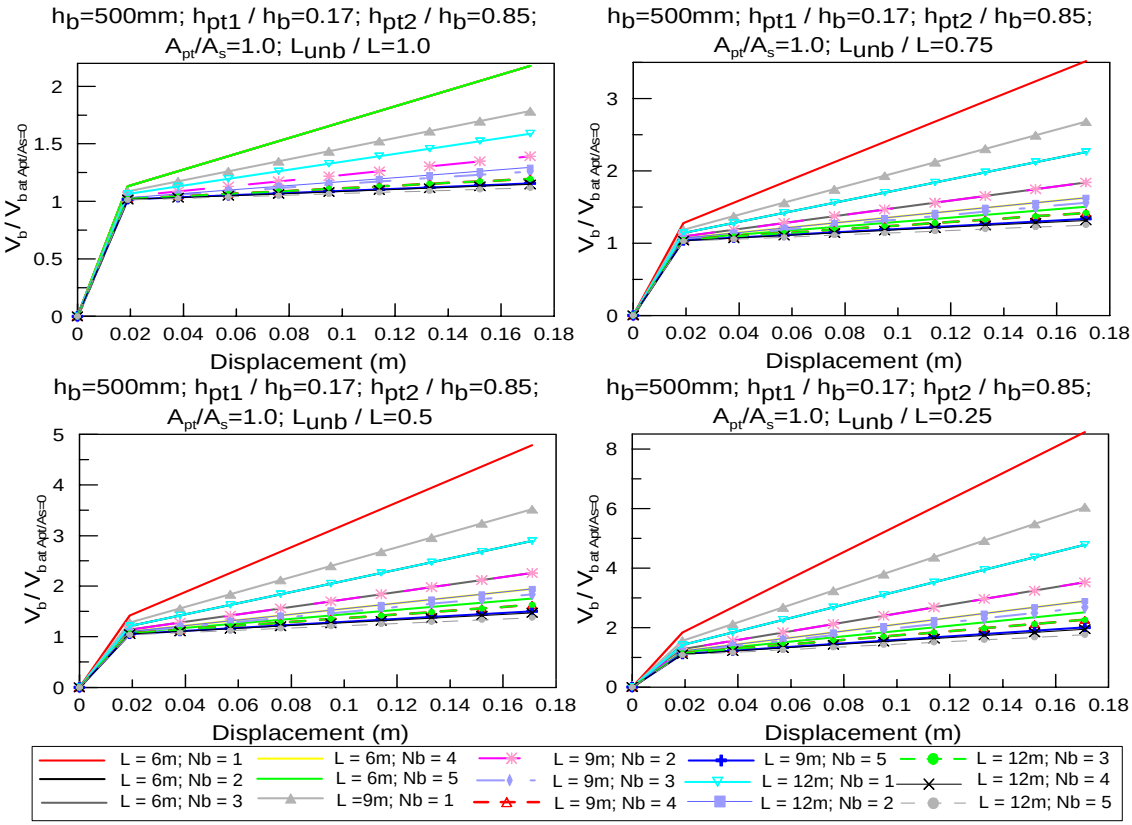

Figure 6.24. Normalized base shear (V_b / $V_{b\ atApt/As=0}$) vs displacement for h_b=500 and A_{pt}/A_s=1.0 varying the number of bays, the bay length and the unbonded length.

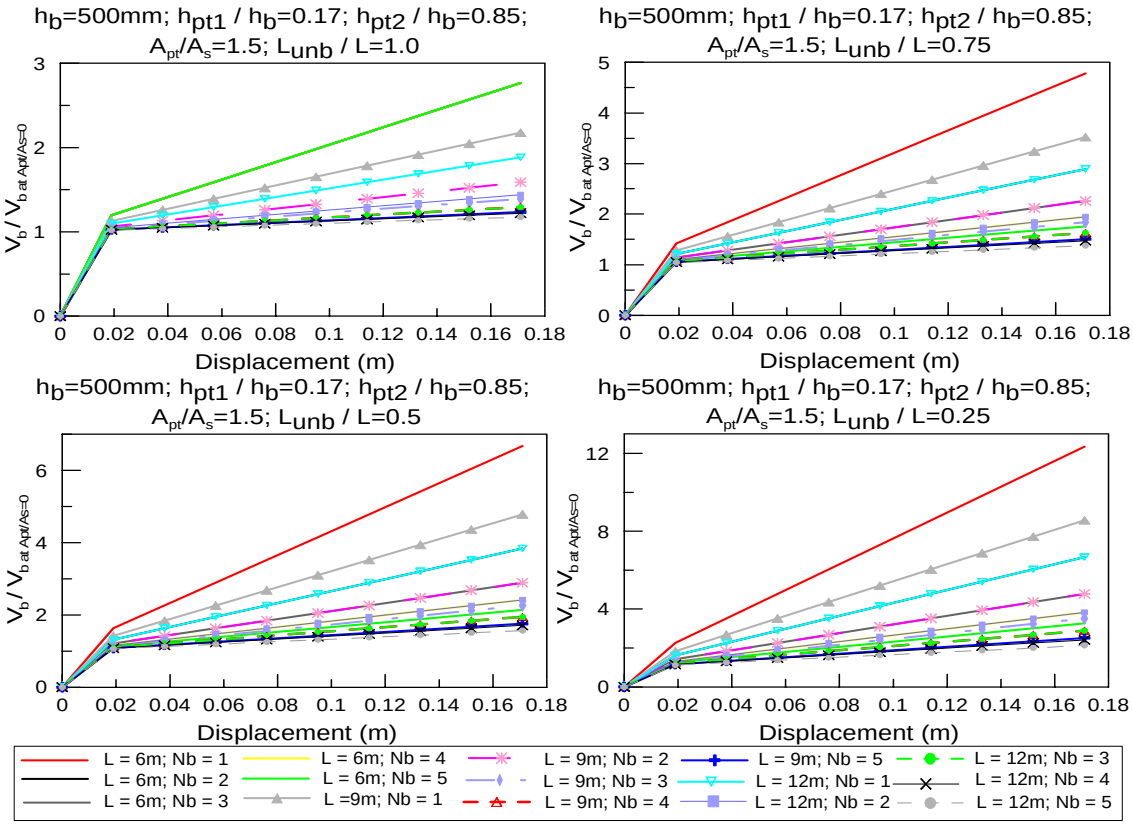

Figure 6.25. Normalized base shear (V_b / $V_{b\ atApt/As=0}$) vs displacement for h_b=500 and A_{pt}/A_s=1.5 varying the number of bays, the bay length and the unbonded length.

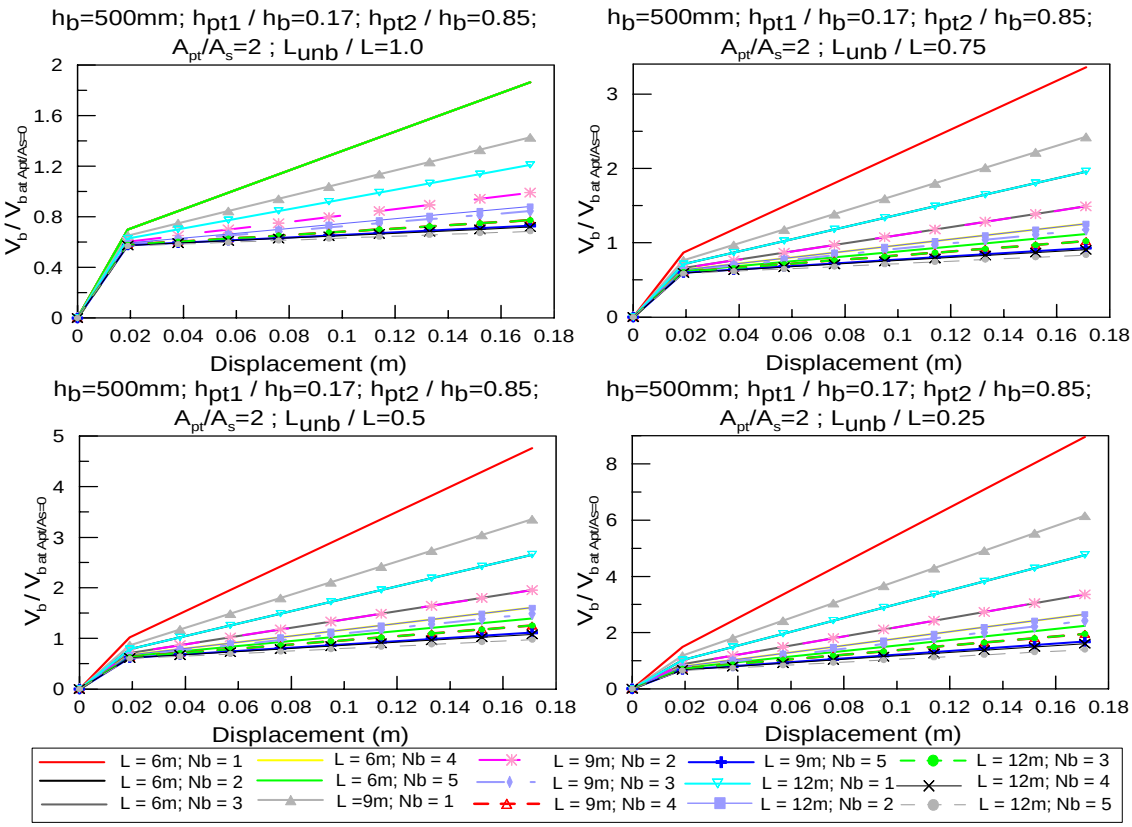

Figure 6.26. Normalized base shear (V_b / $V_{b\ atApt/As=0}$) vs displacement for h_b=500 and A_{pt}/A_s=2.0 varying the number of bays, the bay length and the unbonded length.

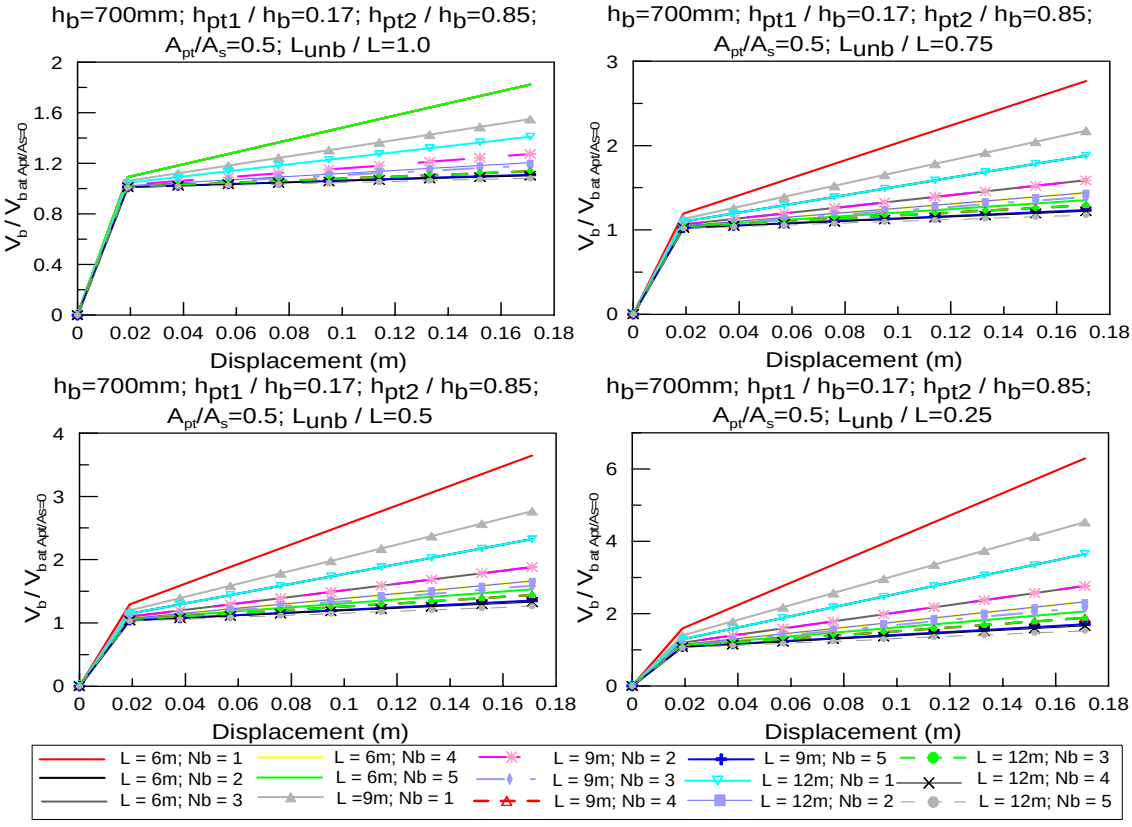

Figure 6.27. Normalized base shear (V_b / $V_{b\ atApt/As=0}$) vs displacement for h_b=700 and A_{pt}/A_s=0.5 varying the number of bays, the bay length and the unbonded length.

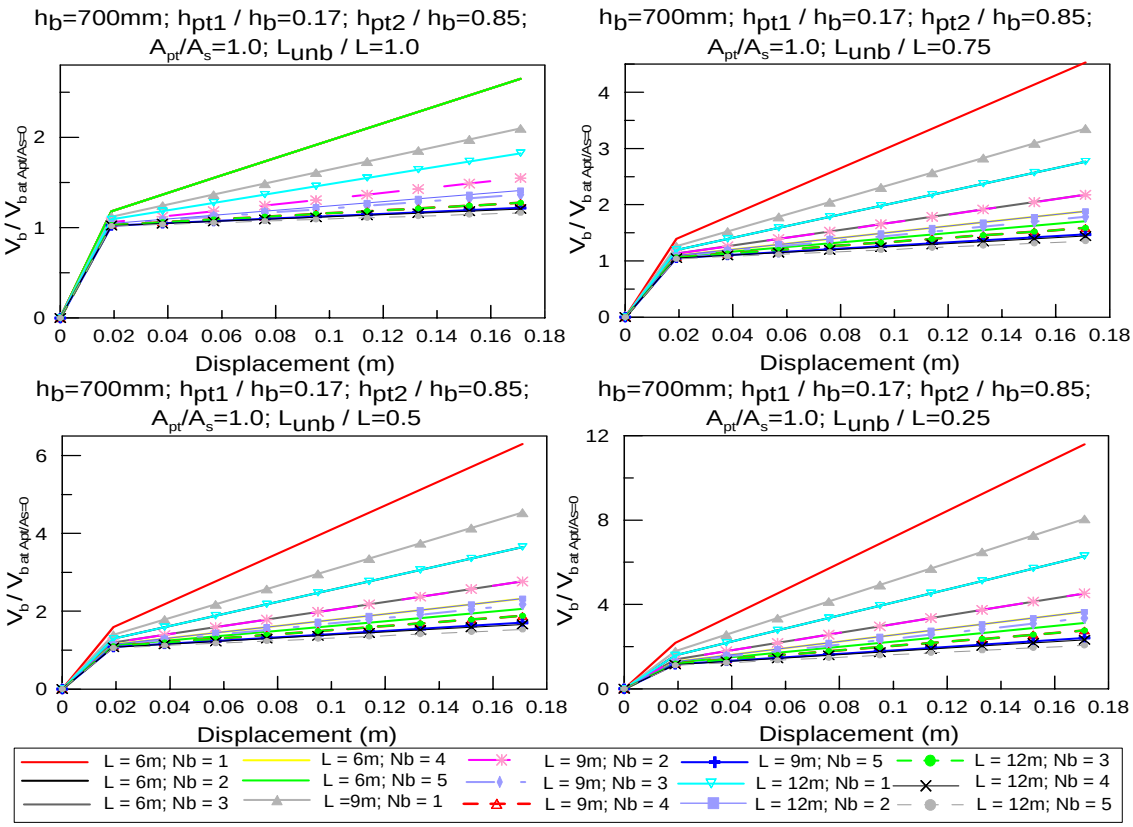

Figure 6.28. Normalized base shear (V_b / $V_{b\ atApt/As=0}$) vs displacement for h_b=700 and A_{pt}/A_s=1.0 varying the number of bays, the bay length and the unbonded length.

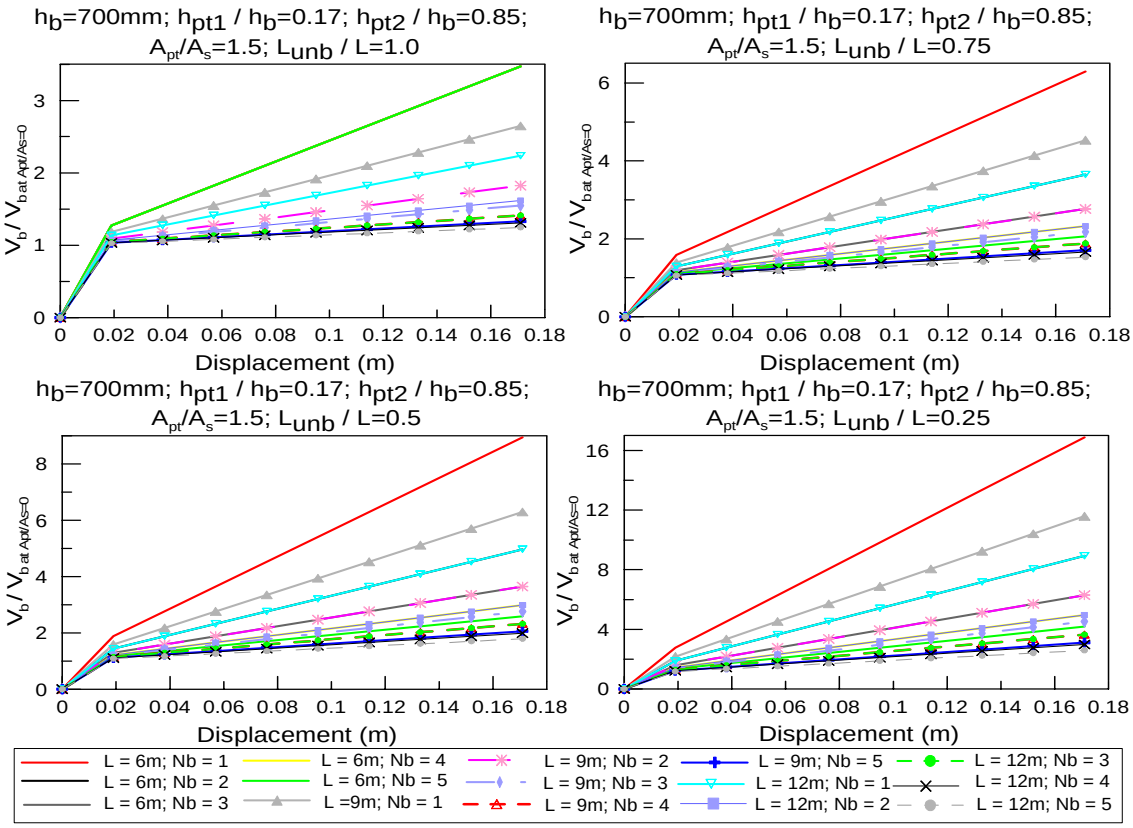

Figure 6.29. Normalized base shear (V_b / $V_{b\ atApt/As=0}$) vs displacement for h_b=700 and A_{pt}/A_s=1.5 varying the number of bays, the bay length and the unbonded length.

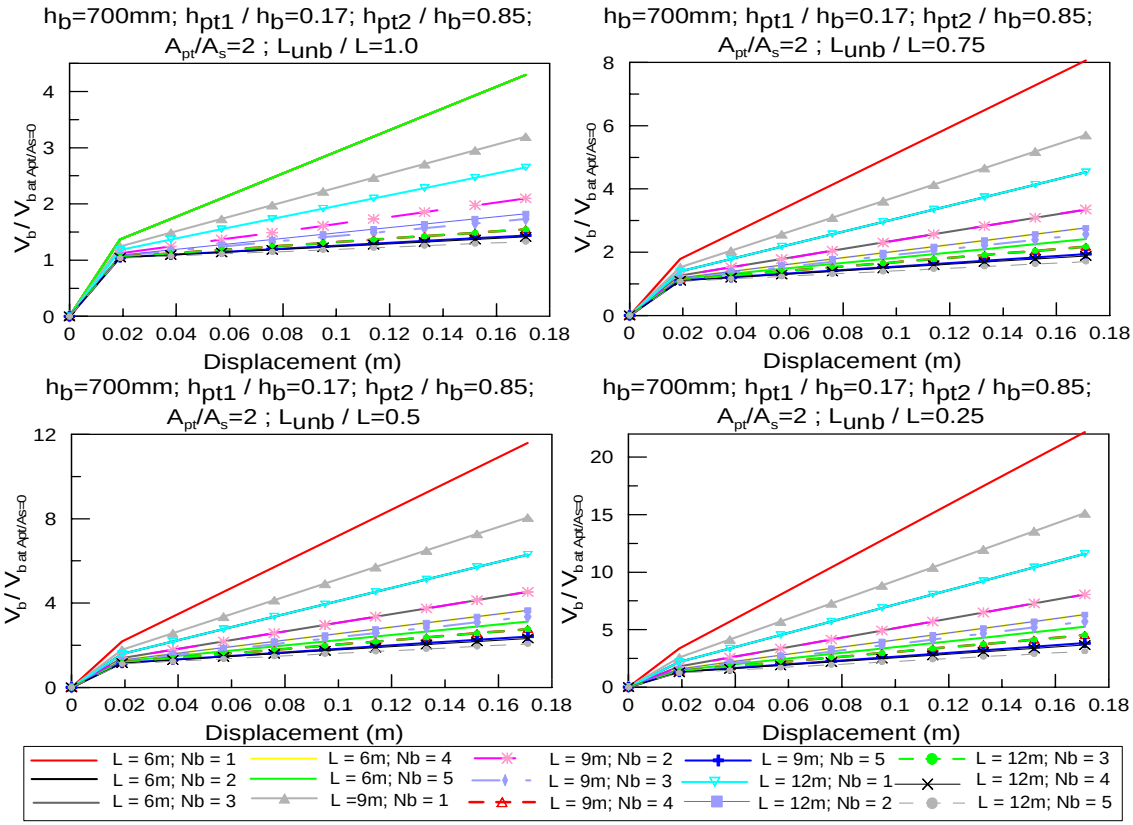

Figure 6.30. Normalized base shear (V_b / $V_{b\ atApt/As=0}$) vs displacement for h_b=700 and A_{pt}/A_s=2.0 varying the number of bays, the bay length and the unbonded length.

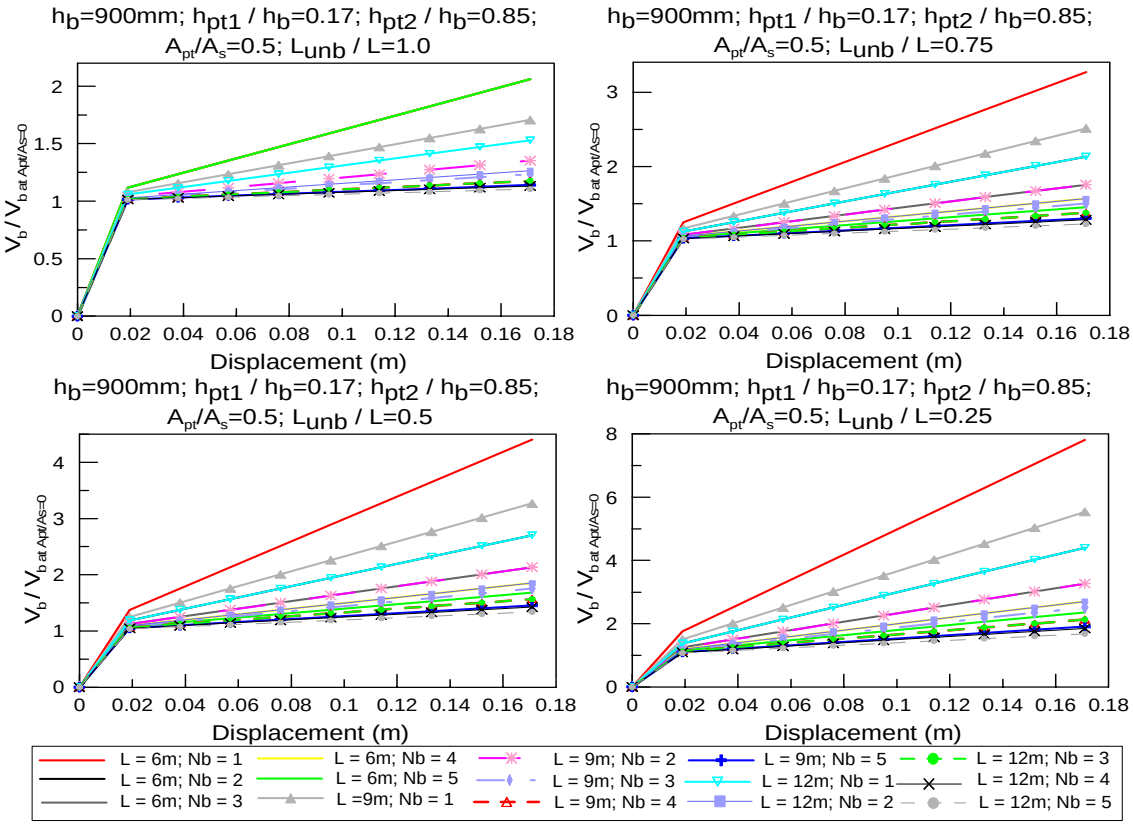

Figure 6.31. Normalized base shear (V_b / $V_{b\ atApt/As=0}$) vs displacement for h_b=900 and A_{pt}/A_s=0.5 varying the number of bays, the bay length and the unbonded length.

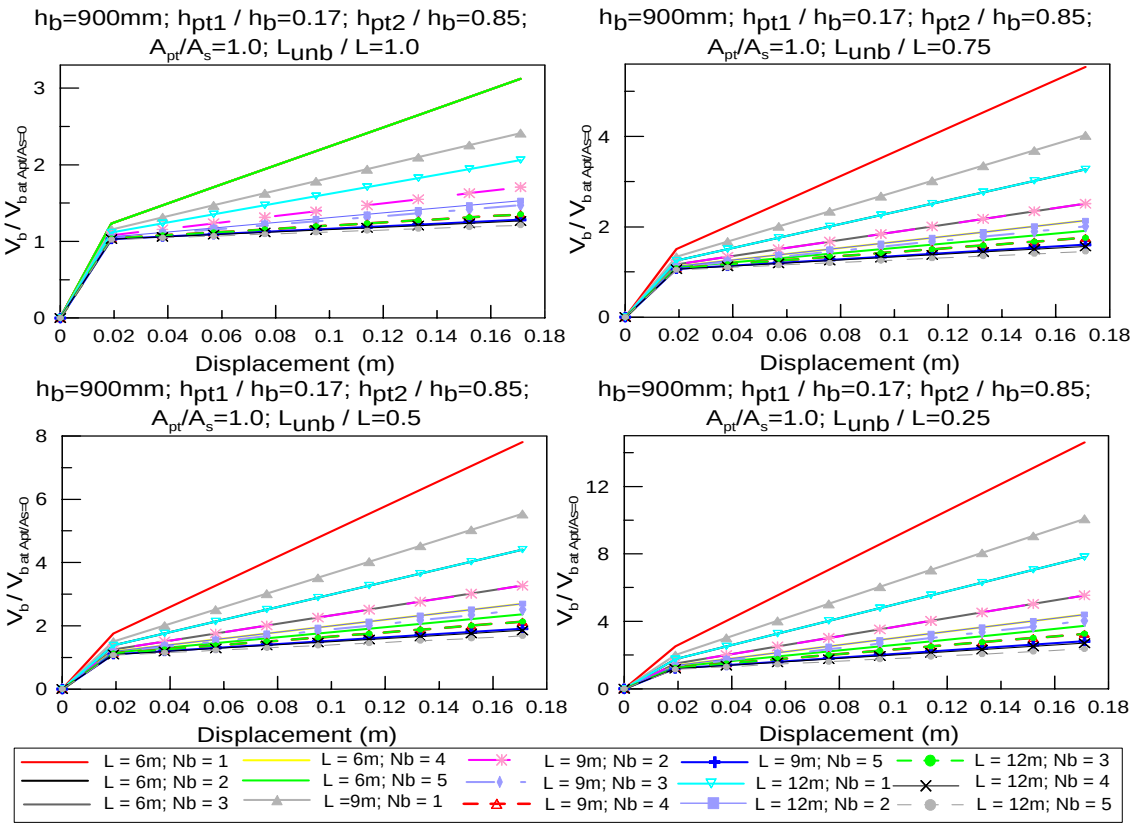

Figure 6.32. Normalized base shear (V_b / $V_{b\ atApt/As=0}$) vs displacement for h_b=900 and A_{pt}/A_s=1.0 varying the number of bays, the bay length and the unbonded length.

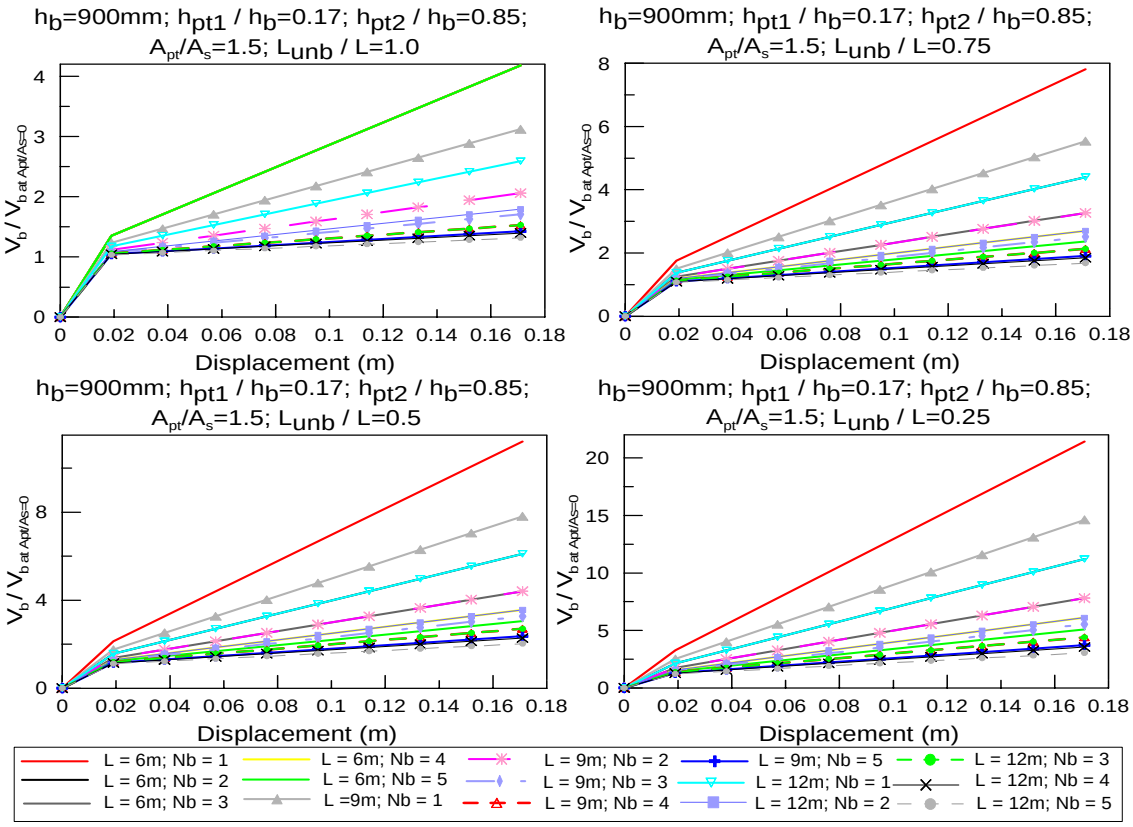

Figure 6.33. Normalized base shear (V_b / $V_{b\ atApt/As=0}$) vs displacement for h_b=900 and A_{pt}/A_s=1.5 varying the number of bays, the bay length and the unbonded length.

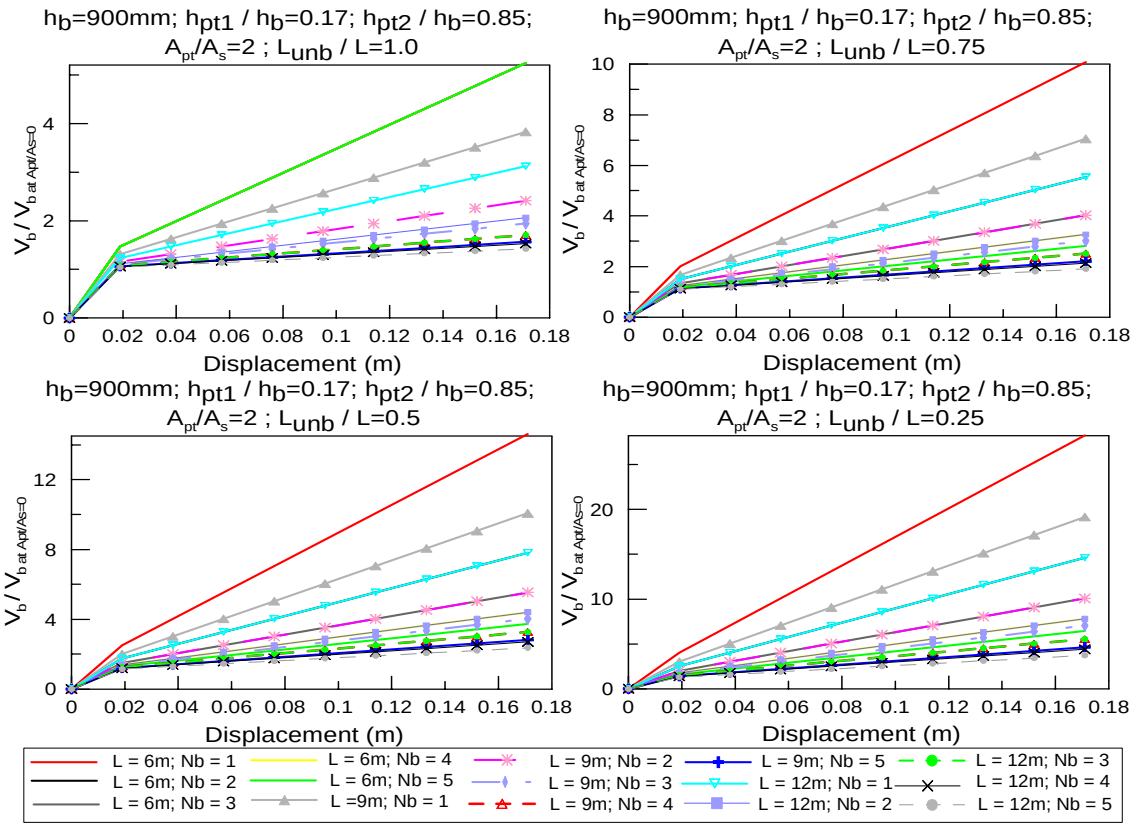

Figure 6.34. Normalized base shear (V_b / $V_{b\ atApt/As=0}$) vs displacement for h_b=900 and A_{pt}/A_s=2.0 varying the number of bays, the bay length and the unbonded length.

6.8 DESIGN EXAMPLE OF A NON-TEARING BEAM-COLUMN JOINT

Figure 6.35 shows an H frame with non-tearing connection with spans of 7.5m long and 3.8m inter-storey height. The structural analysis has determined the beam design moment of $M_{ult} = 400kNm$ at 1.5% drift; therefore, an anti-symmetric tendon profile has been provided and anchored at each column as it was demonstrated in the previous section that in this solution the exterior and interior columns will have a contribution from the post-tensioning moment in addition to the moment contribution of the mild steel external energy dissipaters. For this example no reduction factor will be used for simplicity to understand the concept and application of the equations derived in the previous sections.

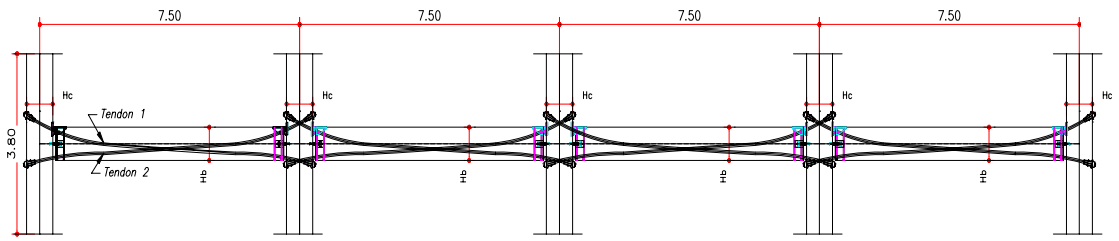

Figure 6.35. Design H-frame.

The compressive strength of the concrete is assumed as f_c' = 40 MPa, with an elastic modulus calculated as $E = 5000\sqrt{f_c'}$. A stress-strain curve assumed for the mild steel dissipaters are shown in Figure 6.36. The steel tensile strength is assumed as $f_y = f_{yh}$ = 300 MPa with a strain hardening of ε_{sh} = 0.02 and ultimate strain of $\varepsilon_{s\,ult}$ = 0.12 with an ultimate stress of $f_{y\,ult}$ = 450 MPa.

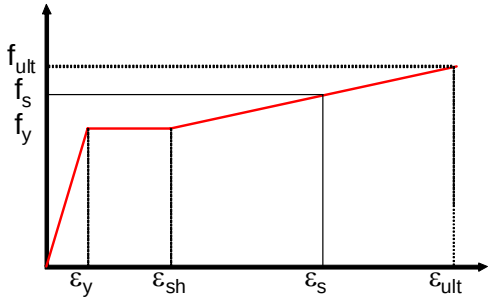

Figure 6.36. Mild steel stress-strain relationship used for design.

The steel tensile strength of the prestressing tendons is assumed as $f_{pt\,y}$ = 1560 MPa with an ultimate stress $f_{pt\,ult}$ = 1860 MPa. The nominal diameter assumed for the tendons is d_{pt} =15.7mm with an area of tendon A_{pt} =150mm^2. The modulus of Elasticity assumed for the prestressing tendons as well as the mild steel bars was E_s = 195 GPa.

In order to reach the desired flexural demand, beam and columns section are shown in Figure 6.37. Assuming mild steel external dissipater fuses of D27.5mm and 4 tendons at each duct ($A_{pt} = 600mm^2$) with an initial post-tensioned force $T_{pt1\,ini} = T_{pt2\,ini} = 600kN$ (53.7% $f_{pt\,ult}$) the increase and decrease in force the post-tensioned tendons can be calculated using (6.4).

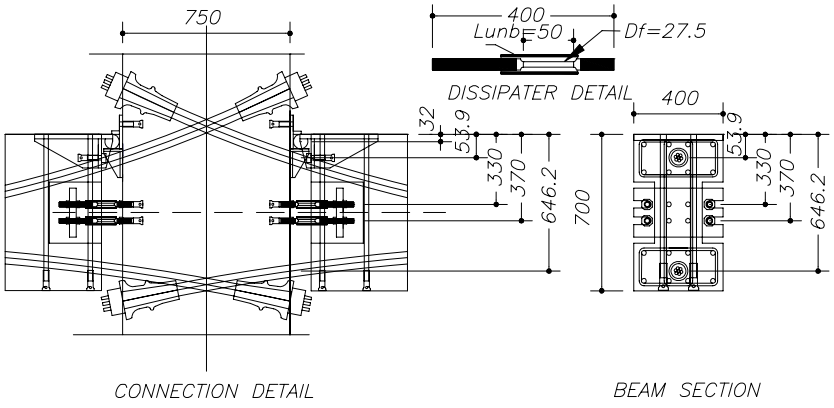

Figure 6.37. Beam section and dissipater details.

Note: no beam and column reinforcement is shown for clarity.

The column rotation established as the design drift is $\theta_b = 1.5\%$,the height of the tendons $h_{pt1} = 53.9mm$ and $h_{pt2} = 646.2mm$, the neutral axis position c=32mm, the unbonded length $L_{unb} = 7.5m$, the modulus of elasticity $E = 195GPa$ and the post-tensioned steel area of $A_{pt} = 600mm^2$, then the changed in post-tensioned force is $\Delta T_{pt1} = -138.6kN$ (shorten) and $\Delta T_{pt1} = 138.6kN$ (elongates). Therefore, the tendon forces are $T_{pt1} = 461.4kN$ and $T_{pt2} = 738.6kN$.

Similarly, the elongation at the level of the mild steel Δ_s is a function of the gap rotation and of its location within the depth of the section; and can be evaluated as

$$\Delta_s = \theta_b (h_s - c) \tag{6.15}$$

where h_s is the location of the mild steel, therefore, for the design beam shown in Figure 6.37, steel elongation is calculated as $\Delta_{s1} = 4.5mm$ and $\Delta_{s2} = 5.1mm$. The strain in the mild steel ε_s can be evaluated as

$$\varepsilon_s = \frac{\Delta}{l'_{unb}} \tag{6.16}$$

Where l'_{unb} is the unbonded length of the mild steel and assumed for this design example of 50mm. Therefore, the strain in the steel is $\varepsilon_{s1} = 0.089$ and $\varepsilon_{s2} = 0.101$.

The tensile stress and steel force within the steel can be calculated through constitutive relationships. Recognising that it is possible for the tension strain to enter the strain hardening region of the stress-strain curve, an approximate multi-linear stress curve is adopted for design as shown in Figure 6.36. Therefore, an evaluation of the strain obtained is required: if the steel strain is within the range of $\varepsilon_y \le \varepsilon_s \le \varepsilon_{sh}$, the tension force in the mild steel can be calculated $T_s = A_s f_y$. Likewise, if the steel strain is greater than ε_{sh}, then the tensile force can be increased linearly as shown in Figure 6.36.

For this particular design example, the steel strain calculated is greater than the strain hardening therefore, the tensile stress are obtained $f_{s1} = 447.7MPa$ and $f_{s2} = 449.3MPa$ and the tensile steel force is $T_{s1} = 531.9kN$ and $T_{s2} = 533.7kN$

Adopting a positive convention for moments (counter-clockwise), for a positive joint rotation (gap opening), the connection moment at the exterior columns can be evaluated at the left and right side $M_{con-ext-left}$ and $M_{con-ext-right}$ following the equations (6.5) or (6.10)

$$M_{pt-ext-left} = 461.4kNx(53.9-32)mm + 738.6kNx(646.2-32)mm = 463.7kNm$$

$$M_{pt-ext-right} = 738.6kNx(53.9-32)mm + 461.4kNx(646.2-32)mm = 299.5kNm$$

$$M_{s-ext-left} = 531.9kNx(330-32)mm + 533.7kNx(370-32)mm = 338.9kNm$$

$$M_{s-ext-right} = -531.9kNx(330-32)mm - 533.7kNx(370-32)mm = -338.9kNm$$

Then $M_{con-ext-left} = 802.6kNm$ and $M_{con-ext-right} = -39.4kNm$.

The connection moments at the interior column depend on the change in the post-tensioned moment ΔM_{pt} at the specific design drift and the mild steel contribution as shown in equation (6.11). The changed in the post-tensioned moment ΔM_{pt} in the connection can be evaluate from $M_{pt-1eft}$ and calculating the initial post-tension moment $M_{pt\ ini}$ which is the initial post-tension force and the distance of the tendons to the centre of the monohinge. Therefore, $M_{pt\ ini} = 381.6kNm$ and hence, $\Delta M_{pt} = 82.1kNm$. The interior connection moments are therefore $M_{con-\text{int}} = 421kNm$. Higher than the demand of $M_{ult} = 400kNm$

Exterior and interior column moments and shears can be evaluating by using equations (6.10) and (6.11). The total storey shear can be obtained using equation (6.13) with a total storey shear of $V_{storey} = 886.3kN$

6.9 CHAPTER SUMMARY

In this chapter the structural behaviour of a hybrid beam column joint and H-frame systems with top hinge (non-tearing) connection has been presented. The behaviour of a hybrid non-tearing connection indicates that the total moment contribution is based on the same pure yielding system moment offset by the initial post-tensioned moment with the initial stiffness determine by the pure yield system and post-yield stiffness by the contribution of both systems (pure yield and linear elastic).

Different configurations of H-frames with multiple spans using non-tearing connections were conceptually evaluated. From these concepts, two solutions were investigated: the first solution used unbonded post-tensioned tendons anchored at each span, while the second, used partially bonded post-tensioning tendons anchored at mid-span and at the exterior columns.

Shear forces and bending moment equations have been proposed for H-frames of one and multiple spans using non-tearing connections. At rest, the initial post-tensioned moments induced column moments that are self equilibrated in each floor. For the first solution, as the gap opens, the exterior and interior column moments changed according to the change in the post-tensioned moment (ΔM_{pt}) and the moment contribution of the mild steel dissipaters (M_s).

The second solution, as the gap opens, the exterior column moments change according to the change in the post-tensioned moment (ΔM_{pt}) but higher than the previous solution because of a smaller unbonded length when compared to the full bay length; however, the interior columns will not have any contribution from the post-tensioning moment as they cancel out and therefore the only contribution for the interior column moments are the mild steel moment connection of the dissipaters (M_s).

Additional parametric analysis for a number of beam column joints and H-frames of one and multiple spans using non-tearing connection has been presented. The analysis has been carried out using a series of equations derived from material and geometric considerations. The parameters analyzed have been the beam section depth, the bay length, the location of the tendon profile along the beam section, the initial post-tensioned force, the unbonded length of the post-tensioned tendons and the steel area content ratio between post-tensioned and mild-steel dissipation devices. Based on this parametric analysis the following conclusions can be made:

1. Results for beam column joints indicate that increasing the depth of the beam section or increasing the location of the tendons from the pivot point, causes higher moments due to post-tensioning.

It was identified that as the unbonded length decreased from fully unbonded to partially bonded, and the bay length increased, the post-tensioned moments increased. However, the change in

the post-tensioned moments is constant. Results also indicated that as the steel area content increased, the total moment increased.

Similarly, as the gap closes (negative rotations), the total moment contribution will be significant reduce due to the prestressing tendons having no force, therefore only the energy dissipation contribution is provided in the connection. To avoid that the post-tensioned tendons reaching zero force at the desired drift level, a minimum of initial post-tensioning force is require to not reach zero force.

2. Parametric analysis on hybrid H-frames systems with non-tearing connections were carried out in terms of local (beam column joint) and global (base shear) response. Results indicated that the first solution will show a better response in terms or base shear. However, this solution seems to be not very economical considering the cost associate with the construction and post-tensioning. The second solution would question the use of tendons in the interior spans if no extra benefit can be taken from them.

Changing the beam section depth of the frames indicates that as the beam section increases, the base shear also increases due to the increase in the lever arm of the post-tensioned moments and mild steel dissipaters. However, increasing the bay length will reduce the response of the frames as the unbonded length increases. Therefore, frames with non-tearing connections present higher lateral responses for short bay lengths although higher initial post-tensioned forces will be required to keep the desired moment capacity at the connection.

For the second solution, results indicated that as the unbonded length decreased from fully unbonded to fully bonded, the total base shear increase. This result indicates that higher base shear can be obtained by reducing the unbonded length by one quarter of the total length.

Finally, simple equilibrium equations and parametric analysis confirmed that increasing the number of bays increases the total base shear. For the first solution, this increase is directly proportional to the sum of all of the energy dissipation moment M_s generated in the beam column joints and the change in moment due to the post-tensioned tendons ΔM_{pt} generated at each span. For the second solution, a substantial reduction of the total lateral shear is deducted as the number of bays increased, ΔM_{pt} is becoming smaller when compared to the moments generated by the dissipation steel M_s and for a higher number of spans this moments can be negligible.

6.10 REFERENCES

6.1 Amaris, A. Pampanin, S., Bull, D., and Carr, A. "Development of a Non-tearing Floor Solution for Jointed Precast Frame Systems," Proceedings of the New Zealand Society of Earthquake Engineering Annual Conference, Parmerston North, New Zealand, 2007.

6.2 Amaris, A. Pampanin, S., Bull, D., and Carr, A. "Experimental Investigation on a Hybrid Jointed Precast Frame with Non-tearing Floor Connections," Proceedings of the New Zealand Society of Earthquake Engineering Annual Conference, Taupo, New Zealand, 2008.

6.3 Ohkubo, M., Hamamoto, T. "Developing Reinforced Concrete Slotted Beam Structures to Reduce Earthquake Damage and to Enhance Seismic Structural Performance," Proceedings of the 13th World conference on Earthquake Engineering. 2004, Vancouver, Canada.

6.4 Au, E. V., "the Mechanics and Design of a Non-tearing Floor Connection Using Slotted Reinforced Concrete Beams," ME thesis, Department of Civil Engineering, University of Canterbury, Christchurch New Zealand, 2010, 335pp.

6.5 Leslie, B.J. "The Development and Validation of a Non-tearing floor Precast concrete Structural System for Seismic Regios," ME thesis, Department of Civil Engineering, University of Canterbury, Christchurch New Zealand, 2010, 481pp.

6.6 Palmieri, L., Saqan, E., French, C., and Kreger, M., "Ductile Connections for Precast Concrete Frame Systems," Proceedings of the Mete Sozen Symposium, SP-162-13, American Concrete Institute, Farmington Hills, MI., Oct. 1996, pp. 313-355.

6.7 New Zealand Standards (NZS). "Appendix B: Special Provisions for the Seismic Design of Ductile Jointed Precast Concrete Structural Systems," *NZS3101:2006, Concrete Standard*, Wellington, New Zealand.

CHAPTER 7
DESIGN AND MODELLING OF PROTOTYPE STRUCTURES USING NON-TEARING FLOOR CONNECTIONS

7.1 INTRODUCTION

The structural behaviour and parametric analysis for a number of beam-column joints and H-frames of single and multiple spans using non-tearing connections was presented in Chapter 6. The local beam column joint response indicates that the total moment contribution is based on a pure yielding hysteresis offset by an initial post-tensioned moment with the initial stiffness being determined only by the pure yield hysteresis and post-yield stiffness being determined by the contribution of both systems (pure yield and linear elastic).

For H-frame systems different configurations were proposed. The first configuration uses unbonded post-tensioned tendons anchored at each span, while the second uses partially bonded post-tensioning tendons anchored at mid-span.

In terms of the global response of the H-frames, it was demonstrated that for the first solution, as the gap opens, the exterior and interior column moments change according to the change in the post-tensioned moment and the moment contribution of the mild steel dissipaters while for the second solution, as the gap opens, the exterior column moments change according to the change in the post-tensioned moment however the change is higher than the previous solution because of a smaller unbonded length in comparison with that of the full bay length. The interior columns will not have any contribution from the post-tensioning moment as they cancel out and therefore the only contribution for the interior column moments are the mild steel moment connection of the dissipaters.

Results indicate that the first solution will show a better response in terms of base shear capacity. However, this solution seems to be uneconomical considering the cost associated with the construction and post-tensioning activities. The second solution is impractical since no extra benefit in terms of additional lateral response can be taken from the use of tendons in the interior spans.

In this Chapter the design and modeling of 5 and 10 multi-storey building prototypes with different solutions will be presented. The buildings will be designed for a traditional hybrid PRESSS type following the direct displacement based design principles in order to ensure that the design limit state was not exceeded, the full distribution of moment and base shear corresponding to a given damage limit state.

As the total base shear will be calculated and distributed throughout the structures, the design of the beam members and their connections will consider three different systems for comparison purposes: traditional hybrid PRESSS, Hybrid using non-tearing connection and a monolithic (cast-in-situ or emulation of cast-in-situ) solution. The prototype buildings and their different configurations will be subjected to push-over analysis to investigate and evaluate the performance of this type of system to lateral loading.

7.2 PROTOTYPE BUILDINGS

A Series of multi-storey frame systems with different stories subjected to pushover analysis and time history analysis have been presented in the literature [7.1]. In this chapter a more detailed and comprehensive design, modelling and adaptive push-over analysis has been carried for frames using non-tearing connections to investigate and evaluate the lateral response. The distribution of moments and shears throughout the frames were of particular interest.

7.2.1 Building typology

Two prototype buildings of five and ten stories were investigated and shown in Figure 7.1. The frame structure adopted corresponds to the prototype in the PRESSS Design Handbook [7.2].

The prototypes have the same plan view geometry with plan dimensions of 24m wide by 30m long. The Lateral resistance is provided by three seismic resisting frames in the longitudinal direction detailed to achieve the desired global displacement demand. Two exterior walls provide seismic resistance in the transverse direction. The building is assumed to have a rigid foundation. A summary of the beam and column dimensions is shown in Table 7.1

7.2.2 Material Properties

The compressive strength of the concrete is assumed as $f_c^{'}$ = 40 MPa, with an elastic modulus calculated as $E = 5000\sqrt{f_c^{'}}$. The steel tensile strength is assumed as f_y = f_{yh} = 300 MPa with

a strain hardening of ε_{sh} = 0.02 and ultimate strain of $\varepsilon_{s\,ult}$ = 0.12 with an ultimate stress of $f_{y\,ult}$ = 450 MPa.

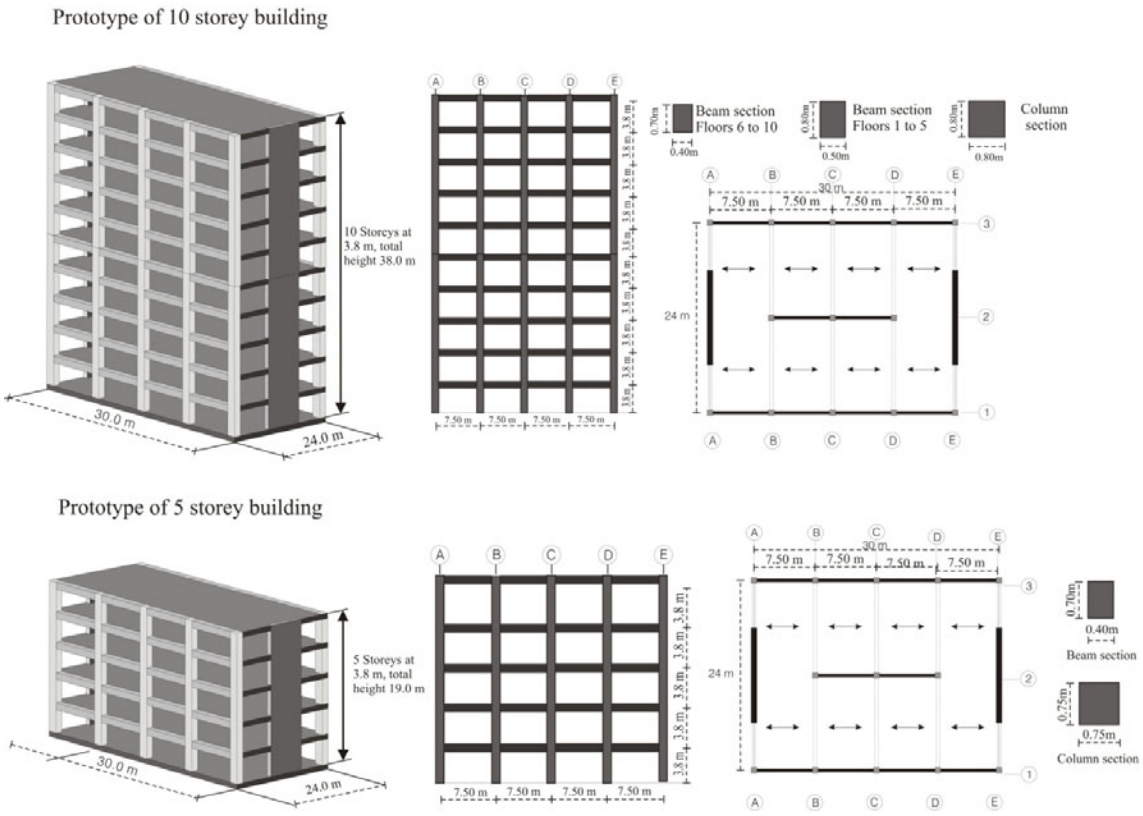

Figure 7.1. 5 and 10-storey Prototype buildings.

Table 7.1 Beam and column dimensions of the prototype buildings.

	Prototype 5-storey				Prototype 10-storey			
N	Columns (mm)	Beams b_w (mm)	Beams h_b (mm)	mass (tonnes)	Columns (mm)	Beams b_w (mm)	Beams h_b (mm)	mass (tonnes)
10	-	-	-	-	800	400	700	531.8
9	-	-	-	-	800	400	700	662.9
8	-	-	-	-	800	400	700	662.9
7	-	-	-	-	800	400	700	662.9
6	-	-	-		800	400	700	662.9
5	750	400	700	527.8	800	500	800	707.9
4	750	400	700	654.3	800	500	800	707.9
3	750	400	700	654.3	800	500	800	707.9
2	750	400	700	654.3	800	500	800	707.9
1	750	400	700	654.3	800	500	800	707.9

The steel tensile strength of the prestressing tendons is assumed as $f_{pt\,y}$ = 1560 MPa with an ultimate stress $f_{pt\,ult}$ = 1860 MPa. The nominal diameter assumed for the tendons is

d_{pt} =15.7mm with an area of tendon A_{pt} =150mm^2. The modulus of Elasticity assumed for the prestressing tendons as well as the mild steel bars was E_s = 195 GPa.

7.2.3 Location

The buildings were located in Wellington on top of shallow soil (soil type C) within 2km of the fault and an importance level of 2 was used, thus requiring a design return period of 500 years.

7.2.4 Loads

7.2.4.1 Dead loads

Dead loads of the floor comprised of precast hollow-core floor units, 65mm topping, and superimposed dead load which include suspended ceiling, services and partitions. However, the roof level does not include partitions.

- Slab 2.5 kPa
- Topping 1.56 kPa (65mm thick)
- SDL 1.0 kPa
- Partitions 0.5 kPa
- Suspended ceiling 0.5 kPa
- External glazing (along the perimeter of the structure) 1.3 kN/m

Beam and column element self weights were also included in the analysis assuming the section properties according with Table 7.1.

7.2.4.2 Live loads

The floor basic live load was according with table 3.1 NZS1170.1:2002 [7.3] and equal to Q_b =3.0kPa. For the roof level a Q_b =1.5kPa was assumed.

Live load combination factors were also assumed according with section 4.3 of reference [7.3] and equal to $\psi_e = 0.3$. Therefore Q_e =0.9 kPa for each floor and Q_e =0.45 kPa for the roof level.

The total seismic mass per floor is the contribution of the dead loads and live loads and is shown in Table 7.1.

7.3 BUILDING DESIGN METHOD

The inappropriateness of the force-based design assumption of initial stiffness and ductility capacity suggests that the resulting base moment and shear will not necessarily satisfy the intended limit state. For that reason, in this study, the buildings were designed for a traditional hybrid PRESSS type solution using displacement-based design principles (DDBD) in terms of basic design requirements. Therefore the full distribution of moments and base shear corresponding to a given limit state can be guaranteed.

The general procedure for a displacement-based design is relatively straight forward and follows a number of key steps. The method aims to provide specific performance criteria as a function of seismic intensity related to the structure; more specifically a target displacement corresponding to a design level earthquake.

The procedure requires the structural system to be converted to an equivalent single degree of freedom system having an effective elastic stiffness, effective mass, effective height and damping corresponding to the target displacement (related to the structural ductility). The procedure is as follows:

- Select a design drift-generally governed as the limiting inter-storey drift offered by the design code or by the maximum allowable displacement ductility of the structural system as suggested by the code i.e. Table 2.5 [7.4].
- Calculate design target displacement for equivalent single degree of freedom structure.
- Estimate the damping of the structure. This is simply related to the expected ductility of the structure as a function of specific dissipation characteristics of the system.
- Enter the displacement response spectra and read off the effective period of the single degree of freedom system.
- Calculate the effective mass, and hence effective stiffness.
- Calculate the base shear.
- Distribute the base shear throughout the structure and design the members accordingly.

7.3.1 Inelastic Mode shape and displacement profile

The generalized displaced shape for the SDOF structure is based upon the inelastic first mode shape representing the structure at the desired limit state, in this case the 5-storey frame building was designed at 2.0% inter-storey drift, while the 10-storey buildings prototype was targeting a 1.5% inter-storey drift. The peak inter-storey drift can be expressed as an elastic (θ_y) rotation plus a plastic (θ_p) rotation and must not exceed the code limit (θ_c) of 2% in this case of $\theta_d = \theta_y + \theta_p \leq \theta_c$.

It should be noted that in some cases the code limit of 2% may not be achieved for the design simply because the increase in effective natural period associated with taller structures is not captured by the spectra. Reducing the target drift from 2.0% to 1.5% will therefore bring the effective natural period within the limits of the design spectra for the 10 storey building.

The critical location of θ_d (Figure 7.2) is likely to be at the first floor in the case of frame buildings and at the top floor in the case of wall structures. Hence for the prototype building frames the normalized displaced profile can be approximated with the following formula as suggested in [7.5].

With n<4

$$\delta_i = h_i / h_n \tag{7.1a}$$

With n>4

$$\delta_i = \frac{4}{3}\left(\frac{h_i}{h_n}\right)\left(1 - \frac{h_i}{4h_n}\right) \tag{7.1b}$$

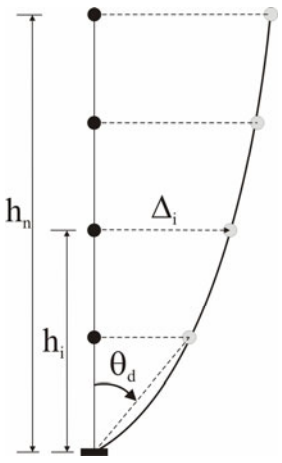

Figure 7.2 Displacement profile.

Where δ_i is the normalized inelastic mode shape, n is the number of storeys in the structure, h_i, and h_n are the heights to the i^{th} storey and roof respectively.

The displacement profile is given by the ratio

$$\Delta_i = \left(\frac{\delta_i}{\delta_1}\right)\theta_d h_1 \tag{7.2}$$

Where n is the number of storeys in the structure, h_i, and h_n are the heights to the i^{th} storey and roof respectively and θ_d is the limit state inter-storey drift.

The effects of higher modes are accounted for by a reduced lateral drift, to allow for an increase in actual dynamic response. The higher mode factor is given in [7.5]:

$$\omega = 1.15 - 0.0034 h_n \leq 1.0 \tag{7.3}$$

The reduced design displacement profile is given by:

$$\Delta_{i,\omega} = \omega \Delta_i \tag{7.4}$$

7.3.2 Effective Mass, displacement and Height

The effective mass is related to the displaced shape and the distribution of mass throughout the height of the structure and can be calculated as proposed in [7.5]

$$m_e = \frac{\sum_{i=1}^{n} m_i \Delta_i}{\Delta_d} \tag{7.5}$$

Where Δ_d corresponds to the equivalent displacement at the effective height of the SDOF structure (Figure 7.3)

$$\Delta_d = \frac{\sum_{i=1}^{n} \left(m_i \Delta_i^2\right)}{\sum_{i=1}^{n} \left(m_i \Delta_i\right)} \tag{7.6}$$

Hence the effective height can be calculated

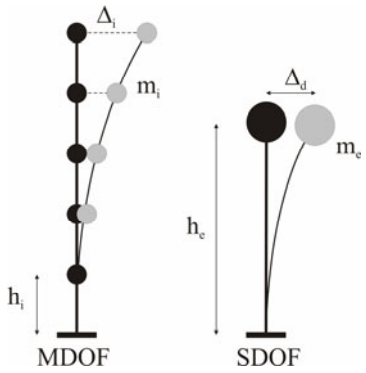

Figure 7.3 Effective mass and height.

$$h_e = \frac{\sum_{i=1}^{n} m_i \Delta_i h_i}{\sum_{i=1}^{n} m_i \Delta_i} \tag{7.7}$$

The Table 7.2 summarises the parameters required to compute the effective mass, effective height and distribution of the shear throughout the height of the building. Table 7.3 shows the results of the results of the equivalent structure.

Hence, for the 5-storey frame $\Delta_{d,\zeta} = 0.224\,m$, $m_e = 2697\,tonne$ and $h_e = 13.2\,m$. Note that m_e equates to 86% of the total mass while h_e equates to 70% of the total building height and $\Delta_{d,\zeta}$ equates to a lateral drift of 1.34% at the height of the equivalent mass.

Table 7.2 Summary of DDBD parameters.

		Prototype 5-storey							Prototype 10-storey						
N	h_i (m)	δ_i (-)	Δ_i (m)	Drift (%)	m_i (t)	$m_i\Delta_i$ (t m)	$m_i\Delta_i^2$ (t m^2)	$m_i\Delta_i H_i$ (t m^2)	δ_i (-)	Δ_i (m)	Drift (%)	m_i (t)	$m_i\Delta_i$ (t m)	$m_i\Delta_i^2$ (t m^2)	$m_i\Delta_i H_i$ (t m^2)
10	38.0	-	-	-	-	-	-	-	1.00	0.44	0.81	531.8	233.2	102.2	8860.6
9	34.2	-	-	-	-	-	-	-	0.93	0.41	0.88	662.9	270.3	110.2	9244.6
8	30.4	-	-	-	-	-	-	-	0.85	0.37	0.96	662.9	248.0	92.8	7540.0
7	26.6	-	-	-	-	-	-	-	0.77	0.34	1.04	662.9	223.8	75.6	5953.2
6	22.8	-	-	-	-	-	-	-	0.68	0.30	1.12	662.9	197.6	58.9	4506.3
5	19.0	1.00	0.30	1.16	527.8	158.3	47.5	3008.5	0.58	0.26	1.19	707.9	181.1	46.3	3440.1
4	15.2	0.85	0.26	1.37	654.3	167.5	42.9	2546.0	0.48	0.21	1.27	707.9	149.0	31.4	2264.6
3	11.4	0.68	0.20	1.58	654.3	133.5	27.2	1521.6	0.37	0.16	1.34	707.9	114.8	18.6	1309.2
2	7.6	0.48	0.14	1.79	654.3	94.2	13.6	716.1	0.25	0.11	1.42	707.9	78.6	8.7	597.6
1	3.8	0.25	0.08	2.00	654.3	49.7	3.8	189.0	0.13	0.06	1.50	707.9	40.4	2.3	153.3

Similarly, for the 10 storey frame, m_e equates to 82% of the total mass while h_e equates to 66% of the total building height and $\Delta_{d,\zeta}$ equates to a lateral drift of 1.39% at the height of the equivalent mass.

Table 7.3 Summary of DDBD parameters.

Prototype	θ_d (%)	Δ_d (m)	m_e (tonne)	h_e (m)
5-storey	2.0	0.224	2697	13.2
10-storey	1.5	0.315	5514	25.3

7.3.3 Effective Damping and Base Shear

Some fundamental relationships are used to calculate the design base shear for the building. The base shear is calculated using the effective stiffness of the substitute structure of the Figure 7.4.

$$V_{Base} = k_{eff}\,\Delta_d \tag{7.8}$$

Where k_{eff} is the effective stiffness of the substitute structure is given by

$$k_{eff} = \frac{4\pi^2 m_e}{T_{eff}^2} \tag{7.9}$$

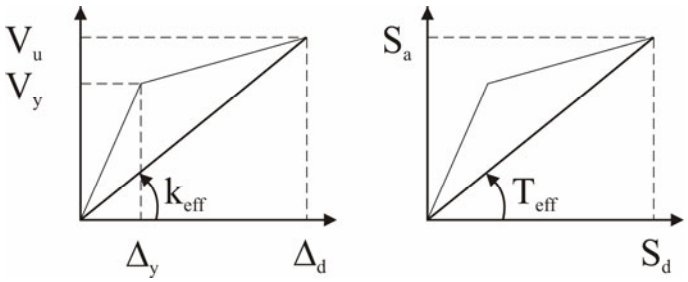

Figure 7.4 SDOF base shear.

Hence the effective period of the equivalent single degree of freedom system is required. The period can be taken from the design spectra, where the target displacement and spectrum is known. However recognising that the design spectrum is representative of a 5% damped structure, a reduction needs to be accounted for the additional damping of the equivalent SDOF structure representative of the expected ductility at the target displacement.

A reduction factor is suggested [7.5] for the design spectrum as a function of ductility as follows

$$\eta = \left(\frac{0.07}{0.02 + \zeta_{eq}}\right)^{\alpha} \geq 0.7 \tag{7.10}$$

Where ξ_{eq} is the equivalent viscous damping ratio of the structure and α is a factor that depends on the ground response characteristics and can be α =0.25 for near field effects or α =0.50 for far field characteristics. Hence, to calculate the effective period from a 5% damped

displacement spectrum, the calculated displacement $\Delta_{d,\zeta}$ is increased by $\frac{1}{\eta}$ with the following relationship:

$$\Delta_{d,5\%} = \frac{\Delta_{d,\zeta}}{\eta} \tag{7.11}$$

Where $\Delta_{d,\zeta}$ is the target displacement converted to an equivalent 5% displacement target $\Delta_{d,5\%}$ for a given period and damping correction factor η.

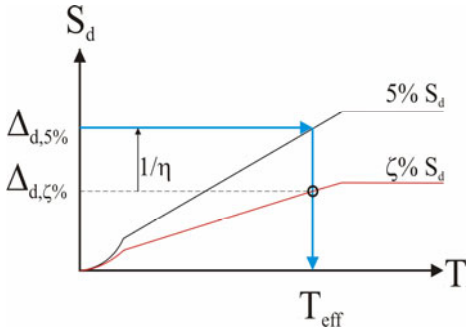

Figure 7.5. Effective period of the equivalent SDOF.

As mentioned in Chapter 6, in order to guarantee full self-centering of a general jointed connection, an appropriate moment contribution ratio is required such that λ (the ratio between the restoring forces and the dissipation forces) is greater than a minimum value which allows for the overstrength of the non-prestressed steel reinforcement or the generic energy dissipating devices and is determined to be α_0 >1.15 [7.6]

$$\lambda = \left(M_{pt} + M_N / M_s\right) \geq \alpha_o \tag{7.12}$$

where M_{pt}, M_N and M_s are the flexural strength contributions of the post-tensioned tendons, the axial load where present, and the non-prestressed steel reinforcement respectively. The Value α_0 is the overstrength factor for the non-prestressed steel reinforcement or the energy dissipating devices. However, for the design of these prototypes, the value assumed was λ=1.25 to obtain a better re-cantering property of the connection minimizing the residual damage.

The equivalent viscous damping of the single degree of freedom system substitute structure is now calculated as proposed in [7.6]

$$\xi_{eq} = \left[5\% + 30\left(1 - \frac{1}{\sqrt{\mu}} \right)\% \right]\left(\frac{1}{1+\lambda} \right) + 5\%\left(\frac{\lambda}{\lambda + 1} \right) \tag{7.13}$$

Where the effective damping depends on the structural system and the displacement ductility factor μ which can be easily obtained by

$$\mu_{\Delta} = \frac{\Delta_d}{\Delta_y} \tag{7.14}$$

Where Δ_d is the equivalent displacement at the effective height, and Δ_y is the yield displacement evaluated as

$$\Delta_y = \theta_y h_e \tag{7.15}$$

Where θ_y is the yield rotation and h_e is the effective height of the single degree of freedom system.

For reinforced concrete frames, the yield drift (drift to the effective height) of a reinforced concrete frame and a frame having beams with unbonded prestressing can be estimated using simple equations proposed in the literature [7.5, 7.8]

- Reinforced concrete frames: $\theta_y = 0.5\varepsilon_y \frac{l_b}{h_b}$ (7.16a)
- Unbonded prestressing frames: $\theta_y = 0.25\varepsilon_y \frac{l_b}{h_b}$ (7.16b)

This implies that precast frames having unbonded prestressing are likely to have a greater stiffness, having a yield displacement of approximately 50% of that of an equivalent reinforced concrete frame with identical member sizes and steel grade. Therefore, the yield drift of the buildings can be calculated where l_b is the bay length and h_b the beam height.

Note that for the 10 storey building prototype a reduction in the beam depth from the 6th storey to the 10th has been applied. This reduction will reduce the yield drift for the upper storeys and a smaller equivalent viscous damping is expected. Therefore, it is proposed [7.5] to reduce the equivalent viscous damping in proportion the ductility of each floor obtained from the corresponding yield rotation as follows.

$$\xi_{eq} = \frac{\sum_{i=1}^{n}\left(\sum_{k=1}^{m} m_k\right)\theta_i \xi_i}{\sum_{i=1}^{n}\left(\sum_{k=1}^{m} m_k\right)\theta_i} \tag{7.17}$$

Where m are the locations of plastic hinges at each beam level, and θ_i is the design drift at level i calculated according to equation (7.18).

$$\theta_i = \left(1 - 0.5\frac{h_i}{h_n}\right)\theta_d \tag{7.18}$$

The damping at level i is based on the drift ductility at that level and equal to $\mu_\theta = \frac{\theta_i}{\theta_{yi}}$. Table 7.4 summarises the effective damping and ductility obtained for each prototype.

Table 7.4 Beam yield rotations, yield displacement, ductility and equivalent viscous damping.

Prototype	floor	L_b (m)	h_b (m)	θ_y (rad)	θ_i (rad)	μ_θ	ξ_{eq}	ξ_{eq} (%)	Δ_y (m)	$\mu_{\Delta i}$	η
5	1	7.5	0.7	0.00402	0.0180	4.5	0.12	11.23	0.05	4.21	0.85
	2				0.0160	4.0	0.12				
	3				0.0140	3.5	0.11				
	4				0.0120	3.0	0.11				
	5				0.0100	2.5	0.10				
	ΣTotal				0.0700	17.4	0.55				
10	1	7.5	0.8	0.00352	0.0143	4.1	0.12	10.55	0.09	3.55	0.86
	2				0.0135	3.8	0.12				
	3				0.0128	3.6	0.11				
	4				0.0120	3.4	0.11				
	5				0.0113	3.2	0.11				
	6		0.7	0.00402	0.0105	2.6	0.10		0.10	3.10	
	7				0.0098	2.4	0.10				
	8				0.0090	2.2	0.09				
	9				0.0083	2.1	0.09				
	10				0.0075	1.9	0.09				
	ΣTotal				0.1088	29.3	1.03				

The effective period is then evaluated using the design spectra coming from NZS 1170.5 2004 [7.7] with elastic site spectrum compatible with the spectral shape factor determined using a subsoil site C, within 2km from the fault and a return period of 500 years. Table 7.5 shows the results for the effective period of the prototype structures.

Table 7.5 Effective Period, stiffness and total base shear.

Prototype	ξ_{eff} (%)	T_{eff} (sec)	K_{eff} (kN/m)	V_b (kN)	V_b / m_e (%)
5-storey	11.2	2.37	6347	1420	5.4
10-storey	10.6	2.95	8361	2634	4.9

The effective stiffness at peak response is thus evaluated in (7.9) and the total base shear is evaluated in equation (7.8).

Hence the lateral design coefficient for the 5 and 10 storey building is equal to 5.4% and 4.9% of the total building weight respectively. Recognising that for this design each of the three seismic frames in the building will have identical strength; DBD distributes the lateral forces within a structure weighted according to the strength of each element, hence the lateral force is distributed evenly between each frame and distributed up the building height according to the previous relationships to give the following,

$$F_i = V_B \frac{m_i \Delta_i}{\sum_{i=1}^{n} (m_i \Delta_i)} \tag{7.19}$$

The base shear was vertically distributed up the building in proportion to the vertical mass and displacement profiles and no additional force at the top was calculated. Table 7.6 shows the distribution of the lateral forces along the height of the frames.

7.3.4 Distribution of internal actions

The internal actions are distributed throughout the structure using the equilibrium approach proposed by reference [7.5].

7.3.4.1 Column axial loads

The non-seismic column axial loads were calculated with respect to the column's tributary area. Therefore considering the seismic frames only, the external columns carry 1/32nd of the total floor load and the interior column carries 1/16th of the total floor load. Columns 4 and 5 in Table 7.6 show the column axial loads for each floor.

Calculation of the earthquake induced axial load N_E requires an estimation of the contra-flexure height of the ground floor columns, based on the total overturning moments.

A common design practice will be to choose base moments such that the point of contra-flexure in the lower story columns occurs between 55% and 65% of the storey height above the base, thus ensuring capacity protection against hinging at the top of the ground floor columns, and an advantageous distribution of moments above and below the first level beams.

The over turning moments generated at each floor can be calculated as the storey shear $V_{S,i}$ times the inter-storey height l_c. Table 7.6 show the values for the cumulative lateral force.

Table 7.6 Lateral forces, overturning moments and column axial load distributions

Frame	floor	h_i (m)	F_i (kN)	Storey shear (kN)	OTM (kNm)	W_{floor} Exterior (kN)	W_{floor} Interior (kN)	N_E (kN)	N_{G+Q} Exterior (kN)	N_{G+Q} Interior (kN)	N_{G+Q-E} Exterior (kN)	N_{G+Q+E} Exterior (kN)
5	5	19.0	373	373	0	162	323	24	162	323	138	185
	4	15.2	394	767	1416	201	401	96	362	724	267	458
	3	11.4	314	1081	4330	201	401	213	563	1126	350	776
	2	7.6	222	1303	8438	201	401	364	763	1527	400	1127
	1	3.8	117	1420	13388	201	401	518	964	1928	446	1482
	0	0.0	0	-	18784	-	-	-	-	-	-	-
10	10	38.0	354	354	0	163	326	22	163	326	141	185
	9	34.2	410	763	1344	203	406	93	366	733	273	459
	8	30.4	376	1140	4245	203	407	214	570	1139	356	783
	7	26.6	339	1479	8575	203	407	380	773	1546	393	1152
	6	22.8	300	1779	14195	203	407	586	976	1952	390	1562
	5	19.0	275	2053	20953	217	434	829	1193	2386	365	2021
	4	15.2	226	2279	28755	217	434	1103	1410	2820	307	2513
	3	11.4	174	2453	37416	217	434	1403	1627	3254	224	3030
	2	7.6	119	2573	46738	217	434	1721	1844	3688	123	3565
	1	3.8	61	2634	56513	217	434	2017	2061	4122	44	4078
	0	0.0	0	-	66521	-	-	-	-	-	-	-

$$OTM_i = V_{S,i} l_c \tag{7.20}$$

With a point of contra-flexure chosen at 60% of the ground floor column height, and with reference in Figure 7.6, hence the earthquake column axial load can be evaluated as

$$N_E = \frac{\sum_{i=1}^{n} OTM_i - 0.6 V_B h_1}{L_{base}} \tag{7.21}$$

Where F_i are the lateral forces calculated according to (7.19), h_i the height of the building at the point of each floor, V_B the total base shear and L_{base} the length between exterior column centre lines.

Hence, the total axial load on each of the ground floor columns can be calculated as the summation of earthquake induced axial loads and gravity loads.

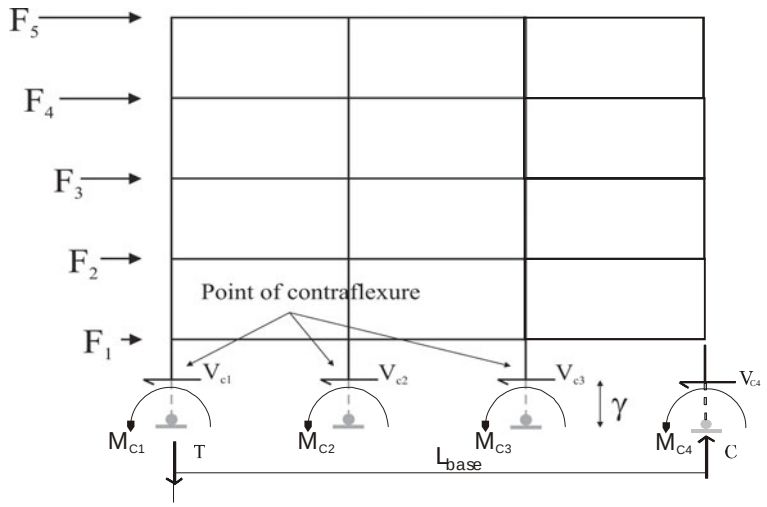

Figure 7.6. Free body diagram, illustrating overturning moments

7.3.4.2 Distribution of beam and column shear and moments

Beam shear is distributed up the height of the building and proportioned to the storey shear at each level.

$$V_{bi} = N_E \frac{V_{S,i}}{\sum_{i=1}^{n} V_{S,i}} \tag{7.22}$$

Where V_{bi} is the beam shear at level i, and $V_{S,i}$ the storey shear at level i and N_E is the tension force in ground column (sum of beam shear).

The beam design moments at the column centrelines can be calculated as

$$M_{bi} = V_{bi} l_b / 2 \tag{7.23}$$

Where l_b is the beam span between column centrelines. Table 7.7 shows the results obtained using the previous equations.

Knowing that the beam design moments are directly related to the beam shear forces, a more appropriate distribution of beam shear up the building height is adopted to provide a more rational design. For the 5 storey building, shears from level 1-3 and levels 4-5 were averaged to have the same construction details. The corresponding beam moment is calculated based on equal top and bottom reinforcement and zero slab influence – resulting in a uniform distribution of beam moment across the frame. Similarly, for the 10 storey buildings, an average between the 1 to 5 and 6 to 10 floors was considered. Table 7.7 shows the results.

Table 7.7 Distribution and design of beam shear forces and bending moments.

Frame	floor	F_i (kN)	Storey shear Vsi (kN)	V_{bi} (kN)	$M_{bi,\,cl}$ (kNm)	$M_{bi,\,cf}$ (kNm)	Average V_{bi} (kN)	Average M_{bi} (kNm)
5	5	373	373	39	147	117	60	179
	4	394	767	80	302	241		
	3	314	1081	113	425	340	133	399
	2	222	1303	137	512	410		
	1	117	1420	149	558	447		
10	10	354	354	41	153	120	127	375
	9	410	763	88	330	260		
	8	376	1140	131	492	387		
	7	339	1479	170	639	503		
	6	300	1779	205	769	605		
	5	275	2053	237	887	698	286	845
	4	226	2279	263	985	775		
	3	174	2453	283	1060	834		
	2	119	2573	296	1112	875		
	1	61	2634	304	1138	895		

7.4 BEAM DESIGN

For comparison purposes, three different beam designs were implemented and subsequently modelled. Firstly a Hybrid PRESSS type solution was designed followed by the Hybrid non-tearing and finally for a monolithic (cast-in-situ or emulation of cast-in-situ concrete) solution.

The longitudinal frames were designed using capacity design principles where beams were designed with average bending moment according to Table 7.7. For comparison analysis, no ϕ reduction factor was used in the designs.

7.4.1 Hybrid PRESSS (Hy) Solution

The design procedure adopted for the hybrid PRESSS building prototypes is according to the Appendix B of the New Zealand Standard code 3101:2006 [7.6], which determine the full self-centering of a general jointed connection shall be achieved by selecting, in the design phase, an appropriate moment contribution ratio λ as the ratio between the restoring forces and the dissipation forces $\lambda = (M_{pt} + M_N)/M_s \geq \alpha_o$ where M_{pt}, M_N and M_s are the flexural strength contributions of the post-tensioned tendons, the axial load where present, and the mild steel reinforcement or energy dissipating device. The Value α_o is the over-strength factor for the energy dissipating device and is determined to be ≥ 1.25.

The actual imposed rotation will differ from the inter-storey drift and will differ for each beam. Some percentage of the lateral drift consists of elastic deformation. It was assumed that the amount of elastic deformation is equal to the yield displacement of the frame. The drift demand decreases up the height resulting from the displaced shape. Furthermore, due to geometry the imposed rotation is greater than the inter-storey drift (or plastic rotation). The amplification is a function of column depth and beam span as explained in Chapter 3. Table 7.8 shows the imposed beam rotation at design displacements.

$$\theta_{imp} = \frac{\theta}{\left(1 - \frac{h_c}{l_b}\right)} \tag{7.24}$$

Assuming a re-centering ratio $\lambda = 1.25$, the amount of post-tensioned and mild steel dissipation can be calculated defining the ratios between energy dissipation and post-tensioning over the total moment as $\alpha = M_s / M_{prov}$ and $\beta = M_{pt} / M_{prov}$. Therefore, the total M_{pt} and M_s contributions required for each connection are $\alpha = 1/(1+\lambda) = 0.44$ and $\beta = \lambda/(\lambda+1) = 0.56$.

While the procedure requires iteration on the neutral axis position within the section, Figure 7.7 and Table 7.9 summarised the beam and column geometry configuration for all the buildings. Final results are shown in Table 7.10.

Table 7.8 Imposed beam rotations at design displacements

Frame	N	Δ_i (m)	Design drift θ_d(%)	θ_y (%)	θ_d-θ_y (%)	θ_{imp} (%)	Average θ_{imp} (%)
5	5	0.300	1.16	0.402	0.76	0.84	0.96
	4	0.256	1.37	0.402	0.97	1.07	
	3	0.204	1.58	0.402	1.18	1.31	1.54
	2	0.144	1.79	0.402	1.39	1.54	
	1	0.076	2.00	0.402	1.60	1.78	
10	10	0.438	0.81	0.352	0.46	0.51	0.68
	9	0.408	0.88	0.352	0.53	0.60	
	8	0.374	0.96	0.352	0.61	0.68	
	7	0.338	1.04	0.352	0.68	0.77	
	6	0.298	1.12	0.352	0.76	0.85	
	5	0.256	1.19	0.402	0.79	0.88	1.06
	4	0.210	1.27	0.402	0.87	0.97	
	3	0.162	1.34	0.402	0.94	1.06	
	2	0.111	1.42	0.402	1.02	1.14	
	1	0.057	1.50	0.402	1.10	1.23	

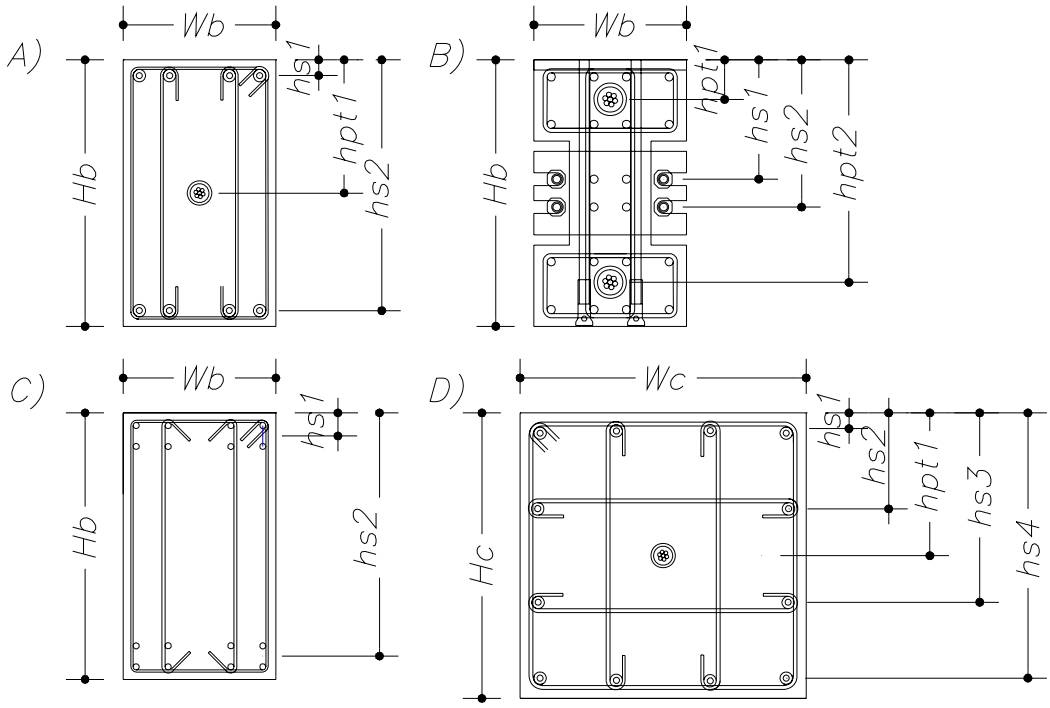

Figure 7.7. Beam and Column section details: A) Hybrid PRESSS, B) Hybrid Non-tearing, C) Monolithic and D) Column base.

Table 7.9 Beam section details for all the prototype buildings.

Frame	Floor	Solution type	b_w (mm)	H_b (mm)	c (mm)	h_{s1} (mm)	h_{s2} (mm)	h_{pt1} (mm)	h_{pt2} (mm)
5	4 and 5	Hybrid PRESSS	400	700	-	58	642	350	-
		Hybrid Non-tearing			32	330	370	54	646
		Monolithic			-	55	646	-	-
	1 to 3	Hybrid PRESSS	400	700	-	78	623	350	-
		Hybrid Non-tearing			32	330	370	54	646
		Monolithic			-	84	616	-	-
10	6 to 10	Hybrid PRESSS	400	700	-	78	623	350	-
		Hybrid Non-tearing			32	330	370	112	646
		Monolithic			-	55	646	-	-
	1 to 5	Hybrid PRESSS	500	800	-	82	718	400	-
		Hybrid Non-tearing			40	360	440	112	693
		Monolithic			-	58	742	-	-

7.4.2 Hybrid Non-tearing ($Hy_{\_non\text{-}tear}$) Solution

It was found from Chapter 6 that the implementation of a fully unbonded post-tensioned solution anchored at each bay is a better solution in terms of overall response (which provides more lateral resistance) when compares with a solution using partially bonded tendons anchored at mid-span. Therefore, for the frame designs purposes, the first option is considered in the design.

Chapter 4 and 6 shows that lower lateral capacity can be seen with hybrid systems with non tearing connections due to the low initial post-tensioned stiffness. The initial post-tensioned moment $M_{pt\,ini}$ and the post-tensioned moment at the design drift level will not contribute significantly to the lateral resistance. However, the change in the post-tensioned moment contribution ΔM_{pt} does contribute in the connection.

Therefore, in order to keep the same storey shears as the hybrid and monolithic systems, it is necessary to provide the required moment capacity at the connection such that the change in the post-tensioned moment contribution ΔM_{pt} and the steel moment contribution M_s satisfy the demand given in Table 7.7. Equations (6.4), (6.7) and (6.10) presented in Chapter 6, can be easily evaluated to obtain the desired moment capacity and equation (6.14) to calculate the storey shear based on beam capacities.

Chapter 6, shows that the initial post-tensioned force will not contribute to the change in the post-tensioned moment ΔM_{pt} which instead increases the moments and shear demand at the exterior columns. Reasonable values of $\Delta M_{pt} / M_s$ =0.1 to 0.3 are recommended. Values close to 0 indicate full capacity in the connection coming from the external energy dissipaters, while higher values than 0.5 will indicate that the post-tensioned moment contribution is significantly large; however, internal moments and shears at the exterior columns will be excessively large and difficult to accommodate in typical column sections. Therefore, steel moment contributions M_s will be higher than the change in the post-tensioned moment contribution ΔM_{pt}. Solutions to increase ΔM_{pt} are based on increasing the number of tendons, reducing the bay length or increasing the beams depth

Adopting the same geometry used for the hybrid frame, the connection design for the hybrid non-tearing models were based on the combination between the require connection flexural capacity and the lateral storey shear. Therefore, a low initial post-tensioned force to keep internal column shear forces into acceptable limit was taken into account; while increasing the number of tendons in addition to the moment contribution of the external energy dissipation was require to provided not only the moment capacity at the connection but also the storey shear. Figure 7.7 show the beam details in conjunction with Table 7.9 and the total moments obtained are shown in Table 7.10 for the three buildings.

7.4.3 Monolithic Solution (Mon)

The design of an equivalent monolithic solution would require the same beam section properties and the same design moment. The flexural beam reinforcement required can be calculated as

$$A_{s,req} = \frac{M}{f_y (h_{s2} - h_{s1})} \tag{7.25}$$

Where M is the average moment from Table 7.7, f_y the yield strength, h_{s2} is the distance from the centroid of the tension reinforcement to the extreme concrete compression fiber and h_{s1} the distance from the extreme concrete compression fiber to the centroid of the top reinforcement (assumed cover thickness was taken as 30mm and 12mm stirrups as shown in Figure 7.7). Table 7.9 shows the beam details and Table 7.10 the moment capacity obtained for each building.

Table 7.10 Beam design for different solutions

Frame	Floor	Solution Type	Average θ_{imp} (%)	Average M_{bi} (kNm)	$T_{pt\ ini}$ (kN)	As_{pt} (mm^2)	$M_{pt\ ini}$ (kNm)	$M_{pt\ left}$ (kNm)	$M_{pt\ right}$ (kNm)	ΔM_{pt} (kNm)	As_{prov} (mm^2)	L_{unb} (mm)	M_s (kNm)
5	4 and 5	Hybrid	0.96	179	300	300	-	108	108	-	3-D12	150	63
		Hy Non-tear			300	300*	191	219	163	28.1	4-D19.5	50	142
		Monolithic			-	-	-	-	-	-	2-D25	-	174
	1 to 3	Hybrid	1.54	399	600	600	-	228	228	-	2-D25	150	173
		Hy Non-tear			600	600*	382	469	295	87.0	4-D27.5	50	314
		Monolithic			-	-	-	-	-	-	2 layers 2-D28	-	393
10	6 to 10	Hybrid	0.68	375	700	750	-	224	224		2-D25	150	164
		Hy Non-tear			750	750*	521	561	481	40	4-D30.8	55	348
		Monolithic			-	-	-	-	-	-	4-D25	-	348
	1 to 5	Hybrid	1.06	845	1200	1200	-	482	482	-	3-D28	150	360
		Hy Non-tear			1800	1800*	1305	1475	1135	170	4-D38.5	55	675
		Monolithic			-	-	-	-	-	-	5-D32	-	825

*correspond to a total area of tendons in each duct.

7.5 COLUMN DESIGN

The shear in the ground floor columns is distributed in such a way that the shear ratio between the exterior and interior columns be 1:2.

$$V_{c\ ext} = \frac{V_{S,i}}{\psi(n_{frames} - 2) + 2} \tag{7.24a}$$

$$V_{c\ ext} = \psi \frac{V_{S,i}}{\psi(n_{frames} - 2) + 2} \tag{7.24b}$$

Where $V_{S,i}$ is the storey shear at level i, ψ is the shear ratio distribution between exterior and interior columns and n_{frames} is the number of columns in each frame and equal to $n_{frames} = n_{bays} + 1$ where n_{bays} number of bays. Table 7.11 shows the column shear distribution.

Table 7.11 Distribution and design of column shear forces and bending moments.

Frame	floor, i	V_{ci}, Exterior (KN)	V_{ci}, Interior (KN)	M_{ci}, Exterior (KNm)	M_{ci}, Interior (KNm)
5	5	46.6	93.2	146.5	293
	4	95.9	191.8	-30.5	-61
	4			271	542
	3	135.1	270.2	-93.3	-186.6
	3			331.7	663.4
	2	162.8	325.6	-181.8	-363.6
	2			330.4	660.8
	1	177.5	355.0	-288.4	-576.8
	1			269.8	539.6
	ground			-404.6	-809.2
10	10	44.2	88.4	152.8	305.6
	9	95.4	190.9	-15.2	-30.4
	9			314.7	629.4
	8	142.4	284.9	-47.9	-95.8
	8			444.5	889
	7	184.9	369.7	-96.8	-193.6
	7			542.3	1084.6
	6	222.3	444.7	-160.2	-320.4
	6			608.4	1216.8
	5	256.7	513.3	-236.4	-472.8
	5			650.8	1301.6
	4	284.9	569.8	-324.5	-649
	4			660.4	1320.8
	3	306.7	613.3	-422.2	-844.4
	3			637.9	1275.8
	2	321.6	643.1	-527.4	-1054.8
	2			584.3	1168.6
	1	329.2	658.4	-637.7	-1275.4
	1			500.4	1000.8
	ground			-750.6	-1501.2

Similarly, the columns were designed following capacity design principles allowing for plastic hinges at the base of the columns and no other plastic hinge formations over the column height.

The column section located at the ground floor is designed to the actions derived from the distribution of the internal actions resulting from the displacement-based design (Table 7.11). The distribution of the ground floor column moments was distributed in such a way to ensure a steel ratio 1:2 for both the exterior and interior columns.

In order to optimise the advantages arising from the use of precast elements, the columns in the Hybrid frames were designed at the column base to match the moment capacity of the DBD moment using unbonded mild steel inserted into drossbach ducts (Figure 7.7). These added additional moment contribution to that of the axial load applied at the centre of the columns for the load case N_{G+Q_u}. However, in Hybrid and Hybrid non-tearing systems, due to the use of precast elements, pinned column bases may be also possible in the design of this type of structures.

The columns bases for the monolithic models were designed as a monolithic connection taking into account the axial contribution change due to earthquake actions. Therefore, the total moment capacity was designed for an axial load case of N_{G+Q-E} in addition to the mild steel bars in the drossbach ducts. No consideration for minimum steel reinforcement was made as the NZS3101 limits columns to a minimum of 0.8% of steel reinforcement. Table 7.12 shows the results for each solution.

It should be recognized that this example only attempts to generate a lateral base shear, distribute it between the lateral resisting systems, and then design the connections in detail. While some design relating to curtailment is provided, the specific detailing and curtailment along the individual elements according to the combinations of seismic and gravity loading is omitted.

Table 7.12 Column base design for different solutions

Frame	Model	Column	W_c (mm)	H_c (mm)	h_{s1} (mm)	h_{s2} (mm)	h_{s3} (mm)	h_{s4} (mm)	As_{prov} (mm^2)	$M_{axial\ G+Q}$ (kNm)	$M_{axial\ G+Q-E}$ (kNm)	M_s (kNm)	M_{total} (kNm)
5	Hybrid	Interior	750	750	77	375	673	-	8-D20	625	-	237	862
		Exterior							8-D10	340	-	73	413
	Mon	Interior							8-D20	-	626	238	864
		Exterior							8-D20	-	155	263	418
10	Hybrid	Interior	800	800	77	400	723	-	8-D16	1369	-	156	1525
		Exterior							8-D10	731	-	66	797
	Mon	Interior							8-D20	-	1371	245	1616
		Exterior				292	507	722	12-D28	-	16	787	804

7.6 ANALYTICAL MODELS

The gap opening for the Hybrid PRESSS and Hybrid non-tearing or the plastic hinge region for the monolithic system were modelling using different hysteretic rules assigned to each spring property to correctly represent the inelastic behaviour at the beam-column connection which is evaluated based on a global member compatibility condition. The non-linear finite element program Ruaumoko2D [7.9] was used in the analyses.

After a lot of attention given to the behaviour of the skeleton structure, more recently the focus of research in Earthquake Engineering has concentrated on the behaviour of the floor system within the overall 3D behaviour of the building and the effects of beam elongation [7.10, 7.11, 7.12].

These effects could be relevant in the response of the first-story columns since the building foundation at this level may try to restrain elongation of the beams of the first story at the formation of their plastic hinges. This restriction may cause shear force in the columns not considered in conventional analysis, with the possibility of also creating additional plastic hinges in the columns (weak-column, strong-beam mechanism) and possible collapse of the structure or in loss of support for precast floor systems due to an elongation of the beam elements [7.13].

In Monolithic reinforced concrete frame systems, axial elongation or axial growth of plastic hinges in beams occurs with increasing plastic rotation of the hinge. In unbonded post-tensioned precast frames, significant beam elongation begins when the gap at the beam-column interface opens to about half of the beam depth.

It is worth emphasising that beam elongation effects are typical of both cast-in-situ concrete and precast concrete frames. Two contributions to beam elongation are typically recognized: a) the material contribution due to the cumulative residual strain within the steel, and b) the geometrical contribution due to the presence of a neutral axis and actual depth of the beam. The non-tearing solution is conceived to prevent elongation. The only longitudinal effects are caused by the initial post-tensioning forces acting on the beams elements.

Although this elongation is not treated explicitly in the model building codes and even more importantly, it is not a standard procedure in the modelling of structures in the common design practice, it can be seen that beam elongation effects has an strong influence on the seismic performance of ductile cast-in-place reinforced concrete frame structures and therefore, the consequences of these actions are investigated using an appropriate structural model in this research.

Five different models have been implemented for the three prototypes to compare the behaviour of the systems for comparison purposes: Hybrid PRESSS without beam elongation (Hy), Hybrid PRESSS including beam elongation (Hy_beam-elong), Hybrid non tearing connection

(Hy_non-tear), monolithic without beam elongation (Mon) and monolithic including beam elongation (Mon_beam-elong).

For all the models, all columns were assumed to have fully fixed base boundary conditions with foundations remaining elastic and rigid. Column bases for the Hybrid models were modelled using two rotational spring elements. A bi-linear elastic hysteresis model represents the axial moment contribution while a bi-linear inelastic model represents the moment contribution of the mild steel. For the monolithic models, an axial force-yield moment interaction surface spring using a Takeda hysteresis model was implemented to account for the interaction between axial force and yield moments to represent the monolithic connection (Figure 7.8).

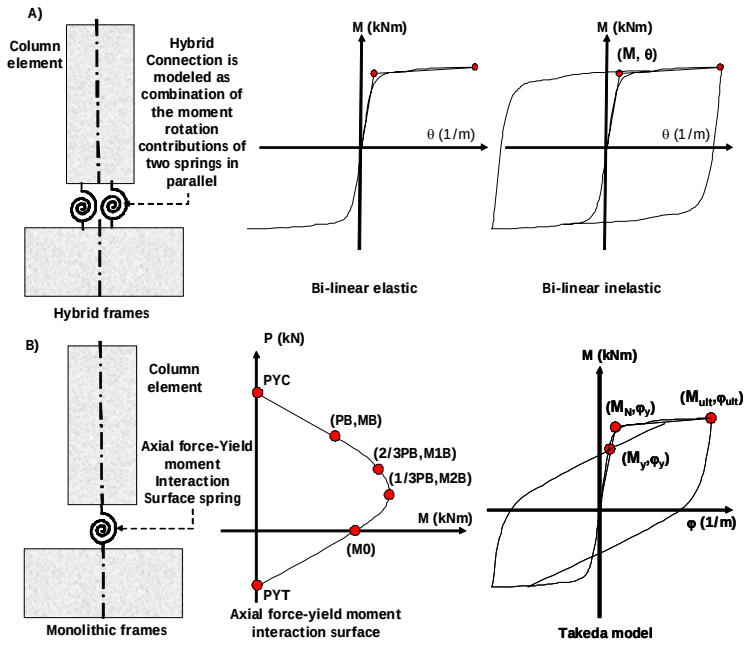

Figure 7.8. Modelling at column base: A) Hybrid frames B) Monolithic frames.

The frames provided the only form of lateral response resistance in the longitudinal direction and were designed following capacity design principles; allowing inelastic action to occur only at column bases and beam ends to form a weak-beam strong-column mechanism. Therefore beams and columns were modelled as elastic elements with a reduced gross inertia of 0.4 and 0.6 as proposed [7.7]. Beam-column connections were model elastically assuming the column width (W_c) and the beam depth (h_b).

Other assumptions were made to the models in order to simplify the analyses and isolate the particular dynamic effects sought in this study:

In order to simplify the analyses and isolate the particular dynamic effects sought in this study, the following assumptions were made with respect to the models used:

- Shear deformation were allowed for in the definition of beam and column elements. The shear area A_s was taken as $5/6h_b$ or b_w, where h_b and b_w are the beam and column depth respectively.

- Floor diaphragms were assumed in-plane with adequate system connections to transfer floor inertia forces to the perimeter frame.

7.6.1 Hybrid PRESSS Excluding (Hy) and Including beam elongation (Hy_beam-elong)

The Hybrid PRESSS type building was modeled using a lumped plasticity model approach with moment rotation properties defined according to the procedure proposed in [7.14]. Two moment rotational springs in parallel (Figure 7.9) were thus implemented at the beam column interface: the post-tensioned steel is modelled with a non-linear elastic hysteretic rule, while a bilinear (elasto-plastic with hardening) hysteretic rule is used for the mild steel contribution.

When considering the hybrid model with beam elongation (Hy_beam-elong), a compound element consisting of multi-axial springs in parallel with elasto-plastic hysteresis behaviour was placed at the interface to represent the reinforcing steel in the plastic hinge region (Figure 7.10) as proposed [7.15]. This approach allows the variation of the neutral axis position at the joint opening. The multiple compression only springs were evenly distributed along the joint interface.

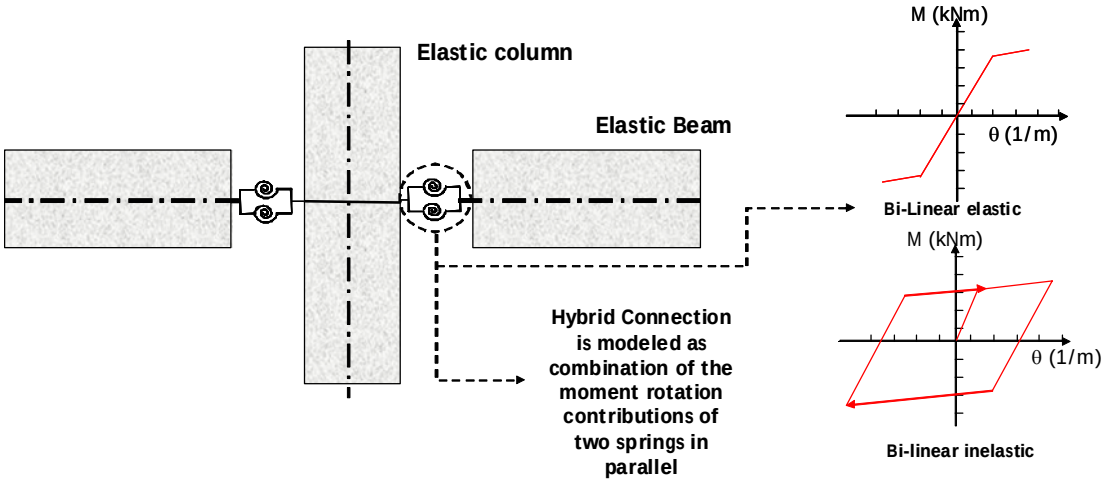

Figure 7.9 Hybrid PRESSS model excluding beam elongation

The compound element will have an axial stiffness determined by $A_s E / L_p$ where A_s is the area of the mild steel provided, E the steel modulus of elasticity and L_p the plastic length which can be evaluated as $L_p = L_{unb} + 0.022 d_b f_y$ [7.8].

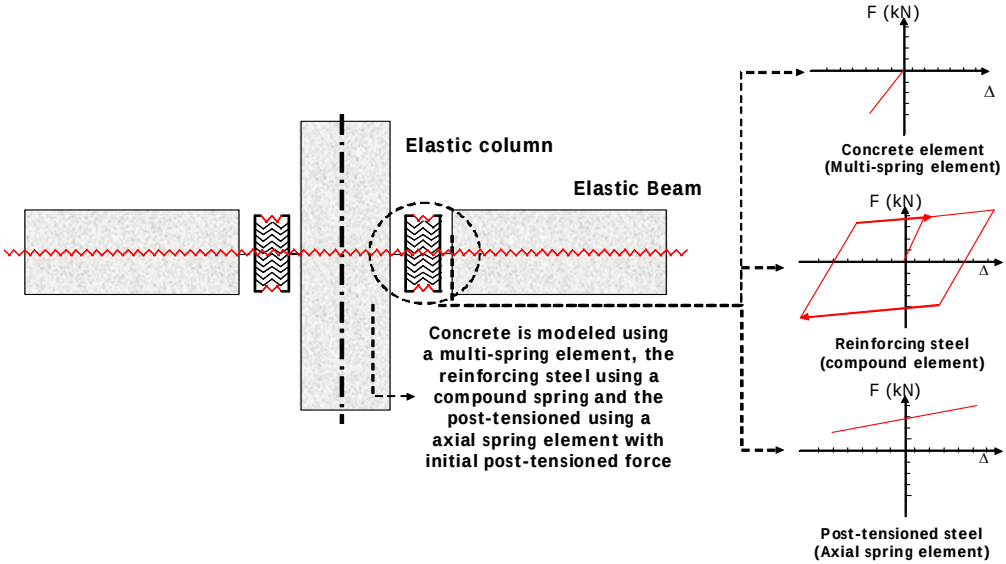

Figure 7.10 Hybrid PRESSS model including beam elongation

The post-tensioned tendons were modelled with a spring element connected from end to end of the exterior columns with an initial post-tensioned force applied on the hysteresis model (Figure 7.10). The axial stiffness was assumed $A_{pt} E / L_{base}$ where A_{pt} is the area of the post-tensioned tendons, E the steel modulus of elasticity and L_{base} the total length between exterior columns.

The concrete is represented using a multi-spring element with a gap-hysteresis loop (compression-only behaviour) with axial stiffness $A_g f'c / h_b$ where A_g is the beam section area, $f'c$ the compressive strength of the concrete and h_b the beam section depth (Figure 7.10). A calibration factor was required to include the interaction of the post-tensioned tendon forces and the multi-spring element. Additionally, the combination of axial stiffness in parallel to the multi spring and beam elements was taken into account to represent the total stiffness of the beam element model without beam elongation.

Shear was transfered across the interface by slaving vertically the nodes at the beam end and column face while the horizontal displacements and the rotations of the nodes are independent.

7.6.2 Hybrid Non-tearing (Hy_non-tear)

The 5 storey Hybrid Non-tearing building was modelled considering two types of model: the first model used moment rotational springs at the beam column interface and the second model used a axial spring model. The 10-storey frame building was modelled using moment-rotational springs.

For the moment rotational model the post-tensioned tendons were modelled with a linear elastic hysteresis behaviour with an initial post-tensioned force $M_{pt\,ini}$, and a slope corresponding to the increase in the initial post-tensioned moment by ΔM_{pt} at the design drift level, while the external energy dissipater was model with a bi-linear inelastic hysteresis behaviour (Figure 7.11).

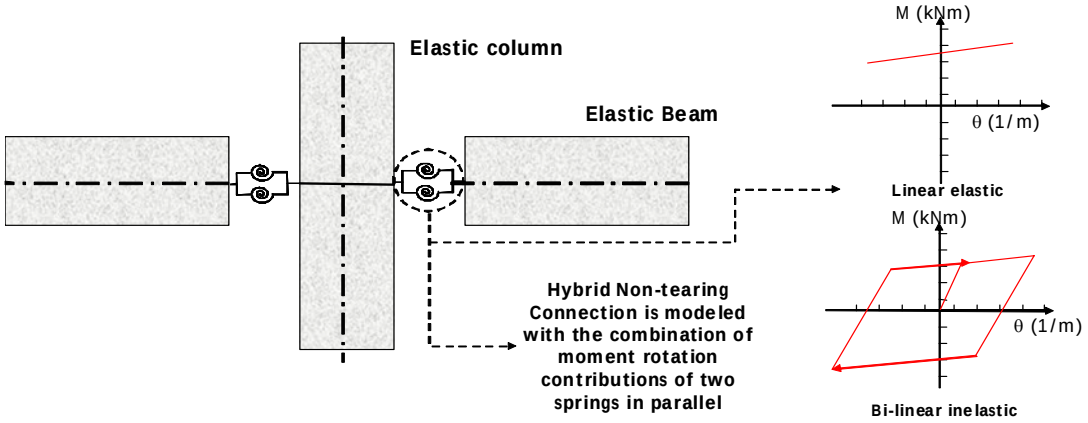

Figure 7.11 Hybrid non-tearing moment rotation model

This longitudinal spring model uses axial stiffness as input parameters (Figure 7.12). The monohinge was modelled using a linear elastic hysteresis. The axial and transversal stiffness was modelled with a high value which represents the steel hinge. Although the monohinge will be in compression only due to the high axial forces in the tendons the element could also be modelled as an elastic element with only compression stiffness.

The external energy dissipaters were modelled using a longitudinal spring with a bi-linear inelastic hysteresis with an axial stiffness determined by $A_s E / L_{unb}$ where A_s is the area of the mild steel provided, E the steel modulus of elasticity and L_{unb} the unbonded length of the dissipater which normally corresponds to the fuse length.

The post-tensioned tendons were modelled with a spring element connected from the centrelines of the columns with an initial post-tensioned force applied on the hysteresis model (Figure

7.12). The axial stiffness was assumed $A_{pt}E/L_b$ where A_{pt} is the area of the post-tensioned tendons, E the steel modulus of elasticity and L_b the bay length between columns.

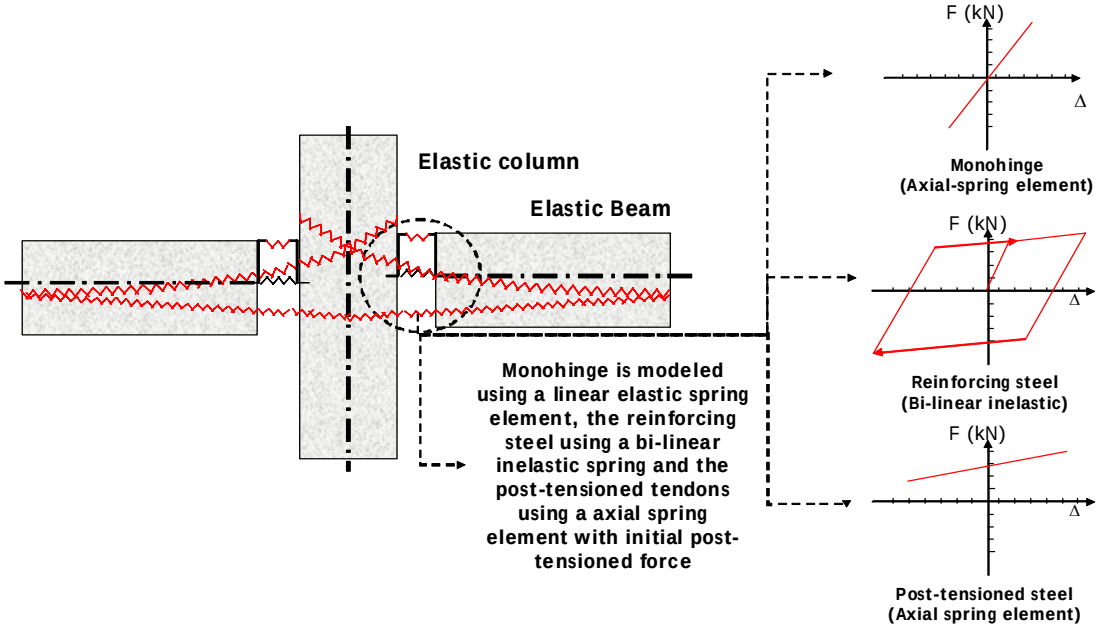

Figure 7.12 Hybrid non-tearing axial spring model

7.6.3 Monolithic excluding beam elongation (Mon) and including beam elongation (Mon_beam-elong)

A simple inelastic rotational spring model (Figure 7.13) was used in the Monolithic model excluding beam elongation to simulate the plastic hinge region in the beam-column joint region with Takeda hysteresis rule implemented in the Ruaumoko program [7.9] assuming an unloading coefficient $\alpha = 0.5$ and reloading coefficient $\beta = 0.2$.

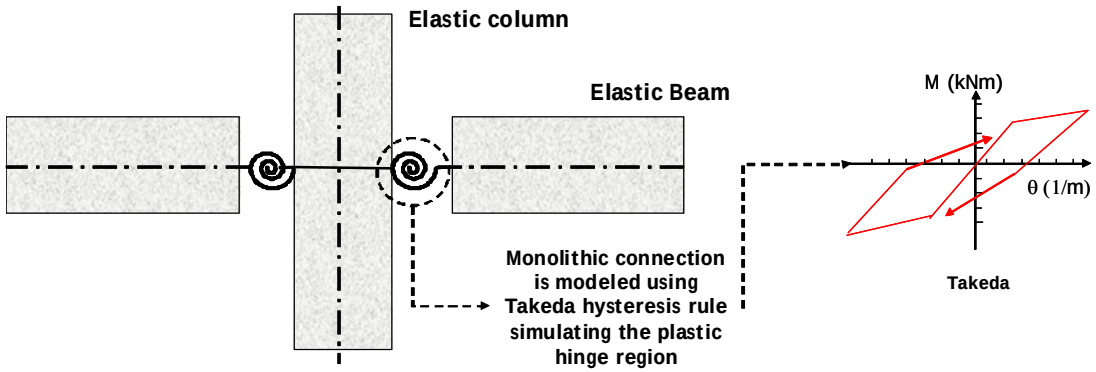

Figure 7.13 Monolithic beam column model excluding beam elongation.

In order to include beam elongation effects in the Mon_beam-elong model, a compound element is placed at the interface to represent the reinforcing steel in the plastic hinge region using elasto-plastic hysteresis behaviour (Figure 7.14).

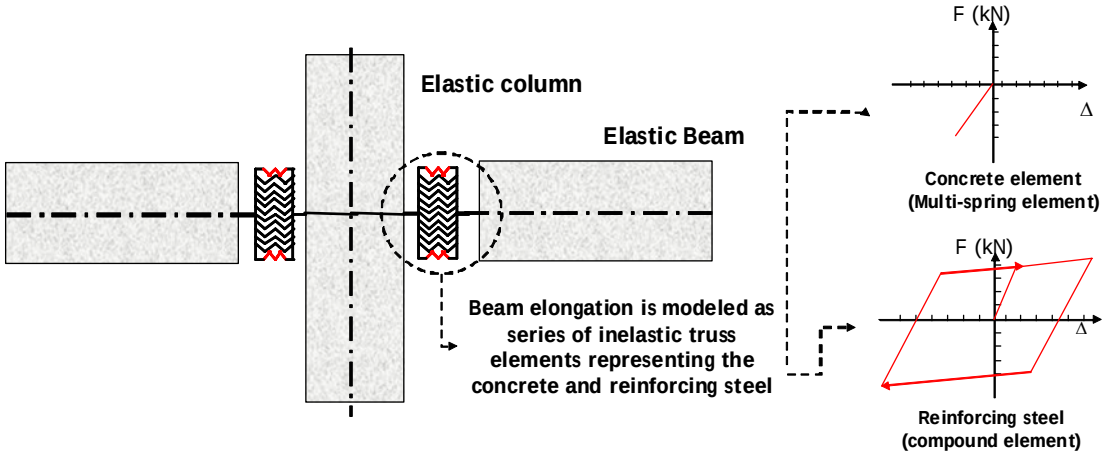

Figure 7.14 Monolithic beam column model including beam elongation

The concrete is represented by a multi-spring element with Bi-linear with slackness hysteresis rule which only acted in compression. The axial stiffness consisted of the gross area of the beam section times the concrete modulus of elasticity and divided by plastic hinge length given by the plastic hinge length assumed as $Lp = 0.08l + 0.022d_b f_y$ [7.8] where l is the distance between the maximum moment and the inflection point, d_b the bar diameter and f_y is the yield strength of the reinforcement.

No plastic deformations were allowed in the concrete to avoid instability in the frame model and the strength/stiffness degradation due to cyclic loading is neglected. Shear is transferred across the interface by vertically slaving the nodes at the beam end and column face while the horizontal displacements and the rotations of the nodes are independent.

The calibration of the stiffness of the beam element was increased considering that the multi-spring elements work in series with the beam element which beam axial force-moment interaction is included.

7.7 ADAPTIVE PUSH-OVER ANALYSIS

A lateral load, initially distributed in an inverse triangular shape, was applied to the frames and pushed until a 2.0% and 1.5% of top roof displacement which is equivalent to 380mm and 570mm for the 5 and 10 storeys frames respectively.

7.7.1 5-Storey Models

7.7.1.1 Comparison between moment rotation and axial spring models

Comparison between total base shear vs. roof displacement for the moment rotational model and axial model is presented in Figure 7.15-left with identical results.

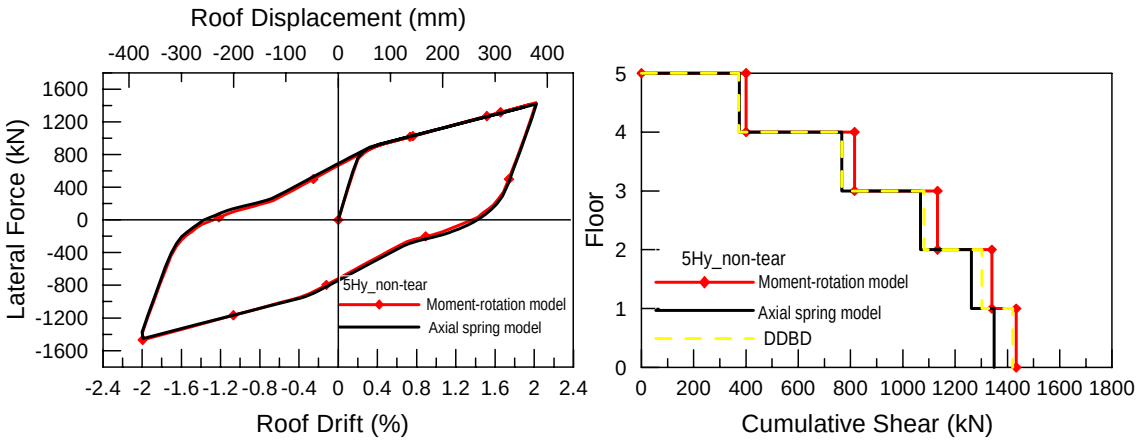

Figure 7.15 5-storey frame comparison model: Total base shear-roof drift (left) and Cumulative inter-storey shear (right).

The cumulative inter-storey shear (Figure 7.15-right) showed small differences especially at the bottom storeys, however the results are very similar. Considering the number of nodes and the specific node coordinates to generate the geometry and create the proper action in the joint, in addition to the increase in number of elements that the longitudinal spring model requires, the moment rotational model seems to be more appropriate. Although, when the determination of more refined internal force distributions in the elements (e.g. beam axial forces due to post-tensioned tendons) the axial model is more appropriate.

7.7.1.2 Total base shear

Figure 7.16 shows the total base shear for the 5-storey models until the frames reached 2.0% roof drift (where drift is defined as the displacement of the exterior column at the top floor divided by the building height). The base shear corresponding to the model Hy_non tear has a total base shear at 2.0% roof drift of 1434 kN, 3.5% and 6.3% higher than Hy_beam elong and Hy models respectively.

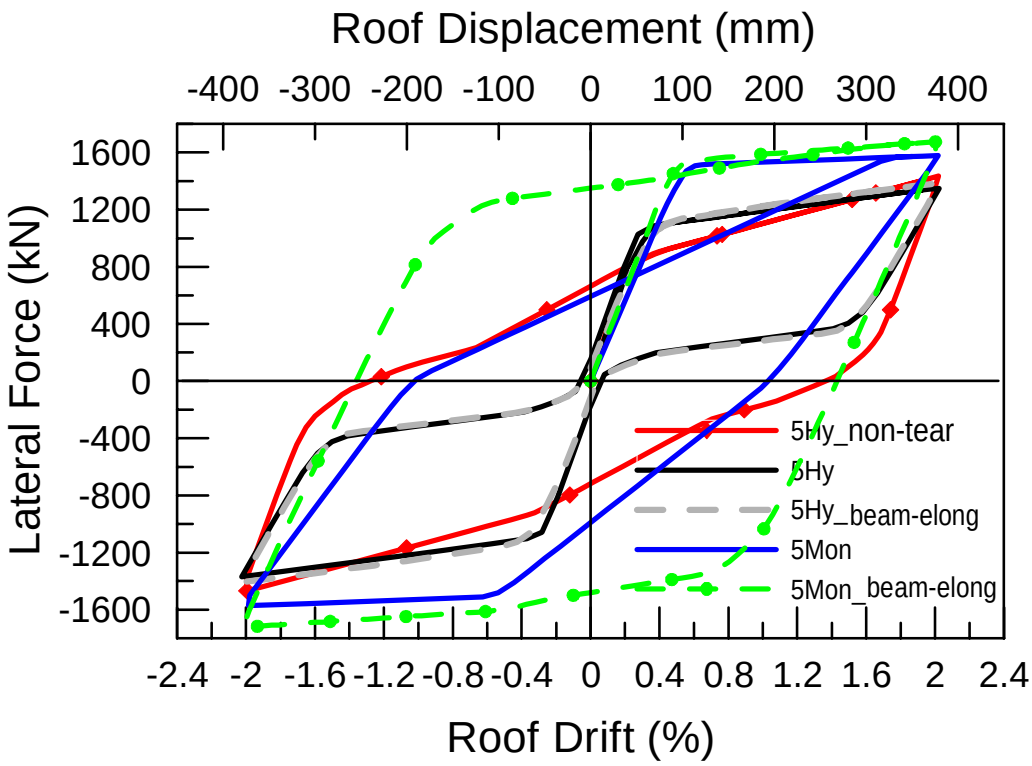

Figure 7.16 5-storey models: Total base shear-roof drift

Similarly, Figure 7.16 also shows the total base shear of the monolithic models excluding and including beam elongation. The Mon_beam-elong model was the strongest of all the models. At 2.0% roof drift, the base shear was 1673 kN, 4.4% and 16.6% higher than the Mon and Hy_non tear models.

Conversely, for a given design load or base shear, the Mon_beam-elong model underwent less deformation than the Mon model when frames were in the post-elastic range. Results for this analysis confirm that Hybrid PRESSS frame systems and Hybrid non-tearing connections would be in general more flexible, though reaching the target strength at a given level of drift. It is worth noting though that the initial stiffness up to the yielding of the mild steel bars (at around 0.4% roof drift) is similar between all models. Thus, the system will maintain its natural and desired monolithic behaviour for small intensity earthquakes (i.e. low return period).

Figure 7.17 shows the cumulative shear for the 5 storey models. It can be seen that the hybrid PRESSS model has very similar cumulative shear profile as the direct displacement based design (DDBD) and similar results are obtained for Hy_beam elong and Hy_non tear models. Higher cumulative inter-storey shears are observed for the Mom and Mom_beam elong models.

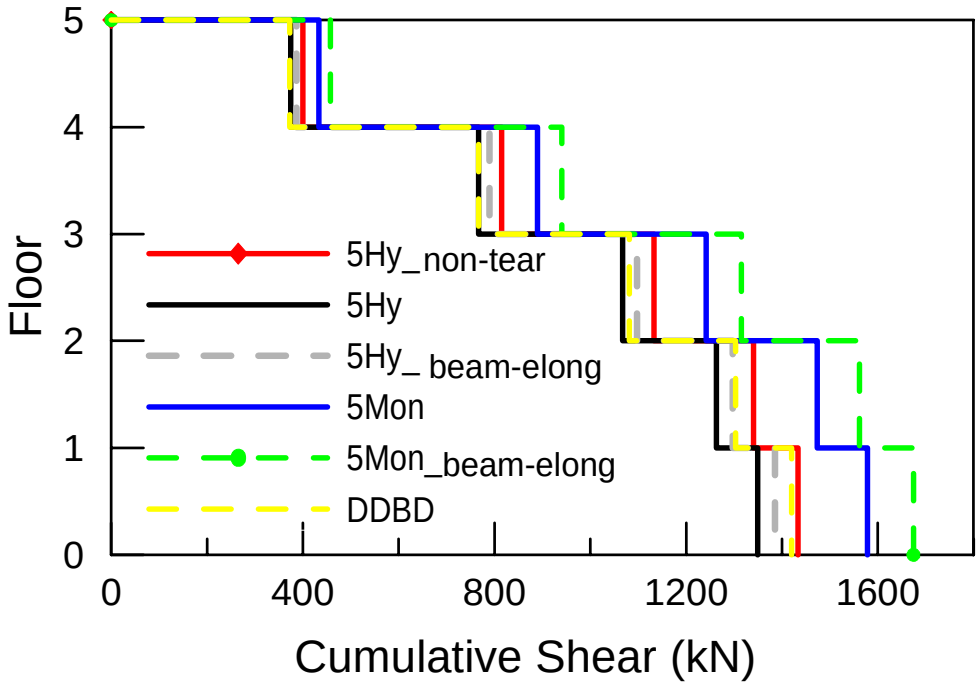

Figure 7.17 5-storey models: Cumulative inter-storey shear (right)

7.7.1.3 Equivalent viscous damping

The equivalent viscous damping ratio is defined as the energy dissipated in a vibration cycle of the actual structure to an equivalent viscous system [7.16]. For a structure, the resisting force-displacement relation obtained under cyclic loading is illustrated in Figure 7.18. The energy dissipated in the structure is given by the total area A_{Total} enclosed by the hysteresis loop and the elastic area $A_{elastic}$ is calculated from the assumed linear elastic behaviour based on the secant stiffness of the system. This definition is formulated by equation (7.25).

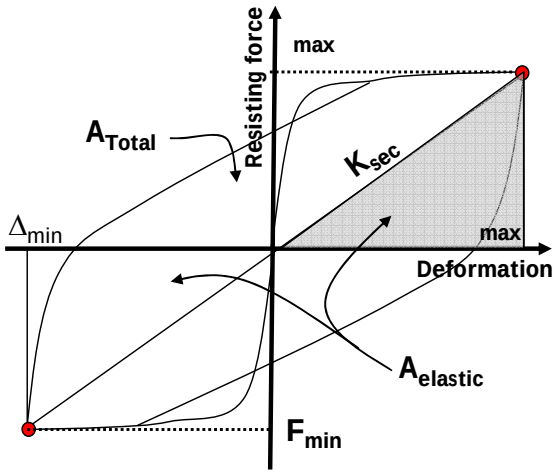

Figure 7.18 Secant stiffness and equivalent viscous damping ratio representation.

$$\xi_{eq} = \frac{A_{Total}}{4\pi A_{elastic}} \tag{7.25}$$

To discuss the energy dissipation characteristics of the frames, the equivalent viscous damping ratio (ξ_{eq}) was calculated under the total base shear – top roof drift and can be obtained at the effective height. Table 7.13 shows the results obtained for the 5-storey frame models.

The equivalent viscous damping for the Hy and Hy_beam elong 5 storey models was 16.9% and 17.0% viscous damping at 2.0% roof drift. The Hybrid non tearing model shows an increase of the energy dissipated of about 47% with respect of the Hy model. Similar results were obtained for the monolithic frame while the monolithic excluding and including beam elongation shows an equivalent viscous damping of 24.9% and 37.1% respectively.

Table 7.13 Equivalent viscous damping for 5 storey models at 2.0% maximum roof drift.

Model	ξ_{eq} (%)
	5 storeys
Hy	16.9
Hy_non tear	24.8
Hy_beam-elong	17.0
Mon	24.9
Mon_beam-elong	37.1

7.7.1.4 Effect of beam axial elongation

Figure 7.19-left shows the exterior columns horizontal displacements in each floor at 2.0% top roof drift ratio for Hy, Hy_beam-elong and Hy_non-tear models. As a result of beam elongation, a different column rotation is recorded at the first story. The beam elongation in the Hy_beam-elong at the first floor was 33mm, while value of 41mm was recorded for the second storey. The elongation of the beams in each bay of the frame corresponds to 1.2% and 1.5% of the member depth respectively. It is clear that the lateral column displacement of the Hy model is, approximately, an average of the two lateral displacements of the Hy_beam-elong model.

Figure 7.19-right shows very similar results for the Mon_beam-elong and the Hy_non-tear models. The hybrid non-tear have no elongation. However, the beam elongation in the Mon_beam-elong at the first floor was 38mm, while for the second floor was 48mm. These elongations of the beams in each bay of the frame are 1.3% and 1.7% of the member depth for the first and second floor respectively.

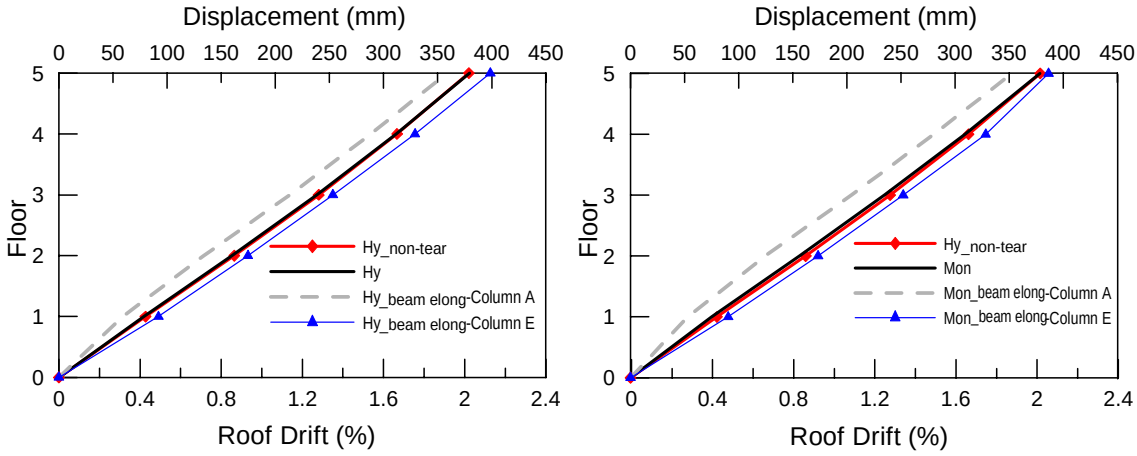

Figure 7.19 5-Storey models: column floor displacement vs. roof drift for Hybrid systems (left) and Monolithic systems (right).

Table 7.14 presents the numerical results obtained as the differences in the lateral displacement of the right and left exterior column at each floor for the 5 frame models including beam elongation. It appears that the total beam elongation at the first floor is restricted by the foundation. The elongation of the beam in each bay of the 5 storey frame is between 1.3% and 1.7% of the beam height. These ranges compare well with the reported range for cast-in-place reinforced concrete frames of 2% to 4% [7.17].

Table 7.14 Exterior column floor horizontal displacements for 5Hy_beam-elong and 5Mon_beam-elong models.

Floor	5 storeys			
	$H_{y\_beam\text{-}elong}$ (mm)	$\%h_b$	$M_{on\_beam\text{-}elong}$ (mm)	$\%h_b$
0	0.0	0.0	0.0	0.0
1	33.0	1.2	37.5	1.3
2	40.9	1.5	48.7	1.7
3	39.7	1.4	48.0	1.7
4	41.0	1.5	48.1	1.7
5	39.8	1.4	33.8	1.2

The increase in the beam length due to elongation is one of the main effects of beam elongation which is restricted by the foundation inducing axial compression/tension forces in beams at different floors. Also variations in the beam elongation at different floors may cause the same effect. Therefore, the axial forces that develop in the beams from restrained elongation (compression) or from restraining beam elongation of adjacent floors (tension) are denoted as axial forces in beams. As a result of these axial forces, the bending moment capacity of the beam connections may be increased or decreased with a loss or gain of ductility.

The elongation of the beams induces bending moments in columns. The additional bending moments are called secondary moments in columns due to the beam elongation and are generally proportional to the distance of the column from the frame centreline. These two effects cause self-equilibrating forces in the frame including the forces at the foundation. These forces increase the moment capacity of beams and columns at certain locations, but decrease the moment capacity at other locations. Thus, the global frame behaviour is not affected by the beam elongation, and the frame base shear-roof displacement curves are similar for the Hy and Hy_beam-elong models and for the Mon and Mon_beam-elong models as shown in Figure 7.16. However, the local element behaviour is significantly affected by the beam elongation and therefore is carefully studied in this research.

7.7.1.5 Axial forces in beams

Figures 7.20 and 7.21 shows the beam axial forces for the 5-storey frame for the four bay first and second floors due to beam elongation. In the Figure 7.20 which corresponds to the Hybrid model including beam elongation the beams from the first floor started from a compression load of 550kN while for the second floor is about 600kN. The prestress force may be changed by flexure in the columns caused by the prestress as presented in other research [7.18]. At maximum top displacements, there is a linear increase of the beam axial force for the first floors while for the second floor the beam axial force remains almost constant.

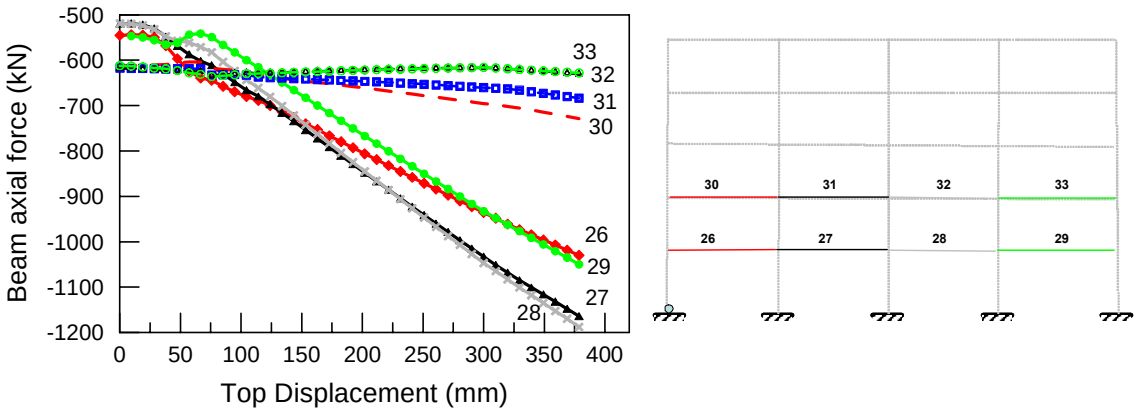

Figure 7.20 5-Storey models: axial force in beams for the 5Hy_beam-elong (left) and beam numbers for the frame (right).

The type of axial force (compression or tension) developed in the rest of the floors is not easily predicted, and depends on the extended restraining effect of the foundation and the relative beam elongation at different floors. The maximum axial forces for the 5Hy_beam-elong model from the first floor level to the roof, are -1118, -731, -647, -500 and -388kN, respectively,

which corresponds to 86, 22, 8, 66 and 29% of the initial post-tensioning forces which were 600kN for the 1st and 3rd floors and 300kN for the 4th and 5th floors.

Figure 7.21-left corresponds to the beam axial forces in the 5-storey Hybrid non-tearing model using longitudinal spring elements. Similar to what was presented by the 5Hy_beam-elong model, beam axial forces from the first floor started from a compression force of 1000kN while for the second floor is about 1100 kN. Similarly as for the 5Hy_beam-elong model, the prestress force changed by flexure in the columns caused by the prestress. At maximum top displacements beam axial forces remain constant for the first and second floors.

The maximum axial forces for the 5Hy_non-tear model from the first floor to the roof level are: -1034, -1129, -1077, -648 and -541kN, respectively, which corresponds to 16, 6, 11% less of the initial post-tensioning force for the 1st and 3rd floors ($T_{pt\ ini}$ =1200kN). For the 4th floor an increase of 8% of the initial post-tensioned is observed followed by a reduction of 11% for the 5th floor ($T_{pt\ ini}$ =600kN). By comparison, the maximum axial forces in the first two floors of frame Hy_beam-elong model represents 86% and 22% of the initial post-tensioning forces. Thus the effect of beam elongation on the behaviour for the Hy_beam-elong model is larger than that of the Hy_non tear model.

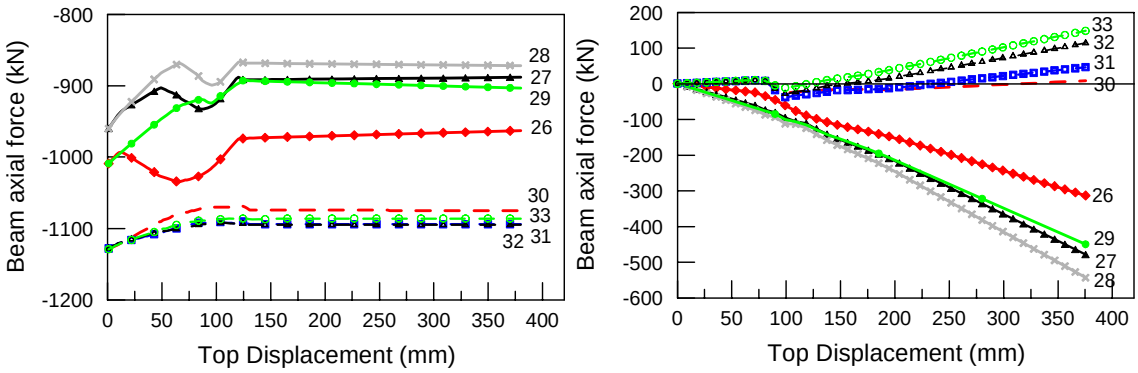

Figure 7.21 Axial force in beams for 5Hy_non-tear (left) and 5Mon_beam-elong models (right).

Figure 7.21-right shows the axial forces in the beams for the four bays of the first and second floors due to beam elongation. In the figure, all curves start from zero forces and after applying the lateral forces, the first and second floor beams are mostly under axial compression and tension forces, respectively.

This is usually the case due to the horizontal restraint provided to the columns by the foundation. However, the type of axial force which is compression for the first floor and tension for the second floor developed in the rest of the floors is not easily predicted, and

depends on the extended restraint effect of the foundation and the relative beam elongation at different floors. The maximum axial forces for the Mon model, for the first floor level to the roof, are -543, 148, 184, -110 and 69kN, respectively. The foundation restraining effect is dominant for the floors near the foundation, while the relative beam elongation effect may be dominant for the upper stories.

7.7.1.6 Effect of axial forces on beam flexural behaviour

Figure 7.22 shows the beam end moment for the first and second floor vs. roof displacement for the 5Hy and 5Hy_beam-elong models. The difference between the 5Hy and 5Hy_beam elongation models represents the axial force effect. Figure 7.22-left shows that the effect of axial compression force on the first floor beams is to decrease the bending moment capacity, decreasing the yield rotation, and increasing the ultimate rotation of the beams. The effect of axial compression force in the beam second floors not only reduces the bending moment capacity but also the yield moment. The largest increase and decrease in bending moment capacity due to axial compression forces was 12% and -20% respectively.

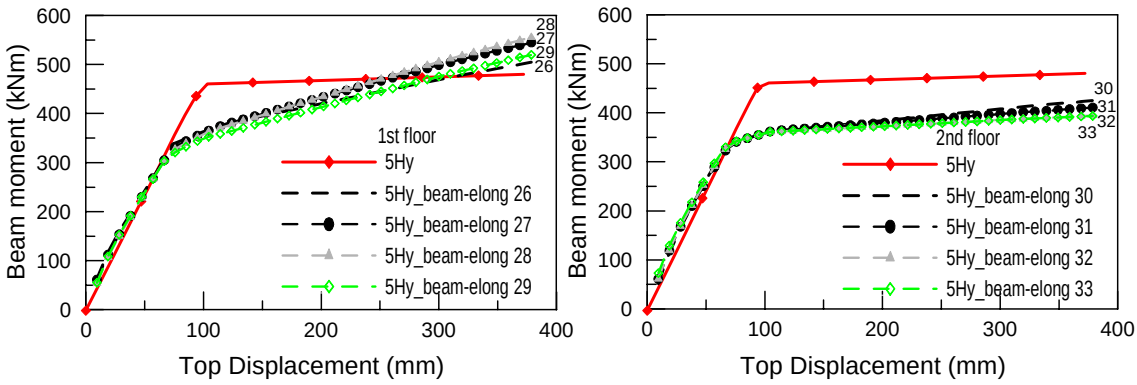

Figure 7.22 Exterior beam end moment of the first floor (left) and second floor (right) for the 5Hy and 5Hy_beam-elong models.

Figure 7.23 shows the beam end moment for the first and second floor vs. roof displacement for the 5Hy_non-tear model using the longitudinal spring model which takes into account the axial compression forces of the post-tensioning tendons which also introduces an initial bending moment at the beam ends corresponding to the initial post-tensioned moments at the connections.

The Figure 7.23-left shows that the effect of axial compression force on the beam moments for the first floor changed slightly between bays. In contrast, the effect of axial compression force on the beam moments for the second floors remains constant (Figure 7.23-right). The increase

in bending moment capacity due to axial compression forces in the first floor was within the 5%.

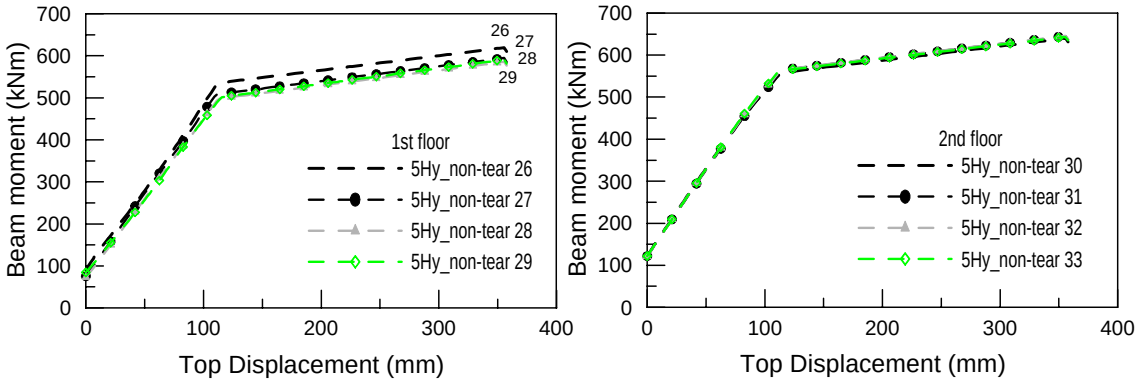

Figure 7.23 Exterior beam end moment of the first floor (left) and second floor (right) for the 5Hy_non-tear frame using axial spring elements.

Figure 7.24 shows the beam end moment for the first and second floor vs. roof displacement for the 5Mon and 5Mon_beam-elong models. The difference between the 5Mon and 5Mon_beam elong models represents the axial force effect.

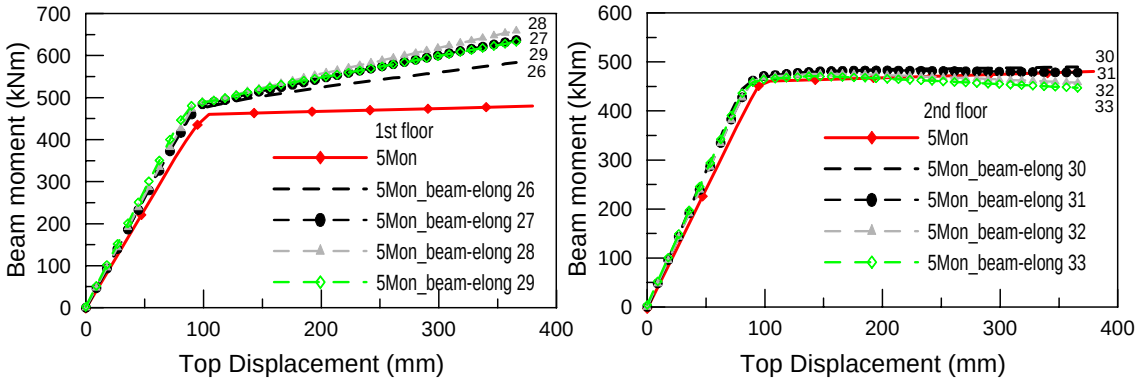

Figure 7.24 Exterior beam end moment of the first floor (left) and second floor (right) for the 5Mon and 5Mon_beam-elong models.

Figure 7.24-left shows that the effect of axial compression force on the first floor beams is to increase the bending moment capacity, increase the yield rotation, and decrease the ultimate rotation of the beams. In contrast, the effect of axial tension force in the beam second floors is to decrease the bending moment capacity, decrease the yield rotation, and increase ultimate rotation of the beams. The largest increase and decrease in bending moment capacity due to axial compression forces was 39% and -8% respectively.

7.7.1.7 Column flexural demands

Figure 7.25 shows the maximum column flexural demands normalized by the beam bending moment for the 5Hy and 5Hy_beam-elong models at the maximum top displacement which also can reflect the effects of the beam elongation on the column flexural demand. Figure 7.25-left shows flexural demands on exterior columns and Figure 7.25-right shows flexural demands on interior columns.

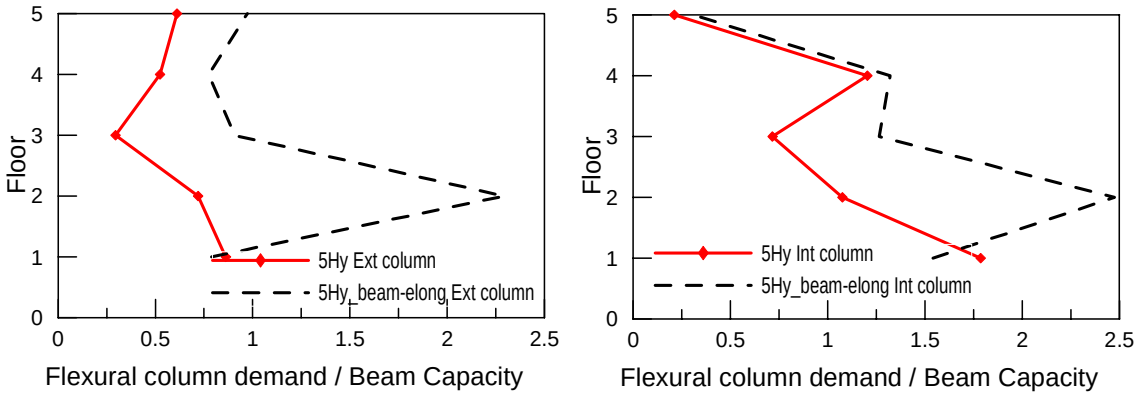

Figure 7.25 Maximum column flexural demands of 5Hy and 5Hy_beam-elong models: Exterior columns (left) and Interior column (right).

The 5Hy model does not include the effect of beam elongation. As shown in the Figure 7.25, the column flexural demands for the 5Hy_beam-elong model are always greater than those of the 5Hy model, and the differences are significant at locations where the beam elongation effect is more pronounced specially at the second floor. It should be noted that the differences in flexural demands for the 5Hy_beam-elong model and the 5Hy models include the secondary moments in columns from restraining the elongation of the beams, as well as, the extra moment transferred to columns by equilibrium due to the increase in the bending moment capacity of the beams.

Capacity design according with the NZS3101 [7.4] requires that for frames where sidesway mechanisms with plastic hinges forming only in columns are not permitted at the ultimate limit state, the design moments and axial loads in columns shall include the effect of possible beam overstrength, concurrent seismic forces, and magnification of column moments due to dynamic effects, in order to provide a high degree of protection against the formation of a column sway mechanism.

The design detail requires the overstrength actions in the columns at each potential plastic primary plastic region on the basis of the detailing used for the region, the critical load

combination which may occur in each region and the likely maximum material strength in each potential plastic region.

When determining the design action in columns the nominal flexural strength of the columns shall be equal to or greater than that required to sustain overstrength moments that act on the column from all beam intersecting the column amplified by appropriate dynamic magnification factor. The design overstrength factors for the column flexural capacity required for the 5Hy_beam-elong model requires more than 2.25 and 2.5 times for the exterior and interior columns respectively.

Figure 7.26 shows the maximum column flexural demands for the columns of the 5Hy_non-tear model for the moment rotational and the axial spring models at the maximum top displacement. The 5Hy_non-tear using moment rotational spring model does not include the effect of beam axial forces.

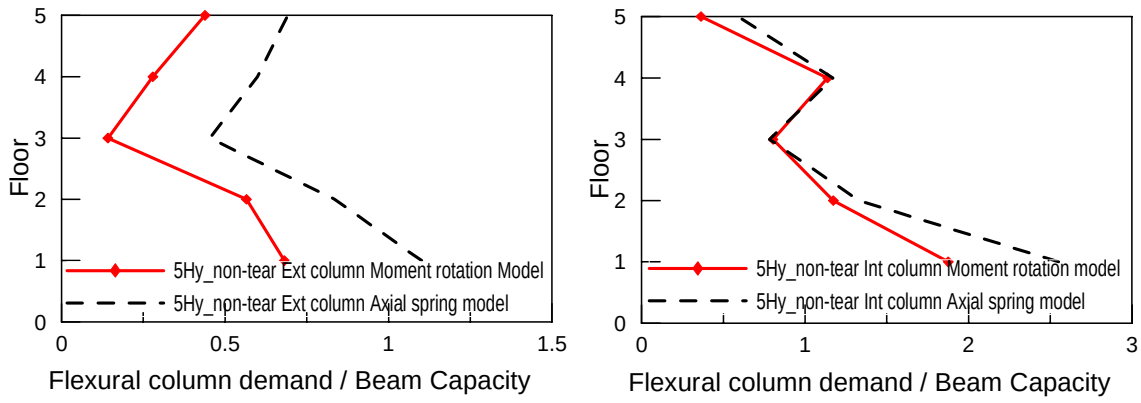

Figure 7.26 Maximum column flexural demands of 5Hy_non-tear with moment rotational moment and 5Hy-non-tear using axial spring models: Exterior columns (left) and Interior column (right).

The column flexural demands for the 5Hy_non-tear using axial spring model are always greater or equal than those of the 5Hy_non-tear with moment rotational model. Comparison between the two models shows that the flexural column demand for the 5Hy_non-tear using an axial spring model are always greater or equal than those of the 5Hy_non-tear with moment rotational model.

For the exterior column, this difference is because the initial post-tensioned force induced an additional initial moment which is not in equilibrium when compared to the flexural column demand in the interior columns which cancels out from the left and right initial moments.

For capacity design, the design overstrength factors for the flexural column demand obtained for the 5Hy_non-tear-model was 1.25 and 2.5 for the exterior and interior columns respectively.

Figure 7.27 displays the effects of the beam elongation on the column flexural demand for the 5Mon and 5Mon_beam-elong models. Similar as found for the 5Hy_beam-elong and 5Hy_non-tear models, the column flexural demands for the 5Mon_beam-elong model are greater than those of the 5Mon model except for the first floor where the effects of beam elongation are not taken into account have more flexural column demand. However, the differences between the two models are significant at locations where the beam elongation effect is more pronounced specially at the second floor.

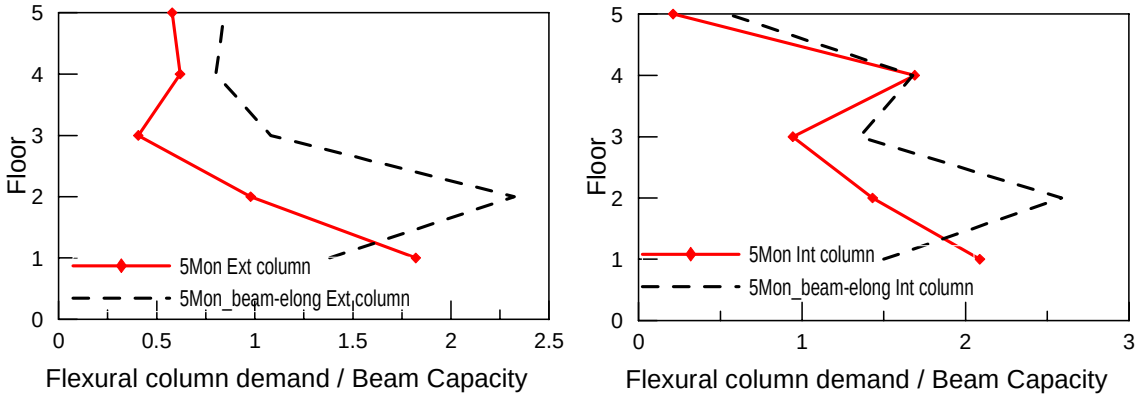

Figure 7.27 Maximum column flexural demands of 5Mon and 5Mon_beam-elong models: Exterior columns (left) and Interior column (right).

For capacity design requirements, the design overstrength factors obtained for the column flexural capacity for the 5Mon_beam-elong model were 2.25 and 2.5 for the exterior and interior columns respectively.

7.7.2 10-Storey Models

7.7.2.1 Total base shear

For the 10-storey building prototype models, the Hy_non-tear model was the strongest of all the models (Figure 7.28). The total base shear of Hy_non tear was 2763kN at 1.5% of roof drift, 8.9% and 7.8% higher than Hy and Hy_beam-elong models respectively. Similarly, the total base shear of the monolithic models excluding and including beam elongation were 8.3% and 6.5% lower than Hy_non-tear model respectively.

However, the Hy_non tear model shows an initial stiffness similar to the other system until the first yielding of the bars at 0.3% of the total roof displacement, but very high post-linear stiffness induced by the sum of all post-tensioned moment contributions at each connection.

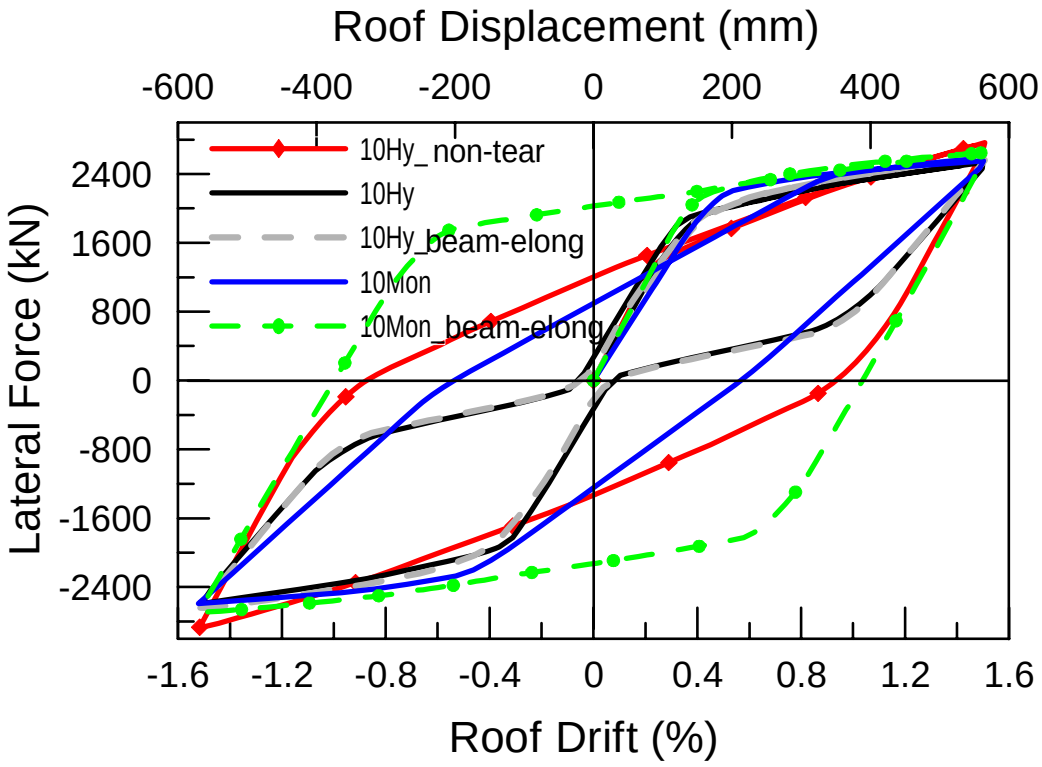

Figure 7.28 10-storey models: Total base shear-roof drift (left)

Similar to that found for the 5-storey models, for a given design load or base shear, the Mon model underwent less deformation than the Hy and Hy_non tear models when frames were in the post-elastic range. Therefore, as a result, the Hy and Hy_non-tear models would, in general, be more flexible, though reaching the target strength at a given level of drift. It is worth noting though that the initial stiffness, up to the yielding of the mild steel bars (at around 0.3% roof drift) is similar between all models. Thus, the Hybrid non tearing model will maintain its natural and desired monolithic behaviour for small intensity earthquakes (i.e. low return period).

Figure 7.29 shows the cumulative shear for the 10 storey models. It can be seen that the Hy and Mon models have similar cumulative shear profiles when compared with the direct displacement base design. However, for the Hy_non tear model an increase of the cumulative shear for the first 5 floors is observed when it is compared with the Hy and Mon models including DBDD cumulative shear profile.

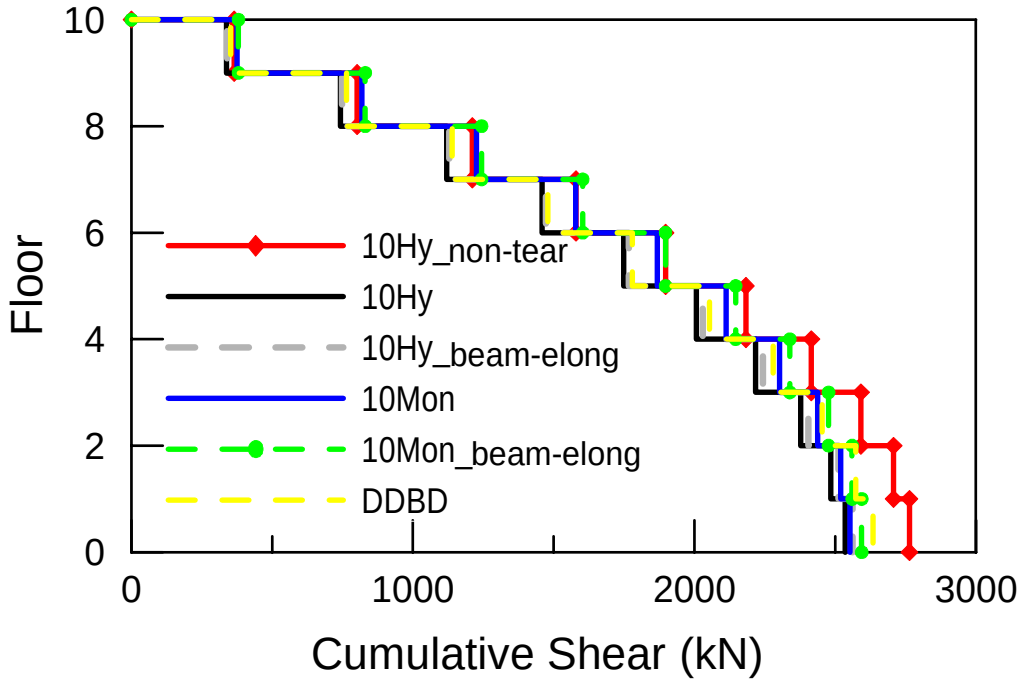

Figure 7.29 10-storey models: Cumulative inter-storey shear (right)

7.7.2.2 Equivalent viscous damping

Table 7.15 present the equivalent viscous damping for the 10 storey Hy and Hy_beam elong models with the same value of 14.8% at 1.5% roof drift. The Hybrid non tearing model shows an increase of the energy dissipated of about 47% with respect to the Hy model. Similar results were obtained for the monolithic frame while the 10Mon and 10Mon_beam-elong showed an equivalent viscous damping of 18.9% and 34% of equivalent viscous damping respectively.

Table 7.15 Equivalent viscous damping for 10 storey models at 1.5% maximum roof drift.

Model	ξ_{eq} (%)
	10 storeys
Hy	14.8
Hy_non tear	21.9
H_y_beam-elong	14.8
Mon	18.9
Mon_beam-elong	34.3

7.7.2.3 Effect of beam axial elongation

Figure 7.30-left shows the exterior columns horizontal displacements in each floor at 1.5% top roof drift ratio for Hy, Hy_beam-elong and Hy_non-tear models. As a result beam elongation in the Hy_beam-elong model at the first and second floors were 31.5mm and 39.6mm respectively.

A reduction of the horizontal displacement is observed from the third to tenth storey where no beam elongation was observed.

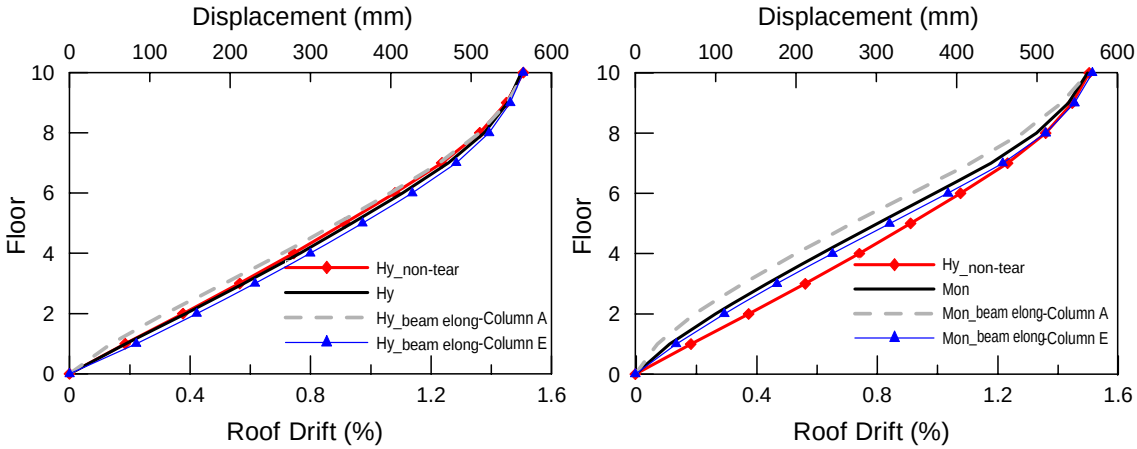

Figure 7.30 10-Storey models: column floor displacement vs. roof drift for Hybrid systems (left) and Monolithic systems (right).

Figure 7.30-right shows very similar results for the Mon_beam elong and the Hy_non-tear models. The beam elongation in the Mon_beam-elong at the first floor was 23.2mm with an increase for the upper storeys from 37.1mm to 46.9mm to the fifth floor and a reduction for the sixth floor to the top floor up from 46.3mm to 5.9mm (6.6% to 0.8% of the member depth) respectively.

Table 7.16 presents the numerical results obtained as the differences in the lateral displacement of the right and left exterior column at each floor for the 10 frame models including beam elongation. It appears that the total beam elongation at the first floor is restricted by the foundation. The elongation of the beam in each bay of the 10 storey frame is between 0% (means no beam elongation) to 1.7% of the beam depth. These ranges compare well with the reported range for cast-in-place reinforced concrete frames of 2% to 4% [7.13].

Notice that the horizontal displacements are smaller for the Hy_beam-elong model when they are compared with the Mon_beam-elong model due to the post-tensioned tendons that help to close the gap when the structure sways. Also it can be seen that beam elongation effects are very similar at the second storey for the 5 and 10-storey frames. However, along the height, beam elongation is predominantly higher for the 5-storey than the 10-storey frame.

Table 7.16 Exterior column floor horizontal displacements for 10Hy_beam-elong and 10Mon_beam-elong models.

Floor	10 storeys			
	$H_{y\_beam\text{-}elong}$ (mm)	$\%h_b$	$M_{on\_beam\text{-}elong}$ (mm)	$\%h_b$
0	0.0	0.0	0.0	0.0
1	31.5	1.0	23.2	0.7
2	39.6	1.2	37.1	1.2
3	37.8	1.2	42.8	1.3
4	34.4	1.1	45.3	1.4
5	31.4	1.0	46.9	1.5
6	27.6	1.0	46.3	1.7
7	21.1	0.8	40.2	1.4
8	12.0	0.4	28.8	1.0
9	3.6	0.1	16.1	0.6
10	-1.1	0.0	5.9	0.2

7.8 CHAPTER SUMMARY

In this chapter the design and modelling of 5 and 10 multi-storey building prototypes with different solutions have been presented. The buildings were designed for a traditional hybrid PRESSS type solution following direct displacement based design principles in order to ensure that the design limit state was not exceeded, the full distribution of moment and base shear corresponding to a given damage limit state.

The building prototypes have plan dimensions of 24m wide by 30m long. Lateral resistance is provided by three seismic resisting frames in the longitudinal direction detailed to achieve the desired global displacement demand. Two exterior walls provide seismic resistance in the transverse direction. The building is located in Wellington on top of a shallow soil (soil type C) within 2km from the fault and it is given an importance level 2, which requires a design for a return period of 500 years.

The DDBD method provides specific performance criteria as a function of seismic intensity related to the structure; more specifically a target displacement corresponding to a design level earthquake. The procedure requires the structural system to be converted to an equivalent single degree of freedom system having an effective elastic stiffness, effective mass, effective height and damping corresponding to the target displacement (related to the structural ductility).

The selection of the design-drift was 2.0% and 1.5% of the inter-storey drift for the 5 and 10 storey buildings respectively. The reason for the smaller design-drift level of the taller structure was because the code limit of 2% was not achieved by the design simply because the increase in

effective natural period associated with taller structures was not captured by the spectra. Therefore, reducing the target drift from 2.0% to 1.5% will therefore bring the effective natural period within the limits of the design spectra.

As the total base shear was calculated and distributed throughout the structures, the design of the beam members and their connections were considering three different systems for comparison purposes: traditional hybrid PRESSS, Hybrid using non-tearing connection and a monolithic (cast-in-situ or emulation of cast-in-situ concrete) solution.

Beams and columns were modelled by elastic elements with a reduced gross inertia while beam-column connections were modelled elastically assuming the gross area equivalent of the column width and the beam depth sections. The gap opening for the Hybrid PRESSS and Hybrid non-tearing or the plastic hinge region for the monolithic system were modelled using different hysteretic rules assigned to each spring property to correctly represent the inelastic behaviour at the beam-column connection which is evaluated based on a global member compatibility condition. The non-linear finite element program Ruaumoko2D was used in the analyses.

Additionally, the effects of beam elongation increasing the curvature demand (and rotation demand of the ground floor columns) are neglected in common practice. The consequences of these actions were investigated using an appropriate structural model. Therefore, for comparison purposes five different models had been implemented for the two frames to compare the behaviour of the systems: Hybrid PRESSS without beam elongation (Hy), Hybrid PRESSS including beam elongation (Hy_beam-elong), Hybrid non tearing connection (Hy_non-tear), monolithic without beam elongation (Mon) and monolithic including beam elongation (Mon_beam-elong). For the 5 storey Hy_non-tear model two models were considered: the first model was using moment rotational spring at the beam column interface and the second model was using a axial spring model.

Column bases for the Hybrid models were modelled using a rocking connection with two rotational spring elements representing the axial moment contribution and moment contribution of the mild steel. For the monolithic models, an axial force-yield moment interaction surface spring using a Takeda hysteresis model was implemented to account for the interaction between axial force and yield moments representing the monolithic connection.

The two prototype buildings and their different configurations were subjected to push-over analysis to investigate and evaluate the performance of this type of systems to lateral loading. In general, the response of the hybrid system using a non-tearing connection was very

satisfactory under push-over analysis. Results indicated that lateral stiffness was lower for the hybrid non-tearing connection when compared with the traditional hybrid systems. However, the total base shear for the same imposed drift level was very similar. Therefore, as a result, the Hy and Hy_non-tear models would be, in general, more flexible, though reaching the target strength at a given level of drift. It is worth noting though that the initial stiffness up to the yielding of the mild steel bars (at around 0.35% roof drift) is similar between all models. Thus, the Hybrid non tearing model will maintain its natural and desired monolithic behaviour for small intensity earthquakes (i.e. low return period).

Comparison between total base shear vs. roof displacement and cumulative storey shear for the 5Hy_non-tear using moment rotational model and longitudinal model showed the same or very similar results. However, considering the number of nodes and the specific node coordinates to generate the geometry and create the proper action in the joint, in addition to the increase in number of elements that the longitudinal spring model requires, the moment rotational model seems to be more appropriate. Although, when it is required to determine a more refined internal forces distribution in the elements (e.g. beam axial forces due to post-tensioned tendons) the longitudinal model is more appropriate.

For the 5-storey frames, the equivalent viscous damping for the Hy and Hy_beam elong models was 17% viscous damping at 2.0% roof drift. The Hybrid non tearing model shows an increase of the energy dissipated of about 47% with respect of the Hy model while the monolithic excluding and including beam elongation shows an equivalent viscous damping of 24.9% and 37.1% respectively. For the 10 storey Hy and Hy_beam elong models an equivalent viscous damping of 15% at 1.5% roof drift was obtained. The Hybrid non tearing model shows an increase of the energy dissipated of about 47% with respect of the Hy model while the 10Mon and 10Mon_beam-elong shows an equivalent viscous damping of 18.9% and 34% of equivalent viscous damping respectively.

Beam elongation effects change the distribution of moments and shears throughout the frame. For the non tearing solution storey shears remain constant. It can be seen that the traditional monolithic and hybrid PRESSS systems are affected by beam elongation especially in the first storey where the shears were larger. The hybrid model show a reduction of the beam elongation when it is compared with the monolithic model due to the post-tensioned forces which help to close the gap at the connection, specially for the top floors of the 10-storey model where in some cases the columns where pulling together.

For the 5-storey model, beam elongation was higher in the second floor of the frame where the plastic hinge elongated 48.7mm for the monolithic system and 40.9mm for the hybrid system (1.7% and 1.5% of the beam section respectively). For the 10-storey model, beam elongation were also higher on the second floor for the Hybrid model including beam elongation with 39.6mm (1.2% of the beam depth) while for the monolithic model the highest beam elongation occurred on the fifth and sixth floors with 46.9mm and 46.3 (1.5% and 1.7% of the beam depth) respectively. It is important to mention that the beam section reduced from 800mm in the 5^{th} floor to 700mm on the sixth floor.

Axial forces in beams for the 5-storey frames were investigated as a consequence of beam elongation and the increase in the beam length due to elongation restricted by the foundation. Similarly, as a result of these axial forces, bending moment capacity of the beam connections was also investigated. For the 5Hy_beam-elong and 5Hy_non-tear models the first and second floor beams remained in compression.

However, for the 5Mon_beam-elong model the first and second floor beams are mostly under axial compression and tension forces, respectively. This is usually the case due to the horizontal restraint provided to the columns by the foundation. The type of axial force developed in the rest of the floors is not easily predicted, and depends on the extended restraining effect of the foundation and the relative beam elongation at different floors. The foundation restraint effect is dominant for the floors near foundation, while the relative beam elongation effect may be the dominant for the upper storeys.

Also, the elongation of the beams induces bending moments in the columns. The additional bending moments are called secondary moments in columns due to beam elongation and are generally proportional to the distance of the column from the frame centreline. These two effects cause self-equilibrating forces in the frame including the forces at the foundation. These forces increase the moment capacity of beams and columns at certain locations, but decrease the moment capacity at other locations. Thus, the global frame behaviour is not affected by the beam elongation, and the frame base shear-roof displacement curves are similar for the Hy and Hy_beam-elong models and for the Mon and Mon_beam-elong models. However, the local element behaviour is significantly affected by beam elongation and therefore is carefully studied in this research.

Effects of axial forces on beam flexural behaviour indicated that for the 5Hy_beam elong model the bending moment increases the beam capacity at the first floor while reducing the yield moment and the beam capacity at the second floor. For the 5Mon_beam-elong model, results

indicated that the effect of axial compression force on the first floor beams increase the bending moment capacity, increase the yield rotation, and decreases the ultimate rotation of the beams. In contrast, the effect of axial tension force in the beam second floors is to decrease the bending moment capacity, decrease the yield rotation, and increase ultimate rotation of the beams.

Column flexural demands were calculated for the exterior and interior columns of the 5-storey frame models and normalized by the beam bending moment. The 5Hy and 5Mon models do not include the effect of beam elongation and the column flexural demands for the 5Hy_beam-elong and 5Mon_models are always greater than those of the 5Hy and 5Mon models, and the differences are significant at locations where the beam elongation effect is more pronounced specially at the second floor.

For capacity design requirements, the ratio between column over beam flexural capacity for the 5-storey Hybrid and Monolithic including beam elongation models were 2.25 and 2.5 for the exterior and interior columns respectively. For the Hybrid with non-tearing model, this ratio was 1.25 and 2.5 for the exterior and interior columns respectively.

A series of time history analysis will be carried out in Chapter 8 on the models herein presented. Special attention will be given for the Hybrid frames using non-tearing floor connections to investigate and evaluate the performance of this type of system to earthquake loading.

7.9 REFERENCES

7.1 Amaris, A. Pampanin, S., Bull, D., and Carr, A. “Numerical Investigations on the Seismic Response of Multi-storey Hybrid Post-Tensioned Precast Concrete Frames with Non-tearing Floor Connections,” Proceedings of the New Zealand Society of Earthquake Engineering Annual Conference, Christchurch, New Zealand, 2009.

7.2 New Zealand Concrete Society. “PRESSS Design handbook” Editor Stefano Pampanin, 2010.

7.3 New Zealand Standards (NZS). “Structural Design Actions: Permanent, Imposed and other Actions,” NZS1170.1. 2004, Wellington, New Zealand.

7.4 New Zealand Standards (NZS). “Concrete Structures Standard, Part 1: The design of concrete structures,” NZS3101. 2006, Wellington, New Zealand.

7.5 Priestley, M.J.N. Calvi, G.M. and Kowalsky M.J. “Displacement-Based Seismic Design of Structures”. IUSS PRESS, Pavia, Italy. 2007, pp. 721

7.6 New Zealand Standards (NZS). "Appendix B: Special Provisions for the Seismic Design of Ductile Jointed Precast Concrete Structural Systems," NZS3101:2006, Wellington, New Zealand.

7.7 New Zealand Standards (NZS). "Structural Design Actions: Earthquake Actions," NZS1170.5. 2004. Wellington, New Zealand.

7.8 Paulay, T. & M.J.N. Priestley. "Seismic Design of Reinforced Concrete and Masonry Buildings. John Wiley, New York, 1992, 744pp.

7.9 Carr, A. "RUAUMOKO program for Inelastic Dynamic Analysis – User Manual". Department of Civil Engineering, University of Canterbury, Christchurch, New Zealand, 2006

7.10 Fenwick, R.C. and Fong, A., "The Behaviour of Reinforced Concrete beams Under Cyclic Loading," Research Report, Department of Civil Engineering, University of Auckland. 1979

7.11 Douglas, K.T., "Elongation in Reinforced Concrete Frames," PhD Thesis, Department of Civil Engineering, University of Auckland. 1992.

7.12 Fenwick, R. C. and Megget, L. M., "Elongation and Load Deflection Characteristics of Reinforced Concrete Members containing Plastic Hinges," Bulletin of the New Zealand National Society for Earthquake Engineering, 26, 1, pp. 28-41, 1993

7.13 Matthews, J., D. Bull, and Mander J., "Hollowcore floor slab performance following a severe earthquake. Concrete Structures in Seismic Regions," Proceeding of the First fib Symposium. Athens, Greece. 2003.

7.14 Pampanin S., Priestley N., and Sritharan S. "Analytical Modelling of the Seismic Behaviour of Precast Concrete Frames Designed with Ductile Connections," Journal of Earthquake Engineering. 5 (3). Imperial College Press. 2001, 329-367pp.

7.15 Kim, J. "Behaviour of hybrid frames under seismic loading" Ph.D. Thesis, Civil Engineering, University of Washington, 2002.

7.16 Chopra, A. K., "Dynamic of Structures – Theory and Applications to Earthquake Engineering". International Edition. New Jersey: Prentice Hall, 1995

7.17 Fenwick, R. and Davidson, B., "Elongation in ductile seismic-resistant reinforced concrete frame," Priestley, N., Collins, M., and Seible, F., editors, Recent Development in Lateral Force Transfer in Buildings, Proceedings of the Tom Paulay Symposium, pp. 143-170, Farmington Hills, MI. American Concrete Institute. 1995

7.18 Murahidy, A. G. "Design, Construction, Dynamic Testing and Computer Modelling of a Precast Prestressed Reinforced Concrete Frames Buildings with rocking Beam-Column Connections and ADAS Elements," ME thesis, Department of Civil Engineering, University of Canterbury, Christchurch New Zealand, 2004, 166pp.

CHAPTER 8
NUMERICAL STUDIES ON MULTI-STOREY FRAMES USING NON-TEARING FLOOR CONNECTIONS

8.1 INTRODUCTION

Chapter 7 showed the design and modeling of 5 and 10 multi-storey building prototypes with different type of connections (e.g. Hybrid PRESSS, Hybrid non-tearing and Monolithic). The buildings were designed for a traditional hybrid PRESSS type following the direct displacement based design principles in order to ensure that the design limit state was not exceeded.

Total base shear was calculated and distributed throughout the structures, the beam designs and their connections were considered for the three different systems for comparison purposes: traditional hybrid PRESSS, Hybrid using non-tearing connection and a monolithic (cast-in-situ or emulation of cast-in-situ concrete) solution.

Additionally, the effects of beam elongation increasing the curvature demand (and rotation demand of the ground floor columns) are neglected in normal designs. The consequences of these actions are also investigated using an appropriate structural model. Therefore, for comparison purposes five different models have been implemented for the three prototypes to compare the behaviour of the systems: Hybrid PRESSS without beam elongation (Hy), Hybrid PRESSS including beam elongation (Hy_beam-elong), Hybrid non tearing connection (Hy_non-tear), monolithic without beam elongation (Mon) and monolithic including beam elongation (Mon_beam-elong).

The prototype buildings and their different configurations were subjected to push-over analysis in Chapter 7 to investigate and evaluate the performance of this type of system to lateral loading. In general results indicated that beam elongation effects change the distribution of moments and shears throughout the frame. It can be seen that the traditional monolithic and hybrid PRESSS systems are affected by beam elongation especially at the first stories where the shears were larger; however, for the hybrid non-tearing these effects were not appreciated. The hybrid PRESSS model including beam elongation showed a reduction of the beam growth effects when compared with the monolithic model due to the post-tensioned forces which help to close the gap at the connection, specially for the top floors of the 10-storey model where in some cases the columns where pulling together.

Similarly, results also showed that the response of the hybrid system using non-tearing connection was very satisfactory under push-over analysis. Although lateral stiffness was lower for the hybrid non-tearing connection when compared with the traditional hybrid systems. However, the total base shear for the same imposed drift level was very similar. Therefore, as a result, the Hy and Hy_non-tear models would be generally more flexible, though reaching the target strength at a given level of drift. It is worth noting though that the initial stiffness up to the yielding of the mild steel bars (at around 0.35% roof drift) was similar between all models. Thus, the Hybrid non tearing model will maintain its natural and desired monolithic behaviour for small intensity earthquakes (i.e. low return period).

This Chapter presents a series of time history analysis will be carried out on the models designed in Chapter 7 and special attention will be given for the Hybrid frames using non-tearing floor connections to investigate and evaluate the performance of this type of system when subjected to earthquake loading.

8.2 MODELLING ASSUMPTIONS

The program Ruaumoko 2D [8.1] was used with appropriate modelling assumptions and hysteretic models, as defined in Chapter 7. However, this time history analysis study did not include P-Δ effects and additional assumptions are required to model the building prototype under time history analysis.

8.2.1 Viscous Damping

The presence of damping additional to that developed from hysteretic action is often accounted for in dynamic analysis. However the appropriateness of this assumed contribution, the values used and the form of application are not generally agree on, making this a somewhat subjective decision. In Ruaumoko a Rayleigh damping model can be used with either initial stiffness or tangent stiffness, where the only difference is either the use of initial elastic stiffness or the current tangent stiffness. Rayleigh viscous damping is determined from a sum of proportional mass M and stiffness K terms:

$$C = \alpha M + \beta K \tag{8.1}$$

The coefficients α and β are computed to give the required level of viscous damping at two different frequencies. These results increased damping as frequency increases, and therefore

higher damping is applied to higher modes. As highlighted in the Ruaumoko 2D, this can lead to very unrealistic damping values being applied to higher modes. This is especially important for structures subjected to strong-ground motion, such as the records used in this analysis.

A viscous damping value of 5% is typically assumed for reinforced concrete structures as a standard value in the analysis. This may be appropriate for elastic analysis, but when hysteresis models are incorporated into an inelastic analysis, this may overestimate the actual damping. Hysteresis rules are based on laboratory testing, and should be representative of the total structural damping, in both the elastic and inelastic ranges. Non-structural damping will also contribute, and a value of 2-5% seems reasonable to take this into account.

Ruaumoko recommends the use of Rayleigh damping based on the tangent stiffness matrix. In the latter case, values of damping for the higher modes should be less than 100% of critical damping. The use of the initial stiffness matrix results in an unrealistic increase in viscous damping when a member becomes inelastic. However, it is thought that this may help to offset the large damping that may result in higher modes through inappropriate use of the Rayleigh model.

In this analysis, a Rayleigh damping model based on the tangent stiffness matrix has been used. A value of 5% damping was applied to the first and second mode for the 5-storey frames while 5% for the first and third mode for the 10-storey frames. Ruaumoko generates the proportionality constants α and β from these values.

8.2.2 Input Ground Motions

The selection of specific ground motion for the design and analysis of an earthquake resistant structure should be based on the critical ground motions, which will drive the structure to a limit state in its response (e.g. collapse). The severity of a ground motion can be examined through two groups: the ground motion time-histories characteristics such as the peak ground acceleration (PGA) or velocity (PGV) or from elastic response spectra for the ground motion.

As stated in Chapter 7, the buildings were located in Wellington on top of a shallow soil (soil type C) within 2km from the fault and were given an importance level 2, Therefore, the frames were designed with a design earthquake (DEQ) proposed by the NZ 1170:5 with a probability of exceedance of 10% in 50 year corresponding to an average return period of 500 years.

An initial set of five earthquake motions were selected and scaled to represent the likely ground motion for the 500-year return period. The three record components were from the Northridge earthquake, Superstition Hills and one from the Landers earthquake. These records were scaled to match the design spectra over the full length of acceleration and displacement spectrum for site class C by a procedure stipulated in the current design standards NZ1170:5 Earthquake Actions [8.2]. The earthquake magnitudes, the closest source distances to the rupture planes for crustal events, the soil classification and the scaling factor are given in Table 8.1.

Table 8.1 Earthquake ground motions selected to investigate seismic intensity levels.

Earthquake Event	Year	Mw	Station	Rclosest (km)	Soil Type (NEHRP)	Unscaled PGA (g)	Unscaled PGV (cm/s)	Scaling Factor	Scaled PGA (g)	Scaled PGV (cm/s)	Scaled PGV/PGA ratio
Superstition Hills	1987	6.7	Brawley	18.2	D	0.1335	17.2	2.45	0.327	42.2	0.131
Northridge	1994	6.7	Canoga Park – Topanga Clan	15.8	D	0.356	32.1	0.90	0.322	29.0	0.092
Northridge	1994	6.7	N Hollywood – Coldwater Can	14.6	C	0.271	22.2	1.20	0.326	26.7	0.084
Northridge	1994	6.7	Sylmar - Olive view Med Ctr	5.30	D	0.84	129.60	0.33	0.281	43.3	0.157
Landers	1992	7.3	Lucerne Valley	0.53	A	0.72	97.60	0.68	0.491	66.5	0.138

Figure 8.1 (top), shows the elastic acceleration and displacement response spectra obtained using the design earthquake (DEQ) proposed by the NZ1170:5 with a probability of exceedence of 10% in 50 year corresponding to an average return period of 500 years and the five real scaled records acceleration and displacements using 5% damping. Although the dispersion generated using five earthquake records it is noted how the average shows a good representation of the design spectra provided by the accelerograms. However, at a period between 2.5 and 3.5 seconds the average spectral displacement does underestimate the spectral displacement specified for the NZ1170.5.

The NZ 1170:5 objective stated that structures should be capable of sustaining the actions of the maximum credible earthquake (MCE) with a return period of 2475 years with a small margin of safety against collapse. This chapter assess each 5 and 10-storey frame model by a sensitivity analysis by changing intensities from 0.5x to 2.0x the earthquake intensity. The variations in the intensity were also included to assess the sensitivity of the dynamic behaviour to intensity, in particular with respect to the commonly held notion that Capacity Design [8.3] effectively desensitises the structure to variations in earthquake characteristics.

Similarly, Figure 8.1 (bottom) shows the elastic acceleration and displacement response spectra obtained for the maximum credible earthquake (MCE) proposed by the NZ1170:5 with a probability of exceedance of 2% in 50 years corresponding to an average return period of 2475

years and the five real scaled records at 2.0 times the earthquake design intensity. It can be seen a good representation of the MCE is provided by the five real scaled earthquake records in terms of acceleration and displacement.

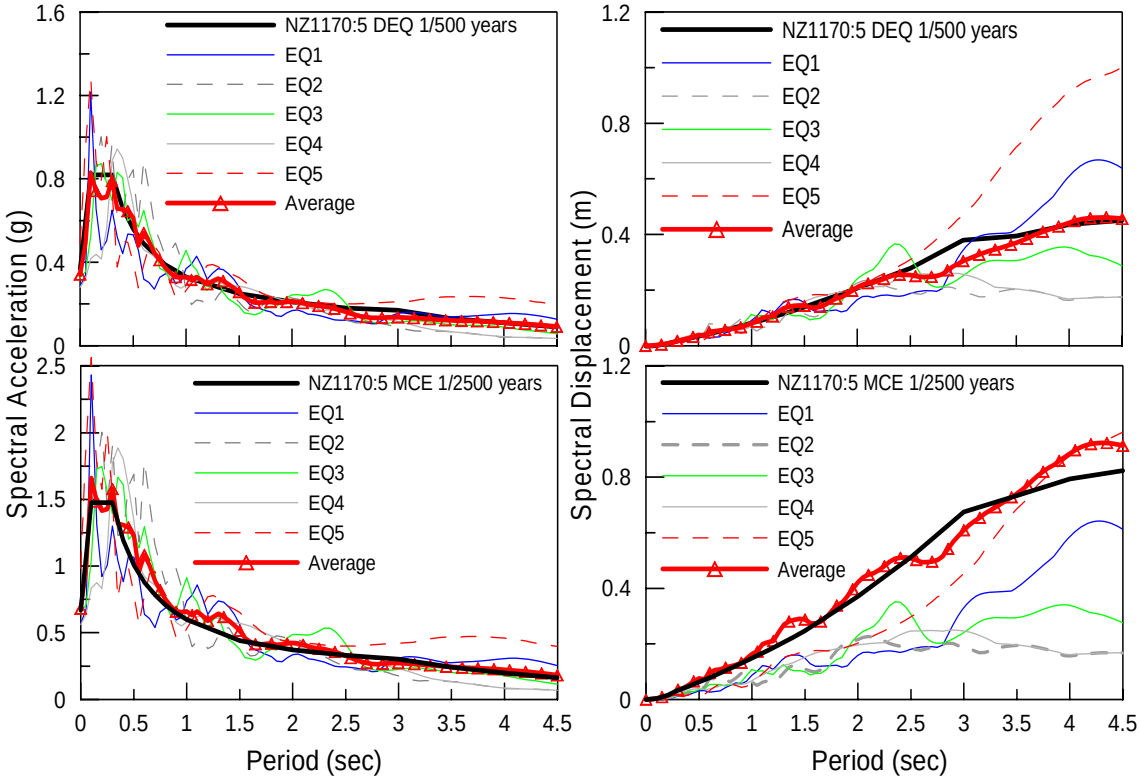

Figure 8.1 Comparison of five scaled acceleration and displacement spectra with the NZ1170-5 elastic design spectrum (top) and Maximum credible earthquake (bottom) (5% damping).

A second set of 30 earthquake motions were selected and scaled to represent the likely ground motion for the 500-year return period. 20 records were considered for far field and 10 for near field faults events. The suite of the first 20 earthquakes is an ensemble of scaled historical "far-field" strong ground motion records from California representative of typical earthquakes having a probability of exceedance of 10% in 50 years. These records were related to soil types C or D (NEHRP categories), with hypocentre depth ranging between 14 and 25km, and were generated by earthquakes of moment magnitude M_w ranging from 6.7 to 7.3. The adoption of the Californian earthquake set is for consistency with previous studies [8.4].

The second suite of earthquakes is an ensemble of 10 historical near-field earthquake records, selected based on their PGV/PGA ratio (at least 0.189 gs m-1) and distance from fault (less than 10km). The source mechanism and soil type are selected such that a range of different properties are considered. Although the soft soil (type E) records typically exhibit large amplifications that are site-specific, the records are included in order to investigate the behaviour of the hybrid systems with non-tearing connections in all types of soil conditions. That is the same reason for

selecting records with various source mechanisms. The earthquake magnitudes, the closest source distances to the rupture planes for crustal events, and the scaling factor are given in Tables 8.2 and 8.3 for the far and near fields sets respectively.

Table 8.2 Earthquake ground motions selected considering far field events

Name	Earthquake Event	Year	Mw	Station	Rclosest (km)	Soil Type (NEHRP)	Scaling Factor	Scaled PGA (g)	Scaled PGV (cm/s)	Scaled PGV/PGA ratio
EQ1	Superstition Hills	1987	6.7	Brawley	18	D	2.45	0.327	42.2	0.131
EQ2	Superstition Hills	1987	6.7	El Centro Imp. Co. Cent	14	D	1.21	0.351	49.6	0.144
EQ3	Superstition Hills	1987	6.7	Plaster City	21	D	1.45	0.225	29.9	0.135
EQ4	Northridge	1994	6.7	Beverly Hills 14145 Mulhol	20	C	0.39	0.184	24.2	0.134
EQ5	Northridge	1994	6.7	Canoga Park – Topanga Clan	16	D	0.90	0.322	29.0	0.092
EQ6	Northridge	1994	6.7	Glendale – Las Palmas	25	D	3.00	1.071	36.9	0.035
EQ7	Northridge	1994	6.7	LA – Hollywood Stor FF	26	D	1.22	0.283	22.4	0.081
EQ8	Northridge	1994	6.7	LA – N Faring Rd	24	D	1.82	0.496	28.7	0.059
EQ9	Northridge	1994	6.7	N Hollywood – Coldwater Can	15	C	1.20	0.326	26.7	0.084
EQ10	Northridge	1994	6.7	Sunland – Mt Gleason Ave	18	C	1.37	0.192	19.8	0.105
EQ11	Loma Prieta	1989	6.9	Capitola	15	D	0.53	0.255	19.4	0.078
EQ12	Loma Prieta	1989	6.9	Gilroy Array #3	14	D	1.18	0.558	85.3	0.156
EQ13	Loma Prieta	1989	6.9	Gilroy Array #4	16	D	0.95	0.287	74.0	0.263
EQ14	Loma Prieta	1989	6.9	Gilroy Array #7	24	D	2.57	0.580	42.1	0.074
EQ15	Loma Prieta	1989	6.9	Hollister Diff. Army	26	D	0.82	0.227	29.2	0.131
EQ16	Loma Prieta	1989	6.9	USGS Anderson Dam -DS	20	D	1.43	0.343	29.1	0.086
EQ17	Cape Mendocino	1992	7.1	Fortuna Fortuna Blvd	24	C	1.86	0.215	55.7	0.264
EQ18	Cape Mendocino	1992	7.1	Rio Dell Overpass – FF	19	C	0.67	0.298	29.5	0.101
EQ19	Landers	1992	7.3	Desert Hot Springs	23	C	1.33	0.203	27.7	0.139
EQ20	Landers	1992	7.3	Yemo Fire Station	25	D	1.16	0.243	34.4	0.145

Figure 8.2 and 8.3 shows the elastic acceleration and displacement response spectra obtained using the design spectrum and the scaled records selected using 5% damping for far and near field events respectively. The dispersion generated using 20 far field earthquake records is appreciable for low period ranges up to 0.75 sec, the mean spectral acceleration shows a good agreement for all the period range up to 4.5 seconds; however, the mean spectral displacements under estimate the code spectra displacement.

Table 8.3 Earthquake ground motions selected considering near field events

Name	Earthquake Event	Year	Mw	Station	Rclosest (km)	Soil Type (NEHRP)	Source Mechanism	Scaling Factor	Scaled PGA (g)	Scaled PGV (cm/s)	Scaled PGV/PGA ratio
EQ21	Northridge	1994	6.7	Rinaldi Receiving Station	6.5	B	Reverse Normal	0.33	0.280	55.4	0.202
EQ22	Northridge	1994	6.7	Jensen Filter Plant	7.01	B	Reverse Normal	0.42	0.179	44.8	0.255
EQ23	Imperial Valley	1979	6.6	El Centro Array #5	3.95	D	Strike Slip	0.68	0.258	61.5	0.243
EQ24	Imperial Valley	1979	6.5	El Centro Array# 7	0.56	D	Strike Slip	0.48	0.220	52.0	0.241
EQ25	Kobe	1995	6.9	Takatori	1.47	E	Strike Slip	0.333	0.203	42.4	0.212
EQ26	Kobe	1995	6.9	Port Island (0 m)	3.31	E	Strike Slip	0.427	0.135	32.0	0.242
EQ27	Loma Prieta	1989	6.9	Saratoga W Valley	9.31	D	Reverse Oblique	0.558	0.185	34.3	0.189
EQ28	Chi Chi	1999	7.6	TCU068	9.96	D	Reverse Oblique	0.384	0.217	67.8	0.318
EQ29	Chi Chi	1999	7.6	CHY101	0.32	A	Reverse Oblique	0.512	0.225	58.9	0.266
EQ30	Kocaeli	1999	7.4	Gebze	10.92	A	Strike Slip	1.575	0.384	79.2	0.210

The average spectral acceleration dispersion generated using 10 near field earthquake records (Figure 8.3) under estimated the spectral acceleration at low periods but showed good agreement for a range of period greater than 0.6 sec. Similarly, the mean spectral displacement shows a good agreement for a range of periods up to 3.0 sec but estimates the code spectral displacement for periods greater than 3 sec.

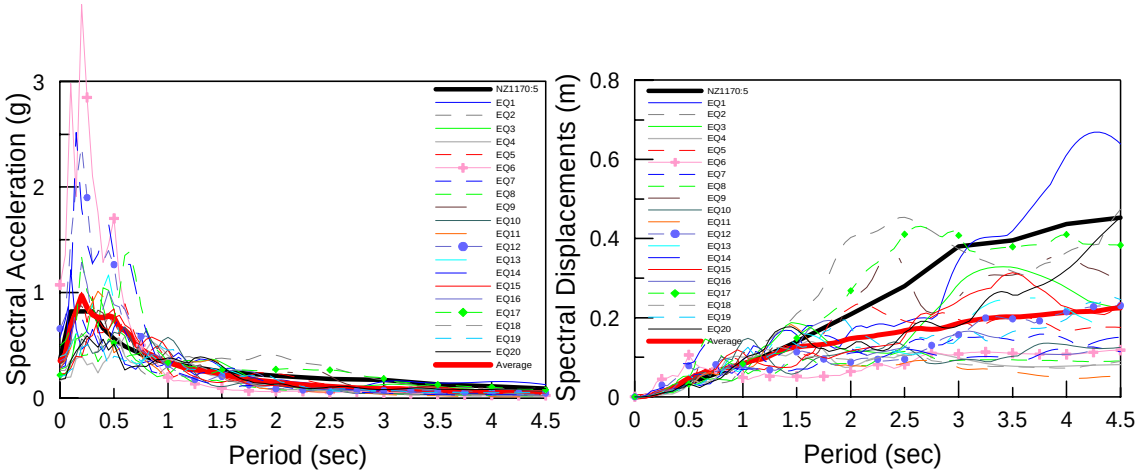

Figure 8.2 Comparison of 20 far field scaled acceleration (left) and displacement (right) spectra with the NZ1170:5 elastic design spectrum (5% damping)

Figure 8.4 shows the comparison between the 1170:5 elastic design spectrum with the minimum, maximum and mean values obtained from the far field and near field acceleration and displacement earthquake records.

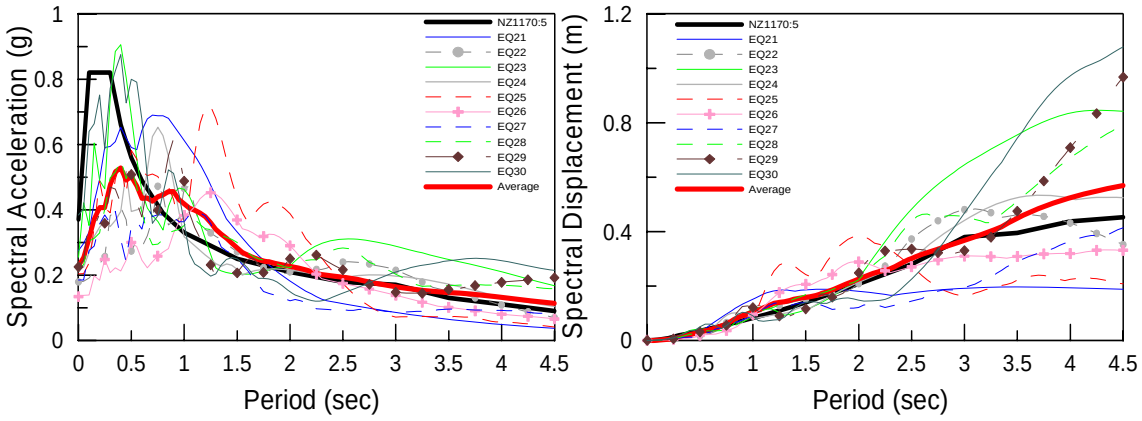

Figure 8.3 Comparison of 10 near field scaled acceleration (left) and displacement (right) spectra with the NZ1170:5 elastic design spectrum (5% damping)

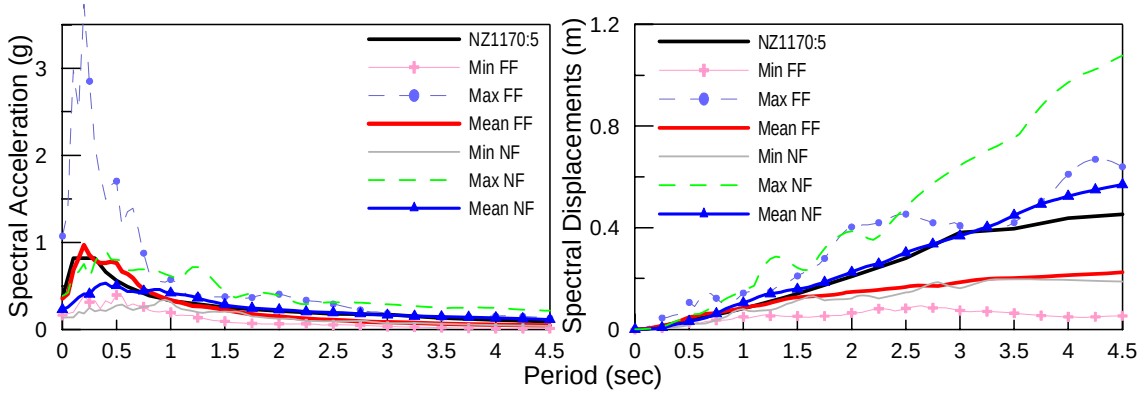

Figure 8.4 Minimum, mean and maximum response for far (left) and near (right) field scaled displacement spectra compatible with NZ1170:5 elastic design spectrum (5% damping).

8.3 INELASTIC TIME-HISTORY RESULTS FOR DIFFERENT EARTHQUAKE INTENSITIES

The dynamic characteristics of the models were studied for maximum displacements, inter-storey drift and cumulative shear using the previous five real scaled earthquakes motions compatible with the design spectra NZ1170:5 for Wellington soil type C and return period of 500 years. Mass was placed at each beam-column interface. Tangent stiffness Rayleigh damping was used with 5% of critical damping at the first and second mode for the 5-storey models, and first and third mode for the 10-storey models.

8.3.1 Mean Maximum and Absolute Maximum Inter-storey Drift Profiles

Figures 8.5 to 8.7 show the mean maximum (mean) and absolute maximum (max.) drift envelopes for each 5-storey model at 0.5x, 1.0x, 1.5x and 2.0x the earthquake intensities. In general, any of the mean and maximum drift values of the 5-storey frames do not exceed the design drift limit of 2.0% at the design intensity.

Figure 8.5 shows the comparison between the 5Hy_non-tear frames using moment rotation and axial spring models at different intensities. Results indicate very small differences for the mean and maximum drift values. There were no differences as the earthquake intensity increased between models.

The 5-storey model using non-tearing connections (Figure 8.5) showed mean and maximum values of 0.4% and 0.6% drift respectively located at the second floor for half of the earthquake intensity. Increaseing the earthquake intensity from 0.5x to 1.0x, mean inter-storey drift values increase by double while maximum values increase more than double with a total of 1.4% drift located at the second floor and reduces along the height of the frame.

As the intensity increased to 1.5, mean and maximum drift values are almost linearly distributed along the height of the frame with values 1.25% and 2.25% drift located at the second and third floor respectively. Finally, at two times the design intensity, a constant mean inter-storey drift of 1.85% is observed along the height of the frame. However, maximum inter-storey drift occurs at the first floor with a value of 3.75% drift with a posterior reduction along the height of the frames with 2.9% roof drift.

Comparison between the 5Hy_non-tear (Figures 8.5) with the 5Hy (Figure 8.6-Left) and 5Mon (Figure 8.7-Left) models show similar mean and maximum inter-storey drift (0.4% and 0.6% drift respectively) for half of the earthquake intensity. As the earthquake intensity increases, the mean drift values are similar between the three models with values of 0.8%, 1.25% and 1.9% drift at 1.0x, 1.5x and 2.0x the earthquake intensity respectively.

At the design earthquake intensity, the 5Hy model showed a maximum of 1.8% drift value higher than the 5Hy_non-tear and 5Mon models with maximum values of 1.4% and 1.3% drift respectively.

At higher earthquake intensities, the 5Hy model shows maximum values of 3.0% and 6.5% drift at 1.5 and 2.0x the design earthquake intensity, while the 5Hy_non-tear model shows smaller maximum drift with values of 2.25% and 3.5% drift at the same design intensities respectively. Similarly, the 5Mon model shows similar maximum drift values as the 5Hy_non-tear model with 2.25% and 3.3% drift at 1.5x and 2.0x the design earthquake intensity respectively.

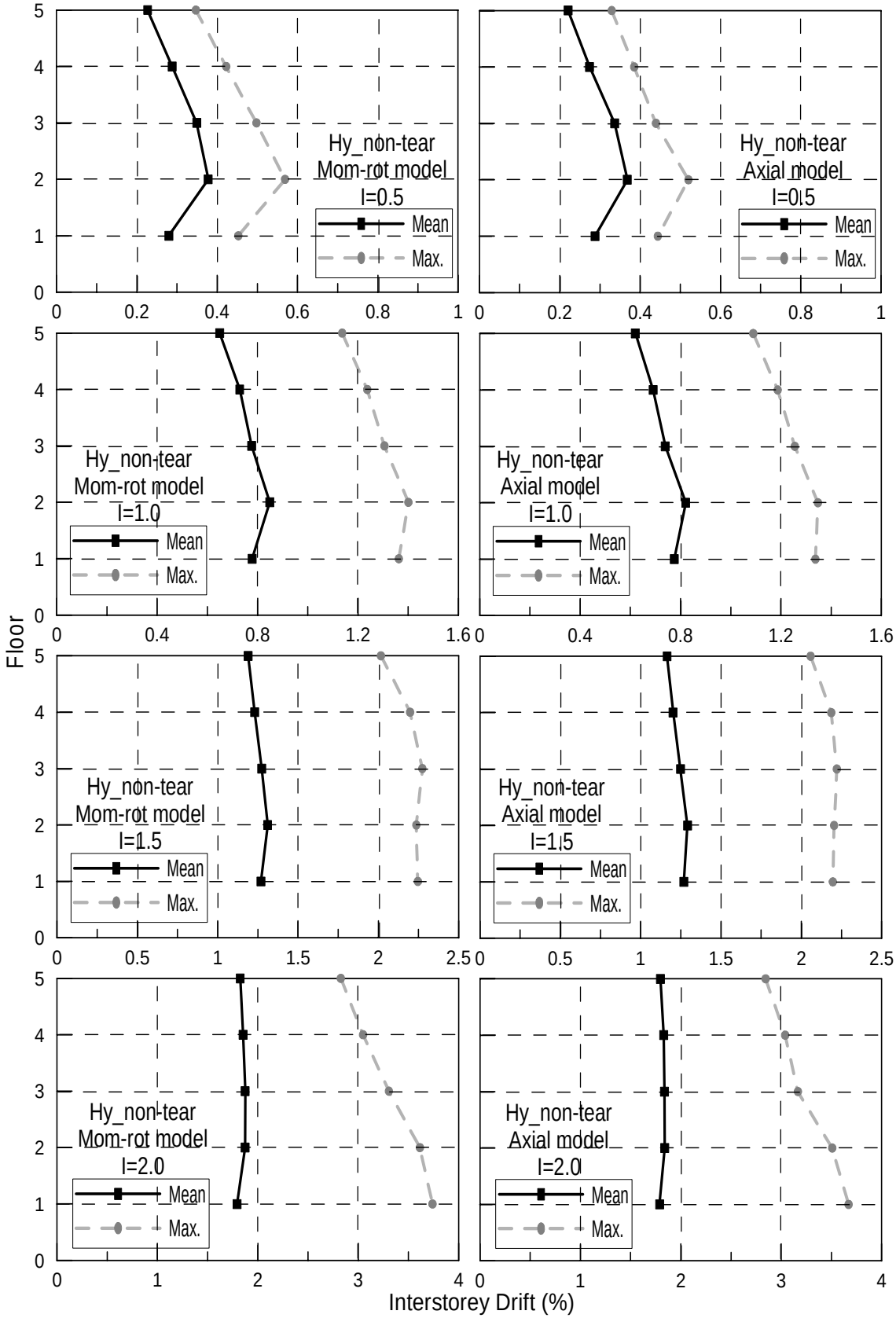

Figure 8.5 Mean and absolute maximum drift profiles for 5Hy_non-tear frame using moment rotation (left) and axial spring (right) models using a set of 5 natural scaled earthquakes for different intensities.

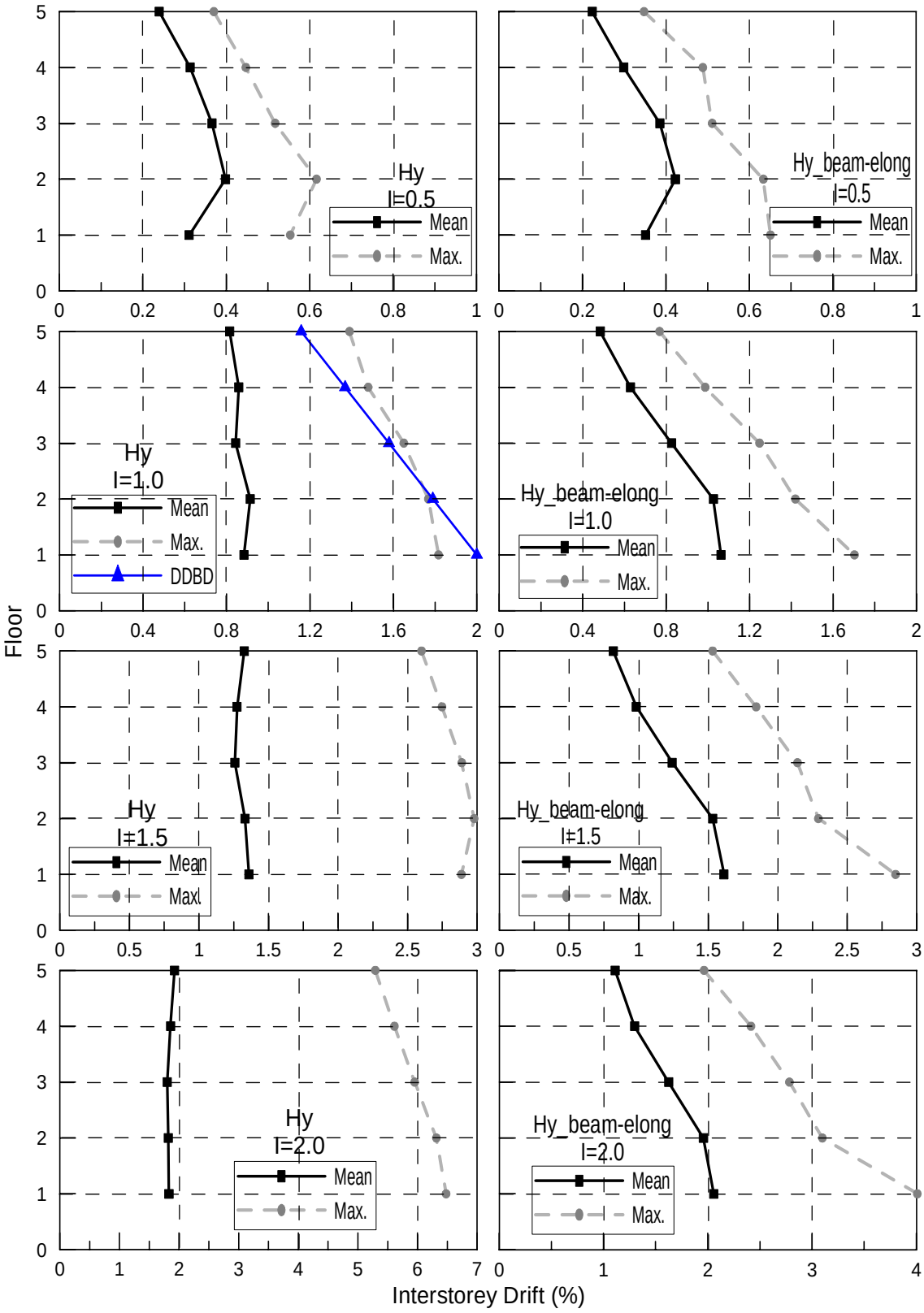

Figure 8.6 Mean and absolute maximum drift profiles for 5Hy (left) and 5Hy_beam-elong (right) frames using a set of 5 natural scaled earthquakes for different intensities.

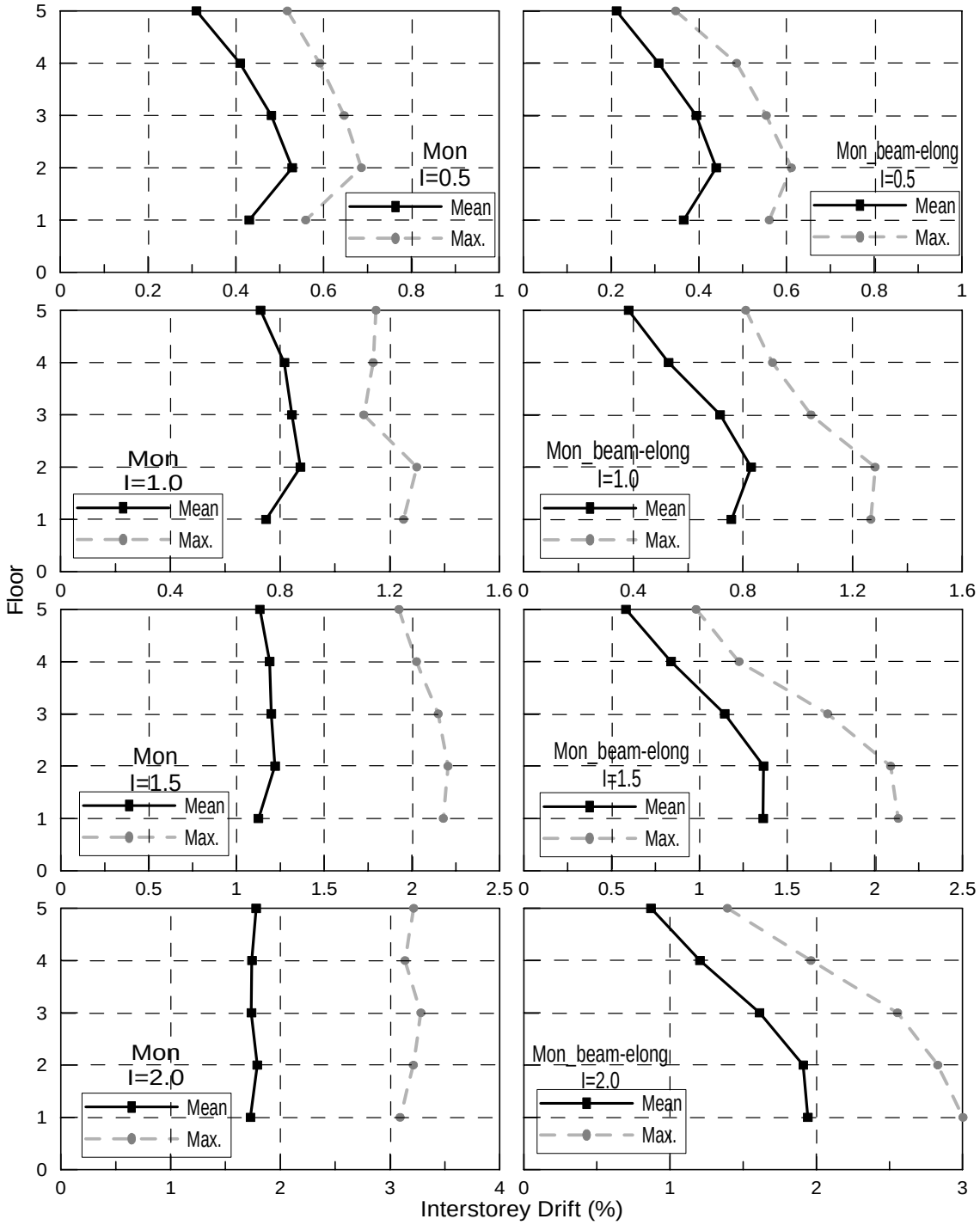

Figure 8.7 Mean and absolute maximum drift profiles for 5Mon (left) and 5Mon_beam-elong (right) frames using a set of 5 natural scaled earthquakes for different intensities.

Comparison between the 5Hy_non-tear (Figures 8.5) with the 5Hy_beam-elong (Figure 8.6-right) and 5Mon_beam-elong (Figure 8.7-right) models shows that the models with beam elongation present higher mean and maximum drift values at the first two floors and then reduce along the height of the building while for the 5Hy_non-tear the mean and maximum drift values remain almost constant along the height of the building. At half of the earthquake intensity, mean maximum drift values are similar for all the three models while maximum drift values are

higher for the 5Hy_beam-elong model with 0.65% drift when compared to the 5Hy_non-tear and 5Mon_beam-elong models with 0.55% and 0.6% drift values respectively.

At the design earthquake intensity, the 5Hy_beam-elong model shows higher mean and maximum values (1.1% and 1.7% drift respectively) than the 5Hy_non-tear and the 5Mon_beam-elong models with 0.8% and 1.35% mean and maximum drift respectively. At 1.5x the earthquake intensity, the 5Hy_non-tearing model shows a mean drift value of 1.25% drift, smaller than 1.55% and 1.4% drift when compared to the 5Hy_beam-elong and 5Mon_beam-elong models respectively. For maximum drift values, the 5Hy_non-tear and the 5Mon_beam-elong models shows very similar values of 2.2% drift while the 5Hy_beam-elong model shows a higher maximum value of 2.85% drift.

Finally, at 2.0x the design intensity, the 5Hy_beam-elong model shows mean and maximum value of 2.0% and 4.0% drift respectively higher than the 5Hy_non-tear model with 1.85% and 3.7% mean and maximum drift respectively. For the 5Mon_beam-elong model, smaller mean and maximum drift values were observed with 1.95% and 3.0% drift respectively.

Comparison between the 5Hy and 5Hy_beam-elong models (Figure 8.6) and 5Mon and 5Mon_beam-elong models (Figure 8.7) indicate similar mean and maximum inter-storey drift values located in the first floor for the different earthquake design intensities. However, the mean and maximum values are smaller for the models considering beam elongation along the height of the frame when compared with the rest of the models.

Figures 8.8 to 8.10 show the mean maximum (mean) and absolute maximum (max.) drift envelopes for each 10-storey model at 0.5x, 1.0x, 1.5x and 2.0x the earthquake intensities. In general, any of mean and maximum drift values of the 10-storey frames does not exceed the design drift limit of 1.5% at the design intensity, except for the 10Hy_beam-elong model at the first floor with 1.57% maximum drift and a localized maximum drift value of 1.55% at seventh floor for the 10Mon model.

Figure 8.8 shows the mean and maximum inter-storey drift for the 10Hy_non-tear model. At half of the design intensity, mean and maximum drift were 0.4% and 0.7% drift while at the design earthquake intensity mean and maximum drift were 0.65% and 1.0% drift located at the seventh floor. However, as the earthquake design intensity increases, the mean inter-storey drift values are almost constant in the lower storeys (floor 1 to 7) with mean drift values of 1.1% and 1.65% drift for 1.5x and 2.0x earthquake intensity respectively. Maximum values occur at the

first floor and linearly reduce along the height of the frame with 2.15% and 3.9% drift respectively for 1.5x and 2.0x the earthquake intensity respectively.

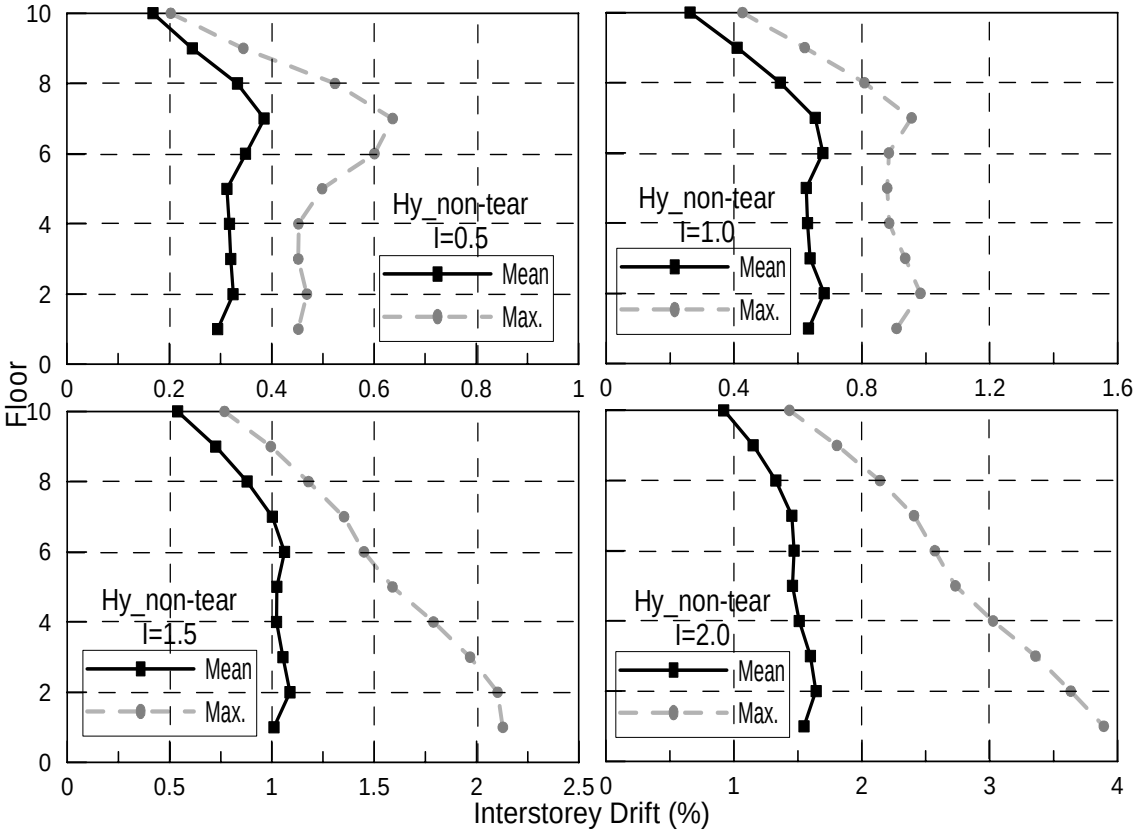

Figure 8.8 Mean and absolute maximum drift profiles for 10Hy_non-tear frames using a set of 5 natural scaled earthquakes for different intensities.

Comparison between the 10Hy_non-tear model (Figure 8.8) with the 10Hy and the 10Hy_beam-elong models (Figure 8.9) show that at half of the design intensity all models have similar behaviour in the drift profile. The mean and maximum drift values were the same for the 10Hy_non-tear model respect with the 10Hy_beam-elong model located at the seventh floor (0.45% and 0.65% mean and maximum drift respectively) and slightly higher for the 10Hy model with 0.5% and 0.7% mean and maximum drift respectively.

At the design earthquake intensity, the 10Hy_non-tear model has smaller mean and maximum inter-storey drift in comparison with the 10Hy and 10Hy_beam-elong models. Mean and maximum values for the 10Hy_non-tear model are 0.7% and 1.0% drift respectively located at the second floor while for the 10Hy model a mean value of 0.9% drift is located at the seventh floor while the maximum value is at the second floor with 1.45% drift. Similarly, the 10Hy_beam-elong model presents a similar mean drift value with respect to the 5Hy model; however, higher maximum drift values are observed at the first floor with 1.57% inter-storey drift.

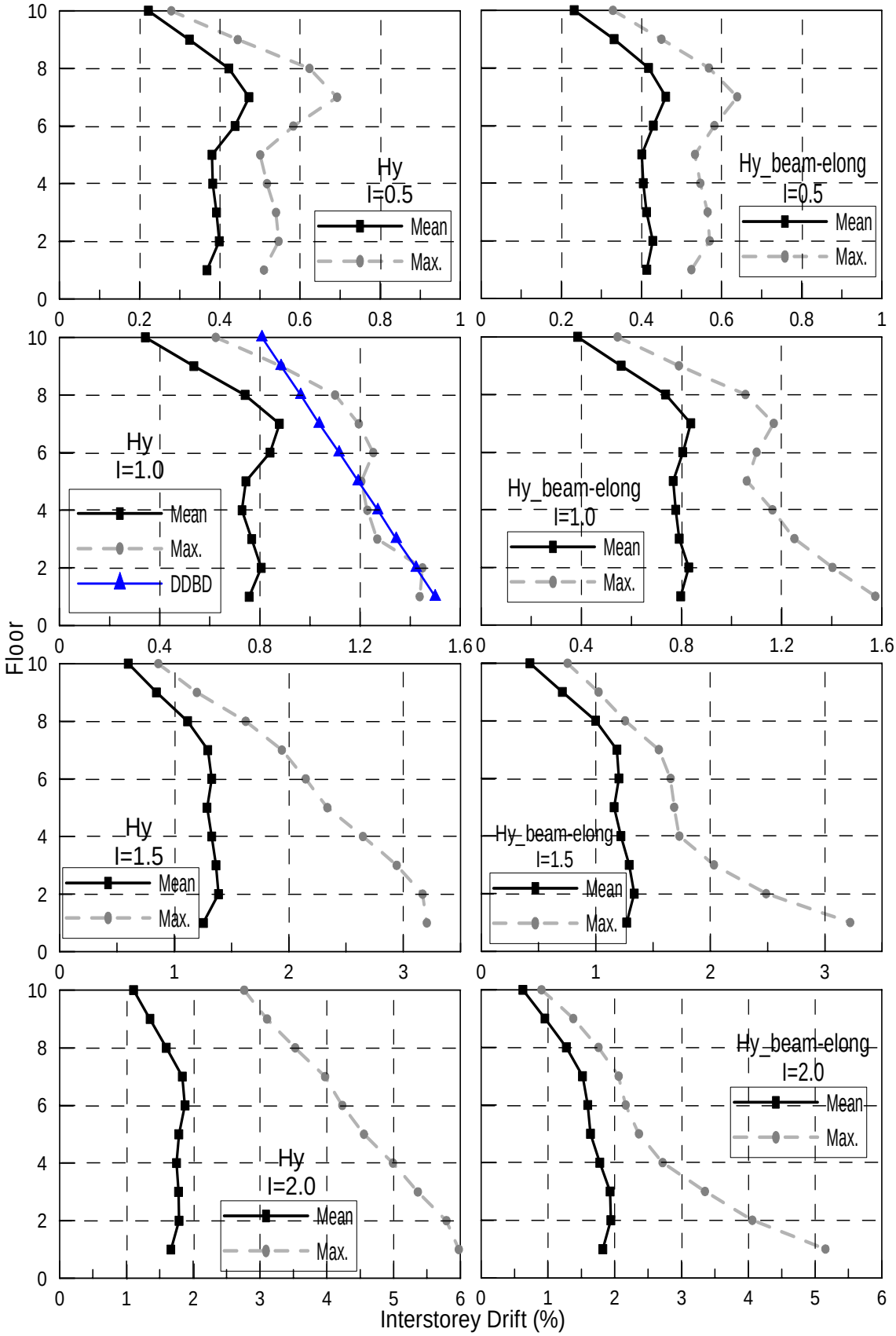

Figure 8.9 Mean and absolute maximum drift profiles for 10Hy (left) and 10Hy_beam-elong (right) frames using a set of 5 natural scaled earthquakes for different intensities.

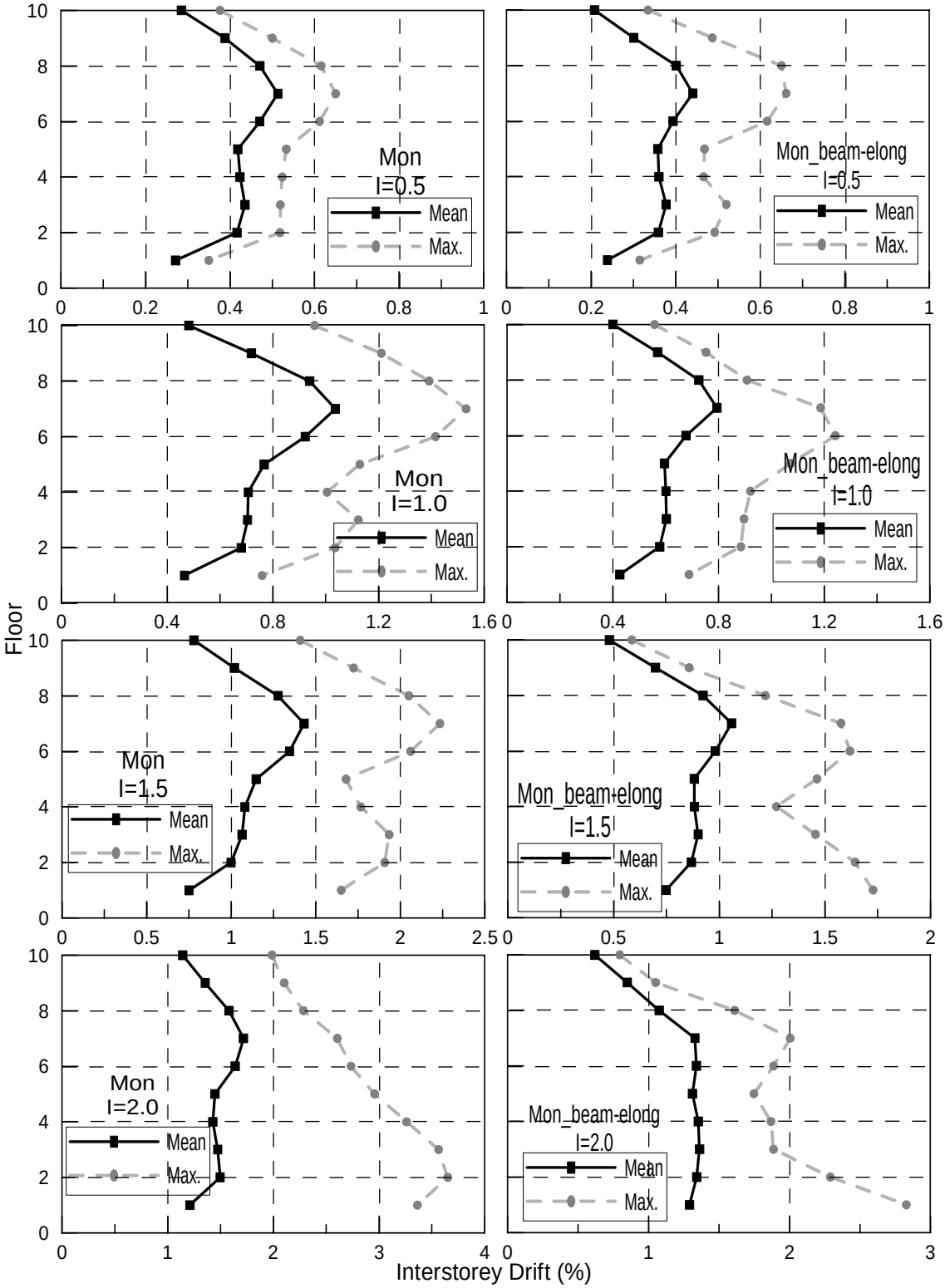

Figure 8.10 Mean and absolute maximum drift profiles for 10Mon (left) and 10Mon_beam-elong (right) frames using a set of 5 natural scaled earthquakes for different intensities.

At 1.5x the earthquake intensity, the 10Hy and 10Hy_beam-elong models show similar mean and maximum drift profiles. Mean values are almost constant along the height of the frames with 1.35% higher drift than the 10Hy_non-tear model with 1.1% drift. Maximum drift values

are located at the first floor for all the models. The 10Hy_non-tear model has maximum drift value of 2.1% drift while the 10Hy and 10Hy_beam-elong models show higher values 3.2% drift; however the 10Hy_beam-elong model reduces the maximum drifts located at the first floors more rapidly with height than does the 10Hy model.

Finally, at two times the earthquake design intensity, the 10Hy_non-tear model shows a mean of 1.5% drift smaller than the obtained for the 10Hy and 10Hy_beam-elong models (1.95% and 2.0% drift respectively). The 10Hy and 10Hy_beam-elong models show maximum values of 6.0% and 5.15% drift respectively higher than the 10Hy_non-tear model with 3.9% drift.

Comparison between the 10Mon and 10Mon_beam-elong models show that up to the design earthquake intensity both mean and maximum drift values are similar between the two models. As the earthquake intensity increases, both models have very similar mean values, however maximum drift values are smaller for the 10Mon_beam-elong model.

Comparison between the 10Hy_non-tear model (Figure 8.8) with the 10Mon and 10Mon_beam-elong models (Figure 8.10) shows that the 10Hy_non-tear model has smaller mean and maximum drift values along the height of the frame at half of the earthquake design intensity. The mean and maximum drift values were the same for all the models with values of 0.4% and 0.65% drift respectively located at the seventh floor.

At the design earthquake intensity, the 10Hy_non-tear model has smaller mean and maximum inter-storey drift when compare to the 10Mon and 10Mon_beam-elong models. Mean and maximum drift profiles for the 10Mon and 10Mon_beam-elong model increase along the height of the frames up to the seventh floor while for the 10Hy_non-tear model, is approximately constant.

Mean and maximum values for the 10Hy_non-tear model are 0.7% and 1.0% drift respectively at the second floor while for the 10Mon model mean and maximum values are 1.0% and 1.05% drift respectively located at the seventh floor. Similarly, the 10Mon_beam-elong model presents the mean and maximum values of 0.8% and 1.25% drift at the seventh floor respectively

At 1.5x the design earthquake intensity, the 10Mon model shows mean and maximum values of 1.45% and 2.25% drift located at the seventh floor, higher than the 10Hy_non-tear model with values of 1.10% and 2.13% drift located at the first floor.

The 10Mon_beam-elong model shows a similar mean value of 1.10% drift located at the seventh floor when compared with the 10Hy_non-tear model. However, the 10Mon_beam-elong model show maximum drift value of 1.75% drift located at the first floor smaller than the 10Hy_non-tear model with a value of 2.1% drift.

Finally, at two times the earthquake design intensity, the 10Mon_beam-elong model shows smaller mean and maximum values (1.35% and 2.85% drift respectively) when compared to the 10Hy_non-tear model (1.65% and 3.9% drift) and 10Mon model (1.75% and 3.65% drift).

Comparison between the 10Mon and 10Mon_beam-elong models shows that mean and maximum drift values are similar up to the design earthquake intensity. As the earthquake intensity increases, both models have very similar mean values, however maximum drift values are smaller for the 10Mon_beam-elong model.

8.3.2 Mean Maximum and Absolute Maximum Displacement Profile

Figures 8.11 to 8.16 show the mean maximum (mean) and absolute maximum (max.) displacement profiles for the 5 and 10-storey frame models at different earthquake intensities. Results indicate that for 0.5 and 1.0x the earthquake intensities, the 5 and 10-storey models with non-tearing connections undergo less deformation than all the other models when the frames were in the post-elastic range. As the earthquake design intensity increases, the 5 and 10-storey Mon_beam-elong models underwent higher deformations than all the other models at the bottom floors and smaller deformation at the top floors when the frames were in the post-elastic range.

Similar results were observed for the 5 and 10-storey Hy_beam-elong models where displacements were smaller than the models excluding beam elongation effects. These results indicate that Hybrid PRESSS frame systems excluding beam elongation behave similarly to the Hybrid non-tearing connections and would in general be stiffer at the first floors and more flexible at the roof level.

Figures 8.11 to 8.13 show the mean and maximum displacement profiles for the 5-storey fames at different earthquake intensities. In general, the mean displacements were similar between the models at different earthquake intensities. The maximum displacement for the hybrid PRESSS and hybrid non-tearing models show similar profiles in comparison with the displacements obtained using the direct displacement base design principles.

Models including beam elongation show a parabolic displacement distribution where lower storeys present bigger displacements while for models excluding beam elongation effects and using non-tearing connections a linear distribution displacement profile is observed.

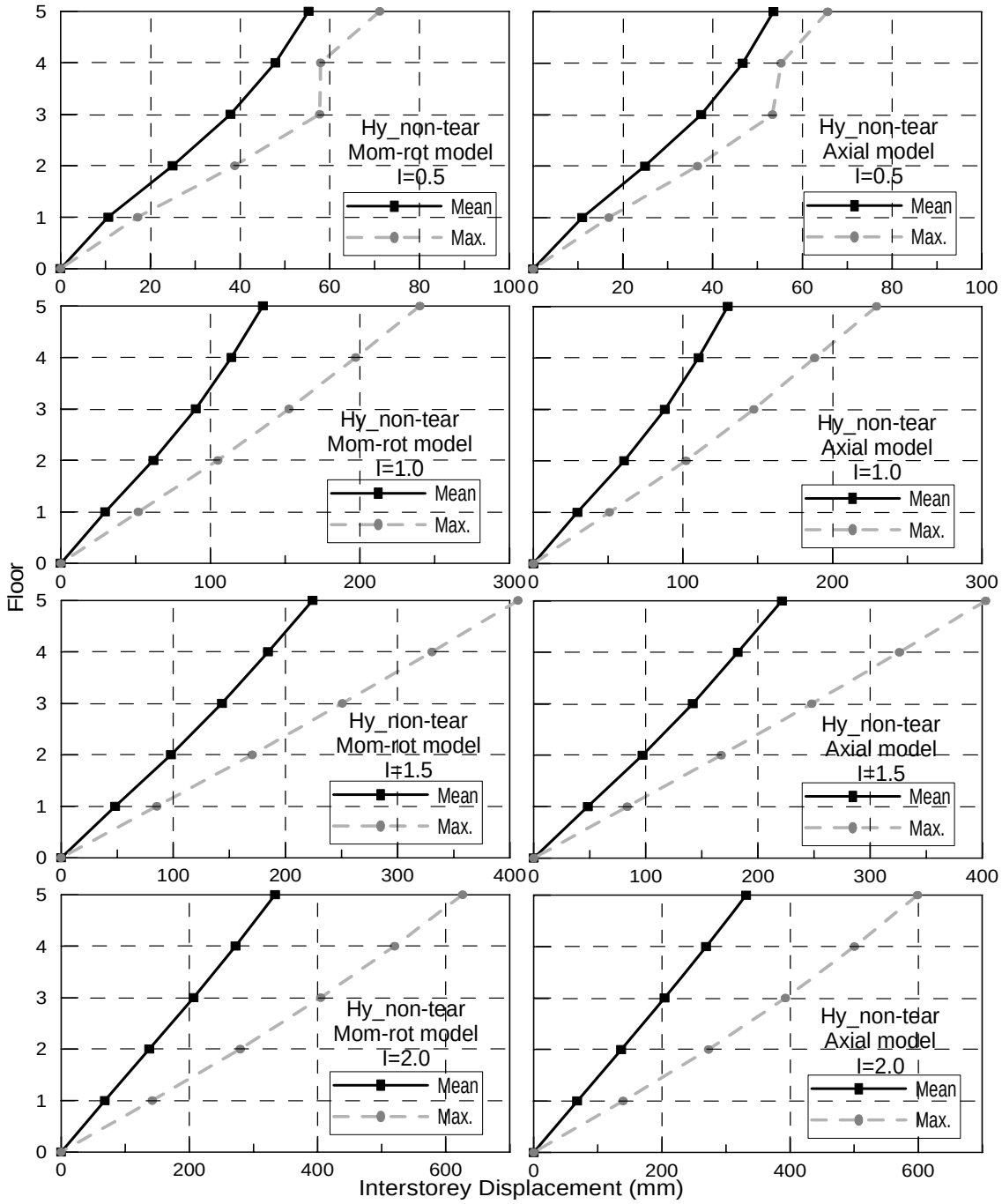

Figure 8.11 Mean and absolute maximum displacement profiles for 5Hy_non-tear frame using moment rotation (left) and axial spring (right) models using a set of 5 natural scaled earthquakes for different intensities.

No difference in the displacement profiles between the 5Hy_non-tear frame considering moment rotation and axial spring model is observed. Comparison between the 5Hy_non-tear model with the 5Hy model show similar mean displacement profile at all intensities. However,

maximum displacements are higher for the 5Hy model when compared to the rest of the models for all the intensities. Similarly, maximum displacements are observed between the 5Hy_non-tear and the 5Mon models for all the intensities.

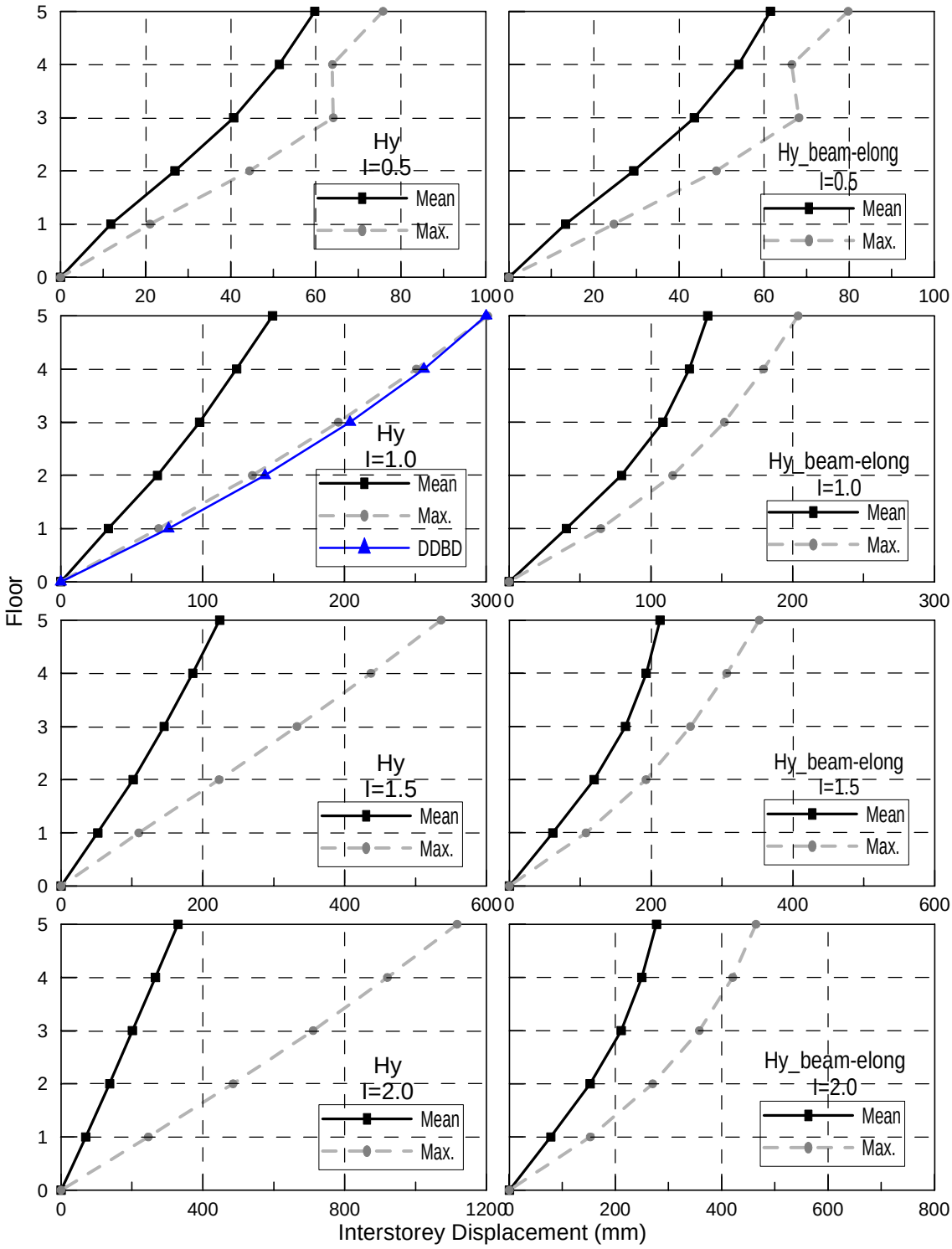

Figure 8.12 Mean and absolute maximum displacement profiles for 5Hy (left) and 5Hy_beam-elong (right) frames using a set of 5 natural scaled earthquakes for different intensities.

For the 5Hy_beam-elong model and 5Mon_beam-elong model show an increase in the displacements at the lower floors due to effects of beam elongation which is more evident at higher earthquake intensity levels.

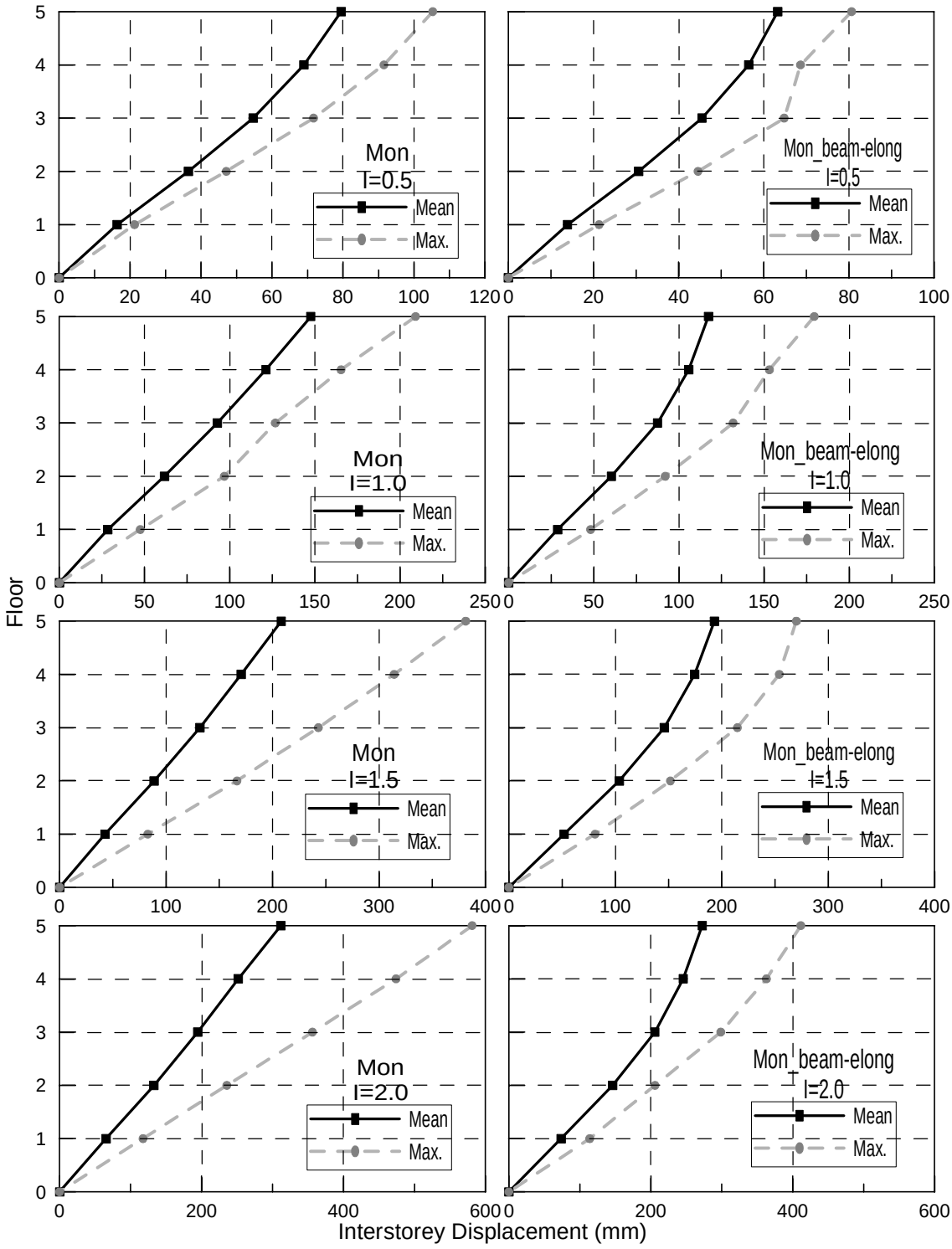

Figure 8.13 Mean and absolute maximum displacement profiles for 5Mon (left) and 5Mon_beam-elong (right) frames using a set of 5 natural scaled earthquakes for different intensities.

Finally, the 5Mon_beam-elong model shows smaller mean displacement values when compared with the rest of the models. The 5Mon model shows higher mean displacement values when compared with the 5Hy_non-tear and 5Hy models at half of the design earthquake intensity; however, as the earthquake intensity increases, the 5Mon model shows smaller mean displacement values than the 5Hy_non-tear and 5Hy models.

At 0.5x and 1.5x the design earthquake intensities, mean displacements are reduced or increased approximately by the same intensity amount for all the models. However, at 2.0x the earthquake design intensity, maximum displacements increase between 2.25 and 2.5 times more for all the models, except for the 5Hy_beam-elong model which maximum displacements are higher by a factor of 2.0.

Figures 8.14 to 8.16 show the mean maximum (mean) and absolute maximum (max.) displacement profiles for the 10-storey fames at different earthquake intensities. In general, the mean and maximum displacements for the 10Hy_non-tear model were smaller than the 10Hy and 10Hy_beam-elong models the for all earthquake intensities (except for the maximum displacement obtained for the 10Hy_beam-elong model at 2.0x the design intensity level). The maximum displacement for the hybrid PRESSS model shows similar profile in comparison with the displacements obtained using direct displacement base design principles.

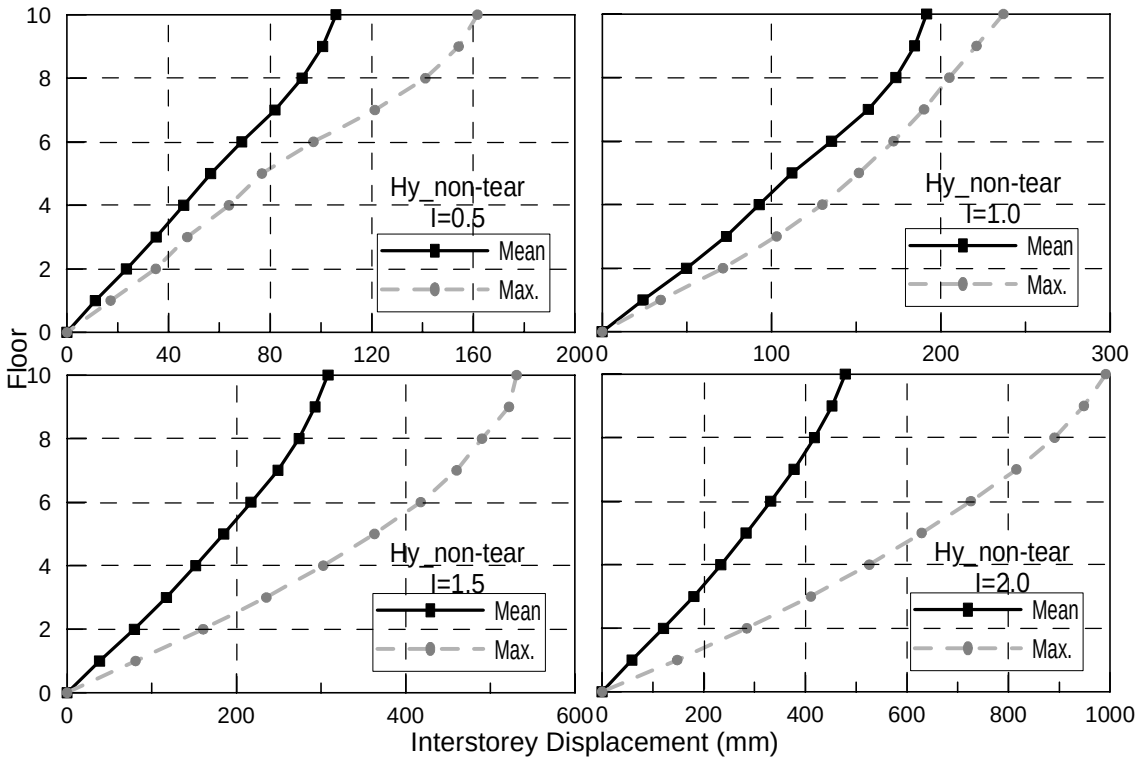

Figure 8.14 Mean and absolute maximum displacement profiles for 10Hy_non-tear frames using a set of 5 natural scaled earthquakes for different intensities.

Similarly, comparison between the 10Hy_non-tear model with the 10Mon and 10Mon_beam-elong models indicate that the 10Hy_non-tear model shows smaller top mean and maximum displacements at 0.5x and 1.0x the design earthquake intensities. However, as the earthquake intensity increases, the 10Mon_beam-elong model shows smaller mean and maximum displacements when compared to the 10Mon and 10Hy_non-tear models.

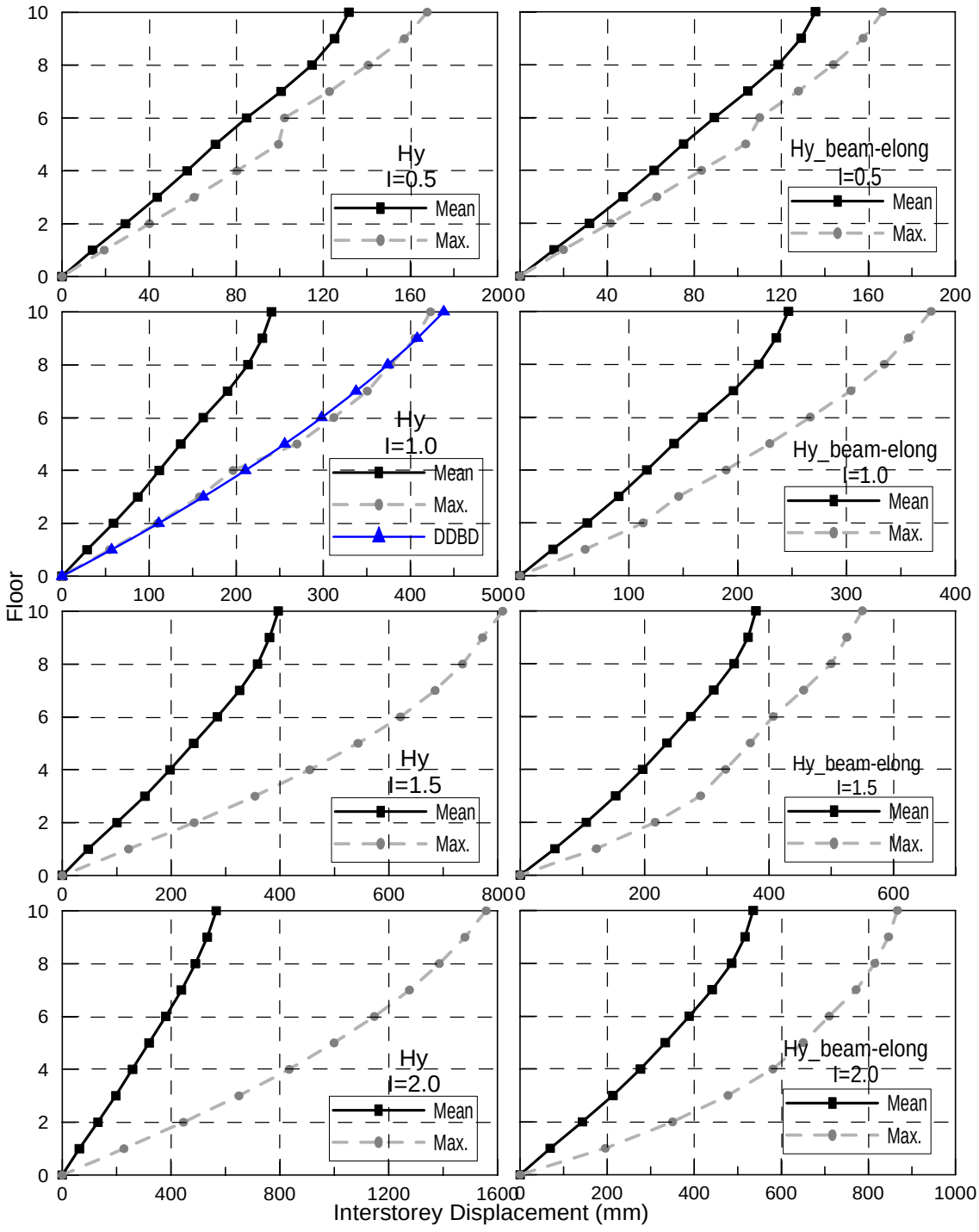

Figure 8.15 Mean and absolute maximum displacement profiles for 10Hy (left) and 10Hy_beam-elong (right) frames using a set of 5 natural scaled earthquakes for different intensities

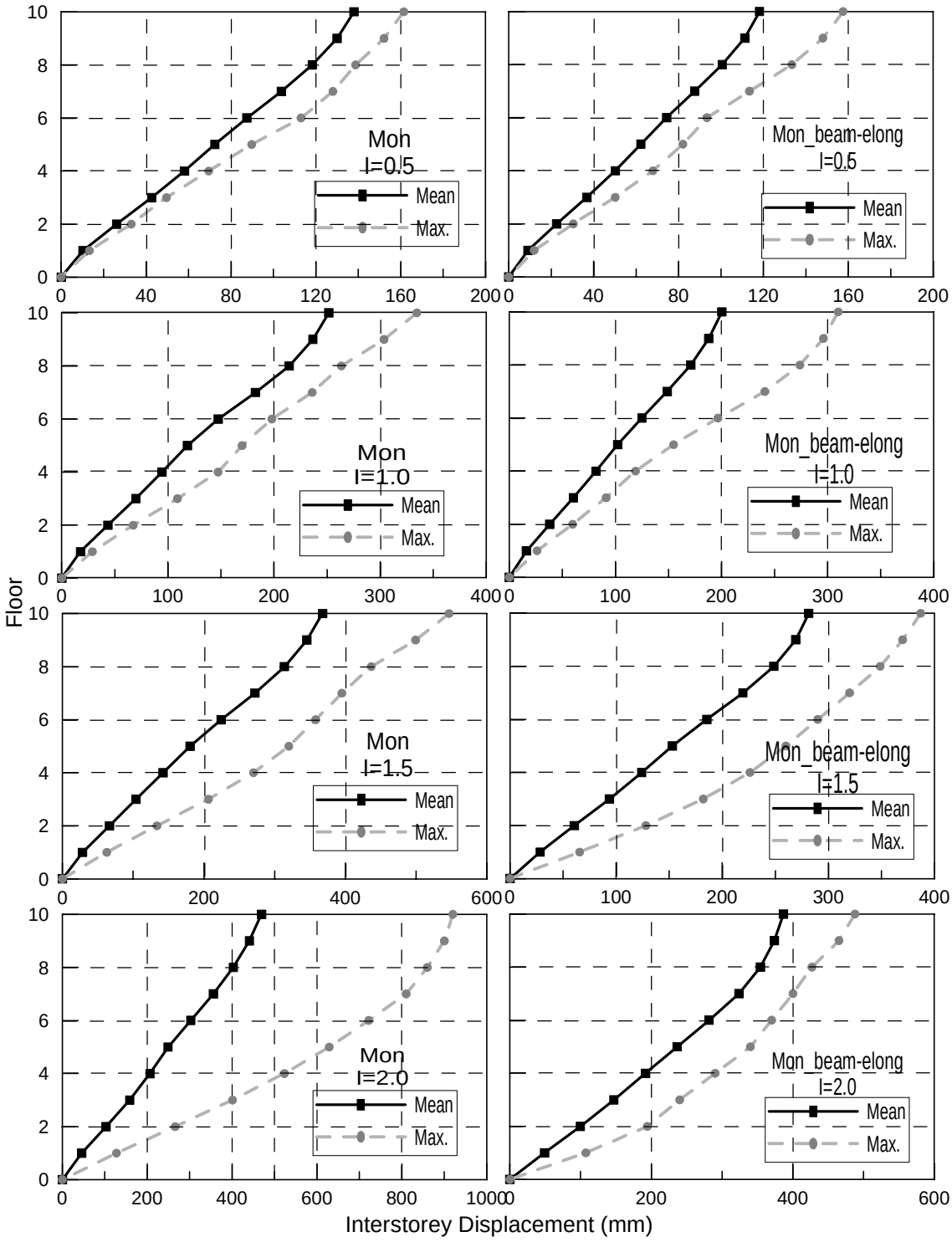

Figure 8.16 Mean and absolute maximum displacement profiles for 10Mon (left) and 10Mon_beam-elong (right) frames using a set of 5 natural scaled earthquakes for different intensities

At 0.5x the design earthquake intensity, mean displacements are reduced approximately by the same intensity amount for all the models. At 1.5x the design earthquake intensity, the 10Hy_non-tear model increases the maximum displacements by 1.5 times. However, for the

10Hy and 10Hy_beam-elong models mean displacements increased more than the intensity level (1.5x) along the height of the frames.

Similarly the 10Mon and 10Mon_beam-elong models show an increase of the mean displacements similar as the intensity level except at the first floor where the maximum displacements increased 1.6 and 1.75 times more respectively.

Finally at 2.0x the earthquake design intensity, the mean displacements increased 2.5 times more for the 10Hy_non-tear model, while for the 10Hy and 10Hy_beam-elong models, the mean displacements increased about 2.25 times more.

The 10Mon and 10Mon_beam-elong models show an increase of the mean displacement at the base about 2.5 and 3.0 times respectively for the earthquake design intensity of 2.0, but this increment reduces along the height of the building up to 2.0 times the mean displacement at the upper floors.

8.3.3 Mean Cumulative Shear Profile

Figure 8.17 shows the mean cumulative shear envelopes for each 5-storey model at 0.5x, 1.0x, 1.5x and 2.0x the earthquake intensities. In general, the 5Hy_non-tear model show the smallest total base shears while the 5Mon_beam-elong model presents the highest for each level of earthquake intensity when compared with the rest of the models.

No difference in the mean shear is observed between the 5Hy_non-tear frames using moment rotation and axial spring models at all earthquake intensities. Comparison between the 5Hy_non-tear with the 5Hy models shows that base shear was 13.2% and 14.9% higher for the 5Hy model at 0.5x and 1.0x the earthquake intensity respectively. However, at 1.5 and 2.0x the design intensity level, the 5Hy_non-tear model has a slightly smaller base shear with respect to the 5Hy model with only 3.1% and 8.5% respectively.

The 5Hy_beam-elong model shows higher base shear than the 5Hy and 5Hy_non-tear models for all earthquake intensities. As the earthquake intensity increases, the base shear differences between the 5Hy_beam-elong with the 5Hy_non-tear models increases very significantly due to the effects of beam elongation.

At half of the earthquake design intensity, the 5Hy_beam-elong model shear is 16.1% higher that the 5Hy_non-tear model, but at 1.0x the earthquake intensity, this difference increases to

59.3%. For higher earthquake intensities, the differences continue increasing (rather than decreasing as per the 5Hy model) to 71.5% and 80.3% for 1.5x and 2.0x the earthquake intensity respectively.

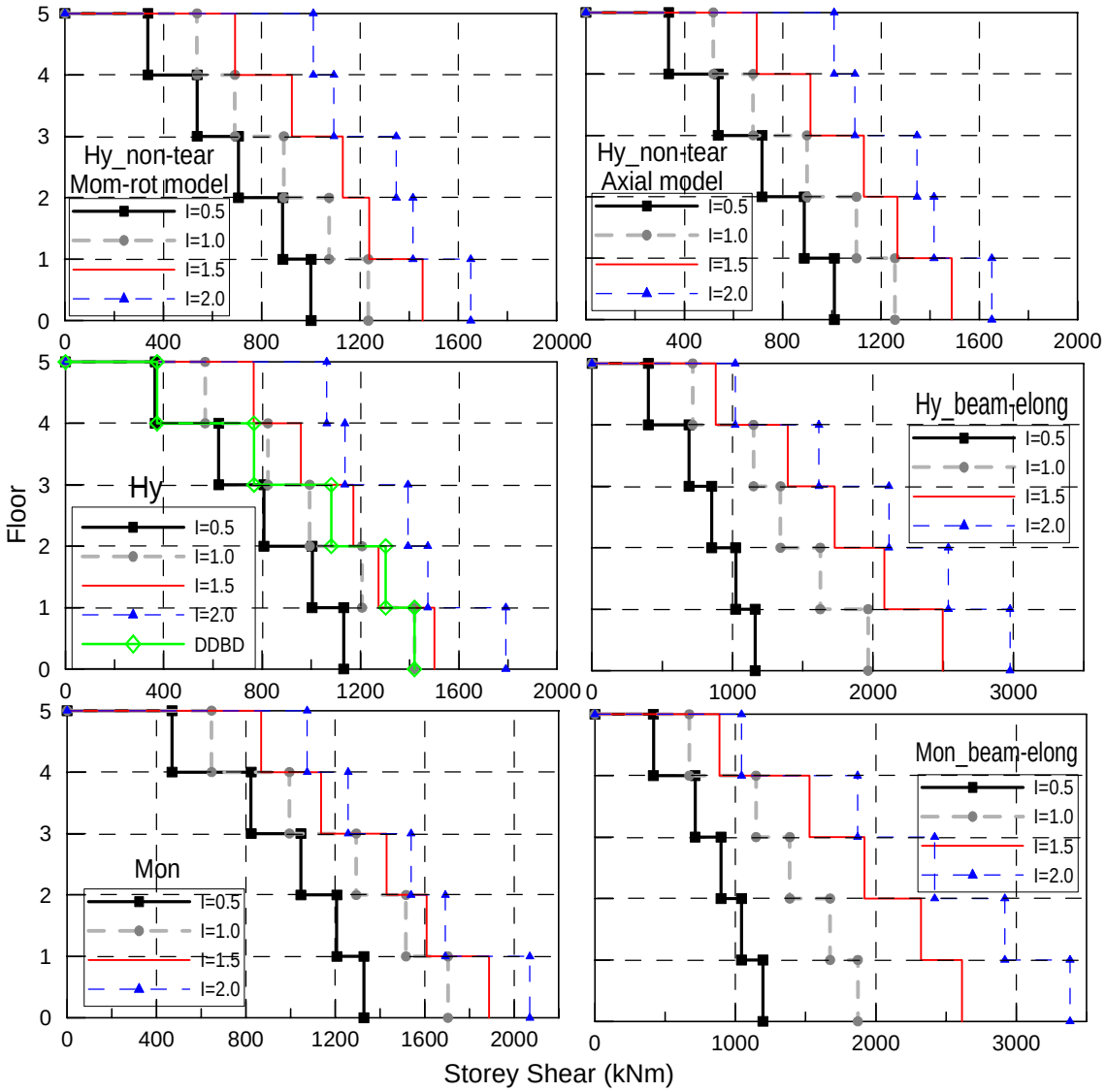

Figure 8.17 Mean Storey shear profiles for 5-storey frames using a set of 5 natural scaled earthquakes for different intensities.

Comparison between the 5Hy_non-tear and the 5Mon models shows that the base shear was 32.8% and 38.1% higher for the 5Mon model at 0.5x and 1.0x intensity level respectively. However, at 1.5x and 2.0x the earthquake design intensity, the difference in base shear for the 5Hy_non-tear model reduces with respect to the 5Mon model to 29.7% and 25.4% respectively.

As mentioned earlier, the 5Mon_beam-elong model presents the higher base shear when compared with all the models at all the earthquake intensities. At 0.5x and 1.0x the earthquake intensity, the 5Mon_beam-elong model is 36.7% and 73.3% higher that the 5Hy_non-tear model

respectively. As the earthquake intensities increases, the base shear differences between the 5Mon_beam-elong with the 5Hy_non-tear models increase significantly due to the effects of beam elongation (similar as the 5Hy_beam-elong model). Therefore, for higher earthquake intensities, the differences continue increasing (rather than decreasing as per the 5Mon model) to 205% and 234.5% higher for 1.5x and 2.0x the earthquake intensity respectively.

Figure 8.18 shows the mean cumulative shear envelopes for each 10-storey model at different earthquake intensities. Similarly as observed in the 5-storey models, the 10Hy_non-tear model shows the smallest total base shears while the 10Mon_beam-elong model presents the highest for each earthquake intensity when compared with the rest of the models.

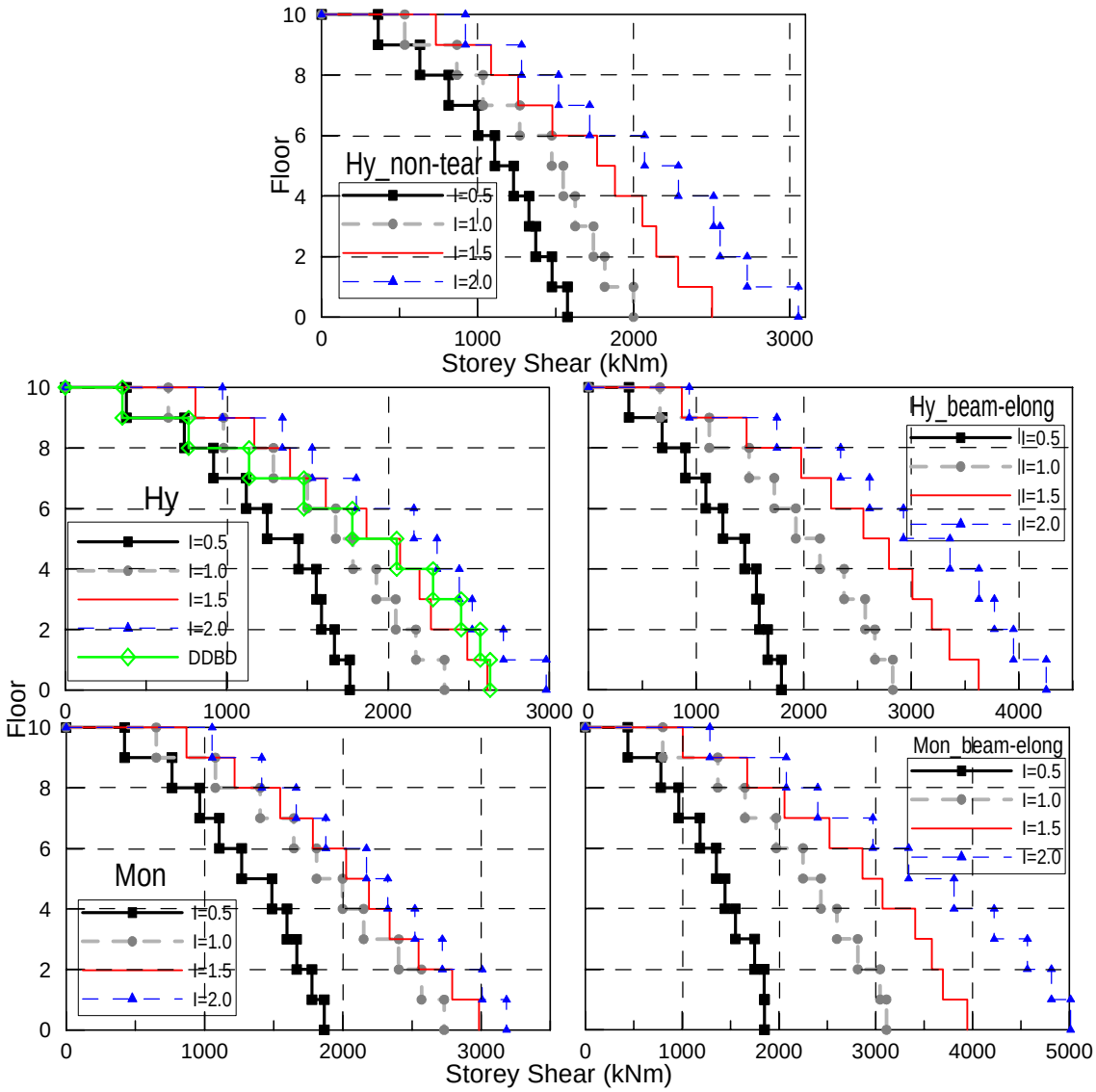

Figure 8.18 Mean Storey shear profiles for 10-storey frames using a set of 5 natural scaled earthquakes for different intensities

Comparison between the 10Hy_non-tear and the 10Hy models shows that base shear was 11.9% and 17.6% higher for the 10Hy model at 0.5x and 1.0x the earthquake intensities respectively. However, at 1.5x and 2.0x the intensity level, the 10Hy_non-tear model has closely smaller base shear with respect to the 10Hy model with only 4.0% and 1.0% difference respectively.

The 10Hy_beam-elong model shows higher base shear than the 10Hy and 10Hy_non-tear models for all earthquakes intensities. As the intensity level increases to 1.5x and 2.0x, the base shear differences between the 10Hy_beam-elong with the 10Hy_non-tear models increase dramatically due to the effects of beam elongation.

At half of the earthquake intensity, the 10Hy_beam-elong model base shear is 13.7% higher than that of the 10Hy_non-tear model, but at 1.0x the earthquake intensity, this difference increases to 41.5%. For higher earthquake intensities, the differences remain similar at 44.9% and 39.3% for 1.5x and 2.0x the intensity level respectively.

Comparison between the 10Hy_non-tear with the 10Mon models shows that base shear was 18.5% and 36.7% higher for the 10Hy model at 0.5x and 1.0x the intensity level respectively. However, at 1.5x and 2.0x the design intensity, the base shear for the 10Hy_non-tear model reduces with respect to the 10Mon model to 19.3% and 4.2% respectively.

As was observed in the 5-storey model, the 10Mon_beam-elong model presents a higher base shear when compared with all the models at all the earthquake intensities. At 0.5 and 1.0x the intensity level, base shear of the 10Mon_beam-elong model is 17.4% and 55.6% higher that the 10Hy_non-tear model respectively. As the earthquake intensities increases, the base shear differences between the 10Mon_beam-elong with the 10Hy_non-tear models remain similar as the effects of beam elongation are not significantly higher as those found for the 5-storey frame. Therefore, 1.5x and 2.0x the intensity level, the differences remain similar with 57.7% and 64.1% higher for the 10Mon_beam-elong model.

8.3.4 Mean Residual Drift and Displacement

As part of developing performance-based design and assessment concepts, residual deformations are accepted as being important in the overall definition of adequate structural response to earthquake demands. Therefore, this section describes the residual drift and displacements to assess the seismic performance of the hybrid systems using non-tearing connections in the design of seismic resistant structures.

Recent investigations [8.5, 8.6, 8.7 and 8.8] have advanced the understanding of residual displacement behaviour and have led to proposal for design methods that estimate and explicitly account for permanent deformations. Despite these efforts, little consideration is currently given to residual deformations in the codes around the world and especially in the New Zealand standard when assessing the seismic performance or in the design of seismic resistant structures.

The American Society of Civil Engineers (ASCE) 41-06 "Seismic Rehabilitation of Buildings" [8.9] includes some limits in residual deformations which correspond to different performance levels for commonly used structural systems. However, no permanent residual drift is given for hybrid precast concrete systems as they are characterized to have self-centering properties with minimum or negligible damage.

The ASCE 41-06 introduces four discrete structural performance levels described as: immediate occupancy (S-1), life safety (S-3), collapse prevention (S-5) and not considered (S-6). The drift values given by the ASCE 41-06 are typical values to illustrate the overall structural response associated with various structural performance levels and not provided as drift limit requirements. Therefore, for concrete frames a 1% drift value with negligible permanent drift is given for the immediate occupancy performance level (S-1). Similarly, a transient drift of 2% with 1% permanent drift is suggested for life safety structural performance level (S-3) and 4% transient or permanent drift for collapse prevention structural performance (S-5).

Figures 8.19 and 8.20 show the residual drifts obtained for the 5 and 10-storey models at different earthquake intensities. In general, the Hybrid model using non-tearing connections presents highest maximum residual drifts located at the roof level, while the hybrid PRESSS including and excluding beam elongation models have the smallest residual drifts due to the self-centring properties.

Additionally, residual drifts for the 5 and 10-storey Hybrid PRESSS and Monolithic models excluding beam elongation remain relatively constant along the height of the frame. However, for the Hybrid PRESSS and Monolithic models including beam elongation maximum residual drift are located at the first floors with a reduction up the height of the building.

A maximum of 0.25% residual drift at the roof level is observed for the 5Hy_non-tear model at 2 times the earthquake intensity which is far below what is recommended by the ASCE 41-06 for any of the structural performance levels indicated above.

Previous studies [8.10, 8.11, 8.12 and 8.6] have shown that the post-yield stiffness to initial stiffness ratio is the principal factor governing the residual deformation response of a structure. In particular these studies showed that systems exhibiting a post-yield stiffness ratio (on development of a full lateral mechanism) greater than 5% will have significantly reduced permanent displacements.

As described in Chapter 4, hybrid system with a non-tearing connection, has small initial and post-yield stiffness (due to the low stiffness of the post-tensioning) when compared with the high initial stiffness of the Hybrid PRESSS system. Furthermore, higher displacements (more flexible) are observed in the hybrid systems with non-tearing connections due to the relatively low initial stiffness until the lateral resistance is achieved.

Improvements in the lateral stiffness can be obtained by using an equivalent amount of steel reinforcement from the monolithic connection in the energy dissipaters and/or locating the dissipaters at the bottom face and therefore higher mild steel moment contribution will be obtained. Additionally, Chapter 5 showed the results obtained using the use of a rubber pad working only in compression located at the gap of the connection which can be sufficient to increase the stiffness when the gap closes. It is require in the design that the rubber compression forces will not surpass the forces in the monohinge. However, further numerical analyses on the post-yield stiffness in the steel stress-strain behaviour of the dissipaters are recommended in order to improve the residual deformations in Hybrid systems with non-tearing connections.

Figure 8.19 shows the residual drift for the 5Hy_non-tear model shows same value of 0.027% at the first floor for 0.5x and 1.0x the earthquake intensity level. This residual drift is higher than the 0.004% drift value obtained for the 5Hy model and very similar for the 5Hy_beam-elong model with a value of 0.025% drift. At the design intensity level, the 5Hy and 5Hy_beam-elong models show a residual drift of 0.009% and 0.04% respectively.

As the intensity increases to 1.5x and 2.0x the design earthquake intensity, residual drift for the 5Hy_non-tear model are 0.05% and 0.08% at the first floor respectively while for the 5Hy model residual drift values are 0.015% and 0.03% for the same intensity levels located at the same first floor. The 5Hy_beam-elong model presents higher residual drift values of 0.035% and 0.043% when compared to the 5Hy model but smaller than the 5Hy_non-tear model.

Similarly, comparison between the 5Hy_non-tear model with the 5Mon and 5Mon_beam-elong frames indicate smaller residual drifts for the 5Mon_beam-elong model. At half of the

earthquake design intensity, the 5Hy_non-tear model has 0.027% residual drift, higher than 0.002% and 0.005% obtained from the 5Mon and 5Mon_beam-elong models respectively. At the design earthquake intensity, the 5Hy_non-tear shows 0.027% residual drift which is smaller than the 5Mon model with 0.058% drift; however, the 5Mon_beam-elong model shows a residual drift of 0.017% smaller than the 5Hy_non-tear and 5Mon models.

As the intensity increases to 1.5x and 2.0x, the residual drifts for the 5Hy_non-tear model are 0.05% and 0.08% at the first floor respectively while for the 5Mon model residual drift values are 0.12% and 0.18%. The 5Mon_beam-elong model presents smaller residual drift values of 0.036% and 0.057% when compared with the 5Hy_non-tear and 5Mon models.

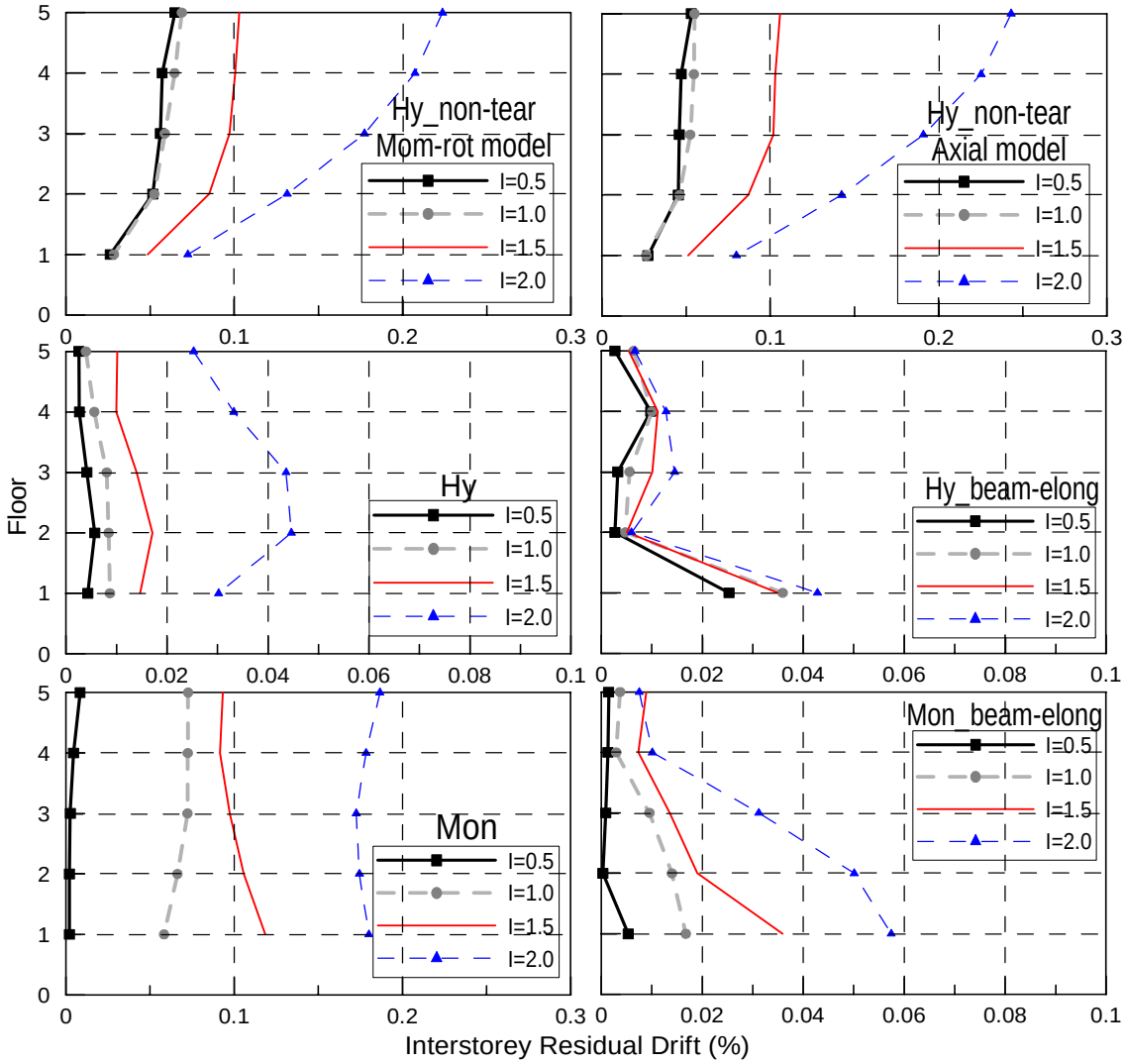

Figure 8.19 Mean residual drift profiles for 5-storey frames using a set of 5 natural scaled earthquakes for different intensities

Figures 8.20 shows the residual drift obtained for the 10-storey model. In general, the behaviour of the 10-storey frames was similar to that observed for the 5-storey buildings. The

10Hy_non-tear model shows smaller residual drifts occurring at the first floor and gradually increases along the height of the building while for the models excluding beam elongation, the residual drift remain relatively constant along the height of the frame. However, for the models including beam elongation maximum residual drift occurs at the first floors and a reduction along the height of the building. Mean residual drift of 0.18% was observed for the 10Hy_non-tear model at the roof level for 2.0x the design earthquake intensity.

The 10Hy_non-tear model shows similar residual drift with a value of 0.02% for 0.5x and 1.0x the earthquake intensity. This value is higher when it is compared with the 10Hy model with 0.002% residual drift, and similar with the 10Hy_beam-elong model with a value of 0.032% residual drift. At the design earthquake the intensity, the 10Hy and 10Hy_beam-elong models show a residual drift of 0.004% and 0.04% respectively located at the first floor.

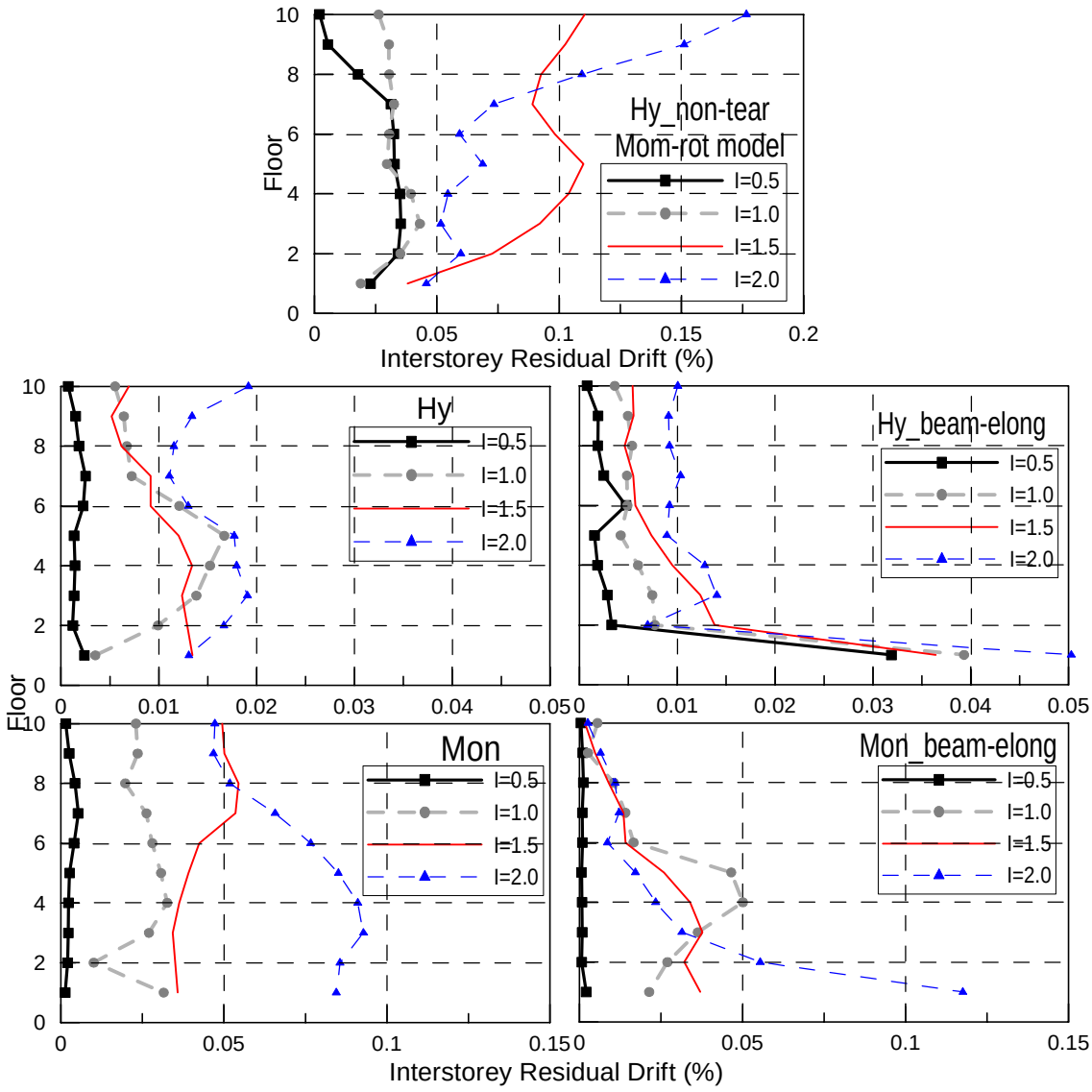

Figure 8.20 Mean residual drift profiles for 10-storey frames using a set of 5 natural scaled earthquakes for different intensities

At 1.5x and 2.0x the design earthquake intensity, the 10Hy_non-tear model shows residual drift of 0.038% and 0.046% at the first floor respectively while for the 10Hy model residual drift is the same with a value of 0.013%. The 10Hy_beam-elong model presents very similar residual drift values when compared to the 10Hy_non-tear model with residual drift values of 0.036% and 0.05% respectively.

Similarly, comparison between the 10Hy_non-tear model with the 10Mon and 10Mon_beam-elong models indicates smaller residual drift for the 10Hy_beam-elong model at the first floor, however, residual drifts are higher at top floors for the 10Hy_non-tear model.

At half of the earthquake intensity, the 10Hy_non-tear model has 0.02% residual drift higher than the 0.001% and 0.002% for the 10Mon and 10Mon_beam-elong model respectively. At 1.0x the earthquake intensity, the 10Hy_non-tear shows 0.019% residual drift smaller than 0.032% and 0.021% for the 10Mon and 10Mon_beam-elong models respectively.

At 1.5 and 2.0x the design earthquake intensity, the residual drifts for the 10Hy_non-tear model are 0.038% and 0.046% respectively at the first floor, while for the 10Mon model residual drift values are 0.036% and 0.084%. The 10Mon_beam-elong model presents higher residual drift values of 0.037% and 0.11% when compared to the other models.

Figure 8.21 shows the residual displacements obtained for the 5 -storey model. The 5Hy_non-tear, 5Hy and 5Mon models show smaller residual displacements occurring at the first floor and linearly increase along the height of the buildings while for the models including beam elongation, the 5Hy_beam-elong residual displacements slightly reduce along the height of the frame, while for the 5Mon_beam-elong the maximum residual displacements increase along the height of the building.

Comparison of residual displacement at the first floor shows that for the 5Hy_non-tear model the same residual displacement is observed with a value of 1mm at 0.5 and 1.0x the earthquake intensity, higher than 0.16mm for the 5Hy model and very similar for the 5Hy_beam-elong model with a value of 0.96mm residual displacement. At 1.0x the intensity, the 5Hy and 5Hy_beam-elong models show a residual displacement of 0.33mm and 1.37mm respectively.

As the intensity increases to 1.5x and 2.0x, the residual displacement for the 5Hy_non-tear model are 1.94mm and 3.03mm at the first floor respectively while for the 5Hy model residual

displacement values are 0.56mm and 1.15mm. The 5Hy_beam-elong model presents higher residual displacement values of 1.33mm and 1.63mm when compared to the 5Hy model.

Similarly, comparison between the 5Hy_non-tear model with the 5Mon and 5Mon_beam-elong models indicates smaller residual displacements for the 5Mon_beam-elong model. At half of the earthquake intensity, the 5Hy_non-tear model has 1.0mm residual displacement, higher than 0.8mm and 0.2mm obtained for the 5Mon and 5Mon_beam-elong model respectively. At 1.0x intensity level, the 5Hy_non-tear shows smaller residual displacements (1.0mm) when compared to the 5Mon model (2.22mm). However, the 5Mon_beam-elong model shows a smaller value when compared to the 5Hy_non-tear model with a value of 0.64mm.

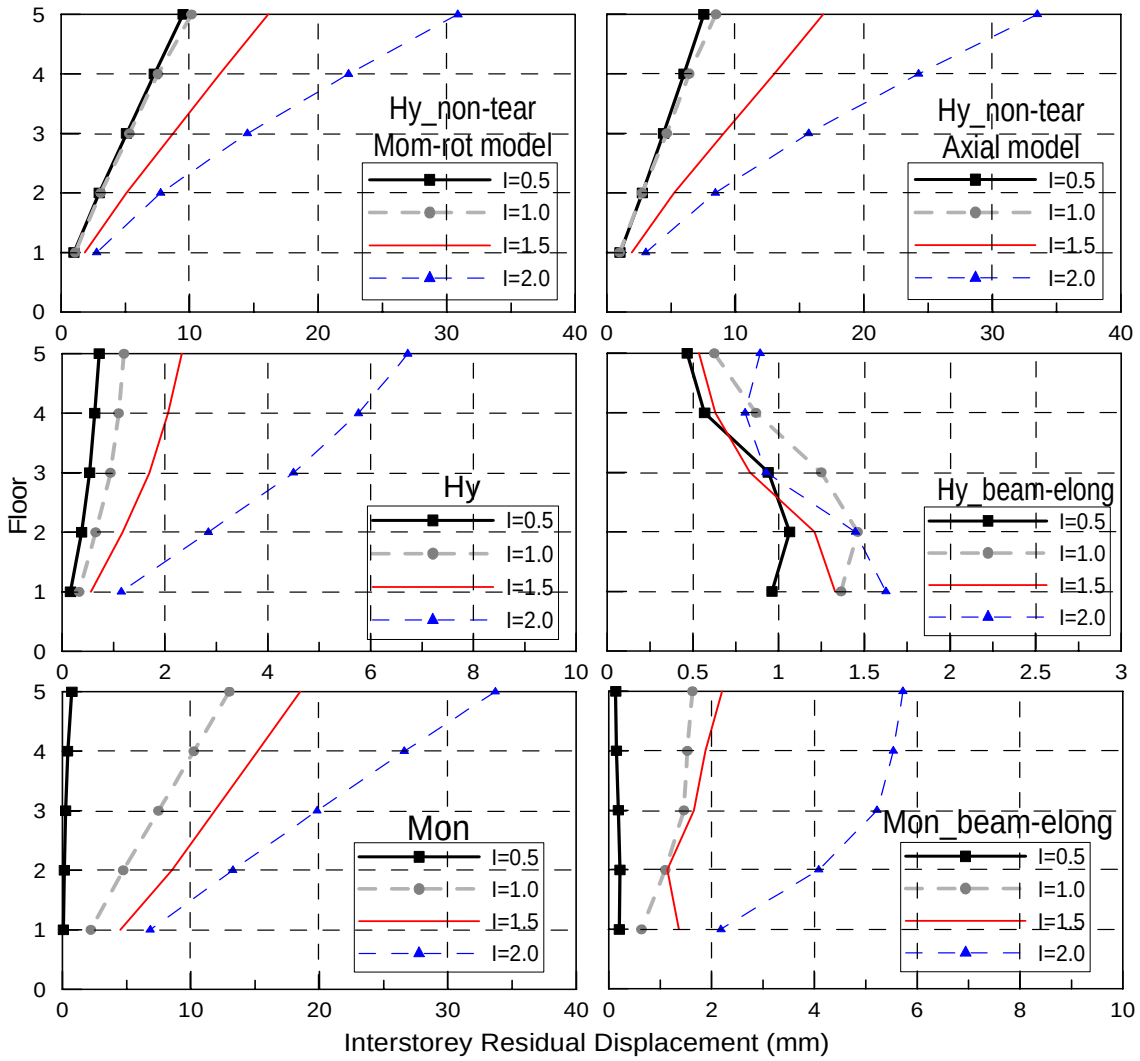

Figure 8.21 Mean residual displacements profiles for 5-storey frames using a set of 5 natural scaled earthquakes for different intensities

As the intensity increases to 1.5 and 2.0 times, the residual displacement for the 5Hy_non-tear are model are 1.94mm and 3.03mm respectively at the first floor while for the 5Mon model

residual displacement values are 4.50mm and 6.84mm. The 5Mon_beam-elong model presents smaller residual drift values of 1.36mm and 2.18mm when compared to the other two modes.

Figure 8.22 shows the residual displacements obtained for the 10 -storey model. In general, the behaviour of the 10-storey frames was similar to those observed for the 5-storey buildings. The 10Hy_non-tear, 10Hy and 10Mon models show smaller residual displacements occurs at the first floor and linearly increases along the height of the buildings while for the models including beam elongation maximum residual drift occurs at the first floors and a reduction along the height of the building for the 10Hy_beam-elong model, but an increase for the 10Mon_beam-elong model.

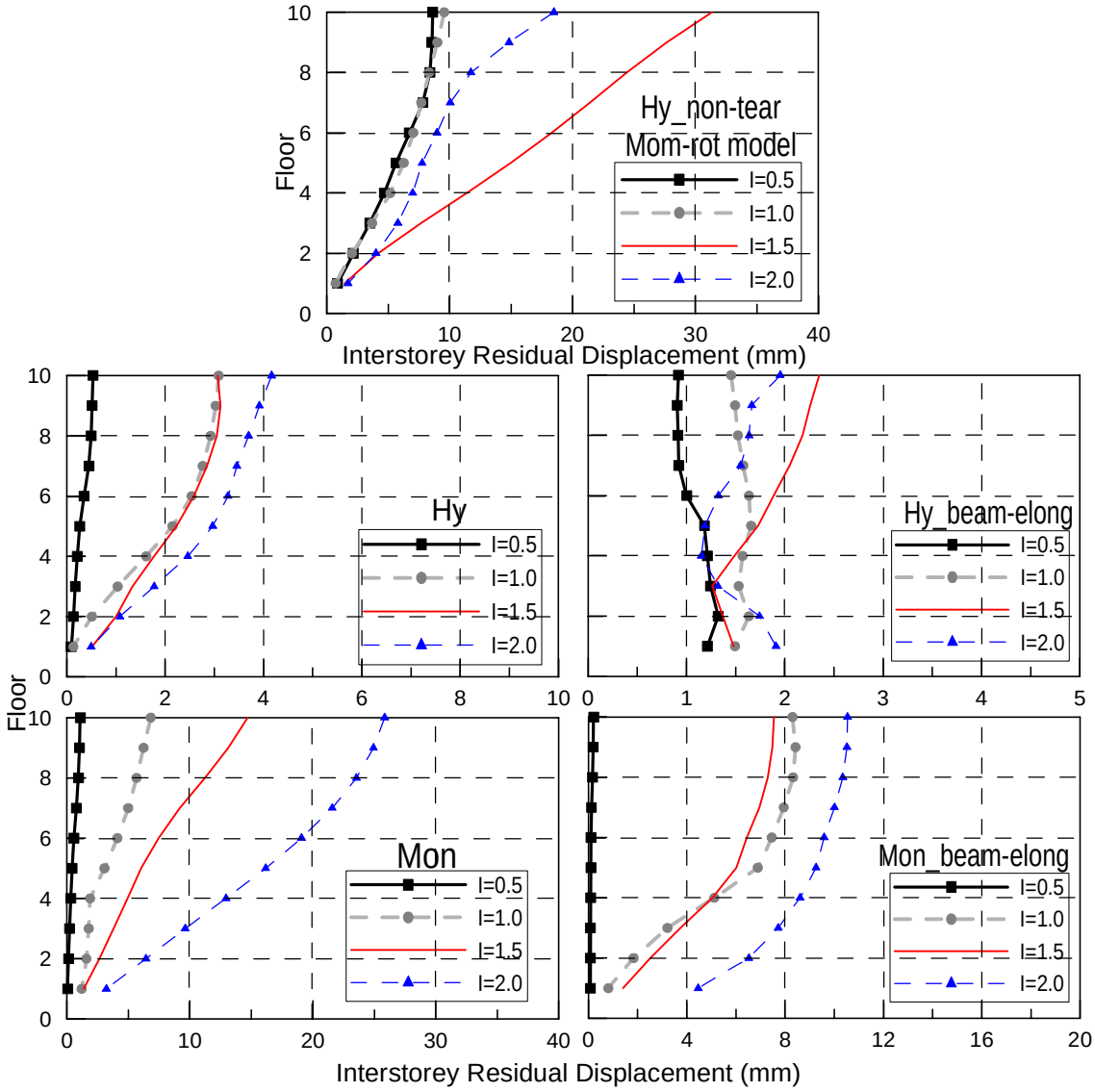

Figure 8.22 Mean residual displacements profiles for 10-storey frames using a set of 5 natural scaled earthquakes for different intensities

The 10Hy_non-tear model shows similar residual displacement at intensities 0.5x and 1.0x with values of 0.8mm at the first floor. At 0.5x the intensity level, the 10Hy model shows a residual displacement of 0.09mm, smaller than the 10Hy_non-tear frame and the 10Hy_beam-elong model with a value of 1.21mm residual displacement. At 1.0x the intensity, the 10Hy and 10Hy_beam-elong models show a residual displacement of 0.13mm and 1.49mm respectively.

At 1.5x and 2.0x the intensity level, the 10Hy_non-tear model shows residual displacements of 1.44mm and 1.74mm at the first floor respectively while for the 10Hy model residual displacement is the same with a value of 0.51mm. The 10Hy_beam-elong model presents very similar residual displacement values when compared to the 10Hy_non-tear model with values of 1.48mm and 1.91mm for 1.5x and 2.0x intensities respectively located at the first floor.

Similarly, comparison between the 10Hy_non-tear model with the 10Mon and 10Mon_beam-elong models indicates smaller residual displacement for the 10Hy_beam-elong model at the first floor, however, residual displacements are higher at top floors for the 10Hy_non-tear model.

At half of the earthquake intensity, the 10Hy_non-tear model has 0.8mm residual displacement at the first floor higher than the 0.05mm and 0.08mm values obtained for the 10Mon and 10Mon_beam-elong model respectively. At 1.0x the earthquake intensity, the 10Hy_non-tear shows 0.8mm residual displacement, smaller than 1.2mm and 0.8mm for the 10Mon and 10Mon_beam-elong models respectively.

As the intensity increases to 1.5x and 2.0x, residual drifts for the 10Hy_non-tear model are 1.44mm and 1.74mm at the first floor respectively, while for the 10Mon model residual displacement values are 1.36mm and 3.21mm. The 10Mon_beam-elong model presents higher residual displacements values of 1.41mm and 4.47mm when compared to the other models.

8.4 INELASTIC TIME-HISTORY RESULTS FOR FAR AND NEAR FIELD EARTHQUAKES RECORDS

8.4.1 Mean Maximum and Absolute Maximum Inter-storey Drift Profile

Figures 8.23 and 8.24 show the mean maximum (mean) and absolute maximum (max.) drift envelopes for each 5-storey model for far and near field earthquakes. In general, any of mean drift values of the 5-storey frames do not exceed the design drift limit of 2.0%. However, some

maximum drift values greater than the drift limit were observed at the first floor for the 5-storey hybrid and monolithic models including beam elongation.

Figure 8.23 shows the inter-storey drift for the 5-storey frames using different connections for far field earthquakes. No significant differences in the mean or maximum drift values can be observed for the 5Hy_non-tear frames using moment rotation and axial spring models. The mean values were almost constant varying from 0.5% drift in the first floor to 0.69% drift at the top floor. The maximum drift value was higher at the second floor with a value of 1.58% drift and gradually reducing to 1.33% drift at the top floor.

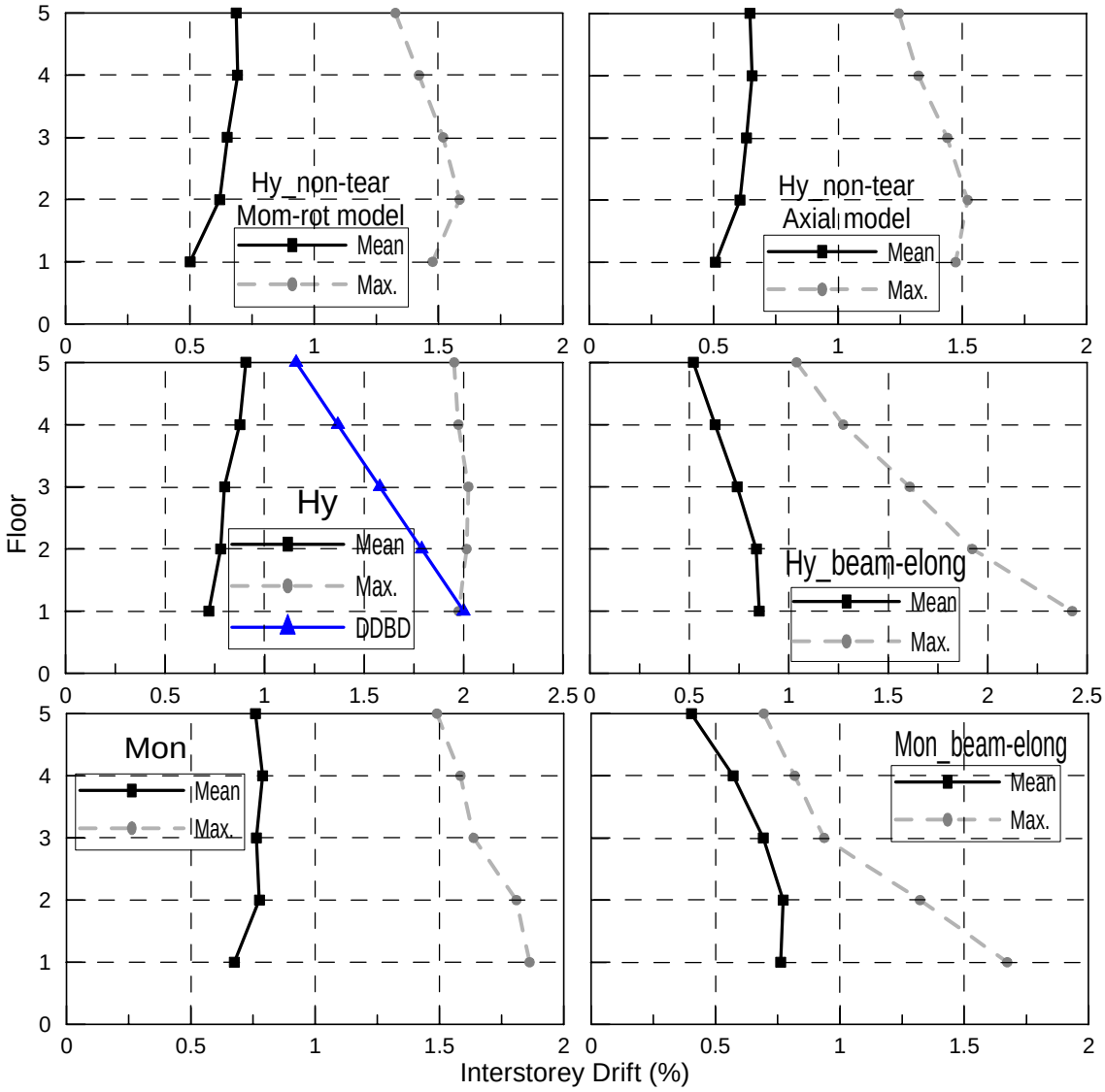

Figure 8.23 Mean and absolute maximum drift profiles for 5-storey frames using far field records.

The 5Hy_non-tear model shows smaller mean and maximum inter-storey drift values at the first floor (0.5% and 1.47% drift) when compared with the 5Hy and 5Mon models with values 0.72% and 1.98% drift for the 5Hy and 0.68% and 1.86% drift for the 5Mon models.

Comparison between the 5Hy_non-tear with the 5Hy_beam-elong and 5Mon_beam-elong models show that the models with beam elongation present higher mean and maximum drift values at the first two floors and then reduce along the height of the building while for the 5Hy_non-tear the mean and maximum drift values remain relatively constant along the height.

The mean drift values for the 5Hy_beam-elong and 5Mon_beam-elong models are 0.85% and 0.76% drift at the first floor higher than the 5Hy_non-tear model with a value of 0.72% drift. However at the top floor the 5Hy_beam-elong and 5Mon_beam-elong models show a mean drift value of 0.52% and 0.40% respectively, while the 5Hy_non_tear model presents a higher value of 0.65% drift. Maximum drift values for the 5Hy_beam-elong and 5Mon_beam-elong models are higher at the first floor with a value of 2.42% and 1.67% drift respectively, while a smaller maximum drift of 1.58% is observed for the 5Hy_non-tear model which occurs at the second floor.

Figure 8.24 shows the inter-storey drift for the 5-storey frames using different connections for near field earthquakes. Comparison between far field and near field response shows a small increment in the mean and maximum drift for the 5-storey models using Hybrid PRESSS type or non-tearing connections. However, for the 5Mon and 5Mon_beam-elong models mean and maximum drift values increase for the 5Mon_beam-elong model and slightly reduce for the 5Mon model.

Similar as what was found for the far field earthquake records, no significant differences are shown for the mean and maximum drift values for the 5Hy_non-tear frames models using moment rotation and axial spring models for the mean and maximum drift values.

Comparison between the 5Hy_non-tear model with the 5Hy and 5Mon models show the 5Hy model with mean value of 0.90% drift higher than the other two models with values of 0.71% and 0.88% drift for the 5Hy_non-tear and 5Mon models respectively at the second floor. Maximum drift values for the 5Hy model are almost constant along the height of the building with a value of 1.7% drift, while the 5Mon and 5Hy_non-tear models shows maximum drifts of 1.43% and 1.67% at the third floor respectively.

Comparison between the 5Hy_non-tear and the 5Hy_beam-elong and 5Mon_beam-elong models show similar results as found for the far field events including beam elongation having higher mean and maximum drift values at the first two floors and then reduce along the height

of the building while for the 5Hy_non-tear the mean and maximum drift values remain almost constant along the height.

Mean drift values of 0.98% and 0.79% are found for the 5Hy_beam-elong and 5Mon_beam-elong models respectively. These values are higher than the values found for the 5Hy_non-tear model with a mean value of 0.61% drift. However at the top floor the 5Hy_beam-elong and 5Mon_beam-elong models show a mean drift value of 0.51% and 0.42%, smaller than the 5Hy_non_tear model with a value of 0.59% drift. Maximum drift values for the 5Hy_beam-elong and 5Mon_beam-elong models are higher at the first floor with a value of 2.39% and 2.47% respectively, while smaller maximum drift of 1.43% is observed for the 5Hy_non-tear model at the third floor.

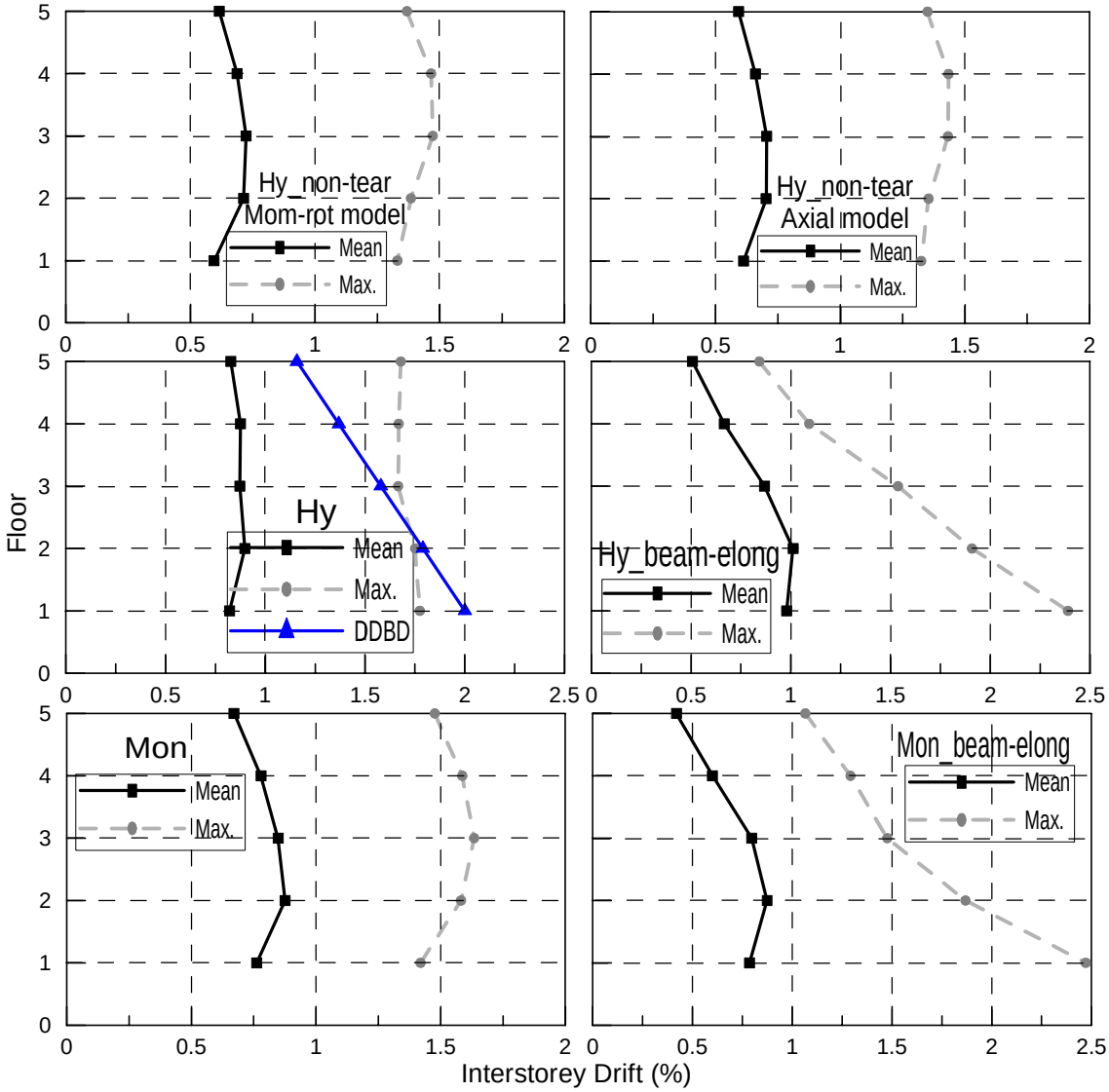

Figure 8.24 Mean and absolute maximum drift profiles for 5-storey frames using near field records.

Figures 8.25 and 8.26 show the mean maximum (mean) and absolute maximum (max.) drift envelopes for each 10-storey model for far and near field earthquakes respectively. In general, any of the mean drift values of the 10-storey frames do not exceed the design drift limit of 1.5%. However, maximum drift values greater than the drift limit were observed for almost all the models except the hybrid model with non-tearing connections.

Figure 8.25 shows the inter-storey drift for the 10-storey frames using different connections for far field earthquakes. Mean and maximum drift values for the 10Hy_non-tear frame were almost constant along the height of the frame with a maximum mean of 0.62% drift located at the seventh floor and a linear reduction to the roof. Maximum drift values are higher at the second floor with a value of 1.29% drift and gradually reducing to 0.49% drift at the top floor.

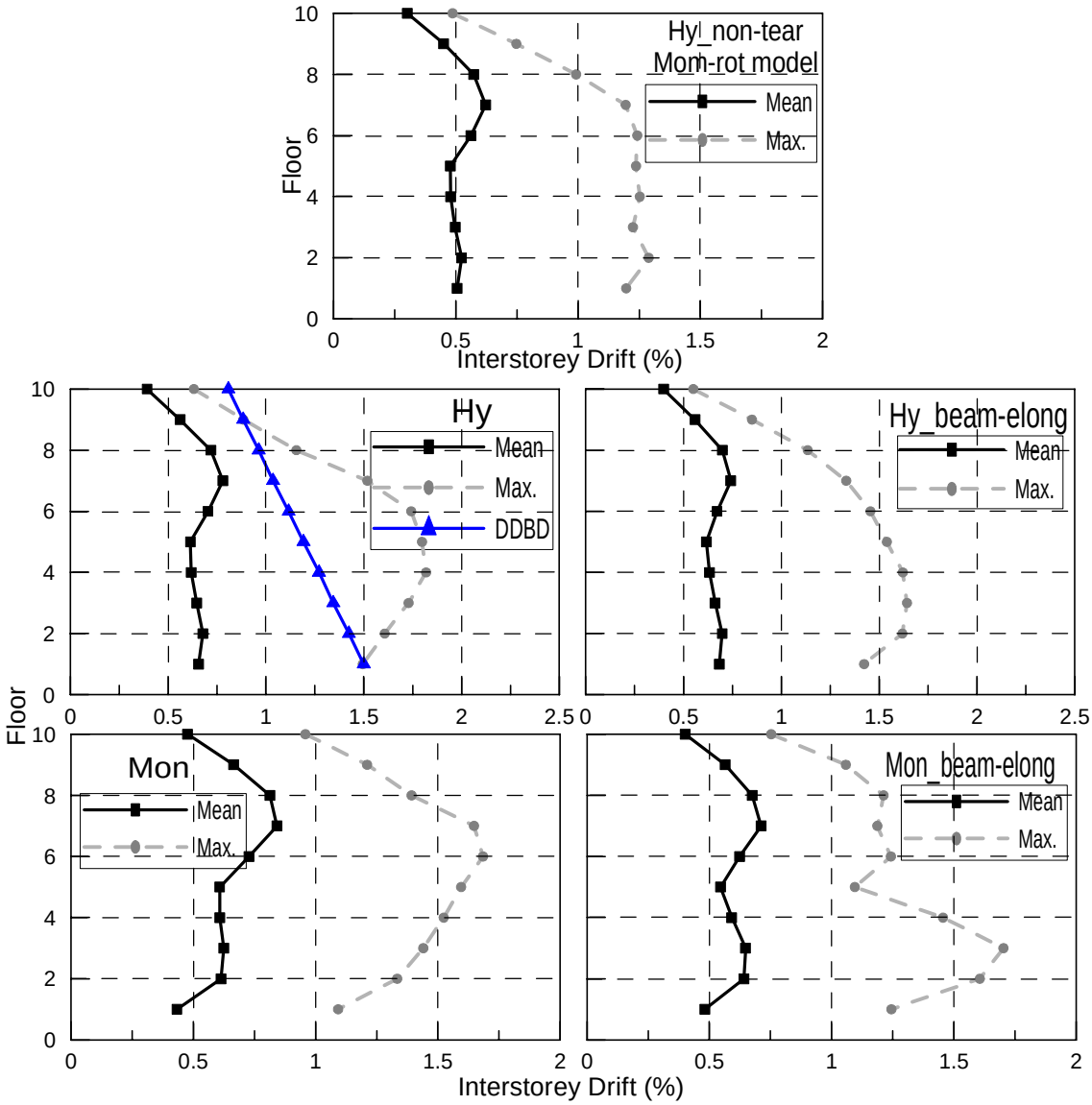

Figure 8.25 Mean and absolute maximum drift profiles for 10-storey frames using far field records.

The 10Hy_non-tear model shows smaller mean drift value (0.62% drift) with respect to the 10Hy and 10Mon models with values of 0.78% and 0.84% drift located at seventh floor. Maximum drift values for the 10Hy and 10Mon models occur at the fourth and seventh floor with maximum values of 1.82% and 1.68% drift respectively while the 10Hy_non-tear model shows a maximum of 1.29% drift located at the second floor.

Comparison between the 10Hy_non-tear with the 10Hy_beam-elong and 10Mon_beam-elong models show that the frames with beam elongation present higher mean and maximum drift values at the first two floors and then reduce along the height of the building while for the 10Hy_non-tear the mean and maximum drift values remain almost constant along the height.

Mean drift values for the 10Hy_beam-elong and 10Mon_beam-elong models are 0.74% and 0.71% drift located at the seventh floor, higher than the 10Hy_non-tear model with value of 0.62% drift. Similarly, maximum drift values for the 10Hy_beam-elong and 10Mon_beam-elong models are higher at the third floor with values of 1.64% and 1.70% drift respectively, while a smaller maximum drift of 1.29% is observed for the 10Hy_non-tear model located at the second floor.

Figure 8.26 shows the mean and maximum inter-storey drifts for the 10-storey frames using different connections for near-field earthquakes. Comparison between far-field and near-field response shows an increase in the mean and maximum drift levels for all the models.

The 10Hy_non-tear model shows mean values of 0.99% drift, higher than the 10Hy model with values of 0.78% drift at the second floor. However, the 10Mon model shows a mean value of 1.18% drift at the seventh floor which is higher than the 10Hy_non-tear and 10Hy models with mean values of 0.72% and 1.03% drift respectively.

Maximum drift values for the 10Hy model were almost constant up to the sixth floor of the frame with a value of 2.05% drift and then reduced at the top floor, while the 10Mon model shows an increase in the maximum drift from the first to the seventh floors with values of 1.10% and 1.98% drift respectively. The 10Hy_non-tear model shows a relatively constant maximum value of 1.5% drift along the height of the building.

Comparison between the 10Hy_non-tear with the 10Hy_beam-elong and 10Mon_beam-elong models show higher mean and maximum drift values were obtained for near field effects when compared with far field response. The 10Hy_beam-elong and 10Mon_beam-elong models present higher mean and maximum drift values at the first two floors and then reduce along the

height of the building with a small increase at the mid-height of the frames. For the 10Hy_non-tear model the mean and maximum drift values remain almost constant along the height of the frame with a reduction at mid-height of the frame.

Mean drift values for the 10Hy_beam-elong model is 0.98% drift located at the first floor, higher than the 10Hy_non-tear model with a value of 0.78% drift. The 10Mon_beam-elong mode has a mean drift value of 0.66%; however, at the seventh floor the 10Hy_beam-elong and 10Mon_beam-elong models show a mean drift value of 1.03% and 0.94% respectively, while the 10Hy_non_tear model presents a smaller value of 0.72% drift.

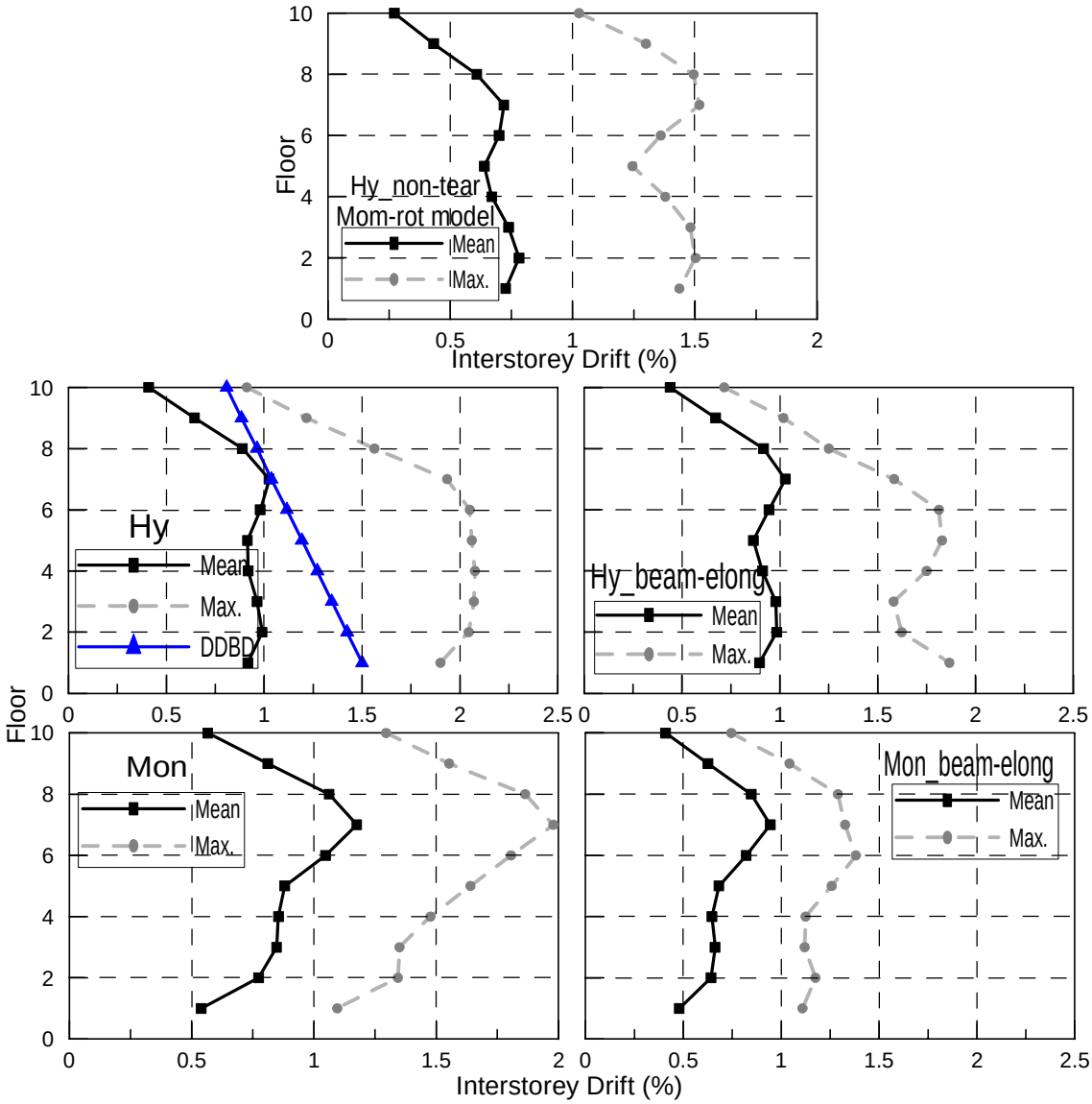

Figure 8.26 Mean and absolute maximum drift profiles for 10-storey frames using near field records.

The maximum drift values for the 10Hy_beam-elong model is 1.87% drift located at the first floor, higher than the 10Hy_non tear and 10Mon_beam-elong models with drift values of 1.44%

and 1.18% respectively. However, the 10Mon_beam-elong and 10Hy_beam-elong models show an increase in the maximum drift of 1.38% and 1.83% in the sixth floor while the 10Hy_non-tear model shows relatively constant maximum drift values of 1.5% along the height of the building but at mid-height a small reduction is observed (1.3% drift).

8.4.2 Mean Maximum and Absolute Maximum Displacement Profile

Figures 8.27 and 8.28 show the mean maximum (mean) and absolute maximum (max.) displacement profiles for the 5-storey fames for the far field (Left) and near field (Right) events. In general, comparison between the far and near field earthquakes indicates that near field events increase the displacements profiles along the height of the buildings.

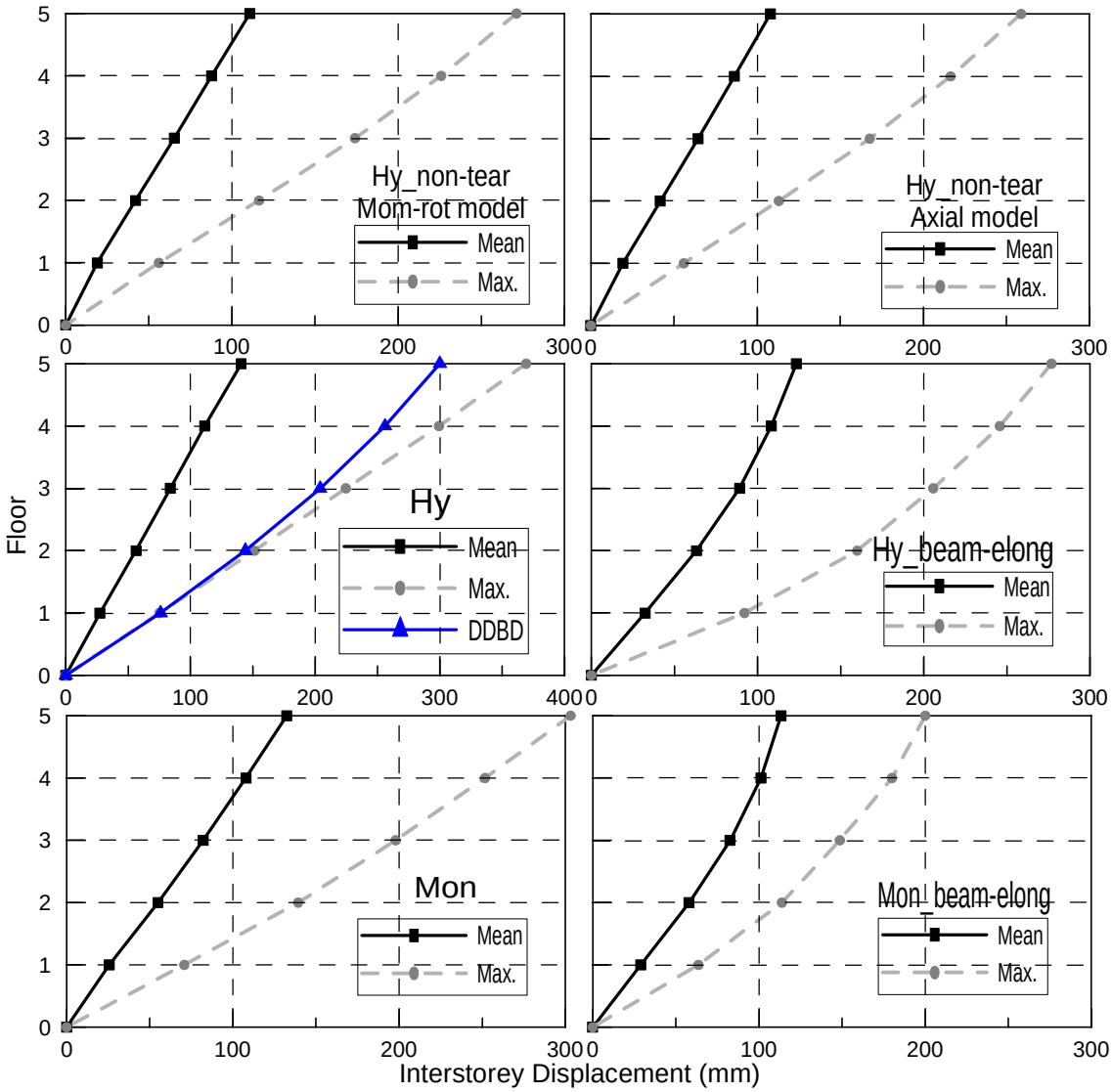

Figure 8.27 Mean and maximum displacement profiles for 5-storey frames using far field records.

The maximum displacement for the hybrid PRESSS model shows a better approximation for near field events when it is compared with the displacements obtained using the direct displacement base design principles (DDBD) while for far field earthquakes, the expected top displacements from the DDBD profiles is smaller than those obtained for the maximum of the set of 20 far field earthquake records.

The mean displacements were similar between the Hybrid PRESSS and monolithic models; however, the model using non-tearing connections undergo less deformation with a linear distribution displacement profile. Models including beam elongation show a parabolic displacement distribution where lower storeys present higher displacements than the models excluding beam elongation effects and using non-tearing connections.

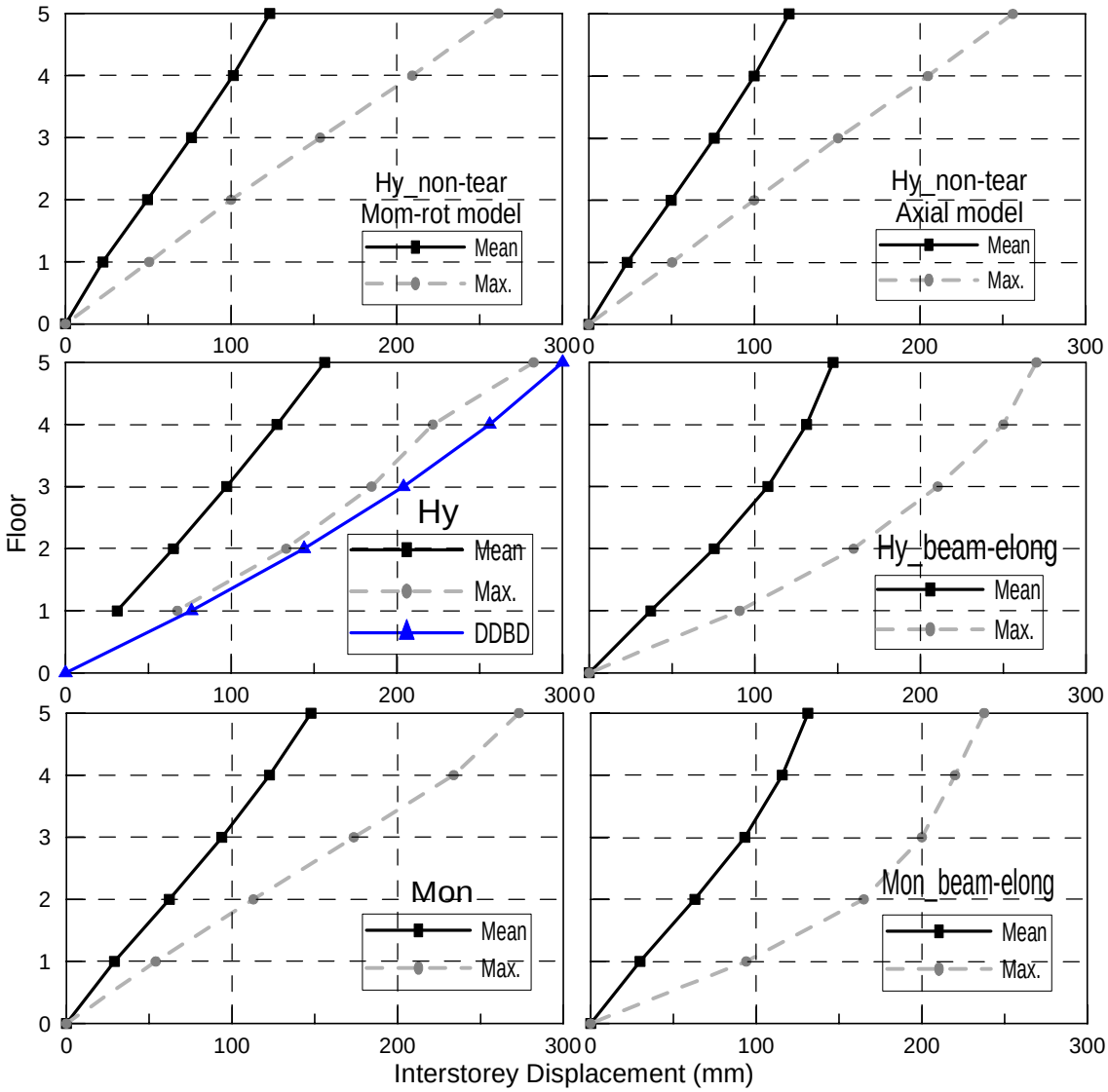

Figure 8.28 Mean and maximum displacement profiles for 5-storey frames using near field records.

No difference in the displacement profiles between the 5Hy_non-tear frame considering moment rotation and axial spring model is observed. Comparison between the 5Hy_non-tear model with the hybrid PRESSS and monolithic models excluding and including beam elongation indicates that the models using non-tearing connections undergo smaller displacements. The 5Hy model has higher roof displacements, however, the 5Hy_beam-elong model shows higher displacements at the first three floors.

Figures 8.29 and 8.30 show the mean and maximum displacement profiles for the 10-storey fames for far field (Left) and near field (Right) events. Similar as found for the 5-storey models, comparison between far and near field earthquakes indicates that near field events increase the displacement profiles along the height of the buildings.

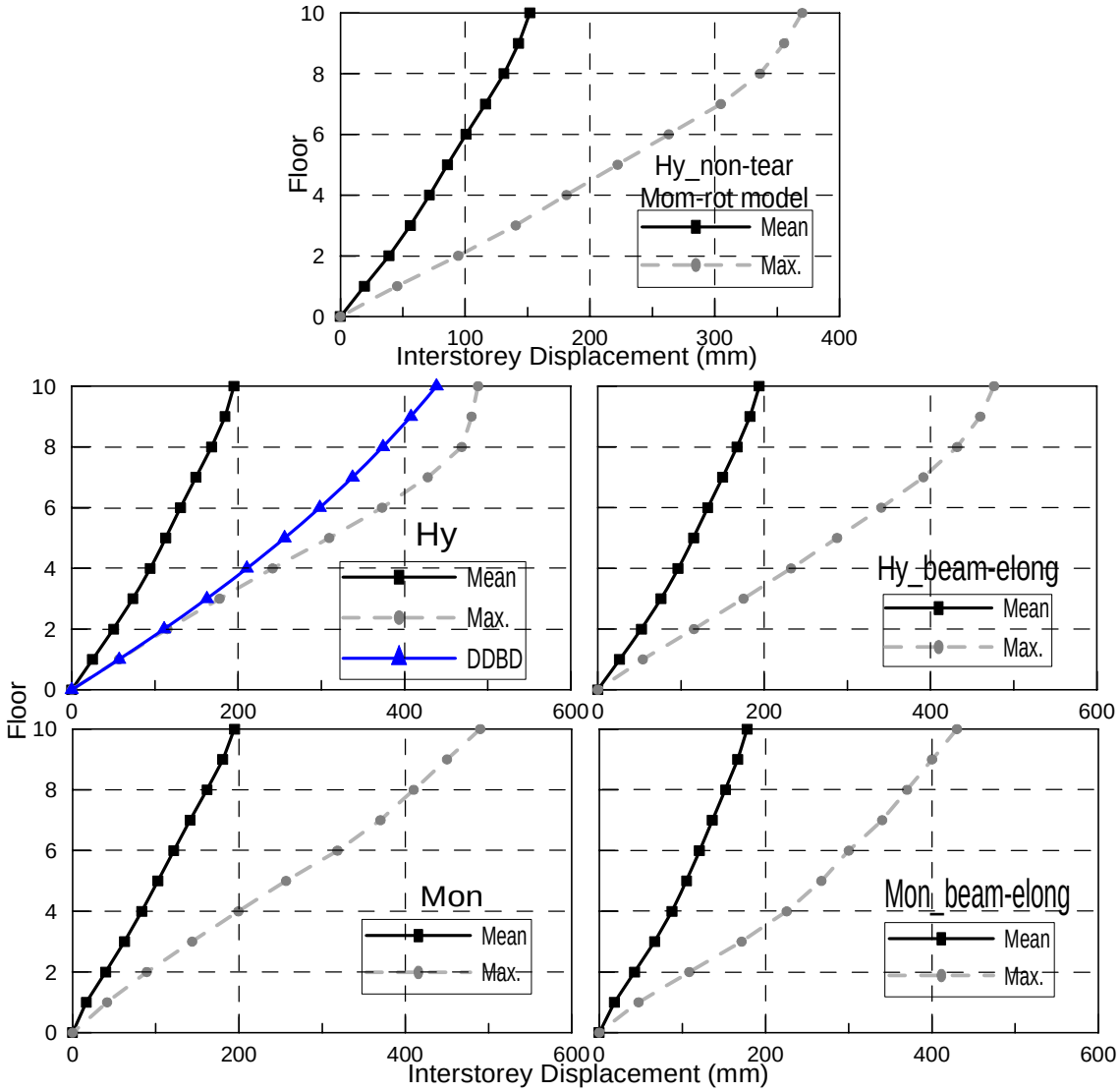

Figure 8.29 Mean and maximum displacement profiles for 10-storey frames using far field records.

The maximum displacement for the hybrid PRESSS model shows better approximation for far field events when it is compared with the displacements obtained using direct displacement base design principles (DDBD) while for near field earthquakes, the expected top displacements from the DDBD profiles is smaller than those obtained for the maximum of the set of 10 near field earthquakes records.

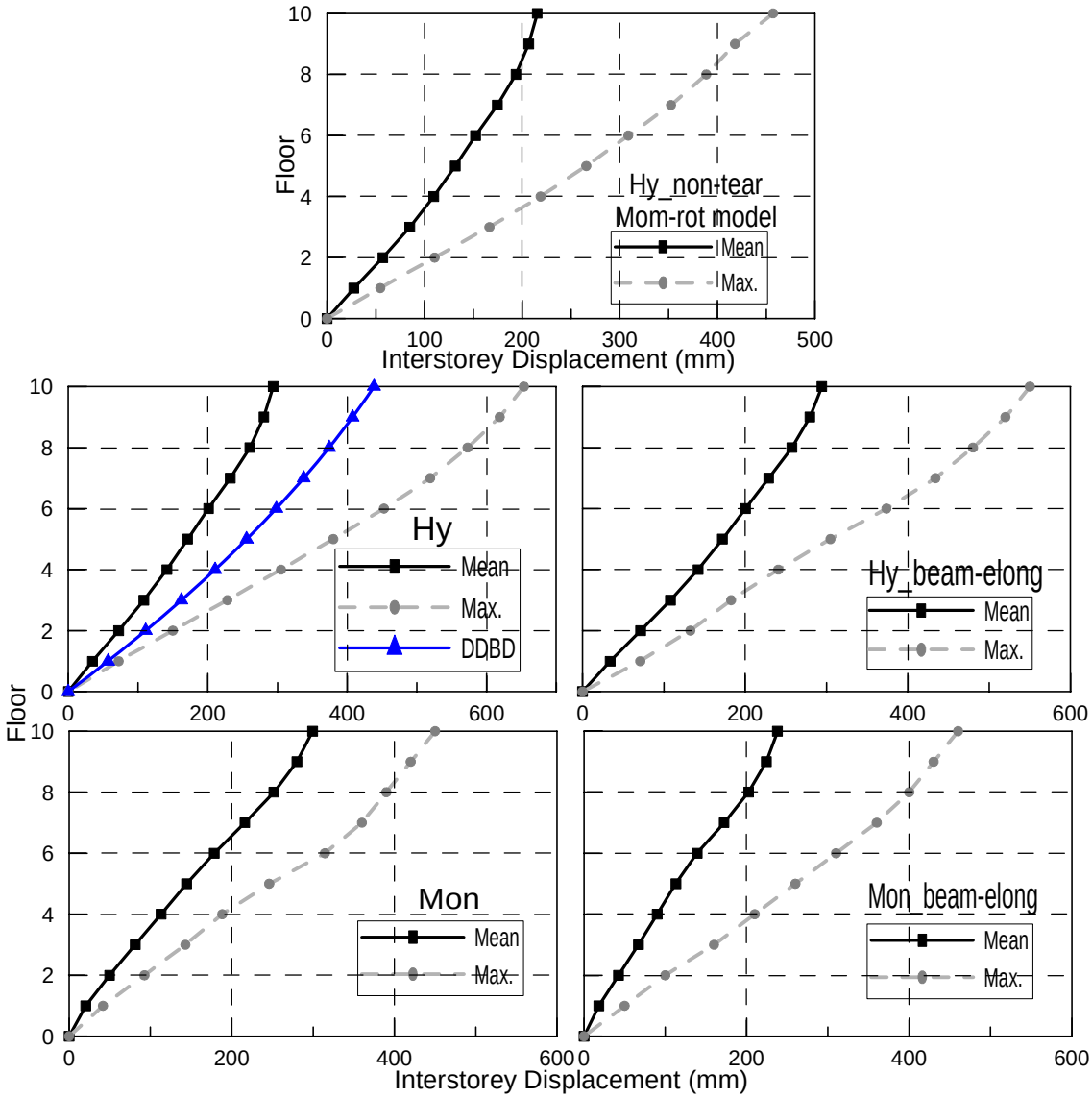

Figure 8.30 Mean and maximum displacement profiles for 10-storey frames using far field records.

Maximum displacement profiles for the 10Hy_non-tear model were smaller than the rest of the models for far field earthquakes. However, for near field events, the 10Mon_beam-elong model has smaller displacements than the rest of the models.

Comparison between the 10Hy and 10Hy_beam-elong models indicates no major differences in the maximum displacements for far field and near field events. However, higher displacements

are observed for the 10Mon when is compared with the 10Mon_beam-elong model especially at the top floors.

8.4.3 Mean Cumulative Shear Profile

Figure 8.31 shows the mean cumulative shear envelopes for each 5-storey model for far field (left) and near field (right) earthquakes. In general, the 5Hy_non-tear model shows smallest total base shears while the 5Mon_beam-elong model has the highest value when compared with the rest of the models. Comparison between far and near field events indicates higher storey shear at the top floors for far field earthquake records, while a small reduction of the cumulative shear at the lower floor levels for near field events.

The 5-storey hybrid PRESSS model shows good agreement for both far and near field when compared with the shear profile obtained using direct displacement base design principles. No difference was observed between the 5Hy_non-tear frames using moment rotation and axial spring models. Similarly, comparison between the 5Hy_non-tear with the 5Hy models shows that base shear was 14.9% and 12.1% higher for the 5Hy model for far field and near field events respectively.

The 5Hy_beam-elong model shows higher base shear than the 5Hy and 5Hy_non-tear models for both far and near field events. Base shear differences between the 5Hy_beam-elong with the 5Hy_non-tear models increases very significantly due to the effects of beam elongation. The 5Hy_beam-elong model is 56.2% and 51.3% higher that the 5Hy_non-tear model for far and near field events.

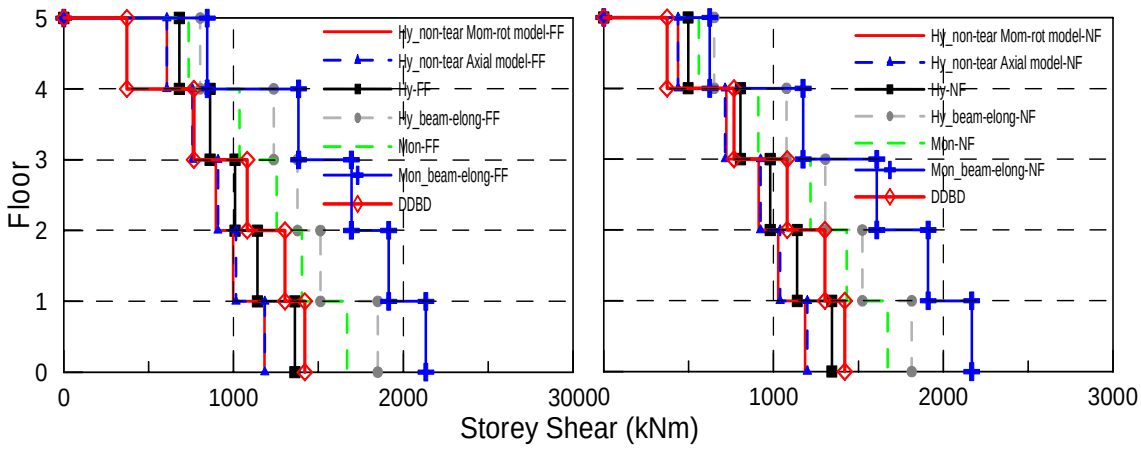

Figure 8.31 Mean Storey shear profiles for 5-storey frames: far field records (left) and near field records (right).

Comparison between the 5Hy_non-tear with the 5Mon models shows that the base shear was 40.9% and 39.5% higher for the 5Mon model for far and near field events respectively. As mentioned before, the 5Mon_beam-elong model presents the higher base shear when compared with all the other models. For far and near field earthquakes, the 5Mon_beam-elong model base shear is 80.1% and 80.8% higher than the 5Hy_non-tear model.

Figure 8.32 shows the mean cumulative shear envelopes for each 10-storey model for far (left) and near field (right) earthquakes. Similarly to what was observed in the 5-storey models, the 10Hy_non-tear model shows the smallest total base shears while the 10Mon_beam-elong model presents the highest for far and near field events when compared with the rest of the models. Comparison between far and near field indicates higher storey shear at the top floors for far field earthquake records, while a small reduction of the cumulative shear at the lower floor levels for near field events.

The 10-storey hybrid PRESSS model shows good agreement for near field earthquakes when it is compared with the shear profile obtained using direct displacement base design principles. However, higher DDBD shear profile distribution is observed when is compared with the 10-storey hybrid PRESSS model for far field earthquake records.

Comparison between the 10Hy_non-tear with the 10Hy and 10Hy_beam-elong models show that the base shear was 16.1% and 9.7% higher for the 10Hy model for far and near field events respectively. The 10Hy_beam-elong model shows higher base shear than the 10Hy and 10Hy_non-tear models for both far and near field events. Base shear differences between the 10Hy_beam-elong with the 10Hy_non-tear models increase very significantly due to the effects of beam elongation. The 10Hy_beam-elong model is 32.4% and 23.5% higher that the 10Hy_non-tear model for far and near field events.

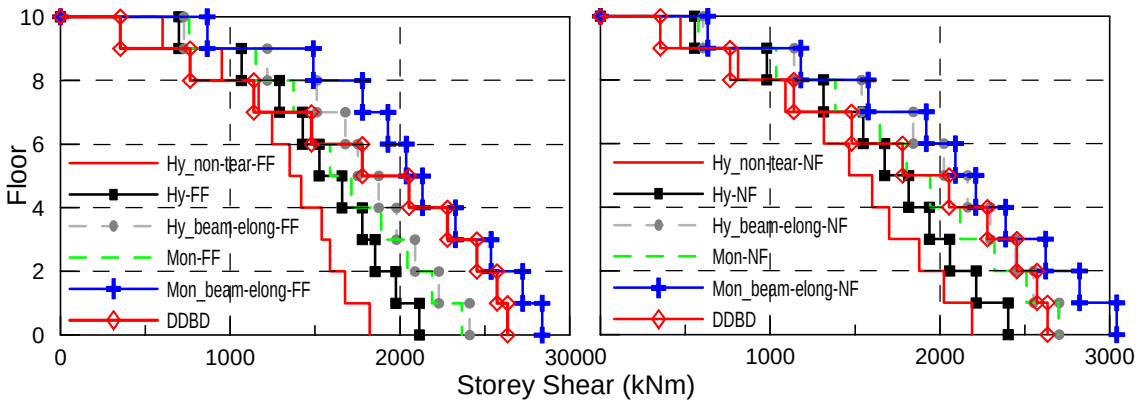

Figure 8.32 Mean Storey shear profiles for 10-storey frames: far field records (left) and near field records (right).

Comparison between the 10Hy_non-tear with the 10Mon models shows that the base shear was 29.8% and 23.3% higher for the 10Mon model for far and near field earthquakes respectively. The 10Mon_beam-elong model presents the higherest base shear when compared with all the models. For far and near field earthquakes, the 10Mon_beam-elong model base shear is 55.8% and 38.9% higher than the 10Hy_non-tear model.

8.4.4 Mean Residual Drift and Displacements

Figures 8.33 and 8.34 shows the residual drift profiles obtained for the 5 and 10-storey models for far (left) and near field (right) earthquake records. In general, the Hybrid model using non-tearing connections presents highest maximum residual drifts located at the roof level, while the hybrid PRESSS has the smallest residual drift due to its self-centring properties. Comparison between far and near field results indicate higher residual drifts for the 5Hy_non-tearing and monolithic models under near field event records while near field earthquake records do not increases the residual drift for the Hybrid PRESSS models due to their re-centering properties.

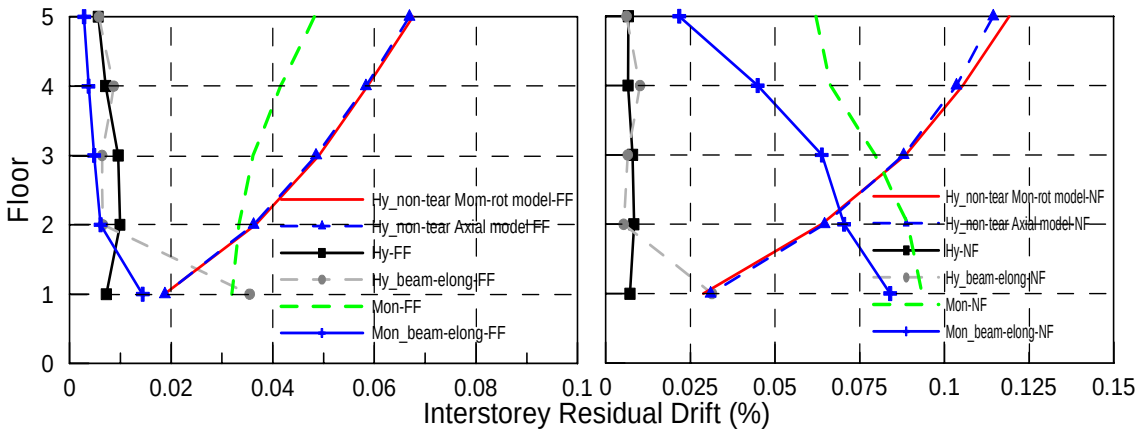

Figure 8.33 Mean residual drift profiles for 5-storey frames: far field records (left) and near field records (right).

The 5 and 10-storey Hy_non-tear models show smaller residual drifts occurred at the first floor and these gradually increased along the height of the buildings while for the models excluding beam elongation, residual drifts remain relatively constant along the height of the frame. However, for the models including beam elongation maximum residual drifts are located at the first floors with a reduction along the height of the building.

Figure 8.33 shows the 5Hy_beam-elong model has 0.035% residual drift, higher than the 0.019% and 0.007% drift obtained for the 5Hy_non-tear and 5Hy models respectively at the

first floor for far field events. At the roof level, the 5Hy_non-tear model shows 0.068% residual drift, higher than the 0.006% residual drift obtained from the 5Hy and 5Hy_beam-elong models.

Near field earthquake records show no increases in the residual drifts for the 5Hy and 5Hy_beam-elong models while the 5Hy_non-tear model shows a higher residual drift of 0.029% and 0.12% at the first and top floors respectively.

Similarly, comparison for far field earthquake records between the 5Hy_non-tear model with the 5Mon and 5Mon_beam-elong models indicates smaller residual drifts for the 5Hy_non-tear model at the first floor, but at the roof level, higher residual drifts are obtained when compared to the model with non-tearing connections. At the first floor, the 5Mon_beam-elong model has 0.014% residual drift, smaller than 0.032% and 0.019% obtained from the 5Mon and 5Hy_beam-elong models respectively. At the roof, the 5Hy_non-tear model, shows 0.068% residual drift, higher than 0.048% and 0.003% for the 5Mon and 5Mon_beam-elong models respectively.

The near field earthquake record results indicated that the 5Mon_beam-elong and the 5Mon models show similar residual drifts with values of 0.084% and 0.093% respectively while the 5Hy_beam-elong model shows a smaller residual drift of 0.029% at the first floor. However, at the top floor, the 5Hy_non-tear model has 0.12% residual drift, higher than the 0.062% and 0.022% obtained for the 5Mon and 5Mon_beam-elong models.

Figure 8.34 shows a residual drift of 0.042% for the 10Hy_beam-elong model, higher than 0.013% and 0.023% for the 10Hy and 10Hy_non-tear models respectively at the first floor for far field earthquakes. At top floor level, the 10Hy_non-tear shows maximum residual drift of 0.057%, higher than 0.013% drift obtained for the 10Hy and 10Hy_beam-elong models.

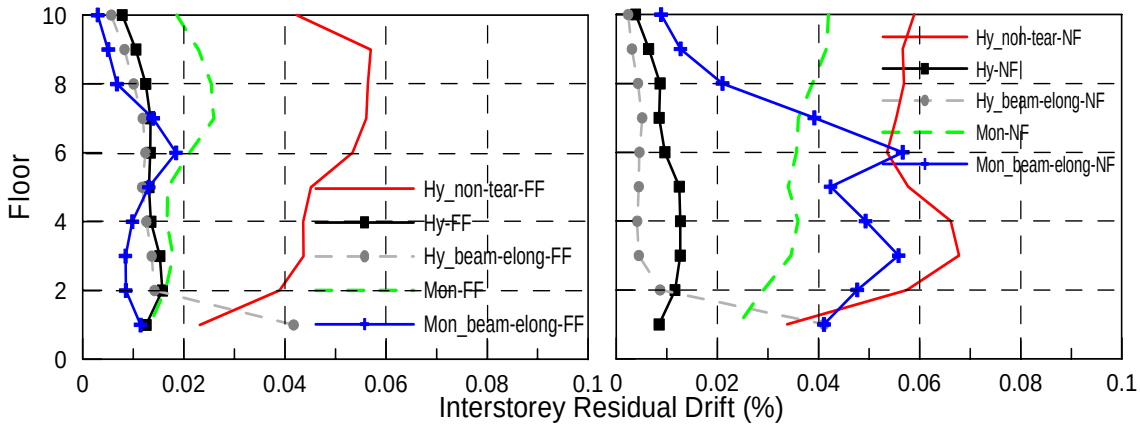

Figure 8.34 Mean residual drift profiles for 10-storey frames: far field records (left) and near field records (right).

Near field earthquake records show no increases in the residual drifts for the 10Hy and 10Hy_beam-elong models while the 10Hy_non-tear model shows a higher residual drift of 0.07% at the third floor.

Similarly, comparison between the 10Hy_non-tear model with the 10Mon and 10Mon_beam-elong models indicates smaller residual drifts observed at the first floor for the 10Hy_non-tear model for far field earthquake records. However, at the roof level, higher residual drifts are obtained compared to the model with non-tearing connections. At the first floor, the 10Mon_beam-elong model showed 0.011% residual drift, smaller than 0.013% and 0.023% obtained from the 10Mon and 10Hy_beam-elong models respectively. At roof displacements, the 10Hy_non-tear shows 0.057% residual drift, higher than 0.026% and 0.018% for the 10Mon and 10Mon_beam-elong models respectively.

Near field earthquake records indicate that the 10Mon_beam-elong has higher residual drifts of 0.041% when compared with 0.024% and 0.034% for 10Mon and 10Hy_non-tear models at the first floor respectively. However, at the upper floors, the 10Hy_non-tear model shows 0.059% residual drift, higher than the 0.042% obtained from the 10Mon model. The 10Mon_beam-elong model shows higher residual drift at mid-height of the building with a value of 0.057%

Figures 8.35 and 8.36 show the residual displacements obtained for the 5 and 10-storey model for far (left) and near (right) field earthquake records. In general the 5 and 10-storey frames with non-tear connections show smaller residual displacements occurring at the first floor and linearly increasing along the height of the building while for the Hybrid PRESSS model the residual displacements remain almost constant along the height of the frame.

Comparison between the far and near field events indicate higher residual displacements for the near field earthquake records specially for the 5 and 10-storey frames using non-tear connections and the Monolithic models including and excluding beam elongation effects while for the Hybrid PRESSS models no major difference in the residual displacements are observed.

Figure 8.35 shows the residual displacement for far field events. Results indicated that the 5Hy_non-tear model has 0.71mm residual displacement at the first floor and increases linearly up to the roof with residual displacements of 8.41mm. The 5Hy model shows smaller residual displacement with a value of 1.43mm at the roof. Similarly, the 5Hy_beam-elong model shows a residual displacement of 1.35mm at the first floor, higher than the 5Hy and 5Hy_non-tear model, and remains almost constant along the height of the building.

The 5Mon model shows similar residual displacements as those observed for the 5Hy_non-tear model for far field events. At the first floor, the 5Mon shows residual displacement higher than the 5Hy_non-tear model but smaller at the roof level with values of 1.71mm and 7.0mm residual displacement at first and top floor displacement respectively. However, the 5Mon_beam-elong at the first and top floor shows 0.55mm and 1.01mm residual displacements smaller than those found for the 5Mon and 5Hy_non-tear models.

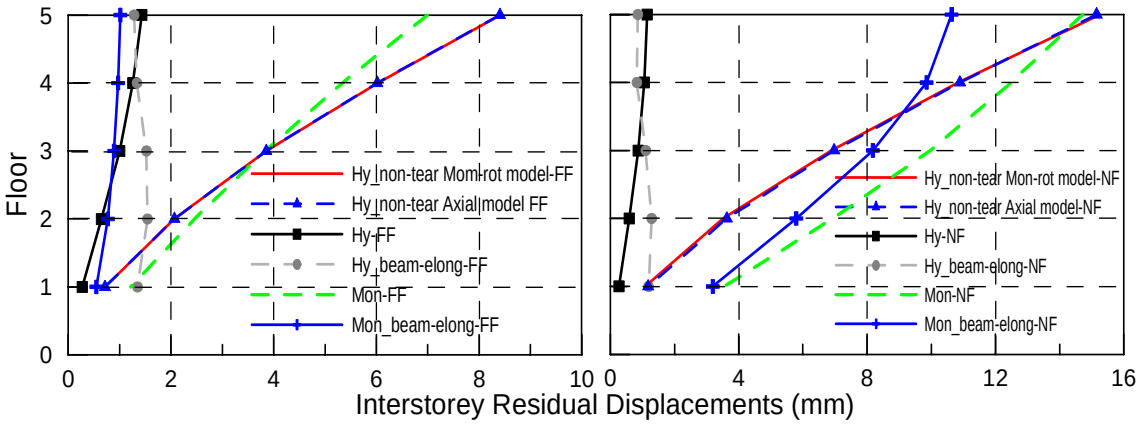

Figure 8.35 Mean residual displacement profiles for 5-storey frames: far field records (left) and near field records (right).

Near field earthquake records indicate higher residual displacement for the 5Hy_non-tear model with values at the first and top floor of 1.09mm and 15.26mm respectively while no major changes in the residual displacements are observed for the Hybrid PRESSS models due to the self-centering properties.

Near field events for the 5Mon and 5Mon_beam-elong models indicate an increase in the residual displacements similar to those observed for far field earthquake records. At the first floor, a residual displacement of 3.55mm and 3.19mm is observed for the 5Mon and 5Mon_beam-elong models respectively. These values are higher than the 5Hy_non-tear model with value of 1.09mm. However, at roof level, residual displacements increase in the 5Hy_non-tear model up to 15.26mm, higher than 14.72mm and 10.63mm for the 5Mon and 5Hy_non-tear models.

Figure 8.36 shows the residual displacement for far field events. Results indicate that the 10Hy_non-tear model has 0.88mm residual displacement at the first floor and this increases linearly up to the roof level with residual displacements of 15.64mm. The 10Hy model shows smaller residual displacement values with 4.45mm residual located at the top floor. Similarly, the 10Hy_beam-elong model shows a residual displacement of 1.59mm at the first floor, higher

than the 10Hy and 10Hy_non-tear model, and increases along the height of the building with a roof residual displacement of 4.37mm.

The 10Mon model shows residual displacements higher than the 10Mon_beam-elong model but smaller than those observed for the 10Hy_non-tear model for far field events. At the first floor, the 10Mon model shows residual displacement of 0.5mm and 7.2mm at the first and top floors respectively. However, the 10Mon_beam-elong at the first and top floor shows 0.44mm and 3.48mm residual displacements, smaller than those found for the 10Mon and 10Hy_non-tear models.

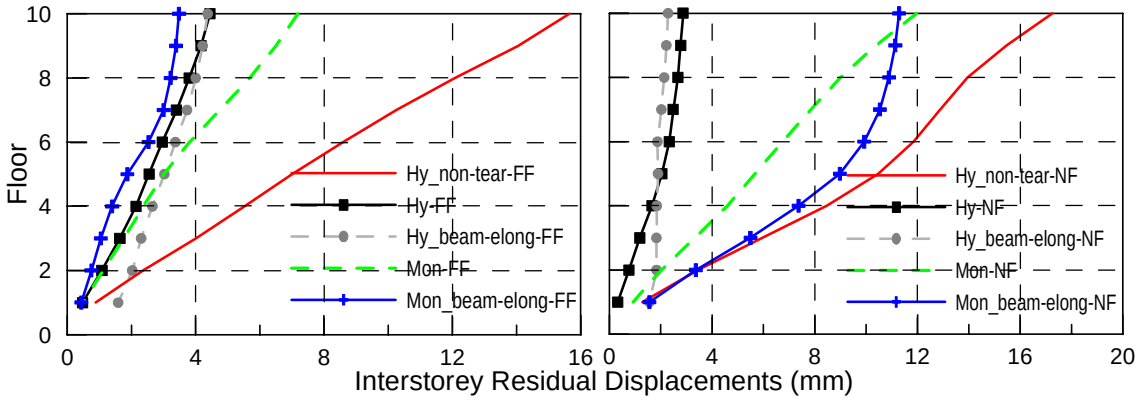

Figure 8.36 Mean residual displacement profiles for 10-storey frames: far field records (left) and near field records (right).

Near field earthquake records indicate higher residual displacement for the 10Hy_non-tear model with values at the first and top floor of 1.29mm and 17.25mm respectively while no major changes in the residual displacements were observed for the Hybrid PRESSS models due to its self-centering properties.

Near field events for the 10Mon and 10Mon_beam-elong models indicate an increase in the residual displacements similar to those observed for far field earthquake records. At the first floor, residual displacements of 0.92mm and 1.56mm are observed for the 10Mon and 10Mon_beam-elong models. There values are smaller than the 10Hy_non-tear model with value of 1.29mm. However, at roof level, residual displacement increases in the 10Hy_non-tear model up to 17.25mm, higher than 11.98 and 11.28mm for the 10Mon and 10Hy_non-tear models.

8.5 CONCLUSIONS

In this chapter a series of time history analyses were carried out on two frames of 5 and 10 storey building prototypes designed with different solutions. Special attention was given to the Hybrid frames using non-tearing floor connections to investigate and evaluate the performance of this type of system under earthquake loading. Comparison with more traditional solutions was also presented.

The buildings were assumed to be located in Wellington on top of a shallow soil (soil type C) within 2km from the fault and where given an importance level of 2, Therefore, the frames were designed with a design earthquake (DEQ) proposed by the NZ 1170:5 with a probability of exceedance of 10% in 50 year corresponding to an average return period of 500 years.

An initial set of five earthquake motions were selected to match the design spectra over the full length of the acceleration and displacement spectrum by a procedure stipulated in the current design standards NZ1170:5 Earthquake Actions. For each 5 and 10-storey frame models the set of five inelastic time-history earthquake records were performed at intensities of 0.5x, 1.0x 1.5x and 2.0x the code scaled intensity. The earthquake intensity level of 2 represents the maximum credible earthquake (MCE) stipulated in the NZ1170:5 with a return period of 2475 years and a probability of exceedence of 2% in 50 years.

A second set of 30 earthquake motions was selected and scaled to represent the likely ground motion for the 500-year return period. 20 records were considering for far field and 10 for near-fault events. The first suite of 20 earthquakes is an ensemble of scaled historical “far-field” strong ground motion records from California representative of typical earthquakes having a probability of exceedance of 10% in 50 years. The second suite of earthquakes is an ensemble of 10 historical near-field earthquake records, selected based on its PGV/PGA ratio, distance from fault, soil type and source failure mechanisms.

Conclusions for the inelastic time history changing the earthquake intensity and the ground motions characteristics such as far or near field can be made:

8.5.1 Mean Maximum and Absolute Maximum Inter-storey Drift

In general, any of the mean and maximum drift values for the 5-storey frame models do not exceed the drift limit of 2.0% for the far field records; however, some maximum drift values greater than the drift limit were observed at the first floor for the hybrid model including beam

elongation. Similarly, for far field records, the hybrid and monolithic models including beam elongations showed higher drift limits than 2.0% located at the first floor.

For the 10-storey frame models, none of the mean drift values exceed the design drift limit of 1.5%. However, maximum drift values greater than the drift limit were observed for almost all the models except the hybrid model with non-tearing connections.

At 0.5x and 1.0x the design earthquake intensity, the 5 and 10-storey hybrid system with non-tearing connections shows similar or smaller mean inter-storey drifts when compared with all the other models. Models including beam elongation showed higher mean and maximum inter-storey drift values at the first two floors and these then reduce along the height of the building. For the 10-storey hybrid frame with non-tearing connections a higher drifts were observed at the seventh floor.

At 1.5x and 2.0x the design earthquake intensity, the mean inter-storey drift values for the 5-storey frames were similar between the models which exclude beam elongation while higher maximum inter-storey drift values are observed for the hybrid PRESSS models excluding and including beam elongation when compared to the other models. A reduction of the mean and maximum inter-storey drift is observed for the models considering beam elongation at the upper storeys.

At the same intensity levels, the 10-storey hybrid frames including and excluding beam elongation have higher mean and maximum drift values when compared with the hybrid with non-tearing connections. However, the monolithic model including beam elongation shows smaller mean and maximum drift values than the hybrid with non-tearing connections. The maximum drift value occurs at the first floor for all the models; the hybrid model including beam elongation reduces the maximum drift values more rapidly with height than the rest of the models.

Comparison between far and near field earthquake events indicated that for the 5- storey hybrid frames using non-tearing connections the mean inter-storey drift values increase for near field events, while maximum drifts are higher for far field events. However, for the 10-storey hybrid frames with non-tearing connections the mean and maximum drifts increases for near field earthquake records. Distribution of the inter-storey drift profiles changes significantly where the maximum drifts occurs in the first floors for far field events, while for near field maximum drift occurs at the upper floors.

5-storey Hybrid PRESSS models including and excluding beam elongation indicate that mean drift values increase for near field events, while maximum drifts are higher for far field events. However, for the 10-storey models, near field earthquake records increase the mean and maximum drift.

Similarly, the 5-storey monolithic models including and excluding beam elongation indicate that mean drift values are not affected by the near field effects. However, maximum drifts are highly affected by near field earthquakes especially for the monolithic model including beam elongation. For the 10-storey monolithic model excluding beam elongation, mean and maximum drift profiles are higher for near field earthquake records, however, for the 10-storey model including beam elongation, smaller mean and maximum drift values are observed for far field events.

8.5.2 Mean Maximum and Absolute Maximum Displacement Profile

Results indicated that for 0.5x and 1.0x the earthquake intensities, the 5 and 10-storey models with non-tearing connections undergo smaller deformations than the other models when frames were in the post-elastic range. As the earthquake design intensity increases, the 5 and 10-storey Monolithic beam elongation models underwent higher deformation than all the models at the bottom floors and smaller deformations at the top floors when frames were in the post-elastic range.

Similar results were observed for the 5 and 10-storey Hybrid including beam elongation models where displacements were smaller than the models excluding beam elongation effects. These results indicate that Hybrid PRESSS frame systems excluding beam elongation behave similarly to the Hybrid non-tearing connections and would be in general stiffer at the first floors and more flexible at the roof level.

Comparison between far and near field earthquakes indicated that near field events increase the displacement profiles along the height of the buildings.

8.5.3 Mean Cumulative Shear Profile

In general, the 5 and 10-storey hybrid frame with non-tearing connections shows the smallest total base shears while the Monolithic including beam-elongation model presents the highest base shear for all the earthquake intensities when compared with the rest of the models. The Hybrid PRESSS with beam elongation model shows higher base shear than the Hybrid PRESSS

excluding beam elongation and Hybrid with non-tearing connections for all earthquakes intensities.

As the earthquake design intensity increases, total base shear for the 5 and 10-storey hybrid PRESSS and monolithic including beam elongation models increases with respect to the hybrid non-tear model due to the effects of beam elongation while the base shear reduces for the hybrid PRESSS and monolithic excluding beam elongation models.

Comparisons between far and near field events indicate higher storey shear at the top floors for far field earthquake records, while a small reduction of the cumulative shear at the lower floor levels for near field events.

8.5.4 Mean Residual Drift and Displacement

In general, the 5 and 10-storey Hybrid model using non-tearing connections showed similar small residual drift and displacements located at the first floor when compared with all the other models. However, residual drift and displacements gradually increase up the height of the building with highest residual drifts and displacements located at the roof level when compared with the other models. However, mean residual drift and displacements recorded at roof level for the hybrid models using non-tearing connections were far below the permanent drift recommended for any of the structural performance levels suggested by the ASCE 41-06.

The 5 and 10-storey Hybrid PRESSS and Monolithic models excluding beam elongation, residual drift remain relatively constant along the height of the frame. However, for the Hybrid PRESSS and Monolithic models including beam elongation the maximum residual drifts are located at the first floors with a reduction up the height of the building. The 5 and 10-storey hybrid PRESSS including and excluding beam elongation models have the smallest residual drift and displacements due to their self-centring properties of the system.

Previous studies have shown that the post-yield stiffness in the reinforcing steel stress-strain behaviour is highly influential in the reduction of residual deformations. In particular these studies showed that systems exhibiting a post-yield stiffness ratio (on development of a full lateral mechanism) greater than 5% will have significantly reduced permanent displacements.

Time history analysis has underlined that hybrid systems with non-tearing connections have small initial and post-yield stiffness (due to the low stiffness of the post-tensioning) when compared with the high initial stiffness of the Hybrid PRESSS system.

Improvements in the lateral stiffness can be obtained by using an equivalent amount of steel reinforcement from the monolithic connection in the energy dissipaters and/or locating the dissipaters at the bottom face and therefore higher mild steel moment contribution will be obtained. Additionally, Chapter 5 showed the results obtained using the use of a rubber pad working only in compression located at the gap of the connection which can be sufficient to increase the stiffness when the gap closes. It is require in the design that the rubber compression forces will not surpass the forces in the monohinge. However, further numerical analyses on the post-yield stiffness in the steel stress-strain behaviour of the dissipaters are recommended in order to improve the residual deformations in Hybrid systems with non-tearing connections.

8.6 REFERENCES

8.1 Carr, A. "RUAUMOKO program for Inelastic Dynamic Analysis – User Manual". Department of Civil Engineering, University of Canterbury, Christchurch, New Zealand.

8.2 New Zealand Standards (NZS). "Structural Design Actions: Earthquake Actions," NZS1170.5. 2004, Wellington, New Zealand.

8.3 Paulay, T. and Priestley, M.J.N. "Seismic Design of Reinforced Concrete and Masonry Buildings. John Wiley, New York, 1992, 744pp.

8.4 Christopoulos, C., Filiatrault, A. and Folz, B., "Seismic response of self-centering hysteresis, SDOF systems." EESD, 31, 1131-1150pp. 2002

8.5 Christopoulos, C., Pampanin, S. and Priestley, M.J.N. "Performance-based Seismic Response of Frame Structures including Residual Deformations. Part1: Single-degree-of-freedim systems," Journal of Earthquake Engineering, Vol 7, No. 1, 97-118pp. 2003

8.6 Christopoulos, C., and Pampanin, S. "Towards performance-based Seismic Design of MDOF Structures with Explicit consideration of residual deformation," ISET journal, special issue on "Performance-Based Seismic Design, 2004.

8.7 Ruiz-Garcia, J. and Miranda, E. Residual displacement ratios for assessment of existing structrures," Earthquake Engineering and Structural Dynamics, 35, No. 3, 315-336pp. 2006.

8.8 Pettinga, J.D, Priestley, M.J.N. Pampanin, S, and Christopoulos, C., "Effectiveness of simple approaches in mitigating residual deformations in buildings," Earthquake Engineering and Structural Dynamics, 36:1763–1783pp, 2007

8.9 American Society of Civil Engineer Standard No. ASCE/SEI 41-06 "Seismic Rehabilitation of Existing Buildings ASCE/SEI 41/06," 1st Edition. American Society of Civil Engineers , May-2007, 423 pp

8.10 MacRae, G.A. and Kawashima, K. "Post-Earthquake Residual Displacements of Bilinear Oscillators," Earthquake Engineering and Structural Dynamics, 26, 701-716pp, 1997.

8.11 Kawashima K, MacRae GA, Hoshikuma J, Nagaya K. "Residual displacement response spectrum," Journal of Structural Engineering May 523–530. 1998.

8.12 Pampanin S, Christopoulos C, Priestley MJN. Performance-based seismic response of frame structures including residual deformations. Part II: Multi-degree-of-freedom systems. Journal of Earthquake Engineering; Vol 7:no. 1:119–147pp, 2003.

CHAPTER 9
CONCLUSIONS AND RECOMMENDATIONS FOR FUTURE WORK

9.1 INTRODUCTION

The research areas covered by the dissertation include the experimental response and analytical validation of advanced hybrid beam-column sub-assemblages with different configurations subjected to uni and bi-dimensional quasic-static loading protocols. The experimental response and analytical validation of two beam-column joints using two types of connections able to reduce the damage in the floor by reducing the effects of beam elongation is also presented. Additionally, further refinements and constructability issues were investigated under the experimental and analytical validation of a major two-story one-bay frame using non-tearing floor connections.

Based on the non-tearing floor connections experimentally validated, a series of parametric analyses for beam-column joints and H-frames were investigated. Furthermore, the analysis and design of two prototype frames using different solutions was presented. The frames were analysed under cyclic adaptive push-over and nonlinear dynamic time-history analysis in order to investigate analytically the response characteristics of hybrid frames using non-tearing connections, as well as how the beam growth affects the frames response to earthquake loading, computational models for hybrid PRESSS frames and conventional reinforced concrete frames were developed and compared with the ones using non-tearing connections.

This chapter summarizes the results and presents the conclusions from the previous chapters of this dissertation divided into those relating to the experimental, modelling and design sections. Also, several areas of future research are recommended.

9.2 CONCLUSIONS

9.2.1 Experimental Response on Beam-Column Subassemblies Using Advanced Hybrid Connections Under 2 and 3-Dimensional Quasic-Static Cyclic Loading

Uni and bi-dimensional cyclic testing of alternative and innovative dry jointed ductile connections able to accommodate higher seismic demands highlighted a superior level of

performance when compared to an equivalent monolithic connection. Damage of the unbonded post-tensioned beam-column joints were superficial with most of the inelastic deformations confined to the sacrificial energy dissipaters (mild steel). The suitability of a number of connection types for post-tensioned connections is confirmed through testing and constructability.

The response of the hybrid system under a bi-directional (four clove) testing regime was very satisfactory and the additional effects of bi-axial loading were negligible, when compared with the uni-directional response. At high drift levels, torsional effects on the beam were observed during the tests leading to losses of prestress in the tendon as well as to general stiffness degradation in addition to a highly demanding testing protocol, excessive strain demand in the dissipaters were observed leading to a premature fracture.

The shear transfer mechanism was investigated by relying either on friction due to the post-tensioned tendon contributions, and/or the dowel action in the mild steel. Additionally, other sources of shear transfer were investigated by using metallic slotted connections using single or double mechanical hinges acting as shear keys.

Internal or external supplemental damping devices relying on mild steel and implemented following a passive control approach were investigated. Internal mild steel dissipaters were inserted in embedded metallic corrugated ducts and grouted as proposed in the implementation of traditional Hybrid PRESSS connections. However, external replaceable mild steel dissipaters were proposed due to the “un-damageable” properties of the hybrid systems, where only the energy dissipaters act as sacrificial fuses and might be required to be substituted after an earthquake event. Location can be either protruding from the beam face or hidden inside of a cage for architectural purposes.

Different arrangements for the longitudinal post-tensioned tendons profile were studied: straight, draped tendons/cable profile solutions or combination of profiles depending on the contribution of the gravity and lateral loads effects, considering different levels of seismicity (target design earthquake) as well as of the assigned role of the system during the seismic response (i.e. gravity-load only system, seismic resisting system or intermediate solutions).

Experimental results showed that traditional hybrid PRESSS systems substantially reduced their secant stiffness with the gap opening; specially the unbonded post-tensioned solution. However, the proposed advanced solution using double hinge concept with external mild steel dissipater

had shown a decreased degradation in secant stiffness as the external dissipaters do not have bond deterioration.

All the experimental results showed that the equivalent energy dissipation ratio increased with an increased story drift. The monolithic specimen showed a higher equivalent viscous damping in comparison with the hybrid solutions. However, higher displacement ductility levels were obtained by the hybrid solutions.

Hybrid connections and especially the unbonded post-tensioned only solution showed much less residual displacement than the monolithic solution due to the self-centering properties of the connection. The advanced hybrid solution showed minimum residual displacements compared to the other connections. However, solutions with parabolic profile (which provides asymmetric behaviour in terms of strength) in addition to the energy dissipation and friction can cause higher residual displacements than expected.

9.2.2 Modelling the Monotonic and Cyclic Response of the Advanced Hybrid Beam-Column subassemblies

The analytical-experimental comparisons, mostly based on pure predictions (i.e. pre-testing numerical simulations) confirmed a very satisfactory accuracy of the simplified modelling proposed and adopted to describe the behaviour of the hybrid connections with different arrangements and configurations. Modelling the cyclic behaviour of the dissipaters gives a very close approximation to the experimental results. Furthermore, the rotational spring model shows a good approximation in terms of overall strength. However, the model is unable to properly capture the unloading stiffness due to the inaccuracy of the moment-rotation parameters adopted to model the hysteresis steel rules.

9.2.3 Experimental Response on Beam-Column Subassemblies using non-tearing floor Connections Under 2 and 3-Dimensional Quasic-Static Cyclic Loading

Two types of connection able to reduce the damage in the floor by reducing the effects of beam elongation have been implemented. The first approach consists of using standard precast rocking/dissipative frame connections referred to “gapping” connection in combination with an articulated or “jointed” floor which uses mechanical devices to connect the floor and the lateral beams which can accommodate the displacement incompatibilities in the connection. No damage in the floor in addition to no over-strength or any interaction was reported when compared to bare frame without floor system.

The second approach to reduce the floor damage has been investigated implementing a "non gapping" connection or also called non-tearing-floor connection using a top hinge at the beam-column interface, while still relying on more traditional floor-to-frame connections (i.e. topping and continuous starter bars). This connection was able to obtain an efficient floor to lateral load resisting system connection, while negating the problems associated to the beam elongation effects.

Experimental results on beam-column joint subassemblies using a top hinge connection has indicated that the total moment contribution is based on the energy dissipaters moment (pure yielding hysteresis behaviour) offset by the initial post-tensioned moment (linear elastic behaviour). The initial stiffness is determined by the pure yield system and post-yield stiffness by the contribution of both systems (pure yield and linear elastic).

9.2.4 Experimental Response of the two storey, single bay, precast concrete frame system using non-tearing floor Connections Under 2-Dimensional Quasic-Static Cyclic Loading

The suitability of the development of a "non gapping" connection or non-tearing floor system was investigated through a simplified connection design based on stress-strain relationships, implementation and experimental validation on a 2-Dimensional, two storey one bay precast concrete frame with the use of a steel top hinge, anti-symmetric unbonded post-tensioned tendons, and external and replaceable energy dissipaters. This connection was able to obtain an efficient floor to lateral load resisting system connection, while negating the problems associated to beam elongation effects with very satisfactory results.

Although the innovative floor solution presented herein significantly reduces the effects of beam elongation, further refinements will include improvements in the energy dissipater devices as well as to guarantee the actual constructability (tolerances issues) targeting a wider adoption by the construction industry. One possible solution could be the reduction in length of the dissipater to increase the bucking capacity and a smoth transition zone slope about 3:1 between the fuse and the bar.

It was demonstrated experimentally that a global re-centring/dissipating response (typically referred to as flag-shape behaviour) can be controlled either by only relying upon the contribution of the self weight of the structure and/or by adding unbonded post-tensioned

tendons such that full re-centring can be achieved by the ratio between axial force and dissipation.

Experimental results showed that the systems using an unbonded post-tensioned solution substantially reduced their secant stiffness in comparison with the hybrid systems with external dissipaters which increased the secant stiffness of the frame.

The equivalent viscous damping is highly dependent of the size of the fuse of the dissipater (steel dissipation content). Dissipaters with larger fuse diameters will have better cyclic performance (more anti-buckling restraint) and higher equivalent viscous damping under higher drift levels.

9.2.5 Modelling the Monotonic and Cyclic Response of the Non-Tearing Floor Connections

Two models were used to reproduce and validate the experimental results of the beam-column joint and frame using non-tearing floor connections: the first model is based on the moment rotation spring model acting in parallel at the connection. The second lumped plasticity model is based on the combination of three longitudinal springs. The two models can reproduce the experimental results with reasonable accuracy in the overall strength response.

In terms of local response, the linear elastic hysteresis model used to represent the unbonded post-tensioned tendons showed very good agreement with the experimental response. Simple rules can be adopted to predict the behaviour of the energy dissipaters. However, due to the poor behaviour in compression and excessive buckling and bearing effects of the energy dissipaters exhibited in the tests new designs are highly recommended and a selection of the respectively hysteresis behaviour needs to be careful selected.

For the validation of the experimental results, modelling the energy dissipaters were using more refined hysteresis rules to capture the cyclic behaviour of the dissipaters and obtained a close approximation to the experimental results. However, the hysteresis rules were unable to properly capture the unloading stiffness and the buckling observed during the tests in the dissipaters.

Comparison between the two models indicates that the longitudinal spring model can better represent the overall response in terms of the force displacement as the additional stiffness of the mono hinge is taken into account while for the moment rotational model only the post-

tensioned stiffness and dissipater contributions are considered. However, considering the number of nodes and the specific nodes coordinates to generate the geometry and create the proper action in the joint, in addition to the increase in number of elements that the longitudinal spring model requires, the moment rotational model seems to be more appropriate. Although, when the determination of more refined internal force distributions in the elements are required (e.g. beam axial forces due to post-tensioned tendons) the longitudinal model is require.

9.2.6 Parametric Analysis for Beam-column joints and H-frames with non-tearing floor connections.

A simplified non-tearing beam-column connection derived from material and geometric considerations has been proposed. Based on equilibrium analysis, moment at the connection, shear forces and bending moment equations have been formulated for H-frames of one and multiple spans using non-tearing connections. Different configurations of H-frames with multiple spans using non-tearing connections were conceptually evaluated. From these concepts, two solutions were investigated: the first solution used unbonded post-tensioned tendons anchored at each span, while the second, used partially bonded post-tensioning tendons anchored at mid-span.

At rest, the initial post-tensioned moments induced column moments that are self equilibrated in each floor for both solutions. For the first solution, as the frame sways, the exterior and interior column moments changed according to the change in the post-tensioned moment and the moment contribution of the mild steel dissipaters. For the second solution, as the system sways, the exterior columns moments changed according to the change in the post-tensioned moment but higher than the previous solution due to the smaller unbonded length; however, the interior columns will not have any contribution from the post-tensioning moment as they cancel out and therefore the only connection contribution for the interior column moments are the mild steel moment of the dissipaters.

Parametric analysis on hybrid beam-column joints and H-frames systems of one and multiple spans with non-tearing connections were investigated in terms of local (beam column joint) and global (base shear) response. Results indicate that the first solution will show a better response in terms or base shear. However, this solution seems to be not very economical considering the cost associated with the construction and post-tensioning. The second solution would question the use of tendons in the interior spans if no extra benefit can be taken from them.

Additionally, studies indicated that frames with non-tearing connections present higher lateral response for short bay lengths although higher initial post-tensioned forces will be required to keep the desired moment capacity at the connection. Reasonable values in the changed of post-tensioned moment contribution over the energy dissipation contribution between 0.1 and 0.3 are advisable. Values close to 0 indicate full capacity in the connection coming from the external energy dissipaters, while higher values than 0.5 will indicate that the post-tensioned moment contribution is significantly large; however, internal moments and shears at the exterior columns will be excessively large and difficult to accommodate in typical column sections.

9.2.7 Static Lateral Load Response of the Prototype Frames Using Non-Tearing Connections and Comparison with Traditional Systems.

In general, the response of the 5 and 10-storey hybrid frame systems using non-tearing connection was very satisfactory under cyclic adaptive push-over analysis. Results indicated that lateral stiffness was lower for the hybrid non-tearing connection when compared with the traditional hybrid system. However, the total base shear for the same imposed drift level was very similar. Therefore, as a result, the Hybrid and Hybrid non-tearing models would be in general more flexible, though reaching the target strength at a given level of drift. It is worth noting though that the initial stiffness up to the yielding of the mild steel bars (at around 0.35% roof drift) is similar between all models. Thus, the Hybrid non-tearing model will maintain its natural and desired monolithic behaviour for small intensity earthquakes (i.e. low return period).

Beam elongation effects change the distribution of moments and shear throughout the frame. It can be seen that the traditional monolithic and Hybrid systems are affected by beam elongation especially in the first stories where shear were larger. The Hybrid model showed a reduction of the beam elongation when compared with the monolithic model due to the post-tensioned forces which helped to close the gap at the connection, specially for the top floors of the 10-storey model where in some cases the columns were pulling together.

Also, the elongation of the beams induces bending moments in columns. The additional bending moments are called secondary moments in columns due to beam elongation and are generally proportional to the distance of the column from the frame centreline. These two effects cause self-equilibrating forces in the frame including the forces at the foundation. These forces increase the moment capacity of beams and columns at certain locations, but decrease the moment capacity at other locations. Thus, the global frame behaviour is not affected by the beam elongation, and the frame base shear-roof displacement curves are similar for the Hybrid and Monolithic excluding beam elongation models and for the hybrid and Monolithic with beam

elongation models respectively. However, the local element behaviour is significantly affected by the beam elongation.

Axial forces in beams for the 5-storey frames were investigated as a consequence of beam elongation and the increase in the beam length due to elongation restricted by the foundation. For the Hybrid including beam elongation and Hybrid non-tearing models, the first and second floor beams remained in compression as a result of the post-tensioned forces. However, for the Monolithic including beam elongation model, the first and second floor beams are mostly under axial compression and tension forces, respectively. This is usually the case due to the horizontal restraint provided to the columns by the foundation. The type of axial force which is compression for the first floor and tension for the second floor developed in the rest of the floors is not easily predicted, and depends on the extended restraint effect of the foundation and the relative beam elongation at different floors. The foundation restrain effect is dominant for the floors near foundation, while the relative beam elongation effect may be the dominant for the upper storeys.

The effects of axial forces on beam flexural behaviour indicated that for the 5-storey Hybrid including beam elongation model the bending moment increased the beam capacity at the first and second floors. For the Monolithic including beam elongation model, results indicated that the effect of the axial compression force in the first floor beams increased the bending moment capacity, increasing the yield rotation, and decreasing the ultimate rotation of the beams. In contrast, the effect of axial tension force in the second floor beams is to decrease the bending moment capacity, decreasing the yield rotation, and increasing the ultimate rotation of the beams.

Column flexural demands were obtained for the exterior and interior columns of the 5-storey frame models and normalized by the beam bending moment. The column flexural demands for the Hybrid and Monolithic including beam elongation models are always greater than those of the model where beam elongation is excluded, and the differences are significant at locations where the beam elongation effect is more pronounced specially at the first and second floors. For capacity design requirements, the ratio between column over beam flexural capacity for the Hybrid and Monolithic including beam elongation models were 2.25 and 2.5 for the exterior and interior columns respectively. For the Hybrid with non-tearing model, this ratio was 1.25 and 2.5 for the exterior and interior columns respectively.

9.2.8 Seismic Response of the Prototype Frames Using Non-Tearing Connections and Comparison with Traditional Systems.

A series of time history analyses on two frames of 5 and 10 multi-storey building prototypes with different solutions have been investigated. For each 5 and 10-storey frame models a set of five inelastic time-history earthquake records were performed at intensities of 0.5x, 1.0x 1.5x and 2.0x. A second set of 30 earthquake motions were selected and scaled to represent the likely ground motion for the 500-year return period. 20 records were far field and 10 near field events.

9.2.8.1 Mean Maximum and Absolute Maximum Drift Profile

In general, at half of the design earthquake intensity, the 5 and 10-storey Hybrid system with non-tearing connections showed similar mean inter-storey drifts when compared with all the models. At the design earthquake intensity, any of the mean and maximum drift values for the 5-storey frame models do not exceed the drift limit of 2.0% for far field record at the design earthquake intensity; however, some maximum drift values greater than the drift limit were observed at the first floor for the Hybrid model including beam elongation. Similarly, for far field records, the hybrid and monolithic models including beam elongations showed higher drift limits than 2.0% located at the first floor. For the 10-storey frame models, any of the mean drift values exceed the design drift limit of 1.5%. However, maximum drift values greater than the drift limit were observed for almost all the models except the Hybrid model with non-tearing connections.

At 1.5x and 2.0x the design earthquake intensity, the mean inter-storey drift values for the 5-storey frames were similar amongst the models which exclude beam elongation while higher maximum inter-storey drift values are observed for the Hybrid excluding and including beam elongation models when compared to the other models. Models including beam elongation showed higher mean and maximum inter-storey drift values at the first two floors and then reduce along the height of the building. The 10-storey hybrid frames including and excluding beam elongation have higher mean and maximum drift values when compared with the Hybrid containing the non-tearing connections. However, the monolithic model including beam elongation showed smaller mean and maximum drift values than the Hybrid with non-tearing connections. The maximum drift value occurs at the first floor for all the models; the hybrid model including beam elongation reduced the maximum drift values quicker than the rest of the models along the height of the building.

Comparison between far and near field earthquake events indicated that for the 5- storey Hybrid PRESSS and Hybrid using non-tearing connections the mean inter-storey drift values increased for near field events, while maximum drift levels are higher for far field events. However, for 10-storey Hybrid PRESSS and Hybrid with non-tearing connections mean and maximum drift increase for near field earthquake records. Distribution of the inter-storey drift profiles changed significantly where the maximum drift values occurred in the first floors for far field events, while for near field the maximum drift values occurred in the upper floor levels. Similarly, the 5-storey monolithic models including and excluding beam elongation indicated that mean drift values are not affected by the near field effects. However, the maximum drifts are considerably affected by near field earthquakes especially for the monolithic model including beam elongation. For the 10-storey monolithic model excluding beam elongation, the mean and maximum drift profiles are higher for near field earthquake records, however, for the 10-storey model including beam elongation, smaller mean and maximum drift values are observed for far field events.

9.2.8.2 Mean Maximum and Absolute Maximum Displacement Profile

Results indicated that for 0.5 and 1.0x the earthquake intensities, the 5 and 10-storey models with non-tearing connections undergo less maximum deformation than all models when frames were in the post-elastic range. As the earthquake design intensity increases, the 5 and 10-storey Monolithic beam elongation models underwent higher deformation than all the models at the bottom floors and smaller deformation at the top floors when frames were in the post-elastic range.

The displacements of the 5 and 10-storey Hybrid including beam elongation frames were smaller than those of the models excluding beam elongation effects.

Comparison between far and near field earthquakes indicated that near field events increase the displacement profiles along the height of the buildings.

9.2.8.3 Mean Cumulative Shear Profile

In general, the 5 and 10-storey hybrid frame with non-tearing connections showed the smallest total base shears while the Monolithic including beam-elongation model presented the highest base shear for all the earthquake intensities in comparison to the rest of the models. The Hybrid PRESSS with beam elongation model shows higher base shear than the Hybrid PRESSS

excluding beam elongation and Hybrid with non-tearing connections for all earthquakes intensities.

As the earthquake design intensity increases, the total difference in base shear between the 5 and 10-storey hybrid and monolithic including beam elongation models respect with the hybrid non-tear model increased significantly due to the effects of beam elongation while reducing for the hybrid PRESSS and monolithic excluding beam elongation models.

Comparison between far and near field events indicates higher storey shear at the top floors for far field earthquake records, while a small reduction of the cumulative shear at the lower floor levels for near field events.

9.2.8.4 Mean Residual Drift and Displacement

In general, the 5 and 10-storey Hybrid model using non-tearing connections showed similar small residual drift and displacements located at the first floor when compared with all the other models. However, residual drift and displacements gradually increase along the height of the building with highest residual drifts and displacements located at the roof level when compared with the rest of the models. These mean residual drift and displacements recorded at roof level for the Hybrid models using non-tearing connections were far below the permanent drift levels recommended for any of the structural performance levels suggested by the ASCE 41-06.

The 5 and 10-storey Hybrid PRESSS and Monolithic models excluding beam elongation, residual drift remain relatively constant along the height of the frame. However, for the Hybrid PRESSS and Monolithic models including beam elongation maximum residual drift are located at the first floors with a reduction along the height of the building. The 5 and 10-storey Hybrid PRESSS including and excluding beam elongation models have the smallest residual drift and displacements due to the self-centring properties.

9.3 FUTURE WORK

Although the advanced hybrid solutions here presented have underlined good global and local response experimentally, additionally, further refinements and constructability issues are require to provide a standard configuration for design and contractors.

The development of a non-tearing floor connection by using an articulated floor will require further experimental and analytical validation to determine the location (apart from the zero

vertical deflections) of the shear keys at which the floor is supported to allow a deformation pattern where the beams deflect together with floor.

A non-tearing floor connection proposed with the use of top hinge and external replaceable energy dissipaters showed successful results. However, due to the cyclic mechanism of the connection in net tension and compression, the given shape of the external dissipaters showed poor performance under cyclic behaviour and buckling was predominantly at early cyclic stages. This was in part due to the large length provided between dissipaters restrains. Reducing this length would effectively reduce the proneness to buckling. Additionally, the use of friction devices or viscous dampers to obtain better dissipation behaviour can be investigated.

Although the use of a steel corbel and mono hinge to transmit the shear was experimentally validated with excellent results, analytical and experimental investigation is proposed to have a better understanding of the hysteretic behaviour of the beam-end zone of hybrid systems with non-tearing floor connection under shear and at the connection level.

This thesis has highlighted that hybrid systems with non-tearing connections have small initial and post-yield stiffness (due to the low stiffness of the post-tensioning) when it is compared with the high initial stiffness of the Hybrid PRESSS system.

Improvements in the lateral stiffness can be obtained by using an equivalent amount of steel reinforcement from the monolithic connection in the energy dissipaters and/or locating the dissipaters at the bottom face and therefore higher mild steel moment contribution will be obtained. Additionally, Chapter 5 showed the results obtained using the use of a rubber pad working only in compression located at the gap of the connection which can be sufficient to increase the stiffness when the gap closes. It is require in the design that the rubber compression forces will not surpass the forces in the monohinge. However, further numerical analyses on the post-yield stiffness in the steel stress-strain behaviour of the dissipaters are recommended in order to improve the residual deformations in Hybrid systems with non-tearing connections.

Although numerical analysis showed that hybrid systems with non-tearing floor connections are more flexible, results indicated serviceability requirements will be satisfied. However, further research on dynamic wind response would be required for this aspect of design as it is possible that current code provisions are not fully validated for this type of structure.

The influence of P-Δ effects has not been investigated. This is particularly important for the frames of low ductility where such second-order effects may reduce the stability of the structural response. Another important second-order effect not considered was the influence of torsion on buildings behaviour. The need for 3-dimensional modelling of such behaviour is significant.

Several assumptions have been made in this dissertation in the modelling of the hybrid frames with non-tearing floor connections in the absence of more research. For the frames studied the revisions to the direct displacement-based design method is required followed by the implementation of design procedures to be investigated through a large number of buildings with different configurations.

APPENDIX A
MONOLITHIC FRAME BUILDING PROTOTYPE–DDBD PROCEDURE

A.1 BUILDING TYPOLOGY

This appendix shows the prototype building design of the exterior beam-column joint tested in Chapter 3. The prototype building is a five storey monolithic reinforced concrete building as shown in Figure A.1. The building has plan a square dimensions 13.5m long. Lateral resistance is provided by two seismic resisting frames in the two orthogonal directions, where the central frame is designed to carry gravity loads alone – detailed to achieve the desire global displacement demand.

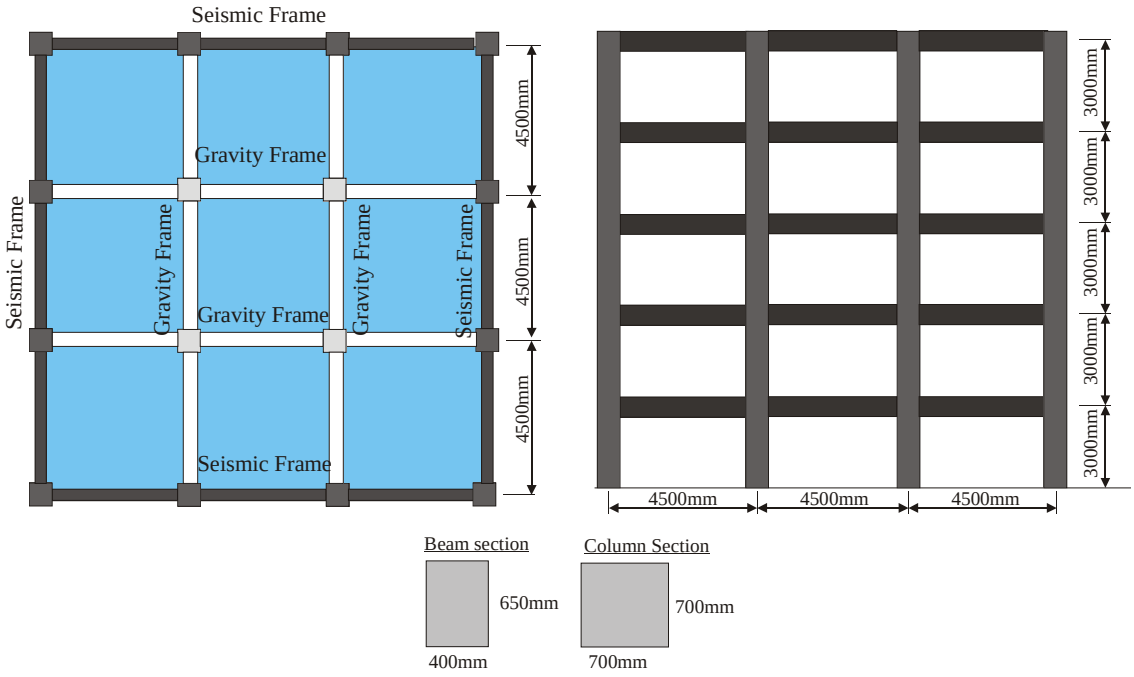

Figure A.1.Prototype Building

The building is located in Christchurch with a soil type C (shallow soil) is adopted from design, with an importance level of 2, requiring design from a 500 year return period event.

A Direct Displacement Based Design (DDBD) procedure is adopted for the design of the seismic frame. This example only attempt to generate a lateral base shear, distribute it between the lateral resisting system and then design the monolithic beam column connection in detail.

While some design relating to curtailment is provided, the specific detailing and curtailment along the individual elements according to a combination of seismic and traditional loading is omitted. The procedure is essentially the same as that used in traditional reinforced concrete design according with Paulay and Priestley [A.1] and Red Book [A.2].

A.2 FLOOR LOADS

A.2.1 Dead loads

Dead loads of the floor comprises of precast hollow-core floor unit, 75mm topping, and superimposed dead:

- Slab 3.0 kPa
- Topping 1.8 kPa (75mm thick)
- SDL 1.0 kPa
- Partitions 0.5 kPa
- Suspended ceiling 0.5 kPa
- Self weight of elements 55 kN + 52 kN = 107 kN/floor

Total Dead load G (including the roof) = 7.0kPa x 13.5m x 6.75m=638 kN/floor

A.2.2 Live loads

Basic live load (according with table 3.1 NZS1170.1:2002) [A3]

- Q_b = 3.0 x 13.5m x 6.75m = 82 kN/floor

Total weight = `107 kN/floor+ 638 kN/floor + 82 kN/floor = 827 kN/floor

A.3 DIRECT DISPLACEMENT-BASED DESIGN

In order to ensure that the design limit state is not exceeded, the full distribution of moment and base shear corresponds to a given damage limit state. The inappropriateness of the force-based design assumption of initial stiffness and ductility capacity suggest that the resulting base moment and shear will not necessarily satisfy the intended limit state. For that reason, in this study, the structure is being designed according to displacement-based design principles in terms of basic design requirements.

The general procedure for a displacement-based design is relatively straight forward and follows a number of key steps. The method sets to provide specific performance criteria as a function of seismic intensity related to the structure; more specifically a target displacement corresponding to a design level earthquake.

The procedure requires the structural system to be converted to an equivalent single degree of freedom system having an effective elastic stiffness, effective mass, effective height and damping corresponding to the target displacement (related to the structural ductility). The procedure is as follows:

- Select a design drift-generally governed as the limiting inter-storey drift offered by the design code or by the maximum allowable displacement ductility of the structural system as suggested by the code i.e. Table 2.5 [A.4].
- Calculate design target displacement for equivalent single degree of freedom structure.
- Estimate the damping of the structure. This is simply related to the expected ductility of the structure as a function of specific dissipation characteristics of the system.
- Enter the displacement response spectra and read off the effective period of the single degree of freedom system.
- Calculate the effective mass, and hence effective stiffness.
- Calculate the base shear.
- Distribute the base shear throughout the structure and design the members accordingly.

The building was assumed to have rigid foundation. The compressive strength of the concrete was $f_c^{'}$30 MPa, and a tensile strength of steel $f_y = f_{yh} =$ 300 MPa were used as the material properties. The total mass per floor is calculated previously with m = 84.3 t.

In order to obtain the moments and shear forces for displacement-based design procedure, it is required to initially determine the design displacement, and the effective mass and damping of the equivalent single-degree of freedom substitute structure.

A.3.1. Displacement Based Design

The generalized displaced shape for the SDOF structure is based upon the inelastic first mode shape representing the structure at the desired limit state, in this case 1.6% of drift. The peak

drift can be expressed as an elastic (θ_y) rotation plus a plastic (θ_p) rotation and must not exceed the code limit (θ_c) of 2% in this case of $\theta_d = \theta_y + \theta_p \leq \theta_c$.

It should be noted that in some cases the code limit of 2% may not be achieved for the design simply because the seismic intensity is not great enough. This will become apparent in the design of a building located in relatively low seismicity (such as Christchurch) where the intensity of the spectra is not large enough to force the building to 2% of drift-hence a reduced target drift should be chosen to satisfy the design spectrum. A maximum drift of 1.6% was targeted in this building.

The critical location of θ_d (Figure A.2) is likely to be at the first floor in the case of frame buildings and at the top floor in the case of wall structures. Hence for building frames the displaced profile can be approximated with the following formula as suggested in [A.6].

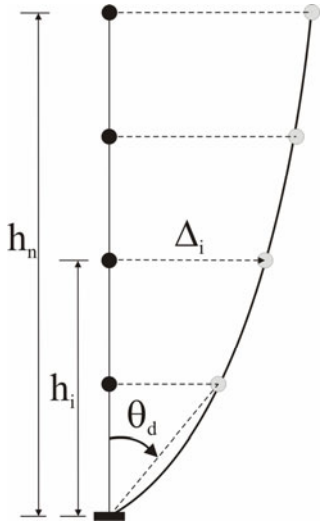

Figure A.2 Displacement profile.

With n<4

$$\delta_i = h_i / h_n \tag{A.1a}$$

With n>4

$$\delta_i = \frac{4}{3}\left(\frac{h_i}{h_n}\right)\left(1-\frac{h_i}{4h_n}\right) \tag{A.1b}$$

The displacement profile is given by the ratio

$$\Delta_i = \left(\frac{\delta_i}{\delta_1}\right)\theta_d h_1 \tag{A.2}$$

Where Where δ_i is the normalized inelastic mode shape, n is the number of storeys in the structure, h_i, and h_n are the heights to the i^{th} storey and roof respectively and θ_d is the limit state inter-storey drift.

The effects of higher modes are accounted for by the a reduced lateral drift, to allow for an increase in actual dynamic response. The higher mode factor is given by:

$$\omega = 1.15 - 0.0034 h_n \leq 1.0 \tag{A.3}$$

The reduced design displacement profile is given by:

$$\Delta_{i,\omega} = \omega \Delta_i \tag{A.4}$$

A.3.2. Effective Mass, displacement and Height

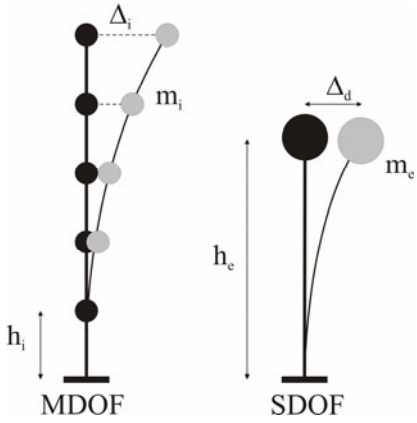

Figure A.3 Effective mass and height.

The effective mass is related to the displaced shape and the distribution of mass throughout the height of the structure and can be calculated as

$$m_e = \frac{\sum_{i=1}^{n} m_i \Delta_i}{\Delta_d} \tag{A.5}$$

Where Δ_d corresponds to the equivalent displacement at the effective height of the SDOF structure:

$$\Delta_d = \frac{\sum_{i=1}^{n}\left(m_i\Delta_i^2\right)}{\sum_{i=1}^{n}\left(m_i\Delta_i\right)} \tag{A.6}$$

Hence the effective height can be calculated

$$h_e = \frac{\sum_{i=1}^{n} m_i\Delta_i h_i}{\sum_{i=1}^{n} m_i\Delta_i} \tag{A.7}$$

The following table summarises the parameters required to compute the effective mass, effective height and distribution of the shear throughout the height of the building.

Table A.1 Summary of DDBD parameters.

Storey, i	Height, h_i (m)	Mass, m_i (tonnes)	δ_i	$\Delta_{i,\omega}$ (m)	$m_i\Delta_i$ (t m)	$m_i\Delta_i^2$ (t m^2)	$m_i\Delta_i h_i$ (t m^2)
5	15	84.3	1.000	0.189	15.97	3.03	239.6
4	12	84.3	0.853	0.162	13.63	2.20	163.6
3	9	84.3	0.680	0.129	10.86	1.40	97.8
2	6	84.3	0.480	0.091	7.67	0.70	46.0
1	3	84.3	0.253	0.048	4.05	0.19	12.1
					52.18	7.52	559.0

Where the distribution of the base shear is given by

$$\frac{F_i}{V_b} = \frac{m_i\Delta_i}{\sum_{i=1}^{n}\left(m_i\Delta_i\right)} \tag{A.8}$$

Hence, $\Delta_{d,\zeta} = 0.144\,m$, $m_e = 362\,tonne$ and $h_e = 10.7\,m$. Note that m_e equates to 85% of the total mass while h_e equates to 71% of the total building height and $\Delta_{d,\zeta}$ equates to a lateral drift of 1.34% at the height of the equivalent mass.

A.3.3. Effective Damping and Base Shear

Some fundamental relationships are used to calculate the design base shear for the building. The base shear is calculated using,

$$V_{Base} = k_{eff}\Delta_d \tag{A.9}$$

Where k_e is the effective stiffness of the substitute structure is given by

$$k_{eff} = \frac{4\pi^2 m_e}{T_{eff}^2} \tag{A.10}$$

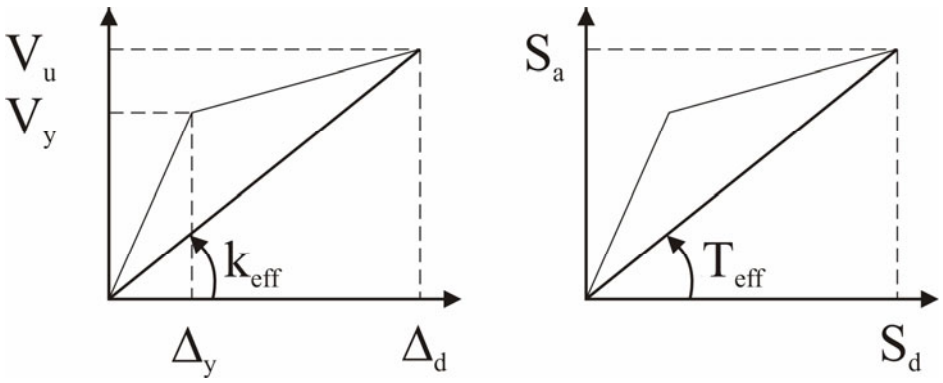

Figure A.4 SDOF base shear.

Hence the effective period of the equivalent single degree of freedom system is required. The period can be taken from the design spectra, where the target displacement and spectrum is known. However recognising that the design spectrum is representative of a 5% damped structure, a reduction needs to be accounted for the additional damping of the equivalent SDOF structure representative of the expected ductility at the target displacement.

A reduction factor is suggested [A.6] for the design spectrum as a function of ductility as follows

$$\eta = \sqrt{\frac{0.07}{0.02 + \zeta_{eq}}} \tag{A.11}$$

Where ξ_{eq} is the equivalent viscous damping ratio of the structure. Hence for the effective period to be read from a 5% damped displacement spectrum the calculated displacement is increased with the following relationship:

$$\Delta_{d,5\%} = \frac{\Delta_{d,\zeta}}{\eta} \tag{A.12}$$

Where $\Delta_{d,\zeta}$ is the target displacement converted to an equivalent 5% displacement target $\Delta_{d,5\%}$ for a given period and damping correction factor η.

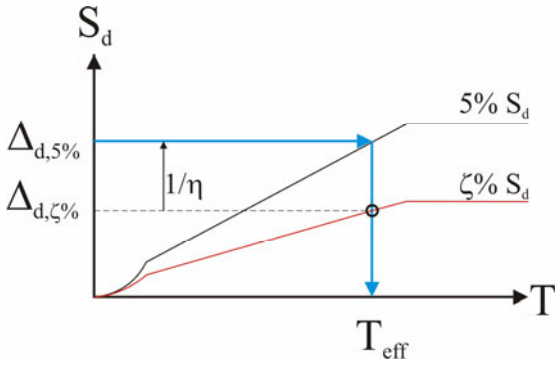

Figure A.5. Effective period of the equivalent SDOF.

As suggested [A.6], the use of an appropriate level of viscous damping for inelastic analysis in order to capture the assumptions made in the design as closely as possible. In the design phase, damping was comprised of two components: elastic viscous damping of 5%, and hysteretic damping, converted to equivalent viscous damping.

The following approximate relationship, based on the shape of the modified Takeda hysteresis rule used to relate damping (ξ_{eq}) expressed as a percentage of critical damping to ductility factor for different structural systems. For reinforced concrete frames:

$$\xi_{eq} = 0.05 + 0.565\frac{(\mu - 1)}{\mu\pi} \tag{A.13}$$

Where the effective damping depends on the structural system and the displacement ductility factor μ which can be easily obtained by

$$\mu = \frac{\Delta_d}{\Delta_y} \tag{A.14}$$

Where Δ_d is the equivalent displacement at the effective height, Δ_y the yield displacement evaluated as

$$\Delta_y = \theta_y h_e \tag{A.15}$$

Where θ_y is the yield rotation at the first is floor and is base on the structural geometry and material sizes and h_e is the effective height of the single degree of freedom system. For a reinforced concrete frame the yield rotation can be estimated can be estimated using simple equations proposed in the literature [A.1, A.6]:

$$\theta_y = 0.5\varepsilon_y \frac{l_b}{h_b} \tag{A.16}$$

Where l_b is the bay length and h_b the beam height. Hence, $\theta_y = 0.00825$

Table A.2 Beam yield rotations.

Bay, j	L_{bj} (m)	h_{bj} (m)	θ_{yj} (rad)	M_j (M_1)	$M_j\theta_{yj}$
1	4.5	0.45	0.00825	1	0.00825
2	4.5	0.45	0.00825	1	0.00825
3	4.5	0.45	0.00825	1	0.00825
Total				3	0.02475

Therefore evaluating the equation (A.15) and (A.14) the yield displacement Δ_y = 0.088 and the ductility of the structure is then μ = 1.63 respectively. Similarly, the equivalent viscous

damping is evaluated in equation (A.13) ξ_{eq} =12.0% and a reduction factor in equation (A.12) η = 0.708.

The effective period is the evaluated into the design spectra is according with NZS 1170.5 2004 [A.7] with elastic site spectrum compatible with the spectral shape factor determined using a subsoil site C, hazard factor of 0.22 (Christchurch) and a return period of 500 years. The result showed a effective period of T_{eff} = 2.83 seconds.

The effective stiffness at peak response is thus evaluated in (A.10) an equal to k_{eff} = 1788 kN/m and the total base shear is evaluated in equation (A.9) as V_{base} = 258 kN.

Hence the lateral design coefficient is equal to 6.2% of the total building weight. Recognising that for this design each of the two seismic frames in the building will have identical strength; DBD distributes the lateral forces within a structure weighted according to the strength of each element, hence the lateral force is distributed evenly between each frame and distributed up the building height according to the previous relationships to give the following,

$$F_i = V_B \frac{m_i \Delta_i}{\sum_{i=1}^{n} (m_i \Delta_i)} \tag{A.17}$$

The base shear was calculated as vertically distributed in proportion to the vertical mass and displacement profiles and no additional force at the top is recommended.

A.4 STRUCTURAL ANALYSIS UNDER LATEARAL FORCES

It is proposed [A.6] that the most effective way to model the structure is place a hinge at the base level, and apply a base resisting moment M_c to the hinge, while representing the column by the elastic cracked-section stiffness.

The values of M_c placed at the base hinges are a design choice, since analysis of the structure under the lateral force vector together with the chosen column-base moments (M_c) will ensure statically admissible equilibrium solution for design moments. In fact this implies some moment redistribution between beam hinges and columns-base hinges, allowing the designer to improve the structural efficiency.

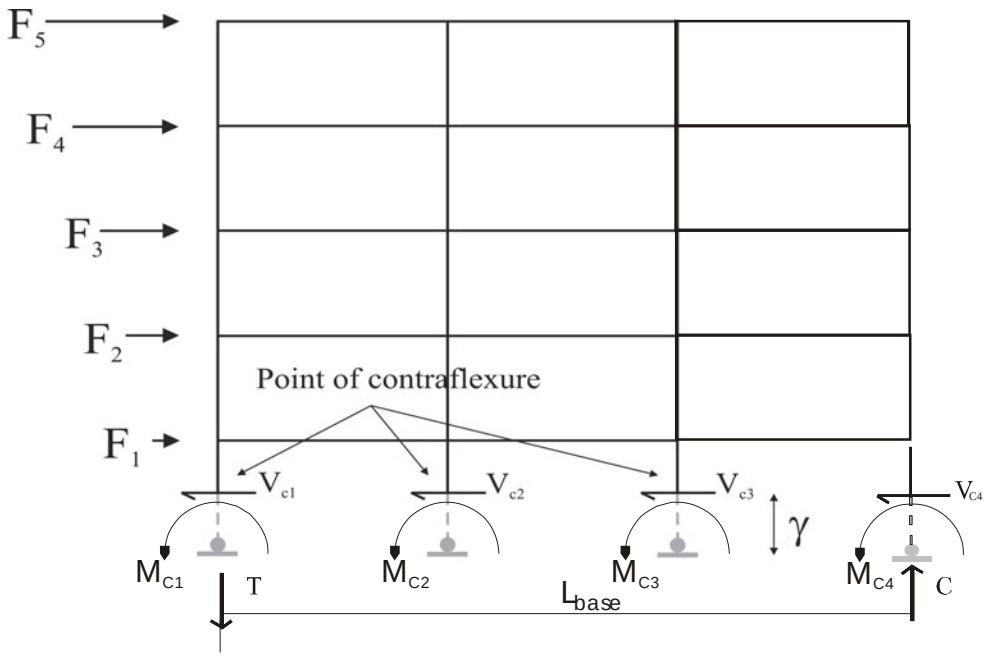

Figure A.6. FDB of building mechanism.

A common choice will be to choose base moments such that the point of contra-flexure in the lower story columns occurs between 55% and 65% of the storey height above the base, thus ensuring capacity protection against hinging at the top of the ground floor columns, and an advantageous distribution of moments above and below the first level beams.

With a point of contra-flexure chosen at 65% of the column height (to be centreline), and with reference in Figure A.6, equilibrium requires that

$$\sum_{j=1}^{m} M_{cj} = M_1 + M_2 + M_3 + M_4 = V_B(0.65h_1) = 503.1kNm \tag{A.18}$$

Considering equilibrium at the foundation level in the Figure A.6, the lateral seismic forces induce column-base moments, and axial load forces in the columns. The total overturning moment (OTM) induce by the lateral forces of the building with n number of storeys is

$$OTM = \sum_{i=1}^{n} F_i h_i \tag{A.19}$$

For a regular building as proposed [A.5], the seismic axial forces will be induced in the exterior columns by the seismic beam shears (V_{bi}) while for the interior columns there is no seismic axial force contribution due to the beam shear at opposite sides of the interior columns will cancel out. Therefore, the OTM induced by the external forces must be equilibrated by the internal forces

$$OTM = \sum_{j=1}^{m} M_{cj} + TL_{base} \tag{A.20}$$

Where $\sum_{j=1}^{m} M_{cj}$ are the column base moments, T the seismic axial force in the exterior column and L_{base} is the distance between the exterior columns. As proposed [A.6], for equilibrium, the sum of the beam shear forces (V_{bi}) along the height of the building is the total seismic axial force. Therefore,

$$T = \sum_{i=1}^{n} V_{bi} \tag{A.21}$$

The beam shear V_b can be evaluated replacing the equations (A.19) and (A.20) with (A.21), therefore,

$$\sum_{i=1}^{n} V_{bi} = \frac{\sum_{i=1}^{n} F_i h_i - \sum_{j=1}^{m} M_{cj}}{L_{base}} \tag{A.22}$$

It is proposed [A.6] to allocate the total beam shear from equation (A.22) to the beam in proportion to the storey shears in the level below the beam under consideration, therefore,

$$\sum_{i=1}^{n} V_{bi} = T \frac{V_{s,i}}{\sum_{i=1}^{n} V_{s,i}} \tag{A.23}$$

Where $V_{s,i} = \sum_{k=1}^{n} F_k$ is the storey shear force and T the seismic axial force. The beam design moments at the column centrelines can be calculated as

$$M_{bi} = V_{bi} l_b / 2 \tag{A.24}$$

Where l_b is the beam span between column centrelines. Table A.3 showed the results obtained using the previous equations.

Table A.3 Distribution of the base shear along the height of the frame.

Storey, i	Height, Hi (m)	miΔi (t m)	Fi (kN)	Vs,i (kN)	OTM (kNm)
5	15	15.97	102.8		
4	12	13.63	65.7	102.8	308.3
3	9	10.86	52.4	168.5	813.7
2	6	7.67	37.0	220.8	1476.2
1	3	4.05	0.0	257.8	2249.5
		48.13	257.8	749.8	

The total shear beam per bay is then $\sum_{i=1}^{n} V_{bi} = 129kN$ and redistribution as proposed (A.23) gives the beam shear at first floor as $V_{b1} = 129(257.8/749.8) = 44.4kN$ and the beam moment M_{b1} = 99.9 kNm.

As mentioned at the beginning of this appendix, objective of this appendix was to design the prototype specimen which will be test in the Structural Laboratory facilities at the University of Canterbury. Therefore the model will be scaled $\beta = 2/3$ such that forces and moments will be scale at $F_{\mathrm{mod}el} = \beta^2 F_{prototype}$ and $M_{b-\mathrm{mod}el} = \beta^3 M_{prototype}$ leading to beam shear force and bending moment of $V_{b-\mathrm{mod}el} = 19.7$ kN and $M_{b-\mathrm{mod}el} = 29.6$ kNm.

A.5 BEAM DESIGN

The beam and columns were designed according to the Concrete Standard NZS3101:2006 [A.4]. The flexural beam reinforcement required can be calculated as

$$A_{s,req} = \frac{M_u}{\phi f_y (d - d')} \tag{A.25}$$

Where M_u = $M_{b-\mathrm{mod}el} = 29.6$, ϕ the strength reduction factor equal to 0.85, f_y the yield strength assumed f_y=300 MPa, d is the distance from the centroid of the tension reinforcement to the extreme concrete compression fibre and assumed as d=300mm, d' the distance from the extreme concrete compression fibre to the centroid of the top reinforcement equal to d'=30mm (assumed cover thickness was taken as approximately 20mm). Then $A_{s,req} = \frac{M_u}{\phi f_y (d - d')} = 435mm^2$ and the beam was provided with 4-D12 with $A_{s\ prov} = 452mm^2$ and $A_{s,prvd} > A_{s,req}$ which also guarantee $A_{s\,\min} \le A_{s\ prov} \le A_{s\,\max}$.

The Beam shear design was check to anti-buckling and confinement condition assuming a spacing of the stirrups of 70mm. The maximum shear forces that can be generated in a beam resulting from simultaneous development of the plastic hinges at `overstrength is $V^* = M_o / l_n$ where l_n is the distance between critical sections that first yield as part of the plastic hinge zone action which is $l_b - h_c/2$ and M_o is the overstrength flexural capacity of the beam that is

calculated as $M_o = (\lambda_o / \phi) M^*_{prov}$ where ϕ is the strength reduction factor assumed 0.85. Therefore, $V^* = \dfrac{50.82}{1.375} = 36.96kN$.

Beam Shear Stresses were also checked and a shear reinforcement was calculated as $A_{v\,req} = (v_n - v_c) b_w s / f_{yt} = 28.6mm^2$ where $v_n = V^* / (\phi b_w d) = 0.49$ but less than the maximum permissible total shear stress. The shear steel provided was $A_{v\,prov} = 2\ legs\ R6@70 = 56.5mm^2$.

Minimum shear reinforcement was required outside of the plastic hinge region. The minimum shear reinforcement required in the beam is calculated from $A_{v\,\min} = 0.35 b_w S_{\max} / f_{yt} = 42mm^2$ where the maximum spacing of reinforcement $s_{\max} = 0.5d = 144mm$ and it was provided $A_{v,prvd} = 2\ \ legs\ \ R6@150 = 56.52mm^2$.

A.6 COLUMN DESIGN

Since flexural over-strengths of the beam M_o=50.82 and is the yielding moment of the beam, column design moment, M^*_{col} can be taken as 25 kNm. Hence, the column design shear force, V^*_{col}, equals to 25kN the M^*_{col} divided by $l_c / 2$, where l_c is the column height equal to 1m.

The longitudinal reinforcement for the column section has been determined using the Column Design Charts. The column axial load and bending moments are for the load case required to be converted to the column design chart axis units. The strength reduction factor for this load case involving overstrength actions is $\phi = 1.0$.

From the design chart, by interpolation, it is found that column requires ρ_t=0.004 which is less than the minimum reinforcement of $\rho_{t\,\min}$=0.008. Providing 12-D12 longitudinal bars in the column section gives $A_{s\,prov} = 1356mm^2 > A_{s\,\min} = 500mm^2$ and the maximum permissible spacing of longitudinal reinforcement is adequate with in the section.

The column axial compression capacity was checked. Where for columns and piers the maximum design axial load under earthquake loading combinations in

compression, $N^* < 0.7\phi N_o$, where $N_o = \alpha_1 f_c^{'}(A_g - A_{st}) + f_y A_{st'}$, and $\alpha_1 = .85$, A_g is the gross column section, A_{st} the steel reinforcement provided. Therefore, $N^* = T = 129kN < \phi N_o = 1214.6kN$.

Confinement reinforcement was provided to the column using rectangular hoops of $d_{tie} = 6mm$. In the end region of columns protected against hinging by the capacity design approach, transverse reinforcement is 70% of

$$A_{sh} = ((1.3 - \rho_t m)s_h h'' / 3.3)(A_g / A_c)(f_c^{'} / f_{yt})(N^* / (\phi f_c^{'} A_g) - 0.006 s_h h''.$$

where $\rho_t m = (A_{st} f_y)/(bh_c 0.85 f_c^{'}) = 0.31$, s_h is the maximum spacing of the stirrups and provided with $s_{h\ prov} = 60mm$, $h^{"}$ the distance between confined concrete is located witin stirrups equal to $h^{"} = 214mm$, A_g the gross area of the column, A_c the confined concrete area equal to $A_c = 45796mm^2$, $f_c^{'}$ and f_y the concrete and steel yield strengths. Therefore, $A_{sh} = -49.22mm^2$ and $A_{sh,prvd} = 2\ legs\ R6@60 = 226mm^2$.

The Column shear design was checked for the anti-buckling and confinement condition assuming a spacing of the stirrups of 60mm. The Potential plastic hinge regions in columns and piers shall be considered to be the end regions adjacent to moment resisting connections over a length from face of the connection as follows:

Where $N^* \le 0.25\phi f_c^{'} A_g$, the greater of the longer member cross section dimension in the case of a rectangular cross section or the diameter in the case of a circular cross section, or where the moment exceeds 0.8 of the maximum moment, taking into account dynamic magnification and overstrength actions, at that end of the member. Therefore, $0.25\phi f_c^{'} A_g = 391kN$ where $\phi = 1.0$ and $N^* = 100kN < 391kN$.

Therefore the potential plastic hinge length can be taken as where the moment exceeds 70% of the maximum moment, taking into account dynamic actions and overstrength actions at that end of the member $M_{col}^* = \phi_o \omega M_E$ where $\phi = 1.0$, w the dynamic magnification factor is between 1.3 and 1.8, then Therefore, $M_{col}^* = 45kNm$.

Shear Reinforcement was provided to the column. The concrete shear contribution in the potential plastic hinge regions of the column must be taken as zero unless the minimum axial compressive stress is greater than 0.1 $f_c^{'}$. Since $N^* / \phi A_g = 1.6 < 0.1 f_c' = 2.5$, then $v_c = 0$.

The nominal shear stress on the column section is $v_n = V_{col}^* / (\phi b_c 0.8 h_c)$ =0.5 MPa, then the area of shear reinforcement required can be calculated as $A_{v\,req} = v_n b_w s / f_{yt} = 25 mm^2$ where $s = 60mm$,. the $A_{v,prvd} = 2\ legs\ R6@60 = 226 mm^2$ in the plastic hinge region.

A.7 EXTERIOR JOINT DESIGN

The horizontal joint shear force is calculated using the equation below with the greatest area of beam reinforcement $V_{jh} = 1.25 f_y A_{st} - V_{col}^*$. The column shear based on the beam overstrength moments at column centerline is $V_{col}^* = 2M_o (l_b / l_{bn}) / (2l_c)$, where l_b is the span length of the beam, l_{bn} is the clear span length of the beam and l_c the column height. Then $V_{col}^* = 23.9kN$ and the horizontal shear force is $V_{jh} = 169.6kN$.

The nominal horizontal shear stress is calculated as $v_{jh} = V_{jh} / b_j h_c = 2.71 MPa < 0.2 f'_c = 5MPa$. The horizontal joint reinforcement required for exterior joints to resist the applied horizontal joint shear force is calculated from $A_{jh} = \frac{6v_{jh}}{f_c'} \beta \left(0.7 - \frac{C_j N^*}{f_c' A_g} \right) \frac{f_y}{f_{yt}} A_s^*$ where $\beta = A_{beam,comp} / A_{beam,tens} = 1$, $6v_{jh} / f_c^{'} = 0.65$ and $C_j = 1$ (one-way joint). Therefore, $A_{jh} = 186 mm^2$ and it will be require to provide 3 legs of R6@60.

A.8 REFERENCES

A.1 Paulay, T. and M.J.N. Priestley 1992. Seismic Design of Reinforced Concrete and Masonry Buildings. John Wiley, New York. 744pp

A.2 RedBook, 1998. Examples of Concrete Structural Design to NZS3101:1995-RedBook, Cement and Concrete Association of New Zealand.

A.3 NZS1170.1. 2002. Structrual Design Actions, Part 1: Permanent, Imposed and other actions, Standards New Zealand.

A.4 NZS3101. 2006. Concrete Structures Standard, Part 1: The design of concrete structures, Standards New Zealand.

A.5 Priestley, M.J.N. "Direct Displacement-Based Design of Precast/Prestressed Concrete Buildings". PCI Journal. Vol. 47 No. 6, Nov-Dec 2002, pp. 66-78

A.6 Priestley, M.J.N. Calvi, G.M. and Kowalsky, M.J. 2007. Direct Displacement-Based Seismic Design of Structures. May 2007. IUSS Press. Pavia, Italy

A.7 NZS1170.5. 2004. Structrual Design Actions, Part 5: Earthquake Actions-New Zealand, Standards New Zealand.